

# V.G Modeling Advanced Electrode Materials

## V.G.1 Electrode Materials Design and Failure Prediction (LBNL)

### Objectives

- Develop continuum models for candidate battery chemistries.
- Perform controlled experiments to obtain model parameters when needed.
- Model reaction distribution in battery electrodes.

### Technical Barriers

- Low energy efficiency; low calendar/cycle life; high cost.

### Technical Targets

- Available energy: 56 Wh/kg (10 mile) and 96 Wh/kg (40 mile).
- $10^{-5}$  discharge power: 750 W/kg (10 mile) and 316 W/kg (40 mile).

### Accomplishments

- Developed a lithium-sulfur (Li-S) cell model incorporating concentrated solution framework.
- Developed a custom Li-S electrochemical cell incorporating a single-ion conductor (SIC) separating a negative electrode chamber from a small (approx. 60  $\mu$ L) catholyte layer. Subsequently performed rate experiments using this custom cell.
- Constructed electrochemical simulation using microstructural spatial domain based on X-ray microtomography reconstruction of a  $\text{LiNi}_{1/3}\text{Co}_{1/3}\text{Mn}_{1/3}\text{O}_2$  (NMC) electrode and compared results with those from a corresponding macroscale model developed previously in our group.

### Introduction

High energy density and long cycle life are critical for reducing the cost of rechargeable batteries and, in turn, electric vehicles. Thick porous electrodes result in large energy densities, and mathematical modeling is useful for understanding electrode processes and optimizing design parameters in such systems. The primary goal of this project is to develop mathematical models for candidate battery chemistries.

The layered NMC cathode material has been selected as the baseline lithium-ion battery system for studying the rate performance associated with the transport limitations in the solid and electrolyte phases. A macroscale model based on this material was previously developed by the Srinivasan group, and these electrodes are now being used as a basis for microscale simulations.

The Li-S system is not well-understood, but could potentially lead to a new generation of low-cost batteries with very high energy densities. This research group has recently begun exploring this next-generation system through complementary modeling and experimental work.

### Approach

The Srinivasan group uses continuum-level mathematical modeling along with controlled experiments on model cells in order to understand the performance and failure modes associated with next-generation battery materials and to design battery materials and electrodes to alleviate these challenges.

#### Project Details

**Venkat Srinivasan (Lawrence Berkeley National Laboratory - PI)**  
Energy Storage and Distributed Resources Division  
1 Cyclotron Road, MS 70R0108B  
Berkeley, CA 94720  
Phone: 510-495-2679; Fax: 510-486-4260  
E-mail: [vsrinivasan@lbl.gov](mailto:vsrinivasan@lbl.gov)

Start Date: October 2012

Projected End Date: September 2016

## Results

### Li-S Cell Experimental Study and Modeling

Figure V- 174 shows Li-S discharge curves at different C-rates (based on a capacity of 1680 mAh/g), from first cycles of coin cells. The discharge profiles are characteristic of Li-S batteries with solid sulfur as the starting material, showing two plateau regions (around 2.4V and 2.1V). The higher plateau region (2.4V) is indicative of sulfur dissolution and the initial reduction process, as solid sulfur is converted to soluble long-chain polysulfide (PS) species (e.g.  $\text{Li}_2\text{S}_8$ ,  $\text{Li}_2\text{S}_6$ ). The subsequent decline in voltage is attributed to the conversion of long-chain to short-chain PS (e.g.  $\text{Li}_2\text{S}_4$ ). The lower plateau region (2.1V) represents reduction of short-chain PS species to final solid discharge product (e.g.  $\text{Li}_2\text{S}$ ).

The discharge profiles show a monotonically decreasing trend in capacity for increasing C-rate. Comparison of the different discharge curves suggests that the differences in the capacity stem from the lower plateau rather than higher one; the latter shows little variation in capacity for differing C-rates, similarly to previous studies. This suggests that the limiting process during discharge is the reduction of short-chain PS to final solid product. It is likely that the film of solid product on the reaction surface has a strong effect on the discharge process.

To identify the limiting process during discharge, the discharge behavior was investigated in a custom cell design with PS solutions of different initial  $\text{Li}_2\text{S}_8$  concentrations. Cells used different reaction substrates: either carbon paper, chosen for its high surface area, or glassy carbon, representing the low-surface area limiting case. To highlight the effects of film growth, an identical low applied current density ( $\text{A}/\text{cm}^2$ ) was used for all cells.

The discharge capacity obtained with carbon paper as a cathode is close to the full theoretical capacity (1,470 mAh/g for solutions of  $\text{Li}_2\text{S}_8$ ) for low concentrations. For example, specific capacities of up to 1,300 mAh/g were obtained for a nominal concentration of 0.05M S (Figure V- 175). A small decline in specific capacity as function of S concentration was observed for the carbon paper system. However, higher total capacity, calculated as the product of the specific capacity and loading mass of sulfur, was obtained for high concentration PS solutions. This indicated that the surface film at the end of discharge should be thicker for higher concentration at the same reaction surface. The decrease of specific capacity may be attributed to the more severe transport limitation in the thicker film at the higher concentrations, which prevents the full utilization of PS. The increase in total capacity with solution concentration suggests that the termination of discharge is not a purely resistive phenomenon resulting from the surface film—if it were, the maximum capacity would be determined by a critical film thickness. Before the film thickness reaches the critical film thickness, both the total and specific capacity would increase with the loading of active material. Beyond the critical thickness, the total capacity would be constant and independent of the loading of active material, while specific capacity would decrease with the loading of active material. However, this conflicts with experimental observations in this work. For example, the specific capacity decreases but total capacity increases as concentration increases from 0.1M to 0.3 M.

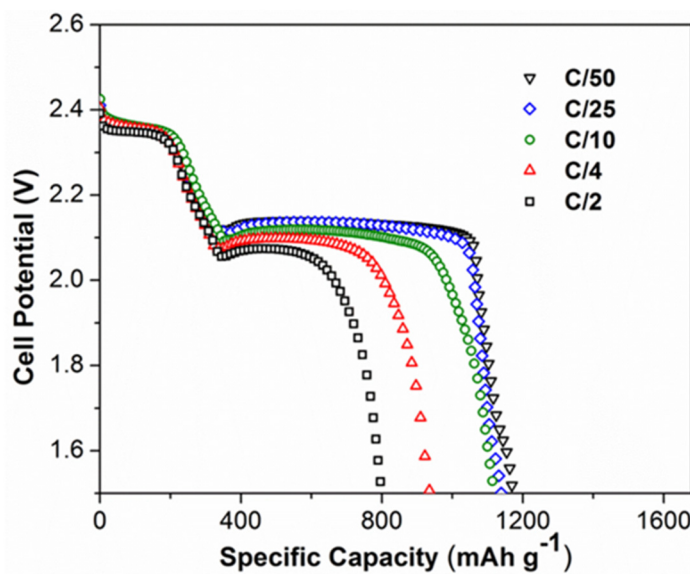


Figure V- 174: Rate performance in first discharge of Li/S batteries

Another possibility is that the decrease of specific capacity may be caused by a side reaction between PS and Li. If the hypothetical side reaction were more serious in a higher concentration solution, the specific capacity would decrease, while the total capacity would increase for higher concentrations, even though the film thickness remains below the critical film thickness. However, the capacity obtained using the flat, non-porous glassy carbon was much lower than with porous carbon. Side reactions cannot explain the difference in capacity, since the discharge time is shorter for glassy carbon than that for carbon paper at each concentration, and therefore the amount of side reaction for glassy carbon is no larger than that for carbon paper. The difference in capacity between glassy carbon and carbon paper can only be attributed to the difference in reaction area and film thickness. The surface area of glassy carbon is much lower than that of carbon paper, resulting in a thicker film on glassy carbon for same amount of current passed. This demonstrates that the capacity limitation is related to the film thickness.

For glassy carbon electrodes, the specific capacities obtained for different solution concentrations were quite close, such as 450 mAh/g and 400 mAh/g for 0.05M and 0.2M S solutions, respectively (Figure V- 175). However, the total capacities increase with solution concentration, as with carbon paper. The film thickness was examined by FIB-SEM and found to increase with concentration. This indicates that the film is not a purely resistive layer. If it were, the film thickness at the end of discharge would be independent of concentration.

The concentration-dependent total capacity and film thickness has been explained by a transport limitation in the formed film that is responsible for premature end of discharge. Furthermore, since only concentration was varied, it is reasonable to believe that ionic PS transport, and not electron transport, is limiting. Electrons should penetrate no farther than a few nanometers into the film near the carbon surface, regardless of solution concentration, so electron transport should be identical for all cases. However, when the bulk concentration outside of the film is higher, concentration gradients and driving forces for transport will be larger, which should permit films to grow thicker before transport through the films cannot sustain desired reaction rates. Furthermore, while the PS concentration might affect film morphology—for instance, by increasing the rate of a hypothetical reaction with freshly formed film, resulting in larger film porosity and facilitating species transport—such a process would affect the morphology and transport process in the outer porous layer, not within the inner porous layer.

A mathematical model based on the proposed film growth mechanism was developed to better characterize cell discharge behavior. As a very thin and porous electrode was used in the experiments, the transport process through the electrode is ignored and a constant reaction distribution in the porous electrode is assumed, leaving the model to focus on film growth and the associated transport process. For simplicity, the film porosity is assumed to be a constant, and ionic diffusion through the film is assumed to follow Fick's law. The modeling results at different C-rates were compared with experimental data, as shown in Figure V- 176. The model results showed good agreement with experimental data, lending support to the proposed mechanism.

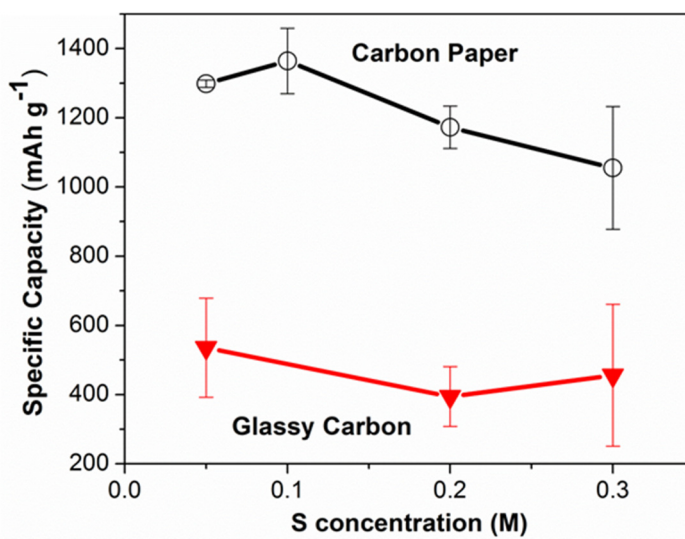


Figure V- 175: Specific capacity as a function of concentration for carbon paper and glassy carbon

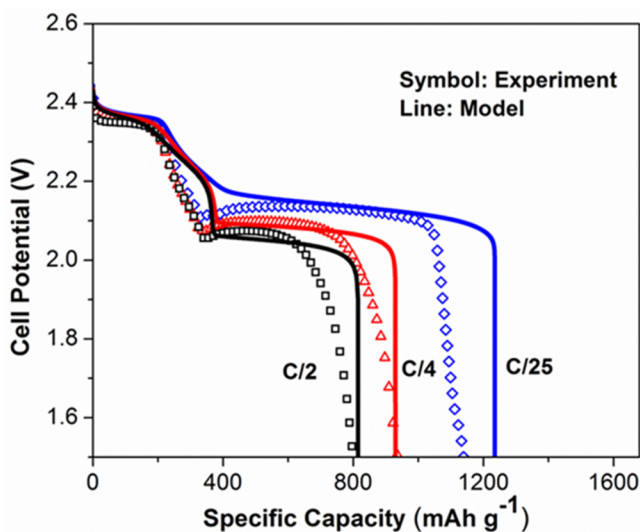


Figure V- 176: Model vs. experimental data at different C-rates (C/2, C/4 and C/25)

the updated model predicts a stronger tendency for Li<sub>2</sub>S to deposit near the separator. The latter result is qualitatively consistent with previous experimental studies at high discharge rates. This suggests that the updated model is a better predictor of cell performance.

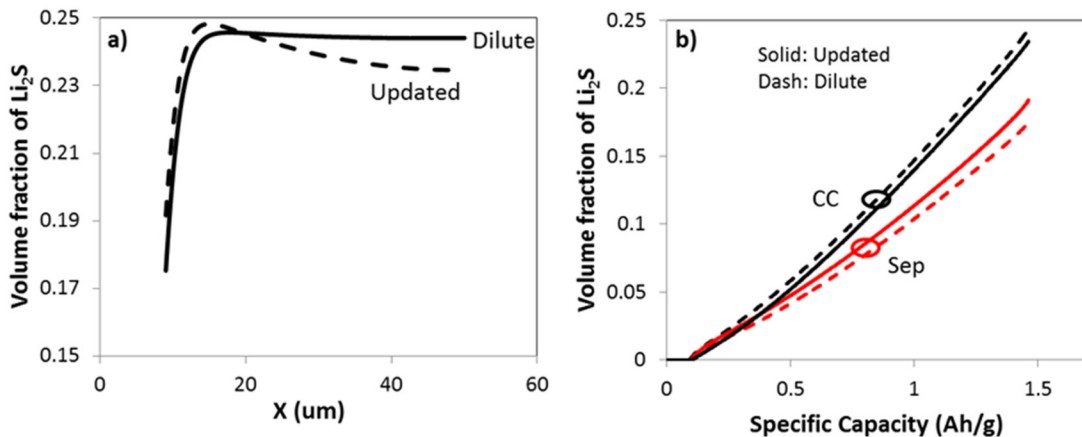


Figure V- 177: Updated model (Updated) and Dilute model (Dilute) predictions of Li<sub>2</sub>S deposition at 3.5 C discharge current throughout cathode at the end of discharge

#### Custom Li-S cell with Small Catholyte Layer

A novel electrochemical cell was designed to incorporate and protect a fragile SIC separating the two sides of the cell while maintaining a small (less than 200 microns thick) catholyte layer and eliminating chemically-incompatible materials. In the present design, the catholyte layer is guaranteed to be thinner (and likely significantly thinner) than 140 μm.

Rate experiments were performed with the fully-assembled cell, including the SIC, using a lithium metal anode, a cathode consisting of elemental sulfur, poly(3,4-ethylenedioxythiophene) (PEDOT), and conductive additive on an aluminum foil current collector, and about 60 microliters of electrolyte solution consisting of 1M bis(trifluoromethane) sulfonimide lithium (LiTFSI) in 1:1 dioxolane (DOL) / dimethoxyethane (DME). It was found that charging at a rate of C/10 or lower reliably produced the two characteristic plateaus during subsequent discharge. Discharging at C/3 yielded a capacity of about 80% (based on capacity determined from a C/12 discharge). The cell was not able to sustain significantly higher currents. Figure V- 178 shows results from one of the experiments: a discharge and charge at a rate of approximately C/12.

To include the porous electrode effect, a theoretical model based on concentrated solution theory, involving concentration-dependent transport properties, was further developed. While many needed model parameters are not yet available, this comprehensive model will be updated as more parameters are determined through our complementary experimental work. Figure V- 177 compares the solid Li<sub>2</sub>S distribution profile at the end of a relatively fast discharge (3.5C), as computed by two models: an updated model with measured electrolyte conductivity ("Updated") and a model based on dilute solution theory ("Dilute"), demonstrating the importance of incorporating accurate transport properties. The sulfur loading of the simulated cell is 1.36 mg/cm<sup>2</sup>, with a cathode thickness of 41 μm. The dilute model simulation shows almost uniform Li<sub>2</sub>S distribution, while

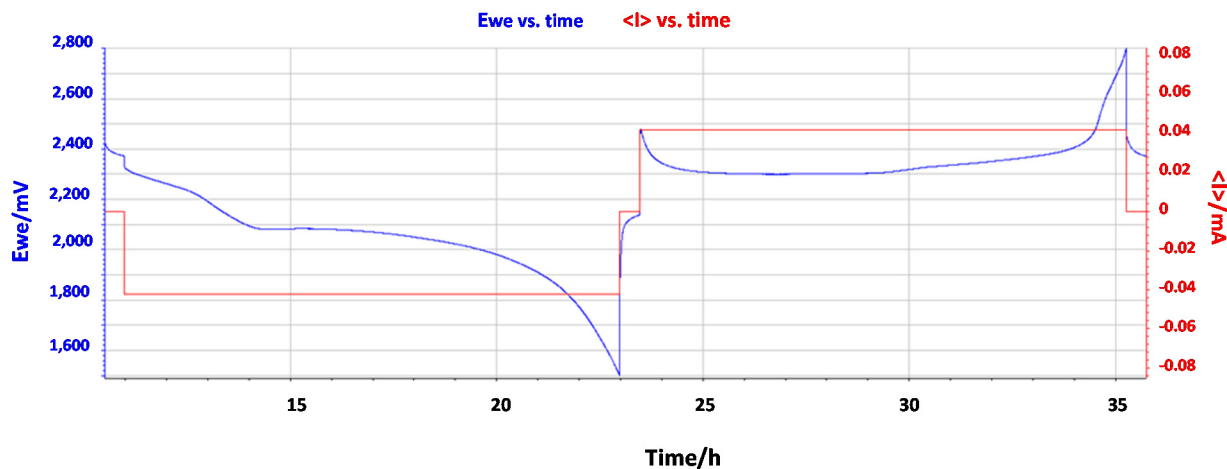


Figure V- 178: C/12 discharge and charge of custom Li-S cell

### Microscale Simulation

A volume reconstruction obtained from our previous X-ray microtomography experiments on NMC electrodes was transformed into surface meshes by first labeling each voxel in the reconstruction as either active material or porous matrix using an intensity threshold selected to match the volume fractions used in our group's earlier work in macroscale simulations of NMC electrodes. The surface meshes generated from the voxel data were imported into the simulation package, repaired as needed, and transformed into simulation domains. These microstructure-derived domains were interfaced with each other and with additional domains with simple shapes representing a positive current collector, a separator, and a lithium negative electrode (Figure V- 179).

A constant-current simulation involving electrochemical reaction, electrical current, and mass transport was constructed and executed. Where applicable, simulation parameters were chosen for consistency with earlier macroscale simulations performed by our research group. The simulated cell potential for a 3C discharge is plotted with experimental and macroscale model results as a function of specific capacity in Figure V- 180. The cell potential from the microscale simulation is seen to be somewhat higher than that observed experimentally and predicted by the macroscale simulation, but the capacity is closer to that obtained experimentally than from the latter. No parameters were adjusted to improve agreement. The discrepancy

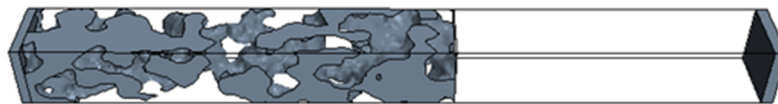


Figure V- 179: Simulation domain showing (from left to right) positive current collector, porous electrode, separator, and lithium negative electrode. For clarity, porous matrix and separator are shown as transparent

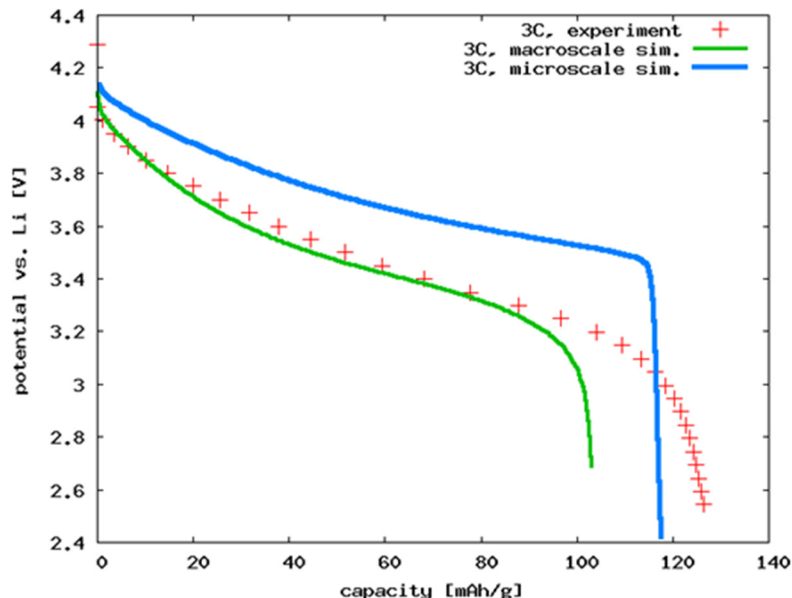


Figure V- 180: Comparison of 3C discharge curves obtained by experiment, macroscale simulation, and microscale simulation

between microscale and macroscale simulation results primarily reflects the difference between solving spatially-averaged equations (involving concepts such as tortuosity) on a geometrically simple domain and solving continuum equations on a spatially detailed domain.

### **Conclusions and Future Directions**

Work in FY 2015 has focused on the development of a macroscale model for Li-S batteries and a microscale model for Li-ion batteries. Combined experimental and modeling efforts have suggested a mechanism for the relationship between PS concentration and film growth. Results from the newly-updated Li-S porous electrode model suggest that the incorporation of concentrated solution theory enables better predictions of cell performance than does the earlier model based on dilute solution theory. A novel Li-S cell that uses a SIC to protect the lithium negative electrode from reaction with polysulfide species, while maintaining a very small (60 microliter) catholyte layer with a SIC, was designed, built, and tested. It was found to deliver 80% of its capacity at a C/3 rate, but was unable to sustain current at significantly higher rates. Spatial domains were constructed from X-ray microtomography of a NMC electrode and used to develop a battery simulation with microscale detail. Results showed reasonable agreement with experimental data. In FY 2016, the Li-S porous electrode model will be developed further through the inclusion of film growth measurements and transport property measurements at a range of concentrations.

### **FY 2015 Publications/Presentations**

1. Higa, K. and V. Srinivasan, "Stress and Strain in Silicon Electrode Models," *Journal of the Electrochemical Society* 162, no. 6 (2015): A1111.

## V.G.2 Predicting and Understanding Novel Electrode Materials from First Principles (LBNL)

### Objectives

- Model and predict the behavior of electrode materials from first-principles.
- Understand the atomistic interactions underlying the behavior and performance of the high-capacity lithium excess and related composite cathode materials.
- Predict new materials using the recently developed Materials Project high-throughput computational capabilities at LBNL.

### Technical Barriers

- Investigating electrode materials with atomistic modeling require rigorous bench marking as well as insight into the materials chemistry and its effect on electrode performance. In the case of the Li-excess materials, it is challenging, as there are an increased number of variables associated with the unknowns regarding possible composite or solid solution structure of the material, the amounts of each phase, synthesis procedure, etc.

### Technical Targets

- Evaluate Li activation barriers in  $\text{Li}_2\text{MnO}_3$  as a function of Li content and Mn migration
- Evaluate the electronic DOS as a function of Li content in  $\text{Li}_2\text{MnO}_3$ .
- Identify stable crystal facets of the layered and spinel phases will be explored, as a function of  $\text{O}_2$  release from surface and oxygen chemical potential.
- Increase the number of predicted battery compounds available on the Materials Project.

### Accomplishments

- The Li migration barriers in pristine, non-defective  $\text{Li}_2\text{MnO}_3$  – both between the TM layer and the Li layer as well as within the Li layer – are found to be comparable to those of  $\text{LiCoO}_2$ .
- Mn migration from the TM layer to the Li layer significantly decreases the Li mobility in  $\text{Li}_2\text{MnO}_3$ .
- These findings indicate that the poor rate capability of  $\text{Li}_2\text{MnO}_3$  is likely due to the surface reconstruction and oxygen loss during the first cycle as well as bulk phase transformation (Mn migration

### Introduction

There is increasing evidence that many of the performance limiting processes present in electrode materials are highly complex reactions occurring on the atomic level. The Persson BMR effort at LBNL is studying these processes using first-principles density-functional theory modeling tools. By understanding the underlying reasons for the electrode materials working performance, improvements or design schemes can be directed at the root cause of the process.

The Li excess cathode materials show great promise for high voltage and high capacity, however, they also present voltage fade, structural degradation and safety concerns. The voltage and capacity fade of the Li excess cathode materials are due to possible 1) dissolution of the transition metal ions and 2) structural transformation reactions as a function of rate and cycling. There are safety concerns relating to oxygen loss and electrolyte breakdown. All these aspects will in turn be addressed in this project and during the first year the main focus was to understand the structural and chemical changes in the layered  $\text{Li}_2\text{MnO}_3$  structure, which is a key material to explain the high capacity in layer-layer or layer-spinel composite electrode materials. Layered

### Project Details

**Kristin Persson**

(Lawrence Berkeley National Laboratory - PI)

Energy Storage and Distributed Resources Division

1 Cyclotron Road

Berkeley, CA 94720

Phone: 510-486-7218

E-mail : [kapersson@lbl.gov](mailto:kapersson@lbl.gov)

Start Date: October 2012

Projected End Date: September 2016

$\text{Li}_2\text{MnO}_3$  has been assumed to be largely electrochemically inactive due to the high oxidation state of Mn (4+ in the discharged state). Additions of  $\text{Li}_2\text{MnO}_3$  to other spinel and/or layered materials have been used to increase the structural stability of the composite materials and allow more Li extraction than for the layered or spinel materials alone. However, many recent experimental works have shown that the  $\text{Li}_2\text{MnO}_3$  component is actually electrochemically active, which demands a re-examination of the conventional belief on the structural and chemical behavior of  $\text{Li}_2\text{MnO}_3$  and the existing explanation of the origin of high capacity in the composite materials.

### Approach

The Persson Group uses atomistic modeling to study the relevant thermodynamic and kinetic processes. The calculations are performed at NERSC and on the Lawrencium cluster at LBNL. To elucidate the atomistic interactions, first-principles zero-temperature calculations are employed and coupled with the cluster expansion technique to examine the structural and chemical space, establish ground states, and resulting electrochemical signature of the materials. To examine temperature-induced properties, statistical mechanics and kinetic Monte Carlo methodologies are utilized.

### Results

We have achieved the following progress:

#### Li Mobility in Pristine $\text{Li}_2\text{MnO}_3$

As illustrated in Figure V- 181, the stable structure of layered  $\text{Li}_2\text{MnO}_3$  has two stable octahedral sites in each layer. The TM-layer has 4g and 2b stable octahedral sites, which contains 2:1 ratio of Mn- and Li-ions respectively, and the Li-layer has 4h and 2c stable octahedral sites. The complete delithiation process is described through our earlier work on the thermodynamic stability of each Li site, indicating the following sequence: i) some Li-ions are extracted from the 4h sites, ii) some Li-ions are extracted from the 2b sites, iii) all Li-ions in the 2c sites are extracted, with some moving into the 4h sites and finally vi) all Li-ions in the 2b and 4h sites are extracted.

To elucidate the kinetic and observed rate limitations in this system, we focused on investigating different delithiation mechanisms in the high Li content regime ( $x > 1.0$ ), in which bulk  $\text{Li}_2\text{MnO}_3$  is predicted to be thermodynamically stable against oxygen loss as well as Mn migration. The single local vacancy, di-vacancy as well as tri-vacancy mechanism as well as Li migration barriers for different Li concentrations were calculated, mapping out the barriers as a function of different local environments. Our calculations indicate that the migrating Li ion experiences significant interactions with its first nearest neighbors, both during the inter-plane (TM to Li-layer) as well as intra-plane (within the Li-layer) diffusion.

For *inter-plane* diffusion, e.g. migration between the TM and the Li layer, we observe that the mobile Li-ions always pass through the tetrahedral site in the Li layer, located directly underneath of the Mn-ion.

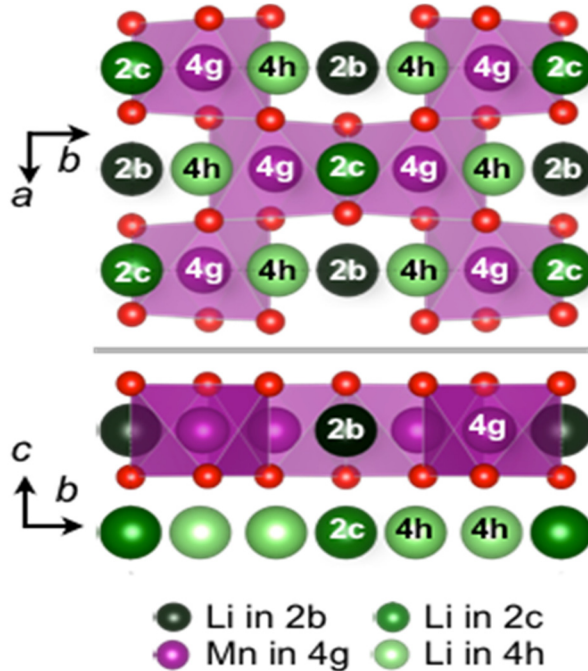


Figure V- 181: Illustration of  $\text{Li}_2\text{MnO}_3$  indicating the 4g, 4h and 2b sites

Figure V- 182 shows Li-ion migration through the single-vacancy intra-layer mechanism. Through this process, 4 out of 6 first neighboring Li-ions are significantly affected, which is evidenced through their displacement from their equilibrium sites during the diffusion process. Through the di-vacancy mechanism, only one nearest neighbor Li is significantly displaced. Hence, the di-vacancy mechanism significantly decreases the migration barrier for between-plane, e.g. inter-layer diffusion, drastically reducing the effective migration barrier from ~600 meV to 150 meV.

Similarly, for *in-plane* (intra Li-layer) diffusion, all possible local configurations were examined, up to tri-vacancy clusters. Here, the single vacancy Li migration barrier was again found to be close to 600 meV, and reduced to 300 meV for the di-vacancy mechanism, which is comparable with in-plane Li diffusion in  $\text{LiCoO}_2$ . Hence, similarly to in-plane diffusion in  $\text{LiCoO}_2$ , we expect the di-vacancy mechanism to become the dominant diffusion mechanism for small deviations from the stoichiometric material.

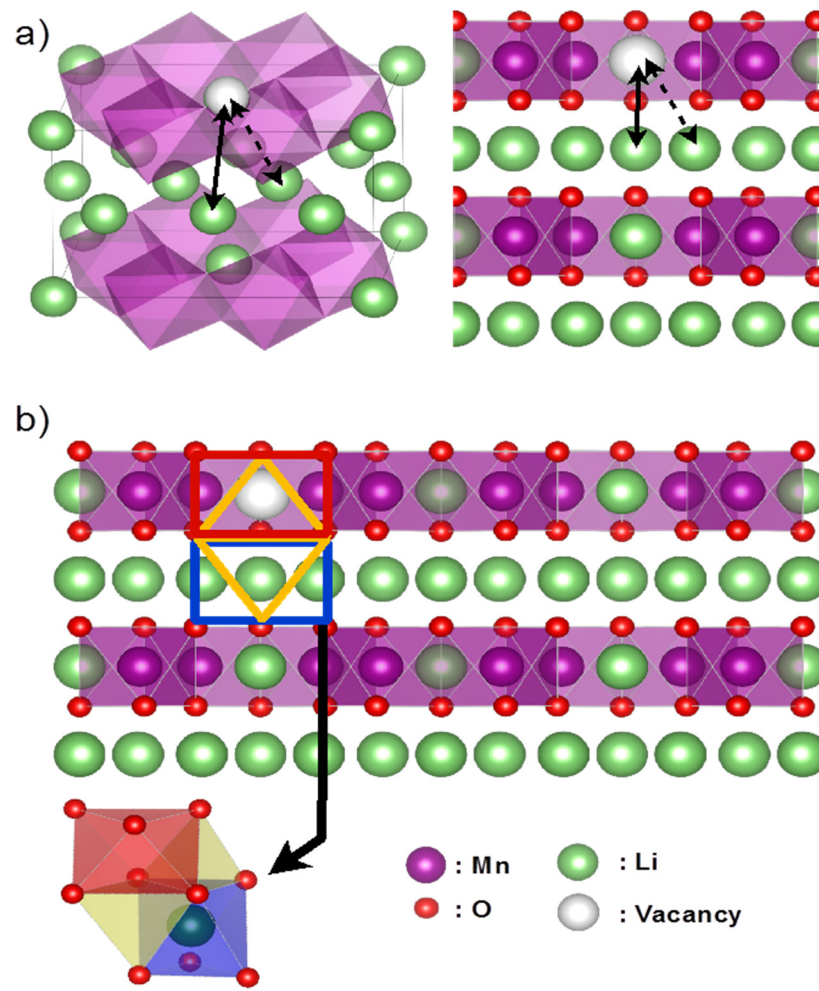
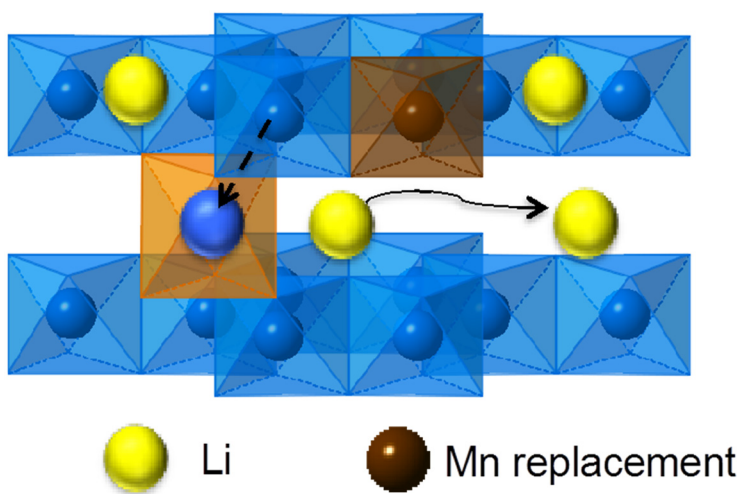


Figure V- 182: Strucure of layered Li-excess material of in the (100) direction and the Li-ion migration process between the transition metal layer and Li-layer

### Li Mobility in Defect, Mn-Migrated $\text{Li}_2\text{MnO}_3$

From our previous work on  $\text{Li}_2\text{MnO}_3$  as well as that of others on layered  $\text{LiMnO}_2$ , we know that Li extraction enhances the instability of the Mn-rich layered structure, and encourages spontaneous Mn migration into the Li layer. Hence, we examine the impact of Li mobility in the Li layer when a few Mn have migrated to the Li layer.



**Figure V- 183:** A schematic of a migrated Mn ion, impacting the Li site preference in the Li layer

in site preference from the octahedral to the tetrahedral Li site in the Li layer. This is consistent with a more stable spinel-like local environment becoming favorable at lower Li concentrations and evidenced by the Mn migration. For *inter-layer* Li migration, the Li migration energy barriers are increased in the presence of a Mn defect for both single- and di-vacancy environments. Hence, we expect Mn migration to cause slow capacity fade as the Li in the TM layer is “locked” or completely depleted following irreversible Mn migration into the Li layer.

### Conclusions and Future Directions

We have found that the inherent Li mobility in pristine  $\text{Li}_2\text{MnO}_3$  is comparable with that of  $\text{LiCoO}_2$  – even considering the Li transfer from the TM layer into the Li layer. Hence, the observed poor rate capability of Li excess materials is likely due to surface and bulk transformations as a function of cycling. The surface has been shown to loose oxygen at high charge (as indicated by our calculations last year), which will result in local surface reconstruction to a more close-packed surface structure. We also previously showed that – at low Li content - the bulk phase becomes increasingly unstable towards Mn migration and defect spinel-like transformation. This is manifested in Li site crossover in the Li layer and severely decreased Li mobility between the TM and the Li layer.

### FY 2015 Publications/Presentations

1. “Predicting and Understanding Novel Electrode Materials from First Principles.”  
ES091\_Persson\_2015\_O, U.S. DOE Vehicle Technologies AMR, 2015.

Figure V- 183 shows a schematic diagram of the Mn defect present in the Li layer while a Li-ion migration process is being undertaken. Here, the highlighted blue atom represents Mn defect in Li-layer, and yellow the Li-ions. Interestingly, we observe that the influence of a single (low-concentration) Mn defect on *intra-layer* (Li moving in the Li layer) single-vacancy Li migration from one octahedral site to another is small. On the other hand, the single Mn defect significantly affects the Li migration path for the *di-vacancy mechanism*, causing a cross-over

## V.G.3 First Principles Calculations of Existing and Novel Electrode Materials (MIT)

### Objectives

- Identify the structure of layered cathodes that leads to high capacity. Clarify the role of the initial structure as well as structural changes upon first charge and discharge. Give insight into the role of Li-excess and develop methods to predict ion migration in layered cathodes upon cycling and during overcharge. Develop predictive modeling of oxygen charge transfer and oxygen loss. Give insight into the factors that control the capacity and rate of Na-intercalation electrodes, as well as Na-vacancy ordering. Develop very high capacity layered cathodes with high structural stability ( $> 250 \text{ mAh/g}$ ).

### Project Details

**Gerbrand Ceder (Massachusetts Institute of Technology – PI)**

Department of Materials Science and Engineering  
77 Massachusetts Avenue, 13-5056

Cambridge, MA 02141

Phone: 617-253-1581

E-mail: [gceder@mit.edu](mailto:gceder@mit.edu)

Start Date: May 2013

Projected End Date: December 2016

### Technical Barriers

- Low rate capabilities
- High cost
- Poor stability
- Low energy density
- Poor understanding of oxygen charge transfer.

### Technical Targets

- Identifying higher capacity Li-ion cathode materials and novel chemistries for higher energy density storage devices

### Accomplishments

- Developed a predictive method for the accurate prediction of oxygen redox activity
- Designed two new high-capacity cathode materials with the disordered rocksalt structure
- Found experimental evidence for oxygen activity in cation-disordered Li-excess materials
- Established oxygen redox activity quantitatively as a new source of capacity for cathodes and developed guidelines for how to activate it reversibly.
- Resolved the Na-vacancy ordering in seven  $\text{Na}_x\text{MO}_2$  Na-intercalation systems

### Introduction

Layered Li-excess cathode materials can deliver very high capacities from 250 up to 300  $\text{mAh g}^{-1}$ , which has been attributed to the additional charge compensation mechanism activated by Li-excess through either the oxidation of  $\text{O}^{2-}$  to  $\text{O}^-$  or the release of  $\text{O}_2$  followed by cation densification. Recently, the design space for Li-excess materials was broadened to rocksalts with partial or complete cation disorder through the understanding that more than 10% Li-excess creates a percolation network of O-TM channels through which Li can diffuse. This opens the possibility to explore and find more candidate cathode materials with very high energy density.

To investigate oxygen charge transfer in Li-excess materials, we have developed a computational methodology that allows the accurate prediction of the relative oxygen and transition-metal redox levels. In parallel, we have experimentally characterized the oxygen redox activity in a number of newly designed cation-disordered materials with Li excess.

Apart from the work on high-capacity Li-ion battery materials, we investigated the fundamentals of Na intercalation. Using high-throughput computations, we determined stable Na-vacancy orderings and the intercalation voltage profiles for several  $\text{Na}_x\text{MO}_2$  systems.

### Approach

**Innovative Approach:** A combination of first-principles computations and experimental synthesis/characterization are being used to evaluate existing and novel materials. Voltages and intercalation curves are calculated with GGA+U, and if highly accurate results are required hybrid functionals (HSE) are used. Phase diagrams are calculated with the Materials Project infrastructure based on high-throughput computations. Configurational disorder for elevated temperature and off-stoichiometry is modeled with either point defect models (when off-stoichiometry is small) or with the cluster expansion for larger disorder. Ion mobility is evaluated with the Nudged Elastic Band Method or with direct Molecular Dynamics Simulations. Thermal stability is investigated with the approach developed previously under this program. Some of the computational work is performed in collaboration with Persson and with the Materials Project. Work on Li-excess layered materials is done in coordination with Persson (computational) and with the experimental efforts in the BMR Program (e.g. Grey).

### Results

We have achieved the following progress:

#### Development of a New Computational Methodology for the Quantitative Prediction of Oxygen Redox Activity

We have developed an accurate first-principles calculation methodology for the predictive modeling of oxygen redox activity, which has been proposed as a possible source of the excess lithium extraction capacity in lithium-rich TM oxide intercalation materials.

The observed electrochemical capacity in Li-excess materials can often exceed that dictated by their transition metal (TM) redox content unlike in common stoichiometric Li-ion cathode materials such as  $\text{LiCoO}_2$ ,  $\text{LiMn}_2\text{O}_4$ , or  $\text{LiFePO}_4$ . To conclusively isolate the source of “excess” capacity with first-principles calculations, however, improvements in accuracy over traditional density-functional theory (DFT) techniques on the level of the general gradient approximation GGA and GGA+U are required. Specifically, a materials system that undergoes possibly both TM and oxygen redox requires investigation with a reliable computational methodology that can accurately predict the charge transfer between oxygen, lithium, and TM atoms as well as their redox potentials.

Our strategy has been to employ hybrid functionals (HSE06), which produce a more accurate representation of the electronic structure due to adding some amount of Hartree-Fock exchange through a tunable mixing parameter  $\alpha$ , specifically optimized to reproduce experimental band gaps (or when unavailable, results from more computationally expensive but accurate GW calculations). Benchmarking the electronic structure of  $\text{LiCoO}_2$ , the optimal  $\alpha$  is found to be 0.17 (red line in Figure V-184) providing excellent agreement with experiment in contrast to GGA and GGA+U calculations which both underestimate the band gap. The computed voltage profiles for  $\text{Li}_{1-x}\text{CoO}_2$  (Figure V-185) demonstrate that HSE06 with the optimized  $\alpha$  (red line) also most accurately reproduces the experimental voltage curve.

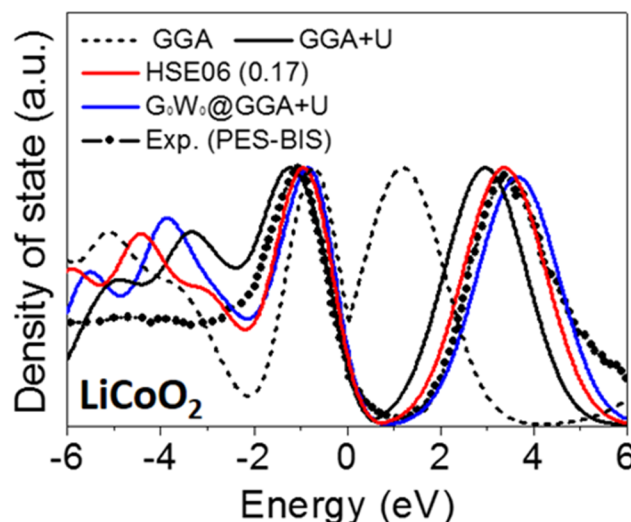


Figure V-184: Density of states (DOS) of  $\text{LiCoO}_2$  as predicted by various electronic structure methods in comparison to experimental spectroscopic measurement

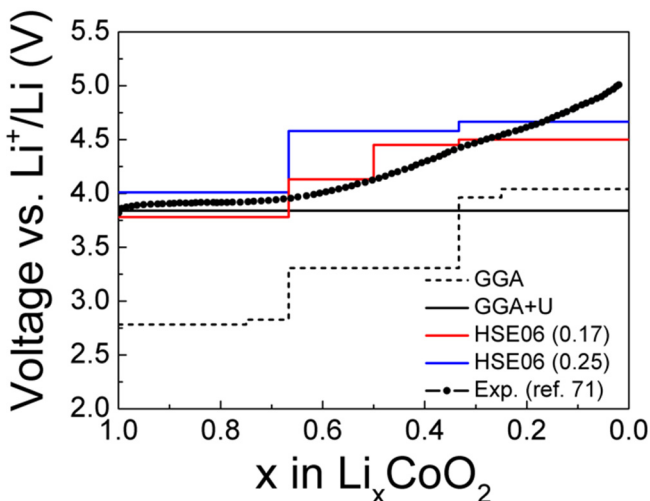


Figure V- 185: Computed voltage profiles of  $\text{Li}_{1-x}\text{CoO}_2$  ( $0 \leq x \leq 1$ ), as predicted by GGA, GGA+U, and HSE with different mixing parameters in comparison to the experimental reference

#### Evidence for Oxygen Redox Activity in $\text{Li}_{1.25}\text{Nb}_{0.25}\text{Mn}_{0.5}\text{O}_2$ —A New High-Capacity Cation-Disordered Material

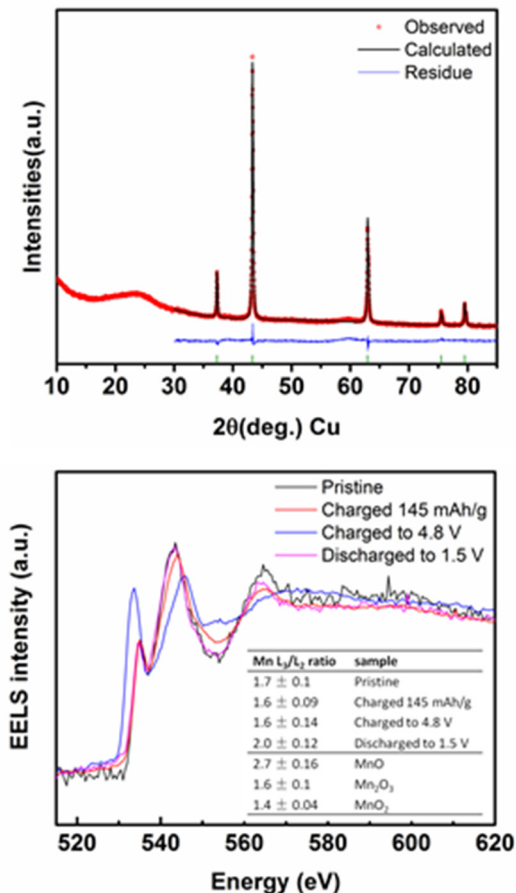


Figure V- 186: XRD shows a pure disordered rocksalt phase; EELS spectra confirm that Mn and O are both redox active

In conclusion, we have successfully benchmarked a new methodology for the accurate prediction of electronic structure properties of TM oxides and lithium TM oxides based on hybrid-functional calculations. These results have been published in Physical Review B.<sup>1</sup> Towards our project objective, our next task will be to apply this methodology to lithium excess TM materials and accurately predict both the TM and oxygen redox potentials so that they can be tuned for optimal performance.

In parallel to the computational method development, our efforts have also been geared towards the design and synthesis of novel ordered and cation-disordered Li-excess materials with high capacity in order to characterize oxygen charge transfer experimentally.

Based on our previous findings that cation-disordered materials can function as cathode material with very high capacities, we designed and prepared a new disordered material,  $\text{Li}_{1.25}\text{Nb}_{0.25}\text{Mn}_{0.5}\text{O}_2$ . As synthesized this material is a pure disordered rocksalt phase. It delivers a large initial discharge capacity of  $287 \text{ mAh g}^{-1}$  and energy density of  $909 \text{ Wh kg}^{-1}$  in the first cycle. (See Figure V- 186.)

Electron energy loss spectroscopy (EELS) results confirm that Mn and O are both redox active. In the first cycle, Mn is oxidized from  $3+$  to  $4+$  upon first charge, and reduced slightly below  $3+$  after the first discharge. In the Oxygen K-edge spectra, an increase of the pre-edge intensity is observed beyond  $145 \text{ mAh g}^{-1}$  Li extraction. This pre-edge is caused by the transition of O 1s electrons to unoccupied 2p orbitals, and therefore indicates the contribution of an oxygen 2p hole, or oxygen oxidation to providing a substantial part of capacity. After the first cycle, the O K-edge largely returns to the pristine state, which suggests a reversible O redox reaction in the first electrochemical cycle. These results clarify that the  $\text{Li}_{1.25}\text{Nb}_{0.25}\text{Mn}_{0.5}\text{O}_2$  material operates reversibly by means of oxygen oxidation and reduction. (See Figure V- 187.)

Together with our previous work on understanding Li transport in Li-excess and disordered materials, we believe that this demonstration of substantial oxygen redox capability is an important new direction to create high capacity cathode materials.

### Oxygen Activity in $\text{Li}_{1.2}\text{Ni}_{1/3}\text{Ti}_{1/3}\text{Mo}_{2/15}\text{O}_2$

In addition to the Nb/Mn-based oxide above, we discovered another cation-disordered high-capacity cathode material with the composition  $\text{Li}_{1.2}\text{Ni}_{1/3}\text{Ti}_{1/3}\text{Mo}_{2/15}\text{O}_2$ . This material also appears to utilize oxygen redox after a certain level of oxygen loss has occurred (Figure V- 188). A more detailed account on the Ni/Ti/Mo-based material will be provided in a future progress report.

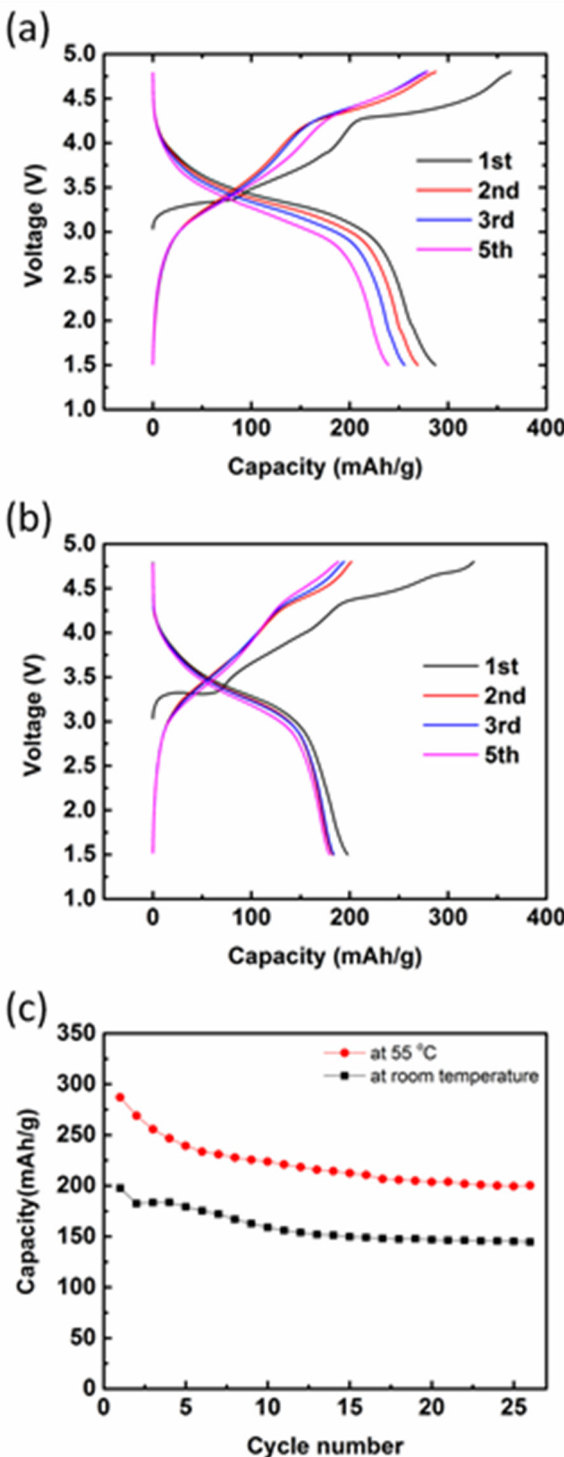


Figure V- 187: Cycling performances of  $\text{Li}_{1.25}\text{Nb}_{0.25}\text{Mn}_{0.5}\text{O}_2$  at 55°C (a) and room temperature (b)

### Na-Vacancy Ordering in Na Intercalation Electrodes

In addition to Li battery materials, one objectives of this project is to explore alternative chemistries, in particular sodium-ion batteries. As an initial step towards understanding and improving electrode materials for Na-ion batteries, we investigated the phase diagram of several Na-intercalation systems. (See Figure V-189.)

Current state of the art Na-ion battery cathodes are selected from the broad chemical space of layered first row transition metal (TM) oxides. Unlike their lithium ion counterparts, seven first row layered TM oxides can intercalate Na ions reversibly, unlike in lithium systems where among the single metal systems only  $\text{LiCoO}_2$  and  $\text{LiNiO}_2$  can exchange lithium reversibly. In contrast to Li-systems, the voltage curves of Na-systems indicate significant and numerous reversible phase transformations during electrochemical cycling. These transformations are not yet fully understood, but arise from Na-ion vacancy ordering and metal oxide slab glide and can significantly affect rate capability.

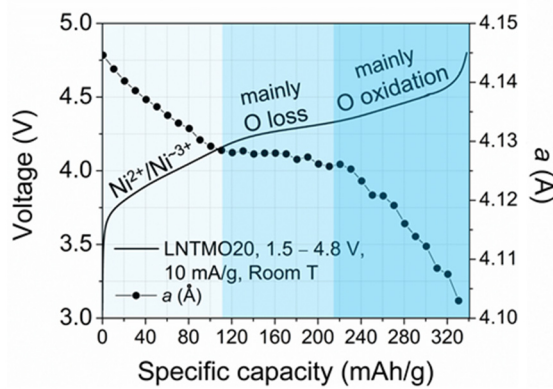


Figure V- 188: First charge profile of  $\text{Li}_{1.2}\text{Ni}_{1/3}\text{Ti}_{1/3}\text{Mo}_{2/15}\text{O}_2$ . The redox processes for different charge states are indicated in the figure

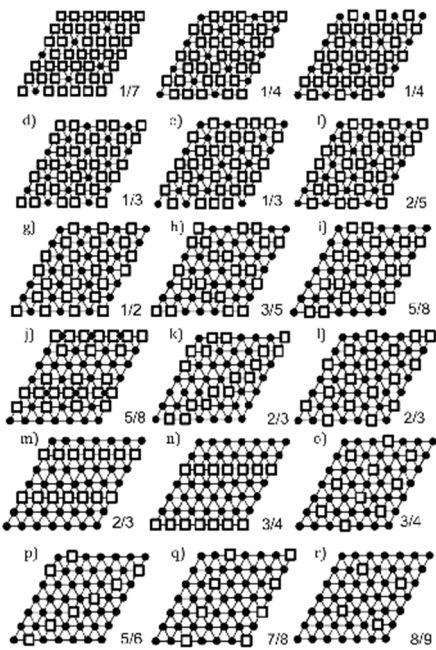


Figure V- 189: Na-vacancy orderings occurring in the  $\text{Na}_x\text{MO}_2$  systems with seven different choices of M

Hence, in this study, we investigated the nature of Na-vacancy ordering transformations within the  $\text{O}_3$  lattice framework. We generate predicted electrochemical voltage curves for each of the Na-ion intercalating layered single TM oxides using a high-throughput framework of density functional theory (DFT) calculations. We determine a set of vacancy ordered phases appearing as ground states in all  $\text{Na}_x\text{MO}_2$  systems, and investigate the effect of ordering interactions between adjacent layers. We calculated a total of approximately 500 possible Na-vacancy orderings for each transition metal system.

From these, any ordering occurring as a ground state in any of the systems was collected and grouped into a collection of 18 low-energy ordering types.

We are currently investigating how some of the phase transformations in the materials can be prevented so that very high rate systems can be developed.

#### FY 2015 Publications/Presentations

1. Seo, D.-H., A. Urban and G. Ceder, "Calibrating transition metal energy levels and oxygen bands in first principles calculations: accurate prediction of redox potentials and charge transfer in lithium transition metal oxides," *Phys. Rev. B* 92 (2015): 115118.
2. Kim, J.C., D-H Seo, G. Ceder, "Theoretical Capacity Achieved in a  $\text{LiMn}_{0.5}\text{Fe}_{0.4}\text{Mg}_{0.1}\text{BO}_3$  Cathode by Using Topological Disorder", *Energy Environ. Sci.* 8 (2015): 1790-1798.
3. Kim, J.C., X. Li, B. Kang, G. Ceder, "High-Rate Performance of a Mixed Olivine Cathode with Off-Stoichiometric Composition", *Chem. Commun.* 51 (2015): 13279-13282.
4. Castelli, I.E., F. Hüser, M. Pandey, H. Li, K.S. Thygesen, B. Seger, A. Jain, K. Persson, G. Ceder, K.W. Jacobsen, "New Light-Harvesting Materials Using Accurate and Efficient Bandgap Calculations", *Adv. Energy Mater.* 5 (2015): 1400915.
5. Kim, J.C., D-H Seo, H. Chen, G. Ceder, "The Effect of Antisite Disorder and Particle Size on Li Intercalation Kinetics in Monoclinic  $\text{LiMnBO}_3$ ", *Adv. Energy Mater.* 5 (2015): 1401916.
6. Jain, A., G. Hautier, S.P. Ong, S. Dacek, G. Ceder, "Relating Voltage and Thermal Safety in Li-ion Battery Cathodes: A High-Throughput Computational Study", *Phys. Chem. Chem. Phys.* 17 (2015): 5942-5953.
7. Sun, W., S. Jayaraman, W. Chen, K. Persson, G. Ceder, "Nucleation of Metastable Aragonite  $\text{CaCO}_3$  in Seawater", *Proc. Natl. Acad. Sci. U.S.A.* 112 (2015): 3199-3204.
8. Liu, M., Z. Rong, R. Malik, P. Canepa, A. Jain, G. Ceder, K.A. Persson, "Spinel Compounds as Multivalent Battery Cathodes: A Systematic Evaluation Based on Ab Initio Calculations", *Energy Environ. Sci.* 8 (2015): 964-974.
9. de Jong, M., W. Chen, T. Angsten, A. Jain, R. Notestine, A. Gamst, M. Sluiter, C.K. Ande, S. van der Zwaag, J.J. Plata, C. Toher, S. Curtarolo, G. Ceder, K. Persson, M. Asta, "Charting the Complete Elastic Properties of Inorganic Crystalline Compounds", *Sci. Data* 2 (2015): 150009.
10. "First Principles Calculations of Existing and Novel Electrode Materials," ES054\_Ceder\_2105\_O, U.S. DOE Vehicle Technologies AMR, 2015.

## V.G.4 First Principles Modeling of SEI Formation on Bare and Surface/Additive Modified Silicon Anode (TAMU)

### Objectives

- Develop fundamental understanding of the molecular processes that lead to the formation of a solid electrolyte interphase (SEI) layer due to electrolyte decomposition on Si anodes.
- Develop a rational selection of additives and/or coatings.

### Technical Barriers

- Description of the electrode surface chemistry; characterization of the electron transfer rate through the SEI layer; description of the SEI layer structure and its evolution as well as that of the electrode during cycling
- Barriers addressed:
- Effects of hydroxylated silica on SEI reactions.
- Characterization of ALD-coated electrodes.
- Characterization of electron transfer beyond tunneling.

### Technical Targets

- Determination of reaction mechanisms as a function of electrolyte composition and voltage.
- Development of a mesoscopic model for SEI nucleation and growth at realistic time/length scales.
- Effects of natural or artificial coating on SEI reactions.

### Accomplishments

- Electron transfer beyond tunneling lengths has been elucidated; role of additives in the nucleation and growth of efficient SEI layers characterized.
- Effects of hydroxyl groups on silicon surfaces have important effects on lithiation but only minor impact on SEI reactions.
- Molecular layer deposition (MLD)-deposited alucone films form a good mechanical barrier while allowing ionic conductivity. However, SEI reactions proceed although the chemical nature of the products is different than that occurring on lithiated silicon or SiO<sub>2</sub>-covered electrodes.
- Aggregation of organic species on LiF or LiO<sub>2</sub> covered electrodes show strong Li..O..Li interactions. The role of the decomposition of the organic products during agglomeration and growth has been assessed.
- A mesoscopic model has been developed to represent nucleation and growth reactions, with input of the first-principles modeling.
- Thermodynamic and chemical stability of SEI films shows clear decomposition of key products. The instantaneous electronic voltage has been monitored.
- The role of solvation on ionic intercalation and SEI reactions has been characterized.

---

### Introduction

Investigation of formation/growth mechanisms of the SEI layer on bare surfaces requires incorporation of effects from surface structure and chemical state: presence of functional groups, surface oxidation, nature of exposed facets, and electrolyte composition including additive species. Finding the correspondence between

#### Project Details

**Perla B. Balbuena (Texas A&M University – PI)**  
Department of Chemical Engineering  
3122 TAMU  
College Station, TX, 77843  
Phone: 979-845-3375 Fax: 979-845-6446  
E-mail: [balbuena@tamu.edu](mailto:balbuena@tamu.edu)

**Jorge M. Seminario (Texas A&M University – co-PI)**  
Department of Chemical Engineering  
3122 TAMU  
College Station, TX, 77843  
Phone: 979-845-3301 Fax: 979-845-3301  
E-mail: [seminario@tamu.edu](mailto:seminario@tamu.edu)

Subcontractor:  
Sandia National Laboratory  
1515 Eubank SE  
Albuquerque, NM 87123

Start Date: October 2012  
Projected End Date: September 2016

additive molecular properties and SEI formation mechanism, structure, and properties in additive-induced SEI layers will allow identification of new/improved additives. Including the state of lithiation of the surface is also a key factor to determine possible changes in the electrolyte reduction mechanism and/or nature of the products. Finally, it is crucial to understand how the electron transfer from the electrode to the electrolyte is modified by deposition of the initial SEI intermediates or products of the SEI formation reaction.

## Approach

**Innovative Approach:** A comprehensive first-principles computational approach employed in this work includes density functional theory, ab initio molecular dynamics, and ab initio-Green's function theory. Static density functional theory (DFT) is utilized within two approaches: cluster models are used to investigate bond dissociation energies, activation barriers for reduction of individual molecules, and polymerization pathways, whereas periodic surfaces representing both quasi-amorphous low lithiated surfaces and well-characterized crystalline  $\text{Si}_x\text{Li}_y$  alloys are used to follow the dynamics of electrolyte decomposition reactions. The electron transfer mechanisms beyond tunneling lengths are investigated on a multicomponent SEI model anode/X1/X2 formed by two or more blocks (X1, X2) stacked over the anode surface  $\text{Li}_{13}\text{Si}_4$ . These models of periodic surfaces in contact with liquid electrolyte mixtures are utilized to investigate mechanisms of SEI nucleation and growth using ab initio molecular dynamics (AIMD). Electron transport through the composite material (electrode/ SEI layer/electrolyte molecule) is also characterized using ab initio Green's functions calculations. In addition, a multiscale modeling approach is utilized to develop a mesoscopic model able to predict SEI layer nucleation and growth at realistic length/time scales (in collaboration with P. Mukherjee, TAMU). Sandia's collaborator Leung developed ab initio procedures to characterize instantaneous electronic voltage of the half cell including anode in contact with electrolyte; this new method allowed identifying voltage effects on SEI reactions. Sandia's collaborator's Rempe focused on the development of accurate classical force fields for ionic solvation in typical non-aqueous solvents. NREL collaborator Chunmei Ban provided detailed experimental information on MLD-deposited alucone-coated Si electrodes.

## Results

We have achieved the following progress:

### Reactivity on Hydroxylated Silica-Covered Silicon Surfaces

DFT optimizations showed the simultaneous incorporation of two Li atoms through breaking of a Si-O bond. All tested Si-O bonds were thermodynamically favorable with an average formation energy of -0.042 eV per Si atom. After structural optimization the Si-O bond is broken, the Si atom is displaced from its tetrahedral position and both the Si and O atoms become threefold coordinated. At low Li content the Si atoms are displaced from their tetrahedral positions and formation of  $\text{Li}_4\text{SiO}_4$ -like structures is predominant. At high Li content formation of Si-Si bonds is observed. This was confirmed through the structural analysis of the Si-Si interaction for several Li contents. The non-lithiated film has a peak around 3 Å for the Si-Si interaction, which indicates the presence of siloxane bridges. However, at elevated Li contents most of siloxane bridges tend to disappear and a Si-Si interaction at 2.29 Å becomes predominant, which is indicative of possible formation of  $\text{Li}_2\text{O}$ -like structures because of the interaction of Li atoms with free O atoms. The presence of surface hydroxyl groups seems to favor the structural reconstruction implied by the displacement of Si atoms. (See Figure V- 190.)

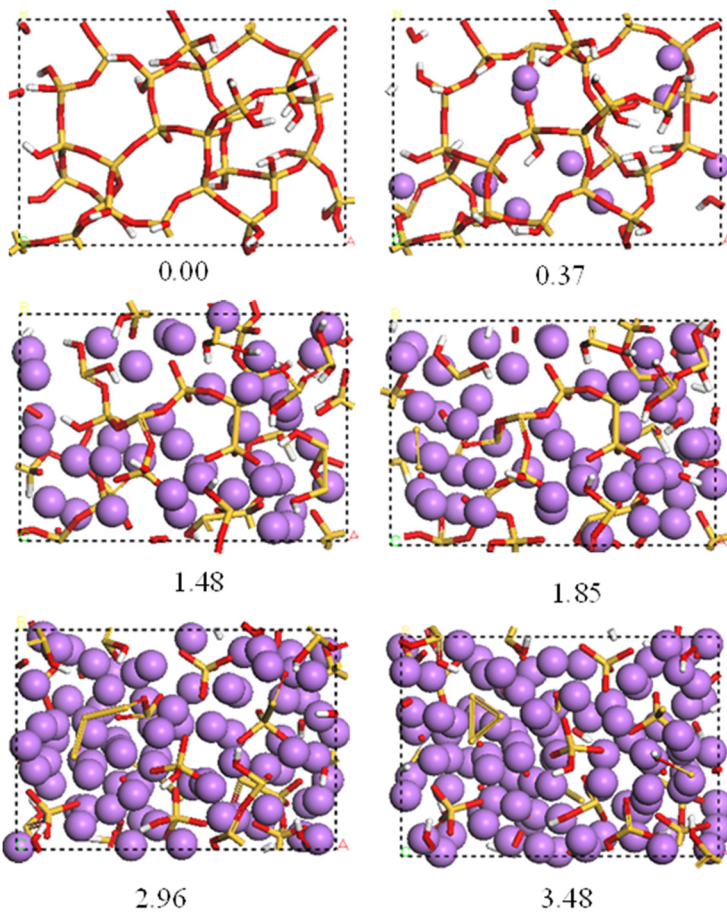
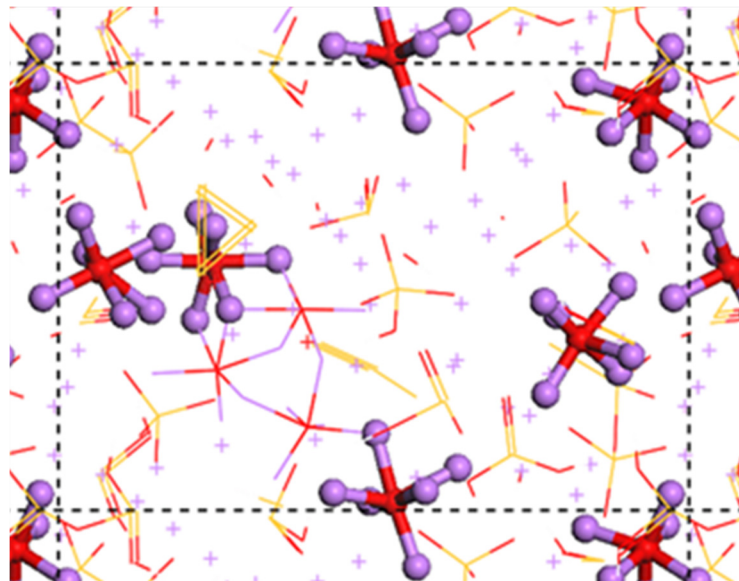


Figure V- 190: Structural evolution as a function of Li/Si content

Figure V- 191: Formation of  $\text{Li}_6\text{O}$  complex at  $\text{Li/Si} = 3.48$ 

Si surfaces. However, the presence of OH groups affect slightly the reaction mechanisms. The results are being compiled in a new manuscript for publication.

The average coordination number of  $\langle \text{Si-Si} \rangle$ ,  $\langle \text{Si-Li} \rangle$ ,  $\langle \text{Si-O} \rangle$ , and  $\langle \text{O-Li} \rangle$  was used to study the bonding mechanism as a function of Li content in Si and O atoms. A quasi linear decrease of the  $\langle \text{Si-O} \rangle$  coordination number from 4 ( $\text{Li/Si} = 0$ ) to 1.78 ( $\text{Li/Si} = 3.48$ ) confirmed the disappearance of the Si-O bonds. The increase in  $\langle \text{Si-Si} \rangle$  linked to the increase in  $\langle \text{O-Li} \rangle$  as the Li content rises indicates that formation of  $\text{Li}_2\text{O}$ -like structures is possibly favored at Li contents near to the saturation point.

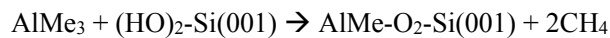
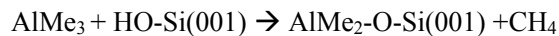
A fraction of O atoms was found to be involved in formation of  $\text{Li}_6\text{O}$  complexes. Detailed view of  $\text{Li}_6\text{O}$  complexes over the surface at the saturation point ( $\text{Li/Si} = 3.48$ ) were observed (See Figure V- 191). As the Li content increases, more O atoms are involved in formation of  $\text{Li}_6\text{O}$  complexes. Stable formation of  $\text{Li}_6\text{O}$  at high Li content in silicon suboxides has been attributed to the presence of surrounding Si atoms.

In summary, hydroxyl groups favor surface lithiation because a structural reconstruction is more favorable when the Si atoms are not fully linked by siloxane bridges. The structural evolution during lithiation shows that Si atoms are displaced from their tetrahedral positions as they are partially reduced, and starting from a  $\text{Li/Si}$  ratio of  $\sim 1.85$ , some Si atoms lose all the Si-O bonds and form Si-Si bonds. The average coordination number is used as an indicator of changes in the bonding mechanism for the Si and the O atoms as a function of Li content. The analysis indicates that breaking of the SiO bonds becomes less favorable at high degrees of lithiation and is accompanied by Si-Si bond formation and nucleation of  $\text{Li}_6\text{O}$  complexes stabilized by Si atoms. SEI reactions on these surfaces were also studied and they show some similarities with those on bare lithiated

## Reactivity on Alucone-Covered Silicon Surfaces

Coating silicon particles with a suitable thin film has appeared as a possible solution to accommodate the swelling of silicon upon lithiation and its posterior cracking and pulverization during cycling of Li-ion batteries. In particular, aluminum alkoxide (alucone) films have been recently deposited over Si anodes and the lithiation and electrochemical behavior of the system have been characterized. However, some questions remain regarding the lithium molecular migration mechanisms through the film and the electronic properties of the alucone film. Here density functional theory, ab initio molecular dynamics simulations, and Green's function theory were used to examine the film formation, lithiation, and reactivity in contact with an electrolyte solution. It is found that the film is comprised of Al-O complexes with 3-O or 4-O coordination. During lithiation, Li atoms bind very strongly to the O atoms in the most energetically favorable sites. After the film is irreversibly saturated with Li atoms, it becomes electronically conductive. The theoretical results are in agreement with those from morphology and electrochemical analyses.

Experimental evidence indicated that the alucone MLD coating removed the native oxide, leading to a covalently bonded and fully nucleated alucone layer (2-5 nm) on Si particles. As the first step of the process, trimethyl-aluminum, a metal precursor for the coating process, reacts with the surface silanol groups of the native oxides. The following corresponding reactions were studied using DFT, where the methyl group is abbreviated as Me:



The calculated reaction energies are -1.86 eV and -3.00 eV respectively, indicative of that both reactions are thermodynamically favorable. This confirms that the alucone coating is covalently bounded to the Si surface, which ensures mechanical integrity in the coated electrode. The adsorbed CH<sub>3</sub>-Al group can react with glycols, such as ethylene glycol and glycerol, followed by the further glycol-TMA reactions, and finally forming amorphous 3D-network structures with chemical composition of -Al<sub>n</sub>(-OCH<sub>2</sub>-CHO-CH<sub>2</sub>O-)<sub>m</sub> (n:m=1). These reaction steps were also found to be exothermic. The overall coating process is accordingly energetically favorable. Further reactions with TMA were carried out to characterize film growth. The DFT calculations showed that the partially oxidized Si(001) surface is distorted in the coating process. The Si atoms bonding with oxygen are typically stretched out of the surface ~0.2 Å. The bond length of new formed Al-O is around 1.7 Å. For the adsorbed Me<sub>2</sub>Al- and MeAl- groups, the bond lengths of Al-C showed no obvious change compared to that in TMA.

The experimentally measured density of the thin film is ~1.6 g cm<sup>-3</sup> – 1.7 g cm<sup>-3</sup> while the film was grown at 140–150°C respectively by our collaborator Ban (NREL). Considering the composition of the film, each single unit of the polymer, -C<sub>3</sub>H<sub>5</sub>O<sub>3</sub>Al<sup>-</sup>, occupies a volume of ~120 Å<sup>3</sup>. Therefore, the 3D-network must be packed very tightly, as the minimum volume of single unit packing is ~103 Å<sup>3</sup>. Based on this information, it was inferred that many crosslinks and branch chains must be formed in the structure, because such connection modes allow utilizing the space maximally. This is in good agreement with experimental results, in which a dense and conformal coating of alucone adhered to the nano-Si particle is observed using high resolution HAADF-STEM.

A cluster model was used to compare the stability of the Al-complexes. As shown in Figure V- 192(top), **A** is built as a 3-O coordinated complex with 3 -O and an Al atom, while **B** and **C** are 4-O coordinated complexes in which C contains CH<sub>3</sub>CH<sub>2</sub>OH as the fourth ligand. The optimized structures have similar Al-O bond length compared to those in the slab model. **B** and **C** are produced by the following addition reactions: **A** + CH<sub>3</sub>CHO<sup>-</sup> → **B** and **A** + CH<sub>3</sub>CHOH → **C**. The corresponding reaction energies are -1.06 and -0.91 eV respectively. Therefore, introducing a 4th ligand into the 3-coordinated Al complex is energetically feasible, and stable in the film structure.

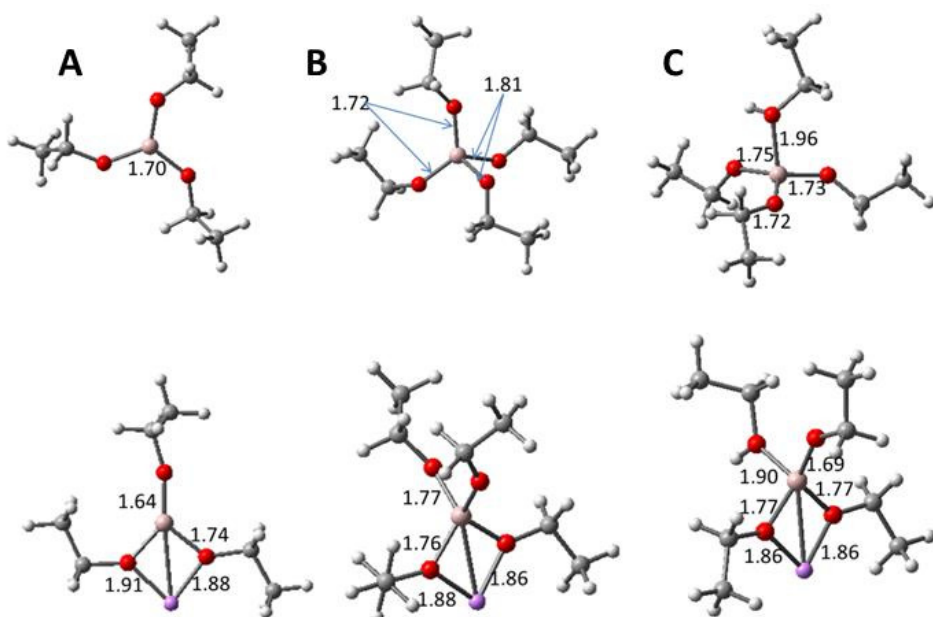


**Figure V- 192:** Cluster models of 3- and 4- coordinated Al complexes. A, 3-O coordination; B, 4-O coordination; C, 4-O coordination with a terminal OH group. Li<sup>+</sup> binding on cluster model A, B, and C. Li<sup>+</sup> ions are denoted as purple spheres. Listed distances are in Å. Light blue, pink, red, grey, and white spheres represent respectively Si, Al, O, C, and H atoms

It is important to understand the possible lithiation in the film, as it may considerably influence the electrochemistry of the Si anodes. On the other hand, the film structure may be modified in the process of lithiation. The structural change could induce some effects on the stability of the film. As a first step, simple cluster models, A, B, and C, were used to investigate lithiation in the alucone film. (See Figure V- 192). For all the configurations, Li<sup>+</sup> is bound with 2 oxygen atoms. The bond length of Li-O is around 1.9 Å. Our calculations indicate that all the configurations can bind Li<sup>+</sup>. The corresponding values of binding energy are -2.63 eV for A, -3.15 eV for B, and -3.30 eV for C, suggesting very strong Li bindings on all the complexes. The result implies that Li ions may reside in the film, thus leading to some irreversible capacity. Notably, Li<sup>+</sup> binding is stronger in the 4-O coordination complex. Thus lithiation may first take place in those sites.

The experimental results indicate the lithiated alucone film is both electronic and ionic conductive. To further investigate this point, two additional models were evaluated: in the first the film is completely saturated with Li atoms located in all possible most favorable lithiation sites as discussed in relation to Figure V- 192. In the second model the film is supersaturated; that is: the Li concentration goes beyond saturation of the most favorable sites; these additional Li atoms were added in random locations to the film. The binding energies of these sequential Li additions were computed. It was observed that the slope of binding energy vs. the amount of Li in the film changes drastically beyond the saturation point with the binding becoming much less favorable. Thus, further Li atoms passing through the film beyond its saturation point will not be strongly retained; instead their diffusion will be facilitated as required during charge or discharge of the battery. The calculated results agree well with the experimental data. The fast lithiation process was confirmed for the coated Si anode by our collaborator Ban (NREL), which enable the coated Si anode to cycle at high cycling rates.

To assess the film electronic conductivity, the Li<sub>18</sub>Si<sub>36</sub> model of the anode was covered by two different films: a “saturated” film represented by C<sub>14</sub>Li<sub>5</sub>Al<sub>5</sub>O<sub>15</sub>H<sub>26</sub> where all the 5 Al-O<sub>x</sub> groups are coordinated with Li, and a “supersaturated” film of composition C<sub>14</sub>Li<sub>11</sub>Al<sub>5</sub>O<sub>15</sub>H<sub>26</sub> where there are 6 extra Li atoms added to random locations in the film. The results are shown in Figure V- 193. In agreement with the experimental results, the calculated electronic conductivity shows that the lithiated film is able to conduct electrons, and such ability increases as the lithiation goes beyond saturation of the film.

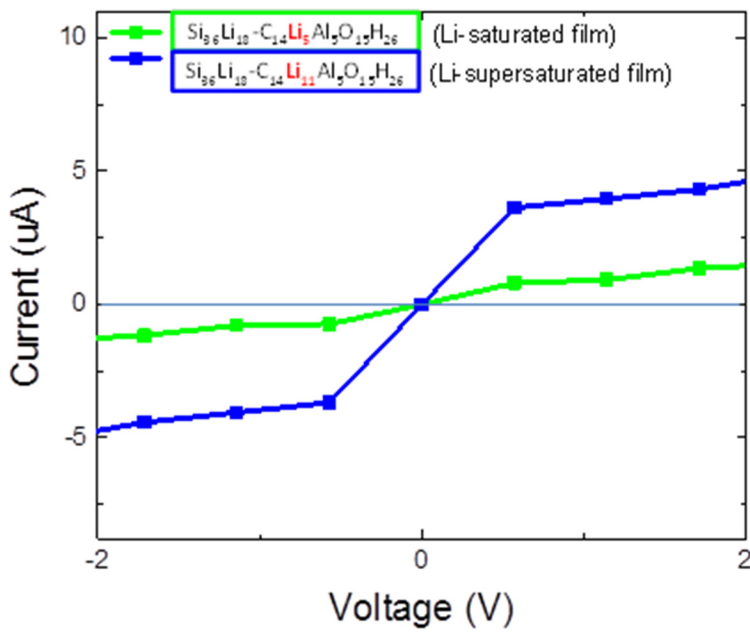


Figure V- 193: Electron current determined for various values of applied voltage for the two model systems. A clear enhancement of the electron conductivity is found in the supersaturated film

A first important issue was found regarding the *stability* of the organic phases tested on a system where a thin Li<sub>2</sub>EDC film was grown directly on a Li<sub>104</sub>Si<sub>32</sub> model anode surface. AIMD simulations revealed that electron transfer from the anode surface to an ethylene dicarbonate (EDC) anion from a Li<sub>2</sub>EDC molecule causes its decomposition into two carbonate anions (CO<sub>3</sub>) and one ethylene molecule (C<sub>2</sub>H<sub>4</sub>). Time evolution of the charges clearly showed charge transfer from the anode to the Li<sub>2</sub>EDC film. To investigate whether these oligomer decomposition reactions may also occur far from the anode surface a multicomponent SEI model anode/X1/X2 formed by two or

more blocks (X1, X2) stacked over the anode surface Li<sub>13</sub>Si<sub>4</sub> was built and tested in contact with the electrolyte solution composed by solvents and salt. The models emulate the initial stages of SEI formation after some X1, X2 compounds (such as LiF or Li<sub>2</sub>O) have nucleated and crystallized over the surface. AIMD simulations were performed to evaluate the time evolution of the system after addition of a radical species: vinyl C<sub>2</sub>H<sub>3</sub><sup>·</sup> and hydroxyl OH<sup>·</sup> radicals were tested in various locations of the simulated system. These radicals only have in common the presence of an unpaired electron and their subsequent extreme reactivity. The analyses clearly showed the composition of one or more molecules and electron transfer through the surrounding environment.

### Electron Transfer during SEI Growth

The first-principles computational studies carried out in this project demonstrate that radical species are responsible for the electron transfer that allows SEI layer growth once its thickness has evolved beyond the electron tunneling regime. In addition, the composition, structure, and properties of the SEI layer depend on the electrolyte, especially on the extent to which they are able to polymerize after reduction. Polymerization mechanisms were analyzed and mechanistic differences for electrolytes yielding a fast and a slow SEI growth were proposed. This new understanding leads to firm guidelines for rational electrolyte design. (See Figure V-194.)

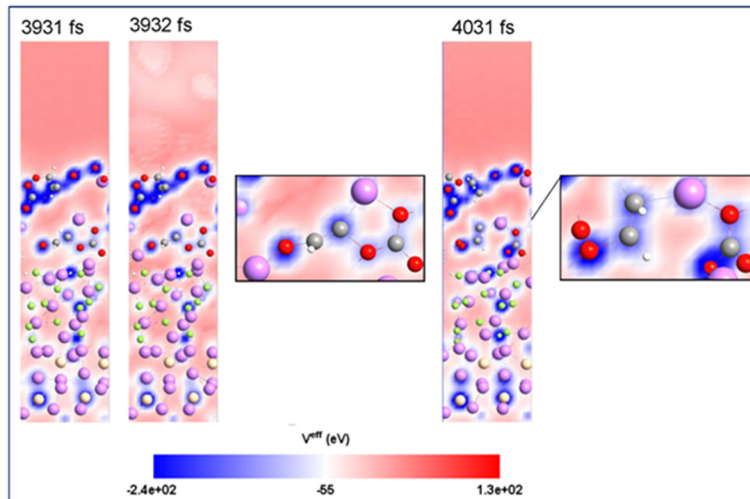
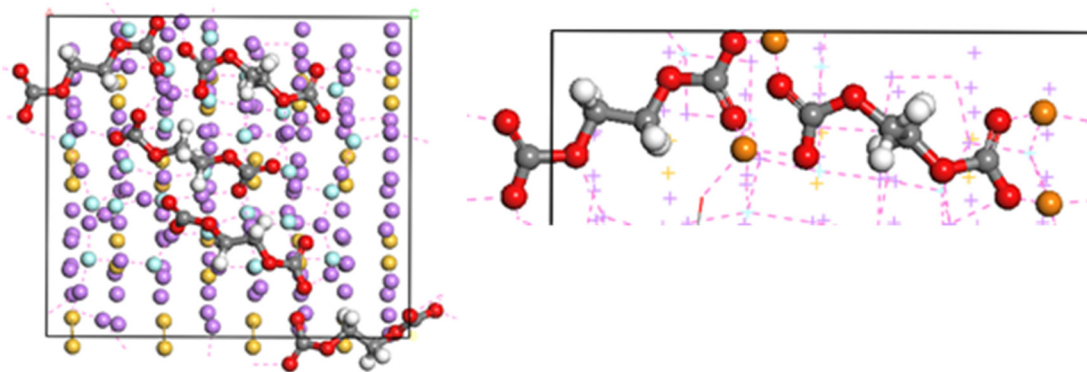


Figure V- 194: Electrostatic potential map follows a reaction occurring at the solid/electrolyte interphase region of the Li<sub>13</sub>Si<sub>4</sub>/LiF/Li<sub>2</sub>VDC surface. The sequence illustrates the events preceding a 2-step decomposition of Li<sub>2</sub>VDC yielding 2 CO<sub>3</sub> groups and C<sub>2</sub>H<sub>2</sub>. One CO<sub>3</sub> anion separates first from the whole molecule (at approximately 3931 fs) and short after (at 4031 fs) the other CO<sub>3</sub> group breaks apart from the acetylene molecule

Another crucial point relates to the effect that the nature of the electrolyte has on SEI growth. The low stability of several organic species derived both from a typical solvent (EC) and a typical additive (VC) was clearly demonstrated in this work. But additives like VC are known to slow down side reactions and form much stable compact films. Therefore, the empirically found clearly different SEI performance between electrolytes without additives (for example EC) and those containing beneficial additives (such as VC or FEC) should be attributed to the fast polymerization rate of the additives. Once the initial decomposition products polymerize, a much lower amount will be available for the formation of unstable oligomer species that may lead to uncontrolled growth because of rapid electron propagation. Thus, solvents/additives able to generate stable polymer-based and inorganic ( $\text{LiF}$ ,  $\text{Li}_2\text{CO}_3$ ) films should be responsible for much more stable SEI layers where growth will fall within the much slower non-adiabatic electron tunneling regime. To investigate possible polymerization mechanisms a series of new computational studies were conducted. It was concluded that polymerization reactions initiated by open VC or open EC radical anions reacting with intact VC molecules are thermodynamically more favorable than those reacting with intact EC molecules, which suggests the greater polymerization tendency of VC-derived species. The fact that intact EC molecules would be polymerized indicates also that these molecules would not be further reduced thus producing much less ethylene gas in agreement with experimental evidence. A possible pathway for poly(VC) formation to be thermodynamically favorable was also found in this work. Thus, it was postulated that VC-containing solutions produce more polymeric species and less short oligomer products, in contrast with pure EC solutions that would produce a thick organic layer of unstable oligomer products. Therefore, if the outer organic layer contains less of the electrochemically unstable species (as in a VC or FEC-based electrolyte), the SEI rate growth will significantly decrease (as observed experimentally) compared with those based on VC (or FEC)-free electrolytes.

#### **Development of a Mesoscopic Model**

The model was developed in two stages: a first-principles analysis of aggregation of lithium ethylene dicarbonate ( $\text{Li}_2\text{EDC}$ ) over bare and coated Si surfaces was performed which provided information about adsorption and aggregation growth rates, as well as confirmed the above discussed electron transfer analysis. An example is shown in Figure V- 195.



**Figure V- 195:** Surface models for  $\text{Li}_2\text{EDC}$  on top of a  $\text{LiF}$  covered surface showing a coverage of  $1.7 \text{ oligomers}/\text{nm}^2$  and  $\text{Li}_2\text{EDC}$  dimer formation

On the basis of rates provided by the first principles analysis, a mesoscopic model was formulated in collaboration with Prof. Mukherjee (TAMU). The microscopic events are: EC molecular adsorption, EC reduction, EC configuration transition, and  $\text{Li}_2\text{EDC}$  formation. The computational domain was divided into identical cubic cells. Initially all the kinetic rates were taken as constant. On this basis, a linear mean growth was found as w function of time. Further analyses showed that thickness  $\delta$  growth rate significantly depends on EC reduction rate  $k_2$  (see Figure V- 196). The effects of EC adsorption rate were also determined. It was found that for very low adsorption rates, the SEI growth is determined by the adsorption rate, whereas higher adsorption rates do not affect SEI thickness growth. In a second stage, a SEI thickness dependent reduction rate was introduced. This reflects the effect of decreased electron concentration as the SEI thickness grows (Figure V- 197). The effect of increase of electron transport resistance on the reduction of the SEI growth thickness was quantified. Further refinements to the model are in progress.

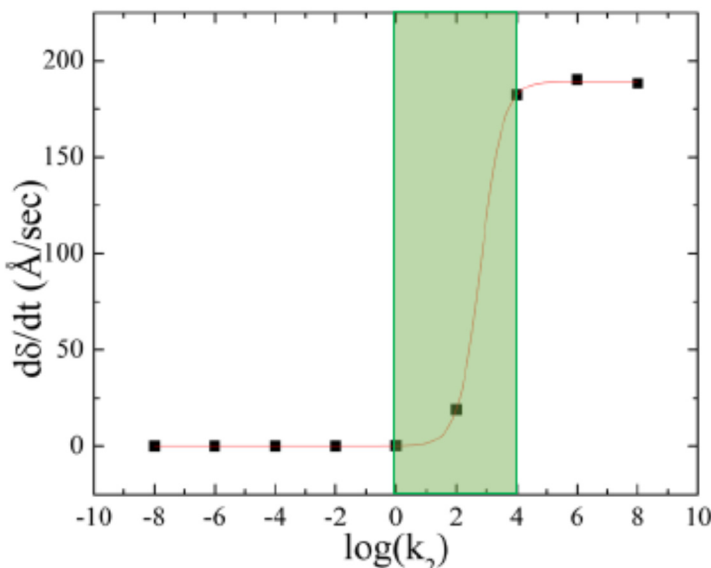


Figure V- 196: Effects of EC reduction rate ( $k_2$ ) on SEI thickness ( $\delta$ ) growth

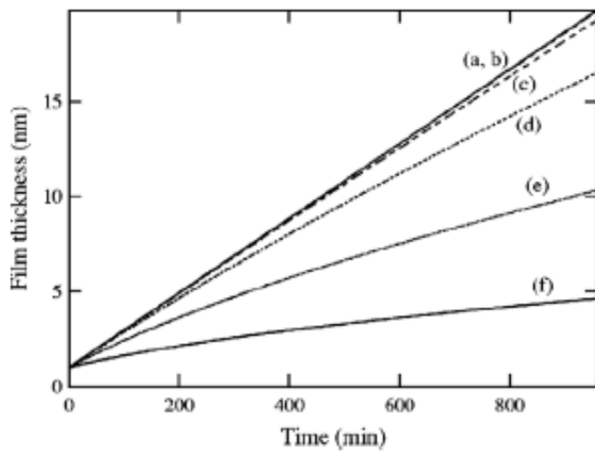


Figure V- 197: Film growth at open circuit. Electron transfer rate was set at various rates taken from the literature

favorable reaction energies at T=0 K. “(s)” and “(g)” refer to solid and gas phases, respectively. However, the full EDC reaction involves breaking strong C-C bonds and may be kinetically hindered. (2) Using Gaussian cluster DFT calculations, we have found no evidence that  $\text{CO}_3^{2-}$  or EDC can be electrochemically reduced above 0 V vs. Li+/Li(s) in the interior (“bulk”) region of the SEI. Thus SEI degradation is not electrochemical, and will likely be initiated at interfaces. (3) We use Li metal (100) and amorphous-Si as model surfaces embodying the two extremes of Li(x)Si contents.  $\text{Li}_2\text{CO}_3$  reacts exothermically to release  $\text{O}^{2-}$  and  $\text{CO}_2^{2-}$  on Li surfaces. The barrier is about 1 eV, i.e., reaction half-life is ~1 hour. Adding surface Si atoms does not facilitate the reaction. EDC reacts to yield  $\text{CO}_2^{2-}$  on both Li and a-Si surfaces, which may ultimately yield  $\text{Li}_2\text{O}$ . This suggests that  $\text{Li}_2\text{O}$  may be the main component at the interface, unless LiF is present (e.g., via additives), and that extensive solid state chemical reactions accompany Si-anode charging/discharging (Figure V- 198). This discovery is also relevant to Li- and Sn-metal anodes; the implications are being explored.

### Coupled Mechanical-Chemical Response and Instantaneous Voltage Effects

Sandia’s main effort (Leung) focused on the examination of SEI formation and evolution on  $\text{Li}(x)\text{Si}$  surfaces with varying Li content (“x”). Particular emphasis was put on elucidating the stability of  $\text{Li}(x)\text{Si}$ -SEI interfaces, using model systems (lithium carbonate ( $\text{Li}_2\text{CO}_3$ ) and lithium ethylene dicarbonate (Li<sub>2</sub>EDC)). This work was performed in collaboration with the Balbuena group and will form the core of an invited presentation at the Electrochemical Society Fall Meeting. The coupled mechanical-chemical response of SEI and electrolyte on  $\text{Li}(x)\text{Si}$  surfaces due to the lateral expansion and contraction of Si as it inserts/de-inserts lithium was also examined. The instantaneous electronic (i.e., the electronic) voltage was monitored and correlated with SEI formation.

There are at least three possible criteria of SEI stability: (1) thermodynamic (i.e., phase diagram study), (2) electrochemical, and (3) interfacial. (1) Thermodynamic stability has been the focus in solid electrolyte studies. It was found (using VASP DFT/PBE calculations) that  $\text{Li}_2\text{CO}_3$  (s) + 4 Li (s)  $\rightarrow$  3  $\text{Li}_2\text{O}$  (s) + C (s) and  $\text{Li}_2\text{C}_4\text{H}_4\text{O}_6$  (i.e., EDC) + 10 Li (s)  $\rightarrow$  6  $\text{Li}_2\text{O}$  (s) + 4 C (s) + 3  $\text{H}_2$  (g) both yield significant (>1.2 eV)

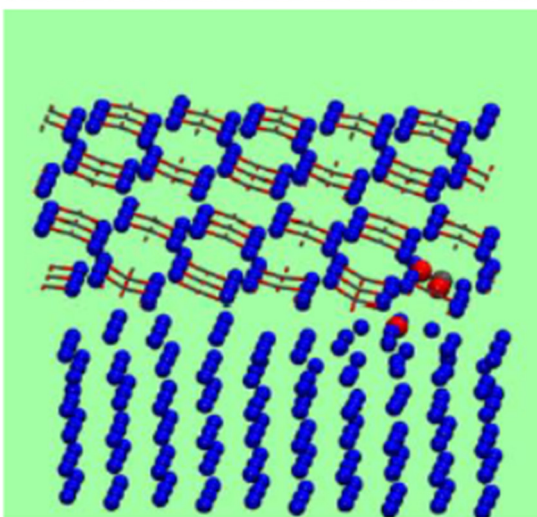
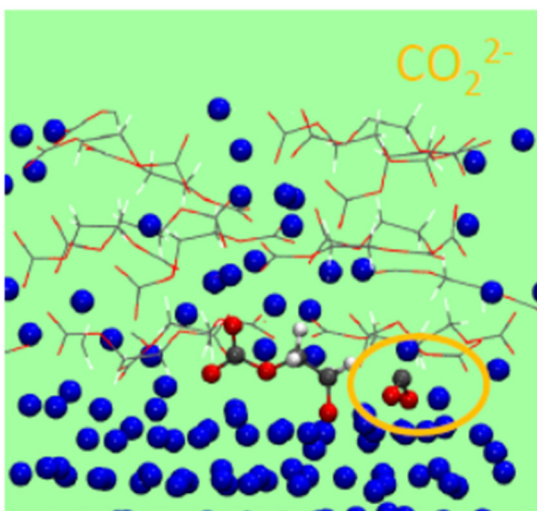


Figure V- 198: Top: EDC film on Li(100) loses a CO<sub>2</sub><sup>2-</sup> spontaneously. Bottom: Li<sub>2</sub>CO<sub>3</sub> film on Li(100) loses a O<sub>2</sub>- (1 eV barrier)

dielectric constant values comparable to the experimental results. The self-diffusion coefficient is another relevant property for ion transport through these solvents. Predicted values of the self-diffusion coefficient based on mean-squared displacements of solvent molecules were reasonably close to the experiments. These

Leung also examined the effect of cracking of a thin LiF film intervening between liquid electrolyte (ethylene carbonate, EC) and amorphous Li(x)Si surfaces as the Li content "x" increased and the lattice was manually expanded (Figure V- 199). The electronic voltage is monitored. EC was predicted to become reductively decomposed in pathways previously found by the Leung and Balbuena groups. The main products are CO, deprotonated ethylene glycol, and carbonate anions -- all two-electron reduction products. EDC, known to be a main SEI product, was not observed in these interfacial calculations. The stability analysis discussed above now explains why: EDC is unstable right at the interfaces. This is in full agreement on the conclusions stated above regarding electron transfer modes.

### Solvation Effects

Force field parameter evaluation is necessary to leap forward from electronic structure calculations to large time-scale studies of transport and diffusion properties in the SEI layer. Rempe's group at Sandia performed classical molecular dynamics (MD) simulations of organic solvents EC and propylene carbonate (PC), which are relevant for energy storage applications. These solvents are widely used because of their high dielectric constants. Hence, it is a necessary step to model dielectric properties using available force field parameters. MD simulations of pure EC and PC were carried out across a wide temperature range (300-600 K). The static dielectric constant and frequency dependent dielectric properties including dielectric relaxation times of these pure solvents were calculated and compared with limited available experimental data. The OPLS-AA parameters for both solvents predicted

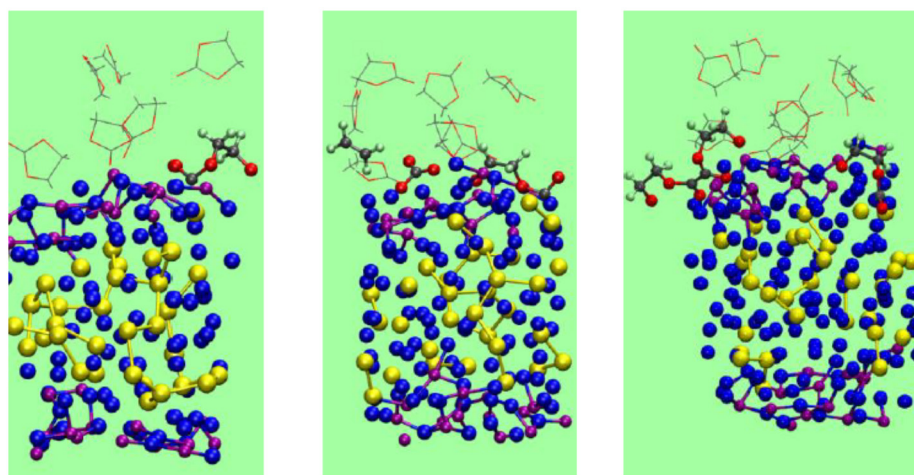


Figure V- 199: Thin liquid EC film decompose on incrementally stretched Li(x)Si surface with increasing "x."

results were submitted to *J. Phys. Chem. B* in September 2015 and will be presented at the Electrochemical Society meeting in October 2015.

### Conclusions and Future Directions

This work has provided dramatic progress to the understanding of the SEI nucleation and growth. The growth of the SEI layer via electron transfer beyond tunneling thicknesses has been clearly demonstrated to take place via instability of the organic SEI products that release radical species able to propagate the electro transfer thus continuing the growth. The contrasted behavior of two electrolyte solutions: one leading to slow growth and another to fast growth was thoroughly detailed and demonstrated in these studies that also addressed the relevance and impact of polymerization reactions. A mesoscopic model has been developed that is able to predict SEI growth for larger time and length scales. The effects of instantaneous voltage and ionic solvation on SEI reactions has been assessed and will be incorporated in future work which will also refine the mesoscopic model with further first-principles information of aggregation reactions.

### FY 2015 Publications/Presentations

1. “First Principles Modeling of SEI Formation on Bare and Surface/Additive Modified Silicon Anodes”, ES214\_Balbuena\_2015\_O, US DOE Vehicle Technologies AMR, 2015.
2. Perez-Beltrán, S., G. E. Ramirez-Caballero, and P. B. Balbuena, “First Principles Calculations of Lithiation of a Hydroxylated Surface of Amorphous Silicon Dioxide,” *J. Phys. Chem. C* 119 (2015): 16424-16431.
3. Ma, Y., J. M. Martinez de la Hoz, I. Angarita, J. M. Berrio-Sanchez, L. Benitez, J. M. Seminario, S-B. Son, S-H. Lee, S. M. George, C. M. Ban, and P. B. Balbuena, “Structure and Reactivity of Alucone-Coated Films on Si and Li<sub>x</sub>Si<sub>y</sub> Surfaces,” *ACS Appl. Mater. Inter.* 7 (2015): 11948-11955.
4. Martinez de la Hoz, J.M., F. A. Soto, and P. B. Balbuena, “Effect of the Electrolyte Composition on SEI Reactions at Si Anodes of Li-Ion Batteries,” *J. Phys. Chem. C* 119 (2015): 7060-7065.
5. Soto, F. A., Y. Ma, J. M. Martinez de la Hoz, J. M. Seminario, and P. B. Balbuena, “Formation and Growth Mechanisms of Solid-Electrolyte Interphase Layers in Rechargeable Batteries,” *Chemistry of Materials*, under review.

## V.G.5 A Combined Experimental and Modeling Approach for the Design of High Current Efficiency Si Electrodes (GM, MSU)

### Objectives

- The use of high capacity Si based electrode has been hampered by its mechanical degradation due to the large volume expansion/contraction during cycling. Nanostructured Si can effectively avoid Si cracking/fracture. Unfortunately, the high surface to volume ratio in nanostructures leads to unacceptable amount of solid-electrolyte interphase (SEI) formation and growth, thereby low current/coulombic efficiency and short life. Based on mechanics models we demonstrate that the artificial SEI coating can be mechanically stable despite the volume change in Si, if the material properties, thickness of the SEI, and the size/shape of Si are optimized. Therefore, the objective of this project is to develop an integrated modeling and experimental approach to understand, design, and make coated Si anode structures with high current efficiency and stability

### Technical Barriers

- The real challenges to developing a model that allows us to design high current efficiency Si electrodes with electrochemically and mechanically stable artificial SEI layer are: a) poor understanding of SEI failure mechanisms; b) lack of accurate mechanical properties of the SEI; and c) difficulty in validation of the model. All of these are due to the extreme challenges associated with characterizing the properties of nano-meter thin SEI layer on lithiated Si in real battery systems. Therefore, we will first address these questions based on simpler thin film electrodes.

### Technical Targets

- Fundamentally understand the mechanical degradation of SEI (including artificial coatings) on Si electrodes.
- Establish a correlation between the capacity loss (or current efficiency) and mechanical degradation of SEI on Si.
- Develop a multi-scale model to predict the stress/strain in the SEI layer on Si.
- Predict and measure the basic material properties required in the mechanics model.
- Use the model the guide the design of nanostructured Si electrode.
- Ultimately assist USABC to achieve its goal on EV energy storage: 200 Wh/kg (EV requirement); 96 Wh/kg, 316 W/kg, 3000 cycles (PHEV 40 mile requirement). Calendar life: 15 years and improved abuse tolerance.

#### Project Details

**Xingcheng Xiao (General Motors LLC – PI)**

Global Research and Development Center

30500 Mound Road

Warren, MI 48090

Phone: 248-912-8132; Fax: 586-986-3691

E-mail: [Xingcheng.xiao@gm.com](mailto:Xingcheng.xiao@gm.com)

**Yue Qi (Michigan State University – co-PI)**

Department of Chemical Engineering and Materials Science

3509 Engineering Building

East Lansing, MI 48824

Phone: 517-432-1243; Fax: 517-432-1105

E-mail: [yueqi@egr.msu.edu](mailto:yueqi@egr.msu.edu)

Subcontractors:

Brown University

Providence, RI 02912

University of Kentucky

Lexington, KY 40506

Start Date: May 2013

Projected End Date: April 2017

## Accomplishments

- Identified important SEI failure modes, such as film delamination and cracking by using combined in-situ electrochemical experiments and modeling techniques (continue comparing individual SEI components).
- Discovered that lithiation of  $\text{Al}_2\text{O}_3$  coatings generates concentration and modulus gradients, which inhibit local stress concentrations and crack propagation.
- Established a material property design methodology for stabilizing SEI on Si.
- Demonstrated the synergistic effects of LiF and  $\text{Li}_2\text{CO}_3$  enhance Li transport and reduce electron transport due to space charge effects. Based on these results, a GO decision was made to continue the design of multi-component and multi-functional artificial SEI coatings.

---

## Introduction

Volume changes of up to ~300 vol.% for Si during lithiation and delithiation leads to fracture of Si and/or loss of electrical contact with the conductive phase or the current collectors. Nano-structured Si effectively mitigates Si cracking/fracture. Unfortunately, the high surface to volume ratio in nanostructures leads to unacceptable amounts of solid-electrolyte interphase (SEI) formation, thereby lowering current efficiencies. Artificial SEI coated Si nanostructures will resolve this contradiction, if the coating can be stable. Based on mechanics models we demonstrate that the SEI coating can be mechanically stable despite the volume change in Si, if the material properties, thickness of the SEI and the size/shape of Si are optimized. Engineering such system is extremely difficult due to the large number of variables involved, especially when many of them are unknown.

In order to develop a validated model, it is critical to fundamentally understand the mechanical and chemical stability of SEI (hereafter, SEI refers to both naturally formed native SEI and artificial SEI coatings) in electrochemical environments, the correlation between the coulombic efficiency and the dynamic process of SEI evolution, and the structural optimization of both the SEI and the Si electrode. However, it is extremely difficult to characterize the structure and to measure the mechanical properties of SEI layers that are tens of nm thick on complicated geometries. In this project, we will take advantage of a thin-film geometry that simplifies the investigations while providing fundamental parameter values. Many measurements (e.g., AFM, indentation, XPS and TOF-SIMS depth profile) can be readily conducted with thin films, whereas similar measurements on particles or nanofibers are difficult. These thin-film electrodes can be appropriately modeled using continuum-based models, thus allowing the direct comparison of measurements with models to support model validation.

## Approach

In this project, four coherent steps will be taken: a) Develop a multi-scale model to predict the stress/strain in the SEI layer (including artificial SEI) on thin-film Si and establish a correlation between the capacity loss (or current efficiency) and mechanical degradation of SEI on Si. b) Use atomic simulations combined with experiments performed on Si-thin-films to provide critical material properties used in the continuum modeling. c) Investigate the impact of the SEI formation on the stress/strain evolution, combined with modeling to quantify the current efficiency related to a variety artificial SEI layers using in situ electrochemical experiments. d) Use the validated model to guide surface coating design and Si size/geometry optimizations that mitigate mechanical degradation to both SEI and Si.

## Results

### **Identifying SEI Failure Mode by Using Combined *In Situ* Electrochemical Experiments and Modeling Techniques**

Based on previous investigations, continuous Si film and patterned model structures were developed. Continuous thin films only expand in the Z direction without fracture or delamination, and thus this serves as a good control system for non-mechanically strained SEI coatings. With the patterned model structure with interfacial sliding, lithiation stretches the SEI layer in the XY direction. The comparison of these two configurations enables us to correlate the irreversible capacity loss with SEI failure. We are controlling the

SoC with different cut off voltages and measuring the corresponding irreversible capacity loss within different voltage ranges. Figure V- 200 shows initial data on irreversible capacity losses from the continuous thin film and patterned model systems. The peak around 0.5V corresponds to SEI formation. Here the continuous Si and patterned samples show similar trends. However, the absolute irreversible capacity shows a sharp rise around 0.25V for patterned samples, which indicates that SEI may become mechanically unstable (crack formation etc.) due to the biaxial expansion. This then leads to more SEI formation and corresponding Li consumption. Applying thin film mechanics to this configuration allows us to accurately describe the deformation of the SEI on the Si islands, and to then relate this to fracture.

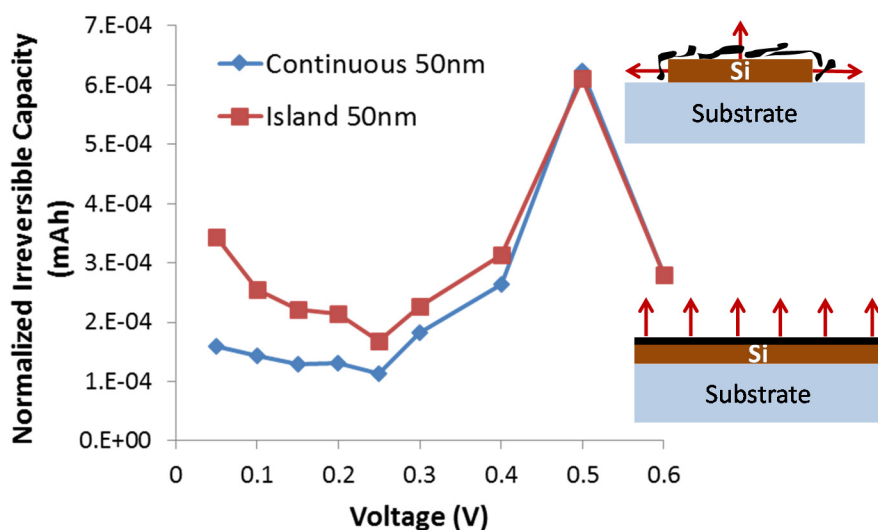


Figure V- 200: Comparison of continuous thin film and patterned model structure allows Si enabled experimental correlation of the irreversible capacity loss with SEI failure

compositional change, mechanical property evolution, mechanical integrity, stress distributions, and fracture behavior were compared for different shell thicknesses. A new mechanics model based on these varying properties was developed to determine if the coating will crack or stay intact (Figure V- 201). Furthermore, we discovered Li atoms insert relatively slowly and gradually into the  $\text{Al}_2\text{O}_3$  coating, forming a well-defined Li density gradient along the shell as the coating is thick enough. This self-generated Li density gradient directly links to an elastic modulus gradient, which plays a critical role to avoid local stress concentration and crack propagation. Based on these results, we propose a modulus gradient coating, softer outside, harder inside, is beneficial to avoid coating fracture thus will protect Si electrode surface and improve its current efficiency.

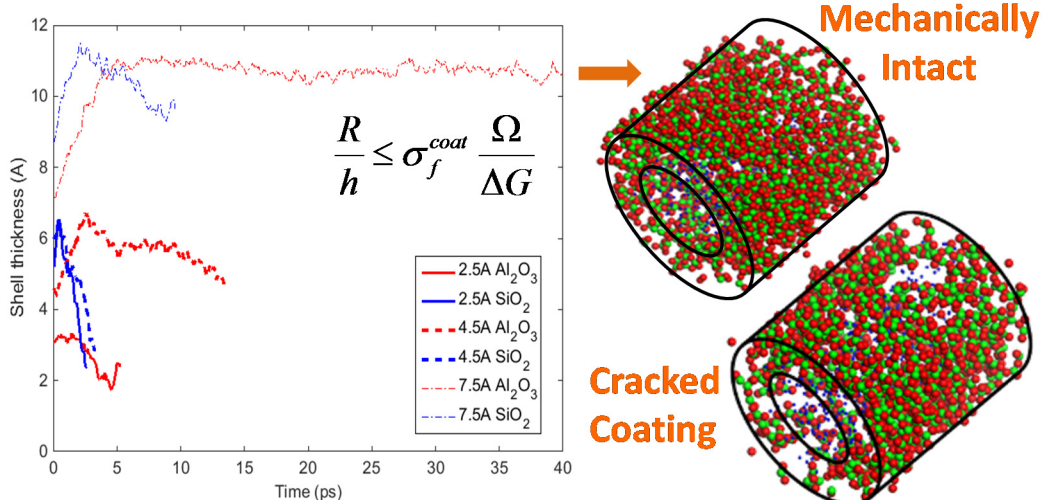


Figure V- 201: Shell failure mechanisms as a function of Si nanowire size and coating thickness. With thicker coatings and Li concentration gradient, the coating is mechanically stable until full lithiation of Si

In parallel to the experimental investigation, detailed SEI failure modes are also revealed by reactive molecular dynamics (MD) simulations. We have developed ReaxFF parameters for Li-Si-Al-O-C system in order to model the reaction and deformation of SEI on a Si during lithiation.

The lithiation process of Si-core/ $\text{Al}_2\text{O}_3$ -shell and Si-core/ $\text{SiO}_2$ -shell nanostructures were simulated. Characteristic behaviors, in terms lithiation rate,

## Established Design Guidance for Stabilizing the Shell

The material properties predicted from atomistic scale were input into continuum models to predict the mechanically stable size of coated Si nano structures. Currently, the two most promising structures are core-shell (predicted in 2014) and yolk-shell. In both structures, there is some retained free space left inside the coating, so Si expands inward in the core-shell structure and outward in the yolk shell structure. In the yolk-shell structure (Figure V- 202), we vary the fracture energy of the coating, corresponding to different coating materials. This design map shows that selecting another coating material will alter the critical size accordingly.

## Development of Promising Multi-Component and Multi-Functional Artificial SEI Coatings

Inspired by the composite nature of naturally formed SEI, we designed lithium carbonate ( $\text{Li}_2\text{CO}_3$ ) and lithium fluoride (LiF) mixed artificial SEI, by codeposition. The improved charge transfer rate of Si electrodes coated with  $\text{Li}_2\text{CO}_3$  mixed with LiF is attributed to faster Li ion transport through the engineered SEI. Considering the bulk properties, it is counterintuitive that introducing LiF into  $\text{Li}_2\text{CO}_3$  would enhance the ionic transport, since the ionic conduction through LiF coated on an anode surface is orders of magnitude lower. However, a multi-scale transport model that considers space charging effects reveals that LiF can facilitate space charge accumulation, which significantly improves lithium transport and reduces electron conduction. The optimal composition in our experiments is 50% LiF. The synergetic effects of LiF and  $\text{Li}_2\text{CO}_3$  interfaces not only facilitate Li ion transport, but also further enhance the passivation function to suppress electrolyte decomposition. These engineered inorganic SEIs consisting of LiF and  $\text{Li}_2\text{CO}_3$  have been successfully applied on thin film Si electrodes and demonstrated improved cycling efficiency due to the combination of electrical insulation and mechanical protection. We envision that this synergy effect will greatly benefit the design of surface coatings/electrolyte additives for Si-electrodes, thus a GO decision was made to further investigate multi-component and multi-functional coatings. (See Figure V- 203.)

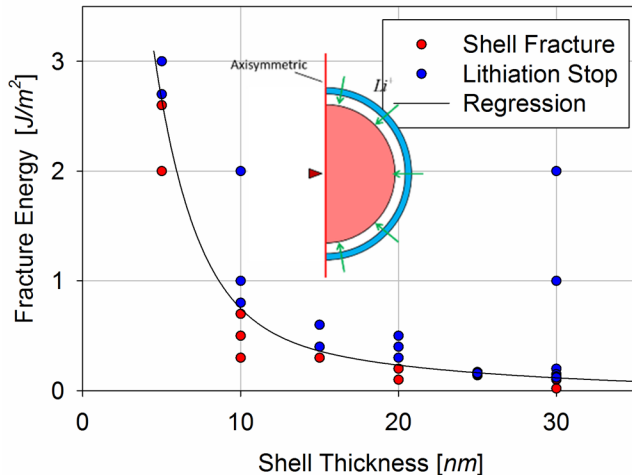


Figure V- 202: Continuum mechanical model identified the critical shell thickness of lithiation in Si-C yolk-shell structure

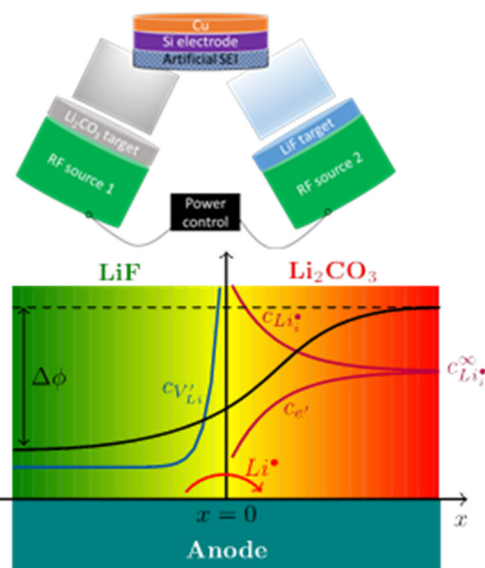
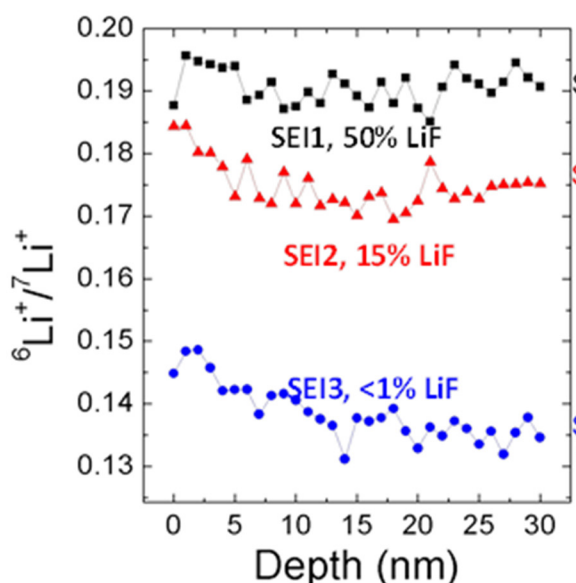


Figure V- 203: Engineered SEI with specified amounts of  $\text{Li}_2\text{CO}_3$  and LiF co-existing on silicon thin film electrodes, showing Li diffusion is peaked with 50% LiF by TOF-SIMS results, due to space charging effect

## Conclusions and Future Directions

1. By using combined in-situ electrochemical experiments and modeling techniques, we were able to identify SEI failure modes, which is mainly due to the fracture during the lithiation process of Si active materials.
2. An artificial SEI layer, with modulus gradient, softer outside, harder inside, is beneficial to avoid coating fracture thus will protect Si electrode surface and improve its current efficiency. A design map based on fracture mechanics was proposed for the selection of desirable artificial SEI and Si nanostructure.
3. Identified functions of individual component in nature SEI, 1) LiF is critical for stabilizing the SEI layer and improving the cycling efficiency, due to the electrical insulating and mechanical protection. 2) The synergetic effects of LiF and  $\text{Li}_2\text{CO}_3$  interfaces, which not only facilitate Li ion transport, but also further enhance the passivation function to suppress electrolyte decomposition.

The next step is to further optimize the composite and structure of SEI layer. Furthermore, by designing Si architecture to minimize the stress and strain generated in SEI in this year, we expect SEI can be stabilized therefore leading to high current efficiency.

## FY 2015 Publications/Presentations

1. Verbrugge, Mark W., Daniel R. Baker, Xingcheng Xiao, Qinglin Zhang, YT Cheng, "Experimental and Theoretical Characterization of Electrode Materials that Undergo Large Volume Changes and Application to the Lithium–Silicon System," *The Journal of Physical Chemistry C* 119, no. 10 (2015): 5341.
2. Zhou, Weidong, Chongmin Wang, Qinglin Zhang, Héctor D. Abruña, Xingcheng Xiao\*, "Tailoring Pore Size of Nitrogen–Doped Hollow Carbon for Confining Sulfur in Lithium–Sulfur Batteries," *Advanced Energy Materials* (2015), DOI: 10.1002/aenm.201401752.
3. Ling, Min, Hui Zhao, Xingcheng Xiao, Feifei Shi, Mingyan Wu, Jingxia Qiu, Sheng Li, Xiangyun Song, Gao Liu and Shanqing Zhang, "Low cost and environmentally benign crack-blocking structures for long life and high power Si electrodes in lithium ion batteries," *J. Mater. Chem. A*, 3 (2015): 2036.
4. Li, Juchuan, Nancy J. Dudney\*, Xingcheng Xiao\*, Mark W. Verbrugge, Chengdu Liang, and Yang-Tse Cheng, "Asymmetric Rate Performance of Si Anodes for Lithium-Ion Batteries," *Advanced Energy Materials* (2014), DOI: 10.1002/aenm.201401627.
5. Zhou, Weidong , Xingcheng Xiao\*, "Polydopamine Coated Nitrogen Confused Hollow Carbon–Sulfur Core–Shell Structure for Improving the Lithium–Sulfur Batteries," *Nano Letters* 14, no. 9 (2014): 5250.
6. Xiao, Xingcheng\*, Weidong Zhou, Ill Ryu, Meng Gu, Chongmin Wang, Gao Liu, Huajian Gao, "Regulated Breathing Effect of Silicon Negative Electrode for Dramatically Enhanced Performance of Li-ion Battery," *Advanced Functional Materials* (2015), DOI: 10.1002/adfm.201403629.
7. Zhang, Qinglin, Xingcheng Xiao, Weidong Zhou, Y. T. Cheng, Mark W. Verbrugge, "Toward High Cycle Efficiency of Silicon-Based Negative Electrodes by Designing the Solid Electrolyte Interphase," *Advanced Energy Materials* 5, no. 5 (2015).
8. Pan, J., Y. T. Cheng, Y. Qi, "General method to predict voltage-dependent ionic conduction in a solid electrolyte coating on electrodes," *Physical Review B* 91, no. 13 (2015): 134116.
9. Wang, Ge Li, Fathy M Hassan, Xingcheng Xiao,\* Zhongwei Chen\*, "Building sponge-like robust architectures of CNT–graphene–Si composites with enhanced rate and cycling performance for lithium-ion batteries," *Journal of Materials Chemistry A* 3 (2015): 3962.
10. Qi, Yue, "Predicting the transport and mechanical properties of the solid electrolyte interphase (SEI) in Li-ion batteries." Chemical and Biomolecular Eng. Department, University of Tennessee, Knoxville, TN. November 25, 2014
11. Qi, Yue, "Predicting the transport properties of the solid electrolyte interphase (SEI) in Li-ion batteries." Paper presented at the MRS 2014 Fall Meeting, Boston, MA. December 2014.
12. Sheldon, Brian W, "Electrochemically Induced Stresses in Energy Storage Materials." Paper presented at the Electrochemical Strain Microscopy Workshop, Oak Ridge, TN, September 2014.
13. Sheldon, Brian W., "Electrochemically Induced Stresses in Energy Storage Materials." Paper presented at the Society of Engineering Science Annual Meeting, West Lafayette, IN, October 2014.

14. Xiao, Xingcheng, "Understanding Degradation Mechanism of Silicon Based High Energy Density Electrode Materials for Lithium Ion Batteries." Keynote lecture, 64<sup>th</sup> Canadian Chemical Engineering Conference, Niagara Falls, ON, October 2014.
15. Xiao, Xingcheng, "Toward high cycle efficiency of high energy density lithium ion batteries." Presented at the 249th ACS Division of ENFL: Applications of Theoretical Chemistry for Energy and Fuel Production, March 2015.
16. Gao, Huajian,"Modeling mechanical degradation in thin film electrodes for high energy density lithium batteries." Presented at the Prager Medal Symposium in Honor of Professor Robert M. McMeeking, The 51st Annual Technical Conference of the Society of Engineering Sciences, West Lafayette, IN, October 2014.
17. Qi, Yue, "Predicting the transport properties of the solid electrolyte interphase (SEI) in Li-ion batteries," Paper presented at the MRS 2015 Spring Meeting, San Francisco, CA. April 2015.
18. Sheldon, Brian W., "Stress Evolution and Degradation Mechanisms in the Solid Electrolyte Interphase," Paper presented at the TMS Annual Meeting, Orlando, FL, March 2015.
19. Sheldon, Brian W., "Stress Evolution and Degradation Mechanisms in Energy Storage Materials," Paper presented at the École polytechnique fédérale de Lausanne, Lausanne, Switzerland, FL, June 2015.

## V.G.6 Predicting Microstructure and Performance for Optimal Cell Fabrication (BYU)

### Objectives

- This work uses microstructural modeling coupled with extensive experimental validation and diagnostics to understand and optimize fabrication processes for composite particle-based electrodes. The first main outcome will be revolutionary methods to assess electronic and ionic conductivities of porous electrodes attached to current collectors, including heterogeneities and anisotropic effects. The second main outcome is a particle-dynamics model parameterized with fundamental physical properties that can predict electrode morphology and transport pathways resulting from particular fabrication steps. These two outcomes will enable the third, which is an understanding of the effects of processing conditions on microscopic and macroscopic properties of electrodes.

### Project Details

**Dean Wheeler (Brigham Young University - PI)**  
Department of Chemical Engineering  
350 Clyde Building  
Provo, UT 84602  
Phone: 801-422-4126; Fax: 801-422-0151  
E-mail: [dean\\_wheeler@byu.edu](mailto:dean_wheeler@byu.edu)

**Brian Mazzeo (Brigham Young University - Co-PI)**  
459 Clyde Building  
Provo, UT 84602  
Phone: 801-422-1240; Fax: 801-422-0201  
E-mail: [bmazzeo@byu.edu](mailto:bmazzeo@byu.edu)

Start Date: October 2012  
Projected End Date: September 2016

### Technical Barriers

- In order for EVs to achieve mass adoption and make a significant dent in U.S and global CO<sub>2</sub> production, the key problems of driving range per charge & cost per kWh must be addressed.  
Barriers addressed:
  - Cell performance: 200 Wh/kg (EV requirement).
  - Life: 3000 cycles (PHEV 40 miles requirement).
  - Calendar life: 15 years
  - Cost: High \$/kWh.

### Technical Targets

- Develop rapid and reliable tools for measuring and predicting electronic and ionic conductivities and 3D microstructures of particle-based electrodes.
- Understand tradeoffs and relationships between fabrication parameters and cell performance.

### Accomplishments

- Developed localized ionic conductivity probe and demonstrated method by testing two candidate electrode materials.
- Used dynamic particle-packing (DPP) model to predict electrode morphology of Toda 523 material.
- Developed fabrication process of micro-N-line probe and demonstrated method by testing two candidate electrode materials.
- Two electronic conductivity probes and the associated computer code were sold to A123 for their use in improving the quality of their electrode fabrication process.

### Introduction

One problem with large-format batteries is ensuring uniformity in the manufacturing process, so that all components perform equally well and no component contributes unduly to performance limitations and failure.

This improvement in manufacturing will not be possible without additional information on the nature of heterogeneities and how they relate to electrode fabrication steps. Even more beneficial is if the information is made available in a timely manner through the use of convenient and reliable experimental and modeling tools.

This work therefore addresses a longstanding unmet industry need to be able to conveniently quantify electronic and ionic conductivities of thin-film electrodes and current collector contact resistance—solving this problem will accelerate process improvement. Additionally, this work remedies our poor understanding of the influence of fabrication parameters on heterogeneities in microstructure, which affect cell energy, power, and cycle life.

## Approach

These objectives will be achieved by a hybrid approach consisting of both experimental and simulation components. These two aspects address fundamental understanding of electrode fabrication processes and their influence on performance.

- Construct novel micro-N-line surface probes that can sample local conductivity of intact battery electrodes. The method overcomes multiple problems with previous methods, allowing reliable measurements of:
  - Bulk film conductivity while electrode still attached to metallic current collector
  - Contact resistance to current collector
  - Effects of pressure and presence of electrolyte
  - Spatial variations and anisotropy
- Construct a particle-dynamics model that can predict electrode microstructure and conductive pathways. The model will uniquely:
  - Predict effects of fabrication variables (slurry composition, drying, calendering, etc.)
  - Be validated with extensive experiments
  - Be built on a nonproprietary software platform that is readily extensible

## Results

For FY2015 an aggressive effort was made to develop and demonstrate three new tools, two experimental and one theoretical. The intention was to prove the concept of the tools this year, then to refine the designs and apply them to multiple materials subsequent to this year. The following progress was achieved:

### Localized Ionic Conductivity Probe

The first activity of FY2015 was to extend the micro-four-line probe ( $\mu$ 4LP) apparatus to enable measurement of local effective ionic conductivity of thin-film battery electrodes. The intention is to create a method to measure ionic conductivity by pressing the probe against the surface of an intact electrode film and the introduction of an electrolyte containing a redox shuttle, which can flow ions between the probe lines and the sample. Work began on this milestone in June 2014, but progress has been more difficult than expected due to materials compatibility issues. In particular, the  $\mu$ m-thin metal lines of the probe tend to be damaged under the action of Faradaic reactions. While the associated This milestone, which was intended to show proof of concept, was completed, development of this technology will continue into FY2016 until the level of reliability is increased.

The current status is as follows. After extensive experimentation with different redox shuttle molecules, supporting electrolyte, and solvents, we have selected a suitable solution that enables current to be carried between the outer lines of the probe through the sample, without electrochemically altering the probe.

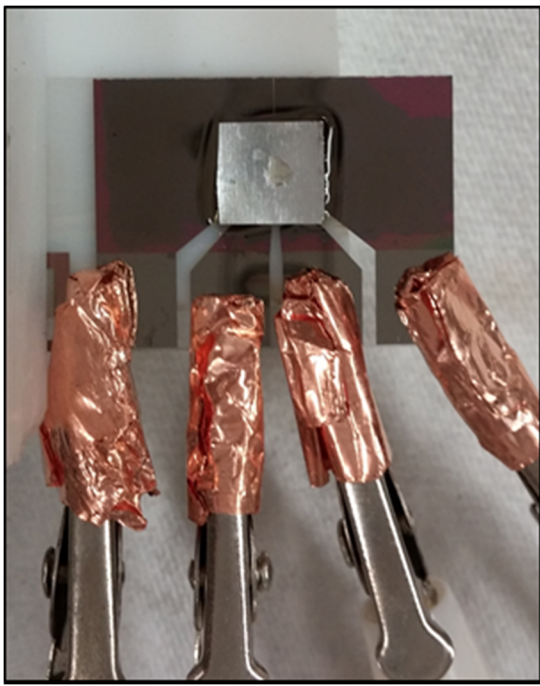


**Figure V- 204:** Micro-four-line-probe with electrode film sample on top. Sampling area for ionic conductivity is  $70 \times 500 \mu\text{m}$

tortuosity results. Thus, although the milestone is completed, the method is judged not to be of satisfactory reliability in its current state. In parallel with other efforts, work will continue on the ionic probe to obtain a more robust design and method.

Initial tests were completed with stacked disks of Celguard 2400 separator ( $25 \mu\text{m}$  thick) acting as a proxy for battery electrode films. Rings of Celguard were also used as spacers to allow a defined thickness of pure liquid electrolyte next to the probe surface. The disks or rings are placed on the surface along with electrolyte and an acrylic cover layer is added, squeezing out any excess liquid. A four-line DC experiment was conducted and an apparent resistance was determined for a sampling volume on the order of  $1-3 \mu\text{L}$ . This was converted to an effective ionic conductivity through use of a shape factor, computed using an algorithm developed previously for electronic conductivity measurements with the  $\mu$ 4LP. Measurements using the initial apparatus indicated that the conductivity of the electrolyte is  $38 \text{ mS/m}$  and of Celguard with electrolyte is  $7.5 \text{ mS/m}$ , which corresponds to a tortuosity of  $1.87$ . This is about  $40\%$  below expectation, based on earlier tortuosity experiments with Celguard 2400.

In subsequent work, six electrode films, two separators, and five probe designs were tested (See Figure V- 204 for an example of one such probe). These proof-of-concept experiments showed large uncertainties in the measurements, namely  $\pm 40\%$  from expected ionic

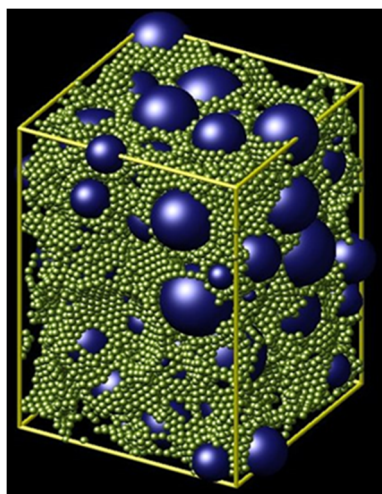


**Figure V- 205:** The DPP model uses superpositions of spheres to represent active material (blue) and carbon/ binder/solvent domains (green)

### Particle Dynamics Model

Under development for over one year, the dynamic particle packing (DPP) model is intended to predict liquid-slurry and dried-film properties from a simple set of input parameters, enabling electrode fabrication process optimization. The model imitates interactions between discrete mesoscale domains containing carbon, binder, solvent, and active materials (see Figure V- 205). The model is implemented in a free and widely available particle simulation platform called LAMMPS, which was built and is maintained by Sandia National Laboratory.

The DPP model has several key advances that allow practical and predictive simulations of the electrode fabrication process to be performed. A combination of about 1000 carbon black particles and associated binder into a homogenous particle (called CBD, for carbon binder domain) of size around  $1 \mu\text{m}$  makes it possible to simulate much larger length scales than previous particle-based models allowed, as shown in Figure V- 205.

The model generates structures from first principles, namely force interactions between the particles and solving Newton's law of motion. While this means the model is more likely to be able to predict structures for a variety of conditions, it also increases the difficulty of parameterizing the model due to the indirect connection between force parameters and the resulting volume-averaged physical properties. Extensive simulations using the BYU supercomputer were used to do this comparison and adjust inter-particle force parameters. An example of the parameterization process is shown in Figure V- 206.

For FY2015 the model was initially tested and validated by comparing to structures and other physical properties of cathode films made from Toda 523 active material, chosen for its spheroidal shapes. At present the simulations have shown remarkable agreement with the following experimental properties measured at BYU: shear-dependent slurry viscosity (See Figure V- 207), volume change upon film drying, solid film elasticity, and solid microstructure (see Figure V- 208). Efforts to validate the model showed that it can predict behavior on length scales not matched by other existing models, has significant agreement with multiple types of experiments, and therefore is likely to become an extremely valuable tool in the battery modeling community. A "Go" decision to continue developing the model was made as part of the milestone in September 2015.

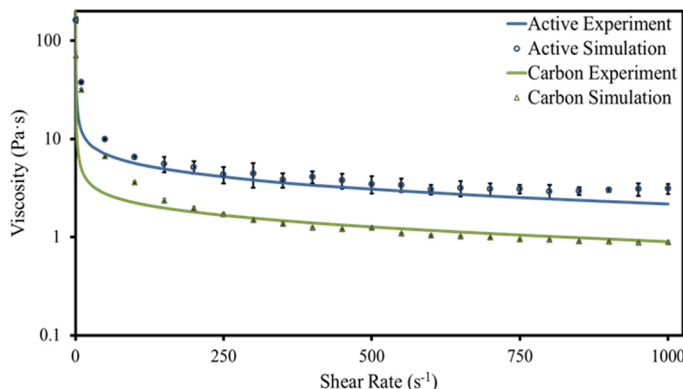


**Figure V- 207:** Viscosity at different shear rates for slurry containing carbon black and binder (green), and for slurry that additionally includes active material (blue), from experiment (line) and simulation (symbols). In some cases error bars are smaller than symbol sizes. Lines are used for experiments due to the close spacing of the data

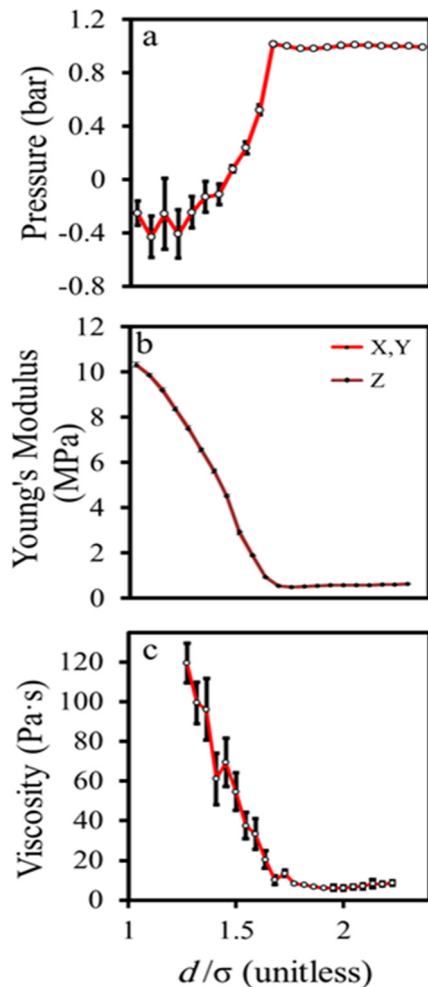


**Figure V- 206:** The effect of changing granular diameter ( $d/\sigma$ ) of CBD particles on simulated properties, while holding other parameters and box volume constant: (a) pressure, (b) elasticity, and (c) viscosity. Error bars (some smaller than symbol size) show 95% confidence intervals from multiple simulations. Lines are a guide to the eye

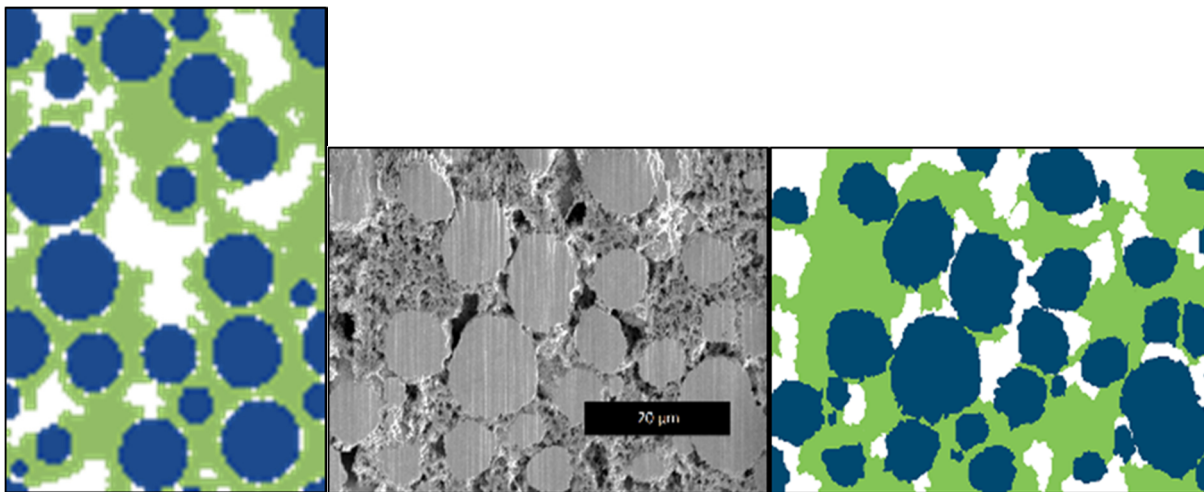


Figure V- 208: Simulated cross section of cathode (left) compared to experimental results. The SEM/FIB image (center) is segmented (right) using computer tools developed at BYU

#### N-line Conductivity Probe

The third major activity of FY2015 was to extend and adapt the micro-four-line probe ( $\mu$ 4LP) apparatus to measure anisotropic electronic conductivity of thin-film battery electrodes. In other words, the apparatus must determine three separate conductive parameters:  $\sigma_x$ ,  $\sigma_y$ , and  $R_c''$ , where  $x$  is an in-plane direction,  $y$  is the out-of-plane direction, and  $R_c''$  is a contact resistance at the current collector. This requires a minimum of three orthogonal experiments completed on a particular volume of the sample. These experiments are made possible with a new micro-six-line probe developed in our group, as shown in Figure V- 209.

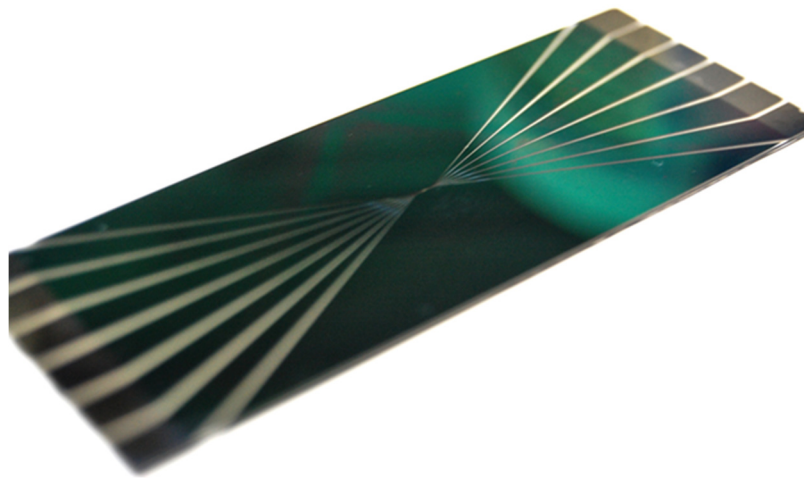


Figure V- 209: Photograph of new 6-line probe, showing dual sets of external connections on the edges of the probe, converging to a  $\mu\text{m}$ -scale sampling region in the center. The probe is mounted in a computer-controlled xyz stage

With the ability to connect to six lines plus the current collector, the user can choose one pair of connections to deliver a perturbing current and another pair of connections to measure an imposed voltage difference, enabling current to flow in different directions. For the initial design, the sampling window of the new six-line probe was similar in dimensions to the old one, namely  $130 \mu\text{m} \times 500 \mu\text{m}$ . To independently and rapidly access each connection on the probe, a computer-controlled multiplexer based on solid-state relays was incorporated into the apparatus.

As before, a detailed computer

model is required in order to invert the experiments and compute the conductive properties. Significant effort was expended to upgrade the model to make it faster, to make it compatible with the six-line-probe, and to incorporate anisotropy.

The probe and inversion routine were tested on two electrode sample films. Both samples in this initial stage were Toda NCM 523 cathodes prepared at Argonne National Lab. A total of six locations were tested on the two films. The average degree of anisotropy was determined to be  $\sigma_x/\sigma_y = 2.9 \pm 0.7$ , though wide variations in this ratio were observed, ranging from 2 to 7. A large part of the variations are likely due to measurement

uncertainty, which will be reduced by optimizing the measurement protocol and weighting factors used in the model. These conductivity results are consistent with the DPP2 model, which suggests an anisotropic conductivity ratio of around 2. This means that conductivity in the out-of-plane direction, which is most needed for electron transport during battery operation, is significantly lower than the in-plane conductivity. This suggests an opportunity for electrode improvement.

### Conclusions and Future Directions

A new surface probe has been developed that can accurately measure conductive properties of intact battery electrodes. Measuring conductivity of intact thin-film electrodes (still attached to metallic current collector) is difficult, and prior methods have not been sufficiently accurate and robust. The new method overcomes these problems and allows simultaneous measurement of two critical properties: bulk film conductivity and contact resistance between the film and the current collector.

In this fiscal year, the probe was extended from 4 lines to 6 lines, opening up the possibility of measuring anisotropic conductivity and providing for additional internal validation of the results. Preliminary work was completed to extend the local measurements to include effective ionic conductivity as well as electronic conductivity. Additional work is required in the upcoming year to make these measurements more reliable and repeatable.

The probe devices are fabricated using semiconductor clean-room techniques. A computer model is used to rapidly interpret the experimental results. The computer model has been incrementally improved, increasing speed of computation and the ability to handle the anisotropic case. A computer-controlled fixture allows the probe to be scanned across the surface of an electrode sample, allowing a local conductivity map to be created. This work has improved understanding of material heterogeneities across thin-film electrodes for Li-ion batteries. In effect, “hot” and “cold” conductivity spots can be identified so that electrode process quality can be improved. One surprising observation was the large degree of conductivity variability, on a millimeter length scale, of commercial-grade electrodes. This likely means that conductivity must currently be “overdesigned” to account for poor performance in some regions of the electrode. Overdesigning for conductivity means that other desirable properties, such as energy density, are sacrificed. In FY 2016 and 2017 this project will more fully examine how those variations change for different electrodes and can lead to performance problems. This will be done by performing measurements on additional materials provided by other battery researchers and by connecting the measured and predicted properties to cell performance models.

### FY 2015 Publications/Presentations

1. Peterson, S. W. and D.R. Wheeler, “Direct measurement of effective electronic transport in porous Li-ion electrodes,” *J. Electrochem. Soc.* 161 (2014): A2175-A2181.
2. Chao, C.-W., D. Bustamante, W. Lange, M.M. Forouzan, B.A. Mazzeo, and D.R. Wheeler, “Dynamic particle packing model for simulating electrode microstructure,” Paper presented at the 2014 MRS Fall Meeting, Boston, MA, November 2014.
3. Cutler, A.D., D.V. Clement, N.S. Gates, J. Flygare, J. Vogel, J.S. Sedgwick, B.A. Mazzeo, and D.R. Wheeler, “Micro-four-line probe for determining spatial conductivity distributions in thin-film battery electrodes,” Paper presented at the 2014 MRS Fall Meeting, Boston, MA, November 2014.
4. Zielke, L., T. Hutzelaub, D.R. Wheeler, C.-W. Chao, I. Manke, A. Hilger, N. Paust, R. Zengerle, and S. Thiele, “Three-phase multiscale modeling of a LiCoO<sub>2</sub> cathode: Combining the advantages of FIB-SEM imaging and X-ray tomography,” *Adv. Energy Mater.* 5, no.5 (2015): 1401612.
5. Monroe, C.W., D.R. Wheeler, and J. Newman, “Nonequilibrium linear response theory: Application to Onsager-Stefan-Maxwell diffusion,” *Indust. Eng. Chem. Res.*, 54, no. 16 (2015): 4460-4467.
6. “Predicting Microstructure and Performance for Optimal Cell Fabrication”, ES220\_Wheeler\_2015\_o, US DOE Vehicle Technologies AMR, 2015.
7. Forouzan, M.M., C.-W. Chao, D. Bustamante, W. Lange, B.A. Mazzeo, and D.R. Wheeler, “Predictive particle-based simulation of the fabrication of Li-ion battery electrodes,” Paper presented at the 227th Meeting of the Electrochemical Society, Chicago, IL, May 2015.
8. Zielke, L., T. Hutzelaub, D.R. Wheeler, C.-W. Chao, I. Manke, A. Hilger, N. Paust, R. Zengerle, and S. Thiele, “Modeling the missing carbon phase in X-ray tomographic reconstructions of a metal-based

- battery cathode," Paper presented at the 12th Symposium on Fuel Cell and Battery Modeling and Experimental Validation (ModVal 12), Freiburg, Germany, March 2015.
- 9. Lanterman, B.J., A.A. Riet, N.S. Gates, J.D. Flygare, A.D. Cutler, J.E. Vogel, D.R. Wheeler, and B.A. Mazzeo, "Micro-four-line probe to measure electronic conductivity and contact resistance of thin-film battery electrodes," *J. Electrochem. Soc.*, 162, no. 10 (2015): A2145-A2151.
  - 10. Flygare, J.D., A.A. Riet, B.A. Mazzeo, and D.R. Wheeler, "Mathematical model of four-line probe to determine conductive properties of thin-film battery electrodes," *J. Electrochem. Soc.*, 162, no. 10 (2015): A2136-A2144.
  - 11. Vierrath, S., L. Zielke, R. Moroni, A. Mondon, D.R. Wheeler, R. Zengerle, and S. Thiele, "Morphology of nanoporous carbon-binder domains in Li-ion batteries - A FIB-SEM study," *Electrochem. Comm.* 60 (2015): 176-179.

## V.H Metallic Lithium and Solid Electrolytes

### V.H.1 Mechanical Properties at the Protected Lithium Interface (ORNL)

#### Objectives

- This project will develop the understanding of the Li metal-solid electrolyte interface through state of the art mechanical nanoindentation methods coupled with solid electrolyte fabrication and electrochemical cycling. Our goal is to provide the critical information that will enable transformative insights into the complex coupling between the microstructure, its defects and the mechanical behavior of Li metal anodes. Work will progress from the study of the component materials toward study of the electrode assembly during electrochemical cycling of the anode. We hope to capture the formation and annealing of defects in the lithium and correlate this with the properties of the solid electrolyte and the interface.

#### Technical Barriers

- Metallic lithium cannot be used as an energy dense anode due to instability and/or high resistance at the interface of lithium metal with various solid electrolytes. This prohibits the use of the metallic anode for high energy dense devices. A deeper analysis of the degradation processes is needed to meet target level performance for EV batteries.
- Cycle life: poor cycle life and calendar life, increasing resistance of Li interface
- Energy density: poor due to thick electrolyte and excess lithium
- Power performance: poor due to interface resistance
- Safety: poor because of roughening of Li

#### Technical Targets

- A detailed characterization of the mechanical properties of several different solid electrolytes and metallic lithium prepared for battery anodes, with particular attention to uniformity of the properties.
- Determination of how the mechanical properties related to the micro- and defect-structure at the solid electrolyte – lithium interface evolve during electrochemical cycling of the Li metal anode.
- New information leading to an understanding of how mechanical stresses and inhomogeneities of the materials and interface impact degradation and failure of the solid electrolyte to stop the formation of lithium dendrites that short circuit the battery.

#### Project Details

**Tien Duong (DOE BMR Program Manager)**

Recipient: ORNL

**Nancy Dudney (PI, ORNL)**

Oak Ridge National Laboratory  
Materials Science and Technology Division

Oak Ridge, TN 37831

Phone: 865-576-4874

E-mail: [dudneynj@ornl.gov](mailto:dudneynj@ornl.gov)

Subcontractors:

**Erik Herbert**, Michigan Technological University  
Materials Science and Engineering  
Houghton, MI  
Phone: 865-566-7035  
E-mail: [eherbert@mtu.edu](mailto:eherbert@mtu.edu)

**Jeff Sakamoto** University of Michigan

Materials Science and Engineering  
Ann Arbor, MI  
Phone: 734-769-2213  
E-mail: [jeffsaka@umich.edu](mailto:jeffsaka@umich.edu)

Start Date: January 2015

Projected End Date: December 2017

## Accomplishments

- Nano-indentation maps with many hundreds of individual points have been collected and statistically analyzed for several promising ceramic solid electrolytes. Intent of the mapping is to identify variation associated with grain boundaries, pores, grain orientations and second phases across the surfaces.
- Using this mapping for commercial electrolytes, glass ceramic plates from Ohara Corp. were found to be more uniform across the surface compared to the Ohara's sintered polycrystalline ceramic plates of similar composition.
- Mapping of an alternative solid electrolyte, LLZO fabricated at University of Michigan, has been studied for different dopant composition, density, grain size and surface preparation. Initial studies showed a high variability of the mechanical properties along the surface. This narrowed greatly as sample preparation improved.
- The capability to use nano-indentation for samples within a glovebox, without extreme measures to eliminate sources of vibration and temperature variation has been demonstrated.
- For lithium metal, several preliminary indentation studies with vapor deposited films, air reacted and freshly rolled surfaces. Due to the plasticity, there is a significant strain rate dependence that requires further study and modified samples. This is the first time that the mechanical properties of thin lithium needed for batteries has been studied.
- For the LLZO electrolytes, we also utilize acoustic impulse excitation to determine the change in mechanical properties during lithium cycling. At this time it appears that crack formation preceeds the formation of Li dendrite shorts.

---

## Introduction

Instability and/or high resistance at the interface of lithium metal with various solid electrolytes limit the use of the metallic anode for batteries with high energy density batteries, such as Li-air and Li-S. To date there are no examples of robust materials and architectures that realize highly efficient cycling of metallic lithium anodes for a lifetime of 1000 cycles due to degradation of the Li-electrolyte interface or failure of the solid electrolyte. A much deeper analysis of these degradation processes are needed, so that materials can be engineered to fulfill the target level of performance for EV, namely 1000 cycles and a 15 year lifetime, with adequate pulse power.

Projecting the performance required in terms of just the Li anode, this requires a high rate of lithium deposition and stripping reactions, specifically about  $40\mu\text{m}$  Li per cycle, with pulse rates up to 10 and 20 nm/s charge and discharge, respectively. This is a conservative estimate, yet daunting in the total mass and rate of material transport. While such cycling is achieved for state-of-the-art batteries using *molten* Na in Na-S and zebra cells, solid Na and Li anodes are proving more difficult, except in special cases such as thin film batteries. With a variety of promising Li solid electrolytes available, now is the time to address this shortcoming so that solid metal anodes can be used to realize breakthroughs in chemistry and safety that move beyond Li-ion.

Mechanical properties studies through state of the art nanoindentation techniques will be used to probe the surface properties of the solid electrolyte and the changes to the lithium that result from prolonged electrodeposition and dissolution at the interface. An understanding of the degradation processes will guide future electrolyte and anode designs for robust performance.

## Approach

Mechanical properties studies through state-of-the-art nanoindentation techniques will be used to probe the surface properties of the solid electrolyte and the changes to the lithium that result from prolonged electrodeposition and dissolution at the interface. An understanding of the degradation processes will guide future electrolyte and anode designs for robust performance. In the first year, the team will address the two critical and poorly understood aspects of the protected Li metal anode assembly: (1) the mechanical properties of the solid electrolyte and (2) the morphology of the cycled Li metal. Candidate solid electrolytes include ceramic and glass-ceramic materials, nominally lithium aluminum titanium phosphate (LATP) from Ohara Corp., lithium lanthanum zirconate with a garnet structure fabricated at UM, and Lipon thin film glass electrolyte fabricated at ORNL. Metallic lithium materials include commercial ribbons and vapor deposited

thin films. In addition to the nano-indentation, the scope was expanded to include acoustic pulse echo measurements during the dc cycling of the lithium.

## Results

This first year was devoted to the mechanical properties of the lithium metal and solid electrolytes as independent samples.

Rapid mapping of the mechanical properties was achieved using nano-indenters and control software developed by NanoMechanics (Oak Ridge, TN). Using a flip stage, this can be done in a glovebox so that the surface can be protected from air exposure.

### Ohara solid electrolytes

Nanoindentation mapping was completed for several pristine ceramic electrolyte samples, including: our ceramic garnet samples, Ohara's polished glass ceramic electrolyte and Ohara's sintered ceramic. The Ohara materials were examined with only minor cleaning of the surface. The difference in the elastic modulus for the glass ceramic (black) and sintered (red) LATP electrolytes is shown in Figure V- 210. For each material we mapped 2 samples, at 100 points per sample. The difference is striking between the glass ceramic and the tape cast and sintered ceramic. The glass ceramic is much more uniform and slightly harder on average than the tape cast sintered body. But both greatly exceed values of the elastic modulus for lithium metal,  $E=11.1$  GPa from theory and 4.9-8 GPa from experiment.

### Metallic lithium

Initial nanoindentation studies of lithium metal were conducted in a glovebox. Samples included vapor deposited Li as well as commercial ribbons, rolled thin as is common for electrode fabrication.

Many samples were not adequate for mapping, requiring better flatness and cleanliness of the surface. Nevertheless, the fixture was set up and successfully operated in an inert atmosphere glove box. Being extremely plastic, the measurements of lithium require a low strain rate and hence thermal stability of the system may need attention. Figure V- 211 and Figure V- 212 illustrate results for thin film lithium on a glass substrate at high (blue) and low (green) strain rate. The strain was applied for 7s (blue) and 32s (green) followed by a 40s hold. During the hold, there is substantially more creep induced by the higher strain rate. The phase angle for the 100Hz modulation, which is an indication of energy dissipation, is surprisingly high for both tests. Rough values for the elastic modulus and hardness agree with values reported in the literature, but more analysis is required. Continuing work will examine thicker films on different substrates, as well as rolled and commercial foils.

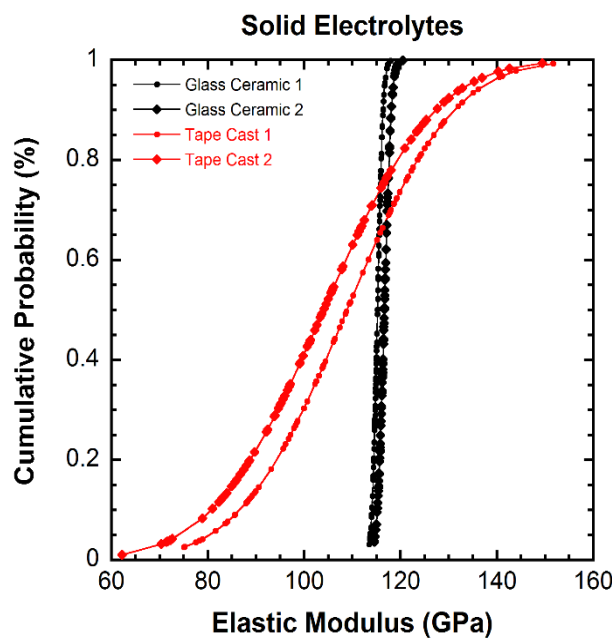


Figure V- 210: Modulus determined from many nanoindentations. Materials are from Ohara

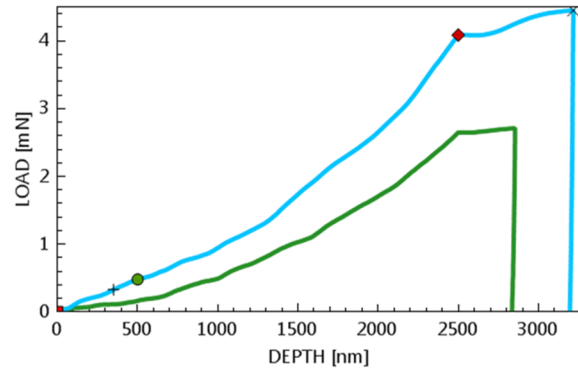


Figure V- 211: Indentation of a  $3\mu\text{m}$  thick Li film at strain rates of  $1/\text{s}$  and  $0.1/\text{s}$ , blue and green respectively

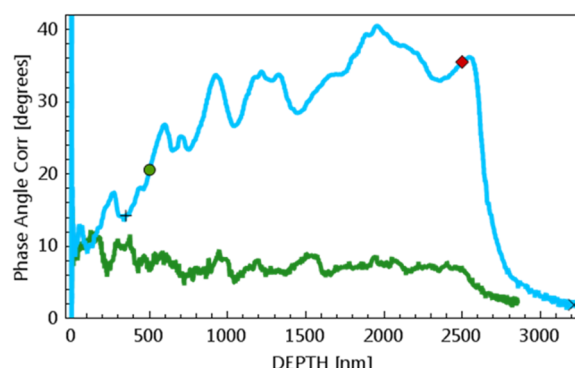


Figure V- 212: Phase angle for  $100\text{Hz}$  modulation corresponding to the indentation tests at left

### Hot pressed LLZO ceramic pellets.

Hot pressed lithium lanthanum zirconate (LLZO) ceramic disks were the most extensively studied to date in order to correlate the mechanical properties with the tendency of this material to form short circuits above a critical dc current density. Samples of LLZO included those with different Al or Ta dopant concentrations, those with different surface preparations, different bulk densities, and before versus after cycling to failure. The nanoindentation results were then compared to pulse echo measurements and theoretical predictions. See V.H.2 for the theory.

Cubic LLZO powder was prepared using solid state synthesis; the nominal composition being  $\text{Li}_7\text{La}_3\text{Zr}_2\text{O}_{12}$ . The powder was then densified using rapid induction hot pressing (RIHP) at  $1100^\circ\text{C}$ . Samples reached densities of 98.9% of theoretical and the transgranular fracture observed by SEM was evidence for a relatively high grain boundary adhesion. Also, there is no evidence of impurity phases.

The quality of the LLZO samples improved greatly between the initial and subsequent indentation studies 8 months later. Typical values for the elastic modulus and hardness of a 97% dense Ta doped sample early in the year were  $E = 141 \pm 15 \text{ GPa}$  and  $H = 8.3 \pm 1.6 \text{ GPa}$ . With improved fabrication, the distribution of values became much narrower for the indentation maps; for dense Ta doped samples we find  $E = 153.8 \pm 2.7 \text{ GPa}$  and  $G = 61.2 \pm 1.1 \text{ GPa}$ . Further, the depth profile of the modulus over  $\sim 500 \text{ nm}$  was very flat for the improved samples, as shown in Figure V- 213. In addition to the sample density, changes were made towards reducing the damage from the surface polishing, and eliminating air exposure that may lead to lithium carbonate and hydroxide at the surface.

Although much has improved since the initial studies of LLZO samples cycled to failure, it is illustrative to show how nanoindentation mapping may provide insight into the nature of the short circuit pathways. For lithium cycling, the surface of  $\sim 1\text{mm}$  thick LLZO pellet was dry-polished in an Ar glove box. The

LLZO pellet was then placed between two lithium foil disks under constant pressure (316 kPa). After preconditioning the interfaces by treating under pressure near the melting temperature, the dc cycling was tested at lower temperatures with a gradually increasing current density. While the cell potential remained stable and followed Ohmic behavior at low currents, at higher current densities, the cell voltage soon became erratic and dropped to nearly 0 V. When disassembled, black spots and lenticular shapes were found to have propagated from pellet face to pellet face. Rapid nanoindentation mapping of the cycled LLZO pellet was

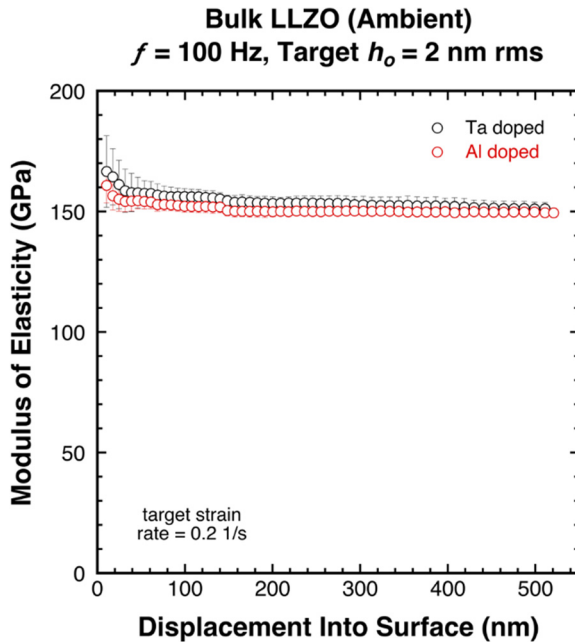


Figure V- 213: Modulus determined from nanoindentation

conducted, initially with the sample protected from air by mineral oil. The surface was mapped in numerous regions with a 10x10 point array at each. A statistically significant difference was found for regions near sites of the degradation forming the visible black features. While the average modulus was independent of the damage, the average hardness, as shown in Figure V- 214, was approximately 25% higher for the damaged regions.

An acoustic impulse excitation (pulse echo) method was developed to provide a real time, nondestructive indication of changes in the average elastic properties during lithium cycling. We observe that the onset of the short circuit is shortly preceded by a change in the wavespeed through the electrolyte. This test utilized a thick LLZO pellet with square cut walls. The acoustic transducers were positioned normal to the direction of the ion current. One result is shown as an example in Figure V- 215.

### Conclusions and Future Directions

In a short period of time, we show excellent capability for measuring the mechanical properties of solid electrolytes and lithium, both before/after cycling of the lithium and also during cycling. The acoustic technique is a promising addition to the program. Each of the solid electrolytes examined have sufficiently high shear modulus to, in principle, resist dendrite incursion, but some surfaces showed a 10% variation in the mechanical properties from point to point. Work suggests that this might be reduced with careful preparation of the ceramic surface. Future work will continue examination of the ceramic and glass electrolytes, while shifting emphasis toward the lithium metal.

Initially tests will examine the lithium before and after cycling, but the ultimate goal is real time studies to see the formation of defects under high current. Only with better understanding of the processes leading to degradation at the ceramic-lithium interface can we make changes to promote extended, safe and efficient cycling with the Li anode.

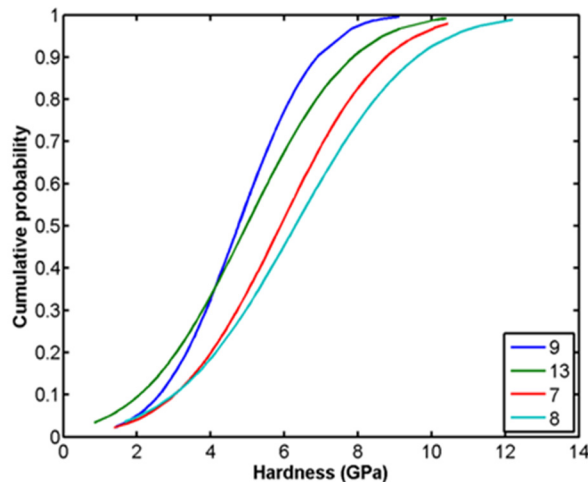


Figure V- 214: Cumulative hardness for selected maps. Areas 7 and 8 had visible dark areas; areas 9 and 13 were still white

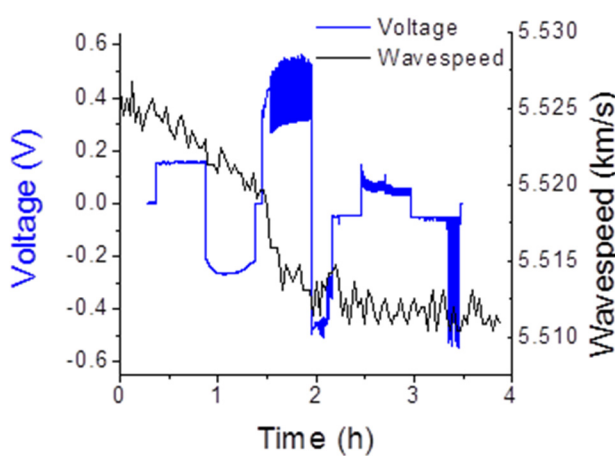


Figure V- 215: Correlation of the pulse echo wavespeed (black) with initiation of failure. The noise in the voltage precedes the eventual short where the voltage drops to zero. In this test, failure occurs at 0.1 and 0.2 mA/cm<sup>2</sup>

### FY 2015 Publications/Presentations

- Journal Article Submitted to *Chemistry of Materials*, “Elastic Properties of the Solid Electrolyte  $\text{Li}_7\text{La}_3\text{Zr}_2\text{O}_{12}$  (LLZO)” Seungho Yu, Robert D. Schmidt, Regina Garcia-Mendez, Erik Herbert, Nancy J. Dudney, Jeffrey B. Wolfenstine, Jeff Sakamoto, and Donald J. Siegel.

## V.H.2 Solid electrolytes for solid-state and lithium-sulfur batteries (University of Michigan)

### Objectives

- *Enable advanced Li-ion solid-state and lithium-sulfur EV batteries using LLZO solid-electrolyte membrane technology.* Owing to its combination of fast ion conductivity, stability, and high elastic modulus, LLZO exhibits promise as an advanced solid-state electrolyte. To demonstrate relevance in EV battery technology, several objectives must be met. First, LLZO membranes must withstand current densities approaching  $\sim 1 \text{ mA/cm}^2$  (commensurate with EV battery charging and discharging rates). Second, low area specific resistance (ASR) between Li and LLZO must be demonstrated to achieve cell impedance values comparable to conventional Li-ion technology ( $\sim 10 \text{ Ohms/cm}^2$ ). Third, low ASR and stability between LLZO and sulfur cathodes must be demonstrated.

### Technical Barriers

- Solid-state electrolytes could enable solid-state batteries to improve performance and safety compared to state-of-the-art batteries. However, the development of viable solid-state membrane technology for use with metallic Li anodes has been impeded by several challenges:
  - Manufacturing of thin membranes and integration of solid-electrolytes with electrodes
  - Demonstrating the electrochemical and mechanical stability against Li

### Technical Targets

- Demonstrate that a solid electrolyte can enable the stable cycling of Li anodes at  $1 \text{ mA/cm}^2$

### Accomplishments

- Demonstrated the ability to control the porosity of LLZO between 1 and 20 vol %. This will enable a study to correlate the maximum current density as a function of porosity.
- Demonstrated that controlling the surface chemistry of a solid electrolyte can reduce the Li-solid electrolyte interface resistance, thereby increasing the maximum current density.
- In collaboration with Task 7.1 (Nancy Dudney and Erik Herbert), the elastic properties of LLZO were determined both through computation and experiments. The values agree within  $\pm 5\%$ . The elastic properties will be used to better understand the role that mechanical properties play in governing the critical current density.

### Introduction

Going beyond Li-ion requires advanced anode, cathode, and electrolyte technology. In theory, the lithium-sulfur (Li-S) system offers over a six-fold increase in specific energy (2567 Wh/kg) compared to state-of-the-art (SOA) Li-ion (387 Wh/kg). However, the potential of the Li-S system has not been realized due to

### Project Details

#### Tien Duong (DOE BMR Program Manager)

Recipient: University of Michigan

#### Chris Johnson (NETL Program Manager)

DE-EE0006821 Recipient: University of Michigan

#### Jeff Sakamoto (University of Michigan – PI)

2350 Hayward Avenue

Ann Arbor, MI 48105

Phone: 734-769-2213

E-mail: [jeffsaka@umich.edu](mailto:jeffsaka@umich.edu)

Subcontractor:

Oak Ridge National Laboratory

Oak Ridge, TN

Subcontractor:

Army Research Laboratory

Adelphi, MD

Start Date: January 2015

Projected End Date: December 2017

electrolyte instabilities. First, other than Lipon, no electrolyte has demonstrated stability against metallic Li. Second, dissolution of Li-polysulfides in SOA liquid electrolytes results in passivation of the Li anode.

## Approach

Our effort will focus on the promising new electrolyte known as LLZO ( $\text{Li}_7\text{La}_3\text{Zr}_2\text{O}_{12}$ ). LLZO is the first bulk-scale ceramic electrolyte to simultaneously exhibit the favorable combination of high conductivity (~1 mS/cm at 298K), high shear modulus (61 GPa) to suppress Li dendrite penetration, and apparent electrochemical stability (0-6V vs Li/Li<sup>+</sup>). While these attributes are encouraging, additional R&D is needed to demonstrate that LLZO can tolerate current densities in excess of 1mA/cm<sup>2</sup>, thereby establishing its relevance for PHEV/EV applications. We hypothesize that defects and the polycrystalline nature of realistic LLZO membranes can limit the critical current density. However, the relative importance of the many possible defect types (porosity, grain boundaries, interfaces, surface & bulk impurities), and the mechanisms by which they impact current density, have not been identified. Using our experience with the synthesis and processing of LLZO (Sakamoto and Wolfenstine), combined with sophisticated materials characterization (Nanda), we will precisely control atomic and microstructural defects and correlate their concentration with the critical current density. These data will inform multi-scale computation models (Siegel and Monroe) which will isolate and quantify the role(s) that each defect plays in controlling the current density. By bridging the knowledge gap between composition, structure, and performance we will determine if LLZO can achieve the current densities required for vehicle applications.

## Results

### Correlating the porosity with current density

To correlate the effect of porosity on the critical current density (CCD) we demonstrated the ability to control the porosity between 1 and 20% in cubic LLZO pellets (Figure V- 216). Materials and mechanical behavior characterization is complete on these pellets and the electrochemical characterization and CCD will be measured in the next quarter. 97% relative density cycled and un-cycled LLZO pellets were also sent to ARL for atomic force microscopy measurements.

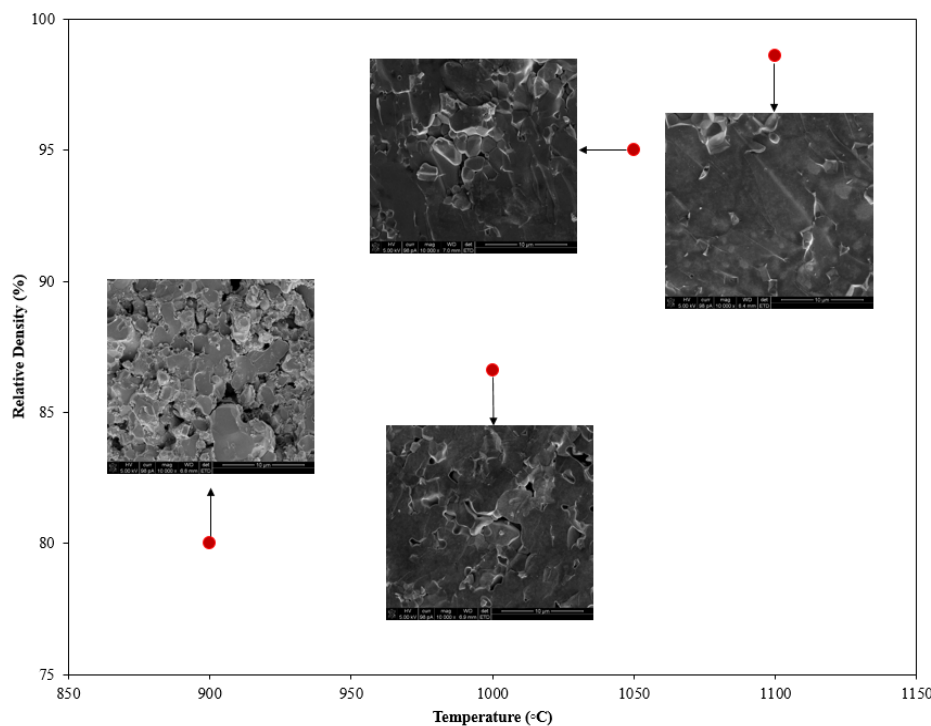


Figure V- 216: Secondary electron SEM images of LLZO fracture surfaces densified between 900 and 1100 C (10,000 X)

### Correlating surface preparation with current density

We successfully correlated the effect of surface contamination with the critical current density (CCD) (Figure V- 217). Using XPS, EIS, and computation analysis, it was determined that a surface treatment must be used to reduce the Li-LLZO interfacial resistance to increase the CCD.

The standard surface preparation, as described by Ren *et al.* [1] and Ishiguro *et al.* [2], typically results in a CCD of  $\sim 0.05 \text{ mA/cm}^2$ , which is comparable to the result in this work.

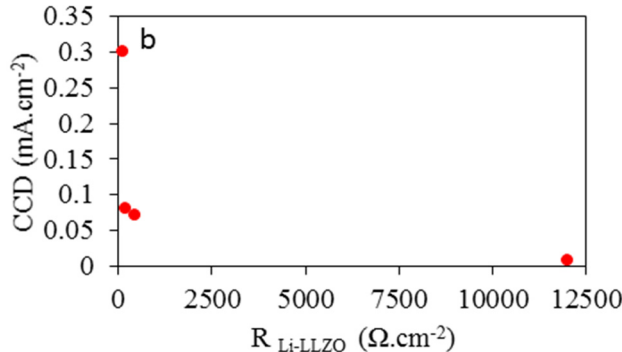


Figure V- 217: Critical current density as a function of the Li-LLZO interfacial resistance, which was controlled by the surface contamination

through the LLZO pellet, and Li-LLZO interface. The Li-LLZO interface resistance was determined by dividing the low frequency semicircle diameters by a factor of two since the cells employed two Li anodes. Using the typical surface treatment as described above, the R<sub>Li-LLZO</sub> is 514 Ohms cm<sup>-2</sup>, which is in excellent agreement with previous result from Ohta *et al.* (530 Ω.cm<sup>-2</sup>) [3]. Using the new surface treatment in this work, the R<sub>Li-LLZO</sub> was determined to be 181

$\Omega\text{.cm}^2$ . By correlating the CCD with R<sub>Li-LLZO</sub>, and achieving relatively low R<sub>Li-LLZO</sub> values, the project is now poised to further reduce R<sub>Li-LLZO</sub>, thus increasing the CCD. By lowering R<sub>Li-LLZO</sub> it is also believed that the role that microstructural defects play in controlling the CCD can now be studied in earnest.

Tracking progress towards the project goal of enabling a 1 mA/cm<sup>2</sup> Li-ion current density at 298 K, the CCD was increased from 0.05 to 0.3 mA/cm<sup>2</sup> after three quarters or work.

### Characterizing the elastic properties of LLZO

High ionic conductivity is a necessary, but not sufficient condition for a viable solid electrolyte: to enable use of a metallic lithium anode, the solid electrolyte must also be stiff enough to suppress Li dendrite formation

Figure V- 218 shows the progress toward reducing R<sub>Li-LLZO</sub> at room temperature. The R<sub>Li-LLZO</sub> was measured using EIS on Li-LLZO-Li cells. In Figure V- 218, the Nyquist plots compare the R<sub>Li-LLZO</sub> based on the surface preparation. The Nyquist plots consist of two distinct resistive components; one at relatively high frequencies between 7 MHz and 200 kHz (the Ohmic drop through the LLZO pellet) and a second in the lower frequency 200 kHz and 1 Hz region (the Li-LLZO interface). The electrochemical impedance spectroscopy (EIS) spectrums were modeled using an equivalent circuit to determine the separate resistive phenomena for Ohmic drop

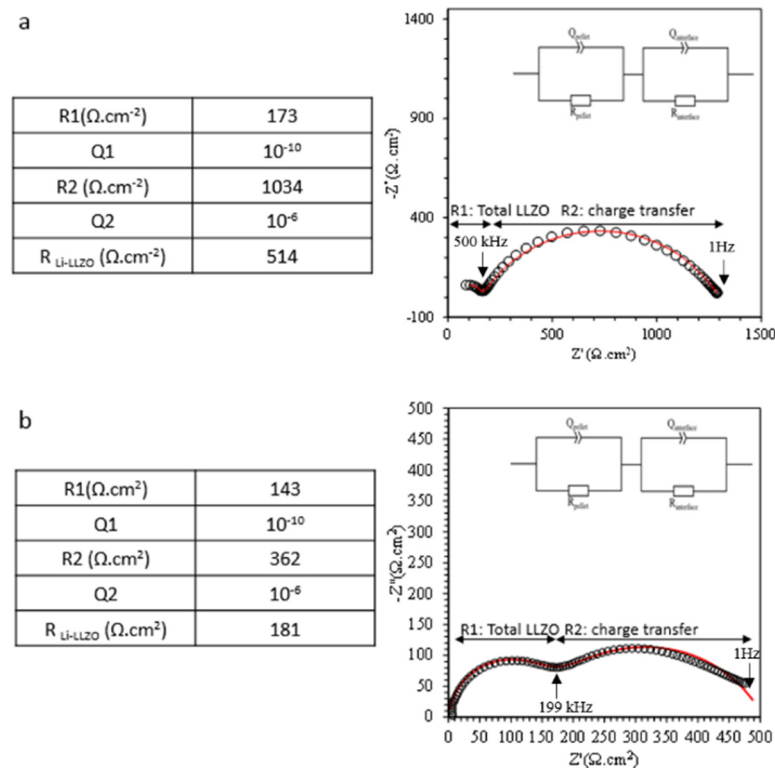


Figure V- 218: EIS data for Li-LLZO-Li cells using the standard surface preparation (a) and the new surface treatment (b)

during cycling. Consequently, the elastic properties of the solid electrolyte are a highly important – yet occasionally overlooked – feature in the design of all-solid-state batteries.

The Siegel, Sakamoto, Herbert, and Dudney Groups collaborated to study and compare, theoretically and experimentally, the elastic properties of the mos promising LLZO formulations.

The study examines the elastic properties of near theoretical density Al and Ta-doped LLZO using impulse excitation, nanoindentation, and density functional theory calculations.

The linear elasticity model of Monroe and Newman suggests that a solid electrolyte having a shear modulus greater than approximately 11 GPa can suppress dendrite formation on a Li anode. The present experiments and calculations yield an averaged shear moduli for Al and Ta-doped LLZO of 58-60 GPa, far exceeding the targeted value.

In addition to characterizing elastic moduli, calculations were also performed to evaluate the brittle/ductile nature of LLZO, and its degree of elastic anisotropy. The ratio of the bulk modulus to the shear modulus,  $B/G$ , indicates the ductile/brittle nature of a solid. According to Pugh's criterion, the critical  $B/G$  value for a transition from brittle to ductile behavior is 1.75. The calculated  $B/G$  values for Al and Ta-doped LLZO are 1.74 and 1.59, respectively, indicating that these compounds are intrinsically brittle, in agreement with fracture toughness data from the literature. Regarding anisotropy, the Zener anisotropy ratio,  $A$ , which describes the elastic anisotropy of a cubic crystal, was evaluated for both LLZO variants. In both cases the elastic properties were found to be relatively isotropic,  $A \approx 1$ , in agreement with other isotropic oxides such as NiO (1.45), and MgO (1.55).

## References

1. Y. Ren, Y. Shen, Y. Lin, C.-W. Nan, *Electrochemistry Communications*, 57 (2015) 27-30.
2. K. Ishiguro, Y. Nakata, M. Matsui, I. Uechi, Y. Takeda, O. Yamamoto, N. Imanishi, *Journal of The Electrochemical Society*, 160 (2013) A1690-A1693.
3. S. Ohta, T. Kobayashi, J. Seki, T. Asaoka, *Journal of Power Sources*, 202 (2012) 332-335.

## Conclusions and Future Directions

In summary, we have studied the effect of surface contamination & impurities of LLZO and the corresponding interfacial resistance (with Li-metal) that ultimately determines the CCD. To address this we have developed a surface treatment method and control the porosity that led to increase in CCD from 0.05 to 0.3 mA/cm<sup>2</sup>. Our next steps are aimed towards increasing the CCD to 1 mA/cm<sup>2</sup> and develop a fundamental understanding towards cell failure (cell shorting) when cycled at higher current density against Li metal. For this purpose, we will utilize advanced characterization methods such as XPS, Raman & electron microscopy in conjunction with multi-scale modeling to identify the key microstructural factors that can sustain higher CCD and stability with Li-metal.

## FY 2015 Publications/Presentations

1. Journal Article Submitted to *Chemistry of Materials*, "Elastic Properties of the Solid Electrolyte  $\text{Li}_7\text{La}_3\text{Zr}_2\text{O}_{12}$  (LLZO)" Seungho Yu, Robert D. Schmidt, Regina Garcia-Mendez, Erik Herbert, Nancy J. Dudney, Jeffrey B. Wolfenstine, Jeff Sakamoto, and Donald J. Siegel.
2. Jeff Sakamoto Moderated a Session at The Battery Show in Novi, MI "The Solid-State Revolution". Speakers from Toyota, Google, Samsung, and Intel participated.
3. Jeff Sakamoto presented at the University of Michigan Energy Institute's Battery Lab Opening Ceremony on October 2, 2015.

## V.H.3 Composite Electrolytes to Stabilize Metallic Lithium Anodes (ORNL)

### Objectives

- Prepare composites of representative polymer and ceramic electrolyte materials to achieve thin membranes which have the unique combination of electrochemical and mechanical properties required to stabilize the metallic lithium anode while providing for good power performance and long cycle life.
- Understand the lithium ion transport at the interface between polymer and ceramic solid electrolytes which is critical to the effective conductivity of the composite membrane.
- Identify key features of the composite composition, architecture and fabrication that optimize the performance and develop practical and scalable fabrication methods.

### Technical Barriers

- A stable lithium anode is critical to achieve high energy density batteries with excellent safety, lifetime and cycling efficiency. In order to match the capacity and performance of current Li-ion cathodes, cycling of the Li metal must meet the challenges listed in Table V- 5.
- To eliminate the need for large excess lithium in the cell expected to cycle 3000 times, the coulombic efficient must exceed 99.99% per cycle.
- This study will identify the key design strategies that should be used to prepare composite electrolytes to meet the challenging combination of physical and chemical and manufacturing requirements to protect and stabilize the lithium metal anode for advanced batteries.

### Project Details

**Tien Duong (DOE BMR Program Manager)**

Recipient: ORNL

**Nancy Dudney (PI, ORNL)**

Oak Ridge National Laboratory

Materials Science and Technology Division

Oak Ridge, TN 37831

Phone: 865-576-4874

E-mail: [dudneynj@ornl.gov](mailto:dudneynj@ornl.gov)

Start Date: October 2011

Projected End Date: September 2016

**Table V- 5: Lithium cycling requirements to match Li-ion cathodes**

Parameter/Requirement	
20-40 µm Li per cycle	no loss to reaction
10-20 nm/sec	no loss to physical isolation
3000 cycles	no roughening or dendrites

### Technical Targets

Success of our composite electrolyte will enable achievement of these DOE goals:

- Enable very high energy Li-S Battery (500 Wh/kg) by 2020 and Li-Air Battery (700 Wh/kg) by 2030
- Fully protect lithium anode for long cycle life (3000 to 5000 deep discharge cycles)
- Ensure lithium remains dense and free of dendrites (Safety)

### Accomplishments

- A subtle variation in processing conditions for composite electrolytes can profoundly alter the ionic conductivity of ceramic-polymer composites. This may well have been overlooked.
- Adsorption of some organic vapors and water can enhance  $\text{Li}^+$  ion transport in ceramic-polymer dispersed composites, multi-layers, and polymer electrolytes.
- Enhancement has been quantified for several different molecules, including dimethyl carbonate and water. Controlled exposure may be a new path to improve properties of composites.

- Demonstrated fabrication of thin electrolyte membranes using techniques that are practical for manufacturing, achieving a thin, dense membrane.

---

## Introduction

A stable lithium anode is critical to achieve high energy density with excellent safety, lifetime and cycling efficiency. This study will identify the key design strategies that should be used to prepare composite electrolytes to meet the challenging combination of physical and chemical and manufacturing requirements to protect and stabilize the lithium metal anode for advanced batteries. By utilizing well characterized and controlled component phases, the design rules developed for the composite structures will be generally applicable toward the substitution of alternative and improved solid electrolyte component phases as they become available. Success in this program will enable these specific DOE technical targets: 500-700Wh/kg, 3000-5000 deep discharge cycles, robust operation.

## Approach

This program seeks to develop practical solid electrolytes that will provide stable and long-lived protection for the lithium metal anode. Current electrolytes all have serious challenges when used alone: oxide ceramics are brittle, sulfide ceramics are air sensitive, polymers are too resistive and soft, and many electrolytes react with lithium and are prone to form lithium short circuits. Composites provide a clear route to address these issues. This program does not seek discovery of new electrolytes, rather the goal is to study combinations of current well known electrolytes. The program emphasizes the investigation of polymer-ceramic interfaces formed as bilayers and as simple composite mixtures where the effects of the interface properties can be readily isolated. In general, the ceramic phase is several orders of magnitude more conductive than the polymer electrolyte, and interfaces can contribute an additional source of resistance. Using finite element simulations as a guide, the composites fabricated in this work must have a large volume fraction, at least 50 vol.% of the conductive ceramic phase and ideally closer to 80 vol.%. This is the only way to achieve both a high elastic modulus and high ion conductivity for a typical polymer+Li salt matrix. Further, care is taken to control exposure to any sources of contamination that may alter the polymer and interface properties by preparing all composites under high purity Ar conditions. Promising compositions and architectures for the composites are fabricated and evaluated for lithium transport properties using AC impedance and DC cycling with lithium in symmetric or half cells. General design rules are determined that can be widely applied to other combinations of solid electrolytes.

## Results

During this year composites of polymer electrolyte and ceramic electrolyte powders have been prepared by several routes. By design, the particular electrolytes are nothing novel. The polymer is polyethylene oxide (PEO) with dissolved Li triflate salt (LiTf); the ceramic powders are from Ohara or are garnet powders of doped lithium lanthanum zirconate (LLZO) from Sakamoto's group. The composites have at least 40 vol.% of the inorganic, with a goal of much higher ceramic loading (~80v.%) to maximize the bulk modulus as well as ion transport. This is far higher than any other reports of dispersed ceramic polymer composites. Composites are largely prepared by melt pressing of the powder mixture. This ensures a totally solvent-free dry processing. While melt pressing has been used for membrane disks of 13mm and 29mm diameter, achieving uniform membranes that are both larger and thinner with high ceramic loading is challenging because the ceramic particles tend to jam rather than flow. Recent membranes prepared from slurries are proving to be attractive. The membrane shown in Figure V- 219 is 50 vol.% ceramic, 6 inches square and about 25  $\mu\text{m}$  thick. The fabrication can easily scale to larger areas and thickness with uniform distribution of submicron ceramic powder.



Figure V- 219: Composite membrane of 50vol.% Ohara glass ceramic powder and PEO+ LiTf salt (on blue background)

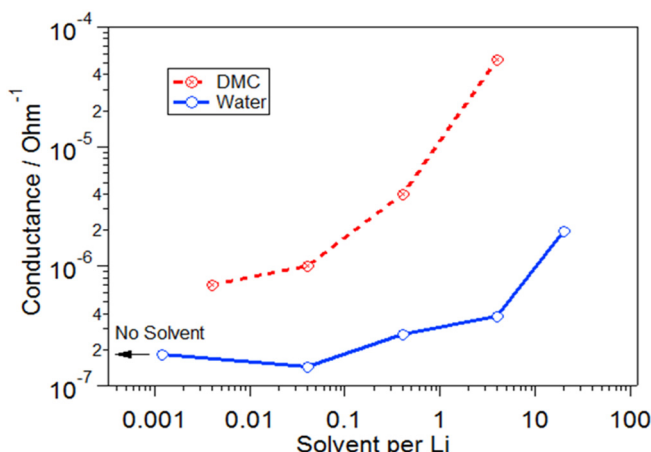


Figure V- 220: Relative conductance after overnight exposure to H<sub>2</sub>O or DMC vapor. Concentration indicates the maximum available quantity of the solvent

For studies of the ionic conductivity, the slurry derived composite membranes are carefully vacuum-dried to remove the solvent. We believe the solvents must be largely removed because the ionic conductivity is identical within experimental error to similar composites prepared by melt processing in a solvent-free Ar atmosphere. Examples of the conductivity for 50v.% ceramic are shown in Figure V- 220. The conductivity at room temperature is about 1 order of magnitude lower than the pure PEO+LiTf electrolyte without any ceramic. This is consistent with our earlier model calculations for the case where, due to a resistive polymer-ceramic interface, the highly conductive ceramic is not contributing to the ionic transport. As the composite relaxes, the conductivity decreases a bit more as the polymer crystallizes. Because determinations of the area-specific, polymer-ceramic interface resistivity is very high for different processing routes, different ceramic materials, and different composite structures, we believe that high resistance is intrinsic for this type of interface.

Our results have demonstrated that exposing the melt formed composites to vapors of various solvents can in some cases greatly enhance the ionic conductivities at low temperatures by several orders of magnitude. This is true upon exposure to water and dimethyl carbonate (DMC) vapor, for example. The enhanced conductivity is shown in Figure V- 221 for a 40v.% melt formed composite. The plot indicates a surprisingly large concentration of molecules relative to the Li; this represents the maximum that needs to be confirmed by further analytical analysis. The conductivity of pure, ceramic-free PEO+LiTf electrolyte is also enhanced by exposure to these solvents, but the effect is not as large as for the composite. This suggests that the molecules facilitate ionic motion across the ceramic-polymer interface so that the ceramic phase participates in the ion transport.

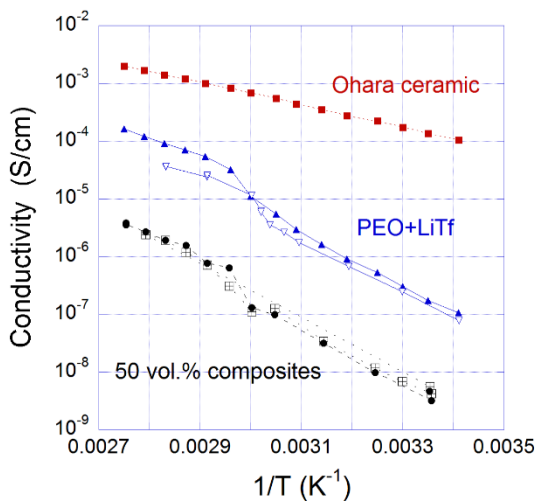


Figure V- 221: Conductivity of two different composite membranes compared to the pure components

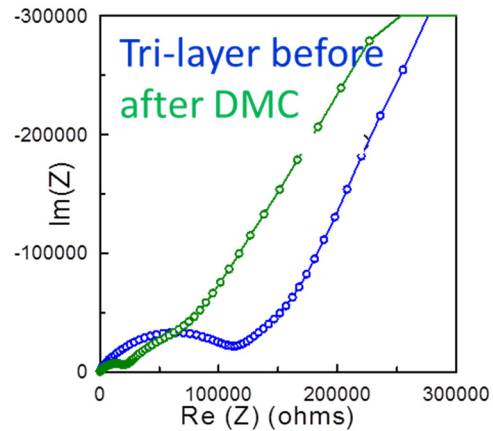


Figure V- 222: Electrochemical impedance of PEO+LiTf coated LLZO ceramic plate. Scans before and after exposure to DMC vapor at room temperature

The properties of the ceramic-polymer interface have also been resolved for a layered composite, generally fabricated as a ceramic electrolyte plate coated on both sides by a polymer electrolyte coating. When the polymer coating is very thin, the contribution of the interface is more easily resolved. One example is shown in Figure V- 222. This plot also shows that exposure to small amount of DMC vapor reduces the resistance of both the ceramic-polymer interface (mid frequency) and the bulk polymer (high frequency). The ceramic itself is too conductive to be resolved at less than 1 MHz.

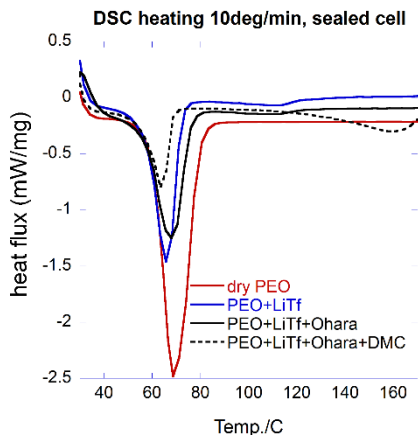


Figure V- 223: DSC scans for designated samples normalized by the total mass

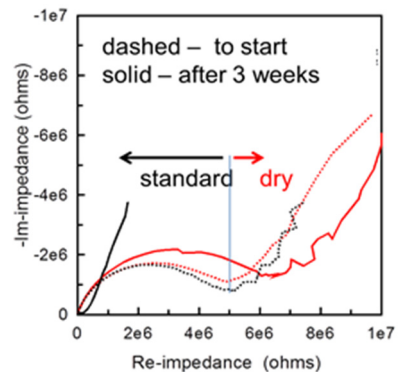


Figure V- 224: Time delayed increase in conductivity after exposure in standard or solvent-free gloveboxes

Figure V- 223 shows differential scanning calorimetry results for the pure polymer and several composites. Dispersed ceramic powders in a polymer are often referred to as a dry plasticizer, however here the dispersed Ohara ceramic powder (20 vol.%, 74 wt.%) has no effect to decrease the endotherm associated with the crystalline transition of the PEO. This further supports our belief that many other studies have unknowingly added a solvent contaminant, such as water, when fabricating polymer-ceramic composites. As shown in the figure, the addition of DMC has a much larger effect on the crystallization than the Ohara particles.

In the previous year, we discovered and reported that the composites are very sensitive to exposure to vapors in a standard glovebox with activated carbon filters used for work with common liquid electrolytes. Even when exposure was limited to just a few minutes, this had profound effect on the ionic conductivity of the composite. Interestingly, the effect was not immediate, but developed over 1-3 weeks as the conductivity increased 3-4 orders of magnitude. This is shown in Figure V- 224. Considerable effort has failed to identify the specific

contaminate(s) or process leading to this effect. It may, for example, be the gradual formation of effective percolation pathways through the composite. Samples were treated with all the solvents, electrolytes, and even water degraded electrolytes that were expected to be present in the glovebox atmosphere at one time or another. Further, gas samples were analyzed and the surface species of various materials from the box were characterized to identify other reaction products or contaminates. Results have been frustratingly inconclusive, yet understanding this effect may have important implications for processing and optimizing the composite electrolytes.

### **Conclusions and Future Directions**

In this year, new slurry processing methods for practical formation of large-area composite membranes with high ceramic loading have been demonstrated. When these membranes are well dried, the conductivities were the same as composites prepared under solvent-free conditions, so the effect of residual trace solvent is minimal. Exposure of the composites and polymer electrolytes to DMC and water vapors enhance the ionic conductivity of the bulk polymer electrolyte and suppress the PEO crystallization. More importantly, these molecules also enhance the ceramic-polymer interface conductance to give a higher and more uniform ion transport across the interfaces and throughout the dispersed particle composite with high ceramic loading. In future work, the alternative slurry processing will be further developed, hopefully achieving a significantly higher ceramic loading with a low ceramic-polymer interface resistance. The sandwich polymer-ceramic samples will be particularly useful for fundamental interface characterizations. Work will continue to try to identify a solvent or additive that promotes the conductivity, but can be stabilized or passivated against the metallic lithium anode. This may eliminate the need for a protective barrier coating, such as Lipon, to stabilize this interface, although achieving uniform plating and striping of the lithium at high rates may require a homogeneous, single-phase interface layer.

### **FY 2015 Publications/Presentations**

1. "Solid Electrolytes for High Energy Density Batteries" Nancy Dudney, Sergiy Kalnaus, and Jeff Sakamoto, Advanced Automotive Battery Conference (AABC), Detroit, June 2015, invited presentation.
2. "Composite Eletrolyte to Stabilize Metallic Lithium Anodes" Nancy Dudney, Annual Merit Review, Washington, DC, June 2015
3. "Designing Solid Polymer Composite Electrolytes for Facile Lithium Transport and Mechanical Strength", Wyatt E. Tenhaeff and Sergiy Kalnaus, Chapter 7, p235, in Handbook of Solid State Batteries, 2<sup>nd</sup> edition, edited by Nancy J. Dudney, William E. West, and Jagjit Nanda, World Scientific Publishing, 2015.

## V.H.4 Overcoming Interfacial Impedance in Solid-State Batteries (University of Maryland)

### Objectives

- Develop a multifaceted and integrated experimental and computational approach to solve the key issue in solid-state Li-ion batteries (SSLiBs), interfacial impedance. Will focus on Garnet-based solid-state electrolytes (SSEs), but the knowledge can be applied to other SSE chemistries. The interfacial impedance in this proposal includes charge transfer, ionic and electronic transport, and interfacial structural/chemical stability over charge-discharge cycling.

### Technical Barriers

- In order to obtain low interfacial impedance solid state batteries, the following technical barriers must be overcome:
- Low specific interfacial area of typical planar solid electrolyte designs.
- Nonconformal electrode-electrolyte interfaces resulting in physical gaps/pores between layers.
- Formation of high impedance interfacial phases during electrolyte/electrode processing.
- Mechanical degradation of interface with electrochemical charge/discharge cycles.

### Technical Targets

- Develop fundamental (computational and experimental) understanding of solid-solid interfacial impedance.
- Develop conformable interfacial layers with 0V to 4.2V stability and  $\leq 100 \Omega \text{ cm}^2$  ASR.
- Demonstrate low anode-electrolyte and cathode-electrolyte interfacial impedances of  $\sim 10 \Omega \text{ cm}^2$ .
- Demonstrate low interfacial impedance in two solid-state battery testbed chemistries:
- Testbed 1: Solid state Li-NMC battery, 350-450 Wh/kg, 200 cycles;
- Testbed 2: Solid state Li-S battery, 350-450 Wh/kg, 200 cycles.

### Accomplishments

- Developed computational models for garnet based interfaces.
- Characterized the interfacial impedance of garnet and LFMO electrodes by EIS.
- Demonstrated that 3D structures on the garnet surface can reduce the interfacial impedance.
- Unflammable PFPE solvent was prepared and PFPE/LiTFSI electrolyte was demonstrated to be electrochemically stable in the voltage region of 0-4.2V providing potential conformable low impedance interfacial layer.
- PVDF-HFP gel membrane was prepared and the stability and impedance of ionic liquid electrolyte in this gel membrane demonstrated, thus providing potential conformable low impedance interfacial layer.

### Introduction

Solid state garnet-electrolyte lithium ion batteries have tremendous potential due to their inherent safety, high voltage stability, and reasonably high conductivity. However, the interfacial impedance between solid state electrolytes and electrode is currently too high. This work will focus on reducing the interfacial impedance, by making controlled structures on the garnet electrolyte surface, and introducing conductive and conformal

#### Project Details

**Christopher Johnson (NETL Program Manager)**  
DE-EE0006860 Recipient: University of Maryland

**Eric Wachsman (University of Maryland - PI)**  
1206 Engineering Laboratory Building  
University of Maryland  
College Park, MD 20742  
Phone: 301-405-8193  
E-mail: [ewach@umd.edu](mailto:ewach@umd.edu)

Start Date: October 2014

Projected End Date: September 2017

interfacial layers between the garnet and the electrodes. These results will address the primary issue and significantly advance solid-state Li-battery technology.

### **Approach**

**Innovative Approach:** The objectives outlined above will be accomplished by optimizing the garnet surface structure and electrode material, and investigating high conductivity conformal interfacial layers.

#### **Effect of Interfacial Structure on Impedance**

While we and others have made tremendous advances in understanding interfacial resistance in solid oxide fuel cells (SOFCs), to date no one has applied these techniques to SSLiBs. Therefore, we use SOFC techniques to develop a fundamental understanding of interfacial impedance in terms of intrinsic charge transfer rates, ionic and electronic transport, and effect of interfacial structure.

Electrochemical impedance spectroscopy (EIS) of solid electrolyte and electrode or interfacial layer pellets are being performed to identify the mechanistic frequency dependence of EIS response for each material as well as blocking electrode and DC measurements to separate out ionic vs. electronic conductivity for each material. Then bilayer electrolyte and electrode/interfacial layer pellets with smooth and controlled interfaces are being fabricated and tested with EIS.

This allows for determination of the specific interfacial impedance, as it will be resolved as an additional EIS frequency response. This interfacial impedance is then being used to calculate the charge transfer reaction rate across the electrolyte/electrode and electrolyte/interfacial layer interfaces. Bilayered pellets with tailored nano/micro-rod interfaces has been fabricated (by templated deposition and additive manufacturing) with different rod length to diameter aspect ratios. The EIS data from these cells is deconvoluted and compared with known ionic and electronic transport rates, and charge transfer rates, to create fundamental models of interfacial impedance as a function of 3-dimensional interfacial structure.

#### **Investigate Interfacial Modifications and Cell Performance**

We are investigating two types of materials as interfacial layers in SSLiBs.

For Type 1, we use nonflammable organic electrolytes such as perfluoropolyethers (PFPE) based electrolytes. It has been confirmed that such organic electrolytes cannot catch fire and are intrinsically safe. Although, PFPE-based electrolytes have very low ionic conductivity ( $\sim 10^{-5}$  S/cm) and can not meet the required power density by itself, PFPE based organic electrolyte can greatly increase the interfaces across electrolyte grain boundaries, or electrolyte/electrode interface for enhancing the battery performance.

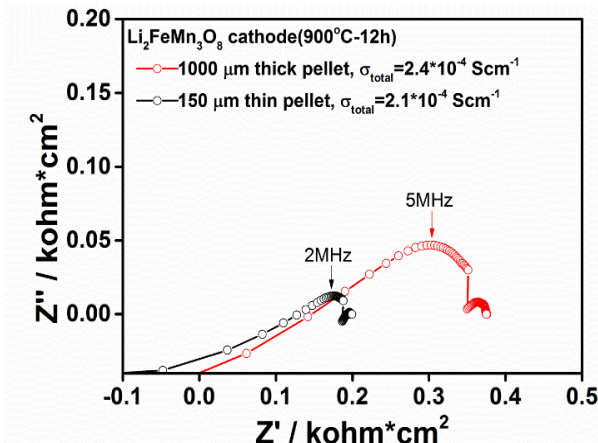
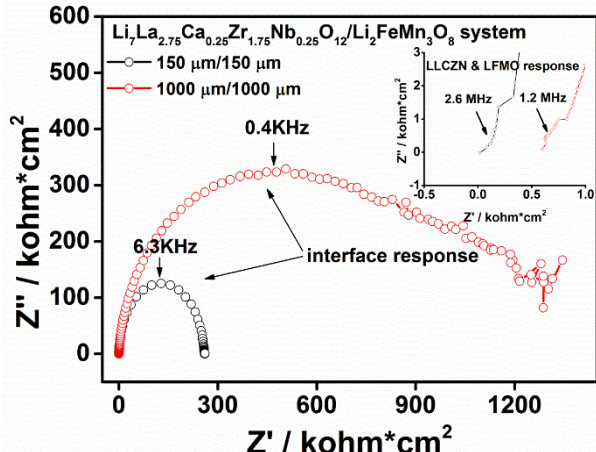
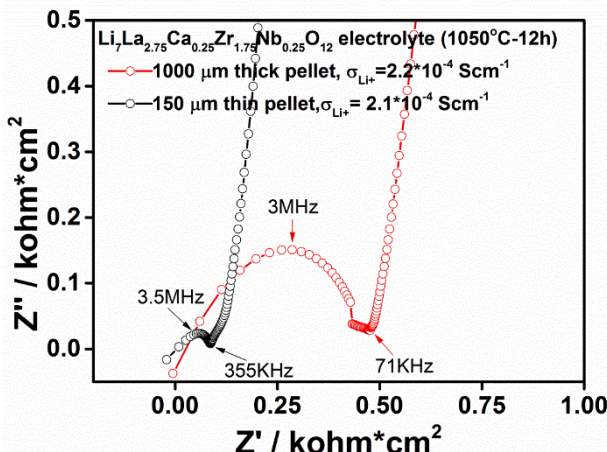
For Type 2, we also use a polymer electrolyte or gel electrolyte, which is Bis(trifluoromethane)sulfonimide lithium salt (LiTFSI) in Poly(vinylidene fluoride-co-hexafluoropropylene) (PVDF-HFP). Although the polymer or gel electrolyte has a much lower ionic conductivity, its thickness is small as an interface layer and thus its contribution in overall impedance is negligible. These soft electrolytes can largely improve the contacts between electrodes and electrolytes toward better charge transport and mechanical integrity.

For each approach, we are fabricating half cells to investigate interfacial impedance and their changes during cycling.

## Results

We have achieved the following progress:

### Characterization of Electrolyte/Cathode interface Impedance



temperature using gold paste current collectors. EIS plots were collected at 50 mV voltage signal over a frequency range of 10 Hz -20 MHz.

Figure V- 225 is the EIS curves of thick and thin LLCZN electrolyte samples. A semicircle and Warburg-type impedance appeared at high and low frequency regions, respectively. The high-frequency semicircle is the sum of bulk and grain boundary responses. The low-frequency tail corresponds to the capacitive behavior of gold blocking electrode. The total lithium-ion conductivity of LLCZN electrolyte is estimated from the intercepts from the semicircle at low frequency side. The thin pellet shows a slightly lower total conductivity than the thick pellet sample.

Figure V- 226 is the EIS curves of thick and thin LFMO cathode samples at initial state (0%SOC). The Nyquist plot contains one depressed semicircle in the high frequency and another semicircle in the medium frequency ascribed to the resistance of Li<sup>+</sup> diffusion through the SEI layer and charge transfer reaction, respectively. The EIS plot indicates similar conductivity exhibited by both the thick and thin pellets of LFMO.

We tested the impedance of LLCZN solid state electrolyte, and its interface impedance with LFMO ( $\text{Li}_2\text{FeMn}_3\text{O}_8$ ) electrodes. The LLCZN( $\text{Li}_{6.8}(\text{La}_{2.95},\text{Ca}_{0.05})(\text{Zr}_{1.75},\text{Nb}_{0.25})\text{O}_{12}$ ) garnet was synthesized by conventional solid state reactions. The starting materials,  $\text{Li(OH)}$ ,  $\text{La(OH)}_3$ ,  $\text{Ca(OH)}_2$ ,  $\text{ZrO}_2$ , and  $\text{Nb}_2\text{O}_5$  were mixed by planetary ball-milling, and then calcined at 700 °C for 48 h. The calcined LLZO-CaNb powder was mixed with additives (both  $\text{Al}_2\text{O}_3$  and  $\text{Li}_3\text{BO}_3$ , only  $\text{Al}_2\text{O}_3$  or only  $\text{Li}_3\text{BO}_3$ ) by planetary ball-milling. The mixture was die-pressed at 10 MPa into a pellet and sintered at 790°C for 40 h in air. EIS of LLCZN electrolyte and LFMO cathode was tested with Solartron 1260 impedance analyzer at room

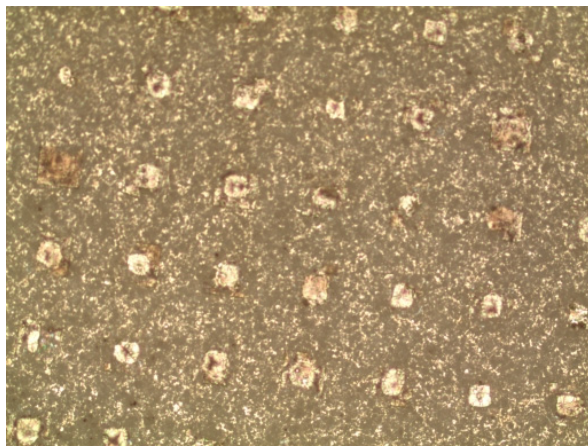


Figure V- 228: Structured garnet surface, white shining areas are deposited garnet columns

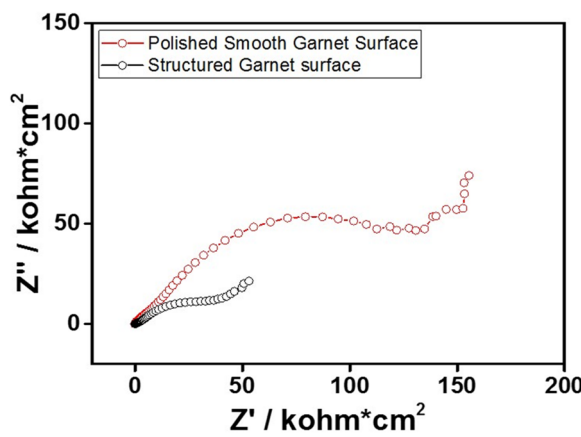


Figure V- 229: Impedance of cathode on smooth and structured garnet electrolyte

Knowing the frequency response of both LLCZN electrolyte and LFMO cathode we then analyzed the system consisting of electrolyte, cathode and their interface. Finely polished electrolyte and cathode with gold electrode on outer side were tightly pressed together. The electrolyte/cathode system was then characterized by EIS. Figure V- 227 shows the Nyquist plots of LLCZN electrolyte/LFMO cathode system. Both thick and thin pellet samples were examined to identify the interfacial effect in the system. The impedance arc is the total resistance of LLCZN electrolyte, LFMO cathode and their interface. The arc in the medium-low frequency range is the dominant interfacial resistance between LLCZN electrolyte and LFMO cathode. The high frequency response in the magnified plot is the sum of LLCZN electrolyte resistance and LFMO cathode resistance.

The garnet/cathode interface impedance was lowered by making structured garnet surfaces. Sintered dense garnet discs were sanded to 150  $\mu\text{m}$  and polished. To make the column structures, polymer mesh was glued on disc surface as a template, after that a garnet slurry was drop coated to fill the open area. The coated sample was dried in oven and sintered at 800  $^{\circ}\text{C}$  for 2h. Figure V- 228 shows the structured garnet surface. The white shining areas are the deposited column structures.

Symmetric cathode/electrolyte/cathode cells were made by screen printing thick cathode slurry on the garnet discs. LFMO cathode was sintered at 500  $^{\circ}\text{C}$  for 1h. Silver paste was used as current collector. Thickness of the cathode was about 20 $\mu\text{m}$ . EIS plots were collected at 50 mV voltage signal in a frequency range of 10 Hz -10 MHz at room temperature. Figure V- 229 is the EIS response of cathode coated as-polished and structured garnet discs which exhibits lower interfacial resistance, compared to that with smooth surface due to the larger interfacial cathode/electrolyte contact area provided by the surface column structure.

### Synthesis and characterization of gel and PFPE based electrolytes.

#### Nonflammable PFPE based electrolyte

PFPE-DMC was prepared from Fluorolink D10 and triethylamine in 1,1,1,3,3-pentafluorobutane at 0  $^{\circ}\text{C}$  under nitrogen atmosphere, followed by dropping a solution of methyl chloroformate in 1,1,1,3,3-pentafluorobutane. After the mixture was stirred at 25  $^{\circ}\text{C}$  for 12 h, the PFPE-DMC product was obtained by filtering and washing with water and brine, followed by evaporation under reduced atmosphere. The PFPE-DMC electrolyte was then produced by

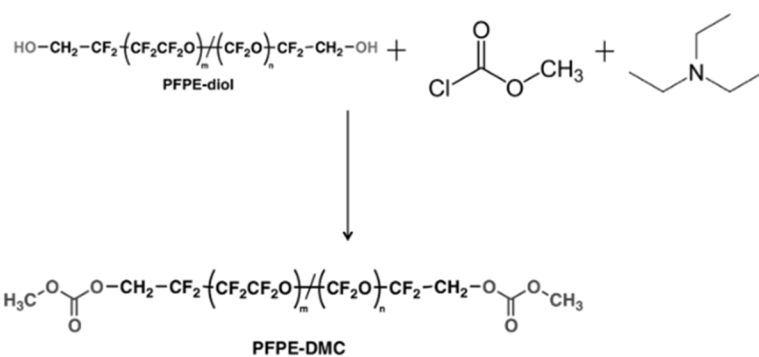


Figure V- 230: Synthesis procedure of PFPE-DMC

dissolving Lithium bis(Trifluoromethanesulfonyl)Imide into PFPE-DMC. The synthesis method of PFPE-DMC is shown in Figure V- 230.

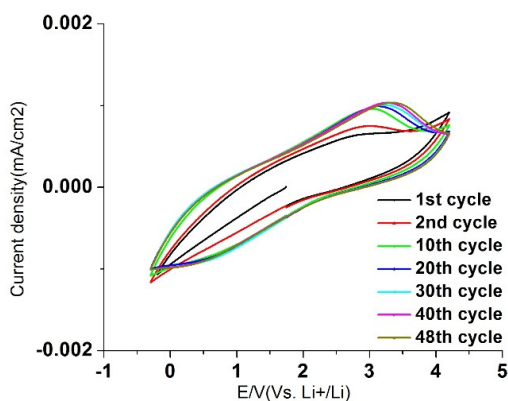


Figure V- 231: Cyclic voltammetric results for LiTFSI/PFPE

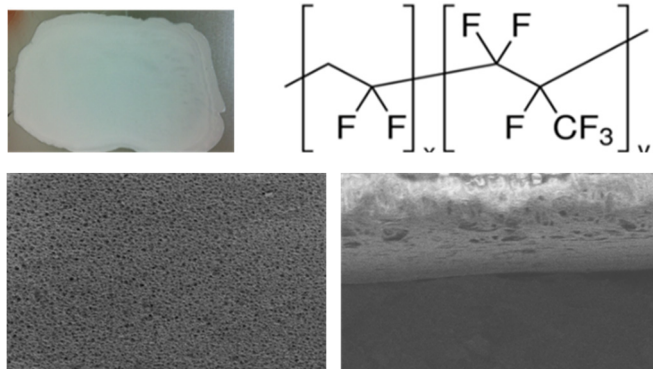


Figure V- 232: Photograph, formula, and top and side SEM images of PVDF-HFP gel membrane

A Li/PFPE/Ti structure in a CR2025 coin cell was used to tested cyclic voltammetry (CV) of the PFPE/LiTFSI electrolyte. The area of the cell is  $1.98 \text{ cm}^2$  (radius=5/16 inch), and the area of Titanium cathode is  $0.712 \text{ cm}^2$  (radius=5/32 inch). The voltage range was  $-0.3 \sim 4.2 \text{ V}$ , and the voltage scan speed was  $1\text{mV/s}$ .

The CV results are shown in Figure V- 231. The reaction current density is less than  $0.002 \text{ mA}$  in  $0.3 \sim 4.2 \text{ V}$  region, which is very small. And after the first few cycles, the CV curve becomes stable. The two facts show that the PFPE electrolyte is electrochemically stable between  $0 \sim 4\text{V}$ . Also, for the PFPE electrolyte, no obvious peaks appear in the voltage region of  $-0.3 \sim 4.2 \text{ V}$ , which means that the Li stripping occurs at a higher voltage than  $4.2 \text{ V}$ , and the Li plating occurs at a lower voltage than  $-0.3 \text{ V}$ . The electrochemical stability of PFPE/LiTFSI in the voltage range of  $0 \sim 4.2 \text{ V}$  ensures that this electrolyte is stable in the reactions of LLCZN garnet electrolyte lithium ion batteries, and can be used as the interfacial layer between garnet and cathode.

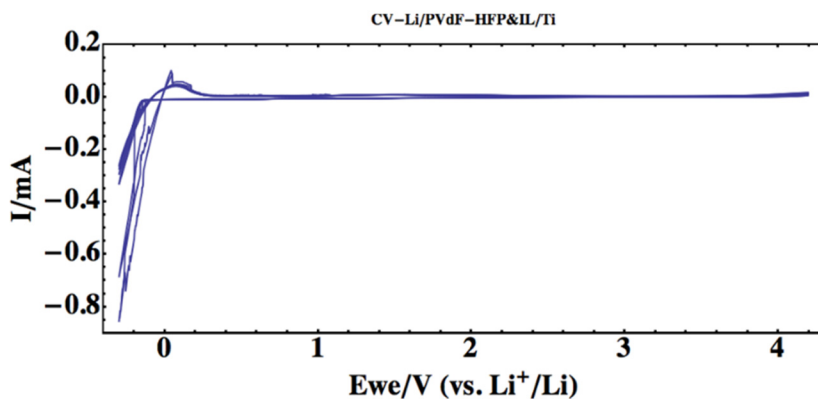


Figure V- 233: CV of Li/PVdF-HFP&IL/Ti system

membrane was obtained. The as-prepared porous membrane was immersed into 1 M LiTFSI in a mixture of 1:1 volume ratio of tetraethylene glycol dimethyl ether and n-methyl-(n-butyl) pyrrolidinium bis(trifluoromethanesulfonyl)imide (Py14TFSI) at room temperature for 30 mins in an argon-filled glovebox.

CV testing cell was set up by sandwiching the gel electrolyte membrane between lithium and titanium disks and sealing the configuration in CR2032 coin cells. The CV (Figure V- 233) at a scan rate of  $1 \text{ mV/s}$  suggests a stable electrochemical window up to  $4.2 \text{ V}$ . The sharp peak at  $-0.2 \text{ V}$  corresponds to the Li plating, while the peak around  $0.1 \text{ V}$  is due to the Li stripping.

#### Gel based electrolyte

A PVDF-HFP based gel polymer was prepared (Figure V- 232) from  $0.25 \text{ g}$  PVDF-HFP dissolved into a mixture of  $4.75 \text{ g}$  acetone and  $0.25 \text{ g}$  DI water (95:5, m/m) under continuous stirring. The solution was cast onto an Al foil and the solvent evaporated at ambient temperature. After drying under vacuum at  $100^\circ\text{C}$  a homogeneous free standing

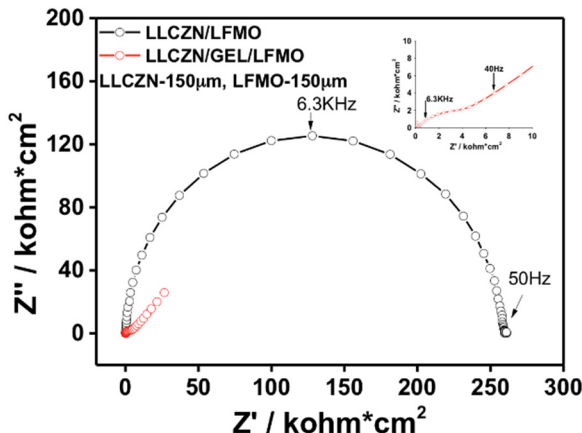


Figure V- 234: EIS of garnet/cathode and garnet/gel/cathode

Figure V- 234 shows the effect of gel polymer on reduction of impedance at the LLCZN electrolyte/LFMO cathode interface. The pristine LLCZN electrolyte/LFMO cathode reveals a huge resistance of  $300 \text{ k}\Omega\cdot\text{cm}^2$ , which consists of bulk resistance of electrolyte and cathode, as well as the significant interfacial resistance between electrolyte and cathode at medium and low frequency range. Introduction of the gel interfacial layer, which provides high Li-ion conduction path, conformal and elastic contact between electrolyte and cathode, results in great reduction of the interfacial resistance, as shown in the medium frequency range in the magnified plot. In addition, the EIS curve shows a different shape, consisting of Warburg-type impedance at low frequency, corresponding to the capacitive behavior of gold blocking electrode.

### Computational modeling of garnet interfaces

First principles modeling of garnet solid electrolyte materials were performed on both tetragonal and cubic LLZ phases. The ordering of Li was determined using computational methods, and the ground state ordering of Li was determined. The Li grand canonical phase diagram of the Li-La-Zr-O system based on first principles computation methods and electrochemical stability of garnet against Li metal was determined (Figure V- 235).

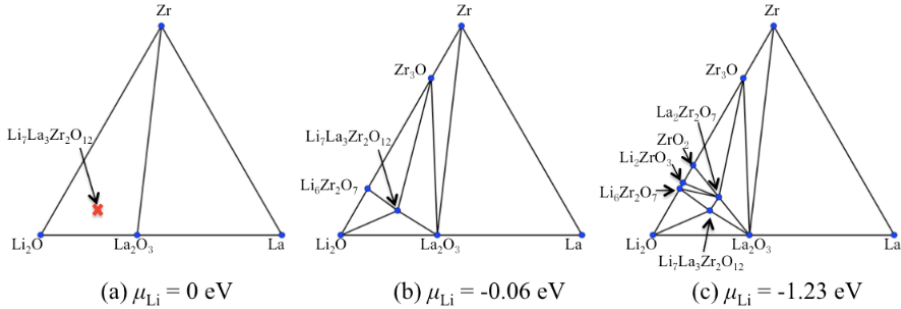


Figure V- 235: Li grand canonical phase diagram of Li-La-Zr-O system

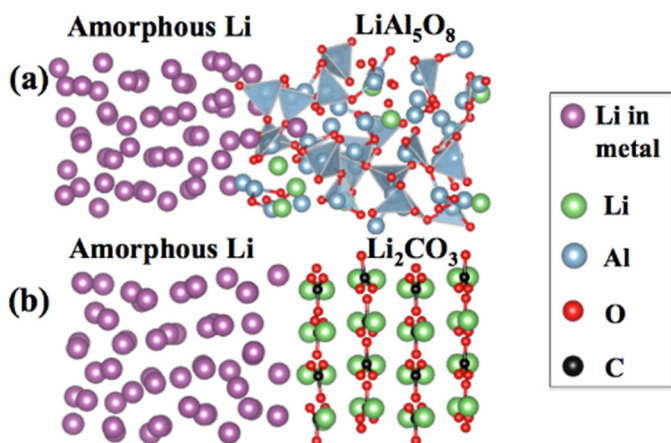


Figure V- 236: Models for the interfaces between Li metal and garnet surface materials

In addition, first principle models were constructed to evaluate the structure and energetics of the electrolyte-electrode interfaces between garnet and Li metal. We found that Li metal has a very weak interfacial binding with  $\text{Li}_2\text{CO}_3$ , which are found on the garnet surfaces, and Li metal binds strongly with oxide materials that may form on the garnet surfaces. The weak interface binding may lead to forming interfacial gaps and intervals, thus a low contact area and a high interfacial resistance. Stronger interface binding would lead to enhanced interfacial contacts with larger contact area and good interfacial conductance. (See Figure V- 236.)

### Model interphase of garnet-electrode of any materials

$x$ LLZO	$x$ LCO	Interphase				
0.0	0.33	La2O3	Li6Zr2O7	Li7Co5O12	Li7La3Zr2O12	Li8CoO6
0.34	0.49	La2O3	Li2O2	Li6Zr2O7	Li7Co5O12	Li8CoO6
0.5		La2O3	Li2O2	Li6Zr2O7	Li7Co5O12	
0.51	0.87	La2O3	La2Zr2O7	Li2O2	Li6Zr2O7	Li7Co5O12
0.88		La2O3	La2Zr2O7	Li2O2	Li7Co5O12	O2
0.89	1	La2O3	La2Zr2O7	Li(CoO2)2	Li7Co5O12	O2

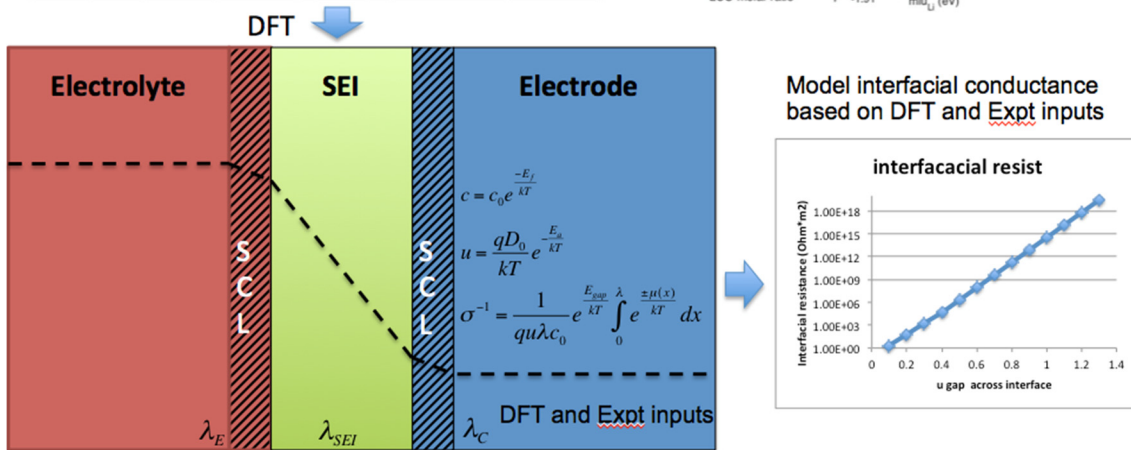
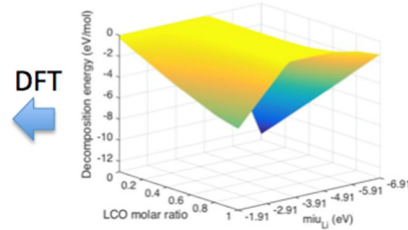


Figure V- 237: Model for garnet-electrode interfaces, which take inputs from first principles calculations and experimental condition parameters

We developed a computational model for garnet-electrode interfaces (Figure V- 237). The comprehensive interface model is based on a large variety of inputs provided by a range of first principles computation and actual experimental parameters to model the interface properties. The interface model has been developed and demonstrated for garnet materials with electrode materials, such as LiCoO<sub>2</sub> and LFMO. The interphase layers between the garnet and the electrode were determined using grand potential phase diagram at the applied voltage of the battery at the input for the model. The formation of the interphase was found to be thermodynamically favorable for the interfaces of garnet with anode and cathode. In addition, the properties of the materials comprising the interphase, such as defect and migration energy, were also evaluated in first principles calculations. The effects of the space-charge layer were incorporated as a part of interface model. Using all these predicted input parameters, the conductivity and interfacial resistance of the interfacial layer were determined. The model is now ready to be applied to any composition of garnet solid electrolyte in contact with any electrode materials. The inputs for the interface model are generated by the first principles computation and experimental parameters. The model was able to demonstrate that a poor interfacial layer causes high interfacial resistance in all-solid-state batteries.

### Conclusions and Future Directions

We have made important progress on the interfacial impedance between solid state electrolyte and electrodes. The interfacial impedance between LLCZN garnet electrolyte and LFMO electrode was tested, and it was found that that extended 3D structures on the garnet surface can reduce the interfacial impedance.

PVDF-HFP gel membranes were fabricated, and their microstructure demonstrated by SEM. CV electrochemical tests have shown that the gel electrolyte is electrochemically stable between 0-4.2V and can thus be used as the interface layer between garnet electrolyte and various high voltage cathodes. The EIS of LLCZN/GEL/LFMO was tested and the total impedance decreased significantly compared with the LLCZN/LFMO system without the interfacial layer.

PFPE nonflammable electrolytes were also fabricated. The CV electrochemical tests of Li/PFPE/Ti shows that it is stable between 0-4.2V, which means that it can be used as the interface layer between garnet electrolyte and various high voltage cathodes.

Future work will focus on investigating the fundamentals of solid-solid interfacial impedance, and different kinds of interface layers by combining experiments and computations. The first task is to determine interfacial

impedance in 3D controlled solid-state structures, and the second task is to finish the battery test using PFPE and gel based electrolyte interfacial layers to see if they can reduce the interfacial impedance, and start to research on other types of interfacial layers: Atomic layer deposition (ALD) based interlayers and  $\beta$ -Li<sub>3</sub>PS<sub>4</sub> (LPS) based interlayers.

### **FY 2015 Publications/Presentations**

#### **Presentations**

1. Eric Wachsman “Ion Conducting Oxides for Electrochemical Energy Conversion and Storage,” September 10, 2015, University of Texas, Austin.
2. Yifei Mo, “Challenges of Solid Electrolyte Materials in All-Solid-State Li-ion Batteries: Insights from First-Principles Calculations”, Materials Research Society, San Francisco, April 6-10, 2015.

#### **Publications**

1. Yizhou Zhu, Xingfeng He, Yifei Mo, “Origin of Outstanding Stability in the Lithium Solid Electrolyte Materials: Insights from Thermodynamic Analyses Based on First Principles Calculations”, ACS applied materials & interfaces (accepted)

# V.H.5 Nanoscale Interfacial Engineering for Stable Lithium Metal Anodes (Stanford University)

## Objectives

- This study aims to render lithium metal anode with high capacity and reliability by developing chemically and mechanically stable interfacial layers between lithium metal and electrolytes, which is essential to couple with sulfur cathode for high-energy lithium-sulfur batteries. With the nanoscale interfacial engineering approach, various kinds of advanced thin films will be introduced to overcome the issues related to dendritic growth, reactive surface and virtually “infinite” volume expansion of lithium metal anode.

## Technical Barriers

- Large volume change of anode during cycling
- High reactivity of lithium metal with electrolyte
- Irreversible consumption of active lithium and electrolyte during battery cycling
- Formation of dendritic lithium with increasing surface area
- Low cycling Coulombic efficiency

## Technical Targets

- Develop various types of nanomaterials as stable interface layer between lithium and electrolyte
- Reduce and prevent growth of dendritic lithium by applying proper interface materials
- Increase Coulombic efficiency of lithium metal anode to >99.5% for 300 cycles
- Develop novel electrolyte additives to further suppress dendritic lithium growth
- Develop novel in situ techniques to study the behavior of lithium metal during electrochemical cycling.
- Study the mechanism governing nucleation of lithium metal

## Accomplishments

- Interconnected carbon nanospheres could regulate the deposition of lithium metal
- Ultrathin two dimensional layers including hexagonal boron nitride and graphene could reduce dendrite formation and improve Coulombic efficiency.
- Demonstrated the guiding effect of polymer nanofibers to improve lithium metal cycling performance.
- Demonstrated improved cycling performance of lithium metal anode with different areal current density and capacity with solutions mentioned above.
- Developed nanoporous lithium metal anode by infusion of molten lithium with “lithophilic” substrates.

## Introduction

To enable the mass adoption of electric vehicles, two key challenges of battery technology need to be addressed: increasing the energy density and reducing the cost. Lithium metal is critical in enabling the next generation of high-energy-density battery technologies that could potentially be very low cost. Battery chemistries based on lithium metal anode, such as Li-S and Li-air could offer about 5-10 times of energy density as compared to the current lithium ion battery technologies. Li metal has long been considered the “holy grail” in Li batteries because as anode, it has the highest specific capacity of around 3860 mAh/g of Li

### Project Details

**Yi Cui (Stanford University, PI)**  
476 Lomita Mall, McCullough 343  
Stanford, CA 94305  
Phone: 650-723-4613; Fax: 650-725-4034  
E-mail: [yicui@stanford.edu](mailto:yicui@stanford.edu)

Subcontractor:  
Stanford University  
Stanford, CA

Start Date: October 2014  
Projected End Date: August 2017

and the lowest potential for maximizing the cell voltage. However, the problems of dendritic and mossy Li formation cause poor safety and low Coulombic efficiency during charge/discharge. Past attempts to address these problems include tuning liquid electrolytes additives, pre-forming surface films, utilizing solid ceramic and polymer electrolytes. These approaches only resulted in limited success. Advanced characterization techniques have helped shed light on the Li growth process, but effective strategies to improve Li cycling remain elusive.

### Approach

**Innovative Approach:** The objectives outlined above will be accomplished by passivating surface of lithium metal anode with nanomaterials that are chemically inert and mechanically stable. Moreover, the protective layer should exhibit good ionic conductivity and mediocre/bad electric conductivity. The major technology innovations will be undertaken to accomplish the objectives of this effort:

1. Dramatically reduce the formation of dendrite on lithium metal anode.
2. Improved Coulombic efficiency together with prolonged cycling life.
3. Reduced consumption of electrolyte.
4. Minimized SEI build up together with stable interface impedance.

### Results

We have achieved the following progress:

#### The synthesis of interconnected carbon nanospheres and its effect on lithium metal anode

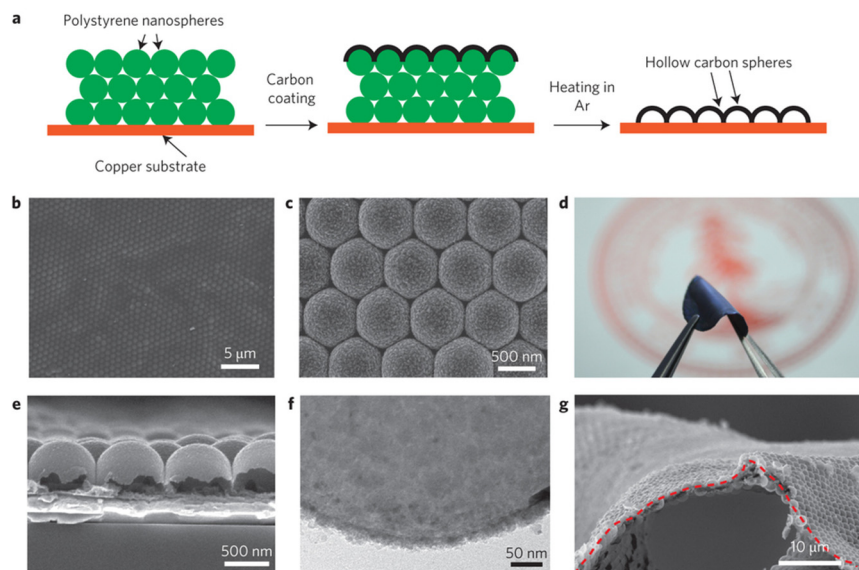


Figure V- 238: (a) Fabrication process for the hollow carbon nanosphere-modified Cu electrode. (b) and (c) SEM images of carbon-coated polystyrene nanoparticle array. (d) to (g) As fabricated hollow carbon nanosphere thin film after removal of template

We have developed a template synthesis method for fabricating the hollow carbon nanospheres, using vertical deposition of polystyrene nanoparticles (Figure V- 238a). A colloidal multilayer opal structure is formed on Cu foil by slowly evaporating a 4% aqueous solution of carboxylated polystyrene particles. The highly monodisperse polystyrene nanoparticles form a close-packed thin film with long-range order (Figure V- 238b). The polystyrene nanoparticles are coated with a thin film of amorphous carbon using flash evaporation of carbon fibres (Figure V- 238c). The samples are then heated in a tube

furnace to 400 °C under an inert atmosphere, forming hollow carbon nanospheres on the Cu substrate (Figure V- 238e). TEM characterization shows that the carbon wall has a thickness of ~20 nm (Figure V- 238f). The hemispherical carbon nanospheres are interconnected to form a thin film, which can be peeled off the Cu surface easily. Loose attachment of the carbon film to the Cu electrode is important in that it allows the protective film to be lifted up, creating space for Li deposition. Mechanical flexibility is also important in accommodating the volumetric change of Li deposition and dissipating the stress exerted on the Li protection layer during cycling. A digital camera image (Figure V- 238d) and SEM image (Figure V- 238g) show that the carbon nanosphere thin film can achieve a bending radius of ~20 μm.

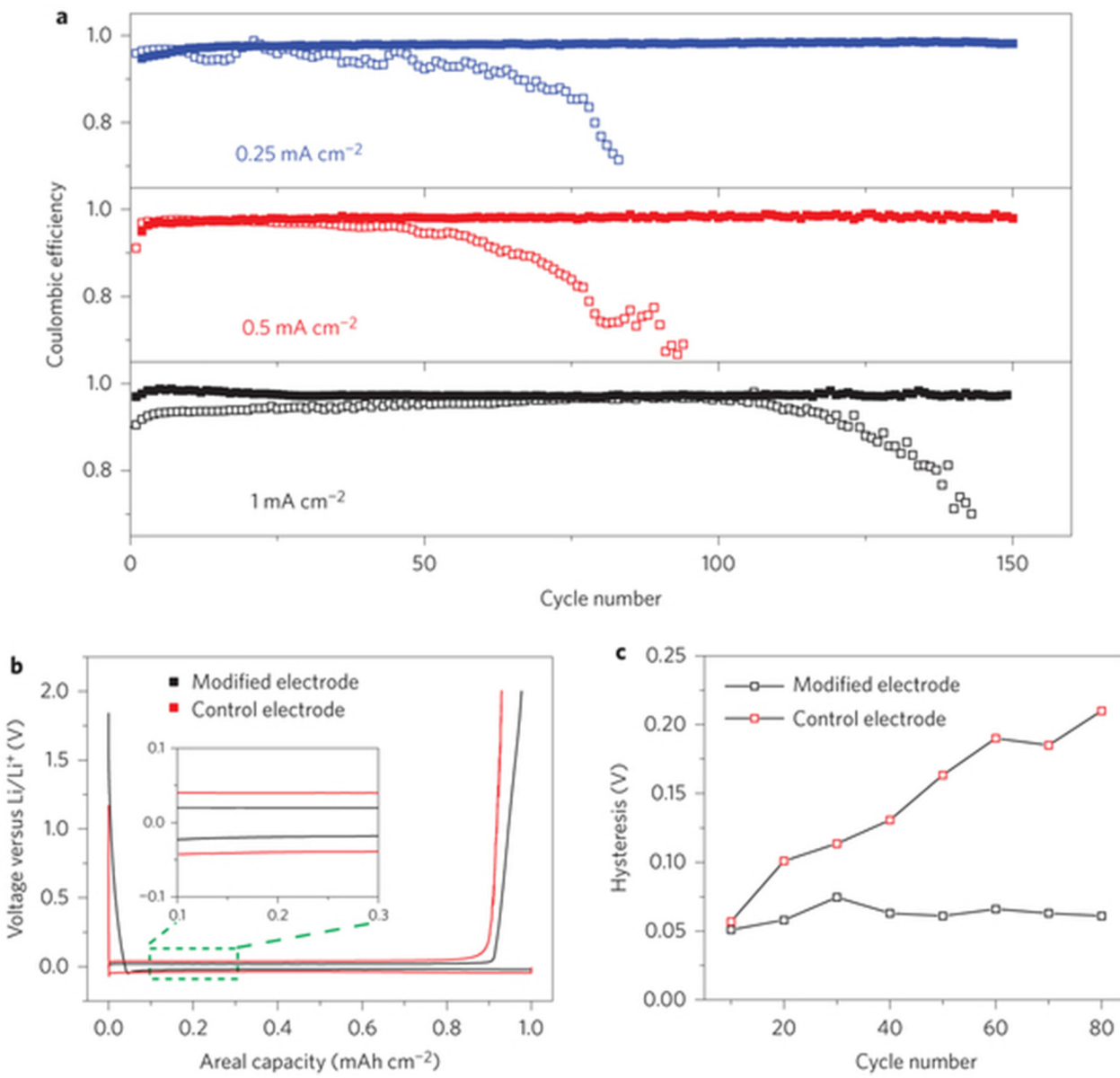


Figure V-239: (a) Cycling performance of hollow carbon nanosphere modified electrode and control Cu electrode. (b) Voltage profiles of the Li deposition/dissolution process. (c) Comparison of the hysteresis of Li deposition/dissolution for the modified electrode and control electrode

The demonstrated stable interfacial layer of carbon hollow nanospheres opens up the opportunity to improve the Coulombic efficiency of Li metal anodes. To standardize the electrochemical performance, ~30 μL electrolytes was used in each coin cell test. In the half-cell configuration Li was electrochemically deposited (at 1 mAh/cm<sup>2</sup>) from the Li metal counter-electrode onto the hollow nanosphere-modified working electrode and then stripped away. In cycle life testing these batteries fail due to the depletion of electrolytes as a result of reaction with the Li metal. Consequently, the internal resistance increases rapidly in batteries that have severe electrolyte decomposition. The analysis of electrochemical performance shows that the cycling performance of the Li metal working electrodes with the carbon nanosphere coating is significantly improved. The Coulombic efficiency is maintained at ~99% for more than 150 cycles at 0.25 mA/cm<sup>2</sup> and ~98.5% at 0.5 mA/cm<sup>2</sup> (Figure V-239a). In comparison, cells without the hollow carbon nanosphere coating show a gradual decrease in Coulombic efficiency, which eventually drops to less than 50% after 100 cycles at 0.25 mA/cm<sup>2</sup> and 0.5 mA/cm<sup>2</sup>. The Li metal batteries in the present study show consistently stable, high-Coulombic-efficiency cycling, which can be attributed to the more uniform Li deposition under the hollow carbon nanospheres, more stable SEI formation on top of the spheres, and reduction of electrolyte decomposition. The effect of stable SEI

formation and reduction of electrolyte decomposition can also be seen in the reduction of polarization (hysteresis) in the voltage profile during Li deposition/dissolution. The Li deposition voltage for the modified electrode is approximately  $-25$  mV (versus Li/Li $^{+}$ ), whereas that for the pristine Cu is  $\sim 50$  mV. The Li dissolution is  $25$  mV and  $50$  mV, respectively (Figure V- 239b). For the electrode without modification, the voltage hysteresis in the Li deposition/dissolution increases gradually as the cycle number increases, with a difference in potential of  $\sim 210$  mV after  $80$  cycles (Figure V- 239c). With the hollow carbon nanosphere modification, the hysteresis is much smaller, only  $\sim 50$  mV after  $50$  cycles.

### The synthesis of ultrathin two dimensional layered materials and its effect on lithium metal anode

We used the method of chemical vapor deposition (CVD) developed recently for synthesis of large-area h-BN. Similar with the CVD growth of graphene, copper foil was heated up to  $1000^{\circ}\text{C}$  in argon and hydrogen at low pressure followed by ammonia borane ( $\text{NH}_3\text{-BH}_3$ ) vapor. A piece of copper foil was loaded into the  $1^{\prime\prime}$  quartz tube of tube furnace. A glass test tube containing certain amount of ammonia borane complex was connected to the upstream of furnace via a quick connector. The system was pumped down to a base pressure below  $10\text{mTorr}$  by rotary pump before mixture of  $20\text{sccm}$  argon and  $10\text{sccm}$  hydrogen was introduced to the furnace. After annealing the substrate at  $900^{\circ}\text{C}$  for  $20\text{min}$ ,  $\text{NH}_3\text{BH}_3$  precursor was vaporized  $\sim 120^{\circ}\text{C}$  by a heat gun.

The partial pressure of precursor gas was maintained  $\sim 100$  mTorr by adjusting the power of heat gun. Typical growth period lasts for  $\sim 10\text{min}$ , after which the furnace temperature ramped down to  $300^{\circ}\text{C}$  with all inlet gas terminated. The partial pressure of precursor was kept at  $\sim 100$  mTorr for up to  $10\text{ min}$ . At the initial stage of growth, discrete triangles of h-BN domains  $\sim 2\ \mu\text{m}$  in edge were found (Figure V- 240b-d). These grains gradually grow and connect with each other and coalescent into a continuous film with line defects along grain boundaries. Within  $10\text{ min}$ , multilayered h-BN films can form and cover the whole copper substrate with a crack hardly visible.

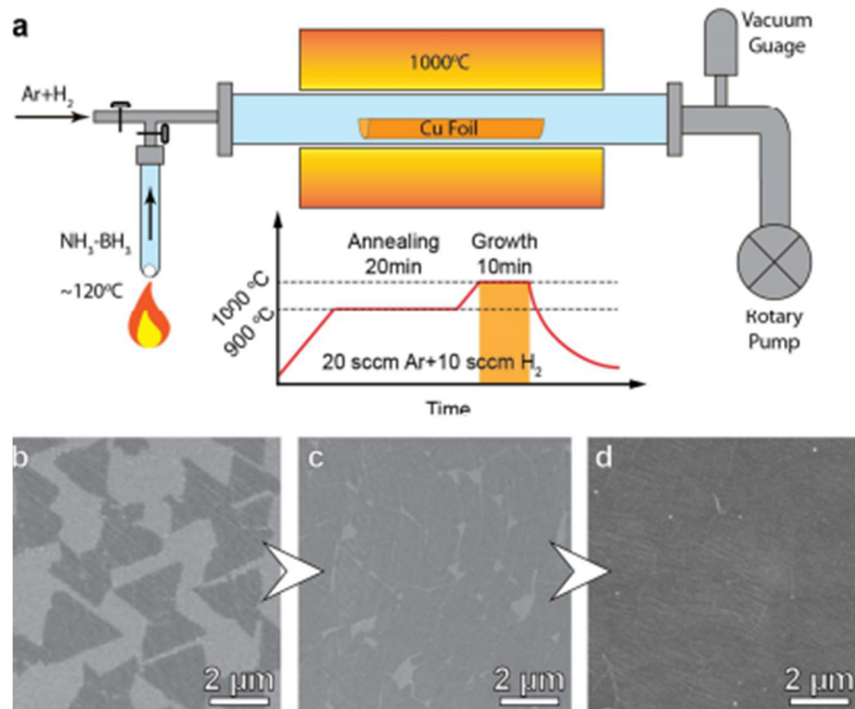


Figure V- 240: Chemical vapor deposition growth of h-BN. (a) Experiment setup for h-BN growth. (b), (c) and (d) SEM images of as grown h-BN sample at different stage

Lithium metal was plated to the Cu substrate galvanostatically afterward. For the bare copper anode, the SEM images (Figure V- 241a) show that wire-shaped Li dendrites and mossy Li with diameter  $1\text{--}2\ \mu\text{m}$  already form after first deposition of  $1.0\ \text{mAh}/\text{cm}^2$  lithium at current rate of  $0.5\ \text{mA}/\text{cm}^2$ . The surface area of dendritic Li is increased drastically, consuming much electrolyte to form SEI. For the h-BN/Cu electrodes, the SEM images (Figure V- 241b) show large size pancake-like Li metal covered by h-BN film. The top surface of Li pancakes seems to be flat. The typical pancake size in the h-BN/Cu electrodes is around  $5\text{--}10\ \mu\text{m}$ .

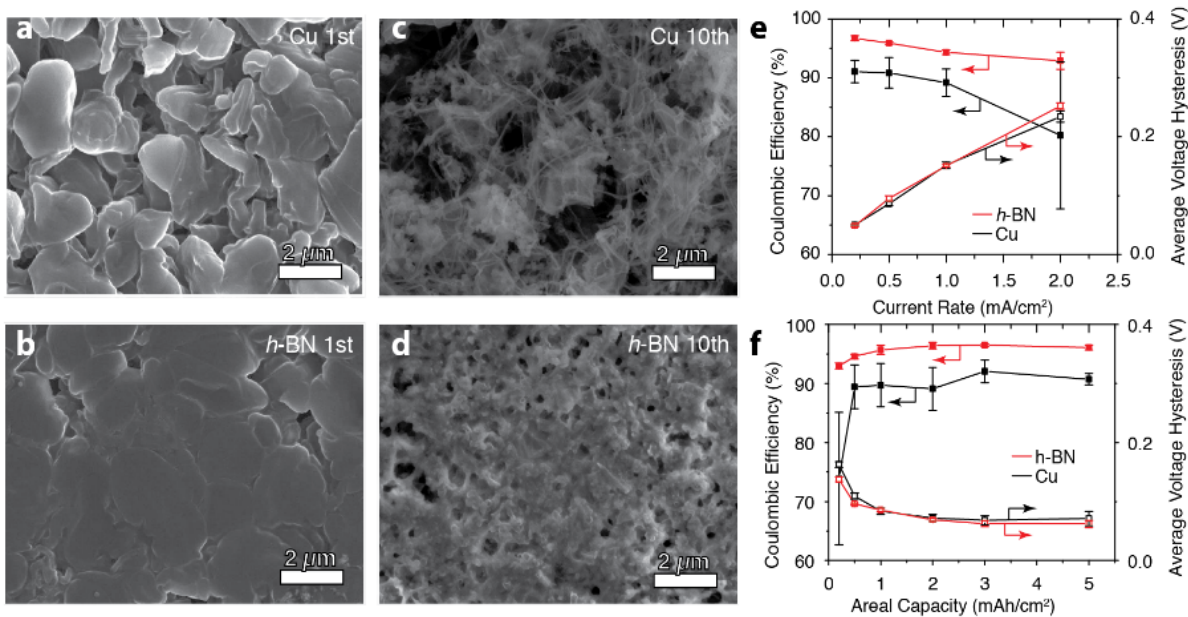


Figure V-241: h-BN as interfacial layer for lithium metal. Morphologies of lithium metal surface without (a and c) and with (b and d) h-BN coating at first cycle (a and b) and tenth cycle (c and d). (e) and (f) Coulombic efficiency and average voltage hysteresis of lithium metal anode upon cycling, with and without h-BN coating at different current densities and areal capacities

It appears that the h-BN layers are sitting on top of Li pancakes. That is, Li metal is sandwiched between h-BN and Cu, further reducing the surface area exposed to the electrolyte. In fact, the successful encapsulation of lithium can significantly suppress lithium reaction with oxygen and moisture in the air. We cannot completely exclude yet the possibility of the SEI formation at the boundaries of h-BN patches, where part of Li metal surface might be still exposed to the electrolyte. However, we expect that the exposed Li surface area is reduced dramatically. The h-BN sheets serve as stable interfacial layers for Li metal deposition. For the cycling performance, the Coulombic efficiency remained high comparing with bare copper at different current densities (Figure V-241e), even in more corrosive organic carbonate electrolyte. More importantly, the unique working mechanism of h-BN in principle allow for effective protection of Li film with different thickness, because the whole layer is always on top of the Li layer during operation.

In order to prove the concept, we explored the dependence of Coulombic efficiency as a function of areal capacity ( $0.2, 0.5, 1.0, 2.0, 3.0, 5.0 \text{ mAh}/\text{cm}^2$ ) at constant current rate of  $0.5 \text{ mA}/\text{cm}^2$ . The Coulombic efficiency of h-BN/Cu electrodes remains high at 95–97% even at these high areal capacities, which are much higher and more stable than the bare Cu electrodes that decay from 92 to 80%. Figure V-241f summarizes the averaged Coulombic efficiency versus areal capacity. The h-BN/Cu electrodes are consistently much better than the bare electrodes for all the areal capacity. For both types of electrodes, the Coulombic efficiency shows noticeable drop for the low areal capacity ( $<0.5 \text{ mAh}/\text{cm}^2$ ). This may arise from the constant amount of electrolyte reaction from the top of electrodes regardless of lithium thickness. For small areal capacity, this amount accounts for a large fraction.

The concept of protecting lithium with inert atomic thin layers could also be extended to graphene. The CVD-grown graphene of high quality on Cu was confirmed by a weak D band and sharp G and 2D bands in Raman spectrum (Figure V-242a). The HR-TEM image of two mismatched graphene layers in Figure V-242b demonstrates the highly crystallized two-dimensional hexagon frameworks. The length of C–C bond was calculated from the FFT pattern as  $\sim 0.141 \text{ nm}$ , which is consistent with the reported value of graphene. Even though graphene is generally regarded as a semimetal with extraordinary carrier mobility, the interlayer conductivity is quite limited. It is also known that electron transfer from the graphene basal plane to outside is sluggish. In addition, any electron transfer can result in the formation of SEI first on graphene basal plane above the Li metal deposition potential. It is thus reasonable to expect that just like the h-BN/Cu electrode, Li metal deposition would take place between graphene and Cu but not on top of graphene. Figure V-242c shows the top surface of graphene/Cu electrodes after lithium deposition with comparable smoothness to that of h-BN, confirming the same deposition behavior. With the protection of graphene film, the cycling performance

of lithium metal anode shows significant improvement over the bare Cu electrodes. The graphene/Cu anodes exhibit high Coulombic efficiency of ~95 and ~93% over 50 stable cycles at current rate of 0.5 and 1.0 mA/cm<sup>2</sup> with areal capacity of 1.0 mAh/cm<sup>2</sup>, respectively (Figure V- 242d). Compared to h-BN, the improvement of Coulombic efficiency is less, which might arise from the smaller average thickness of graphene in our CVD growth. The conductive nature of graphene may also contribute partially considering the possible deposition at active edges.

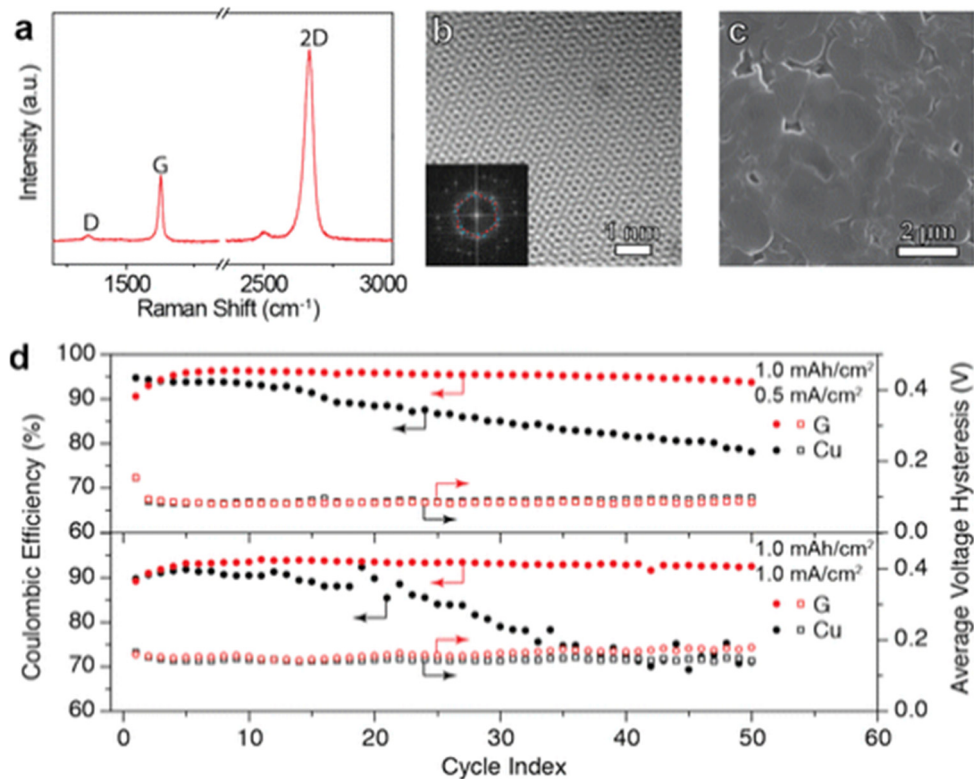


Figure V- 242: Characterizations of graphene and its performance in cycling of Li metal anode. (a) Raman spectrum of graphene film. The wavelength of excitation laser is 632.8 nm. (b) HR-TEM image of mismatched two-layer graphene. Two sets of hexagonal spot patterns were shown in the FFT image inset. (c) Top view SEM image of the first Li metal deposition on graphene protected anode at 0.5 mA/cm<sup>2</sup>. (d) Cycling performance and average voltage hysteresis of Li metal anode with and without graphene protection at different current rate

### Synthesis and performance of oxidized polymer fibers for stable lithium metal anode

We developed a simple two-step process to fabricate the polymer nanofiber network. The precursor solution for our polymer nanofiber was made by adding polyacrylonitrile (PAN) and polyvinylpyrrolidone (PVP) into N,N-Dimethylformamide (DMF) with vigorous stirring (Figure V- 243a). Afterward, we utilize a single-nozzle coelectrospinning method to produce the PAN/PVP nonwoven polymer nanofiber mat onto the collector under a constant voltage (Figure V- 243b). Then the nanofiber mat was transferred to a box furnace and heated at elevated temperature (300 °C) to slightly oxidize the PAN/PVP hybrid nanofiber. The thermal stabilization process involves annealing the polymer fiber at a moderately high temperature of 300 °C in air. In the oxidation/stabilization stage, PAN undergoes a cyclization-oxidation reaction and form a ladder structure with polar functional groups (C=N, C-N, C=O, O-H) working as anchoring points for Li ions.

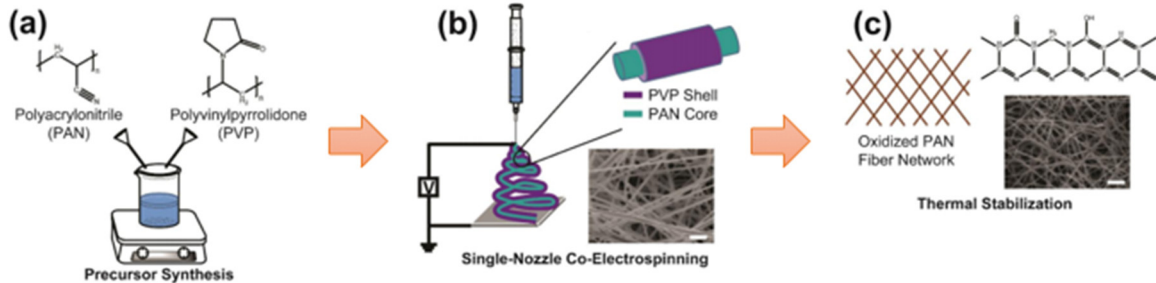


Figure V- 243: Schematics of the fabrication processes of the polymer nanofiber mat. (a) Precursor solution synthesis; (b) PAN/PVP hybrid nanofiber by co-electrospinning and its corresponding SEM image. The resulting nanofiber forms a core-shell structure with PAN as the core and PVP as the shell; (c) Proposed structural formula for oxidized PAN and its corresponding SEM image. PVP is removed from the hybrid fiber through thermal decomposition. Scale bars are  $2 \mu\text{m}$

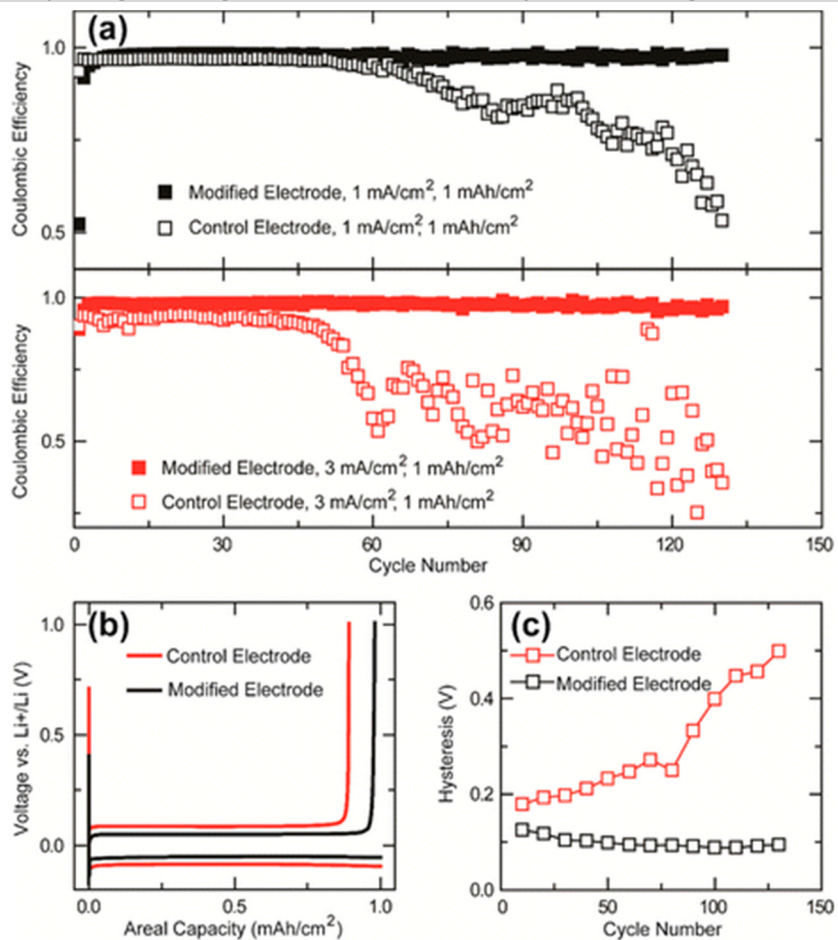


Figure V- 244: Cycling performances of the control Cu electrode and modified Cu-OxPAN electrode at various current rates. (a) Comparison of the Coulombic efficiency of Li deposition on bare Cu and Cu-OxPAN electrode. (b) Comparison of the voltage profiles of the Li plating/stripping process with Li metal as the counter and reference electrode with current density of  $3 \text{ mA}/\text{cm}^2$ . (c) Comparison of voltage hysteresis of the Li plating/stripping process with Li metal as the counter and reference electrode with current density of  $3 \text{ mA}/\text{cm}^2$

bis(trifluoromethanesulfonyl)imide (LiTFSI) in cosolvent of 1,3-dioxolane (DOL) and 1,2-dimethoxyethane (DME) with lithium nitrate (2 wt %) was used as electrolyte. As can be seen from Figure V- 244a, the modified electrode presents a more stable electrochemical cycling and a longer cell life. Under current density of 1 and  $3 \text{ mA}/\text{cm}^2$ , the cells with modified electrodes deliver enhanced Coulombic efficiency of 97.9 and 97.4% over 120 cycles, respectively.

The stabilization step plays a key role since it helps eliminate the residues (organic solvents and water) remained in the nanofiber mat. The as-formed cross-linked PAN fiber has an improved chemical stability in the electrolyte, ensuring little swelling and side reactions during the Li-plating–stripping cycles. After the stabilization process, the oxidized PAN nanofiber could be easily detached from the collector and become a free-standing, mechanically strong film. The oxidized PAN nanofiber leads to increased cycling performance of lithium metal anode. Cells with modified electrode and control electrode were compared in terms of Coulombic efficiency (Figure V- 244a), voltage profile (Figure V- 244b), and hysteresis (Figure V- 244c). Coin cells were assembled by using metallic Li foil as the counter electrode, Cu foil (control), and Cu-OxPAN (modified) as the working electrode.

Lithium

In comparison, the cells with control electrodes exhibit inferior electrochemical cycling performances with an average of 87.6% over 120 cycles (for  $1 \text{ mA/cm}^2$ ) and 71.3% over 120 cycles (for  $3 \text{ mA/cm}^2$ ). The Coulombic efficiencies of control electrodes drop to below 70% after 90 cycles (at  $1 \text{ mA/cm}^2$ ) and 60 cycles (at  $3 \text{ mA/cm}^2$ ), which indicates the depletion of the electrolyte resulted from the intense reaction of Li and electrolyte. The stable cycling of modified cells with Cu-OxPAN electrode even under large current density ( $3 \text{ mA/cm}^2$ ) originates from a homogeneous Li growth, thus a less Li and electrolyte consumption. Electrochemical characterization of Li deposition on Cu-PP electrode (with nonpolar  $\text{CH}_3$  groups) was also performed. The Cu-PP electrode presents a rapid Coulombic efficiency decay, which confirms the importance of polar functional groups.

### Performance of nanoporous lithium fabricated by infusion with ZnO coated polymer matrix

In addition to the well acquainted problem of lithium metal anode such as dendrite formation and low cycling efficiency, virtually infinite volume change also prevents the practical use of lithium metal. Inspired from our previous work in which polymer fiber matrix was adapted as supporting matrix for lithium deposition, we hereby developed an infusion method that creates nanoporous lithium with conformal lithium coating over polymer nanofibers. Figure V- 245 illustrates the fabrication process of the Li-coated PI matrix electrode. We employed a facile electrospinning method to obtain the PI fiber matrix. PI fiber is found to be stable up to  $450^\circ\text{C}$ , which is well above the melting point of Li ( $180^\circ\text{C}$ ). Such high heat-resistance ensures that the matrix can withstand the temperature of molten Li in order to fabricate the metallic Li anode.

Nevertheless, molten Li cannot wet the bare PI matrix. However, we found that a layer of conformal  $\text{ZnO}$  coating applied to the matrix via ALD can render the matrix wet by molten lithium, or “lithiophilic”.

Subsequently, when the core-shell PI-ZnO matrix was put into contact with molten Li,  $\text{ZnO}$  reacted with molten Li and interestingly, extra Li

can be drawn into the matrix, affording a Li-coated PI electrode.

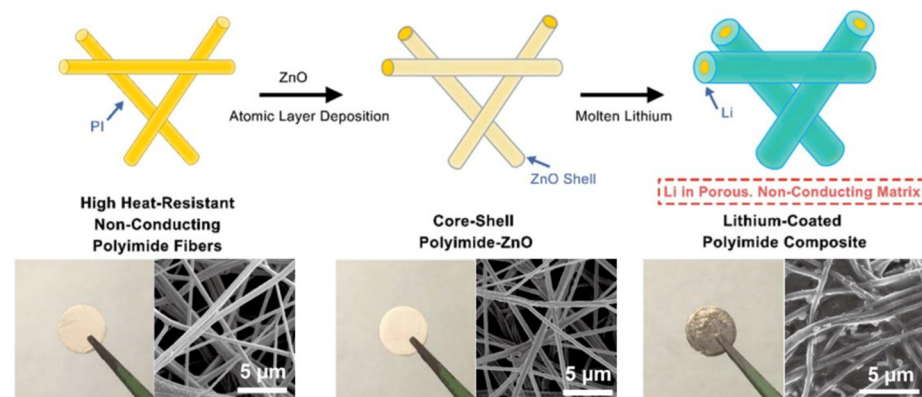


**Figure V- 245:** Schematic of the fabrication of the Li-coated PI matrix. Electrospun PI was coated with a layer of  $\text{ZnO}$  via ALD to form core-shell PI-ZnO. The existence of  $\text{ZnO}$  coating renders the matrix “lithiophilic” such that molten Li can steadily infuse into the matrix. The final structure of the electrode is Li coated onto a porous, non-conducting polymeric matrix

The stripping/plating process of the Li-coated PI matrix was investigated in 2032 coin cells with carbonate-based electrolyte. Interestingly, the electrode exhibited a well-confined stripping/plating behavior (Figure V- 246). Top fibers of the matrix were exposed after stripping away  $5 \text{ mAh/cm}^2$  Li at a current density of  $1 \text{ mA/cm}^2$  (Figure V- 246a), which indicates that the top Li layers were dissolved more favorably during stripping. Subsequently, when  $3 \text{ mAh/cm}^2$  Li was plated, Li was observed to be deposited into the matrix and partially filled the space between the fibers (Figure V- 246b). Finally, when all the stripped Li was plated back (Figure V- 246c), the top surface of the matrix was covered again by Li with no discernable dendrites. The well-confined plating behavior can be rationalized by the removal of the conductive Li component in the prior stripping process, and thus the exposure of the electrically insulating PI surface. Since Li plating only occurs where electrons meet Li ions, the exposed insulating surface was rendered unfavorable for Li nucleation. Instead, the metallic Li confined within the matrix served as the only electron conductor such that the deposition of Li occurred majorly on the underlying reserved Li. In addition, the much larger effective surface area lowered the overall deposition barrier and thus preventing the formation of ‘hot spot’. As a result, uneven Li deposition can be suppressed. On the contrary, if the electrons could be efficiently transported to the electrolyte-facing top surface or the electrodes exhibited limited surface area, undesirable Li stripping/plating behavior may occur after recurrent cycles (Figure V- 246, top-right scheme), as discussed in previous studies.

Direct Li nucleation on the top surface might be easier due to the high availability of both electrons and Li ions, which provides favorable sites for dendrite growth while leaving the interior voids empty.

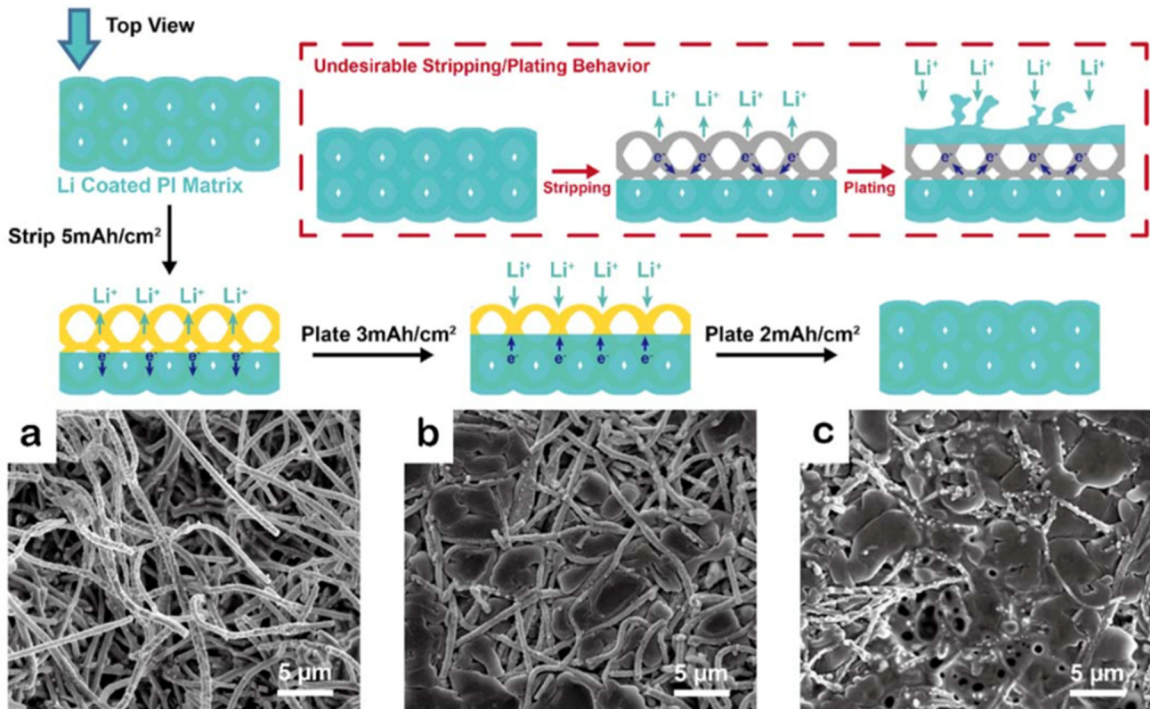
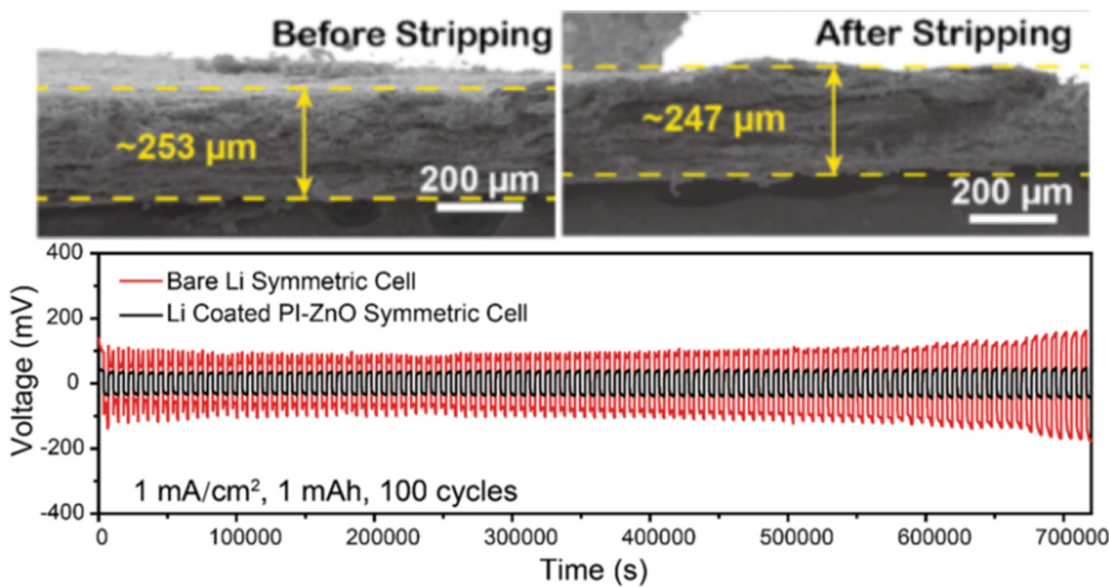


Figure V- 246: SEM images and the corresponding schematics showing the well-confined stripping/plating behavior of the Li-coated PI matrix. Top view SEM images of (a) the exposed top fibers of the Li-coated PI electrode after stripping away  $5 \text{ mAh}/\text{cm}^2 \text{ Li}$ , (b) exposed top fibers partially filled with Li when plating  $3 \text{ mAh}/\text{cm}^2 \text{ Li}$  back and (c) completely filled PI matrix after plating an additional  $2 \text{ mAh}/\text{cm}^2 \text{ Li}$  back

Due to the existence of the host matrix, the issue of infinite volume change associated with the “hostless” Li stripping/plating can now be solved. Even with the complete stripping of Li, the change in electrode thickness was minimal. For example as shown in Figure V- 247 top, the electrode was on average  $\sim 253 \mu\text{m}$  before stripping and remained as  $\sim 247 \mu\text{m}$  after complete stripping, which was merely  $\sim 2.4\%$  of change.

The galvanostatic cycling performance of the Li- coated PI matrix was studied in both carbonate (EC/DEC) and ether based electrolyte and compared with bare Li electrode (Figure V- 247 bottom). At a current density of  $1 \text{ mA}/\text{cm}^2$  in EC/DEC the symmetrical cell of bare Li exhibited a large Li stripping/plating overpotential ( $> 100 \text{ mV}$  vs  $\text{Li}^+/\text{Li}$ ), which increased considerably within the first 100 cycles ( $> 170 \text{ mV}$  in the 100th cycle). In contrast, the Li-coated PI matrix not only showed a much lower overpotential ( $\sim 35 \text{ mV}$  in the initial cycle) but also achieved very stable cycling for at least 100 cycles ( $\sim 40 \text{ mV}$  overpotential in the 100th cycle). These results indicate the improved cycling performance of the nanoporous lithium metal anode fabricated via infusion.



**Figure V- 247:** Electrochemical behaviors of the Li electrodes in EC/DEC electrolyte. (top) Cross-sectional SEM images of nanoporous lithium anode before and after complete lithium stripping. (bottom)Comparison of the cycling stability of the Li-coated PI matrix and the bare Li electrode at a current density of  $1 \text{ mA}/\text{cm}^2$  with fixed capacity of  $1 \text{ mAh}/\text{cm}^2$

### Conclusions and Future Directions

Based on novel nanostructures and nanomaterials, we have developed various methods to resolve the challenges related with lithium metal anode. The initial nanoscale interfacial engineering design already realized several exciting results that have never been realized during the previous half century research on lithium metal anode, including high Coulombic efficiency >99% and long cycling life beyond 150 cycles. At the same time, we have established the standard procedure to evaluate the performance of lithium metal anode, which is essential for our future research. Beyond the successful nanointerface design, we have proposed another effective solution, where nanofibers were incorporated as scaffold for regulated plating and stripping of lithium, in both electrochemical and infusion means. These solutions, though cannot prevent the direct reaction between lithium metal and electrolyte yet, have already suppressed the formation of lithium metal dendrite due to the strong interaction at the nanoscale interface between lithium metal and hosting matrix.

While we are going to continue our successful approaches in the next year, the combinations of interface passivation and scaffold construction would certainly provide a better solution for lithium metal anode, which would control both uniformity and surface reactivity of lithium metal. In addition, the tuning of electrolyte additives, which always played an important role in lithium ion batteries, will also give huge boost to the performance of lithium metal in our future research.

### FY 2015 Publications/Presentations

1. G. Zheng *et al.*, Interconnected hollow carbon nanospheres for stable lithium metal anodes. *Nat. Nanotechnol.* **9**, 618–623 (2014).
2. K. Yan *et al.*, Ultrathin two-dimensional atomic crystals as stable interfacial layer for improvement of lithium metal anode. *Nano Lett.* **14**, 6016–22 (2014).
3. Liang Z. *et al.* Polymer Nanofiber-Guided Uniform Lithium Deposition for Battery Electrodes. *Nano Letters* **15**, 2910-2916 (2015).
4. Liu Y. *et al.* Lithium Coated Polymeric Matrix as Minimum Volume Change and Dendrite Free Lithium Metal Anode. **Submitted**

## V.H.6 Lithium Dendrite Suppression for Lithium-Ion Batteries (PNNL)

### Objectives

- Prevent lithium (Li) dendrite formation on Li-metal anodes used in Li-metal batteries and prevent Li dendrite formation on carbon anodes used in Li-ion batteries during extreme charge conditions such as overcharge, fast charge and charge at low temperatures.
- Explore various factors that affect the morphology of Li deposition, especially under high current density conditions. These factors include solvent-cation reaction, Li-ion additive cation interaction, etc. The long-term stability of these additives also will be investigated.

### Technical Barriers

- Li dendrite growth and low Coulombic efficiency (CE) during Li deposition/stripping are the two major problems hindering the application of Li metal as an anode material in rechargeable Li batteries. Li dendrite growth on carbonaceous anodes in Li-ion batteries also has been a serious safety issue under abusive charging conditions, such as overcharging, charging at high rates, and charging at low temperatures. All of these barriers have hindered commercialization of rechargeable Li-metal batteries as well as state-of-the-art Li-ion batteries for use in plug-in hybrid electric vehicles and pure electric vehicles.

### Technical Targets

- Develop electrolytes to suppress Li dendrite growth on Li metal and graphite anodes and maintain CE at  $\geq 98\%$ .
- Protect graphite electrodes in propylene carbonate (PC)-based carbonate electrolytes with electrolyte additives.
- Achieve over 500 cycles for 4-V Li-metal batteries without internal short circuiting, through optimized electrolyte formulation.

### Accomplishments

- Discovered the mechanism of  $\text{Cs}^+$  additives to effectively protect the graphite anode in PC-rich electrolytes, enhanced the long-term cycling stability of Li-ion batteries based on graphite|| $\text{LiNi}_{0.80}\text{Co}_{0.15}\text{Al}_{0.05}$  (i.e., graphite||NCA) at elevated temperatures, and improved the high rate capability and the low discharge performance of the full cells.
- Discovered that  $\text{Cs}^+$ -containing PC-rich electrolytes can effectively suppress Li dendrite formation on the graphite anode surface during fast-charge conditions.
- Optimized the PC content in  $\text{Cs}^+$ -containing PC-rich electrolytes for graphite||NCA full cells.
- Developed electrolytes with  $\text{Cs}^+$  additive or other solvent mixtures which can maintain 500 stable cycles in  $\text{Li}||\text{LiNi}_{0.4}\text{Mn}_{0.4}\text{Co}_{0.2}$  (i.e., Li||NMC442) cells and retain more than 80% of capacity without internal short circuiting.
- Developed electrolytes to suppress Li dendrite growth and to maintain Li Coulombic efficiency (CE) of above 98%.
- Filed one U.S. Patent Application, published two journal papers, submitted one journal paper, and gave four presentations.

### Project Details

Tien Duong (DOE BMR Program Manager)

Recipient: PNNL

Wu Xu (PNNL – PI)

902 Battelle Boulevard

Richland, WA 99354

Phone: 509-375-6934; Fax: 509-375-2186

E-mail: [wu.xu@pnnl.gov](mailto:wu.xu@pnnl.gov)

Ji-Guang Zhang (PNNL – Co-PI)

902 Battelle Boulevard

Richland, WA 99354

Phone: 509-372-6515; Fax: 509-375-2186

E-mail: [jiguang.zhang@pnnl.gov](mailto:jiguang.zhang@pnnl.gov)

Start Date: October 2012

Projected End Date: September 2016

## Introduction

Li-metal batteries have been called the “holy grail” of energy storage systems because the Li-metal anode has an ultrahigh theoretical specific capacity, low density, and the lowest negative electrochemical potential, but two major problems—Li dendrite growth and low CE of Li deposition/stripping—hinder their commercial application. For a Li-ion battery, Li plating and Li dendrite formation during overcharging, fast charging, or charging at low temperatures also are serious problems that must be solved. A rough or dendritic Li film generated at the anode surface can be self-amplified and lead to internal short circuiting of the battery and even more serious safety problems such as thermal runaway, fire, and explosion. In addition, the use of conventional cathode materials of  $\geq 4$  V in Li-metal and Li-ion batteries requires the electrolytes to be electrochemically stable up to at least 4.5 V, and so far only organic-carbonate solvent-based electrolytes can meet this practical requirement. When PC solvent is added into the ethylene carbonate (EC)-based electrolytes at a content of more than 10% in order to widen the operating temperature range for the batteries, the performance deteriorates because PC is not stable against Li metal and also causes co-intercalation into graphite interlayers, resulting in serious exfoliation of the graphite structure. Electrolyte additives are normally used to form stable solid electrolyte interphase (SEI) layers on Li-metal or graphite surfaces, but such an approach normally leads to thicker SEI layers that negatively compromise other battery characteristics such as rate capability, low-temperature performance, and cycling stability at elevated temperatures. Therefore, a general solution to form a robust, thin, uniform, and compact SEI layer on a Li-metal or graphite anode surface will not only suppress the dendrite growth problem so as to significantly improve the safety of Li-metal and Li-ion batteries, but also enhance their performance in terms of long-term cycling stability, rate capacity, and a wide operating temperature range.

## Approach

**Innovative Approach:** The objectives outlined above will be accomplished by using PC-containing carbonate electrolytes and additives ( $Cs^+$  and others) to form high quality SEI layers to prevent Li dendrite formation on the surface of Li-metal and graphite anodes while maintaining high CE of battery operation. These electrolytes will enhance the cycling stability, rate capability and high/low-temperature stability of Li-metal anodes, graphite anodes, and various  $Li^{+}$ -intercalation cathode materials. As a result, the long-term stability of rechargeable Li-metal batteries and Li-ion batteries will be improved. An areal loading of about  $1.5 \text{ mAh cm}^{-2}$  was used for the cathodes (NCA and NMC442) and the anode (graphite). Various characterization technologies, including high-resolution scanning electron microscopy (SEM), transmission electron microscopy (TEM), X-ray photoelectron spectroscopy (XPS), electrospray ionization mass spectrometry (ESI-MS) and  $^{17}\text{O}$  nuclear magnetic resonance (NMR) spectroscopy will be used to analyze the morphology and composition of the interfacial films on Li-metal and graphite surfaces. The results obtained in these investigations will be combined with density functional theory (DFT) calculations to reveal the mechanism that leads to the enhanced performance in Li-metal and Li-ion batteries.

## Results

We have achieved the following progress:

### Greatly Improved Operating Temperature Window of Li-Ion Batteries Using PC-Rich Electrolyte with $Cs^+$ Additives

In FY2014, we had shown that a small amount of  $CsPF_6$  as the additive in 1 M  $LiPF_6$ /EC-PC-EMC electrolytes can greatly improve the cycling stability of graphite||NCA coin-cell-type full cells at room temperature and elevated temperature (e.g.,  $60^\circ\text{C}$ ), enhance the rate capability, and increase the discharge capacity at elevated temperature. Such performance improvement enabled by the  $CsPF_6$  additive is superior to the conventional SEI additive fluoroethylene carbonate (FEC). It is demonstrated that  $CsPF_6$  can significantly suppress PC co-intercalation into graphite. In FY2015, we further investigated the performance of graphite||NCA full cells using  $Cs^+$ -containing PC-rich electrolytes over a wide temperature range (from  $-40^\circ\text{C}$  to  $+60^\circ\text{C}$ ). Several different electrolytes and additives have been investigated. These electrolytes include

- E2 – Baseline electrolyte: 1 M  $LiPF_6$  in EC-EMC (3:7 by vol.)
- E1 – The PC-rich electrolyte: 1 M  $LiPF_6$  in EC-PC-EMC (5:2:3 by wt.)

- E1VC – The PC-rich electrolyte with vinylene carbonate (VC) additive: 1 M LiPF<sub>6</sub> in EC-PC-EMC (5:2:3 by wt.) with 2 wt.% VC
- E1FEC – The PC-rich electrolyte with FEC additive: 1 M LiPF<sub>6</sub> in EC-PC-EMC (5:2:3 by wt.) with 2 wt.% FEC
- E1Cs – The PC-rich (20%) electrolyte with Cs<sup>+</sup> additive: 1 M LiPF<sub>6</sub> in EC-PC-EMC (5:2:3 by wt.) with 0.05 M CsPF<sub>6</sub>
- E17 – The electrolyte with 10% PC: EC-PC-EMC (2:1:7 by wt.)
- E17Cs – The electrolyte with 10% PC and Cs<sup>+</sup> additive: EC-PC-EMC (2:1:7 by wt.) with 0.04 M CsPF<sub>6</sub>

All the electrolytes were tested in graphite||NCA coin cells. Figure V- 248 compares cycling stability of the cells using electrolytes E2, E1Cs, and E1VC. The stability of the cell with CsPF<sub>6</sub>-containing electrolyte E1Cs [1 M LiPF<sub>6</sub> in EC-PC-EMC (5:2:3 by wt.) with 0.05 M CsPF<sub>6</sub>] exhibits comparable cycling stability at room temperature to the baseline electrolyte E2 (1 M LiPF<sub>6</sub> in EC-EMC (3:7 by vol.) as shown in Figure V- 248A. However, the cell with E1Cs demonstrates much better stability than those with baseline electrolyte E2 at elevated temperature of 60°C, as shown in Figure V- 248B. On the other hand, the cycling stability of VC containing electrolyte E1VC is obviously worse than E1Cs and E2 at both temperatures.

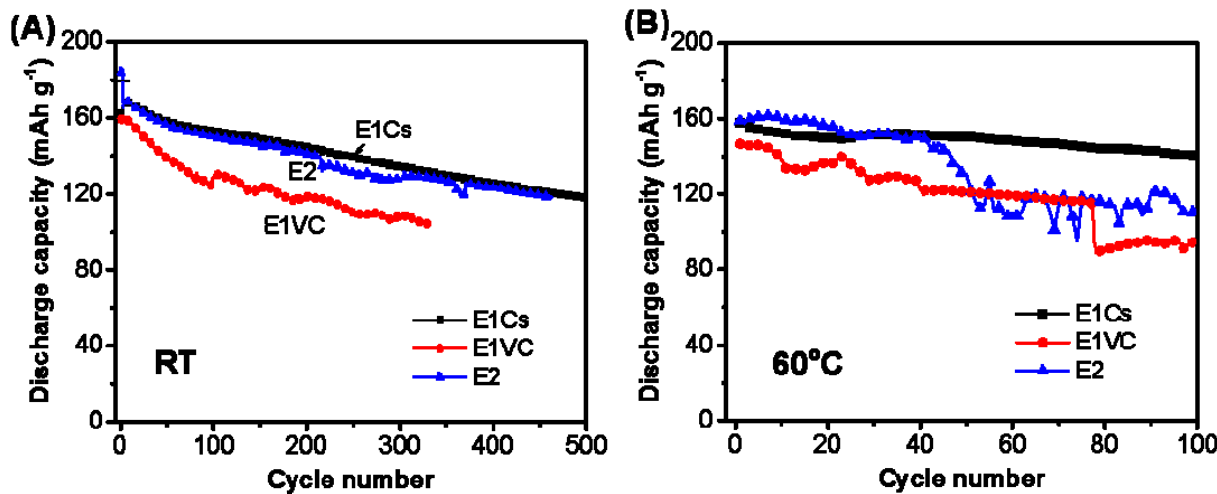


Figure V- 248: Cycling performances of graphite||NCA full cells containing the three electrolytes E1Cs, E1VC and E2 at (A) RT and (B) 60°C

Besides the E1 electrolyte which contains 20% PC solvent [1 M LiPF<sub>6</sub> in EC-PC-EMC (5:2:3 by wt.)], we also tested another electrolyte containing 10% PC solvent [1 M LiPF<sub>6</sub> in EC-PC-EMC (2:1:7 by wt.)] with and without 0.04 M CsPF<sub>6</sub> (E17Cs and E17, respectively). As shown in Figure V- 249, the cell with Cs<sup>+</sup>-containing electrolyte E17Cs has higher Coulombic efficiency, higher reversible capacity and better high-temperature cycling stability than those with the electrolyte but no Cs<sup>+</sup> additive (E17).

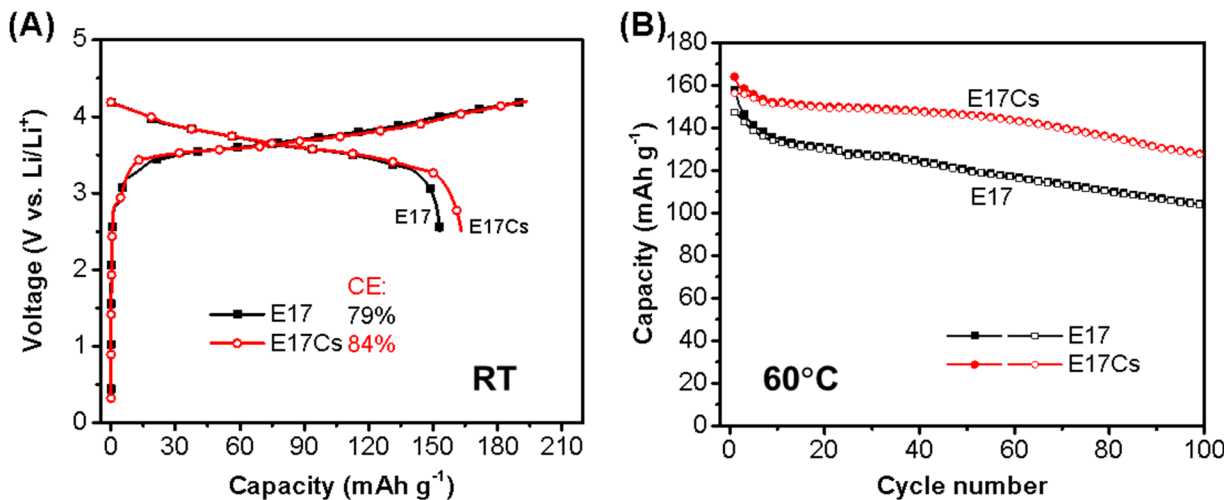


Figure V-249: Comparison of cell performance of graphite || NCA full cells containing two electrolytes, E17Cs and E17. (A) Initial charge/discharge voltage profiles at C/20 rate at RT and (B) cycling stability at 60°C at C/2 rate after two cycles

Figure V-250 compares the low-temperature discharge performance of graphite||NCA full cells with Cs<sup>+</sup>-containing the electrolyte E17Cs and the conventional electrolyte E2. The cells with E17Cs electrolyte maintain a higher discharge capacity at the same temperature conditions than the cell with the electrolyte E2, which has no Cs<sup>+</sup> additive, especially at temperatures below -20°C. For the cells with the Cs<sup>+</sup>-containing electrolyte (E17Cs), the discharge capacity retentions at -30°C and -40°C are 75% (126 mAh g<sup>-1</sup>) and 61% (103 mAh g<sup>-1</sup>) of their room temperature values, respectively. In contrast, for the cells using the electrolyte without Cs<sup>+</sup> additive (E2), the capacity retention drastically decreased to 64% (91 mAh g<sup>-1</sup>) and 18% (25 mAh g<sup>-1</sup>) at -30°C and -40°C, respectively. These results clearly indicate that Cs<sup>+</sup> additive can greatly improve the stability and capacity retention of Li-ion batteries over a wide temperature range (-40°C to 60°C), which is critical for operation of electrical vehicles in extreme weather conditions.

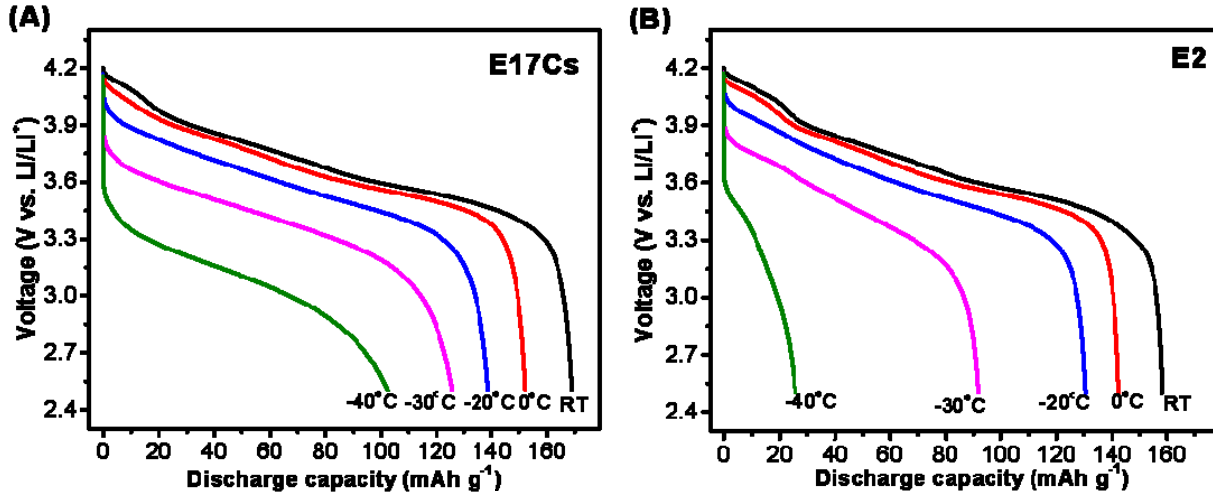


Figure V-250: Comparison of low-temperature performance of graphite || NCA full cells containing two electrolytes, E17Cs (A) and E2 (B). Cells were charged at a C/5 rate at RT, kept for 3 hours at selected low temperature, and then discharged at a C/5 rate at that low temperature

### Characterization of Cycled Graphite Anodes

To investigate the stability of graphite anodes in a PC-rich environment, we first analyzed the graphite anodes obtained from the dismantled Li||graphite half cells that were only charged to 0.3 V for the first time, and there was no Li<sup>+</sup> intercalation into graphite structure yet. The three electrolytes studied included E1, E1FEC and E1Cs. The X-ray diffraction patterns of the graphite anodes shown in Figure V-251A indicate that there is not much difference in the X-ray characteristics of different samples in their bulk region ( $2\theta$  angle of more than 40°), but the broad peak below 20° for graphite from control electrolyte E1 suggests partial exfoliation of

graphite at the edges of the particles, which is also demonstrated in the areas indicated by yellow arrows in the SEM and TEM images (see Figure V- 251B and Figure V- 251C). The pristine graphite has a relatively clean surface (Figure V- 252A). The graphite from the cells using E1 shows significant deposits attached to its surface (Figure V- 252B), which should be the reductive decomposition products of electrolyte components.

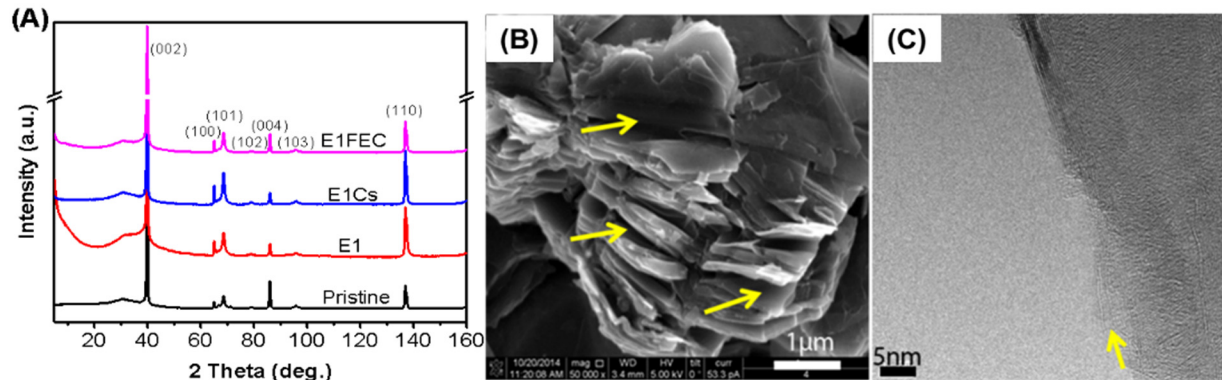


Figure V- 251: (A) Micro-XRD patterns of the graphite electrodes charged to 0.3 V in various electrolytes. SEM (B) and TEM (C) images show the graphite exfoliation in the E1 electrolyte

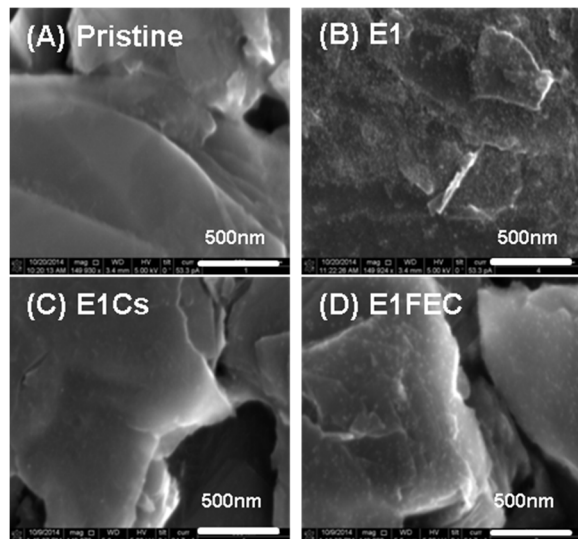


Figure V- 252: SEM images of graphite electrodes: (A) pristine graphite and (B-D) graphite electrodes discharged to 0.3 V in electrolytes of E1 (B), E1Cs (C) and E1FEC (D)

which is consistent with the SEM image in Figure V- 252C. Based on studies of SEIs in the literature, the main components of a common SEI layer include lithium carbonate, lithium alkyl carbonate, and other lithium salts. For the SEI formed in E1Cs, the higher C content and the lower Li content than those formed in E1 and E1FEC suggest that the SEI layer formed in E1Cs consists of more organic species than inorganic species. Time-of-flight secondary ion mass spectrometry results (not shown here) also confirm that the SEI formed in E1Cs contains more oxygen, while the SEI formed in E1FEC is rich in F.

However, the graphite electrode obtained from cells using Cs<sup>+</sup>-containing electrolyte E1Cs has a clean surface with only very limited spots (Figure V- 252C), which is very similar to the pristine graphite. This suggests an ultrathin and uniform SEI layer formed on the graphite surface charged in E1Cs. Figure V- 252D shows many small spots embedded in the SEI layer on the graphite electrode tested in another electrolyte, E1FEC, which also contains no Cs<sup>+</sup> additive.

The morphologies of graphite samples discussed above were further investigated by high-resolution TEM. As shown in Figure V- 253A, the graphite particle in E1 is covered by a thick SEI with the thickness of >6 nm just after the initial charging process without lithiation. Both this thick SEI layer and the deposits shown in Figure V- 252B are results of extensive reductive decomposition of electrolyte components, PC solvent in particular. When FEC is present, a thin (2~4 nm), but uneven, SEI film covered the graphite surface (Figure V- 253B). An ultrathin (<2 nm) and uniform SEI layer was found only in E1Cs (Figure V- 253C),

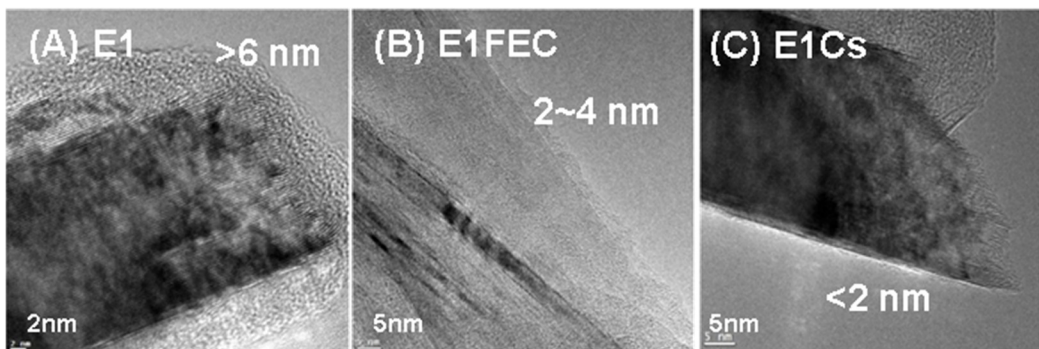


Figure V- 253: TEM images of graphite anodes discharged to 0.3 V from E1 (A), E1FEC (B) and E1Cs (C)

After 100 cycles at 60°C, the graphite anode from E1Cs appears to be clean, and the SEI layer is rather uniform with a thickness of ~1.5 nm (Figure V- 254a, c). This is almost the same as the SEI thickness generated at 0.3 V following the first charge (Figure V- 254C), indicating a stable and uniform interphasial morphology even at high temperature for long-term cycling. However, the SEI layer on the graphite tested in E1FEC contains many particles and the thickness is uneven, varying between 11 and 28 nm (Figure V- 254b, d).

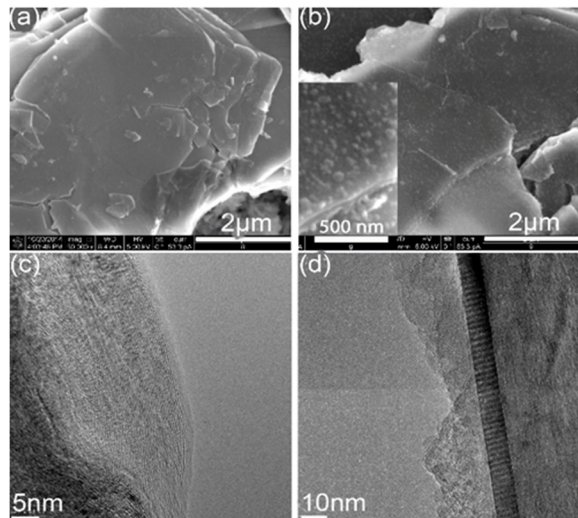
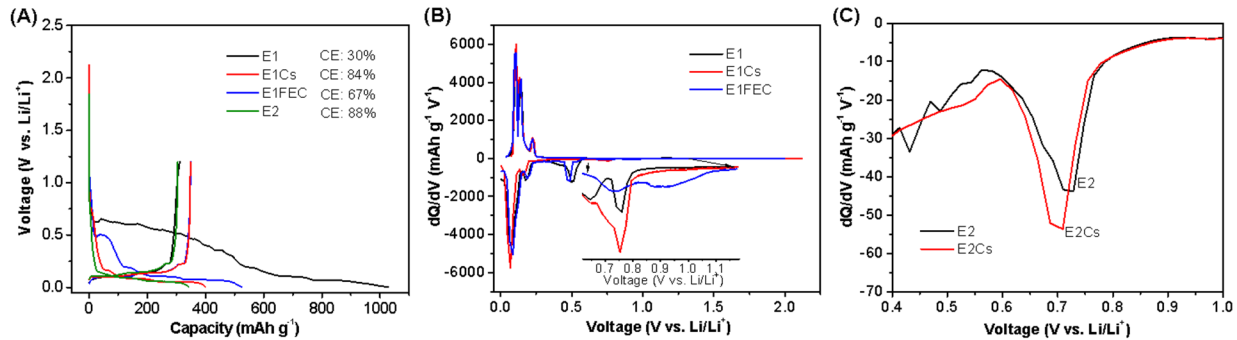


Figure V- 254: SEM images (a, b) and TEM images (c, d) of graphite anodes after 100 cycles at 60°C from graphite || NCA cells with E1Cs (a, c) or E1FEC (b, d)

#### Electrochemical Analysis on Cs<sup>+</sup>-Additive in Li | Graphite Half Cells

As shown in Figure V- 255A, the voltage profile of the Li||graphite half-cell using a PC-rich electrolyte E1 [1 M LiPF<sub>6</sub> in EC-PC-EMC (5:2:3 by wt.)] with no Cs<sup>+</sup> additive exhibits a long plateau above 0.5 V, indicating extensive PC reduction and subsequent graphite exfoliation. This plateau is apparently suppressed in the presence of FEC, but it does not disappear completely. In contrast, the voltage profile of the cell using CsPF<sub>6</sub>-containing electrolyte [E1Cs: 1 M LiPF<sub>6</sub> in EC-PC-EMC (5:2:3 by wt.) with 0.05 M CsPF<sub>6</sub>] completely inhibits this parasitic process. Differential capacity plots in Figure V- 255B provide a more visual comparison, in which the observed conspicuous cathodic peaks at ~0.5 V in E1 or E1FEC, attributed to the PC-reduction process on the graphite, would disappear when Cs<sup>+</sup> is present. A small reductive peak at 0.75 V for all three electrolytes corresponds to the

electrochemical reduction of EC molecules in the Li<sup>+</sup>-(EC)<sub>n</sub> solvates. A third cathodic peak at a higher potential (~0.95 V) in E1FEC is attributed to the reduction of FEC. The peak area or the irreversible capacity corresponding to the peak at 0.75 V for E1Cs is slightly higher than the others, indicating that Cs<sup>+</sup> in E1Cs somehow directs a bit more EC into the reduction process (Figure V- 255B, C).



**Figure V- 255:** Electrochemical behavior of various  $\text{LiPF}_6\text{-CsPF}_6$  electrolytes on graphite surfaces. (A) Lithiation/de-lithiation profiles of  $\text{Li}^+ \mid \text{graphite}$  half cells using electrolytes of E1, E1Cs, E1FEC, and conventional E2. (B and C) Comparison of differential capacity ( $dQ/dV$ ) plots of  $\text{Li}^+ \mid \text{graphite}$  cells using E1, E1Cs, and E1FEC (B), and E2 and E2Cs for the 0.75 V peak (C)

We also used the more soluble CsTFSI salt to replace CsPF<sub>6</sub> additive in the study. Figure V- 256A shows the effect of the solvent components on the lithiation behavior of graphite. Even 0.5 M CsTFSI in pure PC solvent (i.e., E5) cannot help prevent graphite exfoliation. E3 (PC-rich) and E4 (PC-free) show nearly the same lithiation behavior, indicating that the plateau averaged at ~0.75 V is related to Cs<sup>+</sup> and EC. Comparing E4 and E6 (PC-free and Cs<sup>+</sup>-free) suggests that Cs<sup>+</sup> leads to more EC decomposition. Increasing Cs<sup>+</sup> content or EC content shifts the peak at 0.75 V to 0.8 V and increases the peak intensity as well (Figure V- 256B, C). Therefore, EC reduction by the promotion of Cs<sup>+</sup> is responsible for the SEI formation.

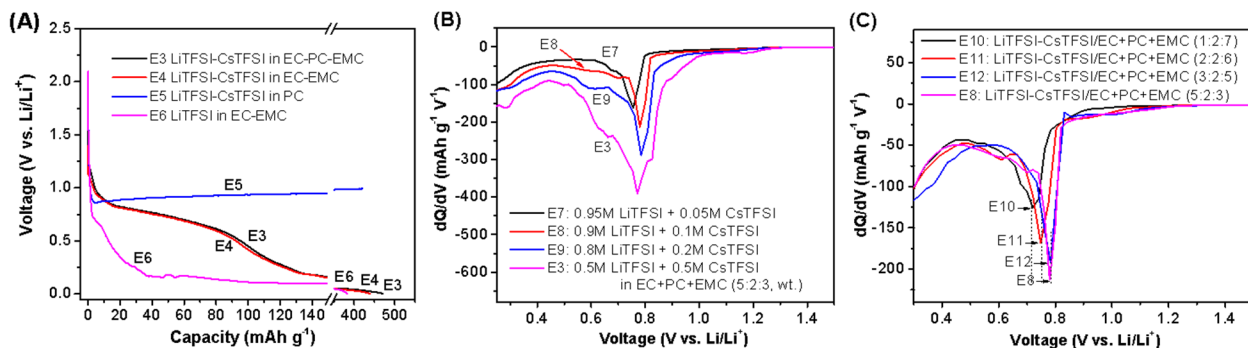


**Figure V- 256:** Electrochemical behavior of various  $\text{LiTFSI}\text{-CsTFSI}$  electrolytes on graphite surfaces. (A) Initial lithiation profiles of graphite in different carbonate electrolytes. (B and C) Comparison of the 0.75 V reduction peaks via  $dQ/dV$  plots for EC-PC-EMC (5:2:3 by wt.) electrolytes at different Cs<sup>+</sup> concentrations (B) and various electrolytes containing 0.9 M LiTFSI and 0.1 M CsTFSI in different EC-PC-EMC mixtures (C). The current density for both lithiation and de-lithiation was 0.075 mA cm<sup>-2</sup> (C/20 rate)

### Protective Mechanism of Cs<sup>+</sup>-Additive on Graphite in PC-Rich Electrolytes

ESI-MS and <sup>17</sup>O NMR spectroscopy were used to determine the solvation preferential and the solvation numbers of Li<sup>+</sup> and Cs<sup>+</sup> with EC and PC molecules. It was found that both Li<sup>+</sup> and Cs<sup>+</sup> prefer to coordinate with PC more than with EC, but Li<sup>+</sup> has preferential solvation ability over Cs<sup>+</sup>. The solvation number for Li<sup>+</sup> is normally 3~4, but only 1~2 for Cs<sup>+</sup>. Therefore, in the Cs<sup>+</sup>-containing, PC-rich electrolytes studied in this work, solvates Li<sup>+</sup>-(PC)<sub>3~4</sub> and Li<sup>+</sup>-(PC)<sub>a</sub>(EC)<sub>b</sub>, where a + b = 3 or 4, are preferentially formed, while Cs<sup>+</sup> can only coordinate with other EC molecules to form Cs<sup>+</sup>-(EC)<sub>1~2</sub> solvates. According to the DFT calculations, the lowest unoccupied molecular orbital (LUMO) energies for Li<sup>+</sup>-(PC)<sub>3~4</sub> and Li<sup>+</sup>-(PC)<sub>a</sub>(EC)<sub>b</sub> solvates are much higher than those for Cs<sup>+</sup>-(EC)<sub>1~2</sub> solvates: about -2~-2.5 eV for the former versus about -3.5~-4.5 eV for the latter. So the Cs<sup>+</sup>-(EC)<sub>1~2</sub> solvates will be electrochemically reduced on graphite surface prior to the Li<sup>+</sup>-(PC)<sub>3~4</sub> and Li<sup>+</sup>-(PC)<sub>a</sub>(EC)<sub>b</sub> solvates. Since the SEI layer formed from EC is of high quality (i.e., uniform, compact, and thin), the intercalation of PC molecules into the graphite structure is completely blocked. This protective mechanism of Cs<sup>+</sup> additive has been illustrated in Figure V- 257.

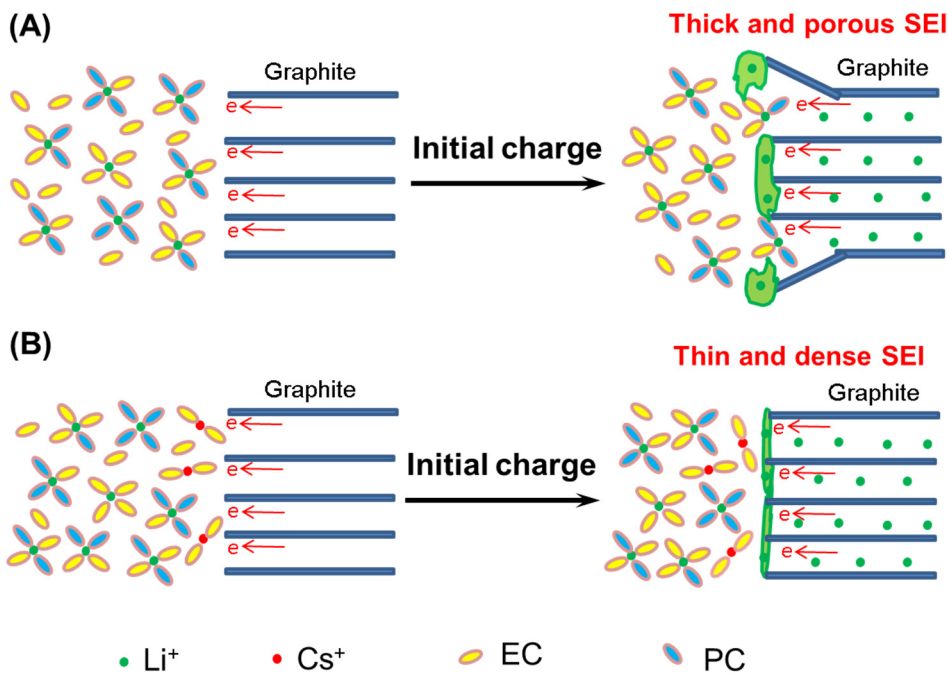


Figure V- 257: Schematic mechanism of SEI film formation promoted by Cs<sup>+</sup>. (A) In a conventional electrolyte, Li<sup>+</sup> favors PC to form solvates. (B) In a Cs<sup>+</sup>-containing electrolyte, due to the preferential formation of Li<sup>+</sup>-(PC)<sub>n</sub> solvates, Cs<sup>+</sup> coordinates with EC molecules and its solvates have priority to be electrochemically reduced

#### Suppression of Li Deposition on Graphite Anode in Cs<sup>+</sup>-Containing PC-Rich Electrolytes

The effect of charge current density on Li dendrite formation on graphite anodes was also investigated in the control electrolyte E2 and a Cs<sup>+</sup>-containing electrolyte, 1.0 M LiPF<sub>6</sub> + 0.05 M CsPF<sub>6</sub> in EC-PC-EMC (3:2:5 by weight) (E20PC-Cs). The voltage profiles of graphite electrodes during discharge to the same capacity of 334 mAh g<sup>-1</sup> (corresponding to 1.5 mAh cm<sup>-2</sup>) at current densities increasing from 0.2 to 2.0 mA cm<sup>-2</sup> are shown in Figure V- 258a-b. The cells with control electrolyte show drastic electrode polarizations with increasing lithiation current density, while the cells with Cs<sup>+</sup>-containing electrolyte have less polarization. After lithiation, the graphite electrodes were retrieved and their morphologies were observed with SEM (see Figure V- 258c-k). In the control electrolyte, some Li dendrites are already observed on the surface of graphite electrode at a discharge current density of 0.5 mA cm<sup>-2</sup> (Figure V- 258d). More Li dendrites are identified at higher current densities of 1.0 and 2.0 mA cm<sup>-2</sup> (Figure V- 258e, f). However, in E20PC-Cs electrolyte, far fewer Li dendrites could be identified on the graphite electrode surface (Figure V- 258g-k). No Li dendrite could be found when the graphite was discharged at 0.2 and 0.5 mA cm<sup>-2</sup>, although sporadic Li dendrites are still observed at higher current densities of 1.0 and 2.0 mA cm<sup>-2</sup> (Figure V- 258j, k). The result illustrates that the Li dendrite formation is suppressed in the CsPF<sub>6</sub>-containing PC-rich electrolyte.

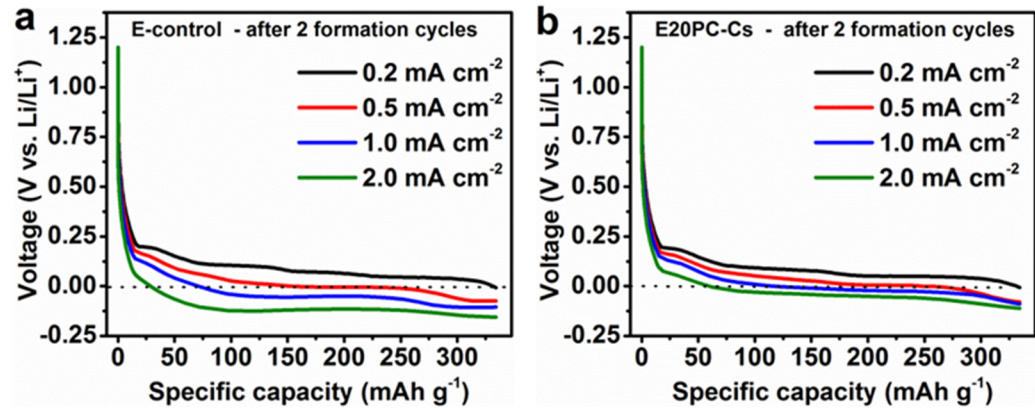


Figure V-258: Lithiation voltage profiles of graphite electrodes in (a) control electrolyte, (b) E20PC-Cs electrolyte at different discharge current densities ranging from 0.2 to 2.0 mA cm<sup>-2</sup>. SEM images showing the Li dendrite formation on the surface of graphite electrodes in control electrolyte E2 (c-f) and in E20PC-Cs electrolyte (g-k) at different current densities: (c, g) 0.2 mA cm<sup>-2</sup>; (d, h) 0.5 mA cm<sup>-2</sup>; (e, j) 1.0 mA cm<sup>-2</sup>; (f, k) 2.0 mA cm<sup>-2</sup>

#### Effect of PC Content on the Performance of Graphite||NCA Full Cells with Cs<sup>+</sup>-Containing PC-Rich Electrolytes

The role of PC content in the presence of CsPF<sub>6</sub> additive (0.05 M) on the performance of graphite electrode in Li||graphite half cells and graphite||NCA full cells was systematically investigated. As shown in Figure V-259, the electrolyte with 20% PC in the solvent mixture shows the best cycling performance for 500 cycles at room temperature (RT). This electrolyte also exhibits the same rate capability as the non-PC control electrolyte but better high-temperature cycling stability. The trend for Li dendrite formation on graphite anodes during fast charge is also alleviated owing to the reduced kinetic barrier for Li<sup>+</sup>-ion transportation through this ultrathin SEI layer. The synergistic effects of the desirable SEI layer formed on the graphite electrode and the presence of low-melting-point PC solvent enable the sustainable operation of the graphite||NCA full cells over a wide temperature range.

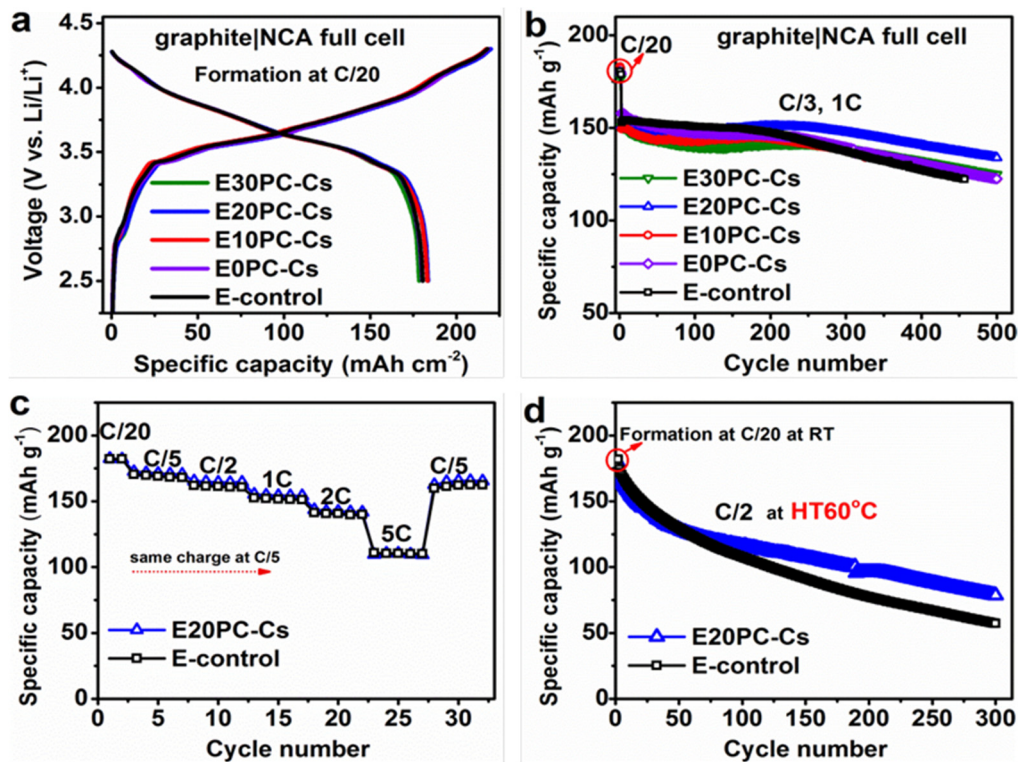


Figure V-259: (a) Initial charge/discharge profiles at C/20 ( $1\text{C} = 1.5 \text{ mA cm}^{-2}$ ) and (b) long-term cycling performance of graphite|NCA full cells using electrolytes containing different amounts of PC at RT. (c) Rate capability at RT. (d) Long-term cycling stability (C/2 rate for charge and discharge) of graphite|NCA full cells using non-PC control and E20PC-Cs electrolytes at an elevated temperature of 60°C

### High Coulombic Efficiency and Long-Term Cycling Stability of 4-V Li-Metal Batteries

The long-term cycling stability of Li|NMC442 coin cells was investigated with ten electrolytes, including three controls based on 1.0 M LiPF<sub>6</sub> in EC/EMC at different ratios (E004, E256 and E448), four based on 1.0 M LiPF<sub>6</sub> + 0.05 M CsPF<sub>6</sub> in EC/PC/EMC at different ratios (E432, E440, E444 and E446), and three other salts-based electrolytes (E319, E319D and E456). NMC442 was used as the cathode due to its good structural stability and thermal stability, and the loading of NMC442 was moderately high at 2.0 mAh cm<sup>-2</sup> so the results would be more realistic. After two formation cycles at C/20 rate, the cells were charged at C/3 rate and discharged at 1C rate in the voltage range of 2.7 to 4.3 V. All tested electrolytes have similar first-cycle charge/discharge voltage profiles. Two control electrolytes (E004 and E256) and two studied electrolytes (E446 and E448) show stable cycling for 500 cycles before the capacity retention reaches 80%, and nearly all of these electrolytes have Coulombic efficiencies above 98% after the first two formation cycles. (Figure V-260).

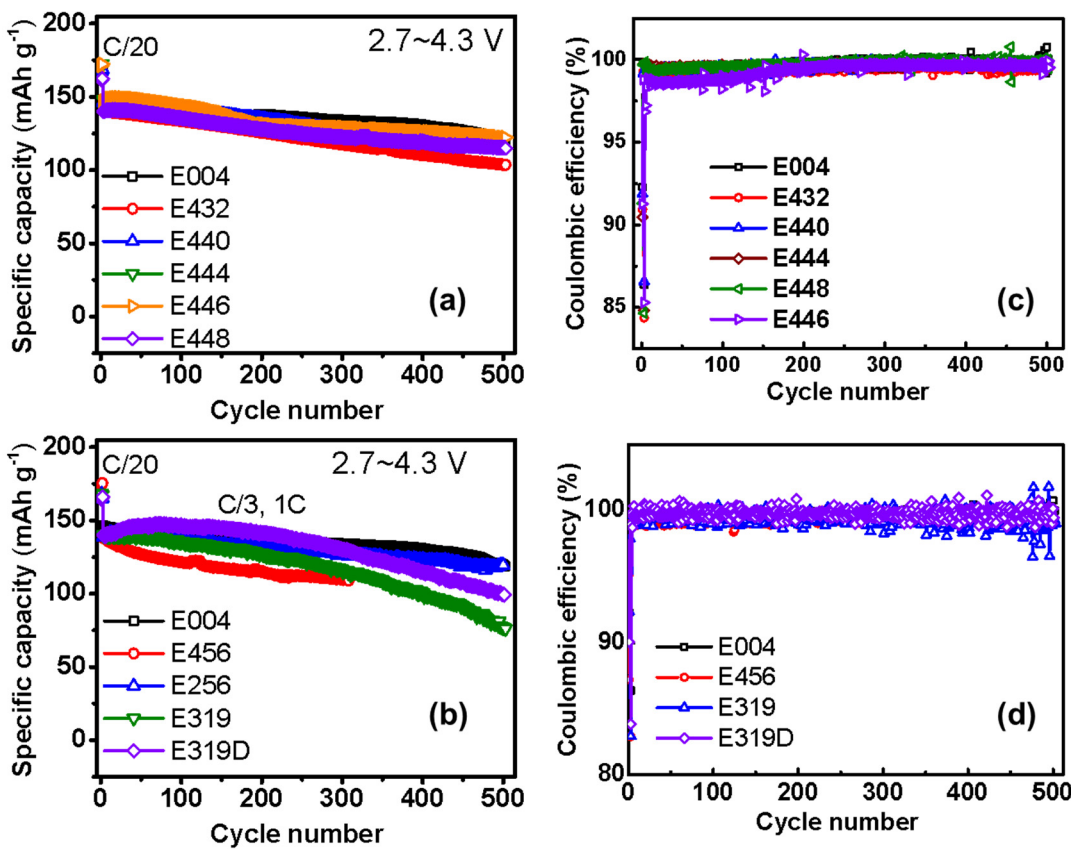


Figure V-260: Long-term cycling stability of Li||NMC442 coin cells with 10 electrolytes at RT. (a, b) Specific capacity vs. cycle number; (c, d) Coulombic efficiency vs. cycle number

### Conclusions and Future Directions

The effects of Cs<sup>+</sup>-additive on the cell performance of graphite||NCA full cells with PC-rich electrolytes were systematically investigated in terms of cycling stability at RT and elevated temperature, rate capability, and low-temperature discharge. The mechanism behind the prevention of graphite exfoliation in PC-rich electrolytes and the enhancement of cell performance were also comprehensively investigated. The Cs<sup>+</sup>-containing, PC-rich electrolytes were found to suppress Li dendrite formation on graphite anode surfaces during fast charging. The tests in Li||NMC442 cells demonstrated that two studied electrolytes can lead to more than 500 stable cycles with capacity retention above 80% and without short circuit. Most of the cells using these electrolytes have high CE above 98%. The fundamental mechanism of the Cs<sup>+</sup> additive to protect graphite anodes in PC-rich electrolytes and improve the performance of full cells will be further investigated in large-size (i.e., 1 Ah) pouch cells in order to attract interest from electrolyte and battery manufacturers and to license this electrolyte technology. The electrolytes for Li-metal batteries in preventing Li dendrite growth during long-term cycling will be further investigated in cells with high-loading 4-V cathodes.

### FY 2015 Publications/Presentations

- W. Xu, H. Xiang, J.-G. Zhang, and R. Cao, Solid electrolyte interphase film-suppression additives, U.S. Patent Application Number 14/565,065, filed on January 12, 2015.
- L. Xiao, X. Chen, R. Cao, J. Qian, H. Xiang, J. Zheng, J.-G. Zhang, and W. Xu, "Enhanced performance of Li||LiFePO<sub>4</sub> cells using CsPF<sub>6</sub> as an electrolyte additive," *Journal of Power Sources*, 2015, **293**, 1062-1067.
- H. Xiang, D. Mei, P. Yan, P. Bhattacharya, S. D. Burton, A. V. Cresce, R. Cao, M. H. Engelhard, M. E. Bowden, Z. Zhu, B. J. Polzin, C. Wang, K. Xu, J.-G. Zhang, and W. Xu, "The Role of Cesium Cation in Controlling Interphasial Chemistry on Graphite Anode in Propylene Carbonate-Rich Electrolytes," *ACS Applied Materials & Interfaces*, 2015, **7**(37), 20687-20695.

4. J. Zheng, P. Yan, R. Cao, M. H. Engelhard, H. Xiang, B. J. Polzin, C. Wang, J.-G. Zhang, and W. Xu, "Improved Performances of Graphite||LiNi<sub>0.80</sub>Co<sub>0.15</sub>Al<sub>0.05</sub>O<sub>2</sub> Lithium-ion Batteries via Manipulating Interphasial Chemistry on Graphite Electrode," under review.
5. W. Xu, L. Xiao, J. Qian, E. Nasybulin, X. Chen, H. Xiang, R. Cao, and J.-G. Zhang, "CsPF<sub>6</sub> as an electrolyte additive for Li|LiFePO<sub>4</sub> batteries," oral presentation at *2014 MRS Fall Meeting & Exhibit*, Boston, MA, November 30-December 5, 2014.
6. W. Xu, J.-G. Zhang, Y. Zhang, J. Qian, L. Xiao, P. Bhattacharya, E. Nasybulin, M. H. Engelhard, R. Cao, H. Xiang, X. Chen, D. Mei, S. M. Russell, A. V. Cresce, and K. Xu, "Lithium dendrite suppression for rechargeable lithium batteries," oral presentation at *2015 International Battery Association and Pacific Power Source Symposium Joint Meeting*, Big Island, Hawaii, January 5-9, 2015.
7. H. Xiang, P. Yan, P. Bhattacharya, R. Cao, M. E. Bowden, J. Qian, B. J. Polzin, C. Wang, J.-G. Zhang, and W. Xu, "A novel additive for enhancing electrochemical stability of graphite anode in PC-rich electrolytes," presentation at *the 227<sup>th</sup> Electrochemical Society Meeting*, Chicago, IL, May 24-28, 2015.
8. W. Xu, H. Xiang, F. Ding, L. Xiao, Y. Zhang, P. Bhattacharya, P. Yan, R. Cao, M. E. Bowden, C. Wang, and J.-G., Zhang, "New electrolyte additives for enhancing anode protection," Invited talk at *2015 International Conference on Electrochemical Energy Science and Technology*, Vancouver, British Columbia, Canada, August 16-20, 2015.

# V.H.7 Daikin Advanced Lithium Ion Battery Technology – High Voltage Electrolyte (Daikin America)

## Objectives

- To develop and optimize an advanced electrolyte containing fluorochemical compounds to achieve:
  - 300 cycles at 4.6 V with a cut off capacity retention of 80%
  - Reduced/no flammability

## Technical Barriers

- This project is focused on the improvement of cycle/calendar life at high voltage (4.6 V) using advanced electrolytes which have improved safety characteristics

## Technical Targets

- Development and optimization of formulations containing fluorinated molecules.
- Increased high voltage cycle life
- Improved safety through intrinsic properties of the electrolyte and reduced interaction with charged electrodes.

## Accomplishments

- Energy gains of up to 50% can be realized by operating existing battery chemistries at higher voltage
- The cycle life of batteries operating at higher voltage (4.35 V) has been greatly improved using Daikin fluorinated electrolyte as evidenced by 60 C cycling data.
- A solvent package has been developed which offers an optimized set of properties including rate performance, increased cycle life and improved safety characteristics. This solvent combination has shown successful (> 250 cycles) cycle behavior in NMC111/graphite batteries
- An additive package has also been identified through cycling data and high precision coulometric techniques employed by Coulometrics.
- Improved safety characteristics have been demonstrated through both overcharge and nail penetration testing
- Sources of gassing in the batteries (electrolyte components, electrode surfaces, voltage and temperature) have been identified which is enabling further development of additives for increased battery life (decreased gassing)
- Fluoroethylene carbonate has been identified as a key source of the gassing at high voltage. The understanding of the behavior of this material important as it has been identified as a key component in the operation of silicon anodes.
- Surface studies which include a suite of Auger, X-ray photoelectron spectroscopy (XPS), and time of flight secondary ion mass spectrometry (TOF-SIMS) have been initiated to determine the nature of films formed by Daikin additives on cathode and anode (graphite, silicon) surfaces.
- The technologies originally evaluated in NMC111/graphite cells are now being evaluated in several additional chemistries to provide a comprehensive look at high voltage electrolyte to DOE.

## Project Details

**Christopher Johnson (NETL Program Manager)**

DE-EE0006437 Recipient: Daikin America, Inc.

**Ron Hendershot**

R & D Director

**Joe Sunstrom**

Senior Applications Development Chemist

2749 Highway 20

Decatur, AL 35601

Phone: 256-260-6314

E-mail: [sunstrom@daikin-america.com](mailto:sunstrom@daikin-america.com)

Subcontractor:

Coulometrics LLC

1086 Duncan Avenue

Chattanooga, TN 37404

Start Date: October 2013

Projected End Date: January 2016

## Introduction

The use of small fluorinated molecules to enhance electrolyte stability is the focus of this project. Fluorinated small molecules show increased chemical and thermal stability due to the inherent strength of the C-F bond. These low molecular weight materials also exhibit viscosities low enough to make viable electrolyte solvents/additives. The stability of these fluorochemicals will allow routine operation to 4.6 V. There are two separate strategies involved to achieve this: 1) increasing intrinsic stability of the electrolyte solvents and 2) design of fluorinated molecules with functional moieties to bond with electrode surfaces as functional films. This technological advance would allow reduction in the number of cells needed for a target application thus reducing overall cost.

## Approach

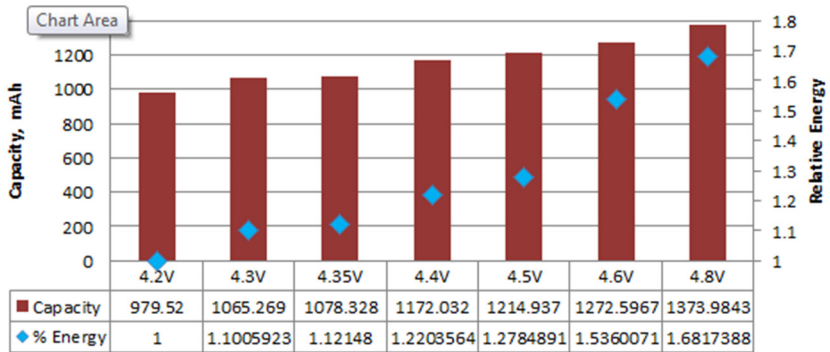
**Innovative Approach:** Drawing on a large library of fluorinated molecules synthesized at Daikin, optimization of high voltage electrolytes will be achieved by a PDCA (Plan-Do-Check-Act) cycle method. Specifically, this involves multiple cycles to optimize electrolyte solvent composition based on intrinsic properties (eg. conductivity, voltage stability). Optimization of SEI and gassing additives will then be superimposed over the optimal solvent combinations to propose candidate electrolytes. This is accomplished by the construction and manipulation of composition/property maps. Finally, the best candidate electrolytes will be evaluated using high performance coulometric techniques and real time cycling data to achieve the target.

## Results

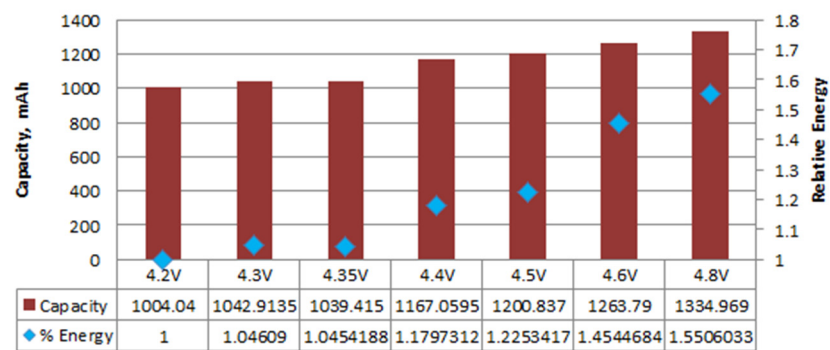
**Cell Performance Impact at Higher Voltages:** Previously, we have shown that significant energy gains can be accomplished by running a commercial cell at elevated voltages. Figure V- 261 shows the energies of a NMC111/graphite cell run at voltages ranging from 4.2 V to 4.8 V. The panels on the right are Daikin fluorinated electrolyte and the panels on the left are a hydrocarbon control. The panels on the top are done at a low rate 0.2 C and the panels on the bottom are at 1 C. The energies are calculated by integrating the capacity curves at each voltage. The energies are then normalized to the energy at 4.2. The data show that the energy increase at 4.5 volts is 31%. This energy gain can also be realized in the hydrocarbon control initially.

Figure V- 262 shows the same analysis for LCO/graphite. In this chemistry, an energy gain of 31% can be achieved at 4.5 V. It should also be noted that there is a linear dependence of the energy on voltage with a discontinuity between 4.5 and 4.6 V for the fluorinated electrolyte. The discontinuity for the hydrocarbon electrolyte occurs between 4.3 and 4.4 V. It has previously been noted in several experiments that the hydrocarbon electrolytes shows degradation at voltages above 4.35 V. For this experiment the NMC11/graphite cells were a commercial cell balanced for 4.2 V operation. These analyses have also now been completed for NCA/graphite and NMC532 graphite.

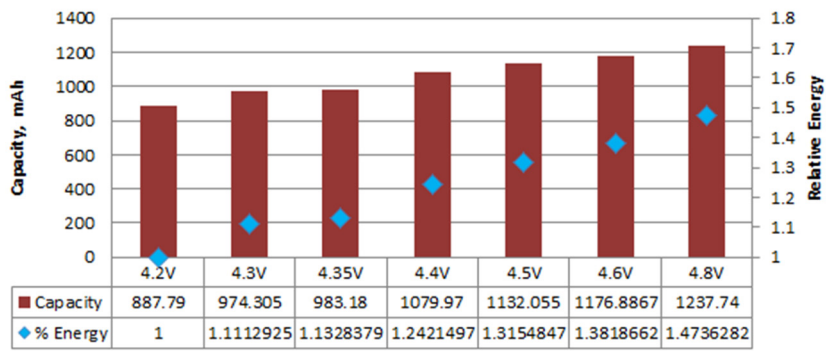
### Fluorocarbon Electrolyte Performance(0.2C)



### Hydrocarbon Electrolyte Performance(0.2C)



### Fluorocarbon Electrolyte Performance(1.0C)



### Hydrocarbon Electrolyte Performance(1.0C)

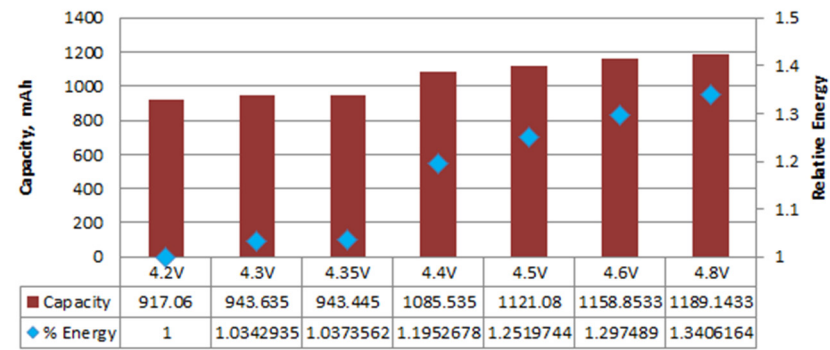


Figure V- 261: Cell Energies at elevated voltages normalized to 4.2 V for NMC111/graphite

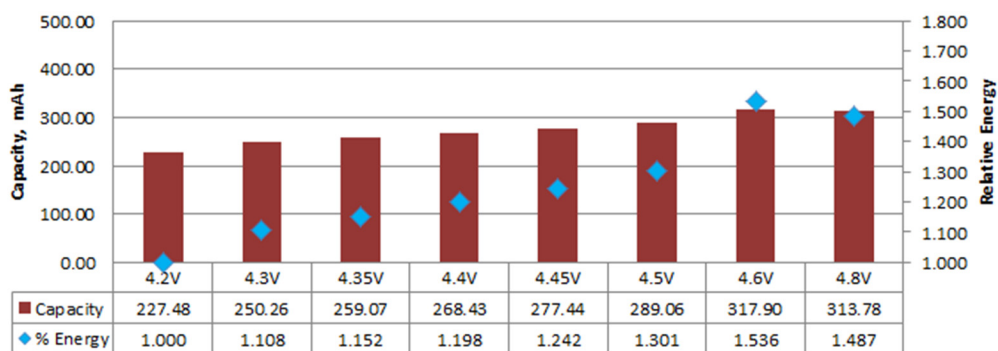
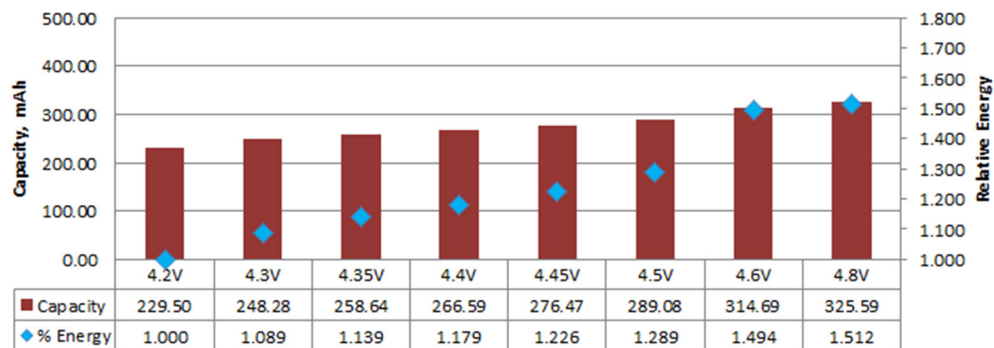
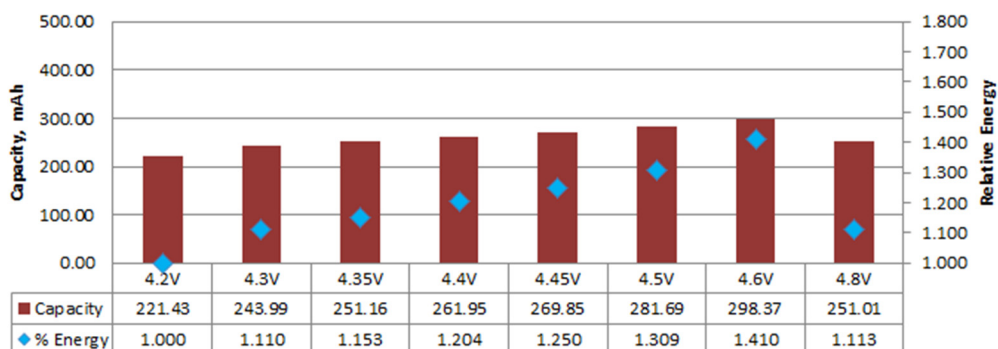
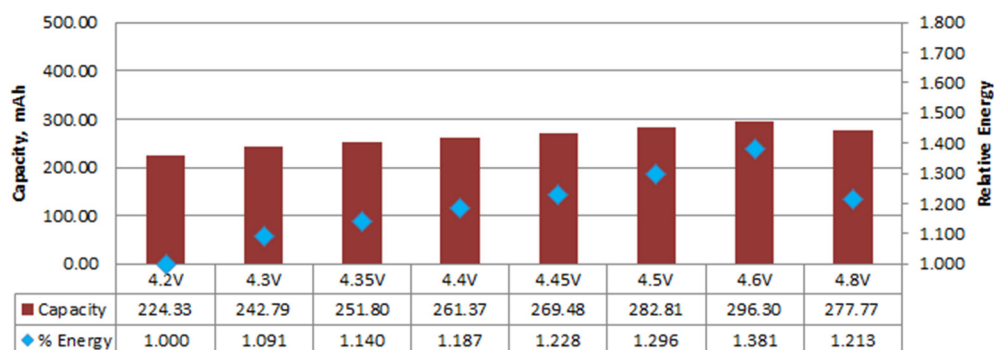
**Fluorocarbon Electrolyte Performance(0.2C)****Hydrocarbon Electrolyte Performance(0.2C)****Fluorocarbon Electrolyte Performance(1.0C)****Hydrocarbon Electrolyte Performance(1.0C)**

Figure V- 262: Cell Energies at elevated voltages normalized to 4.2 V for LCO/graphite

**Optimization of Solvent Package for High Voltage Cycling:** The 4.2 V 72 Hr 60°C storage data (Figure V-263) for several compositions of FEC/organic carbonate/F-solvent were analyzed. The organic carbonate could be EMC, DMC or DEC. All of the samples showed similar capacity retention on storage. The selection criteria, therefore, became the gas generation. The two samples on the left in the graph contain EC as opposed for FEC. It was known that EC would not be suitable for high voltage so the selection pool was further narrowed to electrolytes containing FEC. The two best candidates were 1.2 M LiPF<sub>6</sub> FEC/EMC/F-solvent (2:6:2) and 1.2 M LiPF<sub>6</sub> FEC/DEC/F-solvent (2:6:2). The former was selected due to higher conductivity

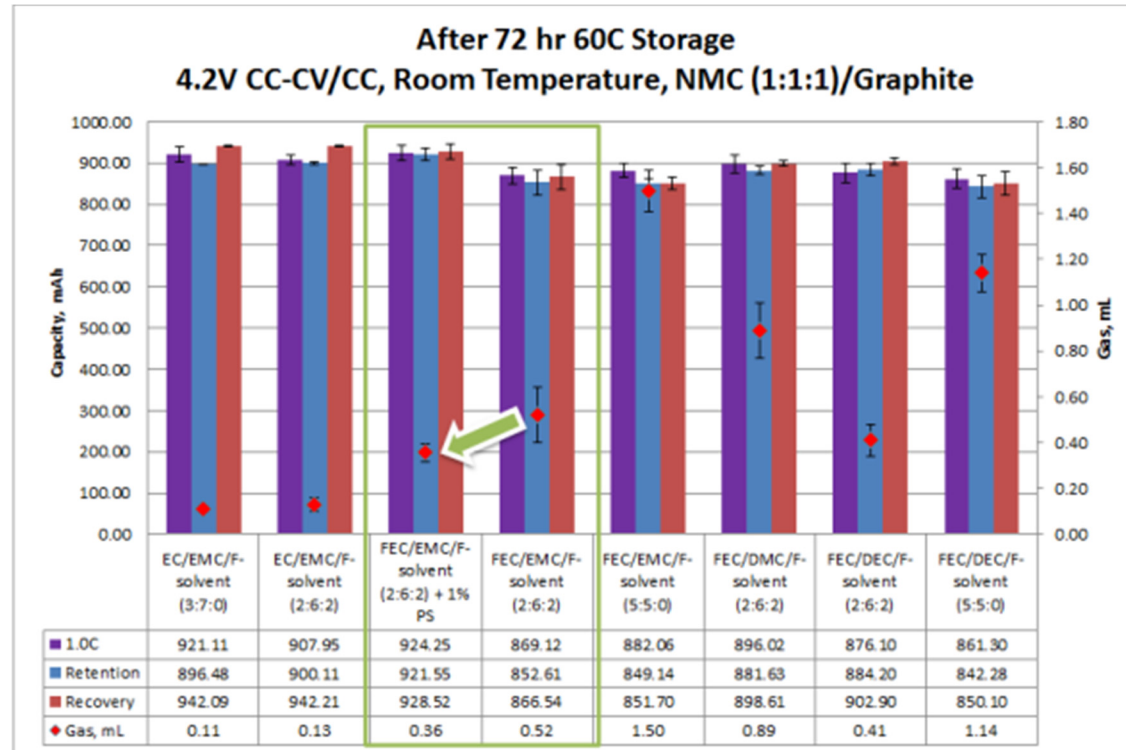


Figure V- 263: Retention and recovery capacities and gassing volume for several solvent compositions

Earlier experiments indicated that the threshold voltage for hydrocarbon decomposition in electrolyte was around 4.35 V. NMC111/graphite cells were filled with the optimized electrolyte solvent package (1.2 M LiPF<sub>6</sub> FEC/EMC/F-solvent + 1% propane sultone PS). The PS was added as an additional precaution against gassing. In addition, cells were also filled with a hydrocarbon control 1.0 M LiPF<sub>6</sub> EC/EMC (3:7) + 1%PS. The cells were then cycled at 1 C and 60 C. The upper cycling voltages were selected to be below (4.2 V), at (4.35 V) and above (4.5 V) the hypothesized decomposition threshold voltage.

The data is shown in Figure V- 264 with the hydrocarbon control and Daikin fluorinated electrolytes in the top and bottom panels respectively. The hydrocarbon control cells cycled at 4.5 V dies very quickly and cells cycled near the 4.35 V decomposition voltage also eventually die. The cells filled with Daikin fluorinated electrolyte continue to cycle at 250 cycles and 60 C.

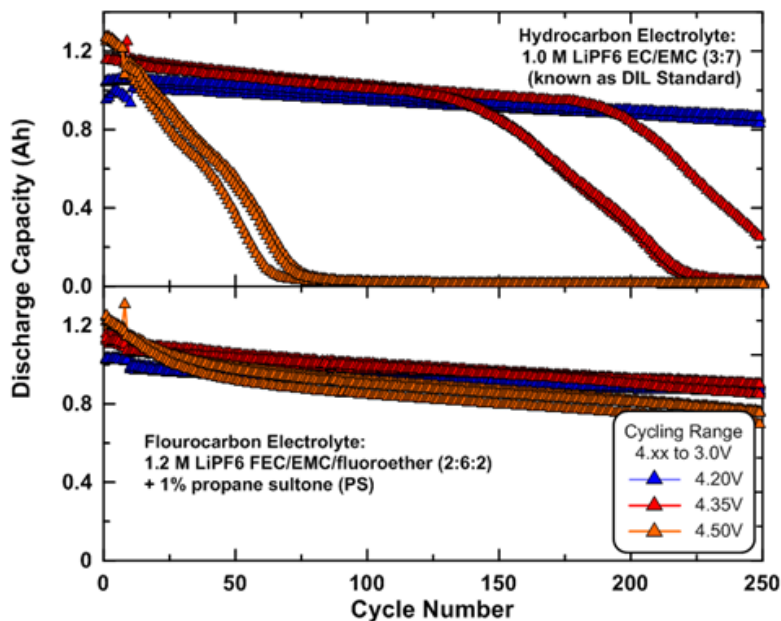


Figure V- 264: NMC111/graphite cells cycled at 1 C and 60 C. at three voltages (4.20, 4.35 and 4.50 V) for both the hydrocarbon control electrolyte (top panel) and Daikin fluorinated electrolyte (bottom panel)

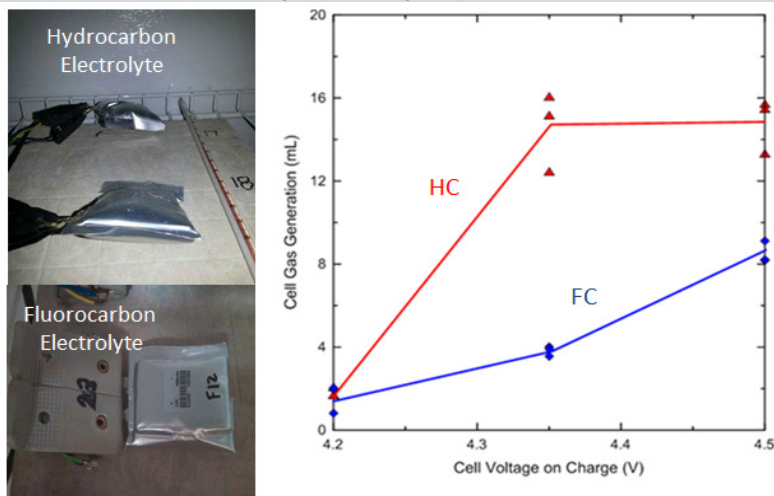


Figure V- 265: Photos of NMC111/graphite cells after the cycling reported in the prior figure. The photos show cells filled with hydrocarbon control electrolyte (top) and the Daikin fluorinated electrolyte (bottom). The post experiment gas volumes vs voltage are graphed in the right

was fixed, various combinations of additives were added. The finished electrolytes were then filled into the NMC111/graphite cells and were examined by high performance coulometric techniques as a screening tool. This work was completed at Coulometrics and is based on the work of Jeff Dahn. When several combinations were identified, new cells were constructed with the candidate electrolytes and were cycled to 4.5 V at 60 C. Figure V- 266 shows the cycling data for various combinations. The hydrocarbon control electrolyte (1.0 M EC/EMC 7:3) is included for reference. All other samples shown in this Figure V- 266 use the optimized Daikin solvent composition as a base. All of the electrolytes with the Daikin fluorinated solvent show same magnitude performance. The effect of the additives is to manipulate the slope of the cycle life curve. This experiment shows the best combination of additives to be 1% Z1 (gassing additive) + 1% FA(fluoroadditive)1 (SEI formation additive)

Figure V- 265 shows photos of the cells immediately following this test. The hydrocarbon cells have visible gassing while the fluorocarbon cells do not. The numerical gassing data is in the right panel.

#### Optimization of Additives:

Following the choice of the appropriate solvent mixture, experiments were then completed to optimize an additive mixture for the NMC111/graphite cell chemistry for operation above 4.35 V. It should be noted that additives by definition are those components existing in a <5% by weight concentration in the mixture. The solvents are considered to be anything in >10% concentration by volume. The additives developed at Daikin may have several functionalities such as: 1. Surface modification agents for anode and/or cathode 2. Direct interaction with contaminants such as HF and 3. Agents which affect solubilities of metal ions at high voltage. The additive and solvent mixtures described in this report were optimized for NMC111/graphite. It will be necessary to develop custom formulations depending in cell chemistry and operational parameters (voltage, temperature, rate).

When the solvent mixture (1.2 M LiPF<sub>6</sub> FEC/EMC/F-solvent)

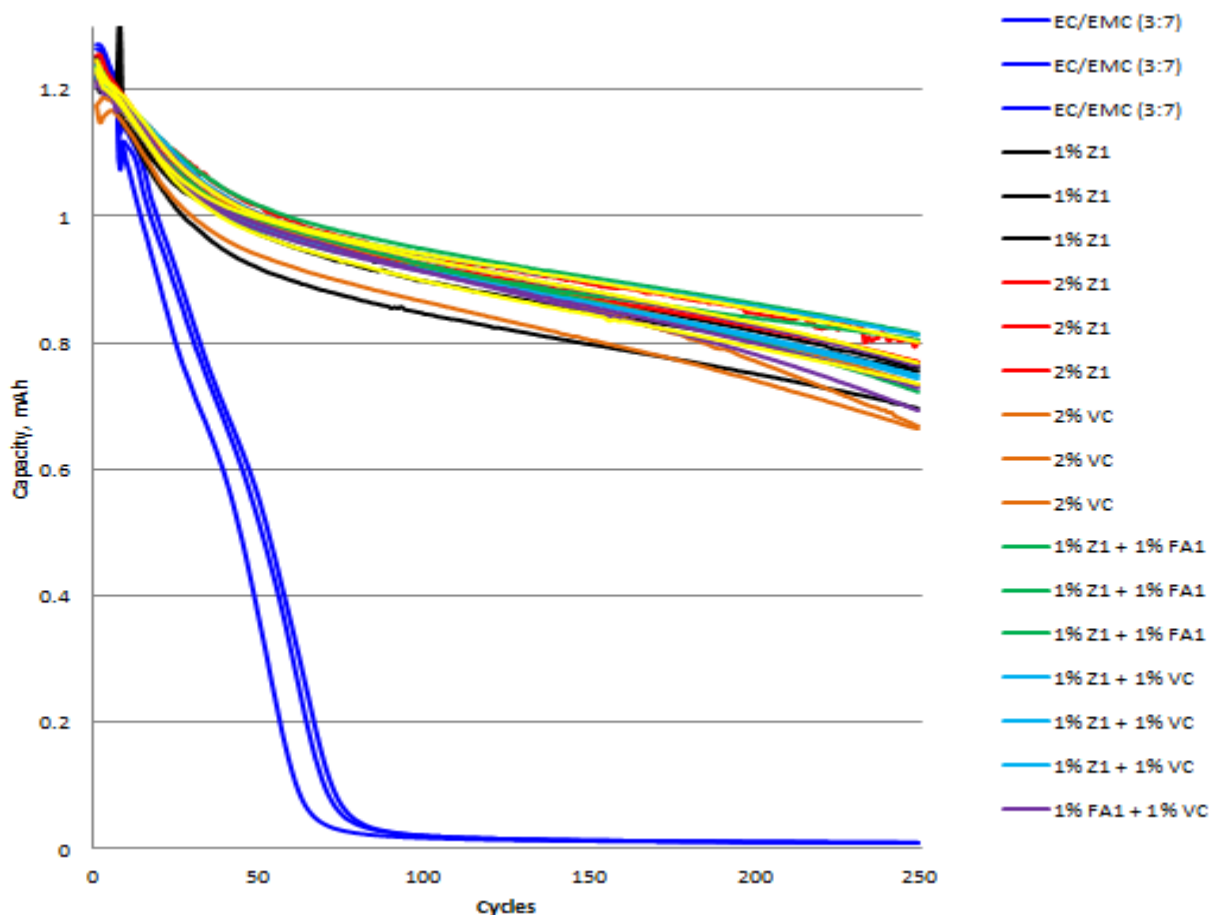


Figure V- 266: Cycle life(1 C, 60 C, 3.0-4.5 V) of fluorinated electrolytes containing different additive packages. The hydrocarbon control electrolyte is shown in blue

Gassing measurements were also performed on various additive mixtures. The cells were filled with the same solvent mixture with variable additive mixtures. The cells were charged to 4.5 V and stored 72 hours at 60 C. The gas volume data for these mixtures is shown in Figure V- 267. The primary result is that mixtures containing vinylene carbonate exhibit more gassing when operated at higher voltages.

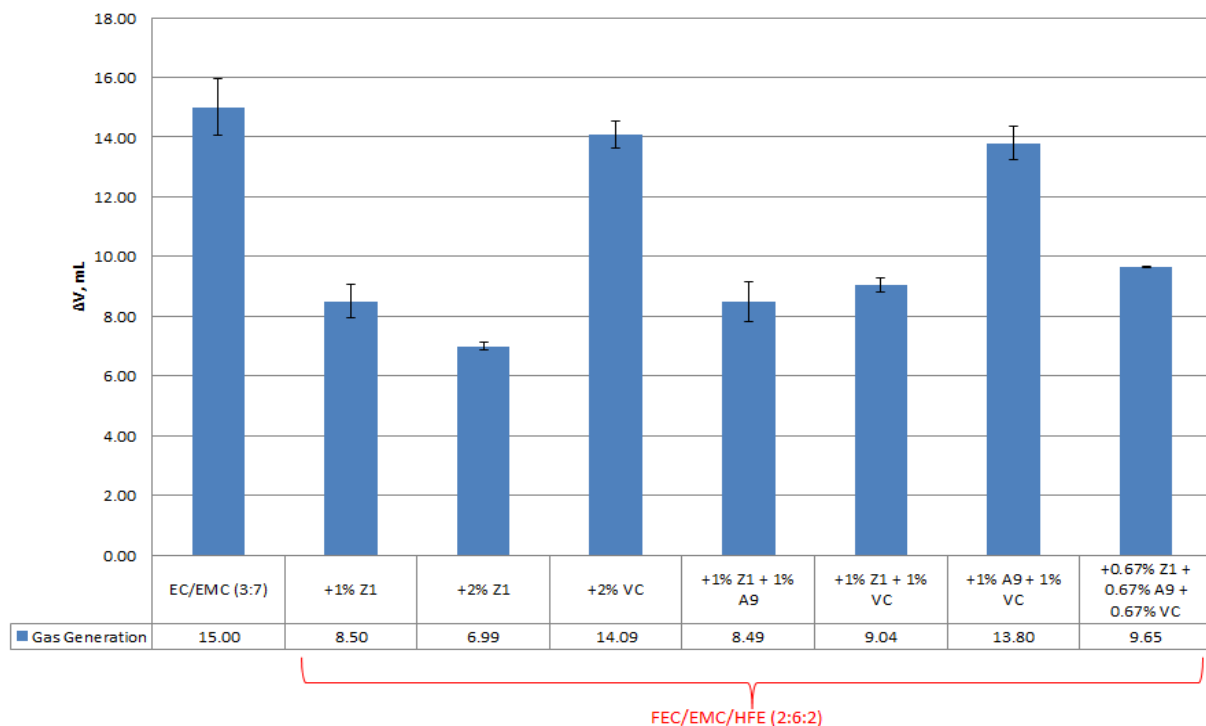


Figure V- 267: Gas volume for NMC111/graphite cells with various additive combinations after 60 C storage at 4.5 V

**Evaluation of preliminary cell:** The final test report for the preliminary cells submitted in February has been issued from Argonne. The cells were 1 Ah NMC111/graphite cells filled with best guess optimal electrolyte 1.2 LiPF<sub>6</sub> FEC/EMC/F-solvent (2:6:2) + 1% additive A. The cycle life testing data is shown in Figure V- 268. The capacity and resistance as a function of cycle number are shown in the top and bottom panels, respectively. The cells completed 80 cycles down to an 80% capacity retention cutoff at 4.6 V most likely due to high resistance change between 50 and 100 cycles. Cells were shutoff at RPT (Reference Performance Test) 3 (150 cycles).

The calendar life test is shown in Figure V- 269. The calendar life did not finish RPT6. The drop in capacity in the 10<sup>th</sup> week is again consistent with a large resistance increase. No post mortem has yet been conducted on these cells. The source of the sudden increase in resistivity has not been determined.

**Gassing Sources:** Superior performance of fluorinated electrolyte at voltages > 4.35 V. Minimal residence time at high voltage is achieved in cycle life experiments. Calendar life experiments were started where the NMC111/graphite cells were CC/CV charged to 4.6 V and allowed to sit at room temperature. The drop in OCV and gas volume were collected over a 600 hour period (see Figure V- 270). The data shows that the fluorinated electrolyte has a lower OCV drop. This is consistent with it being more oxidatively stable. Conversely, the hydrocarbon electrolyte is easily oxidized by the cathode which results in reduced cathode (ie. lower voltage). However, the fluorinated electrolyte has high rate of gassing which is opposite of that seen in the cycle life experiments.

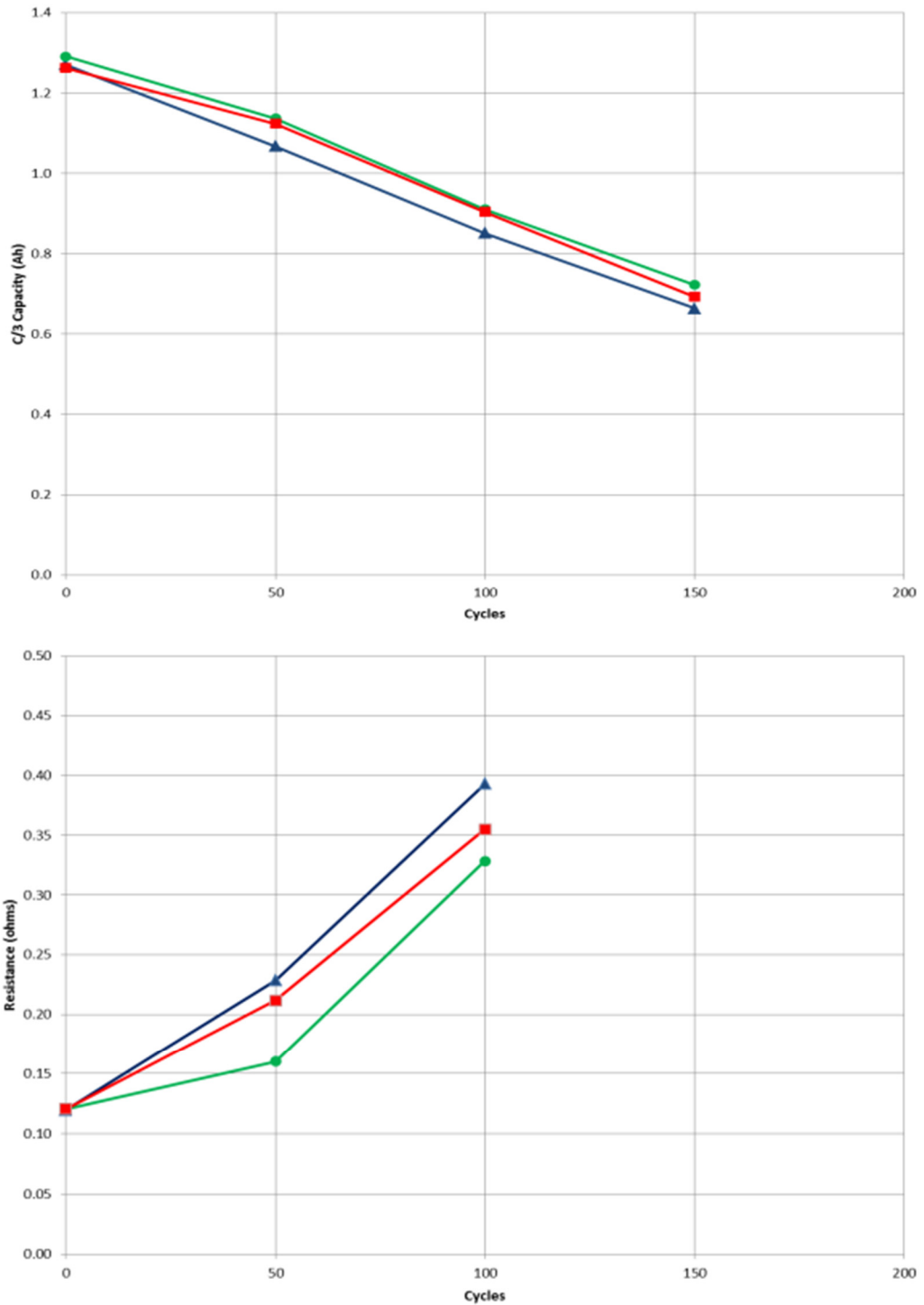


Figure V- 268: Cycle life at 4.6 V Daikin fluorinated electrolyte (capacity - top, resistance –bottom)

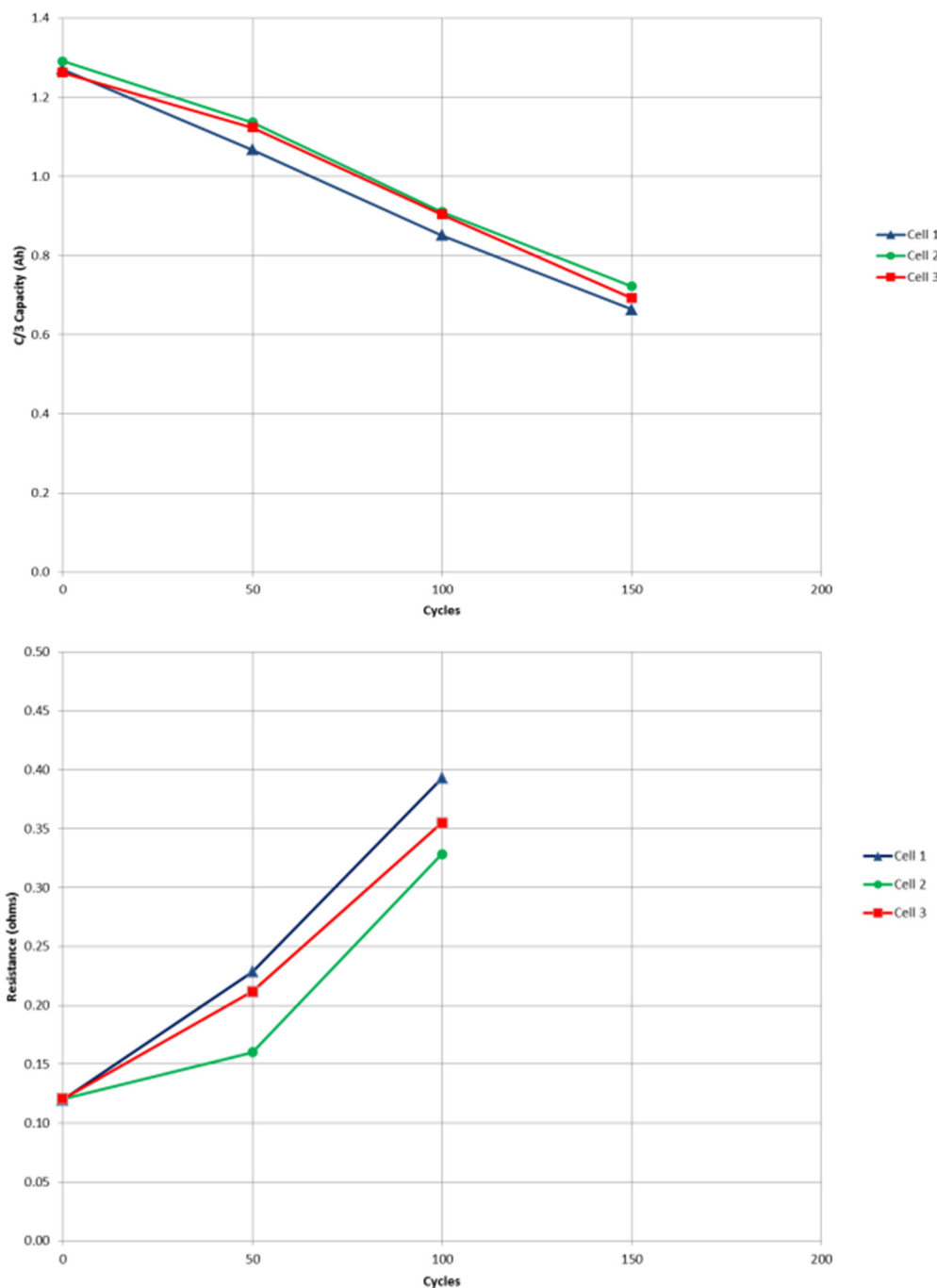


Figure V- 269: Calendar life at 4.6 V Daikin fluorinated electrolyte (capacity - top, resistance –bottom)

The fluorinated electrolyte in the above result contains FEC. In previous communications, we have shown the instability of FEC at high temperature. Figure V- 271 shows a photo of 1. Hydrocarbon control electrolyte (top), 2. Daikin fluorinated electrolyte (middle) and 3. Daikin fluorinated electrolyte with the FEC replaced by EC. The electrolytes were heated ex-situ in PTFE threaded vessels to 60 C (left) and 85 C (right). The electrolyte containing FEC has undergone some decomposition as evidenced by the color change to black. The only possible source of color change is the decomposition of the LiPF<sub>6</sub> salt. Cells built with the “black” electrolyte show similar first capacity and rate performance but cycle poorly.

## 4.6V Calendar Life

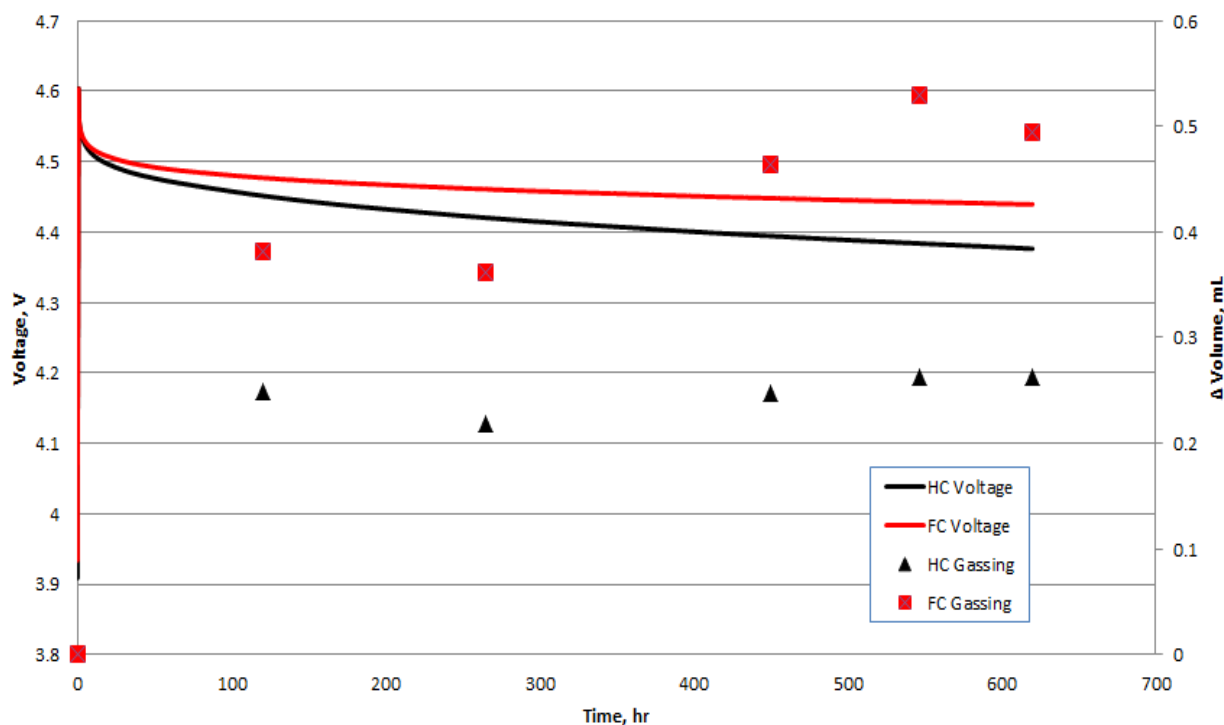
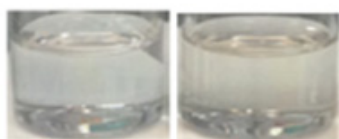


Figure V- 270: RT 4.6 V calendar life fluorinated vs. conventional electrolyte

**60 C**
  
**85 C**
  
**DIL STD - EMC/EC (7:3)**



**DAI-03 - FEC/EMC/FE (2:6:2)**



**EC/EMC/FE (2:6:2)**



Figure V- 271: Three different electrolyte compositions heated to 60C (left) and 85 C(right)

Batteries have been filled with both fluorinated (containing FEC) and conventional electrolyte then were oven aged at 60 C for 72 hours. These batteries were charged from voltages between 4.2 and 4.8 V. The OCV drop and gassing were measured over the 72 hour age (see Figure V- 272). The data show a clear linear dependence of the decomposition of FEC with voltage. The data again shows that the fluorinated electrolyte is more oxidatively stable towards the cathode.

$\Delta$ OCV vs. gas volume data has also been collected for a variety of compositions and is shown in Figure V- 273. There is a clear dependence of gas volume on the concentration of FEC as it varies from 0 to 50 volume percent. The data also shows the benefit of the mixture with propane sultone (PS) resulting in lower gassing. Finally, the data shows the relationship between gassing and the identity of the organic hydrocarbon carbonate. The gassing hierarchy is diethyl carbonate (DEC) < ethyl methyl carbonate (EMC) < dimethyl carbonate (DMC). The electrolyte conductivity and rate performance shows the opposite trend.

**Safety:** Abuse testing (overcharge, nail penetration) has been performed on the Daikin fluorinated electrolyte vs. the hydrocarbon control. The testing has been performed on several chemistries including LCO, NMC111, NCA and NMC532. In all cases, Daikin fluorinated electrolyte performs significantly better than the hydrocarbon control. An example of this can be seen in the photos in Figure V- 274. The photos show an overcharge test on NMC111/graphite cells. The cells filled with hydrocarbon control electrolyte and Daikin fluorinated electrolyte are on the left and right, respectively. The overcharge was to 18 V and the charging current used was 2C. The top left panel shows the beginning of the test, the middle panel shows significant gassing in the hydrocarbon cell and eventually the hydrocarbon cell catches fire. It takes 1452 seconds for the hydrocarbon cell to ignite while it takes 4650 seconds for the Daikin electrolyte to catch fire.

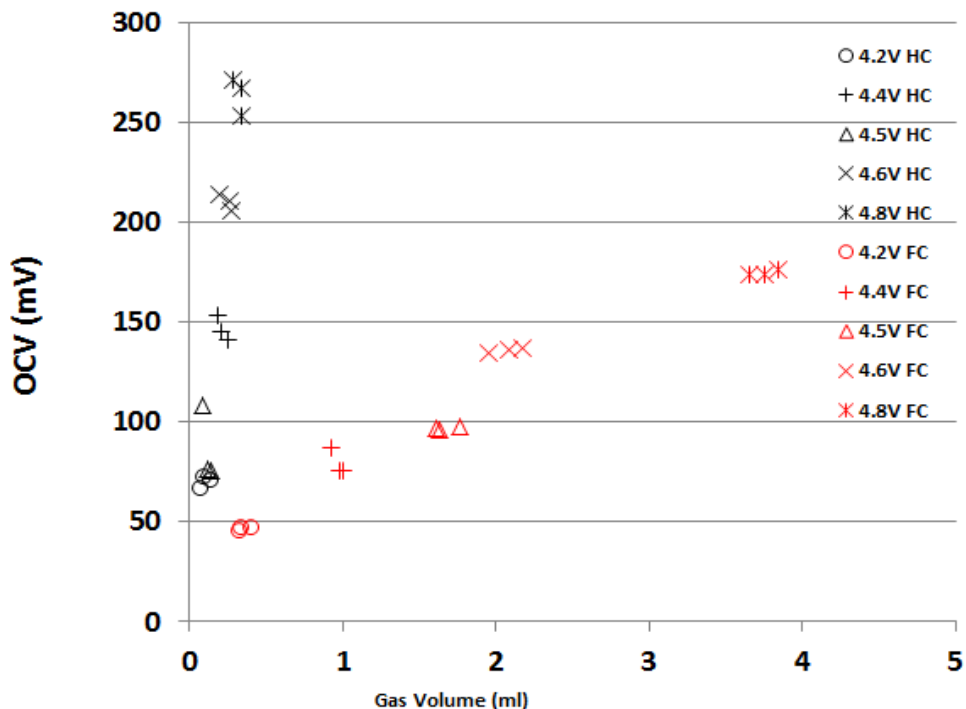


Figure V- 272:  $\Delta$ OCV and gas volume as a function of voltage for both the hydrocarbon control electrolyte (black) and Daikin fluorocarbon electrolyte (red)

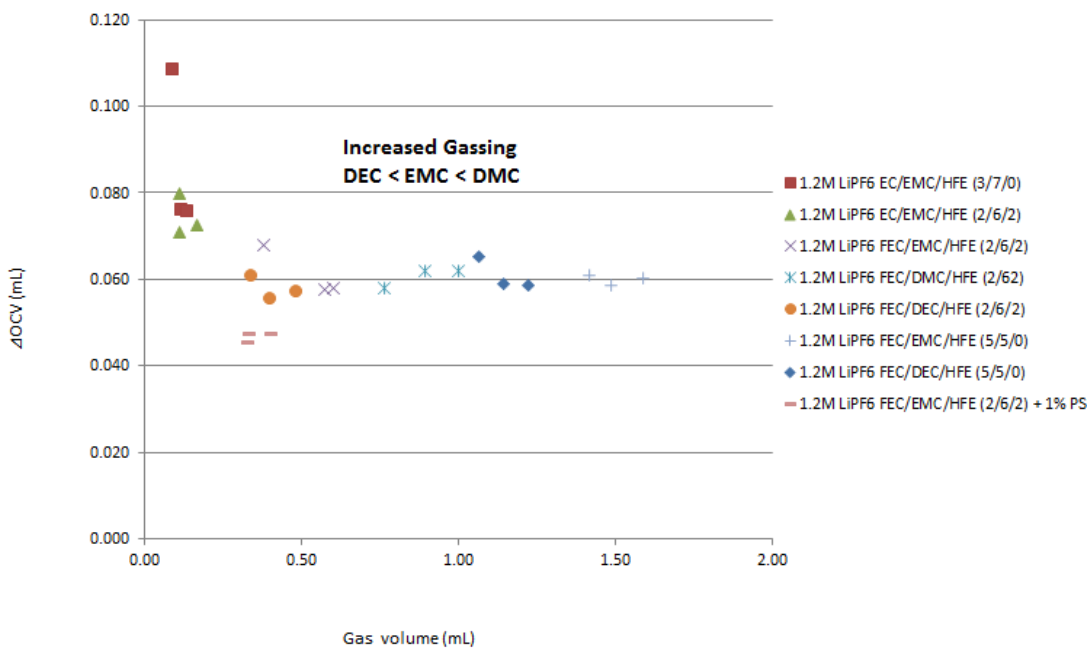


Figure V- 273: DOCV vs. gas volume for various concentrations of electrolyte

### Conclusions and Future Directions

Daikin has made significant improvement in extending the voltage range of the electrolyte in a variety of chemistries. It has been shown that operation of existing commercial chemistries at voltages above 4.5 V results in energy gains >30%. However, hydrocarbon electrolyte is not suitable for operation above 4.35 V due to decomposition. An optimized solvent formula based on FEC/EMC/F-solvent has been developed which allows stable C-rate cycling (>250 cycles) to 4.5 V at 60 C. An additive combination has been successfully identified which affects the slope of the cycle retention curve. 12 interim NMC111/graphite cells had been submitted to DOE for preliminary testing. The cells included the optimized solvent formula but did not contain the additive package. The cells did not pass 4.6 V testing at Argonne. Substantial work has also been completed to identify and understand the source of gassing in the cell. Results show that fluoroethylene carbonate (FEC) is the main contributor to the gassing. The gassing rate is dependent on the FEC concentration, temperature, voltage and oxidizing power of the surface (ie. high nickel). Future work in this area is centered around slowing the kinetics of the gassing reaction by using lower concentrations of FEC and additives to protect the charged cathode surface where the majority of the gassing takes place. The optimization completed in this project was directed at NMC111/graphite cells but now this is being extended/modified for other chemistries. One of the final components of the project is to complete surface analysis (Auger, XPS, TOF-SIMS) to understand the surface chemistry of the Daikin additives. Daikin has also showed safety performance improvement and will continue safety testing.



Figure V- 274: Overcharge testing on NMC111/graphite cells filled with hydrocarbon (left) and Daikin fluorinated electrolyte (right)

## V.H.8 Novel Non-Carbonate Based Electrolytes for Silicon Anodes (Wildcat Discovery Technologies)

### Objectives

The objective of this project is to develop non-carbonate electrolytes that form a stable solid electrolyte interphase (SEI) on silicon alloy anodes, enabling substantial improvements in energy density and cost relative to current lithium ion batteries (LIBs). These improvements are vital for mass market adoption of electric vehicles. At present, commercial vehicle batteries employ cells based on LiMO<sub>2</sub> (M = Mn, Ni, Co), LiMn<sub>2</sub>O<sub>4</sub>, and/or LiFePO<sub>4</sub> coupled with graphite anodes. Next generation cathode candidates include materials with higher specific capacity or higher operating voltage, with a goal of improving overall cell energy density. However, to achieve substantial increases in cell energy density, a higher energy density anode material is also required. Silicon anodes demonstrate very high specific capacities, with a theoretical limit of 4200 mAh/g and state-of-the-art electrodes exhibiting capacities greater than 1000 mAh/g. While these types of anodes can help achieve target energy densities, their current cycle life is inadequate for automotive applications. In graphite anodes, carbonate electrolyte formulations reductively decompose during the first cycle lithiation, forming a passivation layer that allows lithium transport, yet is electrically insulating to prevent further reduction of bulk electrolyte. However, the volumetric changes in silicon upon cycling are substantially larger than graphite, requiring a much more mechanically robust SEI film.

### Project Details

**Bruce Mixer (NETL Program Manager)**  
DE-EE0006453 Recipient: Wildcat Discovery Technologies

**Dee Strand (Wildcat Discovery – PD/PI)**  
6985 Flanders Drive  
San Diego, CA 92121  
Phone: 858-550-1980; Fax: 858-638-7533  
E-mail: [dstrand@wildcatdiscovery.com](mailto:dstrand@wildcatdiscovery.com)

Subcontractor:  
3M  
3M Center, Building 209-2C-26  
St. Paul, MN 55144

Start Date: October 2013  
Projected End Date: June 2016

### Technical Barriers

- In order for EVs to achieve mass adoption and make a significant dent in U.S and global CO<sub>2</sub> production, the key problems of driving range per charge and cost per kWh must be addressed.  
Barriers addressed:
  - Performance: Low Wh/kg & Wh/L
  - Life: Poor cycle life
  - Cost: High \$/kWh

### Technical Targets

Development of non-carbonate electrolyte formulations that

- form stable SEIs on 3M silicon alloy anode, enabling coulombic efficiency > 99.9% and cycle life > 500 cycles (80% capacity) with NMC cathodes;
- have comparable ionic conductivity to carbonate formulations, enabling high power at room temperature and low temperature;
- are oxidatively stable to 4.6V, enabling the use of high energy NMC cathodes in the future; and
- do not increase cell costs over today's carbonate formulations.

### Accomplishments

- Identified anode SEI additives that improved cycle life performance over a baseline formulations containing either ethylene carbonate or propylene carbonate
- Effectively used promising additives to screen a wide range of noncarbonate solvents

- Identified the most effective solvent replacements for cyclic and linear carbonates
- Optimized salt composition and concentration in novel solvent systems to provide improved cycle life relative to a control electrolyte
- Achieved over 300 cycles to 80% capacity retention in full cells with a carbonate-free solvent system with a single SEI additive
- Achieved improved performance relative to the control with novel additives in carbonate based systems
- Demonstrated formulations with improved cycle life did not decrease 1<sup>st</sup> cycle capacity or coulombic efficiency
- Performed initial screening of gas formation in noncarbonate or EC-free formulations which did not show increased gassing over the carbonate control formulations
- Tested several of the carbonate-free and EC-free formulations which showed improved cycle life at higher voltage than the control electrolyte

## Introduction

Silicon-based anodes suffer from major disadvantages relative to graphite. First, during cycling, silicon exhibits a volume change of up to 300% (vs. 5-10% for graphite), causing severe mechanical stress and electrical disconnection of particles. This mechanical stress can be managed by careful control of particle size/morphology, including nanoparticles, nanowires, and nano-pillared materials. Such nanostructured materials have high surface areas (e.g., >10 m<sup>2</sup>/g) and often require a composite matrix to prevent electrochemical sintering. Second, carbonate-based electrolyte formulations do not form a stable SEI on silicon, with subsequent high irreversible capacity losses and poor cycle life (typically >15% and <100 cycles, respectively).

3M has developed several prospective silicon alloy anodes that provide a 100% increase in the composite electrode energy density compared to graphite coatings. In 18650 test cells using a fluorinated ethylene carbonate (FEC)-based electrolyte, 3M has demonstrated a full cell energy increase of 15% to 20% against a standard NMC cathode, with charge depleting cycling for 500+ cycles resulting in 67% capacity retention at a C/2 charge/discharge rate from 2.8V to 4.35V. Catastrophic failure still occurs under long term cycling due to parasitic reactions consuming the electrolyte. This project focuses on the development of formulations that provide stable SEIs using additives in a non-carbonate formulation. Linear and cyclic carbonate solvents do not yield suitably stable SEIs on silicon. In order to avoid simultaneous reduction with the new SEI additives, carbonates need replacement.

## Approach

Wildcat is using a three stage approach to the development of noncarbonate electrolytes for silicon anodes (Figure V- 275). In the first, an additive package was developed in a propylene carbonate (PC) based system. PC does not form a stable SEI on the anode, so the effect of additive(s) on the resulting SEI will be measureable. Once a promising additive package was identified, new solvent candidates were enabled. Therefore, the second stage consisted of identification of novel solvents that provide high ionic conductivity, good low temperature performance, improved thermal stability/safety, and adequate oxidative stability. The development of an effective additive package to form an SEI practically enables electrolyte solvents that might not otherwise be considered, and substantially increases the number of potential candidates. Finally, optimization of the electrolyte is necessary



Figure V- 275: Systematic approach to electrolyte development

in the final stage of the project to ensure that the final solution can meet all of the PHEV/EV cell level goals, including ionic conductivity and oxidative stability to 4.6V.

In the design and development of novel SEI additives, several factors were taken into consideration, as shown in Table V- 6. The concept uses molecular design concepts to create an SEI with improved mechanical and electrochemical performance, enabling longer cycle life on silicon anodes.

**Table V- 6: Molecular design approach for anode SEI additives**

Approach	Factor
Control SEI thickness	Influenced by the relative amount of polymer additive relative to surface area of anode, and the reduction potential of the additive
Control SEI modulus and/or glass transition temperature ( $T_g$ )	Property of polymer influenced by 1) average molecular weight and distribution, 2) chemical composition, 3) effective crosslink density, 4) degree of swelling by solvent.
Control amount of more brittle non-polymeric species	Influenced by other components of the electrolyte such as solvent, other additives, and salts
Control ionic conductivity of SEI	Influenced by polymer composition and other electrolyte components such as the salt

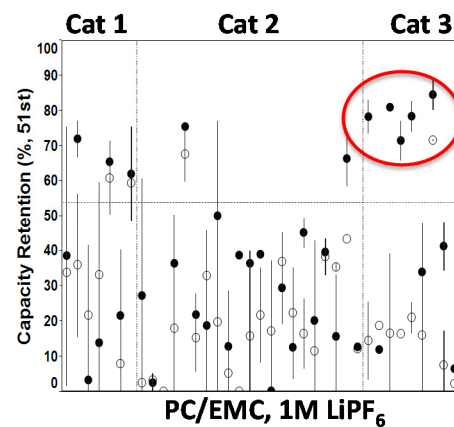
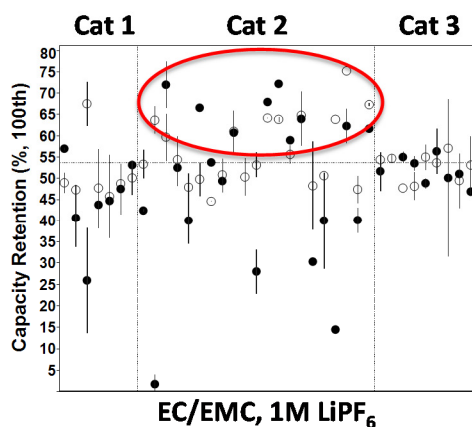
## Results

We have achieved the following progress:

### Identification of SEI Additives for EC-Free Electrolyte Formulations

Today's electrolyte formulations most often contain a blend of a high dielectric constant solvent and a low viscosity solvent. The most common high dielectric constant solvent is ethylene carbonate (EC), which solvates the  $\text{Li}^+$  cations and also, fortuitously, participates in SEI formation on graphite anodes. Propylene carbonate (PC) is another commonly used high dielectric constant solvent. However, it cannot form effective SEI layers on graphite. However, EC (and many other high dielectric constant solvents) tend to have high viscosities, requiring dilution with a low viscosity solvent to work effectively in a battery. Linear carbonates such as ethyl methyl carbonate (EMC) are often used as the low viscosity solvents.

Today's common SEI additives, such as vinyline carbonate (VC) are used within electrolyte formulations that contain a blend of EC with various linear carbonate solvents. We, therefore, tested the electrochemical performance of hundreds of SEI additives in different chemical categories in the presence of EC, which participates in the SEI formation on graphite/silicon, and PC, which does not participate in SEI formation. This allows us to elucidate those additives that can form an effective SEI on their own vs. those that require co-reaction with EC to form an SEI. Figure V- 276 shows a subset of the data, including three categories of additives tested in two different base formulations. All additives were tested at two different concentrations (open and closed circles).



In EC-based formulations, Category 2 additives tended to show improved capacity retention relative to the baseline (dashed line). Yet these same additives showed detrimental

**Figure V- 276: Additives show synergies with differing solvent formulations**

performance relative to the baseline in PC based formulations. Instead, Category 3 additives improved the cycle life performance when used with PC. Category 2 additives were reactive monomer species, such as VC, which appear to form an SEI in a cooperature fashion with EC to form higher molecular weight species. In the absence of the EC, they are unable to create an effective SEI. Category 3 based additives are polymer/oligomeric in nature, providing the necessary higher molecular weight species to the SEI film. Several other promising categories of additives were also identified that resulted in improved cycle life in PC-based formulations.

### Identification of Promising Solvents for Noncarbonate or EC-Free Electrolyte Formulations

Using the additives identified in Phase 1 of the project, we evaluated the performance of large numbers of solvent combinations in full cells containing NMC and 3M silicon alloy anode. Approximate 25 high dielectric (HD) constant solvents and 25 low viscosity (LV) solvents were selected that met criteria of electrochemical stability, physical properties, salt solubility, etc. for use as lithium ion battery electrolytes. Initial screening consisted of blending all the HD solvents with a linear carbonate, EMC, and evaluating with 1M LiPF<sub>6</sub> and a single SEI additive. Cycle life results for the best performing formulations are shown in Figure V- 277.

These HD solvents were then blended with all 25 LV solvents, 1M LiPF<sub>6</sub>, and a single SEI additive for evaluation in full cells. The first cycle discharge capacity and capacity retention of these formulations are shown in a correlation plot in Figure V- 278. In this graph, the baseline performance for both metrics is shown as the gray band (vertical and horizontal). The data points in different colors represent varying combinations of HD and LV solvents. A number of combinations showed performance similar to the standard carbonate control formulation, which are circled in red.

These formulations provide the basis for further iteration and optimization. These best noncarbonate or EC-free formulations can now be improved by optimization of solvent ratios, salts (concentration and combinations), and additives (concentrations and combinations).

### Example of Salt Optimization in Novel Solvent Formulations

While a wide variety of solvents were evaluated, other formulation variables were kept constant thus far. For example, all formulations contained 1M LiPF<sub>6</sub>. Yet, there is no reason to expect that this salt or this concentration will be optimal for entirely new solvent systems. Therefore, optimization is required. Results for an example of the initial salt optimization experiments are summarized in Table V- 7. In the experimental design, each of the best combinations of HD solvents and LV solvents is tested with five different salts. For example, LV solvent A is blended with HD solvents 1, 2, and 3; LV solvent B is blended with HD solvents 1, 2, and 4; etc.

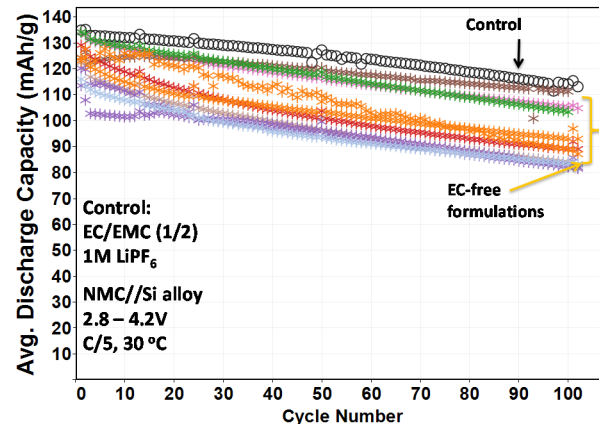


Figure V- 277: Best performing high dielectric constants were identified in EMC blends

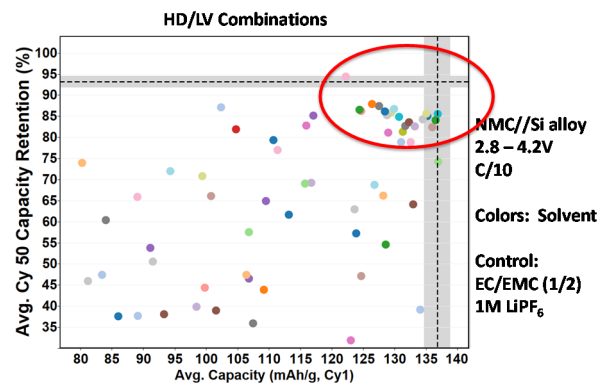


Figure V- 278: Evaluation of best performing high dielectric constant solvents with a variety of low viscosity solvents

For each formulation, the cycle 1 capacity and cycle 100 capacity retention is determined. Results are

**Table V- 7: Salt efficacy is very solvent dependent**

		LiPF6		Salt 1		Salt 2		Salt 3		Salt 4		Salt 5	
LV	HD	Cy1 Capa. mAh/g	Capa. Reten (%)										
Control		134.2	83.6	134.2	83.6	134.2	83.6	134.2	83.6	134.2	83.6	134.2	83.6
A	1	132.4	72.0	122.4	30.3	129.4	21.7	133.1	0.47	129.1	92.1	123.8	82.4
	2	134.1	80.2	122.6	33.0	131.6	33.9	132.7	0.34	129.8	93.3	123.2	80.1
	3	122.9	71.8	80.3	41.5	131.4	53.3	128.7	1.9	125.9	89.0	122.4	82.3
B	1	124.5	78.4	31.1	59.4	125.9	26.3	134.5	76.7	127.3	15.1	131.3	88.2
	2	131.6	75.7	116.6	62.5	131.9	73.9	131.5	84.6	102.3	6.9	127.2	89.6
	4	123.1	86.9	126.1	54.2	131.1	76.0	134.0	79.8	131.9	43.0	132.9	86.3
C	5	133.8	80.8	90.6	54.5	121.6	0.1	137.7	0.1	103.6	1.2	131.8	87.7
	6	131.7		-	-	118.6		135.7		120.4		129.2	
	7	136.5		-	-	118.5		135.1		133.7		129.5	
D	3	134.0	86.9	122.1	66.2	121.2	90.4	135.7	88.8	133.9	81.7	130.4	88.4
E	2	135.5		-	-	130.6		127.3		134.3		125.4	

visualized by color coding the box green if the performance is improved relative to the control, gray if the results are unchanged from the control, and red if the results are worse than the control. In this way, it is easy to see that, for example, Salt 5 tends to be beneficial to LV solvent B blended with HD solvents 1, 2, and 4. These results are the basis for further optimization of salt composition, concentration, and salt combinations to further improve full cell cycle life.

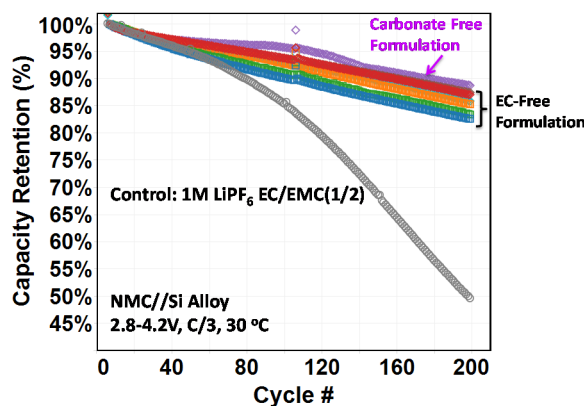


Figure V- 279: Carbonate-free formulations exceed performance of control electrolyte

In parallel with the optimization experiments in novel solvent formulations, we continued to screen additional SEI additives in both EC and PC based formulations. These experiments provide additional options to include new additives in combination with those previously identified. Throughput multiple rounds of high throughput screening, Wildcat achieved continuous improvement in cycle life while building knowledge on structure property relationships as we expand upon promising additives by structural modifications.

Example cycle life results for optimized salts in the novel solvent formulations are shown in Figure V- 279, where cycle life of the noncarbonate or EC-free formulations exceed that of the control. Cycle life results after further optimization are shown in Figure V- 280, where 300 cycles are achieved to 80% capacity retention in carbonate-free formulations. Thus far, all of the formulations contain only a single SEI additive - leaving much headroom for optimization of additives, additive concentrations, and combinations of additives.

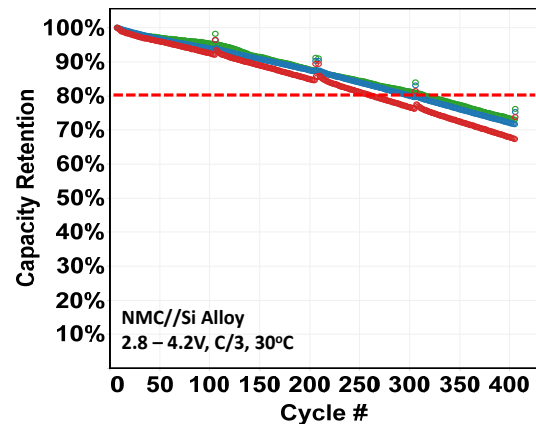


Figure V- 280: Carbonate-free formulations achieve 300 cycles to 80% capacity retention

## High Voltage Testing of Promising Formulations

These promising formulations were tested at higher voltage in full cells, using the same paired electrodes.

The capacity match (based on reversible capacity) at 4.2V was 1.2, leaving some room to increase voltage. Ultimately, higher voltage tests will be done on matched electrodes designed for the higher cathode capacity achieved at higher voltage. However, initial screening was performed on the existing electrodes to determine if these formulations were close to the maximum in operating voltage. These very preliminary results indicate that at least some of the promising formulations can be run at higher voltage. Figure V- 281 shows cycle life results for cells cycled to 4.45V, where several of the EC-free and carbonate-free formulations show promise at higher voltage.

## Additive Optimization

Wildcat is currently executing large experimental designs to optimize SEI additives for the new solvent combinations to achieve the 500 cycle life target. However, due to the slow cycle rates and the relatively long cycle life – results are not currently ready to report.

## Conclusions and Future Directions

We have made dramatic progress in the identification of noncarbonate solvents for use with silicon anodes in lithium ion batteries. The current cycle life of 300 cycles to 80% capacity retention outperforms the control electrolyte. It should be pointed out that further improvements could be made to the carbonate based control electrolyte – which may make it a better selection in the long run. However, this project will result in alternatives to carbonates that may provide other advantages such as high voltage stability, lower volatility, etc. Furthermore, the electrolyte additives being discovered may be valuable across a range of solvent systems (still to be tested).

The remainder of the project will focus on the further optimization of SEI additives within the most promising solvent combinations to achieve the project targets.

## FY 2015 Publications/Presentations

1. "Novel Noncarbonate Electrolyte Formulations for Silicon Anodes," Dee Strand, 32<sup>nd</sup> Annual International Battery Seminar & Exhibit, March/ 2015, Ft. Lauderdale, FL.
2. "Development of Novel Lithium Ion Battery Electrolytes for Silicon Anodes," Bin Li, The Second International Forum on Cathode & Anode Materials for Advanced Batteries, April/ 2015, Hangzhou, China.
3. "Development of In Situ Gas Measurements for Lithium Ion Battery R&D," Ye Zhu, 227<sup>th</sup> ECS Meeting, May/2015, Chicago, IL.
4. "Novel Noncarbonate Electrolyte Formulations for Silicon Anodes", ES219, US DOE Vehicle Technologies AMR, June/2015, Washington, DC.
5. "Development of Novel Electrolytes for Silicon Anodes," Gang Cheng, 4<sup>th</sup> China LIB Electrolytes Conference 2015, June/2015, Yangzhou, China.

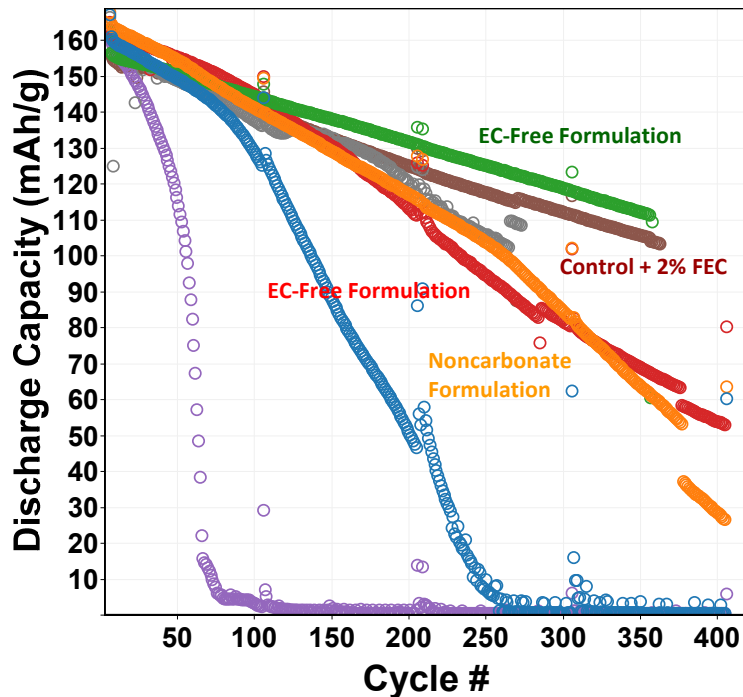


Figure V- 281: Early results on carbonate-free and EC-free formulations show promise at higher voltage

FY 2015 ANNUAL PROGRESS REPORT FOR ENERGY STORAGE R&D

6. "Novel Noncarbonate Electrolytes for Silicon Anodes," Gang Cheng, AABC USA 2015, June/2015, Troy, MI.
7. "Development of Novel Electrolytes for Silicon Anodes," Dee Strand, ABAA8, September/2015, Bilbao, Spain.
8. "Development of Novel Electrolytes for Silicon Anodes," Dee Strand, Batteries 2015, October/2015, Nice, France.

## V.I Lithium Sulfur Batteries

### V.I.1 New Lamination and doping Concepts for Enhanced Li–S Battery Performance (U Pittsburgh)

#### Objectives

- To successfully demonstrate generation of novel sulfur cathodes for Li-S batteries meeting the targeted gravimetric energy densities  $\geq 350$  Wh/kg and  $\geq 750$  Wh/l with a cost target \$125/kWh and cycle life of atleast 1000 cycles for meeting the *EV everywhere* blueprint. The proposed approach will yield sulfur cathodes with specific capacity  $\geq 1400$  mAh/g, at  $\geq 2.2$  V generating  $\sim 460$  Wh/kg, energy density higher than the target. Full cells meeting the required deliverables will also be made.

#### Technical Barriers

- In order for EVs to achieve mass adoption and make a significant dent in U.S and global CO<sub>2</sub> production, the key problems of driving range per charge & cost per kWh must be addressed.  
Barriers addressed:
  - Performance: Low Wh/kg & Wh/L.
  - Life: Poor deep discharge cycles.
  - Cost: High \$/kWh.

#### Technical Targets

- Sulfur Cathode Targets:  $\geq 350$  Wh/kg,  $\geq 750$  Wh/l, high capacity  $\geq 1400$  mAh/g, cyclability ( $\sim 1000$  cycles), loss per cycle  $\leq 0.01\%$  per cycle, CE:  $\geq 99.99\%$ .
- Cell Targets: 350 Wh/kg, 700 Wh/L,  $<\$150$ /kWh.

#### Accomplishments

- Demonstrate synthesis of finely dispersed nanoparticles of sulfur (December 2014) – Completed
- Develop novel lithium-ion conducting (LIC) membrane systems using ab-initio methods displaying impermeability to sulfur diffusion (December 2014) – Completed
- Demonstrate capabilities for generation of novel sulfur 1-D, 2-D and 3-D morphologies exhibiting superior stability and capacity (June 2015) – Completed
- Identification and synthesis of LIC materials for use as coatings for sulfur cathodes (June 2015) – Completed
- Novel encapsulation and sheathing techniques and exploration of unique architectures and generation of 3-D composites displaying superior Li-ion conduction, reversible capacity and stability (June 2015) – Completed
- Identification of suitable dopants and dopant compositions to the improve electronic conductivity of sulfur (October 2015) – Completed
- Fundamental electrochemical studies to understand the reaction kinetics, mechanism and charge transfer kinetics (October 2015) – On-going

#### Project Details

**John Tabacchi (NETL Program Manager)**  
DE-EE0006825 Recipient: The University of Pittsburgh

**Prashant Kumta (The University of Pittsburgh –PI)**  
Attn: Allen A. DiPalma  
123 University Place  
Pittsburgh, PA 15213-2303  
Phone: 412-648-0223; Fax: 412-624-3699  
E-mail: [pkumta@pitt.edu](mailto:pkumta@pitt.edu)

#### Collaborators:

Dr. Moni Datta (University of Pittsburgh)  
Dr. Oleg Velikokhatnyi (University of Pittsburgh)  
Dr. Spandan Maiti (University of Pittsburgh)  
Dr. A. Manivannan (NETL)  
Dr. D. Krishnan Achary (University of Pittsburgh)

Start Date: October 2014

Projected End Date: September 2017

- Go/No-Go (October 2015) decision will be based on the ability to demonstrate improvement in cycling upon use of the LIC coating. – Completed

## Introduction

The increasing demand in the EV industry for low cost, light weight and high energy storage batteries to meet the *EV everywhere* grand challenge, the current focus of research has shifted towards the development of lithium sulfur (Li–S) batteries owing to the high theoretical specific capacity exhibited by sulfur compared to other cathode materials currently available. Li–S battery shows a theoretical capacity of 1675 mAh/g corresponding to the formation of  $\text{Li}_2\text{S}$  which makes sulfur a promising electrode to replace the layered transition metal oxides (~150 mAh/g) and  $\text{LiFePO}_4$  (~170 mAh/g) deployed in present LIB systems. Moreover, the abundance of sulfur in the earth's crust, its ubiquitous availability as a byproduct in the extractive mineral and petrochemical industry, combined with ease of processing, makes it a more economical proposition compared to currently existing cathode materials.

## Approach

**Innovative Approach:** The objectives outlined above will be accomplished by engineering sulfur cathode materials primarily by laminating the electrodes with lithium ion conductor (LIC) coatings in order to prevent polysulfide dissolution and doping in order to improve the electronic and ionic conductivity. The major technology innovations will be undertaken to accomplish the following objectives of this effort:

1. **Phase – 1 (Year 1):** Synthesis, Characterization and Scale up of suitable LIC matrix materials and multilayer composite sulfur cathodes. This phase is completed.
2. **Phase – 2 (Year 2):** Development of LIC coated sulfur nanoparticles, scale up of high capacity engineered LIC coated multilayer composite electrodes and doping strategies for improving the electronic conductivity of sulfur.
3. **Phase-3 (Year 3):** Advanced high energy density, high rate, extremely cyclable cell development.
4. Identify novel LIC coating materials and morphology for composite multilayer sulfur cathode architectures exhibiting: Specific capacity  $\geq 1000$  mAh/g ( $\geq 8$  mAh/cm<sup>2</sup>), cyclability (~1000 cycles), loss per cycle  $\leq 0.05\%$  per cycle, Coulombic Efficiency (CE):  $\geq 99.5\%$ .
5. Optimize the interface engineered multilayer composite LIC coated sulfur cathode architectures exhibiting: Specific capacity  $\geq 1200$  mAh/g ( $\geq 4$  mAh/cm<sup>2</sup>), cyclability (~1000 cycles), loss per cycle  $\leq 0.01\%$  per cycle, CE:  $\geq 99.9\%$ .
6. Synthesize doped sulfur nanoparticles on gram scale and demonstrate improvement in performance, reflected as an increase in sulfur weight percentage and improvement in rate capability of the electrodes.
7. Tie together the three different trees of development i.e. coating development/sulfur particle development/CNT based exploration by identifying suitable configuration integrated electrode (I.E.) with maximum sulfur weight percentage demonstrating high capacity  $\geq 1400$  mAh/g, cyclability (~1000 cycles), loss per cycle  $\leq 0.01\%$  per cycle, CE:  $\geq 99.99\%$ .
8. Assemble 4 mAh high energy density Li-S pouch cells and performance testing.

## Results

The aim of Phase-1 of this project was essentially to identify various materials that can act as lithium ion conductors (LICs) while preventing polysulfide transport and accompanying sulfur loss. The end of Q-4 has a Go/No-go point which is based on the ability to demonstrate that the working hypothesis is valid (i.e. LICs improve Li–S battery cycle life). In order to achieve this target, 4 strategies were employed during Phase-1 of the project: (a) Use of inorganic LICs in the form of pellet coatings (Q1, Q2) (b) fabrication of flexible polymer-sulfur wires (Q2) (c) generation of gel polymer electrolyte (GPE) as an electrolyte medium (Q3) (d) use of complex framework materials (CFM) as trapping agents for sulfur species (Q4). The various strategies and progress achieved therein are described below:

### High areal capacity inorganic LIC coated sulfur nanoparticulate electrodes

Research in the first quarter of Phase-1 involved identification of strategies to improve the characteristics of sulfur electrodes by pursuing a three-pronged approach:

- a) Synthesis of nano-particulate sulfur in order to achieve higher capacities without significant increase in fade rate.
- b) Use of solid state processing i.e. pellet pressing as an effective method to improve the capacity retention in lithium sulfur batteries in comparison to the conventional slurry casting procedure.
- c) Coating of thin solid state lithium-ion conductive (LIC) layer for minimal contact of liquid electrolyte with sulfur preventing dissolution of the polysulfides formed during lithiation of sulfur, while at the same time not presenting problems observed with the use of purely solid state electrolytes.

Among the several approaches identified, the first was to synthesize sulfur nanoparticles (SNPs) size to increase the capacity approaching theoretical limits of sulfur ( $\sim 1675$  mAh/g-Sulfur). The synthesis procedure involved re-precipitation of sulfur dissolved in a basic media followed by acid-driven neutralization. Different concentrations of various molecular acids resulted in colloidal SNPs of various sizes determined by dynamic light scattering (DLS). The average particle size was observed to decrease with lower concentration of the dissolved sulfur solution and also with the decrease in the normality of the acid solution used for generating the colloidal SNPs. Among the various SNPs, particles of  $\sim 600$  nm were found to have ideal electrochemical characteristics. Figure V- 282a and Figure V- 282b show the SEM images of the nano-sulfur and commercial sulfur, respectively. The difference in particle size can be distinctly observed by comparing the two images. The nano-sulfur particles formed by the chemical re-precipitation procedure exhibit agglomerated particle sizes of  $\sim 500$  nm- $2\ \mu\text{m}$  as seen in the SEM micrograph in Figure V- 282a. Commercially obtained sulfur particles used as precursors in the chemical re-precipitation reaction on the other hand, have a wide particle size distribution consisting of 20-150 micron particles as seen in Figure V- 282b. The fine particles of nano-sulfur are expected to have exceptional exposure to the lithium conducting (LIC) layer/conductive additive resulting in high capacity. Similar to the case of nanoparticle amorphous silicon anodes studied for Li-ion batteries, reversible expansion and contraction would not result in particle fracture and accompanying capacity fade. Figure V- 282c shows the morphology of the composite multilayer electrode assembled by the pellet pressing method. The pellet consists of a thin layer of lithium orthosilicate coating the mixture of sulfur and carbon. The uniformity of the coating and lack of macroscopic cracks are confirmed from the same. The inset images depict the disparate architecture existing within the orthosilicate layer and the sulfur-carbon layer. The orthosilicate layer consists of macroscopic particles fused together as a result of the mechanical pressing process. It can also be seen that the layer consists of macroscopic pores ideal for liquid electrolyte percolation. Short solid-state diffusion distances would result and the common issues typically experienced in solid electrolyte based lithium-sulfur batteries would thus be circumvented. The orthosilicate layer is a few microns thick ensuring that sulfur particles are not directly exposed to the liquid electrolyte thus serving to protect and prevent any dissolution of the polysulfides formed. The channel structure existing in the electrode would thus ensure minimal percolation of liquid electrolyte to sulfur particles. In addition to the protection offered by the orthosilicate layer, the pressing procedure ensures the formation of an elegant carbon coating on the sulfur particles. The carbon networks thus act both as electron conducting and lithium ion conducting (LIC) channels. Solid-state lithium ion diffusion through carbon is not hindered and should not pose as a barrier to the ensuing intercalation and de-intercalation processes. Evaluation of electrochemical performance of the various sulfur materials as cathodes was thus performed for the electrodes generated following two methods.

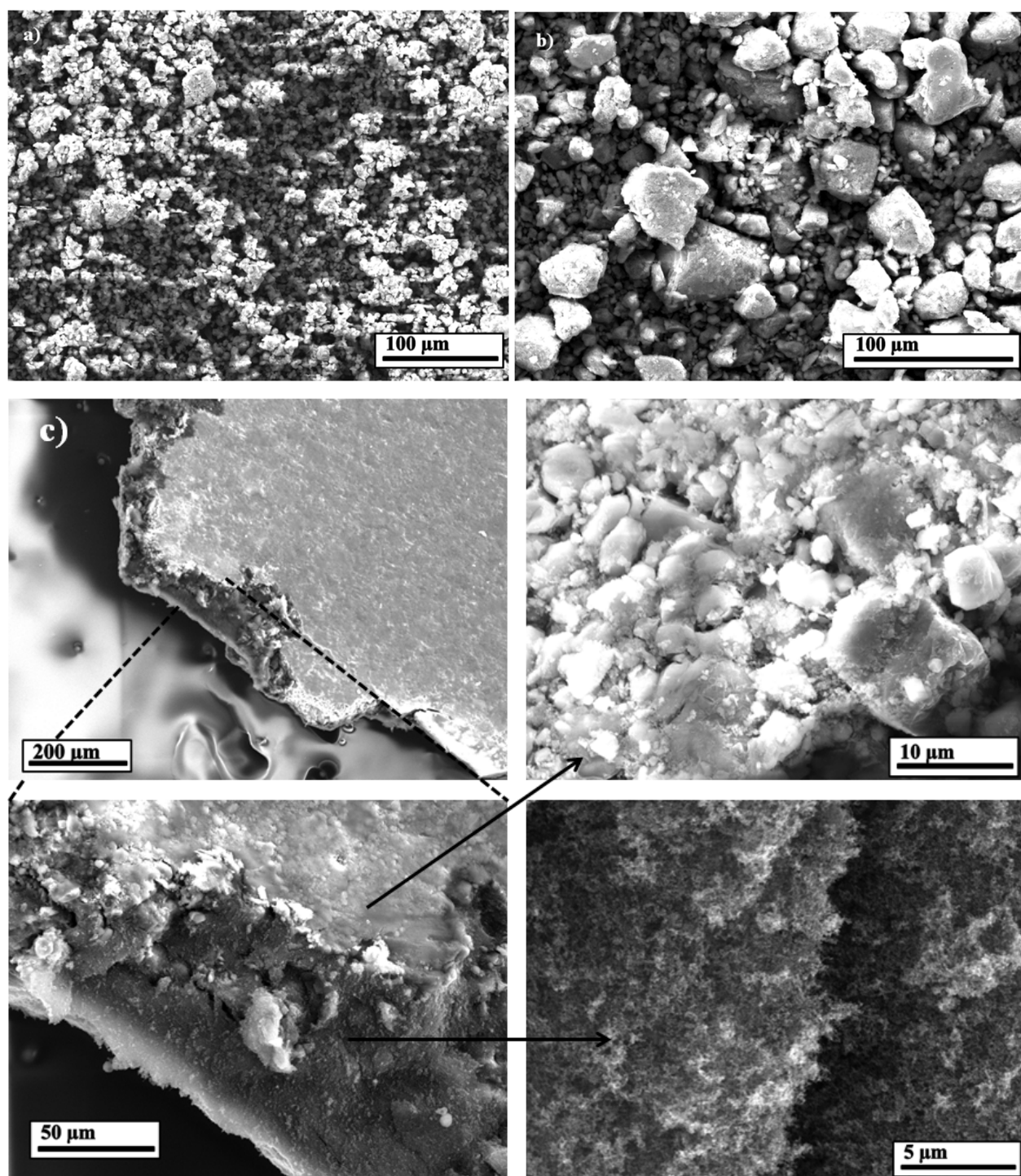


Figure V- 282: Scanning electron microscope images of a) Chemically derived nano sulfur; b) Commercially procured sulfur; c) Composite multilayer electrode architecture with a uniform coating of lithium orthosilicate on a sulfur-carbon mixture. The layer structure is clearly visible in the inset image. The top layer of orthosilicate is porous and consists of macroscopic particles fused as a result of the mechanical pressing. The soft sulfur-carbon inner layer consists of much finer particles of distinctly different morphology

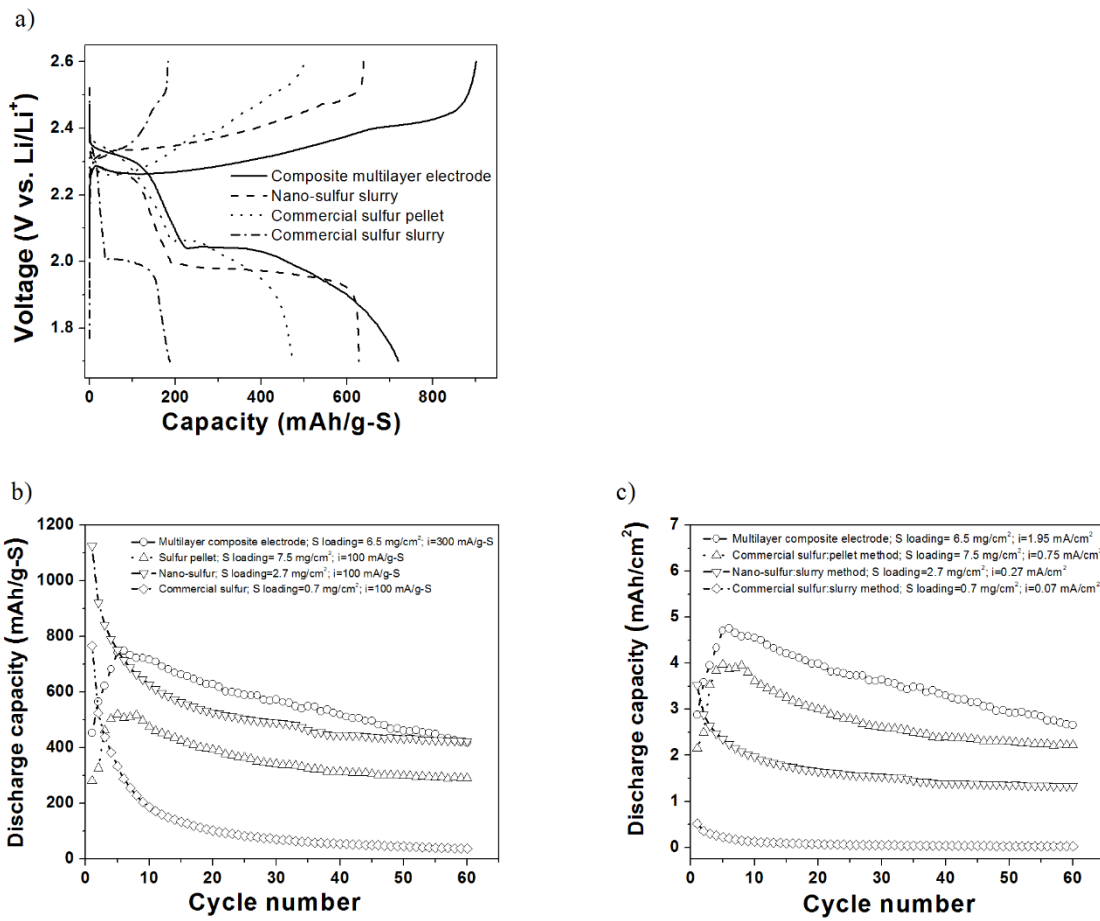


Figure V-283: a) Charge-discharge profiles (sulfur basis gravimetric capacity) of the various electrode architectures; b) Comparison of cycling behavior of the commercial sulfur, nano-sulfur prepared by slurry method, pellet method and the multilayer composite electrode; c) Comparison of cycling behavior (overall electrode areal capacity basis) of the various electrodes

Electrodes of sulfur-carbon (1:1) were prepared by either tape casting from the organic solvent based slurries or mechanically pressed pellets. Figure V-283a shows the 10th cycle charge-discharge profiles of the various sulfur-carbon materials. Characteristic plateaus corresponding to polysulfide formation and subsequent conversion to dilithium disulfide ( $\text{Li}_2\text{S}_2$ ) and dilithium sulfide ( $\text{Li}_2\text{S}$ ) are observed in all the materials. The composite multilayer electrode can be seen to exhibit however, the highest gravimetric capacity of the various materials after 10 cycles as a result of the high capacity yielded by the nano-sulfur (as shown in Figure V-283b also). The nano-sulfur slurry electrode also displays a high capacity as compared to the commercial sulfur pellet and the slurry made from commercially obtained sulfur powder. The cycling stability of the various materials is plotted in Figure V-283b and Figure V-283c (specific gravimetric and areal capacity, respectively). Among the slurry cast electrodes, it can be seen that the nano-sulfur demonstrates the higher capacities and better fade characteristics in comparison to the commercially obtained sulfur. The improvement in capacity can be attributed to the change in particle size seen in Figure V-282a and Figure V-282b. The higher surface area of the 0.3-2  $\mu\text{m}$  particles (as confirmed by DLS) results in enhanced reactivity and thus better capacity. The improvement in cycling performance observed therein could be attributed to reduced particle stresses in smaller particles resulting in much reduced fracture and delamination. In addition, the fine particle size would ensure good contact with the conductive additive preventing the particles from becoming inactive over time as a result of the fracture. The crystalline nature of the fine nanoparticles would at the same time, ensure that the particles would not be completely insulating. The slurry cast nano-sulfur electrode thus has a high initial capacity of  $\sim 1125$  mAh/g-S and a fade rate of 0.86%/cycle as seen in Figure V-283b. This superior performance indicates that sulfur behaves similar to silicon with respect to charge storage capability and cycling stability, in that the reduction in particle size aids both those characteristics. The nano-sulfur slurry

cast electrode has a high initial areal capacity of  $3.5 \text{ mAh/cm}^2$ , stabilizing at  $\sim 1.4 \text{ mAh/cm}^2$ , upon further cycling (Figure V- 283c).

The improvement in charge storage as a result of utilizing the pellet-pressing procedure, especially the composite multilayer electrode architecture is both seen in Figure V- 283b. The use of the pellet pressing procedure yields thicker electrodes, while at the same time allowing for better capacity retention. This results in the significantly higher areal capacities seen in Figure V- 283c. The thick electrodes made from commercially obtained sulfur have an initial areal capacity of  $\sim 4 \text{ mAh/cm}^2$  while the composite multilayer electrode has an areal capacity of  $\sim 4.75 \text{ mAh/cm}^2$ . These are values corresponding to the 5th cycle since these thick electrodes suffer from poor wetting in the initial cycles as would be expected. With further optimization,

we believe we could improve the capacity and cyclability of the electrodes by ensuring that polysulfides would not contribute to loss of electrical contact and would thus get completely converted to  $\text{Li}_2\text{S}$ . Even so, the capacity at the 5<sup>th</sup> cycle is much higher than the current EERE-OVT (Office of Energy Efficiency & Renewable Energy-Office of Vehicle Technologies) target for areal capacity of electrodes of  $4 \text{ mAh/cm}^2$ . It should be also noted that the areal capacities and sulfur loadings on the electrode exceed those previously reported though further optimization is ongoing to improve the overall sulfur weight percentage (to reduce overall electrode thickness). Both electrodes exhibit superior cycling stability though validating the hypothesis that the inorganic LIC materials aid in preventing polysulfide dissolution driven lithium-sulfur battery capacity loss hitherto seen.

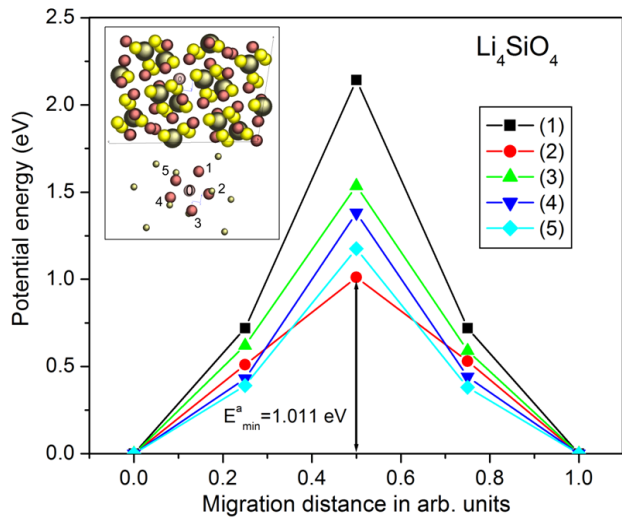


Figure V- 284: Activation barriers for different migration paths of Li-ions in  $\text{Li}_4\text{SiO}_4$ . Inset: pink 0 - Li-ion site; red (1)-(5) – Li vacancy sites for different migration pathways

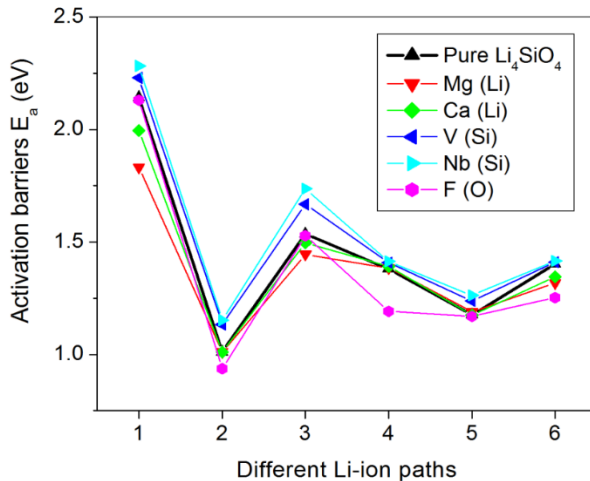


Figure V- 285: Activation barriers  $E_a$  for different migration paths of Li-ions in pure and doped  $\text{Li}_4\text{SiO}_4$

higher activation barriers (up to 2.2 eV). Introduction of aliovalent dopants could create Li-ion vacancies as well as decrease the activation barriers for the ionic migration, thus improving the overall ionic mobility. The ionic conductivity of doped  $\text{Li}_4\text{SiO}_4$  with Mg, Ca, V, Nb, and F has been studied from first principles. Corresponding results shown in Figure V- 285 indicate that  $\text{Mg}^{2+}$  and  $\text{Ca}^{2+}$  replacing  $\text{Li}^{+}$ -ion as well as  $\text{F}^-$  replacing  $\text{O}^{2-}$  ions help decrease the activation barriers for all corresponding Li-ion pathways in comparison to pure  $\text{Li}_4\text{SiO}_4$ . On the other hand, V and Nb substituting Si-ions slightly increase the  $E_a$  due to

### First principles studies into identification of high ionic conductivity LIC coating materials

Improvement in LIC ionic conductivity and polysulfide filtration capability is to be achieved by first principles driven design and experimental development of suitable LIC materials with the aim of further improving cycling capability. Using the nudged elastic band method implemented in VASP (Vienna ab-initio simulation package), various Li-ion migration pathways have been considered and corresponding activation barriers  $E_a$  have been calculated. Corresponding results in Figure V- 284 indicate that the pathway (0-2) requires the lowest activation energy ( $\sim 1 \text{ eV}$ ) for the Li-ion migration from the central position (0) to the Li-vacancy (2). All other pathways demonstrate

the larger ionic radii of  $V^{5+}$  and  $Nb^{5+}$  vs.  $Si^{4+}$ . However, the overall Li-ion conductivity is expected to be improved due to formation of  $Li^{+}$  vacancies and thus, facilitating Li-ion hopping through the crystal lattice. In terms of structural and chemical stability, calculated cohesive energies of the pure and doped orthosilicates indicate that V and Nb slightly decrease the stability, while Mg, Ca and F virtually render the stability invariant. Thus, the present theoretical study helped in identifying Mg, Ca, and F as prospective doping elements facilitating improvement in the Li-ion conductivity without sacrificing the overall structural and chemical stability of the LIC orthosilicate. An experimental validation of this conclusion will be conducted in the closest future.

### Flexible polymer-sulfur wires



Figure V- 286: Image showing the yarn-like nature of the Flex – sulfur wires (Flex-SWs)

Following earlier studies demonstrating significant capacity and stability improvement in sulfur cathodes obtained by using a thin layer of lithium ion conductor (LIC) on sulfur nanoparticles, work in the second quarter involved identification of strategies to further improve the stability by tailoring the sulfur morphology.

Towards this end, flexible sulfur wires (Flex-SWs) were generated using a simple polymer-handling method reported in Q2. The synthesis allows for a polymer-sulfur wire morphology (Figure V- 286) to be obtained with the polymer acting as a structural template

as well as improving the cycling characteristics by facilitating polysulfide retention. Figure V- 287a and Figure V- 287b depict the scanning electron micrograph and corresponding sulfur map of the unique sulfur fiber (Flex-SW) morphology obtained for the first time rendering Flex-SW very amenable for use in compliant, flexible batteries. Figure V- 286 displays the yarn-like quality of the Flex-SWs opening the door for a multitude of unique applications. It can be seen from Figure V- 287b that sulfur is uniformly distributed over the length of the yarn with no obvious segregation. The unique synthesis procedure yields wires which are in-effect encapsulated in a polymer matrix thus directly addressing the primary problem of polysulfide dissolution typically solved by the ubiquitous chemically induced steric hindrance methods. Figure V- 288a shows the cycling response of the various sulfur electrodes including commercial sulfur cast (C-Sulfur:slurry) and pellet-pressed (C-Sulfur pellet); nano-sulfur pellet-pressed with an LIC layer (nano-Sulfur-LIC pellet); Flex-SWs with LIC (Flex-SW pellet-LIC) and void LIC (Flex-SW pellet) layers. The Flex-SW pellet demonstrates superior stability and minimal capacity fade over ~135 cycles (see Figure V- 288b). The Flex-SW pellet demonstrates an initial capacity of ~700 mAh/g which stabilizes to ~450-500 mAh/g over the first 5 cycles. Studies are on-going to understand this stabilization behavior, a typical feature of Flex-SW materials. This 1<sup>st</sup> cycle irreversible loss behavior however is circumvented by use of a thin LIC coating on Flex-SW as seen in Figure V- 288a wherein the FSW-LIC pellet maintains a stable capacity of ~650 mAh/g over 60 cycles (fade rate~0.003%/cycle). Further analysis and optimization is ongoing to improve the capacity and stability of the flexible sulfur-

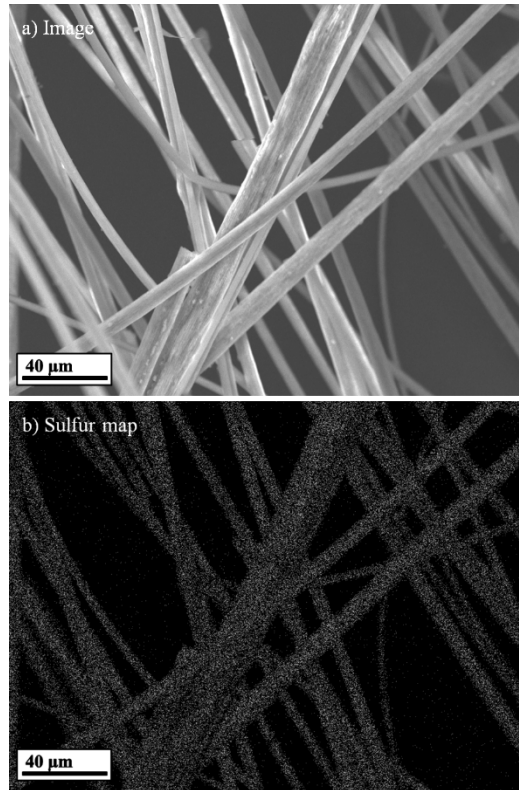


Figure V- 287: (a) SEM image (b) EDAX map of the flexible sulfur-polymer morphology shown in a prior figure

polymer wires. Stable areal capacity of the Flex-SW-pellet materials is  $\sim 2.5 \text{ mAh/cm}^2$  and optimization of sulfur weight percentage is needed to achieve this number to achieve the targeted  $4 \text{ mAh/cm}^2$ .

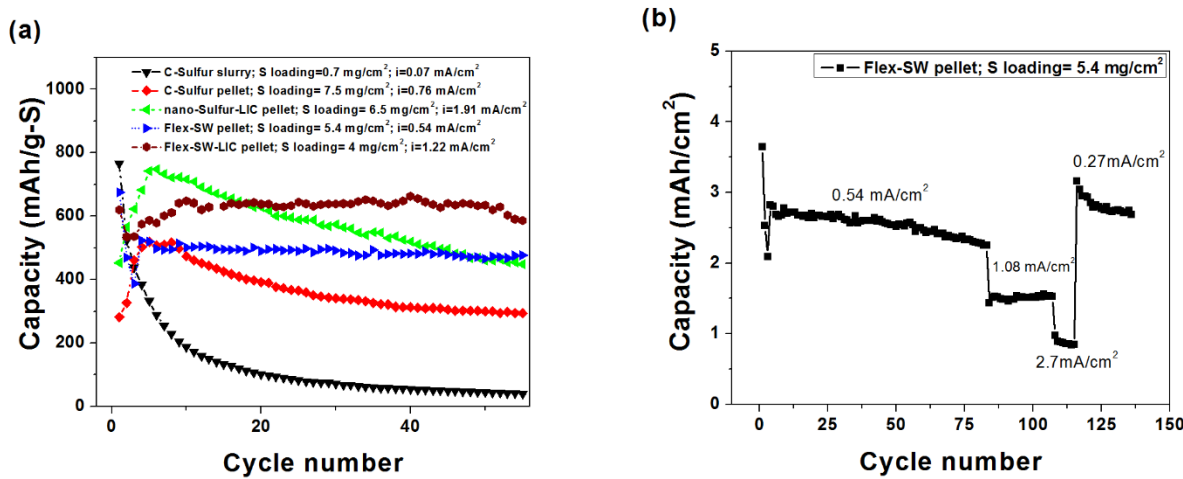


Figure V- 288: (a) Cycling behavior of various sulfur materials (b) Extended cycling and rate dependence of capacity in Flex-sulfur wires seen in a prior figure

#### Polymeric LIC materials (Gel-polymer electrolytes-GPEs)

In addition to inorganic LIC materials, polymer LIC (gel-polymer materials (GPE) containing lithium-ion conductor) materials were explored as a part of continuing studies into the same. These polymeric LIC materials were used in place of conventional polymeric separator materials. Figure V- 289 depicts the improvement in cycling stability of creating composite polymeric core-shell and layer-by-layer composite materials. In order to tackle fade associated with the gel-polymer electrolyte materials, nanoparticulate oxide materials were used as fillers in the GPE matrix. Figure V- 290a shows the TEM images of the oxide nanoparticles used therein and Figure V- 290b depicts the improvement in cycling behavior occurring as a result of the same.

Stability as a result of using doped oxide nanoparticles as filler materials in the polymer material results in a stable capacity of  $\sim 400 \text{ mAh/g}$  seen upto 80 cycles. The polymer electrolyte materials with oxide tethering sites act as both polysulfide filters as well as restainment media ensuring improvement in cycling stability. Optimization work is ongoing involving the gel-polymer LIC electrolyte materials and will be reported in following reports.

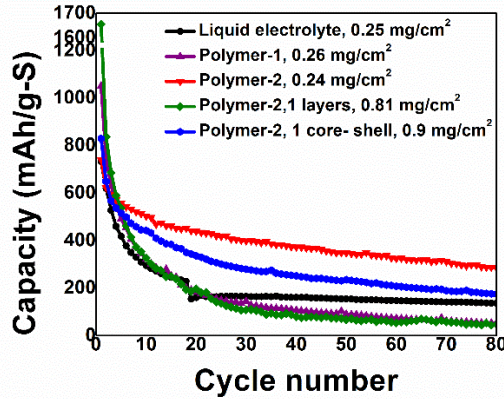


Figure V- 289: Comparison of cycling behavior of various polymeric LIC electrolyte materials

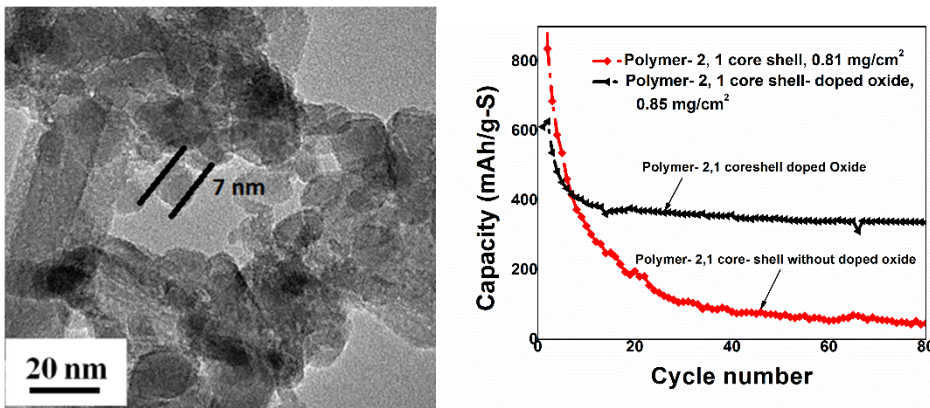


Figure V- 290: (a) Transmission electron microscope (TEM) (left Figure) of oxide nanoparticles used as fillers in the GPE materials (b) Effect of oxide filler material on cycling behavior in polymer LIC materials (right Figure)

### Complex framework materials (CFM)

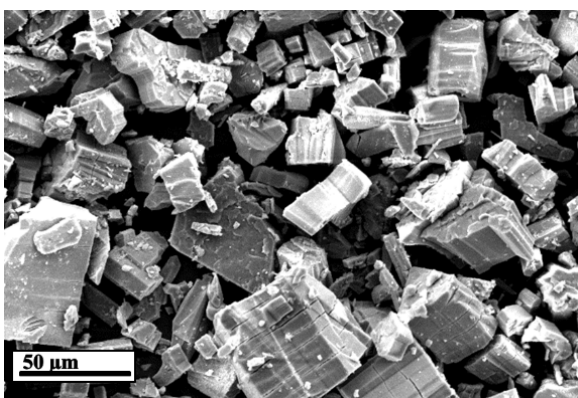


Figure V- 291: Morphology of sulfur-containing nanoporous CFMs

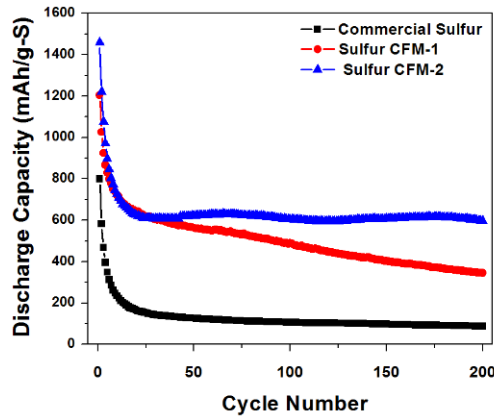


Figure V- 292: Improvement in cycling stability of sulfur cathodes by use of CFM materials

Research on Li – S batteries is mainly focused on three main aspects:(i) Improving the conductivity of Sulfur by using conductive coatings or composites and hence increasing the active material utilization, (ii) Modifying the liquid electrolyte – separator system using a gel – polymer or composite – polymer electrolyte to prevent polysulfide dissolution and (iii) Confining sulfur into porous matrices and hence preventing polysulfide dissolution. Porous materials with pore size comparable to or less than the size of polysulfide species need to be devised in order to completely overcome the problem of polysulfide dissolution. Hence, the use of complex framework materials (CFM) as trapping agents for sulfur species has been explored. The CFM materials containing nanopores are ideal for entrapping the soluble polysulfide species formed during lithiation of sulfur. Figure V- 291 depicts the morphology of certain nanoporous CFMs acting as sulfur – hosts. There is a significant improvement in initial capacity and cycling stability as a result of the use of sulfur-containing CFMs as Li-S battery cathodes and stable cycling has been demonstrated for up to 200 (Figure V- 292) cycles thus-far (further cycling is ongoing). The CFM electrodes exhibit a very low fade rate of ~0.01%/cycle following initial phase change.

**Table V- 8: Cycling characteristics of various sulfur battery systems synthesized and evaluated in this work**

Material	Initial discharge capacity (mAh/g-S)	Initial capacity fade <sup>y</sup> (% capacity)	Fade rate <sup>*</sup> (% capacity/cycle)
C-Sulfur:slurry	766.3	56.53	1.76
C-Sulfur pellet	519.3 <sup>†</sup>	N/A	0.87
nano-Sulfur-LIC pellet	748.2 <sup>†</sup>	N/A	0.79
Flex-SW pellet	675.4	23.09	0.17
Flex-SW pellet-LIC	620.3	5.37	0.003
Polymer 2,1 core-shell-doped oxide	776.26	36.75	0.4
Sulfur CFM-2	1460.4 <sup>^</sup>	54.79	0.01

<sup>x</sup>Fade rate calculated on the basis of 1<sup>st</sup> cycle capacity and 5<sup>th</sup> cycle capacity. <sup>y</sup>Fade rate calculated on the basis of 5<sup>th</sup> cycle capacity and 55<sup>th</sup> cycle capacity. <sup>†</sup>Capacity reported at 5<sup>th</sup> cycle since there was an increase in capacity from 1<sup>st</sup> cycle due to gradual wetting of the electrode.<sup>^</sup>Stabilizes at 20<sup>th</sup> cycle and fade calculated upto 200<sup>th</sup> cycle.

### Conclusions and Future Directions

Table V- 8 summarizes the cycling characteristics of the various sulfur materials explored in Phase-1 of this project. The aim of Phase-1 was to establish methods to improve sulfur cycling characteristics by use of lamination approaches, especially in the form of LIC materials. It can clearly be observed that fade rates have been significantly reduced by using the 4 approaches in Phase-1 described above. Stable capacities of in excess of 600 mAh/g have been observed in two systems with stability for over 150 cycles, the flexible sulfur-polymer composite electrodes and the Sulfur CFM materials. Exceptionally low fade rates of ~0.003%/cycle have been observed which greatly supports the hypothesis of LIC-based engineering. In Phase-2 of the study, emphasis will be laid on improving capacity of these systems with the goal of achieving in excess of 1000 mAh/g for 1000 cycles. The primary driving force for this will be electronic conductivity improvement. In lieu of this, *ab-initio* calculations have been performed in Q4 to identify suitable doping strategies to achieve the same. First principles studies were conducted to understand the effect of dopants on the band-structure and density of electronic states (DOS) of sulfur (Figure V- 293). It can be seen that sulfur which is inherently an insulator following introduction of these dopants leads to sulfur exhibiting semiconducting properties upon the introduction of dopants into the sulfur lattice. Experimental synthesis of the doped sulfur followed by detailed evaluation forms a part of Phase-2 study of the project which will be initiated in year 2 and accordingly, reported in due course. Electronic and ionic conductivity optimization using various experimental strategies will be actively pursued towards making

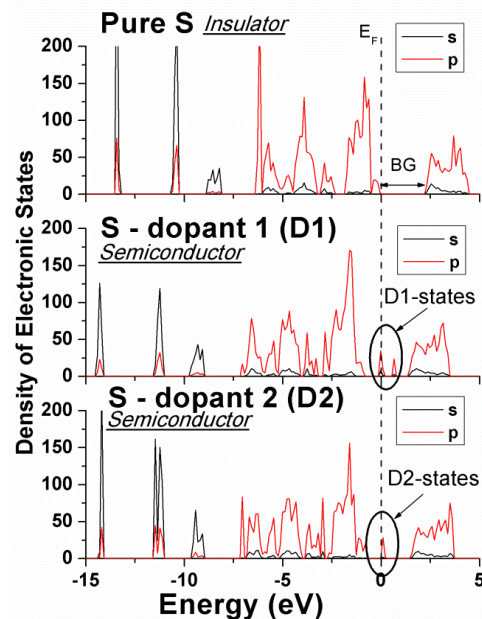


Figure V- 293: Effect of doping on electronic conductivity of sulfur

high rate, high gravimetric and areal capacity sulfur cathodes with exceptional cycling stability. Results of these studies will be reported in due course.

#### FY 2015 Publications/Presentations

1. P. J. Hanumantha, B. Gattu, et al., Journal of The Electrochemical Society, 2014, 161, A1173-A1180.
2. P.J. Hanumantha, B. Gattu, P.M. Shanthi, P.N. Kumta, Provosional Patent, 2015, Application number: 62132014.
3. Jampani, P.H.; Shanthi, P.M.; Gattu, B.; Kumta, P.N. Novel Flexible Sulfur Wire Fabrics (FSF) for Lithium-Sulfur Batteries, The Electrochemical Society (Spring 2015), Chicago, IL
4. Shanthi, P.M.; Jampani, P.H.; Gattu, B.; Velikokhatnyi, O.I.; Kumta, P.N. Effect of Coating and Particle Properties on the Cycling Stability of Li-Ion Conductor (LIC) Coated Sulfur Cathodes, The Electrochemical Society (Spring 2015), Chicago, IL
5. Jampani, P.H.; Gattu, B.; Shanthi, P.M.; Damle, S.S.; Basson, Z.; Bandi, R.; Datta, M.K.; Park, S.K.; Kumta, P.N. Flexible sulfur wires (Flex-SWs) – A Versatile platform for lithium-sulfur batteries, ChemElectroChem (2015), in press.

## V.I.2 Simulations and X-ray Spectroscopy of Li-S Chemistry (LBNL)

### Objectives

- Develop method of characterizing Li-S battery reaction mechanisms consisting of in situ X-ray absorption spectroscopy and molecular simulations
- Examine Li-S charge/discharge reaction mechanisms
- Elucidate physical and chemical nature of Li-S battery reaction intermediates in different electrolytes

### Technical Barriers

- Li-S batteries infamously suffer from dissolution of lithium polysulfide reaction intermediates formed during charge and discharge. These species can dissolve out of the cathode and cause battery capacity to fade and cell failure
- The reaction mechanisms that underly the formation of polysulfide reaction intermediates are still unclear.
- Uncertainty regarding the reactions has historically stemmed from uncertainty in spectroscopic data used to analyze in situ spectro-electrochemical data. Obtaining spectra for isolated polysulfide molecules (rather than a distribution of  $\text{Li}_2\text{S}_x$ ,  $2 \leq x \leq 8$ )

### Technical Targets

- Obtain X-ray absorption spectroscopy (XAS) signatures for lithium polysulfide dianions ( $\text{Li}_2\text{S}_x$ ,  $2 \leq x \leq 8$ ) as well as lithium polysulfide radical anions (e.g.  $\text{LiS}_3$ ). Compare experimentally obtained spectra to those obtained via simulation.
- Build in situ electrochemical/XAS setup and battery cell that enables in situ probing of Li-S reaction intermediates
- Examine Li-S reaction intermediates in situ, both as they are formed during charge/discharge and at time points after charge/discharge has occurred

### Accomplishments

- Experimental XAS were obtained for  $\text{Li}_2\text{S}_x$  intermediates dissolved in poly(ethylene oxide) (PEO) and a diblock copolymer of polystyrene-poly(ethylene oxide) (SEO)
- First ever theoretical calculations of sulfur K-edge XAS of isolated polysulfide dianions and radical anions were obtained for ether-based solvents as well as dimethylformamide
- In situ solid-state pouch cells were developed to enable in situ soft X-ray spectroscopy experiments
- Li-S cells were discharged to various depths of discharge; XAS was used to probe the electrolyte of these batteries. Resulting spectra were analyzed using theoretically calculated XAS, which revealed that during early stages of discharge lithium polysulfide radical anions are formed.
- In situ XAS experiments were performed on discharging Li-S cells
- Concentration and temperature dependence of polysulfide speciation in PEO and SEO were probed and revealed that within the given concentration regime, changes in concentration and temperature have no effect on speciation.

#### Project Details

**John Tabacchi (NETL Program Manager)**  
DE-EE0005443 Recipient: OneD Material, LLC

**Nitash Balsara (LBNL – PI)**  
201 C Gilman Hall  
University of California  
Berkeley, CA 94720  
Phone: 510-642-8973; Fax: 510-643-5037  
E-mail: [nbalsara@berkeley.edu](mailto:nbalsara@berkeley.edu)

David Prendergast  
Materials Sciences Division  
Lawrence Berkeley National Laboratory  
Molecular Foundry  
Berkeley, CA 94720

Start Date: October 2013  
Projected End Date: October 2017

---

## Introduction

Studies of Li-S reaction mechanisms have historically been challenged by the difficulty of differentiating lithium polysulfide reaction intermediates experimentally. The objective of this work is to overcome these issues by leveraging theoretical calculations of polysulfide X-ray absorption spectra. The objectives of this work are to: (1) elucidate the mechanisms by which redox reactions in the sulfur cathode proceed, and (2) study the physical and chemical nature of lithium polysulfide reaction intermediates.

## Approach

**Innovative Approach:** Molecular dynamic simulations of lithium polysulfide dianions and radical anions in various solvents are used to obtain spectra for isolated polysulfide species. This is done using eXcited Core Hole simulations in conjunction with ab initio molecular dynamic motifs of dissolved polysulfide species. Experimental XAS is used to (1) examine Li-S battery reaction mechanisms as they take place in the Li-S cathode, and (2) to probe ex situ, chemically synthesized mixtures of lithium polysulfide species.

1. Obtain experimental XAS for lithium polysulfide species dissolved in SEO, the polymer electrolyte of which will be used for in situ battery experiments
2. Perform theoretical calculations to obtain X-ray spectra that can be used to interpret and analyze experimentally obtained data
3. Perform in situ studies of Li-S reaction mechanisms by probing cells as they are charging/discharging and cells that have been discharged to various depths of discharge.
4. Analyze resulting experimental spectroscopy using theoretically obtained X-ray spectra for individual polysulfide species.

## Results

We have achieved the following progress:

### Calculation of lithium polysulfide radical anion sulfur K-edge spectra

The presence of radical anions in lithium sulfur batteries has become a popular focus of Li-S reaction mechanism studies. The influence that these species have on the redox pathways is an interesting question we aim to elucidate. Similar to polysulfide dianions ( $\text{Li}_2\text{S}_x$ ), spectra for the radical anions are difficult to obtain. Ultramarine powder (lazurite) has previously been used as a spectral standard for sulfur radical anions, however, ultramarine can contain both  $\text{S}_2^-$  and  $\text{S}_3^-$  radicals. Additionally, the sulfur radical in lazurite exist in a highly crystalline environment that is far different than the freely dissolved state of a battery electrolyte. For these reasons, we sought to elucidate the molecular origin of spectral features evident in the sulfur K-edge spectra of sulfur radical anions. Figure V- 294 shows the calculated spectra for the radical  $\text{S}_3^-$  ion, separated into contributions from the central S atom and the two terminal S atoms. Additionally, the contributions of each to the XAS from the majority ( $\alpha$  – dashed line) and minority ( $\beta$  – solid line) spin channels. Electron densities of the core-excited p-orbital star and sigma star orbitals are also shown. Our calculations allow us to both calculate theoretical spectra and elucidate the molecular origin of X-ray features.

***In situ* characterization of polysulfide radical anions present in an ether-based electrolyte of an Li-S battery**

We have successfully constructed modified Li-S pouch cells that enable us to perform *in situ* soft X-ray

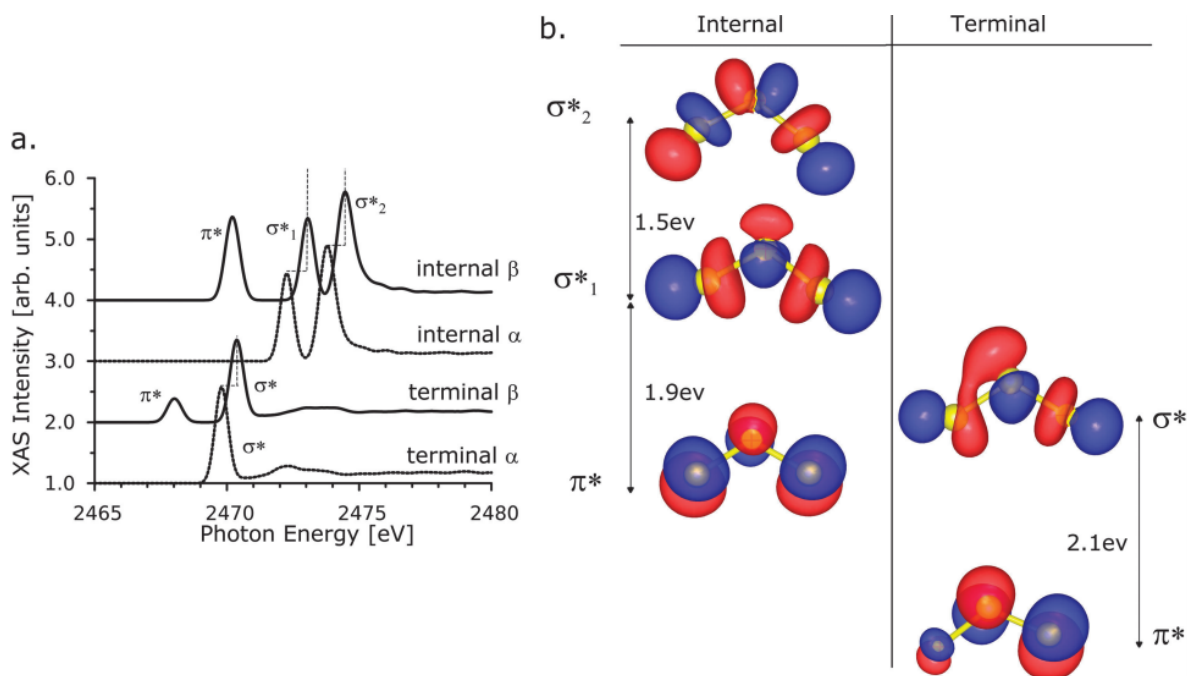


**Figure V- 294:** (a) Calculated S K-edge XAS of the radical S<sub>3</sub><sup>-</sup> ion separated into contributions from the central S atom and the two terminal S atoms. (b) Electron density of the core-excited pi star and sigma star orbitals in the trisulfur radical molecule at 0 K

spectroscopy experiments of lithium-sulfur battery chemistry. Solid state Li-S cells containing a lithium metal anode, a block copolymer electrolyte SEO containing LiClO<sub>4</sub>, and a cathode containing carbon black, elemental sulfur, and SEO were discharged to different depths of discharge, as shown in Figure V- 295 below. Discharging was stopped and the cells were allowed to sit at operating temperature (90 °C) for three days. Cells were then brought to the sulfur K-edge XAS beamline and probed in their native, unaltered state. As shown in Figure V- 295 (a), spectra were obtained in fluorescence mode, through the anode side of the battery. Thus, spectra primarily represent the sulfur species that were given ample time to diffuse out of the battery cathode. The experimental geometry, cell schematic, voltage profiles and spectra in Figure V- 295(d) display two common features: a main-edge peak corresponding to internal sulfur atoms at peak (c) and a pre-edge peak corresponding to terminal sulfur atoms (b). Interestingly, spectrum I also exhibited intensity around 2468-2469 eV. Our previous theoretical calculation of polysulfide radical anion spectra suggested that this feature may be attributed to a sulfur radical anion. Thus, we also calculated the theoretical spectra for radical anions dissolved in TEGDME. The resulting spectrum and corresponding molecular attributed to individual spectral features of the molecule are shown in Figure V- 296.

Our library of theoretically calculated sulfur spectra (S<sub>8</sub>, Li<sub>2</sub>S, Li<sub>2</sub>S<sub>x</sub> ( $2 \leq x \leq 8$ ), and radicals (LiS<sub>3</sub>, LiS<sub>4</sub>, LiS<sub>5</sub>) enables us to interpret the experimental spectra with insight from first principles. The experimental spectra were fit via a linear combination least squares fitting method. The best fit of the experimental data using theoretically calculated spectra is shown for point I in Figure V- 297.

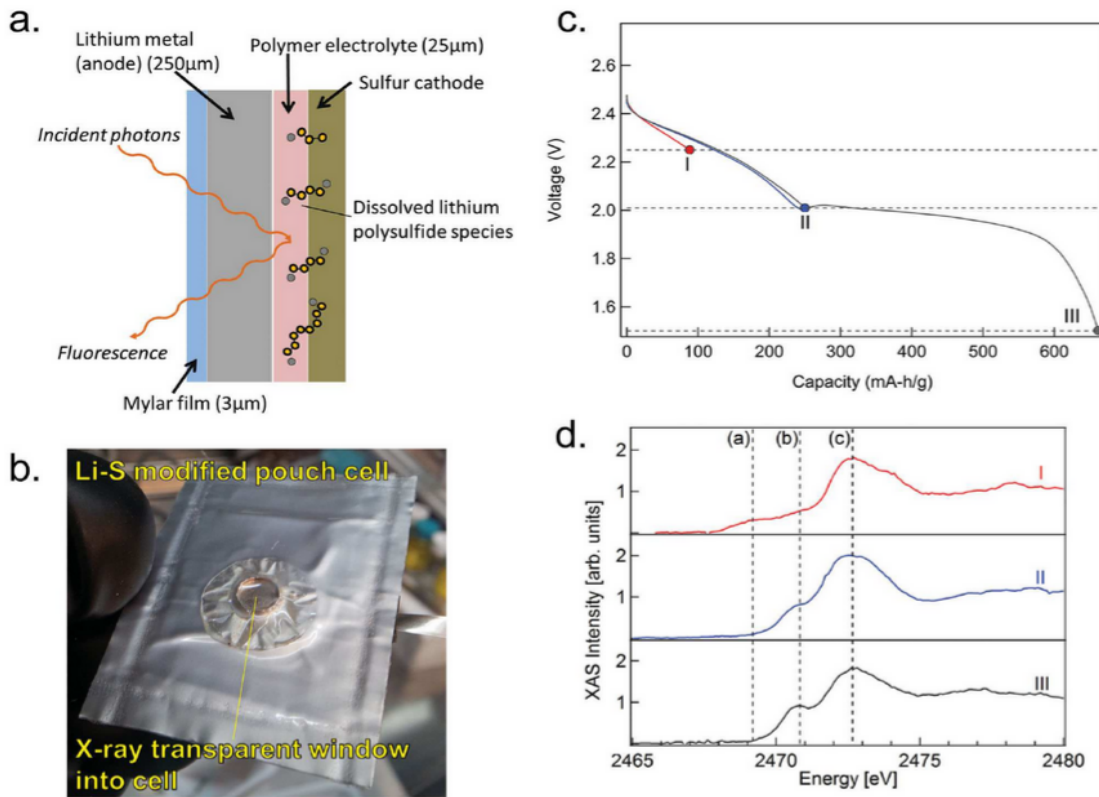


Figure V- 295: (a) Schematic of X-ray experiment, (b) Diagram of modified Li-S pouch cell, (c) Voltage profiles for the three discharged Li-S cells, (d) Sulfur K-edge XANES as a function of discharge for the three points indicated in (c)

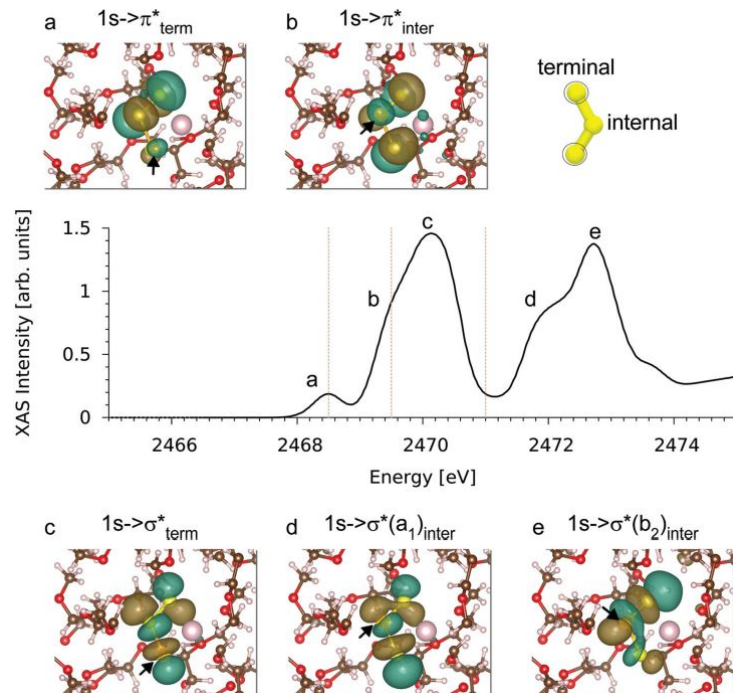
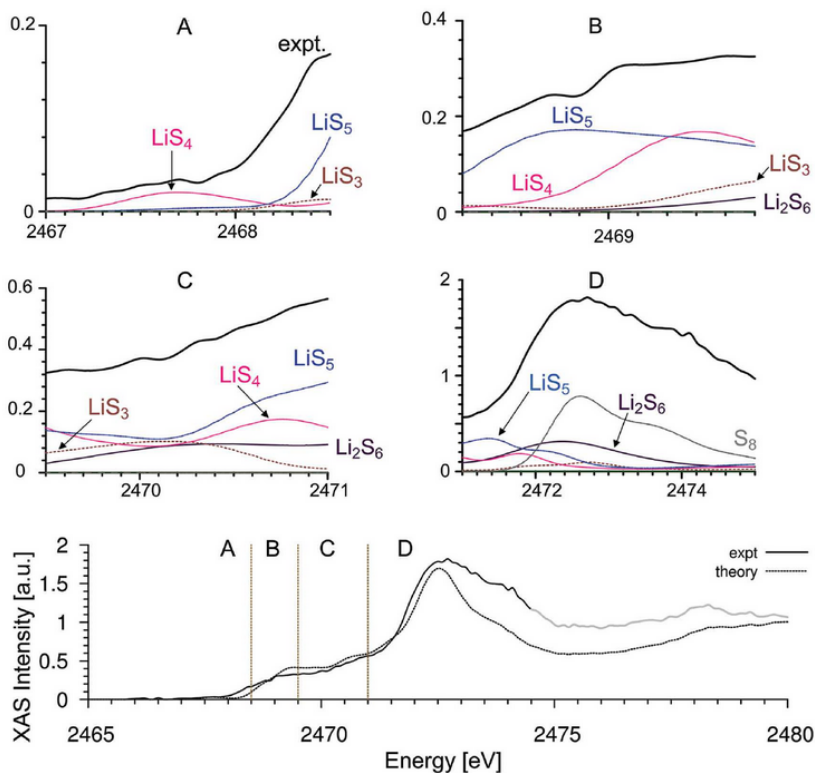


Figure V- 296: First-principles XANES spectra of the trisulfur LiS<sub>3</sub> molecule dissolved in TEGDME, obtained from sampling ab initio molecular dynamics at 298 K. Each of the five major transitions that inform the spectra is indicated



**Figure V- 297:** Sulfur K-edge XAS during initial stage of discharge. We present a best fit of the experimental data (solid line) using independent spectra obtained from first-principles calculations (dashed line). The spectrum is broken into four regions according to the transitions occurring in each region

**Table V- 9: Exact spectral weightings used in linear combination fitting of spectra**

Spectra	Voltage (V)	S8 (%)	Li2S (%)	Radicals (%)	Dianions (short) (%)	Dianions (long) (%)
I	2.25	20	0	62	0	17
II	2.02	2	36	6	45	11
III	1.50	0	39	0	61	0

#### ***In situ* study of solid-state Li-S battery discharge reaction mechanisms**

Li-S cells containing a lithium metal anode, a block copolymer electrolyte SEO containing LiClO<sub>4</sub>, and a cathode containing carbon black, elemental sulfur, and SEO were also used for *in situ*, direct measurement of Li-S reaction mechanisms. Figure V- 298 shows sulfur K-edge spectra obtained during first discharge for a solid-state Li-S pouch cell. The cell was discharged at a slow rate of C/60 to assure that there would be no drastic changes in chemistry while a spectrum was being collected. The inset of Figure V- 298 highlights the increase in spectral intensity in the vicinity of 2469.0 eV as the battery approaches 2.25 V.

The least squares fitting procedure was performed for each spectrum, thus providing a spectral composition of theoretical spectra for each experimental spectrum. These spectral compositions were then converted to molecular compositions, which are shown in Table V- 9. While these were in fact the best fit spectra, they were not the only fit that provided an accurate representation of the experimental spectra. For that reason, Table V- 9 reports the speciation of each spectrum in terms of small ‘families’ of molecules. Table V- 9 shows clear evidence for the presence of radical species at early stages of discharge, but none at later stages of discharge.

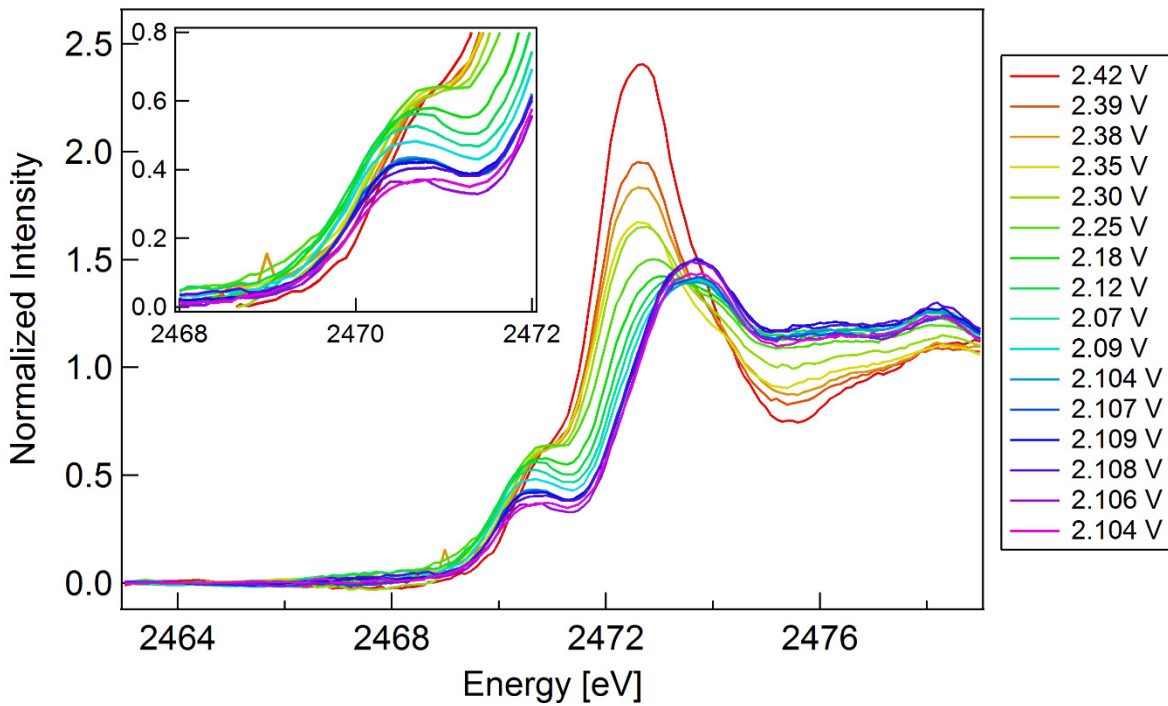
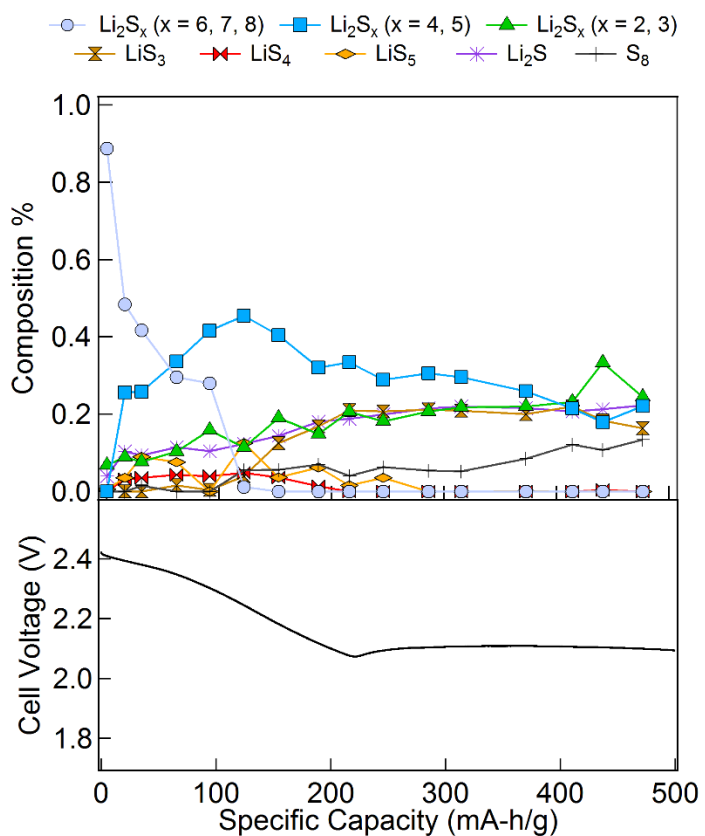


Figure V- 298: Sulfur K-edge XAS obtained for a discharging Li-S battery consisting of a solid polymer electrolytes (SEO) with  $\text{LiClO}_4$ , and a cathode of elemental sulfur, carbon black, SEO, and  $\text{LiClO}_4$ . Discharging was performed at C/60 to assure no significant change in speciation during spectrum collection

Again, theoretical spectra for lithium polysulfides dissolved in TEGDME,  $\text{Li}_2\text{S}$ , and  $\text{S}_8$  were used to analyze the array of spectra. The best fit for each spectrum was determined, and the resulting speciation can be seen in Figure V- 299, along with the voltage profile for the battery. Long chain polysulfide dianions ( $x = 6, 7, 8$ ) are found to dominate early in discharge, followed by mid-chain dianions ( $x = 4, 5$ ), and finally short-chain ( $x = 2, 3$ ). The inset of Figure V- 298 highlights the growth of a low energy feature near 2469.0 eV, which leads to the growth of  $\text{LiS}_3$  radical anions seen in the composition plot. Further analysis of this data is on-going. This data exemplifies the fact that our experimental system is now established for performing in situ studies of Li-S chemistry.



**Figure V- 299:** Speciation of sulfur K-edge spectra shown in the prior figure. Long chain dianions dominate early spectra, followed by mid-chain dianions, and ultimately, low chain dianions. Radical species attributing to the increase in intensity as shown in the inset of the prior figure

computations will be coupled to experimentally obtained spectra for polysulfide species dissolved in DMF. Lastly, we will continue to utilize theoretical spectra to interpret experimental XAS, and also invoke calculations for free energy of formation to better inform us of polysulfide disproportionation tendencies.

#### FY 2015 Publications/Presentations

1. N.P. Balsara, "X-ray Absorption Spectroscopy of Lithium Sulfur Battery Reaction Intermediates" Symposium on Energy Storage, National Meeting of the American Chemical Society, Denver, Colorado, March 24, 2015
2. N.P. Balsara "Segmental Interactions between Polymers and Small Molecules in Batteries and Biofuel Purification" Meeting of the American Physical Society, San Antonio, Texas, March 2 2015
3. N.P. Balsara " Polysulfide Radicals Appearance in Partially Discharged Lithium-Sulfur Battery Analyzed By First-Principles Interpretations of X-ray Absorption Spectra" Meeting of the Electrochemical Society, Phoenix, Arizona, October 14, 2015
4. K.H. Wujcik, "X-ray Absorption Spectroscopy of Lithium Sulfur Battery Reaction Intermediates" Meeting of the American Physical Society, San Antonio, Texas, March 6, 2015
5. T. Pascal, "Probing the Solution Structure and Electronic Charge State of Dissolved Sulfur Molecules using X-ray Spectroscopy", Talk, 2015 ALS User Meeting, PICKLES workshop, Berkeley, CA, Oct, 2015
6. T. Pascal, "X-ray Absorption Spectroscopy as a probe of dissolved polysulfides in lithium sulfur batteries", Talk, 2015 APS Spring Meeting, San Antonio, TX, March 2015
7. T. Pascal, "Establishing key chemical species in electrochemical systems from first principles", Department of Mechanical Engineering seminar, MIT, Cambridge, MA, Feb. 2015
8. T. Pascal, "Probing the Chemistry of Energy Storage Systems using X-rays", Department of Chemistry seminar, NYU, NY, NY, Jan, 2015

#### Conclusions and Future Directions

In FY2015 we have made significant progress toward our goal of performing in situ XAS of Li-S batteries. The library of theoretical spectra needed to interpret experimental XAS has been fully established and studied in great depth. Pouch cells have been designed, built and used to perform in situ XAS studies of cells at different depths of discharge and cells discharging while being probed by X-ray photons. The resulting XAS have been interpreted using our theoretical catalog of spectra. These studies have revealed the presence of lithium polysulfide radical anions at early stages of discharge. Going forward, we plan to perform in situ XAS studies of full discharge/charge processes at different rates of discharge/charge. Using our theoretical calculations we will continue to explore the physical and chemical nature of polysulfide species. In particular, we will leverage molecular dynamics to examine speciation of polysulfide molecules in electron-pair doning solvents like dimethylformamide. Results of these

9. D. Prendergast, "Understanding working interfaces at the Nanoscale", 2015 ALS User Meeting, Invited Talk, Berkeley Lab, October 6, 2015
10. D. Prendergast, "Exploring details of batteries from first principles", 6th World Materials Research Institutes Forum, Invited Talk, Lawrence Livermore National Lab, September 15, 2015
11. D. Prendergast, "What X-ray spectra can teach us about electrochemistry", SUNCAT Seminar, Stanford University, July 28, 2015
12. D. Prendergast, "Revealing nanoscale details of electrochemical systems through first-principles simulations of X-ray absorptionspectroscopy", Australian Synchrotron Seminar, Monash University, Melbourne, June 18, 2015
13. D. Prendergast, "Revealing nanoscale details of electrochemical systems through first-principles simulations of X-ray absorption spectroscopy", NSLS User Meeting Workshop, Brookhaven National Lab, May 20, 2015
14. D. Prendergast, "Establishing key chemical species in electrochemical systems using first-principles simulations", BATT Seminar, Berkeley Lab, March 30, 2015
15. D. Prendergast, "Predicting X-ray spectral fingerprints of energy-relevant processes from first principles", 2014 ALS User Meeting workshop, October 7, 2014
16. Pascal, T. A., et al. (2015). "X-ray spectroscopy as a probe for lithium polysulfide radicals." Physical Chemistry Chemical Physics **17**(12): 7743-7753.
17. Wujcik, K. H., et al. (2015). "Characterization of Polysulfide Radicals Present in an Ether-Based Electrolyte of a Lithium–Sulfur Battery During Initial Discharge Using In Situ X-Ray Absorption Spectroscopy Experiments and First-Principles Calculations." Advanced Energy Materials **5**(16): n/a-n/a.

## V.I.3 Novel Chemistry: Lithium-Selenium and Selenium-Sulfur Couple (ANL)

### Objectives

- The objective of this project is to develop a novel  $\text{SeS}_x$  cathode material for rechargeable lithium batteries with high energy density and long life along with low cost and high safety.

### Technical Barriers

- Dissolution of lithium polysulfides.
- Insufficient life.
- Low round-trip energy efficiency.

### Technical Targets

- A cell with nominal voltage of 2 V and energy density of 600 Wh/kg.
- A battery capable of operating for 500 cycles with low capacity fade.

### Accomplishments

- Suppressed the shuttle mechanism by encapsulating S in porous organic polymer.
- Investigated the impact of solvent on Li-Se chemistry.
- Explored the phase stability of binary S-Se phase diagram.
- Conducted *in situ* XANES of the charge storage mechanism in  $\text{S}_x\text{Se}_y$ .
- Developed porous carbons for encapsulation of  $\text{S}_x\text{Se}_y$ .

### Introduction

The Li-S battery has been the most promising technology for a major leap in the energy density beyond that of present Li-ion batteries. However, the dissolution of lithium polysulfides in non-aqueous electrolytes has been the major contributor to the low energy efficiency and short life of Li-S batteries. In addition, the insulating nature of both end members during charge/discharge (S and  $\text{Li}_2\text{S}$ ) limits the rate capacity. To overcome the conducting barrier, S or  $\text{Li}_2\text{S}$  is generally impregnated in a carbon-conducting matrix for better electronic conductivity, thereby impeding the increase of the loading density of practical electrodes.

### Approach

- Investigate the phase stability of  $\text{SeS}_x$ .
- Confine Se and  $\text{SeS}$  in different carbon matrix, including a porous organic polymer, to suppress the dissolution of lithium polysulfides and polyselenide.
- Understand the specific interaction between S (and Se) and porous substrate and their dissolution in different solvents.
- Develop new encapsulation strategy to further suppress the dissolution of lithium polysulfides or polyselenide.

### Results

#### Study the compatibility between $\text{Li}_2\text{Se}$ and solvents

Figure V- 300 shows that neither Se nor  $\text{Li}_2\text{Se}$  dissolved in the carbonate-based solvent, GenII, a mixture of ethylene carbonate and ethyl methyl carbonate (EC/EMC). We took 1 mL solution from the  $\text{Li}_2\text{Se}$ -containing bottle and added it to the Se-containing bottle. No color change was observed. By contrast, once  $\text{Li}_2\text{Se}$  was

#### Project Details

**Khalil Amine & Zonghai Chen**

Argonne National Laboratory  
9700 South Cass Avenue  
Argonne, IL 60439

Phone: 630-252-3838; Fax: 630-972-4451

E-mail: [amine@anl.gov](mailto:amine@anl.gov)

#### Collaborators:

Prof. Chunsheng Wang (University of Maryland)  
Dr. Yang Ren (Advanced Photon Source, ANL)  
Dr. Chengjun Sun (APS, ANL)

Start Date: October 2014

Projected End Date: September 2018

dissolved in an ether-based solvent and added to an ether-based solvent containing Se, a dark-brown solution formed, corresponding to  $\text{Li}_2\text{Se}_n$  ( $n \geq 4$ ). These results imply that lithium polyselenides are insoluble in conventional carbonate-based solvent. This finding indicates that Li-Se batteries have the substantial advantage of being able to use commercially available electrolyte.

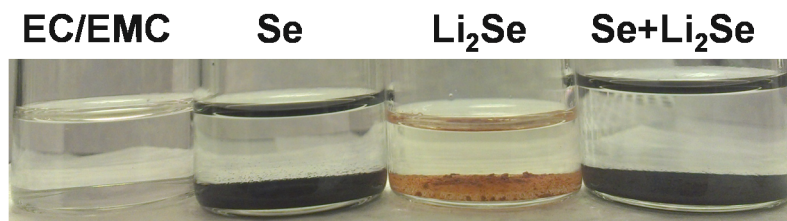


Figure V- 300: Photograph of GenII electrolyte solvent (EC/EMC) alone and with insoluble Se,  $\text{Li}_2\text{Se}$ , and a combination of the two

We carried out *in-situ* X-ray absorption near edge structure (XANES) measurements on a pouch Li-Se cell made with GenII electrolyte that was cycled at a rate of 110 mA/g. The selenium K-edge absorption, at 12,658 eV, arises from the transition of Se 1s core electrons to the unoccupied 4p states. The Se K-edge of  $\text{Li}_2\text{Se}$  shifts to a higher energy (12,660 eV). The abnormal shifts of the  $\text{Li}_2\text{Se}$  Se-edge toward higher energy could be explained by the reduced screening effect. A 2D contour plot of the Se XANES spectra recorded during the cell cycling is presented in Figure V- 301a, with the voltage profile shown in Figure V- 301b. Generally, the energy position of the edge is determined as the lowest energy peak of the first derivative of the XANES spectra, as shown in Figure V- 301c. Correlating Figure V- 301c and Figure V- 301a, we found that the edge positions did not undergo obvious shifts during the cell cycling, even at the fully discharged state (0.8 V), in contrast to the significant energy shifts in the Li-Se cell with ether-based electrolyte. However, the absorption of the Se-edge is weakened when the cell is discharged to 0.8 V.

Another common use of XANES is fingerprinting by linear combination fitting of XANES spectra of known species to determine the components in a mixture. By selecting XANES spectra of the powder materials (Se and  $\text{Li}_2\text{Se}$ ) as standards, we were able to determine the composition of the Se electrode at different states of charge/discharge by linear combination fitting of the XANES spectra measured during cell cycling with the Athena software package. Most of the spectra are well fitted, illustrated by the extremely small residues with reduced  $\chi^2$  from 0.012% to 0.144% shown in Figure V- 301d (black squares). These results are comparable to the values we obtained in multi-phase fitting with reduced  $\chi^2$  from 0.017% to 0.07% in the D2 electrolyte. For Se and  $\text{Li}_2\text{Se}$  two-phase fitting, the spectra of the cell with ether-based electrolyte leads to huge residues, with reduced  $\chi^2$  up to 5.676%, indicating the formation of an intermediate phase. The fitting results in Figure V- 301d suggest that no observable intermediate phases formed in the carbonate-based electrolyte cell, i.e., Se is directly transformed into  $\text{Li}_2\text{Se}$  and the reduction is not complete. About 44% of the Se is reduced into  $\text{Li}_2\text{Se}$  at the end of discharge, with a capacity of 425 mAh/g at a rate of 110 mA/g for a pouch cell. Most important, the *in-situ* XANES results confirmed that no lithium polyselenides formed in the electrochemical reaction during cycling.

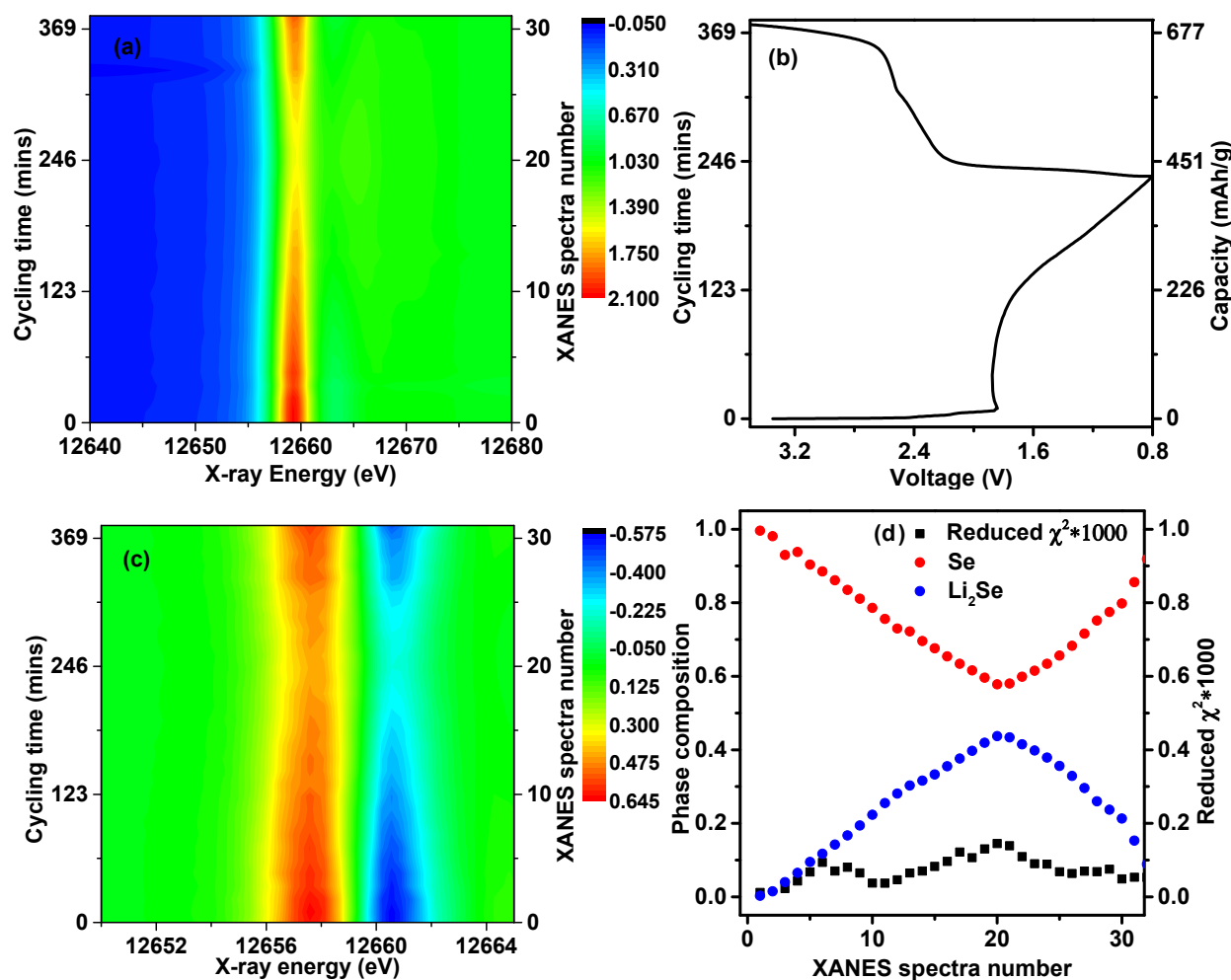


Figure V-301: *In-situ* XANES measurement for Li-Se pouch cell in GenII electrolyte: (a) normalized XANES spectra of the cycling cell, (b) voltage profile, (c) derivative of normalized XANES spectra, and (d) linear combination fitting of residue values and corresponding phase compositions in different state of charge/discharge

### Encapsulating S in porous organic polymer

An easily available porous organic polymer (POP) network (Figure V-302) represents a new class of amorphous polymeric material that has tunable permanent porosity and can act as a host to encapsulate sulfur and suppress the dissolution of lithium polysulfides. The POPs in our study have much higher surface area (up to  $3143 \text{ m}^2/\text{g}$ ) than the porous carbon materials. Moreover, these POPs exhibit dominant micropores with pore size less than 1 nm, as calculated from non-local density functional theory (NLDFT). The highly strained tetrahedral monomer in POPs extends the network three dimensionally, thus enabling the formation of a robust network with less penetration and high surface area.

The charge–discharge voltage profiles of Li–S cells containing POP–sulfur composite are presented in Figure V-303. Figure V-303a shows the first charge and discharge voltage profiles for a POP-A/sulfur cell. The discharge capacity is  $927 \text{ mAh g}^{-1}$  at a current density of  $200 \text{ mA g}^{-1}$ , and the subsequent charge capacity is  $898 \text{ mAh g}^{-1}$ , corresponding to a high coulombic efficiency of 97%. As shown in Figure V-303b, the high coulombic efficiency for the POP-A/sulfur cell is maintained even after 100 cycles, suggesting the successful restraint of polysulfide dissolution and the redox shuttling effect. Such a high coulombic efficiency in the whole cycle range for a sulfur cathode is quite rare. Figure V-303c and Figure V-303d show Li–S cell testing data for POP-B/sulfur and POP-C/sulfur composites. It is notable that the charge and discharge voltage profiles of POP/sulfur composites showed different potential polarization, which might be caused by the different porous structure and the pore volume reduction after the sulfur infusion. As shown in Figure V-303d, both POP-B and POP-C composite cells can achieve high coulombic efficiency in the initial cycle, and the values

are close to 100% in the following cycles, indicating that the shuttle mechanism was completely suppressed in the POP-B and POP-C systems.

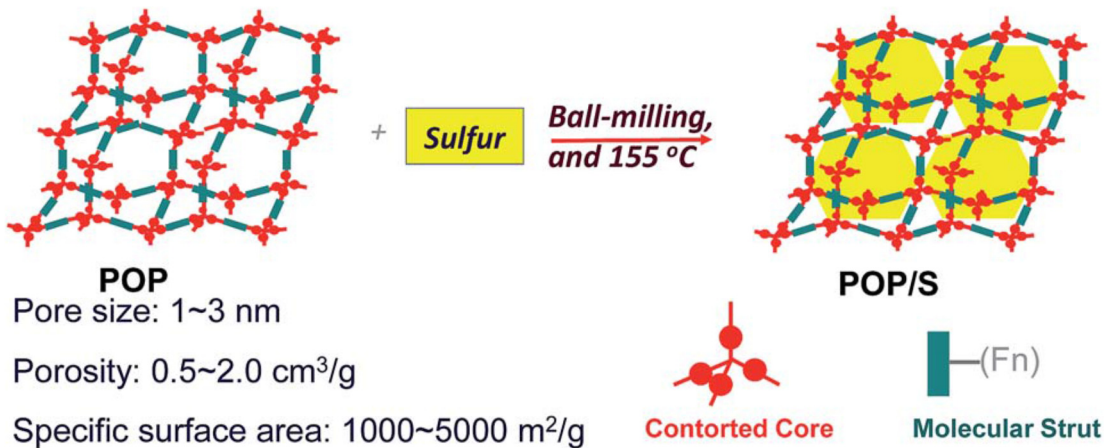


Figure V- 302: Preparation of POP–sulfur composites with micropores as host materials for accommodation of nanosized sulfur particles

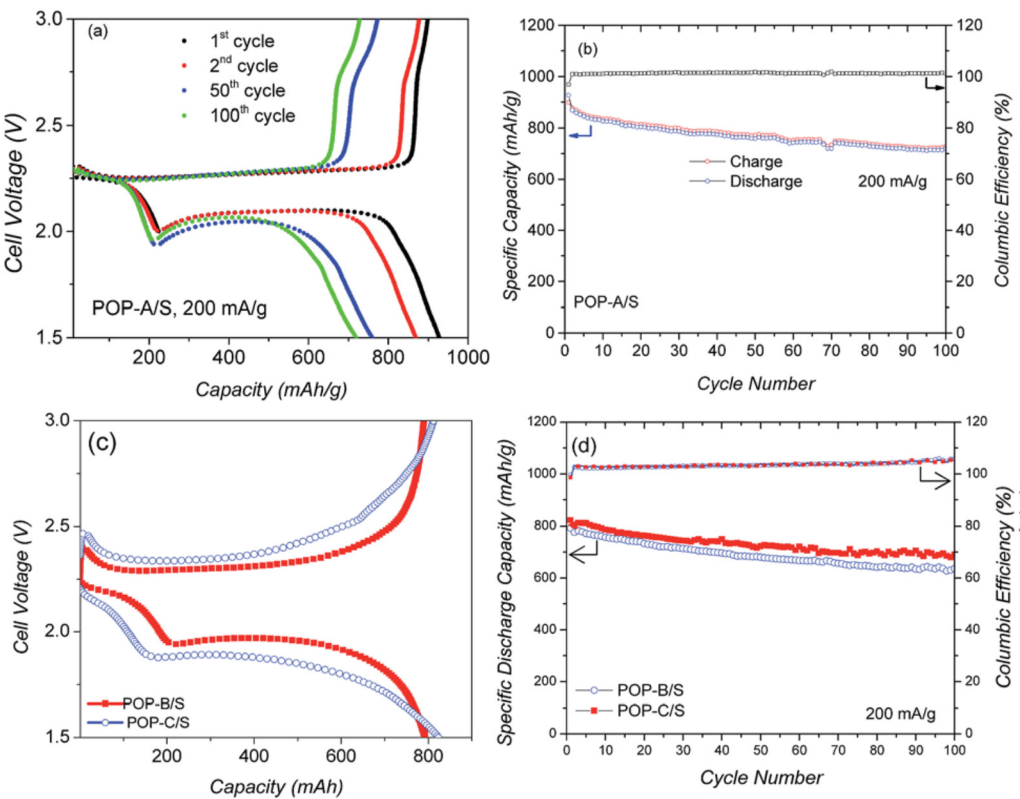


Figure V- 303: Performance of Li–S cells with POP–sulfur composite cathodes cycled between 1.5 and 3.0 V at a current density of 200 mA/g current. Voltage profiles (a) and capacity retention (b) of POP-A/S composite cell; 1st-cycle charge-discharge profiles of POP-B/S and POP-C/S composite cells (c), and cycling performance of POP-B/S and POP-C/S composite cells (d). (Electrolyte: 1 M LiTFSI in 1,3-dioxolane (DOL) and CHF<sub>2</sub>CF<sub>2</sub>CH<sub>2</sub>OCF<sub>2</sub>CF<sub>2</sub>H in a 1:2 volume ratio.)

### Phase stability of S-Se alloys

In order to study the phase stability of Se<sub>x</sub>S<sub>y</sub> against the chemical composition of the final compound, a series of samples was synthesized to establish the S-Se phase diagram. Table V- 10 shows the compositions of the samples synthesized. Raman spectroscopy (see Figure V- 304) clearly shows the signature of a new compound that was formed by mixing S and a proper amount of Se. X-ray diffraction data also showed that the new

compound had a different crystal structure from either S or Se (see Figure V- 305). Two samples of great interest are SeS and  $\text{Se}_2\text{S}_5$ . The former, SeS, was selected because it is amorphous as synthesized; the latter was picked because it has broad diffraction peaks, indicating nano-crystallinity. At the same time,  $\text{Se}_2\text{S}_5$  has more S than SeS, and hence  $\text{Se}_2\text{S}_5$  is expected to have a higher reversible capacity than SeS. Therefore,  $\text{Se}_2\text{S}_5$  was selected for detailed study, and investigation on SeS will be carried out for the coming quarter.

Figure V- 306 shows the evolution of XANES spectra of  $\text{Se}_2\text{S}_5$  material during the charge/discharge process. The absorbance of the material was color-coded in the contour plot shown in Figure V- 306; a red pixel means a high absorbance at the specific time and X-ray energy, while a blue pixel means a low absorbance. The peak at 12655 eV indicates the absorbance of Se while the peak at 12720 eV is the absorbance of  $\text{Li}_2\text{Se}$ . Figure V- 306 indicates that Se was fully converted into  $\text{Li}_2\text{Se}$  during the initial discharge, but only part of the  $\text{Li}_2\text{Se}$  was reversed back to Se during the following charge. It is believed that trapped  $\text{Li}_2\text{Se}$  after the initial discharge is the primary contributor to the initial drop of reversible capacity of a cell using  $\text{Se}_2\text{S}_5$  cathode (see Figure V- 307). Therefore, it is believed that the reversible capacity can be further improved by using an alternative impregnation process to enhance the utilization of  $\text{Li}_2\text{Se}$ .

**Table V- 10: Composition of SexSy prepared for this study**

	Sulfur weight ratio
Se	0
$\text{SSe}_5$	7.5%
$\text{S}_{1.9}\text{Se}_{5.1}$	13.1%
$\text{S}_3\text{Se}_5$	19.6%
SeS	28.8%
$\text{S}_5\text{Se}_4$	33.6%
$\text{S}_{4.98}\text{Se}_{3.02}$	40%
$\text{Se}_2\text{S}_5$	50.3%
$\text{Se}_2\text{S}_6$	54.8%
$\text{S}_4\text{Se}$	61.8%
$\text{S}_{27.64}\text{Se}_{4.36}$	72.0%
$\text{S}_{10}\text{Se}$	80.2%
$\text{S}_{22.2}\text{Se}$	90.2%
S	100.0%

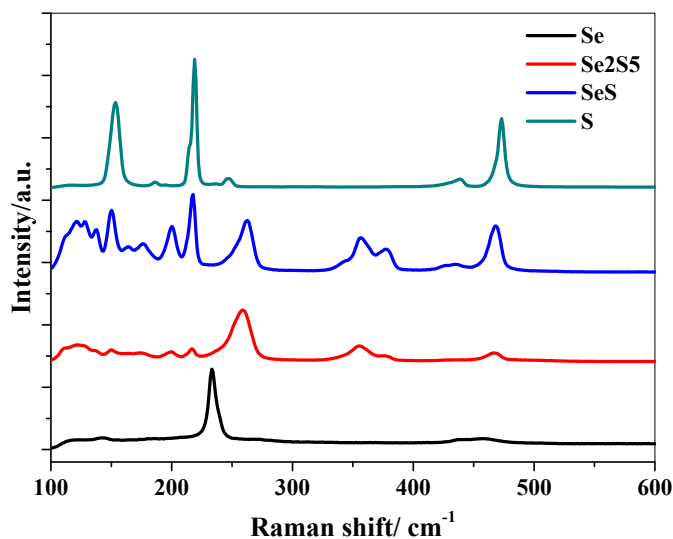


Figure V- 304: Raman spectra of typical  $\text{Se}_x\text{S}_y$  samples

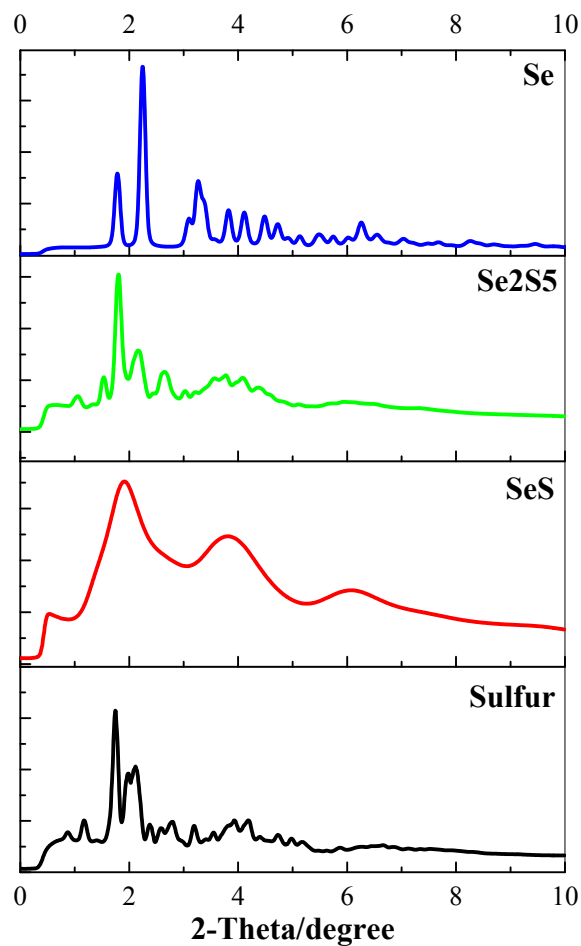
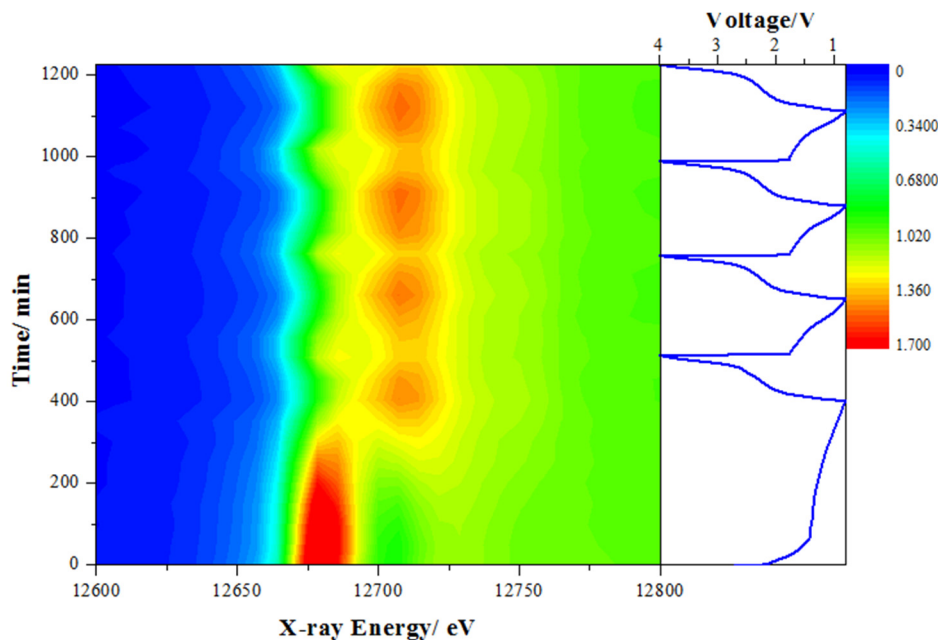
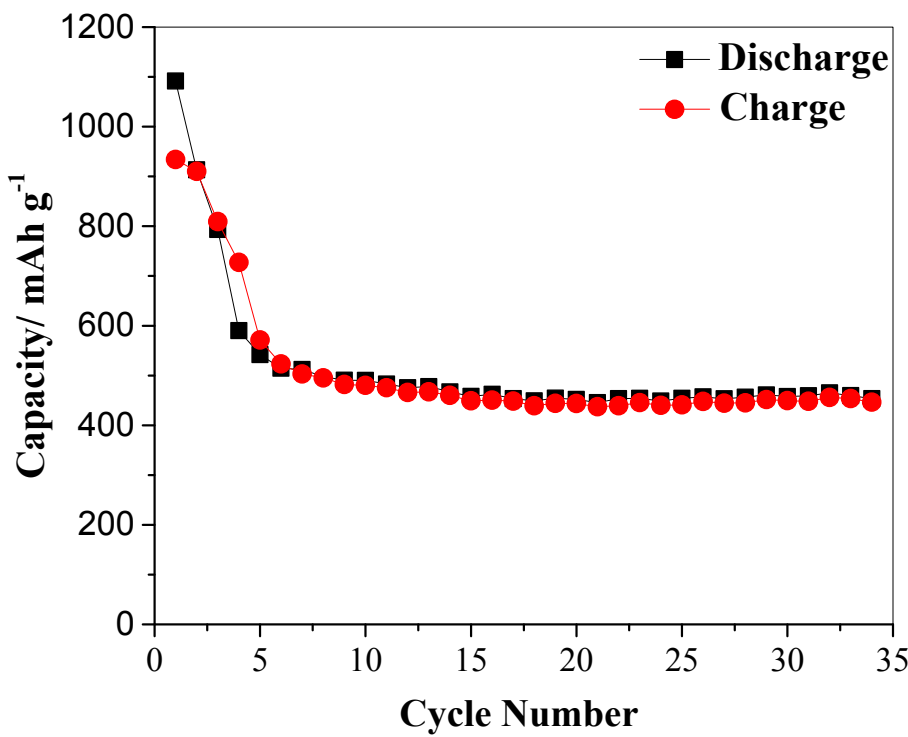


Figure V- 305: High-resolution X-ray diffraction of typical  $\text{Se}_x\text{S}_y$  samples

Figure V- 306: *In situ* XANES of Li/Se<sub>2</sub>S<sub>5</sub> battery using a carbonate-based electrolyteFigure V- 307: Capacity retention of Li/Se<sub>2</sub>S<sub>5</sub> cell using a carbonate-based electrolyte

### Encapsulating Se<sub>2</sub>S<sub>5</sub> in carbon matrix

Our *in situ* X-ray absorption spectroscopy study reported in the previous quarter also showed a low utilization of Se when a carbonate-based electrolyte was used. Here, we tried to improve the utilization of Se<sub>2</sub>S<sub>5</sub> by encapsulating the active material in a nanoporous carbon matrix. Figure V- 308 shows scanning electron

microscopy images of the carbon materials investigated. Conventionally, Ketjenblack is widely used as the conducting agent for electrodes used in lithium-ion batteries, and it was investigated here as a control experiment. Figure V- 308a shows that Ketjenblack is composed of nano-spheres with a diameter of about 50 nm, and that macropores are formed through the agglomeration of nano-balls. To further improve the electric conductivity of the electrode, multiwall carbon nanotubes were added as a complementary conductive agent for Ketjenblack. The active material was prepared by ball-milling a mixture of sulfur (25 wt%), selenium (25 wt%), Ketjenblack carbon black (45 wt%), and carbon nanotube (5 wt%) in an argon environment. Thermogravimetric analysis (TGA) confirmed the proper loading of  $\text{Se}_2\text{S}_5$  active material in the carbon matrix (see Figure V- 309). Electrochemical testing showed that the composite material can deliver a stable capacity of about 400 mAh/g, which is substantially lower than its theoretical capacity (1389 mAh/g). Alternatively, we tried to encapsulate the active material in nanochannels of ordered microporous carbon (OMC) (see Figure V- 308c). For a fair comparison, 50 wt% of  $\text{Se}_2\text{S}_5$  was loaded into OMC. However, no significant improvement on the electrochemical performance was observed for the  $\text{Se}_2\text{S}_5$ /OMC composite.

It is also possible that the low reversible capacity can originate from poor compatibility between the active material and the electrolyte. Our preliminary results shows that the reversible capacity can be improved up to 600 mAh/g by simply replacing the carbonate-based electrolyte with an ether-based one (see Figure V- 310).

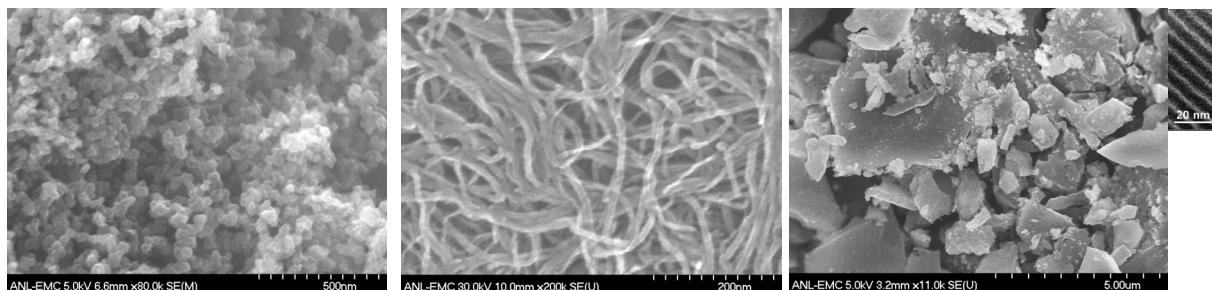


**Figure V- 308:** Scanning electron microscopy images of (a) Ketjenblack carbon black, (b) multiwall carbon nanotube (CNT), and (c) ordered microporous carbon (OMC). The inset in (c) is a transmission electron microscopy image showing micron channels (about 5 nm in diameter) in OMC to host  $\text{Se}_2\text{S}_5$

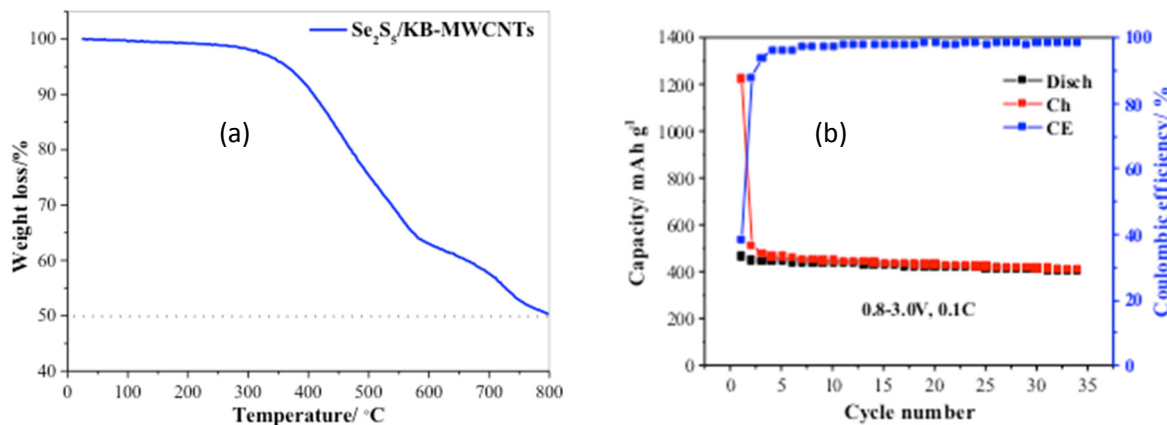


**Figure V- 309:** (a) Weight loss of a  $\text{Se}_2\text{S}_5$ /Ketjenblack-CNT composite during TGA analysis, confirming the proper loading of the active material in carbon matrix, and (b) charge/discharge capacity of cell using the prepared electrode and a carbonate-based electrolyte

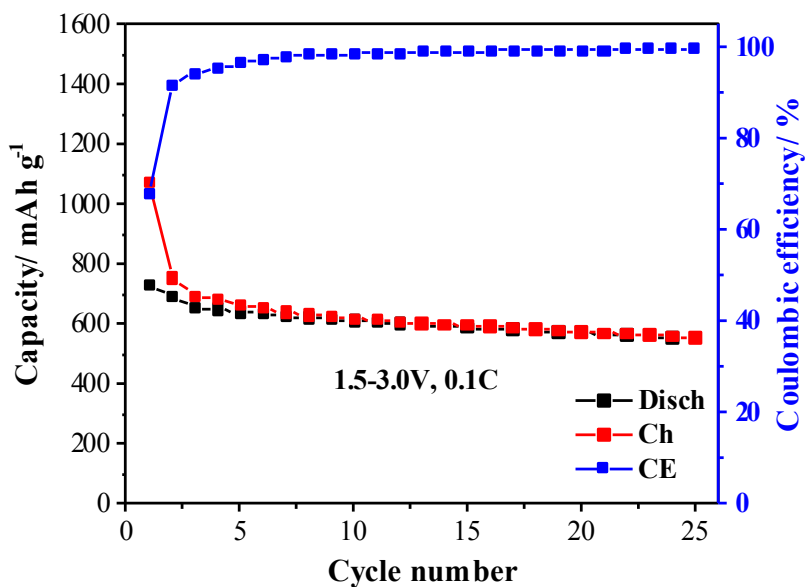


Figure V- 310: Charge/discharge capacity of cell with  $\text{Se}_2\text{S}_5$ /Ketjenblack-CNT electrode. The electrolyte was 1.0 M lithium bis-(trifluoromethanesulfonyl)imide (LiTFSI) in 1,3-dioxolane/1,1,2,2-tetrafluoroethyl-2,2,3,3-tetrafluoropropyl ether (1:1 by volume) with 0.1 M  $\text{LiNO}_3$

#### FY 2015 Publications/Presentations

1. Improved cyclability of a lithium–sulfur battery using POP–sulfur composite materials, Wei Weng, Shengwen Yuan, Nasim Azimi, Zhang Jiang, Yuzi Liu, Yang Ren, Ali Abouimrane and Zhengcheng Zhang, *RSC Adv.*, **2014**, 4, 27518.

## V.I.4 Multi-Functional Cathode Additives (BNL)

### Objectives

- Develop a low cost battery technology for PEV application utilizing Li-S electrochemical system by incorporating conductive transition metal sulfides as multifunctional cathode additives (MFCA) to improve the power performance, consistent with the long-term goals of DOE EV Everywhere Blueprint.

### Technical Barriers

- In order for EVs to achieve mass adoption and make a significant dent in U.S and global CO<sub>2</sub> production, the key problems of driving range per charge & cost per kWh must be addressed.  
Barriers addressed:
  - Performance: Low Wh/kg & Wh/L, Low W/kg & W/L
  - Life: Poor cycle with fast capacity fade.
  - Cost: High \$/kWh.

### Technical Targets

- Benchmark Sulfur electrode: achieve > 50% of theoretical capacity upon activation.
- MFCA coin cells: > 50% of theoretical capacity upon activation.
- Sulfur-MFCA hybrid electrode: > 60% theoretical sulfur utilization upon activation.

### Accomplishments

- Achieved 57% utilization of Li<sub>2</sub>S electrode in the presence of LiI electrolyte additive.
- Established sulfur cathode baseline by achieving more than 50% cathode utilization.
- Evaluated the sulfur loading effect on the sulfur cell activation and sulfur utilization.
- Determined the cycling voltage range of CuS coin cells for good cycle life to be 3.0V to 1.8V.
- Completed FeS<sub>2</sub> coin cell evaluation with activation condition and cycle performance determined.
- Demonstrated good TiS<sub>2</sub> coin cell cycling behavior between 3.0V to 1.5V with initial capacity of 276 mAh g<sup>-1</sup> achieved.
- Completed the proof of concept study demonstrating the discharge power improvement of sulfur electrode in the presence of the metal sulfide cathode additives, including CuS, FeS<sub>2</sub>, TiS<sub>2</sub>, and CoS<sub>2</sub>.
- Observed strong chemical and electrochemical interaction between CuS (or Cu<sub>2</sub>S) and sulfur electrode, resulting in fast coin cell capacity fade. Detailed reaction mechanism study point out S<sub>3</sub> as the reactive intermediate that facilitate the dissolution of copper ion leading fast capacity fade.
- Observed electrochemical interaction between FeS<sub>2</sub> and sulfur with experimental limitation identified.
- Reduced coin cell cycling capacity fade rate with hybrid TiS<sub>2</sub>:S electrode achieved comparing with the sulfur electrode control cell.
- Synthesis of the selected FeS<sub>2</sub> and TiS<sub>2</sub> materials with small particle size have been accomplished.

### Introduction

The Li-S battery system has gained significant interest due to its low material cost potential (35% cathode cost reduction over Li-ion) and its attractive 2.8x (volumetric) to 6.4x (gravimetric) higher theoretical energy density compared to conventional Li-ion benchmark systems. Commercialization of this technology requires to overcome several technical challenges. This effort will focus on improving the cathode energy density, power

### Project Details

**John Tabacchi (NETL Program Manager)**  
DE-SC0012704 Recipient: BNL

**Hong Gan (BNL – PI)**  
P.O. Box 5000  
Upton, NY 11973-5000  
Phone: 631-344-4012  
E-mail: [hgan@bnl.gov](mailto:hgan@bnl.gov)

**Esther Takeuchi (SBU – Co-PI)**  
Stony Brook University  
Phone: 631-216-7414  
E-mail: [esther.takeuchi@stonybrook.edu](mailto:esther.takeuchi@stonybrook.edu)

Start Date: October 2014  
Projected End Date: September 2017

capability and cycling stability by introducing conductive transition metal sulfides as multifunctional cathode additives (MFCA). The primary deliverable of this project during this year is to identify and characterize the best MFCA for Li-S cell technology development.

## Approach

**Innovative Approach:** Transition metal sulfides are evaluated as cathode additives in sulfur cathode due to their high electronic conductivity and chemical compatibility to the sulfur cell system. Electrochemically active additives are also selected for this investigation to further improve the energy density of the sulfur cell system. To facilitate the hybrid electrode and interaction studies, in the first year, the team has evaluated the transition metal sulfide cathode cells and sulfur cathode cells individually to establish the baseline. Then we investigated the interaction between transition metal sulfide additives and the sulfur electrode in the hybrid system. The mechanism associated with MFCA and sulfur interaction at the component and the cell levels is elucidated to aid the further optimization of the electrode and the cell system. In parallel, commercially unavailable selected additives are synthesized for additional electrochemical cell interaction and optimization studies in the following year. The 1<sup>st</sup> year milestones are listed below:

- 1) Baseline Li/S cell demonstration with Sulfur and/or Li<sub>2</sub>S cathode.
- 2) Baseline Li/MFCA cell demonstration with selected transition metal sulfides.
- 3) Li/Sulfur-MFCA concept cell demonstration for cathode-MFCA interaction.
- 4) Preparation and characterization of selected non-commercial MFCA.

## Results

### 1) Baseline Li/S Cell Demonstration with Sulfur and Li<sub>2</sub>S Cathode

To maintain low material and process cost, all the electrodes in this study were prepared by using the commercially available Li<sub>2</sub>S, sulfur, carbon black, and PVDF raw materials with the conventional slurry casting process.

#### A. Li<sub>2</sub>S baseline cells

We have successfully developed baseline Li<sub>2</sub>S and sulfur coin cells and achieved the sulfur utilization of more than 50%. Li<sub>2</sub>S has theoretical capacity of 1166 mAh·g<sup>-1</sup>. The Li<sub>2</sub>S electrode cannot be activated at the charging rate higher than C/40, and it cannot be activated without the presence of electrolyte additives (Figure V- 311). The presence of LiI additive is critical to activate Li<sub>2</sub>S electrode with 50-57% of the theoretical capacity delivered in the subsequent discharge [1]. After activation, the cells can be cycled under C/10 rate with progressive capacity fade over cycles, reaching 200 mAh·g<sup>-1</sup> capacity after 20 cycles (Figure V- 312).

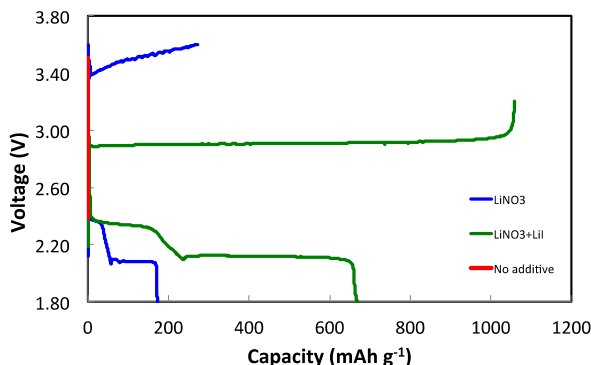


Figure V- 311: Additive effect on Li<sub>2</sub>S cell activation

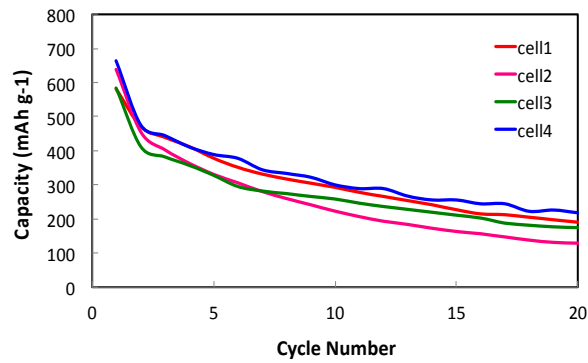


Figure V- 312: Li<sub>2</sub>S cells cycling at C/10 after C/40 activation with LiI additive

## B. Sulfur baseline cells

The theoretical capacity of sulfur electrode is  $1674 \text{ mAh}\cdot\text{g}^{-1}$ . We found that the initial discharge capacity or sulfur utilization of coin cells is highly dependent on the cell discharge rate and sulfur electrode loading. [2] Under low discharge rates (C/10, C/5, and C/2), the cells displayed typical voltage profile with two voltage plateaus at  $\sim 2.4 \text{ V}$  and  $\sim 2.1 \text{ V}$ . However, the voltage profile showed no observable 2.1 V voltage plateau at 1C rate (See Figure V- 313). Nevertheless, sulfur utilization of  $\sim 52\%$  and  $\sim 49\%$  were achieved at C/10 and C/5 respectively. The sulfur cathode loading effect was also investigated under C/5 discharge rate. For cells with sulfur loading equivalent to  $1.2 \text{ mg}\cdot\text{cm}^{-2}$  ( $2.0 \text{ mAh}\cdot\text{cm}^{-2}$ ) or lower, the cells delivered around 50% sulfur theoretical capacity. When the sulfur loading approaches  $2.0 \text{ mg}\cdot\text{cm}^{-2}$  ( $3.0 \text{ mAh cm}^{-2}$ ) or higher, cell voltage exhibited significant polarization and the 2.1 V voltage plateau diminishes (Figure V- 314), resulting in low initial sulfur utilization. The improved sulfur utilization can be achieved for the high sulfur-loading electrode by activating the cells at a slower C-rate, such as C/20. The cycling performance of sulfur electrode with various loading at C/5 rate cycling is shown in Figure V- 315. The cells still deliver  $400 \text{ mAh}\cdot\text{g}^{-1}$  after 50 cycles.

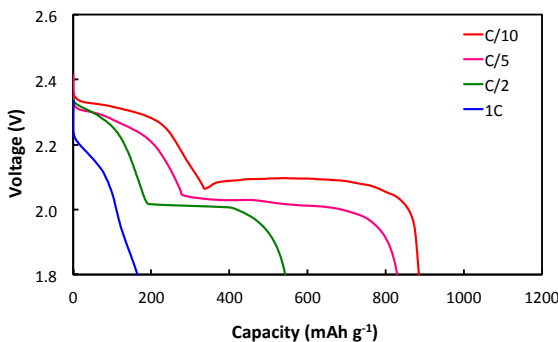


Figure V- 313: S-cell discharge rate capability

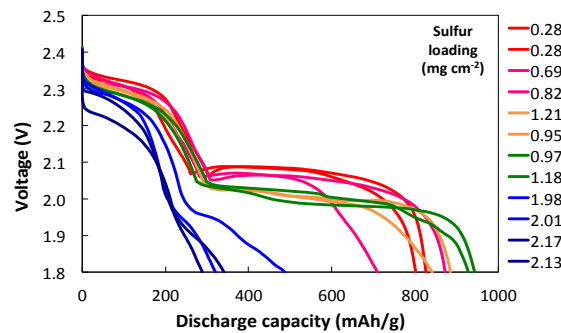


Figure V- 314: Sulfur loading effect on 1<sup>st</sup> discharge

## 2) Baseline Li/MFCA Cell Demonstration with Selected Transition Metal Sulfides

### A. Copper sulfide (CuS)

Covellite CuS has a hexagonal structure at room temperature which can be described as a stacking of CuS and Cu<sub>2</sub>S<sub>2</sub> double layers along the *c*-axis direction (Figure V- 316) [3] (Space group *P6<sub>3</sub>/mmc*, *a* =  $3.79 \text{ \AA}$ , *c* =  $16.34 \text{ \AA}$ ).[4] The weak Van der Waals between the S-S layers allows reaction with Li<sup>+</sup>, yielding a high theoretical capacity of  $560 \text{ mAh}\cdot\text{g}^{-1}$ .[5]

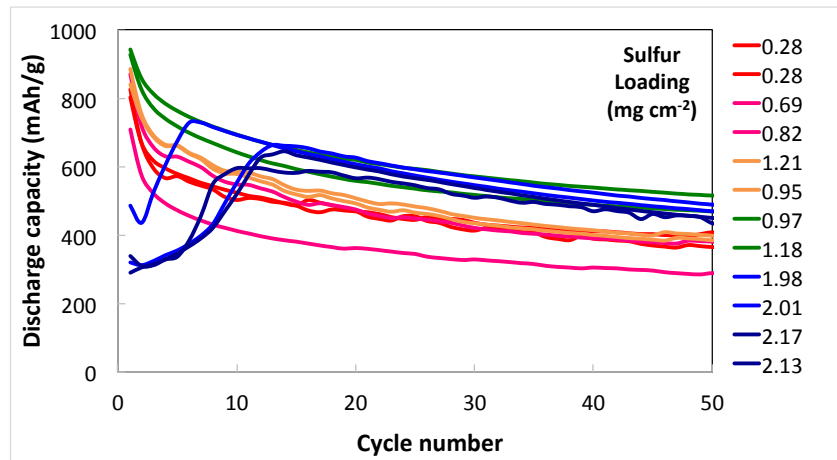


Figure V- 315: Sulfur loading effect on coin cell cycling

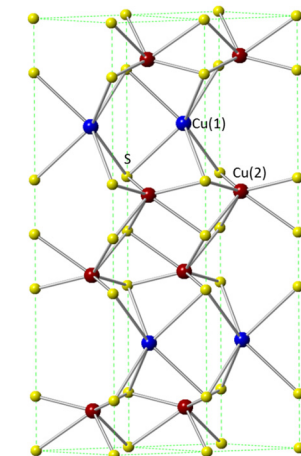


Figure V- 316: CuS structure

CuS cathodes were cycled at C/10 rate in two different voltage ranges: 3.0-1.8 and 3.0-1.0 V vs. Li. Figure V-317(a) and Figure V-317(b) show the discharge profiles of cycle 1, cycle 10 and cycle 50 in the two voltage ranges (cycle 50 is not shown in Figure V-317(b)). In the range of 3.0-1.8 V, there was 245 mAh·g<sup>-1</sup> delivered on cycle 1 with 191 mAh·g<sup>-1</sup> remaining on cycle 20 and 109 mAh·g<sup>-1</sup> remaining on cycle 50. In comparison, in the range of 3.0-1.0 V, there was 434 mAh·g<sup>-1</sup> delivered capacity on cycle 1. However, the capacity degraded rapidly and there was only 7 mAh·g<sup>-1</sup> delivered on cycle 20. The voltage profiles agree well with the previous reports on the cycling behavior of CuS.[6,7] It is shown that the discharge reactions take place at 2.1 and 1.7 V. First plateau corresponds to the lithium insertion into CuS with the formation of  $\text{Li}_x\text{CuS}$ , while the second plateau is related to the irreversible formation of metallic Cu, which is a major source of capacity degradation.[6] Other factors such as volume change during cycling, electrolyte composition and loss of active material due to the solubility of sulfide species also account for the capacity degradation.[8] Figure V-317(c) displays the capacity versus cycle number of CuS cycled at C/10 in the two voltage ranges. It is clear that the cell cycling in the range of 3.0-1.8 V has less capacity loss over 50 cycles. A rate capability was performed on CuS cells, and Figure V-317(d) shows the capacity versus cycle number at 1C, 2C, 5C and 10C. The cell delivered 190, 143 and 97 mAh·g<sup>-1</sup> capacity on the first discharge of 1C, 2C and 5C, respectively. When the cell was cycled at high rate of 10C, the capacity delivered was only 7 mAh·g<sup>-1</sup>.

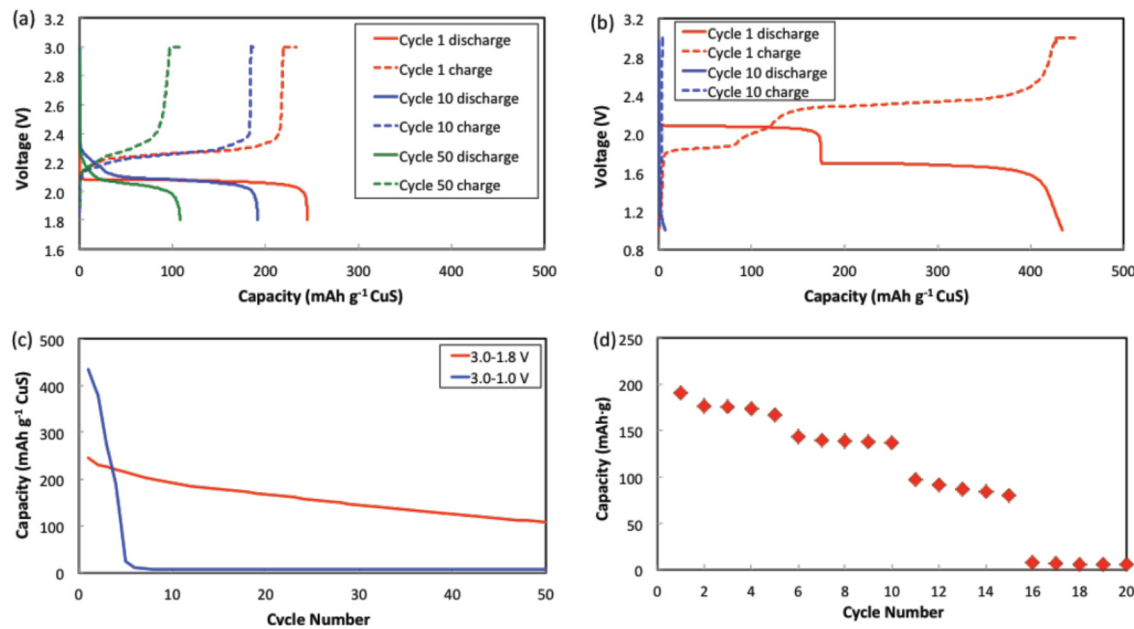


Figure V-317: (a) Voltage profile of CuS cycling between 3.0-1.8 V; (b) Voltage profile of CuS cycling between 3.0-1.0 V; (c) Capacity versus cycle number; (d) Capacity versus cycle number at different rates.

## B. Iron disulfide ( $\text{FeS}_2$ )

Iron(II) disulfide,  $\text{FeS}_2$  can exist in two phases at room temperature: pyrite and marcasite. Pyrite is a NaCl-type structure belonging to the  $\text{Pa}3$  space group where  $\text{Fe}^{2+}$  ions are positioned in a face-centered cubic arrangement and  $\text{S}_2^{2-}$  bonds are located at both the center of the edges and the center of the unit cell, as shown in Figure V-318.[9] Marcasite is similar to pyrite, but has an orthorhombic structure and belongs to space group  $\text{Pmnn}$ , see Figure V-318. [9]

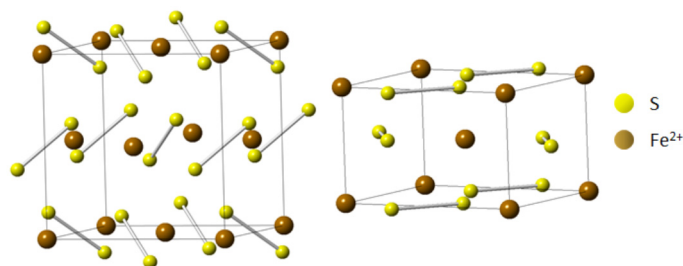


Figure V-318: Structures of pyrite (L), and marcasite (R)

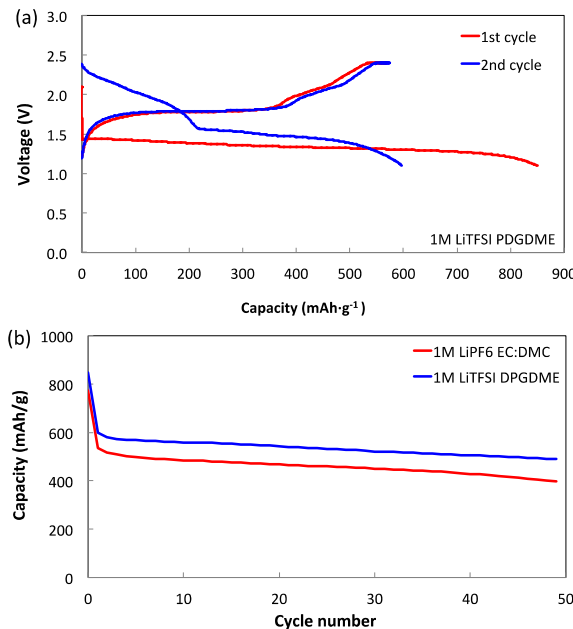


Figure V- 319: Li/FeS<sub>2</sub> cells cycled between 2.5-1.1 V at C/10 (a) voltage profile; (b) Cycling capacity.

profile are observed at about 2 and 1.5 V for both electrolytes, consistent with the literature.[10-12] Further cycling shows the system is reversible and little capacity is lost after the first cycle.

### C. Titanium disulfide (TiS<sub>2</sub>)

TiS<sub>2</sub> has a hexagonal close-packed sulfur lattice with Ti ions in octahedral sites between alternating sulfur sheets ( $P3\bar{1}m1$ ), as shown in Figure V- 320. The TiS<sub>2</sub> sheets are stacked directly on top of one another, giving the S anion stacking sequence of ABAB. The theoretical capacity of Li intercalation is 239 mAh·g<sup>-1</sup> giving a composition of LiTiS<sub>2</sub>.[13] Figure V- 321 shows the electrochemical performance of Li/TiS<sub>2</sub> cells cycled between 3.0 - 1.5 V at a C/10 rate. The specific discharge capacity on cycle 1 was 276 mAh·g<sup>-1</sup> with 266 mAh·g<sup>-1</sup> maintained after 10 cycles.

### D. Cobalt disulfide (CoS<sub>2</sub>)

CoS<sub>2</sub> crystallizes in cubic pyrite structure with lattice constant of  $a= 5.5 \text{ \AA}$  with each Co octahedrally coordinated with 6S atoms, Figure V- 322. CoS<sub>2</sub> has a high theoretical lithium storage capacity of 870 mAh·g<sup>-1</sup>[14]

Li/FeS<sub>2</sub> coin cells were prepared with two different electrolytes: 1M LiPF<sub>6</sub> in EC:DMC (1:1) and 1M LiTFSI in dipropylene glycol dimethyl ether (DPGDME). The coin cells were cycled for 50 cycles between 2.4 and 1.1 V at a C/20 rate. During the first discharge, the capacities achieved for the carbonate and glyme electrolyte systems were 773 and 849 mAh/g, respectively, with higher cycling capacities achieved using glyme electrolyte than with carbonate electrolyte (Figure V- 319a and Figure V- 319b). The voltage profile of the initial discharge and later cycle discharge is very different (Figure V- 319a), indicating that FeS<sub>2</sub> activation is required at low discharge voltage.

Currently, the accepted reaction mechanism for the first discharge process for Li/FeS<sub>2</sub> is described as follows: upon charging, Li<sub>2-x</sub>FeS<sub>2</sub> forms at 2.4 V and a non – stoichiometric pyrrhotite phase, FeS<sub>x</sub> forms when the voltage exceeds 2.45 V.[10] The plateau observed at 1.8 V is in agreement with the literature.[10, 11] Plateaus in the second discharge

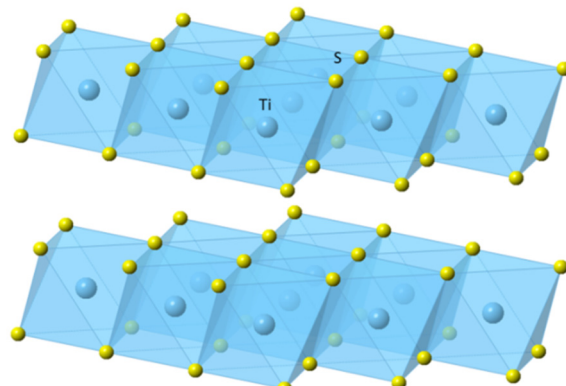


Figure V- 320: TiS<sub>2</sub> structure

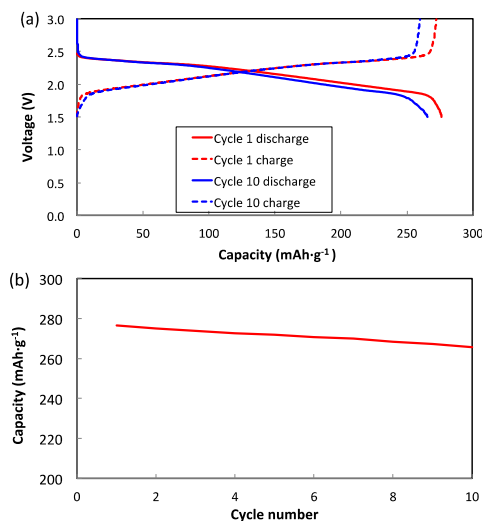


Figure V- 321: Li/TiS<sub>2</sub> cells cycled between 3.0-1.5 V at C/10  
(a) Voltage profile; (b) Capacity versus cycle number.

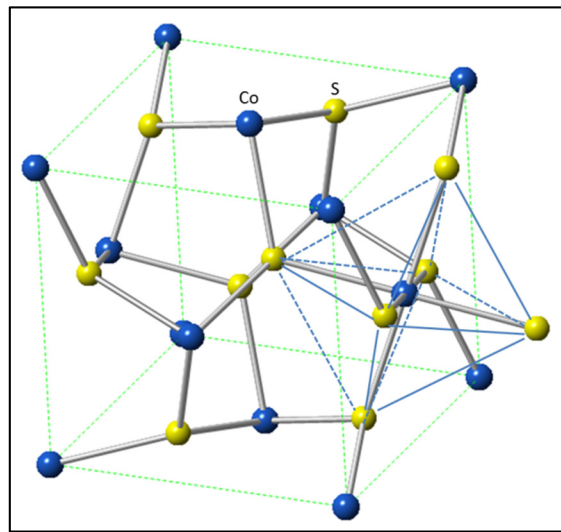


Figure V- 322: CoS<sub>2</sub> structure

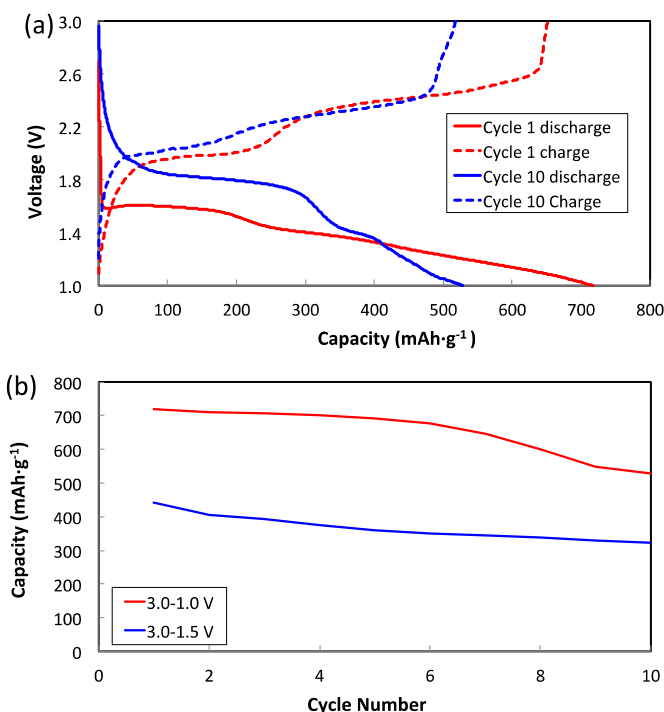


Figure V- 323: Li/CoS<sub>2</sub> cells (a) Voltage profile cycled 3.0-1.0 V at C/30; (b) Capacity versus cycle number.

Figure V- 323(a) shows the voltage profiles of CoS<sub>2</sub> cycled in the voltage range of 3.0 - 1.0 V at a C/30 rate. The first discharge curves was different from subsequent, with a long plateau at ~1.6 V, consistent with previous reports.[15, 16] Initial discharge capacity of 730  $\text{mAh}\cdot\text{g}^{-1}$  was achieved. In comparison, in the voltage range of 3.0 - 1.5 V, the initial discharge capacity reached 440  $\text{mAh}\cdot\text{g}^{-1}$ , but with ~100  $\text{mAh}\cdot\text{g}^{-1}$  capacity loss after 10 cycles, Figure V- 323(b). Thus in the range of 3.0 - 1.5 V, the cell displays less delivered capacity but better cycle stability.

### 3) Li/Sulfur-MFCA Concept Cell Demonstration

We have successfully demonstrated the interaction between multiple transition metal sulfide and the sulfur. Both chemically and electrochemically based interactions were identified. Part of the interaction mechanism has been investigated.

### A. Proof of concept study

Coin cells using hybrid electrodes with formulation according to Table V- 11 were prepared and tested under 1C discharge rate (Figure V- 324). The control cells exhibited severe voltage polarization without the observable 2.1V voltage plateau, resulting in less than 24% sulfur utilization.

Except for CoS<sub>2</sub>, cells with CuS, FeS<sub>2</sub> and TiS<sub>2</sub> presented

the typical sulfur electrode discharge voltage profiles with two clearly distinguishable voltage plateaus, leading to significantly improved sulfur utilization (Table V- 11). Since CuS in the hybrid electrode only contributes 5.3% of the total cell theoretical capacity, the improved sulfur utilization is mainly contributed by the CuS induced power enhancement at high rate discharge. FeS<sub>2</sub> and TiS<sub>2</sub> are expected to follow the same mechanism.

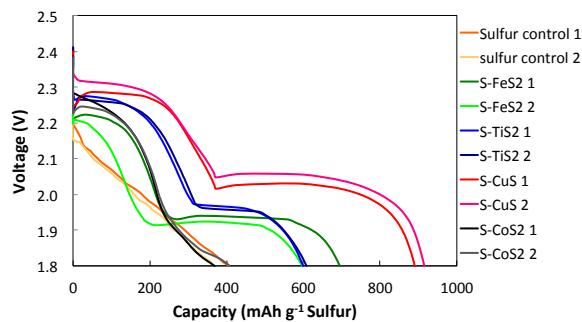


Figure V- 324: Sulfur:MFCA hybrid electrode C-rate discharge

(Figure V- 326), which contributes to the rapid reduction of polysulfide into Li<sub>2</sub>S on anode, leading to fast capacity fade. Although CuS-S system does not cycle well due to this dissolution mechanism, the results point to the importance of good anode SEI.

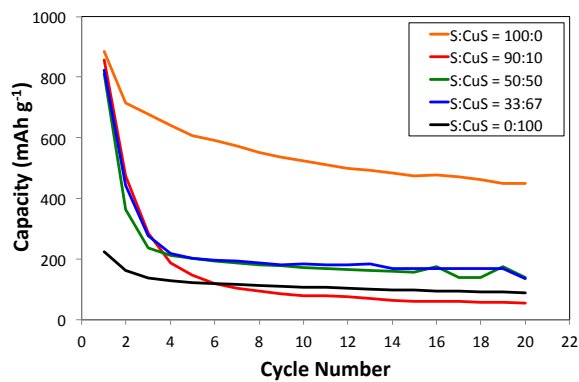


Figure V- 325: S:CuS hybrid electrode cycling

Table V- 11: Hybrid Electrode Formulation for Power Test

MFCA	Sulfur %	MFCA %	Carbon %	PVDF %	S Utilization (1C)
None	45	0	45	10	24%
CuS	45	15	30	10	54%
FeS <sub>2</sub>	50	17	25	8	39%
TiS <sub>2</sub>	50	17	25	8	36%
CoS <sub>2</sub>	50	17	25	8	24%

### B. Interaction of sulfur and copper sulfide

The beneficial effect of sulfur electrode activation by CuS under 1C rate does not maintain at C/10 rate discharge. Although the delivered capacity during the 1<sup>st</sup> discharge is still adequate, the presence of CuS in sulfur electrode at various ratio resulted in severe capacity fade as indicated in Figure V- 325. Mechanistic investigation uncovered the copper dissolution catalyzed by S<sub>3</sub> intermediates as the root cause for this fast capacity fade. The soluble copper species deposit on the anode surface as Cu<sub>2</sub>S to form a more porous and conductive SEI layer

The interaction of sulfur with Cu<sub>2</sub>S was also investigated. Cu<sub>2</sub>S and sulfur interact chemically to form nano-flake shaped crystalline CuS (SEM in Figure V- 327) during electrode preparation. With excess mole % of Cu<sub>2</sub>S vs. sulfur in hybrid cathode, up to 100% sulfur utilization for the 1<sup>st</sup> discharge under C/10 and C/20 rates was observed (Figure V- 327 and Figure V- 328), indicating the complete conversion of sulfur into CuS. For hybrid cathode with S:Cu<sub>2</sub>S > 1:1, dissolution of copper ions in the electrolyte was found to be detrimental to the cell capacity retention – consistent with the copper dissolution mechanism.

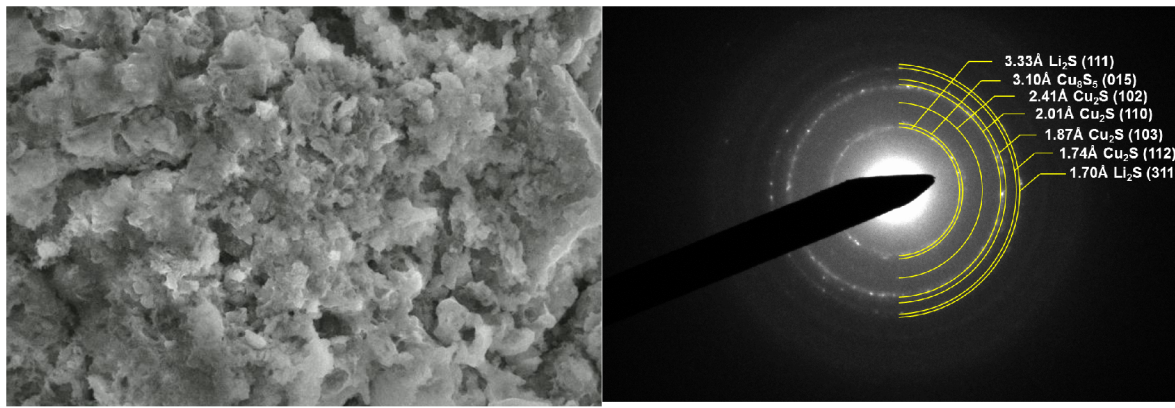
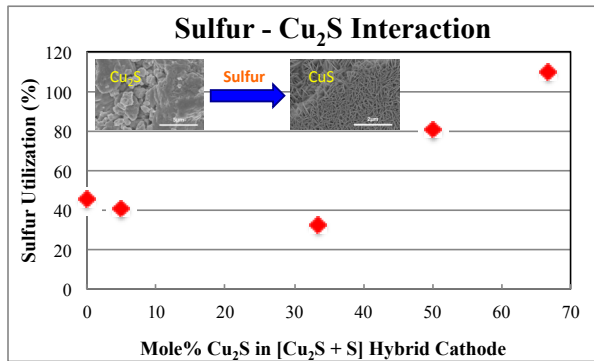
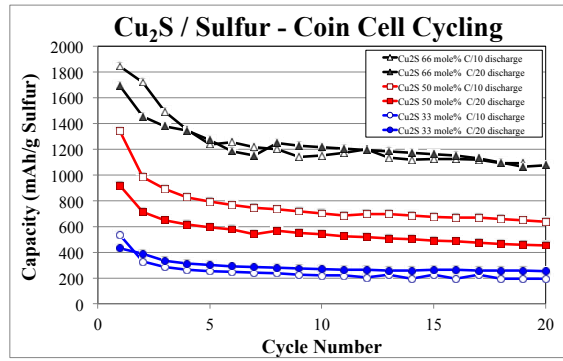
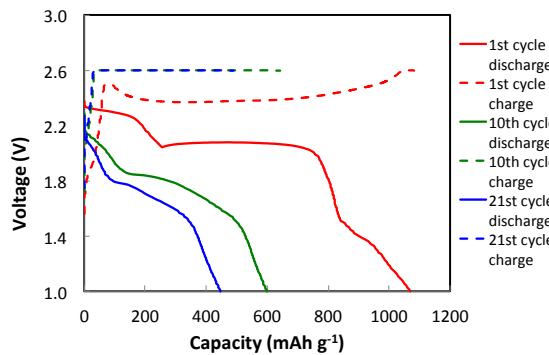
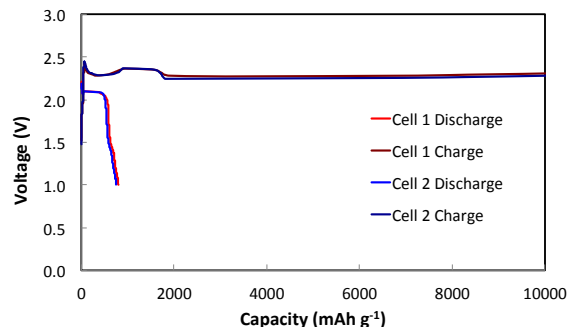


Figure V- 326: S:CuS hybrid cell anode SEI morphology and chemical composition

Figure V- 327: S:Cu<sub>2</sub>S interactionFigure V- 328: S:Cu<sub>2</sub>S cell cycling

### C. Interaction of sulfur and iron sulfide

In order to activate FeS<sub>2</sub>, the hybrid electrode needs to be discharged to 1.0 V in the 1<sup>st</sup> discharge to induce the formation of cyclable new Li<sub>2-x</sub>FeS<sub>2</sub> phase (Figure V- 319a). We found that under such a low discharge voltage, the LiNO<sub>3</sub> electrolyte additive is reduced on cathode [17] causing internal cell impedance growth with fast charge voltage polarized to 2.6 V cut off in a few cycles (Figure V- 329), which is detrimental to the cell cycle life. However, by removing LiNO<sub>3</sub> from electrolyte the cell exhibited severe shuttling effect at the C/5 charge rate (Figure V- 330). Therefore, two contradiction factors prevent the FeS<sub>2</sub> utilization in the hybrid electrode. Alternative approach needs to be developed.

Figure V- 329: FeS<sub>2</sub> activation w/ LiNO<sub>3</sub>Figure V- 330: FeS<sub>2</sub> activation w/o LiNO<sub>3</sub>

Unlike the S:Cu<sub>2</sub>S system shown in Figure V- 327, XRD showed no material phase change by just physical mixing FeS and sulfur during electrode preparation. However, a new FeS<sub>2</sub> phase along with Fe was detected

by TEM electron diffraction (Figure V- 331) after just one cycle of S:FeS hybrid electrode. The nature of this phase transition is electrochemically induced, rather than chemically induced.

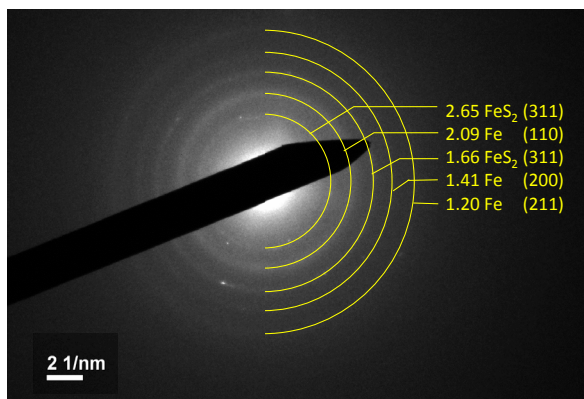


Figure V- 331: ED of cycled S:FeS electrode

discharge (Figure V- 332). In addition, the hybrid electrode exhibited lower capacity fade rate (Figure V- 333). Our results are in agreement with literature reports. [18, 19]

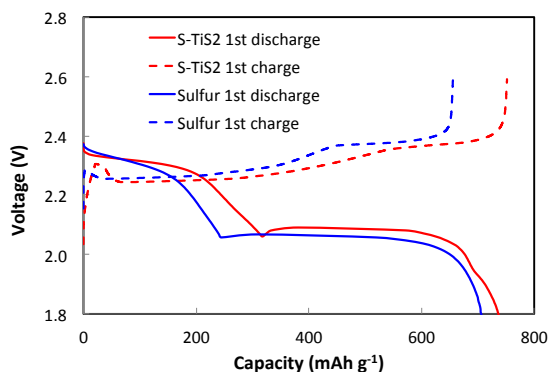


Figure V- 332: S:TiS₂ voltage profile

#### D. Interaction of sulfur and titanium sulfide

The effect of electrochemically active and chemically stable TiS<sub>2</sub> additive was also investigated in hybrid cathode with weight ratio S:TiS<sub>2</sub> = 3:1, in which TiS<sub>2</sub> contributing to 4.5% of the total cathode theoretically capacity. Both control and hybrid cathode coin cells were electrochemically cycled between 2.6 to 1.6 V under C/5 rate. Similar capacities were delivered by control and hybrid electrode in the initial cycle based on the sulfur loading. The 1<sup>st</sup> cycle voltage profile clearly showed an voltage shoulder near the end of discharge for the hybrid electrode at around 1.9 V, indicating the participation of TiS<sub>2</sub> during cell

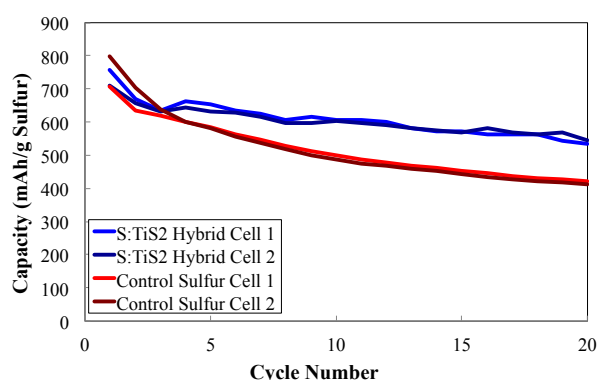


Figure V- 333: S:TiS₂ hybrid cell cycling

#### 4) Preparation and Characterization of Selected Non-Commercial MFCA

Based on the above proof of concept study, FeS<sub>2</sub> and TiS<sub>2</sub> are selected for follow up studies. Material synthesis and characterization are focused on these two metal sulfides.

##### A. Iron disulfide (FeS<sub>2</sub>)

Preparation of iron(II) disulfide, FeS<sub>2</sub> is under investigation using a hydrothermal route, using nanosized iron oxide, sodium thiosulfate, and sulfur as reagents in a tartaric acid – sodium tartrate buffer.[20] Iron(III) oxide (Fe<sub>2</sub>O<sub>3</sub>) and iron(II,III) oxide (Fe<sub>3</sub>O<sub>4</sub>) have been tested as reagents, with a focus on use of nanosized iron oxides as precursors. X-ray powder diffraction confirmed complete conversion of magnetite to iron(II) disulfide with no trace of iron oxide precursors, while transmission electron microscopy verified retention of parent oxide particle size and morphology in the sulfide product. Gram scale quantities were successfully prepared.

##### B. Lithium titanium disulfide (LiTiS<sub>2</sub>)

Lithiated-TiS<sub>2</sub> material was prepared by electrochemically lithiating TiS<sub>2</sub>. The product LiTiS<sub>2</sub> had a hexagonal structure (space group  $P\bar{3}m1$ ), similar to that of the TiS<sub>2</sub> parent material. Power XRD showed (001) peak shift to lower  $2\Theta$  after lithiation, indicating expansion of the interlayer distance upon lithiation. Gram scale quantities of LiTiS<sub>2</sub> were generated.

Synthesis of a Li<sub>2</sub>S-TiS<sub>2</sub> composite was also investigated based on an adaptation of a recently reported synthesis method.[21] Li<sub>2</sub>S powder was dispersed in anhydrous solvent then mixed with TiCl<sub>4</sub> to generate a TiS<sub>2</sub> coating on the Li<sub>2</sub>S core. The ratio of Li<sub>2</sub>S and TiCl<sub>4</sub> was varied to obtain the core-shell structure with

different thicknesses of TiS<sub>2</sub>. Post synthesis heating to crystallize the TiS<sub>2</sub> coatings was investigated. Milligram scale products were generated, and gram scale quantities of Li<sub>2</sub>S-TiS<sub>2</sub> composite are in preparation.

### Conclusions and Future Directions

A Li-S battery research program has been built up with baseline Li<sub>2</sub>S and sulfur coin cells established. Using commercially available raw material and conventional electrode preparation process, we have achieved and demonstrated more than 50% sulfur utilization during cell activation. LiI additive must present for acceptable Li<sub>2</sub>S electrode activation with up to 57% theoretical capacity delivered. For sulfur electrode cells, the discharge rate and electrode loading are identified as important factors that strongly impact the sulfur electrode activation/utilization and the the cell cycling performance. The conversion of electrolyte soluble polysulfide to the insoluble Li<sub>2</sub>S<sub>2</sub> and Li<sub>2</sub>S, is the key step to for high sulfur utilization. Factors promote this conversion and the subsequent discharge on the 2.1 V voltage plateau will be investigated for improved sulfur utilization.

Baseline transition metal sulfides coin cells investigation identified the cell testing condition for metal sulfide activation with the best predicted capacity retention. For CuS, cycling between 3.0V to 1.8V is recommended for hybrid cell study. Activation of FeS<sub>2</sub> and CoS<sub>2</sub> require the 1<sup>st</sup> discharge to voltage cut off below 1.5 V, followed by phase transition after the 1<sup>st</sup> charge. TiS<sub>2</sub> can be cycled between 2.6V to 1.8V without the need of special activation. These testing conditions are designed into the subsequent hybrid cell study.

During this year, we have completed the proof of concept study investigating the interaction between sulfur and several transition metal sulfides, CuS, FeS<sub>2</sub>, CoS<sub>2</sub> and TiS<sub>2</sub>. The high rate discharge of sulfur electrode is shown to be significantly improved by mixing these metal sulfide additives with sulfur electrode. Up to 50-125% delivered capacity improvement are demonstrated at 1C activation discharge rate for metal sulfide additive cells relative to the sulfur control cells – support the original proposal that the conductive metal sulfide may boost the discharge rate capability of the sulfur electrode.

We have discovered very complicated interaction between metal sulfide and sulfur, depending on the type of transition metal. Cu<sub>2</sub>S chemically reacts with sulfur to form CuS during the electrode preparation process. While FeS exhibits interaction with phase transformation only after being cycled electrochemically. Activation of FeS<sub>2</sub> in the hybrid electrode proves to be difficult due to the two contradicting factors that is the limiting factors required by the sulfur system. Alternative approach will be developed in the future FeS<sub>2</sub> hybrid electrode study. While the high ordered polysulfide prevents the dissolution of CuS, the low ordered S<sub>3</sub> polysulfide intermediate, which strongly interacts with CuS, is identified to be the root cause for copper dissolution, resulting in dramatic capacity fade for S:CuS hybrid electrode during the slow cell cycling. Mechanistic study indicates the strong influence of the anode SEI properties on the sulfur cell cycling capacity fade. TiS<sub>2</sub> is stable towards sulfur and is electrochemically active, contributing to the hybrid electrode cycling capacity. The major contribution of TiS<sub>2</sub> additive is the reduced cell cycling capacity fade rate. Optimization of hybrid electrode using TiS<sub>2</sub> with different particle size and morphology as well as different electrode/cell design will be followed.

Two metal sulfide additives have been selected for optimization study, FeS<sub>2</sub> and TiS<sub>2</sub>. Synthetic methodologies have been developed with gram scale nano-particle sized FeS<sub>2</sub> synthesized for characterization and follow up test. Gram scale electrochemically lithiated TiS<sub>2</sub> (Li<sub>x</sub>TiS<sub>2</sub>) was also obtained. Synthetic methodology development and preparation of gram scale quantities of Li<sub>2</sub>S-TiS<sub>2</sub> composite is underway. In the new fiscal year, we will initiate the MFCA additive and hybrid electrode optimization studies.

### References

1. Stefano Meini, Ran Elazari, Ariel Rosenman, Arnd Garsuch, and Doron Aurbach, *J. Phys. Lett.*, 5, 915-918 (2014).
2. Sung-Hwan Kang, Xiaohui Zhao, James Manual, Hyo-Jun Ahn, Ki-Wan Kim, Kwon-K Cho and Jou-Hyeon Ahn, *Phys. Status Solidi A* 211, No. 8, 1895-1899 (2014).
3. S. Conejeros, I. d. P. R. Moreira, P. Alemany and E. Canadell, *Inorganic Chemistry*, 53, 12402 (2014).
4. X. Rui, H. Tan and Q. Yan, *Nanoscale*, 6, 9889 (2014).
5. G.-Y. Chen, Z.-Y. Wei, B. Jin, X.-B. Zhong, H. Wang, W.-X. Zhang, J.-C. Liang and Q. Jiang, *Applied Surface Science*, 277, 268 (2013).

6. J. S. Chung and H. J. Sohn, *Journal of Power Sources*, 108, 226 (2002).
7. Y. Wang, X. Zhang, P. Chen, H. Liao and S. Cheng, *Electrochimica Acta*, 80, 264 (2012).
8. B. Jache, B. Mogwitz, F. Klein and P. Adelhelm, *Journal of Power Sources*, 247, 703 (2014).
9. D. Rickard and G. W. Luther, III, *Chem. Rev. (Washington, DC, U. S.)*, 107, 514 (2007).
10. R. Fong, J. R. Dahn and C. H. W. Jones, *J Electrochem Soc*, 136, 3206 (1989).
11. Y. Wang, X. Qian, W. Zhou, H. Liao and S. Cheng, *RSC Advances*, 4, 36597 (2014).
12. T. A. Yersak, H. A. Macpherson, S. C. Kim, V. D. Le, C. S. Kang, S. B. Son, Y. H. Kim, J. E. Trevey, K. H. Oh, C. Stoldt and S. H. Lee, *Advanced Energy Materials*, 3, 120 (2013).
13. M. S. Whittingham, *Chemical Reviews*, 104, 4271 (2004).
14. J.-C. Xing, Y.-L. Zhu, Q.-W. Zhou, X.-D. Zheng and Q.-J. Jiao, *Electrochimica Acta*, 136, 550 (2014).
15. Y. Wang, J. Wu, Y. Tang, X. Lü, C. Yang, M. Qin, F. Huang, X. Li and X. Zhang, *ACS Applied Materials & Interfaces*, 4, 4246 (2012).
16. Q. Wang, L. Jiao, Y. Han, H. Du, W. Peng, Q. Huan, D. Song, Y. Si, Y. Wang and H. Yuan, *The Journal of Physical Chemistry C*, 115, 8300 (2011).
17. Sheng S. Zhang, *J Elecrochem Soc*, 159, A920-A923 (2012).
18. Arnd Garsuch, Stefan Herzog, Lucas Montag, Andrea Krebs, and Klaus Leitner, *ECS Electrochemistry Letters*, 1 (1) A24-A26 (2012).
19. Yu-Sheng Su, Arumugam Manthiram, *Journal of Power Sources* 270 (2014) 101-105.
20. J. Xia, J. Jiao, B. Dai, W. Qiu, S. He, W. Qiu, P. Shen and L. Chen, *RSC Adv.*, 3, 6132 (2013).
21. Z. W. Seh, J. H. Yu, W. Li, P.-C. Hsu, H. Wang, Y. Sun, H. Yao, Q. Zhang and Y. Cui, *Nature Communications*, 5, 5017 (2014).

#### FY 2015 Publications/Presentations

1. Presentation to DOE ABMR review meeting (Jan. 22, 2015).
2. Ke Sun, Dong Su, Qing Zhang, David C. Bock, Amy C. Marschilok, Kenneth J. Takeuchi, Esther S. Takeuchi, and Hong Gan, "Interaction of CuS and Sulfur in Li-S battery system," *J. of Electrochem. Soc.* Accepted for publication.
3. Hong Gan, Patrick, J. Looney, "Multi Functional Cathode Additives for Battery Technologies", Filed USPTO, Feb. 2015.
4. Hong Gan, Ke Sun, "Hybrid Cathodes for Li-ion Battery Cells", Filed USPTO Provisional, April 2015.

## V.I.5 Development of High Energy Lithium Sulfur Batteries (PNNL)

### Objectives

- Develop high energy lithium-sulfur (Li-S) batteries.
- Investigate the fundamental reaction mechanism of polysulfides in thick sulfur electrodes.
- Perform advanced characterizations to advance the fundamental understanding in Li-S batteries.
- Technical Barriers
- High cost of materials and synthesis routes
- Limited energy density and cycling ability.

### Technical Targets

- Study the electrochemical behaviors of thick sulfur electrodes built at relevant scales.
- Investigate the chemistry/electrochemistry of polysulfides in Li-S batteries.
- Decouple lithium metal anode issue from Li-S batteries.

### Accomplishments

- Identified the key challenges in preparation and application of thick sulfur electrodes in Li-S batteries.
- Discovered sulfur radicals and their interactions with electrolytes during cycling.
- Developed new Li-ion sulfur batteries to decouple the lithium metal anode issue from the system to enable focused study on sulfur cathode.

---

### Introduction

As one of the most promising next-generation battery technologies, the Li-S battery system has recently been intensively investigated by groups around the world. Although the number of publications increased exponentially, many challenges still need to be addressed for the practical application of Li-S batteries for vehicle electrification. The poor cycling stability, low round-trip efficiency, and severe self-discharge of Li-S batteries are all rooted in the dissolution of long-chain polysulfide species. To overcome these hurdles, focused research on sulfur cathodes built at relevant scales is urgently needed.

### Approach

To ensure the knowledge gathered from the Li-S battery research is transferrable to industry, the following approaches have been adopted.

### Project Details

#### Jie Xiao (PI)

Pacific Northwest National Laboratory  
Energy and Environment Directorate  
902 Battelle Boulevard  
Richland, WA 99352  
Phone: 509-375-4598; Fax: 509-375-2186  
E-mail: [jie.xiao@pnnl.gov](mailto:jie.xiao@pnnl.gov)

#### Jun Liu (Co-PI)

Pacific Northwest National Laboratory  
Energy and Environment Directorate  
902 Battelle Boulevard  
Richland, WA 99352  
Phone: 509-375-4443; Fax: 509-371-6242  
E-mail: [jun.liu@pnnl.gov](mailto:jun.liu@pnnl.gov)

Start Date: October 1, 2011

Projected End Date: September 30, 2016

- Studied the electrochemical behavior of thick sulfur electrodes ( $3\text{-}4 \text{ mAh/cm}^2$ ).
- Investigated the reactions between sulfur radicals and different electrolytes.
- Decoupled lithium metal anode problems from the system by using novel electrolyte and graphite anode.

## Results

### 1. Electrochemical properties of thick sulfur electrodes

Based on our sulfur fabrication method (Patent application #61/521,191) developed in FY14, the relationship between the electrode preparation process and their electrochemical properties was further studied to understand polysulfide reactions at relevant scales ( $3\text{-}4 \text{ mAh/cm}^2$ ).

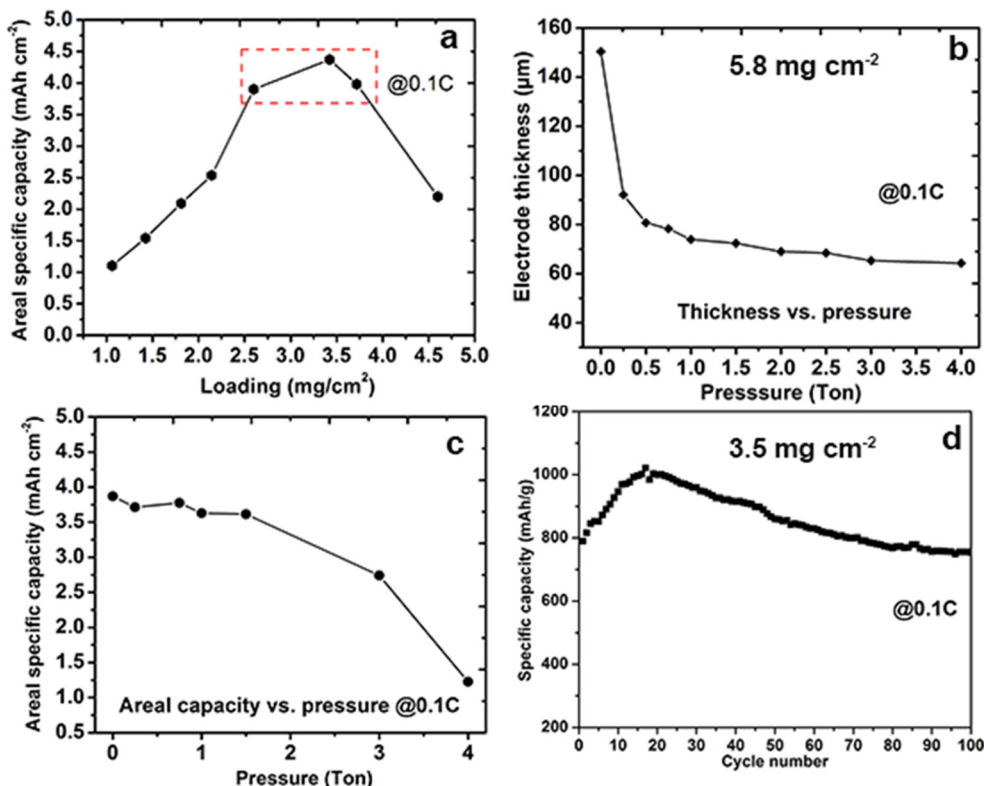
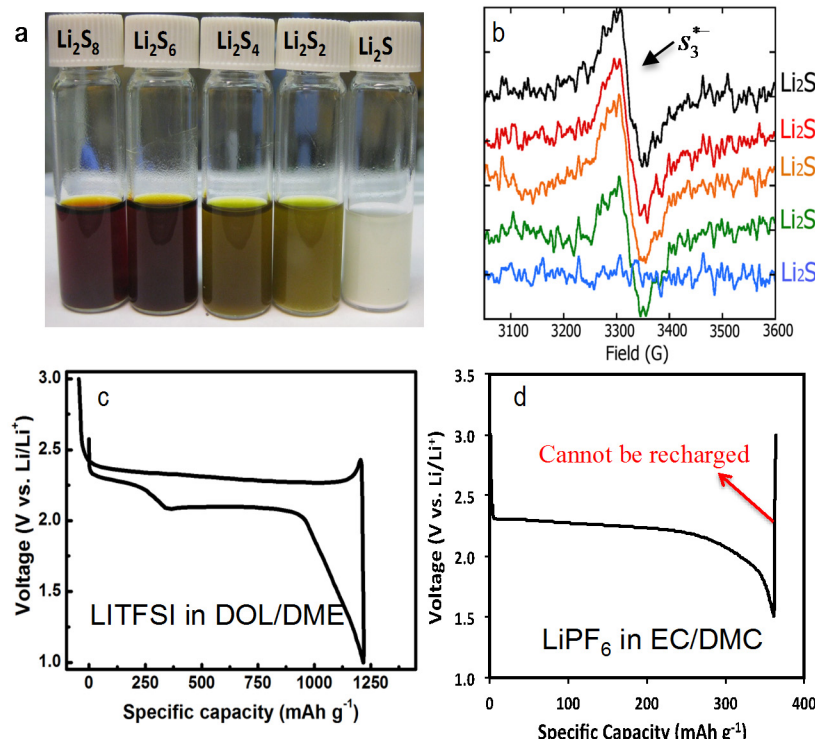


Figure V-334: (a) Areal specific capacity dependence on the sulfur loading obtained at 0.1C, (b) electrode thickness as a function of calendering pressure, (c) areal capacity dependence on pressure applied for calendaring the electrode, and (d) cycling stability of cells cycled at 0.1C ( $1\text{C}=1000 \text{ mAh/g}$ )

Figure V-334a compares the deliverable areal capacity from sulfur electrodes with different areal loadings of sulfur. The balanced utilization rate of sulfur and conductivity (both ionic and electronic) of the whole electrode was reached at ca.  $3.5 \text{ mg/cm}^2$  sulfur loading, leading to a peak capacity of  $4.5 \text{ mAh/cm}^2$  at 0.1C. Figure V-334b shows the thickness changes of a thick sulfur electrode ( $5.8 \text{ mg/cm}^2$ ) under different calendering pressures. Even a small pressure of 0.25 ton (T) induced a significant thickness decrease from 150 to  $90 \mu\text{m}$ , indicating relatively loose structure of the original electrode composed of sulfur/carbon composite. Further increase of pressure to above 1 T only slightly decreased the electrode thickness. The purpose of this step was to adjust the porosity and tortuosity of as-prepared electrodes. Of note, the optimized sulfur loading in Figure V-334a could change depending on the current density and electrode wettability. For example, it was found that the electrolyte penetration into the interior sulfur cathode became very difficult when the electrode thickness was decreased. Since ether-based solvent had to be used for Li-S batteries, the application of vacuum was not feasible. If the wetting of the entire thick electrode was resolved, the optimized loading of sulfur, e.g., the loading corresponding to the highest areal capacity, could be further increased to benefit practical applications.

The specific areal capacity displayed significant dependence on the rolling pressure, i.e., the porosity, of the electrode (Figure V- 334c). As the pressure increased from 0 to 1.5 T, the areal capacity deliverable from the same electrode did not change much and remained between 3.5 and 4 mAh/cm<sup>2</sup>. The electrode thickness reduction benefited the final volumetric energy density of the cell, while the slightly decreased porosity helped to reduce the amount of electrolyte needed to completely wet the electrodes but still maintain a decent sulfur utilization rate. Further increasing the pressure to greater than 2 T, a large capacity reduction was seen. However, if the pressure applied was greater than 2 T, the continuous electrolyte diffusion pathway was blocked in the highly densified electrodes. Therefore, not only did the electrolyte wetting become an issue at the beginning, the ionic conductivity of the whole electrode also greatly decreased, leading to a much lower capacity (Figure V- 334c). For thick electrode preparation, both the areal mass loading and electrode porosity/tortuosity needed to be balanced carefully, as they may vary with different types of carbon materials and sulfur fractions. The thick electrode (3.5 mg/cm<sup>2</sup> of sulfur, pressed at 0.2 T) showed good cycling stability (Figure V- 334d), comparable to or even better than the thin-film Li-S cells, for the first 100 cycles. At 0.1 C, the sample S80/IKB delivered a capacity of 750 mAh/g<sup>1</sup> in 100 cycles. After 100 cycles, the limiting step of cycling was transferred to the anode side, as discussed in last year's report.

## 2. Reactions between sulfur radicals and electrolytes



**Figure V- 335:** a) Comparison of chemically synthesized  $\text{Li}_2\text{S}_x$  series products in DOL/DME solvent. Concentration of each sample is 0.2 M based on elemental sulfur. b) EPR spectra of  $\text{Li}_2\text{S}_x$  series products. Sulfur radicals were detected in  $\text{Li}_2\text{S}_8$ ,  $\text{Li}_2\text{S}_6$ ,  $\text{Li}_2\text{S}_4$  and  $\text{Li}_2\text{S}_2$ , while there was no resonance signal from commercial  $\text{Li}_2\text{S}$ . c) The first discharge/charge curve of a Li-S battery tested in LITFSI-DOL/DME. d) The first discharge/charge curve of a Li-S battery tested in  $\text{LiPF}_6$ -EC/DMC

In FY14, *in situ* electron paramagnetic resonance (EPR) was developed to capture signals from  $s_3^*$  radicals generated during cycling. The sulfur radicals were found to facilitate the conversion among different polysulfide chains. The interactions between sulfur radicals and different electrolytes were then further investigated; the results are shown in Figure V- 335. Polysulfides with different chain lengths were prepared simply by mixing lithium and sulfur powders in 1,3 dioxolane/1,2-dimethoxyethane (DOL/DME) solvents, followed by heat treatment at 60°C. Although the as-prepared polysulfides are labeled with stoichiometric numbers of Li and S in Figure V- 335a, other  $\text{Li}_2\text{S}_x$  species also coexisted and formed equilibrium with each other. The long-chain  $\text{Li}_2\text{S}_8$  and  $\text{Li}_2\text{S}_2$  were dark yellow emulsions. Commercial  $\text{Li}_2\text{S}$  was completely insoluble and precipitated out from the solvent. The EPR revealed that  $s_3^*$  radicals, derived from  $\text{S}_6^{2-}$  anions, coexisted in all polysulfide species except in  $\text{Li}_2\text{S}$  (Figure V- 335b), confirming that an equilibrium, rather than a specific polysulfide species, was present in each  $\text{Li}_2\text{S}_x$ .

$\text{Li}_2\text{S}_6$  completely dissolved in the solvents showing dark red color, while  $\text{Li}_2\text{S}_4$  and  $\text{Li}_2\text{S}_2$  were dark yellow emulsions. Commercial  $\text{Li}_2\text{S}$  was completely insoluble and precipitated out from the solvent. The EPR revealed that  $s_3^*$  radicals, derived from  $\text{S}_6^{2-}$  anions, coexisted in all polysulfide species except in  $\text{Li}_2\text{S}$  (Figure V- 335b), confirming that an equilibrium, rather than a specific polysulfide species, was present in each  $\text{Li}_2\text{S}_x$ . This can be assigned to the spontaneous carbonate/dimethyl carbonate (EC/DMC) cannot be used for Li-S batteries. It is notable that most reported Li-S battery research employed lithium disproportionation/dissociation reactions of polysulfides. When a small amount of carbonate solvent such as propylene carbonate (PC) was added in these chemically synthesized  $\text{Li}_2\text{S}_x$  preparations, all resonance signals

disappeared after 40 min (data not shown here), indicating that carbonate solvents reacted and consumed all the sulfur radicals in the solutions. This explains why a conventional electrolyte such as LiPF<sub>6</sub> in ethylene bis(trifluoromethanesulfonyl)imide (LiTFSI)-DOL/DME electrolyte (Figure V- 335c) without mentioning the reason, although this recipe is not a typical formula for Li-ion batteries. It is very likely that those radicals easily attacked the alkyl carbonate solvents, leaving by-products at the end of discharge. Those by-products were electrochemically inactive, so Li-S cells cannot be recharged at all if tested in the traditional electrolyte (Figure V- 335d). Even for ether-based electrolytes, the long-term stability between sulfur radicals and the electrolyte is still questionable.

### 3. Lithium metal anode problems decoupled from the system by using novel electrolyte and graphite anode

It was found that when thick sulfur electrodes were used, lithium metal “corrosion” became the dominant issue, which limited the stable cycling of Li-S cells. That is because the solid electrolyte interface (SEI) accumulation on the lithium side quickly built up cell impedance and led to fast capacity degradation. To decouple the lithium metal problem from the system, an intercalation compound such as graphite was preferred to construct a new prototype of Li-ion batteries, because graphite has limited volume expansion during cycling and accumulation of the SEI on the anode surface was thereby avoided. However, graphite needs ethylene carbonate (EC) to form a protective SEI layer to prevent solvent co-intercalation. Unfortunately, EC was not compatible with polysulfide and its derived radicals as discussed in Figure V- 335. Recently, it was discovered at PNNL that 5 M LiTFSI in pure DOL was able to realize reversible cycling of graphite in the absence of EC. Therefore, the new electrolyte provided an ideal opportunity to remove the problems related to lithium metal in the Li-S battery system and efforts can focus on addressing challenges on the sulfur cathode side.

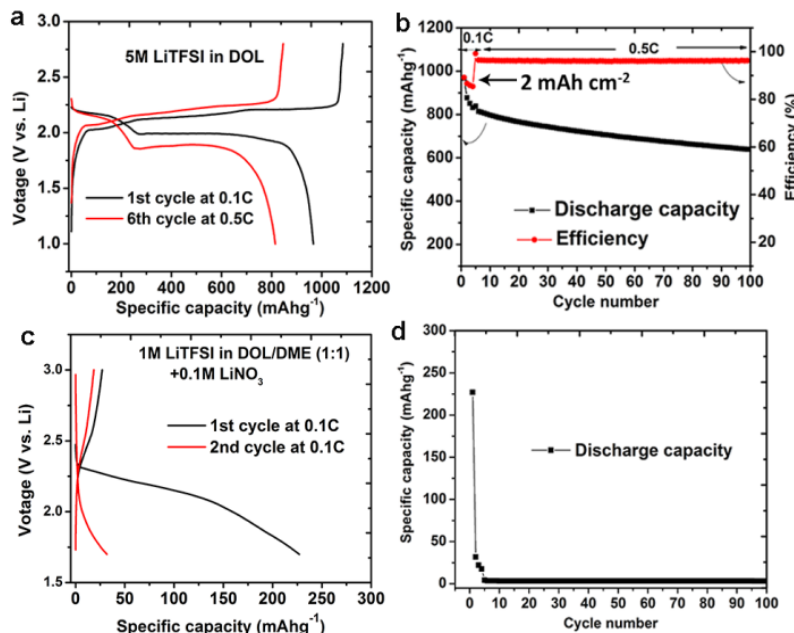


Figure V- 336: (a) Charge/discharge curves of graphite/sulfur full cell (LG/S) at different C rates in 5 M LiTFSI/DOL electrolyte without additive LiNO<sub>3</sub> and (b) its corresponding cycling stability and Coulombic efficiency. (c) Charge/discharge curves of LG/S full cell at 0.1 C in 1 M LiTFSI-DOL/DME with 0.1 M LiNO<sub>3</sub> and (d) its corresponding cycling performance. Areal capacity of sulfur cathodes: 2 mAh/cm<sup>2</sup>. 1C = 1000 mA/g

as 815 mAh/g was delivered, suggesting good kinetics of Li<sup>+</sup> across the electrolyte, both electrodes, and their interfaces. After around 100 cycles (Figure V- 336b), a high capacity retention of 81.3% was achieved at 0.5 C. Of note, the mass balance between cathode and anode will be optimized to further stabilize the cycling and take full advantage of intercalation anode. In contrast, when a traditional electrolyte, i.e. 1M LiTFSI in DOL/DME, was used, the LG/S full cell cannot be cycled at all (Figure V- 336c-Figure V- 336d); only about 220 mAh/g capacity was obtained during the first discharge, and the cell cannot be recharged. Since no

Preli lithiated graphite (LG) was coupled with a sulfur cathode to construct a full cell by using 5 M LiTFSI/DOL as the electrolyte. Typical discharge/charge curves of sulfur cells were observed (Figure V- 336a), confirming that graphite was not exfoliated in this new electrolyte without EC. At a low rate of 0.1 C, the LG/S cell exhibited high capacities of 980 mAh/g (2 mAh/cm<sup>2</sup>) and 1080 mAh/g for discharge and charge, respectively, with a high Coulombic efficiency of 90.7%. Note that there is no LiNO<sub>3</sub> additive used in this new electrolyte. The high Coulombic efficiency indicated the greatly reduced shuttle reactions in the electrochemical couple of graphite and sulfur are probably due to the removal of the highly reactive lithium anode. When the rate was elevated to 0.5 C after 5 cycles at 0.1C, a capacity as high

effective SEI was formed to protect the graphite lattice in this regular electrolyte, the exfoliation of graphite led to the observed poor electrochemical performance. Accordingly, the capacity decayed to almost zero after the first few cycles.

### Conclusions and Future Directions

A detailed study on the relationships between preparation methods of thick sulfur electrodes and their electrochemical behaviors was conducted. The porosity and tortuosity of thick sulfur cathodes were carefully adjusted to maximize the sulfur utilization rate while maintaining a good cycling stability of Li-S cells. Polysulfide radicals generated from the disproportionation and dissociation reactions of polysulfides were found to react intensively with traditional carbonate-based electrolytes, but are relatively mild to ether-based solvents, providing insights on the electrolyte selection for Li-S batteries. A new electrolyte recipe has been identified to enable reversible cycling of graphite without the presence of EC. A new prototype Li-ion sulfur battery was therefore designed to avoid the corrosion of the lithium metal anode that occurs in conventional Li-S batteries. This concept of a Li-ion sulfur battery provided a unique opportunity to further study the reaction/diffusion pathways of polysulfides within the thick electrodes without influence from the lithium metal side.

Future work will continue to increase sulfur loading to more than 4 mg/cm<sup>2</sup> and solve the wetting issues in such thick sulfur electrodes. The new electrolyte recipe, coupled with the graphite anode, will be employed in the Li-ion sulfur cells to eliminate the corrosion effect of the lithium anode. Therefore, a more accurate understanding of sulfur cathodes can be gained, which may help develop innovative approaches to address the challenges in Li-S batteries at relevant scales.

### FY 2015 Publications/Patents/Presentations

1. Q. Wang, J. Zheng, E. Walter, H. Pan, D. Lv, P. Zuo, H. Chen, Z.D. Deng, B.Y. Liaw, X. Yu, X.-Q. Yang, J.-G. Zhang, J. Liu and J. Xiao, "Direct Observation of Sulfur Radicals as Reaction Media in Lithium Sulfur Batteries," *J. Electrochem. Soc.*, **2015**, 162, A474-A478.
2. D. Lv , J. Zheng, Q. Li, X. Xie, S. Ferrara, Z. Nie, L. B. Mehdi, N. D. Browning, J.-G. Zhang, G. L. Graff, J. Liu and J. Xiao, "High Energy Density Lithium-Sulfur Batteries: Challenges of Thick Sulfur Cathodes," *Adv. Energy Mater.*, **2015**, DOI: 10.1002/aenm.201402290.
3. D. Lv, P. Yan, Y. Shao, Q. Li, S. Ferrara, H. Pan, G. L. Graff, B. Polzin, C. Wang, J.-G. Zhang, J. Liu and J. Xiao, "High Performance Li-ion Sulfur Batteries Enabled by Intercalation Chemistry," *Chem. Comm.*, **2015**, 51, 13454.
4. J. Xiao, "Understanding the Lithium Sulfur Battery System at Relevant Scales" (Editorial), *Adv. Energy Mater.*, **2015**, 5, 1501102.
5. "Preformation of stable solid electrolyte interface (SEI) film on graphite anode," Application #14/529,840
6. "Electrolyte for lithium-sulfur batteries employing graphite as the anode," Application #14/530,562
7. D. Lv, Y. Shao, Q. Li, S. Ferrara, W. D. Bennett, G. L. Graff, B. Polzin, J.-G. Zhang, W. A. Henderson, J. Liu and J. Xiao, "High Performance Li-ion Sulfur Battery with Graphite as Anode: Electrochemical Properties and Interphase Study," *249th ACS National Meeting & Exposition*, March 22-26, **2015**, Denver.
8. D. Lv, P. Yan, Y. Shao, Q. Li, S. Ferrara, H. Pan, G. L. Graff, B. Polzin, M. H. Engelhard, C. Wang, J.-G. Zhang, J. Liu and J. Xiao, "Li-ion Sulfur Batteries Enabled by Intercalation Chemistry," *Beyond Lithium Ion VIII*, June 2-4, **2015**, Oak Ridge National Laboratory, Tennessee.
9. J. Xiao, "High Energy Li-ion Sulfur Batteries," *2nd PNNL-UNIST Battery Workshop*, August 18, **2015**, Richland.

# V.I.6 Nanostructured Design of Sulfur Cathodes for High Energy Lithium-Sulfur Batteries (Stanford U)

## Objectives

The charge capacity limitations of conventional transition metal oxide cathodes are overcome by designing optimized nano-architected sulfur cathodes. This study aims to enable sulfur cathodes with high capacity and long cycle life by developing sulfur cathodes from the perspective of nanostructured materials design, which will be used to combine with lithium metal anodes to generate high-energy lithium-sulfur batteries. Novel sulfur nanostructures as well as multifunctional coatings will be designed and fabricated to overcome the issues related to volume expansion, polysulfide dissolution and insulating nature of sulfur.

## Project Details

**Yi Cui (PI)**  
Stanford University  
Department of Material Science and Engineering  
476 Lomita Mall, McCullough 343  
Stanford, CA 94305  
Phone: 650-723-4613; Fax: 650-725-4034  
E-mail: [yicui@stanford.edu](mailto:yicui@stanford.edu)

Start Date: January 2013  
Projected End Date: December 2015

## Technical Barriers

The poor cycle life of lithium-sulfur battery is caused by multiple materials challenges: 1) large volume expansion of sulfur upon lithiation; 2) dissolution of intermediate discharge product lithium polysulfides in the electrolyte; 3) insulating nature of sulfur. These problems result in the following technical barriers to good battery performance:

- Loss of active materials
- Rapid capacity decay
- Low Coulombic efficiencies
- Poor rate performance
- Low areal mass loading of active materials.

## Technical Targets

- Develop fundamental material guidelines through structure and property correlations.
- Design novel nanostructured sulfur cathodes to address the material challenges outlined above.
- Develop conductive coatings to improve the rate performance of lithium-sulfur batteries.
- Discover novel nanostructured materials that can trap polydulfide species.

## Accomplishments

- Designed and synthesized various conductive sulfide encapsulated nanostructured Li<sub>2</sub>S cathodes to achieve superior battery rate performance.
- Demonstrated the multiple roles of sulfide coating
- Designed non-conductive oxide coated porous carbon flakes for sulfur and polysulfides confinement.
- Identified the optimal oxide material and the corresponding binding mechanism of polysulfides

## Introduction

Lithium-sulfur batteries can bring about significant improvements to the current state-of-the-art battery technologies due to its high specific energy density and cost saving. The capacity decay of lithium-sulfur battery during cycling is a multifaceted problem. There exist multiple materials challenges that prevent it from reaching the cycling performance suitable for portable electronics and electrical vehicles. The rapid capacity decay of sulfur cathode can be attributed to several reasons: 1) significant volumetric expansion (~80% change) when sulfur is reduced to lithium sulfide (Li<sub>2</sub>S); 2) dissolution of intermediate lithium polysulfides (Li<sub>2</sub>S<sub>x</sub>, 4≤x≤8) in the electrolyte; 3) low ionic and electronic conductivity of both sulfur and Li<sub>2</sub>S.

## Approach

To ensure the knowledge gathered from the Li-S battery research is transferrable to industry, the following approaches have been adopted.

- Studied the electrochemical behavior of thick sulfur electrodes ( $3\text{-}4 \text{ mAh/cm}^2$ ).
- Investigated the reactions between sulfur radicals and different electrolytes.
- Decoupled lithium metal anode problems from the system by using novel electrolyte and graphite anode.

## Results

### 1. Electrochemical properties of thick sulfur electrodes

Based on our sulfur fabrication method (Patent application #61/521,191) developed in FY14, the relationship between the electrode preparation process and their electrochemical properties was further studied to understand polysulfide reactions at relevant scales ( $3\text{-}4 \text{ mAh/cm}^2$ ).

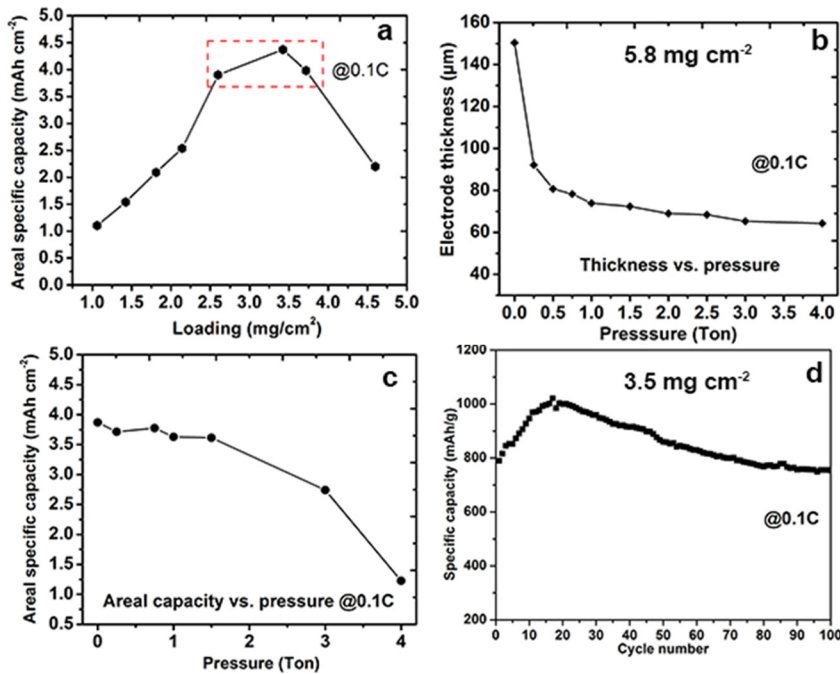


Figure V- 337: (a) Areal specific capacity dependence on the sulfur loading obtained at 0.1C, (b) electrode thickness as a function of calendering pressure, (c) areal capacity dependence on pressure applied for calendaring the electrode, and (d) cycling stability of cells cycled at 0.1C (1C=1000 mAh/g)

Figure V- 337a compares the deliverable areal capacity from sulfur electrodes with different areal loadings of sulfur. The balanced utilization rate of sulfur and conductivity (both ionic and electronic) of the whole electrode was reached at ca.  $3.5 \text{ mg/cm}^2$  sulfur loading, leading to a peak capacity of  $4.5 \text{ mAh/cm}^2$  at 0.1C. Figure V- 337b shows the thickness changes of a thick sulfur electrode ( $5.8 \text{ mg/cm}^2$ ) under different calendering pressures. Even a small pressure of 0.25 ton (T) induced a significant thickness decrease from 150 to 90  $\mu\text{m}$ , indicating relatively loose structure of the original electrode composed of sulfur/carbon composite. Further increase

of pressure to above 1 T only slightly decreased the electrode thickness. The purpose of this step was to adjust the porosity and tortuosity of as-prepared electrodes. Of note, the optimized sulfur loading in Figure V- 337a could change depending on the current density and electrode wettability. For example, it was found that the electrolyte penetration into the interior sulfur cathode became very difficult when the electrode thickness was decreased. Since ether-based solvent had to be used for Li-S batteries, the application of vacuum was not feasible. If the wetting of the entire thick electrode was resolved, the optimized loading of sulfur, e.g., the loading corresponding to the highest areal capacity, could be further increased to benefit practical applications.

The specific areal capacity displayed significant dependence on the rolling pressure, i.e., the porosity, of the electrode (Figure V- 337c). As the pressure increased from 0 to 1.5 T, the areal capacity deliverable from the same electrode did not change much and remained between  $3.5$  and  $4 \text{ mAh/cm}^2$ . The electrode thickness reduction benefited the final volumetric energy density of the cell, while the slightly decreased porosity helped to reduce the amount of electrolyte needed to completely wet the electrodes but still maintain a decent sulfur utilization rate. Further increasing the pressure to greater than 2 T, a large capacity reduction was seen. However, if the pressure applied was greater than 2 T, the continuous electrolyte diffusion pathway was

blocked in the highly densified electrodes. Therefore, not only did the electrolyte wetting become an issue at the beginning, the ionic conductivity of the whole electrode also greatly decreased, leading to a much lower capacity (Figure V- 337c). For thick electrode preparation, both the areal mass loading and electrode porosity/tortuosity needed to be balanced carefully, as they may vary with different types of carbon materials and sulfur fractions. The thick electrode (3.5 mg/cm<sup>2</sup> of sulfur, pressed at 0.2 T) showed good cycling stability (Figure V- 337d), comparable to or even better than the thin-film Li-S cells, for the first 100 cycles. At 0.1 C, the sample S80/IKB delivered a capacity of 750 mAh/g<sup>1</sup> in 100 cycles. After 100 cycles, the limiting step of cycling was transferred to the anode side, as discussed in last year's report.

## 2. Reactions between sulfur radicals and electrolytes

In FY14, *in situ* electron paramagnetic resonance (EPR) was developed to capture signals from  $s_3^{*-}$  radicals generated during cycling. The sulfur radicals were found to facilitate the conversion among different

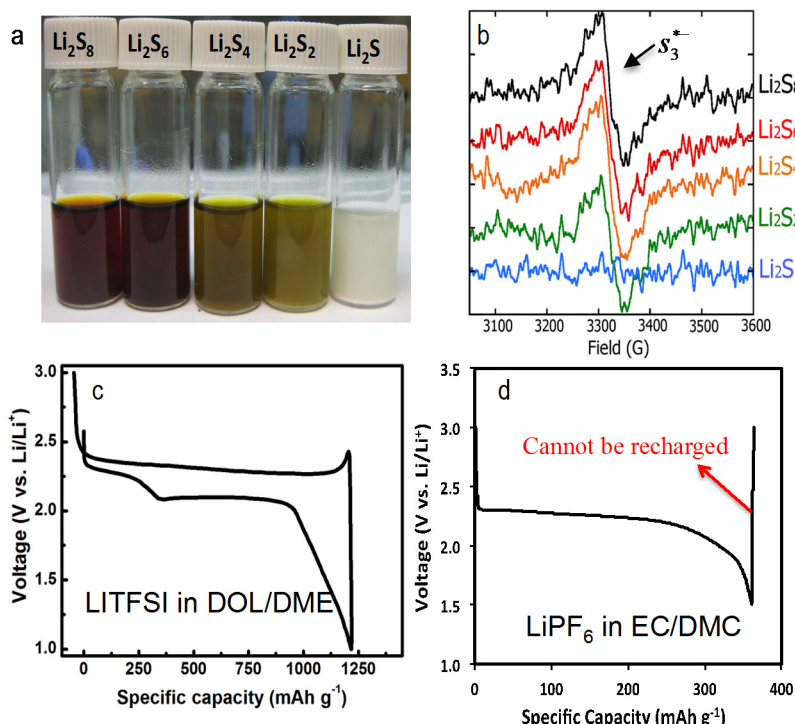


Figure V- 338: a) Comparison of chemically synthesized  $\text{Li}_2\text{S}_x$  series products in DOL/DME solvent. Concentration of each sample is 0.2 M based on elemental sulfur. b) EPR spectra of  $\text{Li}_2\text{S}_x$  series products. Sulfur radicals were detected in  $\text{Li}_2\text{S}_8$ ,  $\text{Li}_2\text{S}_6$ ,  $\text{Li}_2\text{S}_4$  and  $\text{Li}_2\text{S}_2$ , while there was no resonance signal from commercial  $\text{Li}_2\text{S}$ . c) The first discharge/charge curve of a Li-S battery tested in LITFSI-DOL/DME. d) The first discharge/charge curve of a Li-S battery tested in  $\text{LiPF}_6$ -EC/DMC

$\text{Li}_2\text{S}$  (Figure V- 338b), confirming that an equilibrium, rather than a specific polysulfide species, was present in each  $\text{Li}_2\text{S}_x$ . This can be assigned to the spontaneous disproportionation/dissociation reactions of polysulfides. When a small amount of carbonate solvent such as propylene carbonate (PC) was added in these chemically synthesized  $\text{Li}_2\text{S}_x$  preparations, all resonance signals disappeared after 40 min (data not shown here), indicating that carbonate solvents reacted and consumed all the sulfur radicals in the solutions. This explains why a conventional electrolyte such as  $\text{LiPF}_6$  in ethylene carbonate/dimethyl carbonate (EC/DMC) cannot be used for Li-S batteries. It is notable that most reported Li-S battery research employed lithium bis(trifluoromethanesulfonyl)imide (LITFSI)-DOL/DME electrolyte (Figure V- 338c) without mentioning the reason, although this recipe is not a typical formula for Li-ion batteries. It is very likely that those radicals easily attacked the alkyl carbonate solvents, leaving by-products at the end of discharge. Those by-products were electrochemically inactive, so Li-S cells cannot be recharged at all if tested in the traditional electrolyte

polysulfide chains. The interactions between sulfur radicals and different electrolytes were then further investigated; the results are shown in Figure V- 338. Polysulfides with different chain lengths were prepared simply by mixing lithium and sulfur powders in 1,3 dioxolane/1,2-dimethoxyethane (DOL/DME) solvents, followed by heat treatment at 60°C. Although the as-prepared polysulfides are labeled with stoichiometric numbers of Li and S in Figure V- 338a, other  $\text{Li}_2\text{S}_x$  species also coexisted and formed equilibrium with each other. The long-chain  $\text{Li}_2\text{S}_8$  and  $\text{Li}_2\text{S}_6$  completely dissolved in the solvents showing dark red color, while  $\text{Li}_2\text{S}_4$  and  $\text{Li}_2\text{S}_2$  were dark yellow emulsions. Commercial  $\text{Li}_2\text{S}$  was completely insoluble and precipitated out from the solvent. The EPR revealed that  $s_3^{*-}$  radicals, derived from  $\text{S}_6^{2-}$  anions, coexisted in all polysulfide species except in

(Figure V- 338d). Even for ether-based electrolytes, the long-term stability between sulfur radicals and the electrolyte is still questionable.

### 3. Lithium metal anode problems decoupled from the system by using novel electrolyte and graphite anode

It was found that when thick sulfur electrodes were used, lithium metal “corrosion” became the dominant issue, which limited the stable cycling of Li-S cells. That is because the solid electrolyte interface (SEI) accumulation on the lithium side quickly built up cell impedance and led to fast capacity degradation. To decouple the lithium metal problem from the system, an intercalation compound such as graphite was preferred to construct a new prototype of Li-ion batteries, because graphite has limited volume expansion during cycling and accumulation of the SEI on the anode surface was thereby avoided. However, graphite needs ethylene carbonate (EC) to form a protective SEI layer to prevent solvent co-intercalation. Unfortunately, EC was not compatible with polysulfide and its derived radicals as discussed in Figure V- 338. Recently, it was discovered at PNNL that 5 M LiTFSI in pure DOL was able to realize reversible cycling of graphite in the absence of EC. Therefore, the new electrolyte provided an ideal opportunity to remove the problems related to lithium metal in the Li-S battery system and efforts can focus on addressing challenges on the sulfur cathode side.

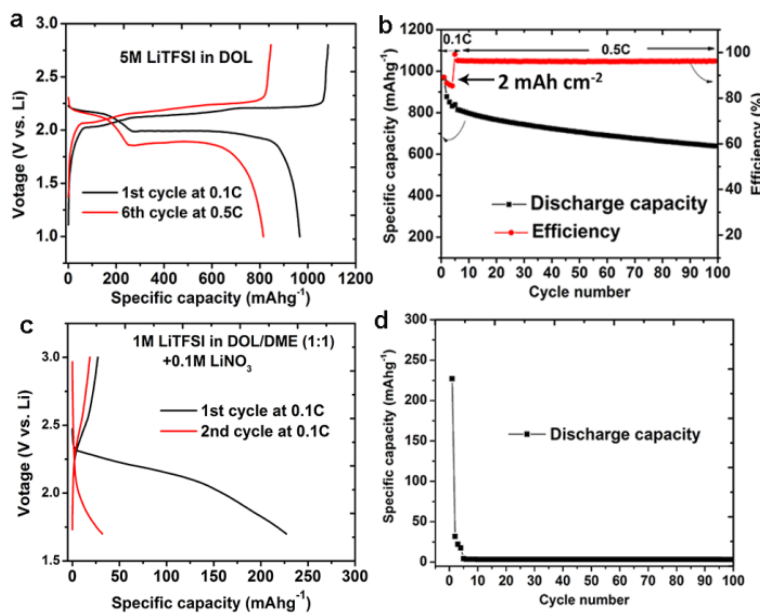


Figure V- 339: (a) Charge/discharge curves of graphite/sulfur full cell (LG/S) at different C rates in 5 M LiTFSI/DOL electrolyte without additive LiNO<sub>3</sub> and (b) its corresponding cycling stability and Coulombic efficiency. (c) Charge/discharge curves of LG/S full cell at 0.1 C in 1 M LiTFSI-DOL/DME with 0.1 M LiNO<sub>3</sub> and (d) its corresponding cycling performance. Areal capacity of sulfur cathodes: 2 mAh/cm<sup>2</sup>. 1C = 1000 mA/g

good kinetics of Li<sup>+</sup> across the electrolyte, both electrodes, and their interfaces. After around 100 cycles (Figure V- 339b), a high capacity retention of 81.3% was achieved at 0.5 C. Of note, the mass balance between cathode and anode will be optimized to further stabilize the cycling and take full advantage of intercalation anode. In contrast, when a traditional electrolyte, i.e. 1M LiTFSI in DOL/DME, was used, the LG/S full cell cannot be cycled at all (Figure V- 339c-Figure V- 339d); only about 220 mAh/g capacity was obtained during the first discharge, and the cell cannot be recharged. Since no effective SEI was formed to protect the graphite lattice in this regular electrolyte, the exfoliation of graphite led to the observed poor electrochemical performance. Accordingly, the capacity decayed to almost zero after the first few cycles.

### Conclusions and Future Directions

A detailed study on the relationships between preparation methods of thick sulfur electrodes and their electrochemical behaviors was conducted. The porosity and tortuosity of thick sulfur cathodes were carefully

Prelithiated graphite (LG) was coupled with a sulfur cathode to construct a full cell by using 5 M LiTFSI/DOL as the electrolyte. Typical discharge/charge curves of sulfur cells were observed (Figure V- 339a), confirming that graphite was not exfoliated in this new electrolyte without EC. At a low rate of 0.1 C, the LG/S cell exhibited high capacities of 980 mAh/g (2 mAh/cm<sup>2</sup>) and 1080 mAh/g for discharge and charge, respectively, with a high Coulombic efficiency of 90.7%. Note that there is no LiNO<sub>3</sub> additive used in this new electrolyte. The high Coulombic efficiency indicated the greatly reduced shuttle reactions in the electrochemical couple of graphite and sulfur are probably due to the removal of the highly reactive lithium anode. When the rate was elevated to 0.5 C after 5 cycles at 0.1C, a capacity as high as 815 mAh/g was delivered, suggesting

adjusted to maximize the sulfur utilization rate while maintaining a good cycling stability of Li-S cells. Polysulfide radicals generated from the disproportionation and dissociation reactions of polysulfides were found to react intensively with traditional carbonate-based electrolytes, but are relatively mild to ether-based solvents, providing insights on the electrolyte selection for Li-S batteries. A new electrolyte recipe has been identified to enable reversible cycling of graphite without the presence of EC. A new prototype Li-ion sulfur battery was therefore designed to avoid the corrosion of the lithium metal anode that occurs in conventional Li-S batteries. This concept of a Li-ion sulfur battery provided a unique opportunity to further study the reaction/diffusion pathways of polysulfides within the thick electrodes without influence from the lithium metal side.

Future work will continue to increase sulfur loading to more than 4 mg/cm<sup>2</sup> and solve the wetting issues in such thick sulfur electrodes. The new electrolyte recipe, coupled with the graphite anode, will be employed in the Li-ion sulfur cells to eliminate the corrosion effect of the lithium anode. Therefore, a more accurate understanding of sulfur cathodes can be gained, which may help develop innovative approaches to address the challenges in Li-S batteries at relevant scales.

#### FY 2015 Publications/Patents/Presentations

1. Q. Wang, J. Zheng, E. Walter, H. Pan, D. Lv, P. Zuo, H. Chen, Z.D. Deng, B.Y. Liaw, X. Yu, X.-Q. Yang, J.-G. Zhang, J. Liu and J. Xiao, "Direct Observation of Sulfur Radicals as Reaction Media in Lithium Sulfur Batteries," *J. Electrochem. Soc.*, **2015**, 162, A474-A478.
2. D. Lv , J. Zheng, Q. Li, X. Xie, S. Ferrara, Z. Nie, L. B. Mehdi, N. D. Browning, J.-G. Zhang, G. L. Graff, J. Liu and J. Xiao, "High Energy Density Lithium-Sulfur Batteries: Challenges of Thick Sulfur Cathodes," *Adv. Energy Mater.*, **2015**, DOI: 10.1002/aenm.201402290.
3. D. Lv, P. Yan, Y. Shao, Q. Li, S. Ferrara, H. Pan, G. L. Graff, B. Polzin, C. Wang, J.-G. Zhang, J. Liu and J. Xiao, "High Performance Li-ion Sulfur Batteries Enabled by Intercalation Chemistry," *Chem. Comm.*, **2015**, 51, 13454.
4. J. Xiao, "Understanding the Lithium Sulfur Battery System at Relevant Scales" (Editorial), *Adv. Energy Mater.*, **2015**, 5, 1501102.
5. "Preformation of stable solid electrolyte interface (SEI) film on graphite anode," Application #14/529,840
6. "Electrolyte for lithium-sulfur batteries employing graphite as the anode," Application #14/530,562
7. D. Lv, Y. Shao, Q. Li, S. Ferrara, W. D. Bennett, G. L. Graff, B. Polzin, J.-G. Zhang, W. A. Henderson, J. Liu and J. Xiao, "High Performance Li-ion Sulfur Battery with Graphite as Anode: Electrochemical Properties and Interphase Study," *249th ACS National Meeting & Exposition*, March 22-26, **2015**, Denver.
8. D. Lv, P. Yan, Y. Shao, Q. Li, S. Ferrara, H. Pan, G. L. Graff, B. Polzin, M. H. Engelhard, C. Wang, J.-G. Zhang, J. Liu and J. Xiao, "Li-ion Sulfur Batteries Enabled by Intercalation Chemistry," *Beyond Lithium Ion VIII*, June 2-4, **2015**, Oak Ridge National Laboratory, Tennessee.
9. J. Xiao, "High Energy Li-ion Sulfur Batteries," *2nd PNNL-UNIST Battery Workshop*, August 18, **2015**, Richland.

## V.I.7 Addressing Internal “Shuttle” Effect: Electrolyte Design and Cathode Morphology Evolution in Li-S Batteries (TAMU)

### Objectives

- Overcome the lithium-metal anode deterioration issues through advanced Li-anode protection/stabilization strategies including (i) in-situ chemical formation of a protective passivation layer and (ii) alleviation of the “aggressiveness” of the environment at the anode by minimizing the polysulfide shuttle with advanced cathode structure design.

### Technical Barriers

- Complexity of carbon mesoporous architectural features and role of the mesostructures for improving electronic conductivity while not sacrificing S-loading and strain accommodation due to volume change; anode surface stabilization; involvedness of the electrolyte chemistry; cathode morphology evolution  
Barriers addressed:
  - Anode SEI reactions in presence of PS species; alternative materials for PS retention.
  - Tuning synthesis of the C/S composite.
  - Characterization of morphology evolution of C/S composite.

### Technical Targets

- Optimization of synthesis of C/S composite and characterization of structure and composition.
- Development of a mesoscopic model for understanding effects of cathode morphology evolution on ionic diffusion and charge/discharge curves.
- Identification of anode SEI reactions in presence of PS species; characterization of cathode chemistry.

### Accomplishments

- Synthesis and characterization of a lab-scale C/S composite material has been achieved .
- Nucleation and growth of  $\text{Li}_2\text{S}$  at the Li-metal surface and SEI reactions on formed film characterized.
- Effects of C porosity on S dissolution, lithiation, and reaction in a C/S environment elucidated.
- Electrode morphology evolution and cathode mesostructure impact on product formation and deposition characterized.

### Introduction

This project provides new information about the chemistry of the composite C/S cathode as a function of its morphology, as well as about the interfacial reactions taking place at the surface of the Li anode in presence of PS species, and the chemical, interfacial, and structural effects on the cell performance and cell life. All of this new information results from a synergetic study involving atomistic and mesoscopic modeling and synthesis and characterization of C/S composites and complete cell and is expected to result in new electrolyte formulations and development of alternative startegies for PS retention at the cathode. Moreover, the final outcome of the project will be the delivery a cell operating for 500 cycles at efficiency greater than 80 %.

### Project Details

**Perla B. Balbuena (Texas A&M University)**  
DE-AC02-05CH11231, Subcontract No. 7060634

**Partha P. Mukherjee (Co-PI, Texas A&M University)**

**Vilas Pol (Co-PI, Purdue University)**

Start Date: October 2014

Projected End Date: September 2017

## Approach

A mesoscale model including different realizations of electrode mesoporous structures generated based on a stochastic reconstruction method allows virtual screening of the cathode microstructural features and the corresponding effects on electronic/ionic conductivity and morphological evolution. Interfacial reactions at the anode due to the presence of polysulfide species and successful additives such as LiNO<sub>3</sub> are characterized with ab initio methods. For the cathode interfacial reactions, data and detailed structural and energetic information obtained from atomistic-level studies is used in a mesoscopic-level analysis. A novel sonochemical fabrication method is used to generate controlled cathode mesoporous structures that are tested along with new electrolyte formulations and alternative materials for retention of PS species based on the knowledge gained from the mesoscale and atomistic modeling efforts.

## Results

We have achieved the following progress:

### Synthesis and Characterization of C/S Composite Cathode Materials

New carbon cavities were developed for encapsulation of non-conducting sulfur. The solid-state synthesis of the carbon substrate is an environmentally-friendly, economical, and single-step procedure. A bio-mass derived precursor is pyrolytically heat-treated to high temperatures between 500 - 1000°C in an inert gas atmosphere. The synthesis process of the carbon-sulfur composites utilizes sonochemistry, the application of ultrasound waves that produce high velocity jet-streams of bubbles according to the acoustic cavitation effect. The total time for ultra-sonication is approximately 5-7 minutes. Lab scale 500 mg C/S composite synthesis is illustrated in Figure V- 340a.

Scanning electron micrograph demonstrates the carbon cavities prepared for the nanosulfur loading. Figure V- 340b demonstrates the sulfur nanoparticle loaded C/S composite. It can be seen that the cavities are almost filled. The amount of sulfur loading is under investigation by TGA analysis. Additional work was dedicated to characterization of the carbon-sulfur composite using techniques including transmission electron microscopy, X-ray powder diffraction, Brunauer-Emmett-Teller (BET) surface area analysis, and Raman spectroscopy. This information was utilized to optimize the chemical nature of the carbon-sulfur composite and its subsequent electrochemical performance.

Although the capacity was initially high for the 60% S and 40% C composite reported earlier, due to reduced conductivity it was observed to fade during cycling. Therefore, synthesis conditions were optimized to produce a sulfur-carbon composite, where the weight of sulfur is 27.89 wt%. This composition was confirmed via thermo-gravimetric analysis (TGA) under inert atmosphere. X-Ray powder diffraction (XRD) is performed to confirm the orthorhombic crystal structure of the sulfur inserted in a carbon “compartment” cavity. Scanning electron microscopy (SEM) and energy-dispersive X-ray spectroscopy (EDS) was carried out to demonstrate the mono-dispersity of nanosulfur in the carbon-sulfur composite. That clarified whether most of the sulfur is loaded inside the carbon “compartment” cavities. The electrochemical performance was carried out using a newly prepared electrolyte composed of 1 M solution of LiTFSI in organic solvent of equal parts DOL/D2. Initial results showed lower capacities and slight fading with cycling. This could be due to insufficient drying of solvent that could have some water content leading to poor electrochemical performance. Thus further work was performed to optimize solvents (DOL and D2) via drying in dried molecular sieves followed by addition of 1 M solution of LiTFSI salt and electrochemical testing of newly developed C/S composite with ~30% S content.

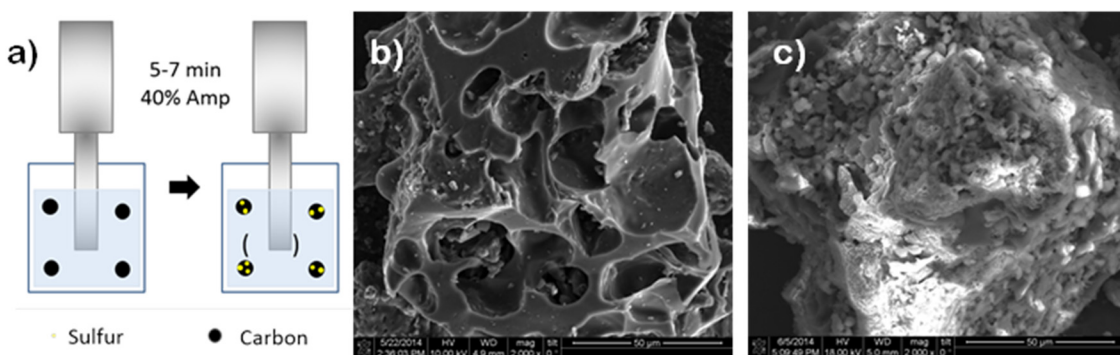


Figure V-340: a) Synthesis procedure for carbon-sulfur composites, b) SEM of carbon micro-compartment as a substrate for nanosulfur loading, c) SEM of carbon micro-compartment after loading sulfur nanoparticles sonochemically

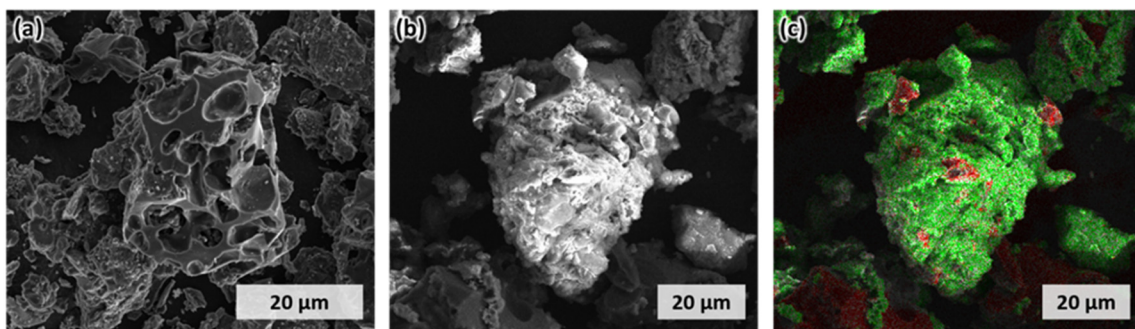


Figure V-341: Schematic for ultrasonic synthesis of CCs-S composite. (a) Scanning electron micrographs of porous bare CCs. (b) Scanning electron micrograph of carbon-sulfur composite produced via the sonochemical sulfur deposition process. (c) Elemental mapping of the carbon-sulfur composite by X-ray dot-mapping. Sulfur is highlighted in green, while carbon is highlighted in red

### Structural evolution as a function of Li/Si content

Sulfur amounts in S-C composite fabricated via sonochemical power were varied and optimized. The composites were characterized with morphological (SEM), compositional (EDS), and structural (XRD) analyses. It was confirmed that most of the nanosulfur is loaded in the carbon compartments (CC). Electrochemical performance was tested on newly prepared electrolyte composed of 1 M solution of LiTFSI in organic solvent of equal parts DOL/D2. Before loading sulfur (Figure V-341a), the as-prepared CCs exhibit small and large cavities that permit sulfur loading retaining an intimate electronic pathway. The CCs demonstrated here were synthesized via a separate, single-step pyrolytic heat treatment of a biomass precursor. After applying ultrasonic irradiation the CCs particles serve as a conductive substrate for sulfur and makes a hybrid composite (Figure V-341b). Nano-sulfur is formed via the action of acoustic cavitation in aqueous solution and nucleated S is loaded into the cavities with the sonochemical microjet effects to produce a homogeneous and conductive carbon-sulfur composite. Elemental dot mapping (Figure V-341c) shows that CCs can accommodate sulfur upon the available compartments. X-ray powder diffraction (XRD, not shown here) identifies the crystal structure of the loaded sulfur in CCs as an orthorhombic allotrope of sulfur known as cyclo-sulfur ( $\alpha$ -sulfur), 46 most stable allotrope at room temperature. The amorphous structure of pristine CCs was studied by Raman spectroscopy and X-ray diffraction. Thermogravimetric analysis (TGA) of S/C composite indicated significant mass loss between 100°C and 200°C confirming 65 wt% of sulfur loading in the C/S composite. The high degree of nano-sulfur loading is manifested in deposition of sulfur within the pores and micron size compartments.

The hybrid electrode comprising 45 wt.% S shows stable performance during rate studies. Hysteresis is shown to increase as the specific current is increased. The upper voltage plateau in the charge curve is seen to be constant. In the presence of a fluorinated electrolyte comprising 1,1,2,2-Tetrafluoroethyl 2,2,3,3-tetrafluoropropyl ether, it is observed that there is a shift in the voltage at which the reduction or oxidation of

sulfur compounds occurs. The voltage profile of the CCs-sulfur composite during different currents is shown in Figure V- 342a. Our theoretical analysis of the SEI reactions on the Li metal surface indicate that DOL and DME are very stable solvents compared with the organic carbonates whereas D2 easily decomposes forming LiF and other organic fragments. The presence of LiF may be responsible for the formation of a more stable and passivating SEI possibly also stabilizing the rapid PS decomposition observed otherwise. When cycled at a constant specific current of 112 mA/g, the carbon-sulfur composite demonstrates an average capacity of approximately 650 mAh/g and minimum 96% coulombic efficiency. This can be attributed to the effective sulfur accommodation in the carbon cavity cathode. However, some consistent capacity fade is seen across the 100 cycles (Figure V- 342b). Further efforts are underway to stabilize specific capacity during long cycling.

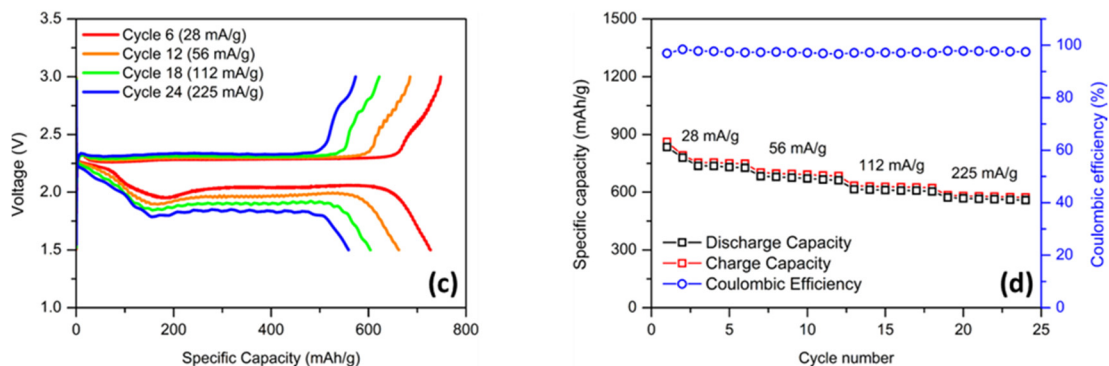
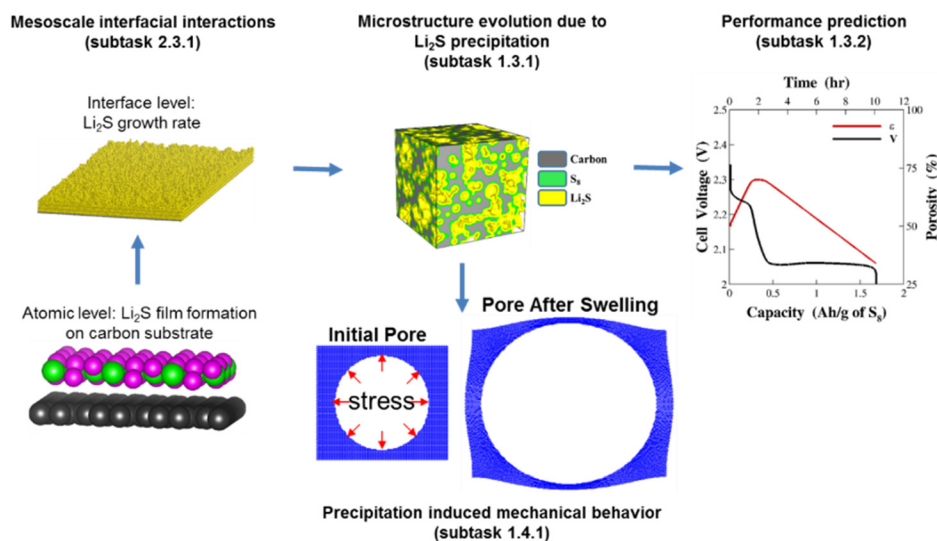


Figure V- 342: a) Synthesis procedure for carbon-sulfur composites, b) SEM of carbon micro-compartment as a substrate for nanosulfur loading, c) SEM of carbon micro-compartment after loading sulfur nanoparticles sonochemically. Structural evolution as a function of Li/Si content

### Mesoscopic Modeling of Cathode Morphology Evolution

A mesoscale approach is developed to appropriately understand the overall Li-S battery behavior as schematically illustrated in Figure V- 343. Interactions between insoluble polysulfides and solid substrate were studied by a first-principles approach at the atomistic scale. It is found that facets of crystalline  $\text{Li}_2\text{S}$  are dominated by  $\text{Li}_2\text{S}$  (111) surface and a  $\text{Li}_2\text{S}$  (111) film can form on carbon substrate. Based on the results from



atomic scale simulations, a coarse-grained lattice model combined with kinetic Monte Carlo (KMC) algorithm was developed to study the  $\text{Li}_2\text{S}$  film growth rate ( $d\delta/dt$ ) at an interfacial level. The growth rate was determined by reactant concentrations ( $C_{\text{Li}^+}$ ) and ( $C_{\text{S}-2}$ ), discharge product solubility ( $\Theta$ ), and cathode microstructure (total pore volume  $V$  and

Figure V- 343: Schematic illustration of the mesoscale modeling approach, which includes  $\text{Li}_2\text{S}$  film formation, cathode microstructure evolution, performance prediction and poromechanics

interface area between solid substrate and electrolyte  $S$ ) as  $d\delta/dt=1.04\times 10^{-6} (VS_0)/(V_0 S)(C_{\text{Li}^+}^2 C_{\text{S}-2})-\Theta$ . This interfacial model was extended to study the cathode surface coverage evolution by explicitly considering  $\text{Li}_2\text{S}$  molecule desorption/diffusion on carbon substrate as shown in Figure V- 344. It is found that the coverage grows faster at the lower temperature. The low temperature can reduce  $\text{Li}_2\text{S}$  desorption rate and diffusion rate.

This condition can facilitate the formation of small Li<sub>2</sub>S nanoislands, which can supply sufficient lateral sites to stabilize free Li<sub>2</sub>S molecules on the carbon substrate.

Stochastic realizations of 3D cathode architectures were reconstructed to investigate the microstructure evolution induced by Li<sub>2</sub>S precipitation. It is found that both the porosity and specific surface area of cathode

tend to decrease as the Li<sub>2</sub>S thickness increases, which finally leads to the decrease of effective ionic conductivity. For cathode microstructures with the same intrinsic specific surface area, the one which has the lowest carbon volume fraction has the highest ability to maintain the specific surface area during the discharge as

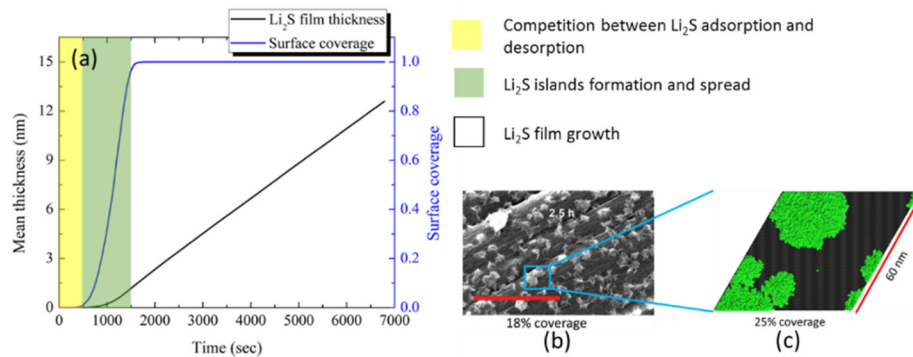


Figure V-344: (a) Li<sub>2</sub>S film thickness and coverage variation versus time. (b) SEM image of Li<sub>2</sub>S nanoislands formation on carbon substrate from F. Y. Fan et al., 2015, Advanced Materials, 27, pp. 5203-5209. (c) Snapshot of Li<sub>2</sub>S nanoislands formation on carbon substrate from Coarse-Grained KMC simulation

shown in Figure V-345. Hence, it is necessary to develop cathode architecture with as high porosity as possible without compromising the mechanical stability.

A macroscale mathematical description of the lithium sulfur cell is developed based on porous electrode theory. The model involves Li<sub>2</sub>S precipitation kinetics from the Kinetic Monte Carlo simulations described above and porous microstructure properties from virtual 3D reconstruction of evolving electrode. The model predicts the discharge behavior of a Li-S cell in terms of discharge voltage over time. The occurrence of plateau is found to be caused by precipitation kinetics of Li<sub>2</sub>S. The experimental results exhibit capacity loss even at very low operating current densities. This must be attributed to explicit capacity fade mechanisms since transport losses are not significant at these operating conditions. Several experimentally argued capacity loss mechanisms have been studied in a simplified model framework to quantify the order of their influence. Li<sub>2</sub>S<sub>2</sub> precipitation and sulfur isolation are found to be dominant causes for capacity loss.

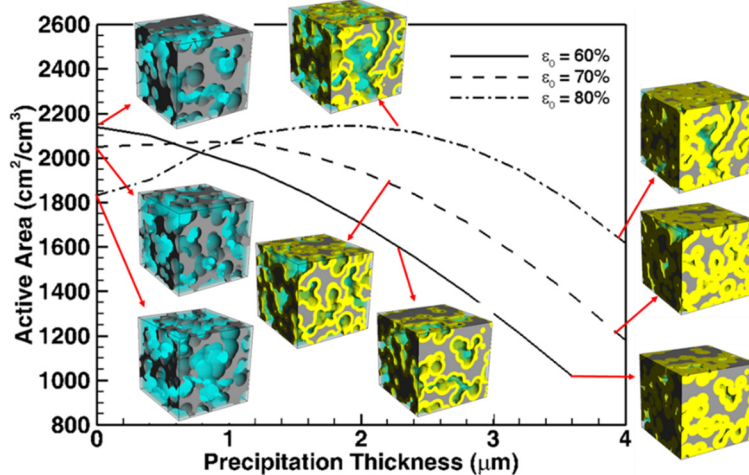


Figure V-345: Effect of Li<sub>2</sub>S film thickness on active area of the cathode frameworks with different porosity

The mechanical degradation of porous cathode induced by Li<sub>2</sub>S precipitation is studied at the single-pore level. The analysis of volume expansion during discharge of a lithium sulfur cell is conducted here by applying the Green-Lagrange strain to capture the large deformation. Maximum stress concentration is observed at sharp corners and they act as crack initiation points. Thin walls are also prone to rupture during the discharge process. Hence cathode microstructures with round shaped and thick pores are beneficial from the mechanical stability perspective.

## Chemistry at the Li metal Anode: SEI Reactions and Interactions with Soluble PS Species

The extreme reactivity of the Li-anode surface in contact with the electrolyte solution in Li-S batteries has been investigated using DFT and AIMD methods. From the electrolyte components used in Li-S batteries, the salt LiTFSI is much more reactive than typical solvents such as DOL and DME. Cleavage of the C-S or N-S bond was found as the starting point for all of the LiTFSI reduction pathways, the first one being the most thermodynamically favorable (Figure V-346). Eventually the salt becomes decomposed into multiple fragments. One of the most important products is LiF but other charged radical anions are derived from C, SO<sub>2</sub>, O, and CSN fragments that mostly become adsorbed onto the metal surface. None of the Li-S solvents tested (DOL and DME) were found to be decomposed during the entire simulation, whereas EC decomposes very quickly via sequential 4 or 2 electron mechanisms in agreement with previous analyses on lithiated silicon anodes and on pure Li surfaces. The primary method of Li<sub>2</sub>S<sub>8</sub> fragmentation away from the anode surface does not involve delithiation; however the most favorable pathway includes reaction of the lithiated PS with additional Li atoms

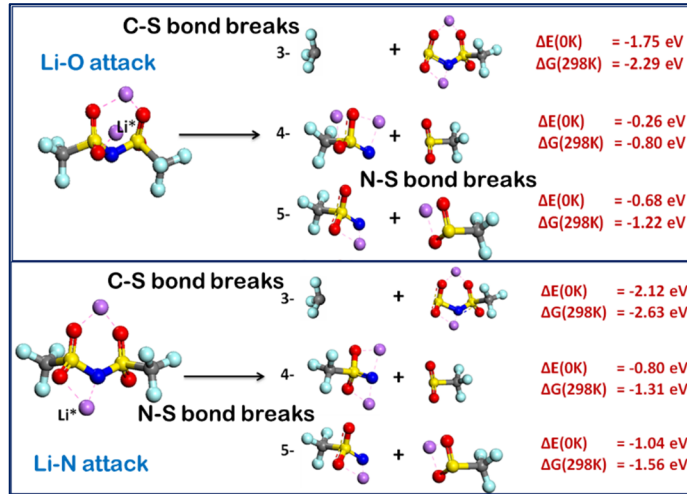


Figure V-346: DFT calculated LiTFSI most favorable decomposition mechanisms from interaction of a Li atom from the surface with a specific location. Top: a Li..O attack is shown leading to C-S and N-S bond breaking. Bottom: a Li..N attack is found favorable through C-S and N-S bond breakings. Color code: Li: purple, O: red, F: light blue, N: blue, S: yellow, C: grey

Figure V-346: DFT calculated LiTFSI most favorable decomposition mechanisms from interaction of a Li atom from the surface with a specific location. Top: a Li..O attack is shown leading to C-S and N-S bond breaking. Bottom: a Li..N attack is found favorable through C-S and N-S bond breakings. Color code: Li: purple, O: red, F: light blue, N: blue, S: yellow, C: grey

**Table V-12: PS reactivity at the anode: Reactions with Li in eV**

Reaction	Gas phase	Gas phase	EC solvent	EC solvent	DOL solvent	DOL solvent
	ΔE (0K)	ΔG (298K)	ΔE (0K)	ΔG (298 K)	ΔE (0K)	ΔG (298 K)
Li <sub>2</sub> S <sub>8</sub> +2Li→Li <sub>2</sub> S+Li <sub>2</sub> S <sub>7</sub>	-3.56	-3.43	-5.53	-5.39	-5.18	-4.85
Li <sub>2</sub> S <sub>8</sub> +2Li→Li <sub>2</sub> S <sub>2</sub> +Li <sub>2</sub> S <sub>6</sub>	-5.63	-5.38	-6.02	-5.92	-5.64	-5.51
Li <sub>2</sub> S <sub>8</sub> +2Li→Li <sub>2</sub> S <sub>3</sub> +Li <sub>2</sub> S <sub>5</sub>	-5.32	-5.17	-6.19	-6.09	-5.78	-5.65
Li <sub>2</sub> S <sub>8</sub> +2Li→2Li <sub>2</sub> S <sub>4</sub>	-6.95	-6.69	-6.28	-6.14	-6.15	-5.68

formation of a Li<sub>2</sub>S layer that was characterized by analyses of bond distances and atomic charges. The decomposition mechanisms of PS on the surface are a function of the initial positions of each PS in relation to the surface. Three different initial positions were tested with PS molecules located close to the surface. The reactions were analyzed based on the time evolution of the chain size (Figure V-347) and also on the time evolution of the charge of each fragment. In all cases, it was found that one chain containing five S atoms is formed from the decomposition of the initial chain. S<sub>5</sub> later decomposes into S<sub>3</sub> + S<sub>2</sub>, and S<sub>3</sub> into S<sub>2</sub> + S. The mechanism for a S<sub>2</sub> dimer decomposition is the slowest and also is always the last step for the complete PS decomposition. Although the tendency is to reduce the chain size, some mechanisms can involve reconstruction of the PS short chains such as S<sub>3</sub>. Charge stabilization towards a value of ~ -2 occurred for individual sulfur atoms, indicating the end of the reaction decomposition of one PS molecule. This agrees with an accumulation of n charges (positive) on part of the lithium atoms and with the time evolution of bond distances. Breaking of S-S bonds does not necessarily indicate formation of two different PS species, and in the majority of the cases there is a cluster formation, where chains share some Li atoms with the anode surface.

in gas phase or in presence of the solvent, with four different fragmentation modes found having similar (very favorable) ΔGs of reaction (Table V-12). In contact with the anode surface, the long-chain PS species is highly decomposed despite the solvent used or the PS initial geometry (ring or linear), resulting in the

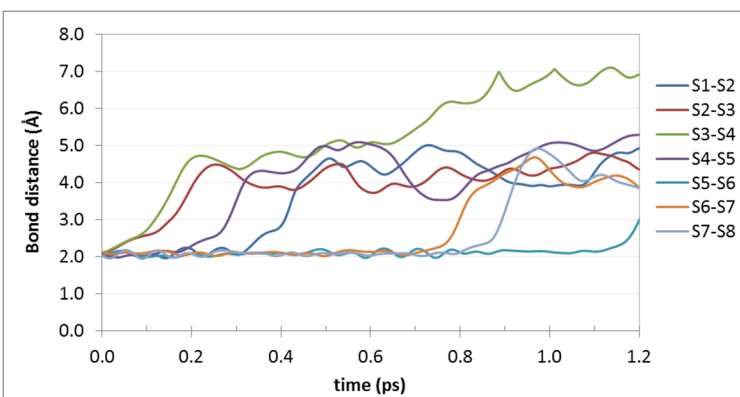


Figure V-347: Time evolution of S-S bond distances on one PS molecule illustrating PS decomposition at the model Li anode surface

crystals.

The process of  $\text{Li}_2\text{S}$  (111) formation on graphene is summarized in Figure V-348. While a single  $\text{Li}_2\text{S}$  molecule adsorbs on graphene first with relative small adsorption energy, the adsorbed  $\text{Li}_2\text{S}$  molecule film interacts with graphene via strong covalent Li-C bonds. When more  $\text{Li}_2\text{S}$  molecules are introduced to pre-adsorbed graphene Structure-I and Structure-II are observed. In Structure-I, the Li-S bond length is 0.27 Å shorter than the Li-S bond in the  $\text{Li}_2\text{S}$  crystal, and the length of the short S-S bridge is 0.35 Å shorter than the S-S distance (4.05 Å) in a typical  $\text{Li}_2\text{S}$  (110) layer. The variation of these geometric parameters is attributed to the lattice parameter mismatch between graphene and the  $\text{Li}_2\text{S}$  (110) layer. On the other hand, the S atoms arrangement in Structure-II is hexagonal, which is similar to that in the  $\text{Li}_2\text{S}$  (111) layer. Each S atom coordinates with four Li atoms, and the S atom at the center of the S hexagon disappears compared to that in a  $\text{Li}_2\text{S}$  (111) surface. Hence Structure-II is a defective  $\text{Li}_2\text{S}$  (111) surface with S vacancies. Figure V-348 illustrates the adsorption energy  $\Delta E$  of adding one  $\text{Li}_2\text{S}$  to the pre-adsorbed graphene layer  $(\text{Li}_2\text{S})_{m-1}$  to form  $(\text{Li}_2\text{S})_m$ . When Structure-I is formed, a  $\Delta E$  of  $\sim -4$  eV is released with respect to the single molecule adsorption, and  $\sim 0.5$  eV more negative for Structure-II, while forming the complete  $\text{Li}_2\text{S}$  layer is a very exothermic process. Hence, it can be inferred that the pre-adsorbed single  $\text{Li}_2\text{S}$  molecule is the seed for the formation of a  $\text{Li}_2\text{S}$  layer on graphene. An important point is the initial nucleation of the  $\text{Li}_2\text{S}$  species in the real environment defined by the electrolyte solution surrounding the C-S cathode. Our AIMD simulations revealed that stable  $\text{Li}_2\text{S}$  molecules can be formed at the very initial stages of  $\text{S}_8$  reduction in the electrolyte phase or close to the carbon pore (Figure V-349). The calculated  $\text{Li}_2\text{S}$  bond length is 2.11 Å; such length is reached and keeps stable in the DOL electrolyte phase.  $\text{Li}_2\text{S}$  molecules can also be formed at the carbon edges. This is because Li ions are also attracted to those locations and the reduction process takes place.

## Cathode Chemistry: Effects of the Carbon Microporosity

An important question is how the various S/C loading ratios may affect battery performance. It is observed that the high S/C ratio causes dramatic capacity fade. One possible reason for such capacity fade is the deposition of  $\text{Li}_2\text{S}$  both on C and on S surfaces leading to isolation of S particles and subsequent capacity reduction. First we carried out a DFT analysis aimed to investigate the  $\text{Li}_2\text{S}$  deposition on carbon surfaces and compared the results with those of growth of  $\text{Li}_2\text{S}$

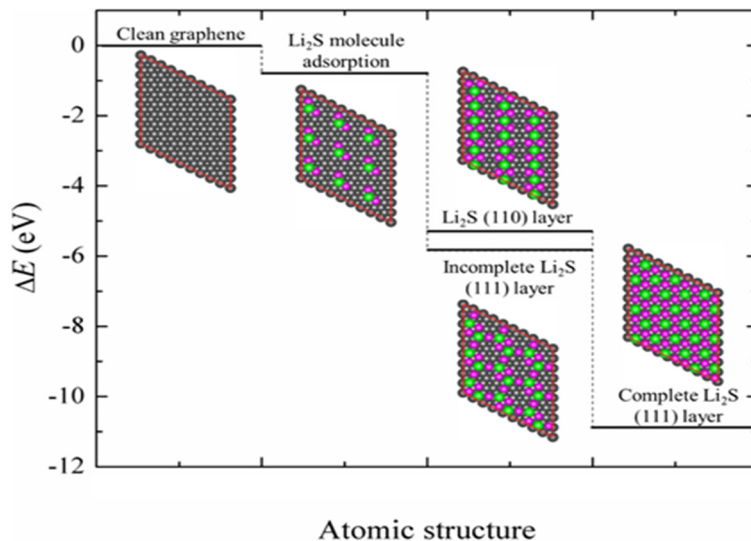


Figure V-348: Energy profile of  $\text{Li}_2\text{S}$  (111) layer formation on graphene calculated with DFT within the vdW-D3 approach. Color code: Green, violet and grey spheres represent S, Li and C atoms, respectively

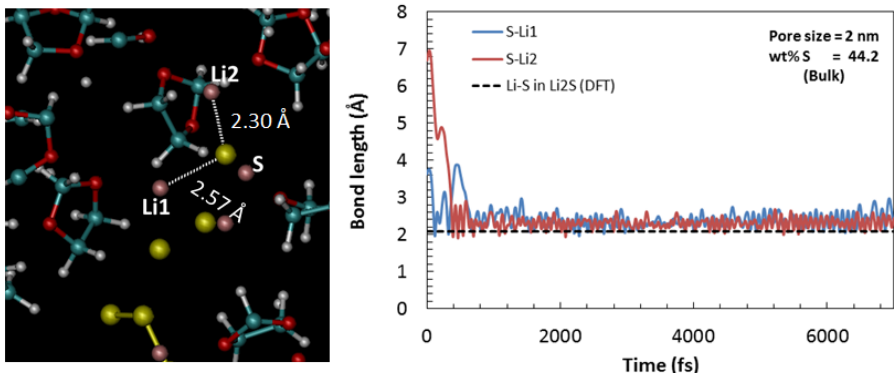


Figure V-349: Formation of  $\text{Li}_2\text{S}$  in the electrolyte phase. The snapshot depicts the  $\text{LiS}$  bond distances during formation of a  $\text{Li}_2\text{S}$  molecule from reduction of a  $\text{S}_8$  ring. The  $\text{LiS}$  bond distances are followed in the graph as a function of time showing evidence of stable  $\text{LiS}$  bonds at  $\sim 400$  and  $600$  fs, respectively. Color code: S: yellow, Li: purple, O: red, H: white, C: light blue

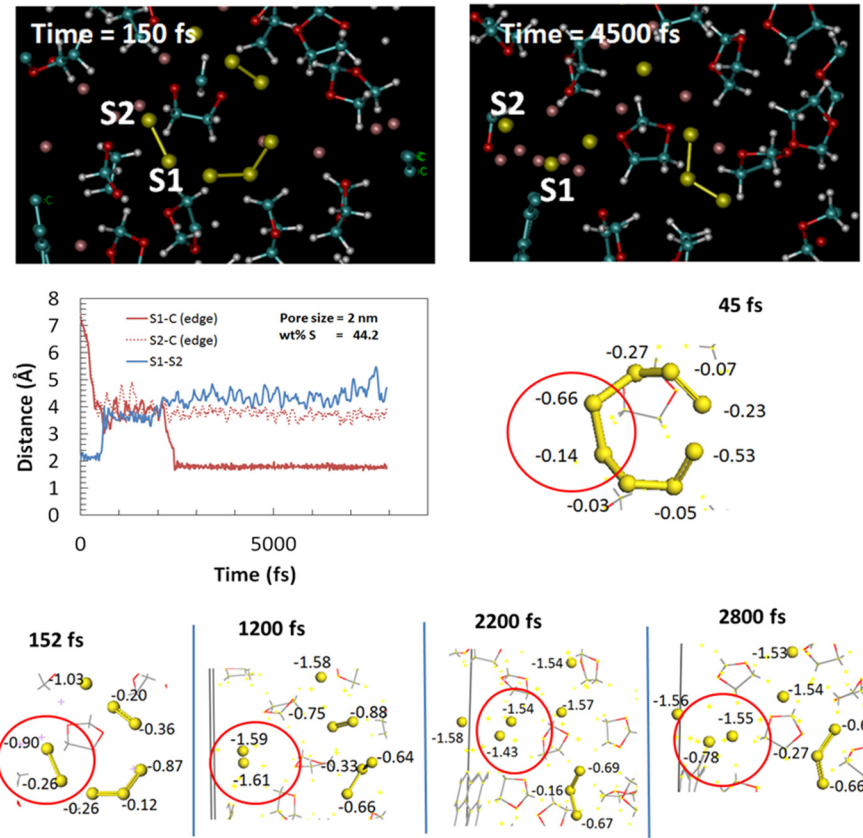


Figure V-350:  $\text{S}_8$  dissolution in the electrolyte phase near the opening of a  $2\text{ nm}$  carbon pore. Top: Snapshots illustrating the initial and final fragmentation of a  $\text{S}_8$  ring. At  $4500$  fs  $\text{S}_3^{2-}$  is still intact. The other  $\text{S}$  dianions are paired with  $\text{Li}$  ions forming short-chain PS species. Bottom: Time evolution of the  $\text{S-S}$  and  $\text{S-C}$  distance of a  $\text{S}_2$  radical anion ( $\text{S}$  atoms labelled  $\text{S}2$  and  $\text{S}1$ ). The snapshots depict Bader charges for the  $\text{S}$  atoms during the reduction process (Li ions are not shown). Formation of several radical anions ( $\text{S}^-$ ,  $\text{S}_2^{2-}$ ,  $\text{S}_3^{2-}$ ) shortly becoming dianions is illustrated. Color code: S: yellow, Li: pink, C: blue, O: red, H: white

variety of materials that hold affinity with  $\text{S}$ , thus acting as potential additional retention of the long chain PS species. As an illustration, Figure V-352 shows

Following the time evolution of the location of the  $\text{Li}$  ions with respect to the electrolyte phase and to the carbon pore, it was found that most of the  $\text{Li}$  ions are located (together with  $\text{S}$  anions) in the vicinity of the C pore edges. This location would favor the nucleation of the solid  $\text{Li}_2\text{S}$  on the carbon surfaces and on the  $\text{Li}_2\text{S}$  crystals as discussed above.

One of the most unwanted consequences of the sulfur lithiation is the dissolution of the long-chain PS species. Our C-S composite material contains two ranges of porosities: one at the micron scale, and another at the nanoscale. We examined the role of the C nanopores in the retention of PS species in the vicinity of the cathode. It was found that pores smaller than  $1.5\text{ nm}$  can double the adsorption energy of long-chain PS species with respect to the adsorption on a graphene sheet (Figure V-351). This suggests that tuning the carbon microstructure it may be possible to significantly improve the battery performance. In addition, our computational studies have also screened a

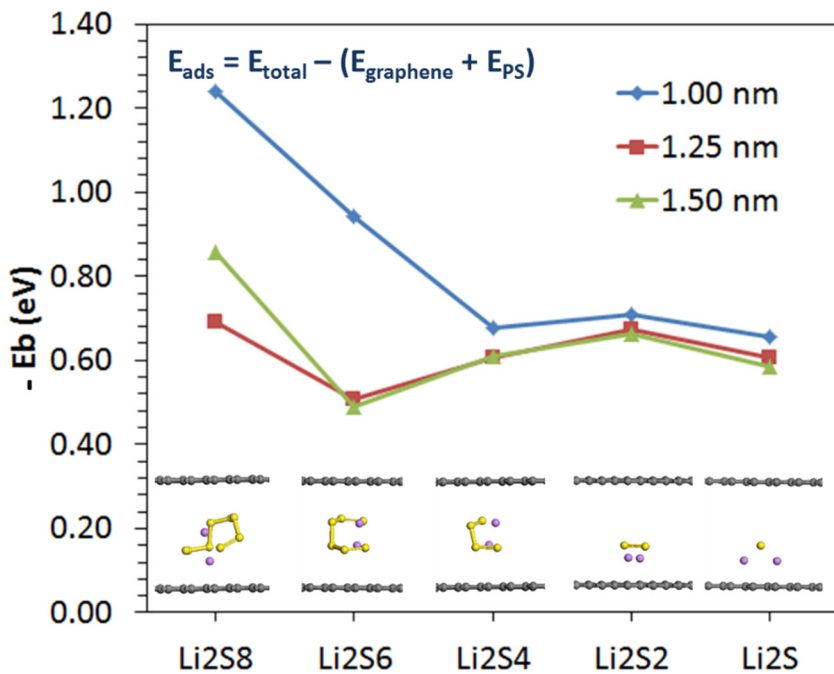


Figure V- 351: Adsorption energies of PS species inside carbon pores of the indicated diameters (1; 1.2; and 1.5 nm)

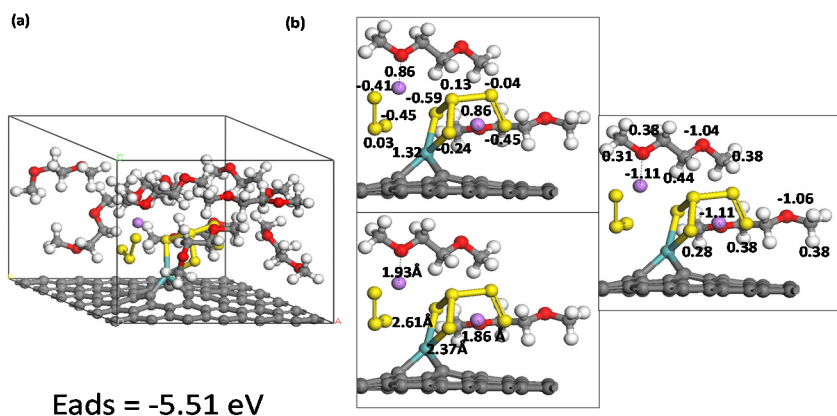


Figure V- 352: Adsorption of Li<sub>2</sub>S<sub>8</sub> dissolved in DME over Mo-doped graphene layers.  
Color code: C: grey, S: yellow, Li: purple, Mo: blue, O: red

order of their influence, and have suggested that Li<sub>2</sub>S precipitation and sulfur isolation are dominant causes for capacity loss. In addition, our studies demonstrated that the polysulfide shuttle and migration to the anode causes the deposition of Li<sub>2</sub>S on the Li metal which does not impede the further reaction of the salt species and formation of SEI layer. Significant deformation of the Li metal surface is caused by the formation of the Li<sub>2</sub>S film. The C nanoporosity has been shown to have a good retention of the long PS species; however additional materials have been computationally tested that favor the retention of long PS species at the cathode side. Current experimental tests are being carried out. We are also investigating the products from LiNO<sub>3</sub> oxidation at the anode side, and plan to investigate its effects at the C-S cathode as well.

## FY 2015 Publications/Presentations

1. "Addressing Internal "Shuttle" Effect: Electrolyte Design and Cathode Morphology Evolution in Li-S Batteries DE-EE-0006832", P. B. Balbuena, BMR meeting, LBNL, Berkeley, January 22, 2015.
2. Z. Liu, D. Hubble, P. B. Balbuena, and P. P. Mukherjee, "Adsorption of Insoluble Polysulfides Li<sub>2</sub>S<sub>x</sub> (x = 1, 2) on Li<sub>2</sub>S Surfaces," Phys. Chem. Chem. Phys., 17, 9032-9039, (2015).

the great increase in adsorption energy (-5.51 eV compared to -1.25 eV in the smallest carbon pore) of a PS Li<sub>2</sub>S<sub>8</sub> linear species dissolved in DME in contact with a Mo-substituted graphene layer. Mo was selected because of its strong affinity with S. Experimental and further computational tests are in progress of this and other materials.

Finally, we are also investigating the role of LiNO<sub>3</sub> as an oxidant and its influence both on the anode and cathode side.

## Conclusions and Future Directions

During the first year of our grant we have done significant progress especially in the refining of the synthesis of our C-S composite material, understanding of the Li-S chemistry both at anode and cathode, and the effect of the cathode morphology evolution on battery performance. Several experimentally argued capacity loss mechanisms have been studied through a simplified model framework to quantify the

3. Luis E. Camacho-Forero, Taylor W. Smith, Samuel Bertolini, and Perla B. Balbuena, "Reactivity at the Lithium-Metal Anode Surface of Lithium-Sulfur Batteries," *J. Phys. Chem. C*, under review.
4. Arthur A. Dysart, Juan C. Burgos, Aashutosh Mistry, Chien-Fan Chen, Zhixiao Liu, Perla B. Balbuena, Partha P. Mukherjee, Vilas G. Pol, "Towards Next Generation Lithium-Sulfur Batteries: Non-Conventional Carbon Compartments/Sulfur Electrodes and Multi-scale Analysis," submitted.

## V.J Lithium-Air Batteries

### V.J.1 Rechargeable Lithium-Air Batteries (PNNL)

#### Objectives

- Develop stable electrolyte and oxygen evolution reaction (OER) catalysts to reduce the charging overvoltage of lithium (Li)-air batteries and improve their cycling stability.

#### Technical Barriers

- During the discharging process, the reduced oxygen species attack all components in a Li-O<sub>2</sub> battery and significantly limit the reversibility of rechargeable Li-O<sub>2</sub> batteries.
- The overvoltage during the charging process of a Li-O<sub>2</sub> battery is too high and leads to low Coulombic efficiency of the batteries.

#### Technical Targets

- Develop electrolytes that are stable during the oxygen reduction reaction (ORR) and OER.
- Improve the stability of air electrodes.
- Integrate new electrolytes and catalytic air electrodes in Li-O<sub>2</sub> batteries.

#### Accomplishments

- Developed in situ grown ZnCo<sub>2</sub>O<sub>4</sub>/single-walled carbon nanotube (SWCNT) composite air electrode material with well protected carbon surface, and systematically investigated the factors affecting the cycle life of Li-O<sub>2</sub> batteries with such nanoparticle catalyst.
- Developed a binder-free air electrode based on a metal oxide catalyst on a carbon cloth with special treatment. Achieved 120 stable cycles for Li-O<sub>2</sub> batteries at a capacity above 1200 mAh g<sup>-1</sup> and 140 cycles at above 1000 mAh g<sup>-1</sup> under the full discharge/charge protocol.
- Demonstrated that highly concentrated LiTFSI-dimethoxyethane (DME) electrolytes significantly improved the stability of Li-O<sub>2</sub> batteries.
- Revealed the fundamental mechanism of enhancement of Li-O<sub>2</sub> stability by using concentrated electrolytes.

---

#### Introduction

Li-O<sub>2</sub> batteries have an ultra-high theoretical specific energy (~5200 Wh/kg when the weights of Li and O<sub>2</sub> are included), and are expected to have a practical specific energy of around 800 Wh/kg, which is approximately four times of that of state-of-the-art Li-ion batteries (~200 Wh/kg). However, development of rechargeable Li-O<sub>2</sub> batteries faces significant challenges including decomposition of electrolytes, large overvoltage that occurs during charging, design of cathode materials with high capacity and stability, and protection of the Li metal anode. More importantly, highly reactive oxygen species (O<sub>2</sub><sup>•</sup>, LiO<sub>2</sub>, O<sub>2</sub><sup>2-</sup>, LiO<sub>2</sub><sup>-</sup>, and Li<sub>2</sub>O<sub>2</sub>) are generated on the air electrode surface via the ORR) during the discharge process of a Li-O<sub>2</sub> battery, and these species attack every components in Li-O<sub>2</sub> batteries and significantly limit the reversibility of Li-O<sub>2</sub> batteries. Therefore, the chemical and electrochemical stability of all Li-O<sub>2</sub> battery components, including the electrolyte solvent, electrolyte salt, cathode material (typically carbon-based), and binder, needs to be reevaluated in an O<sub>2</sub>-rich environment. Novel catalysts also need to be developed to reduce the overvoltage during oxygen evolution reactions to minimize electrolyte decomposition and enhance the cycling stability of Li-O<sub>2</sub> batteries.

#### Project Details

Tien Duong (DOE BMR Program Manager)

Recipient: PNNL

Ji-Guang Zhang (PNNL – PI)

902 Battelle Boulevard

Richland, WA 99354

Phone: 509-372-6515; Fax: 509-375-2186

E-mail: [jiguang.zhang@pnnl.gov](mailto:jiguang.zhang@pnnl.gov)

Wu Xu (PNNL – Co-PI)

902 Battelle Boulevard

Richland, WA 99354

Phone: 509-375-6934; Fax: 509-375-2186

E-mail: [wu.xu@pnnl.gov](mailto:wu.xu@pnnl.gov)

Start Date: October 2012

Projected End Date: September 2016

## Approach

### Innovative Approach:

- Develop new electrolytes that are stable against the reactive reduced-oxygen species.
- Improve the stability of carbon-based air electrodes with selected OER catalysts to encapsulate the carbon surface so as to minimize carbon oxidation and improve the cycling stability of the rechargeable Li-O<sub>2</sub> batteries.
- The stability of the electrolytes and coated air electrodes during discharge-charge processes of Li-O<sub>2</sub> batteries will be systematically investigated to improve the performance of Li-O<sub>2</sub> batteries.

## Results

### *In Situ* Grown ZnCo<sub>2</sub>O<sub>4</sub> on Single Walled Carbon Nanotubes as Air Electrode Materials

We used a facile hydrothermal method to synthesize the ZnCo<sub>2</sub>O<sub>4</sub> (ZCO) catalyst *in situ* on the surface of SWCNTs, thus forming a novel catalyst/carbon composite (refer to ZCO/SWCNTs). After careful characterizations using micro X-ray diffraction (micro-XRD), scanning electron microscopy (SEM), energy-dispersive X-ray spectroscopy (EDX), and transmission electron microscopy (TEM), we found that the nano-sheet-assembled ZCO microspheres were entangled with SWCNTs, and ultrathin ZCO film also were formed on the surface of SWCNTs (see Figure V- 353). This structure could fully utilize the electrocatalytic effect of ZCO in the ORR and OER processes during the discharge and charge cycles of Li-O<sub>2</sub> batteries.

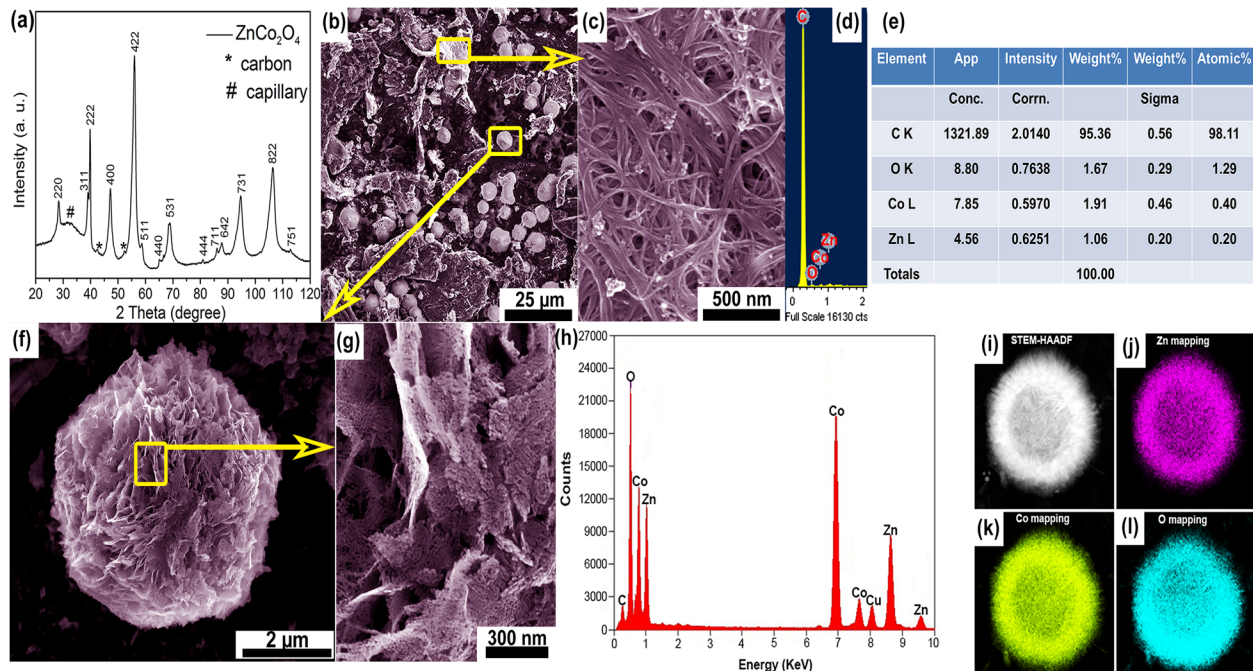
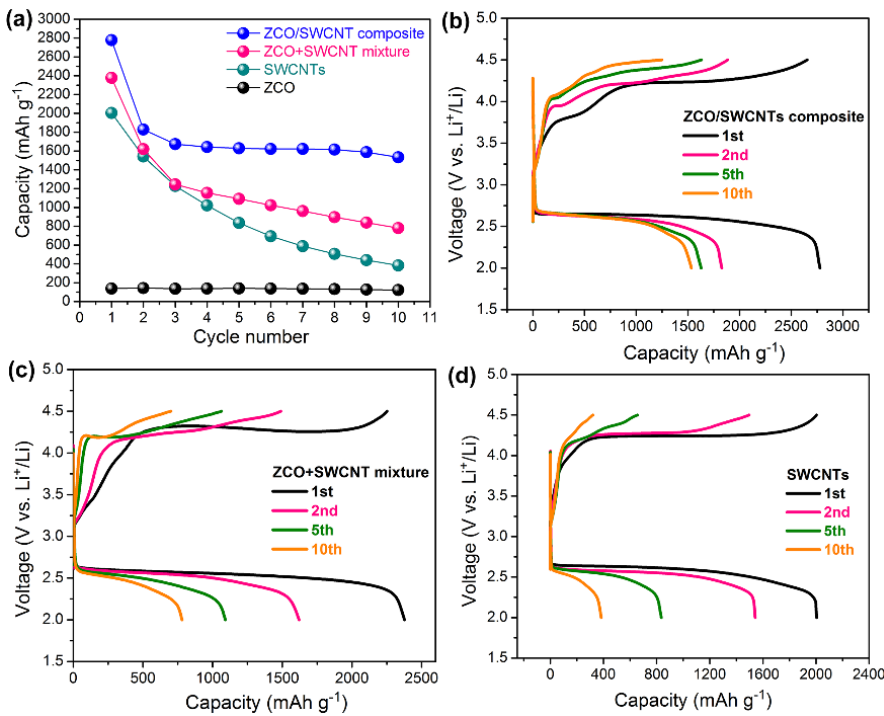


Figure V- 353: a) XRD pattern of ZCO/SWCNTs composite powders. b, c, f, g) SEM images of ZCO/SWCNTs composite powders from low to high magnifications. d) EDX spectrum from the selected area of SWCNTs in ZCO/SWCNTs composite. e) The corresponding weight and atomic percentage from the selected surface area of SWCNTs in ZCO/SWCNTs composite. h) EDX microanalysis on a selected area of a ZCO microsphere. i-l) Corresponding TEM image and EDX mapping images of the ZCO microsphere: selected TEM area i), Zn j), Co k), and O l)

To demonstrate the feasibility of ZCO as an efficient ORR and OER catalyst, the ZCO/SWCNTs composite fabricated by in situ growth method were used as the air electrode in a Li-O<sub>2</sub> cell (type CR2032). Li foil was used as the anode, a glass fiber (GF-B) was used as the separator, and 1.0-M lithium trifluoromethanesulfonate (LiTf) in tetra(ethylene glycol) dimethyl ether (tetraglyme) was used as electrolyte. The cell was cycled at 0.1 mA cm<sup>-2</sup> between 2.0 and 4.5 V (i.e. the full discharge and charge cycling) in airtight Teflon containers filled with ultrahigh purity O<sub>2</sub> at 1 atm pressure. To better evaluate the synergistic effect of both ZCO and SWCNTs, other comparable electrodes, including a ZCO and SWCNTs mixture (prepared by ex situ mixing ZCO powders with SWCNTs), SWCNTs alone, and ZCO powders alone, also were fabricated and characterized under the same measurement parameters.



**Figure V- 354:** a) Comparison of cycling performance of Li-O<sub>2</sub> cells with ZCO/SWCNTs composite, ZCO+SWCNT mixture, sole SWCNTs, and sole ZCO electrodes. b-d) The corresponding voltage profiles of ZCO/SWCNTs composite electrodes b), ZCO+SWCNT mixture electrodes c), and sole SWCNTs electrodes d), respectively, at a current density of 0.1 mA cm<sup>-2</sup> and cycled under full discharge/charge protocol between 2.0 and 4.5 V for first 10 cycles

ZCO/SWCNTs composites have synergistic effects from ZCO and SWCNTs because of the intimate contacts of ZCO and SWCNTs. The coverage of ultrathin ZCO films on the SWCNT surface protects SWCNTs from direct attack by superoxide radical anion (O<sub>2</sub><sup>•-</sup>) generated during ORR; therefore, the electric conductivity of the air electrode is enhanced by SWCNTs.

The effect of the cycling protocol on the performance of Li-O<sub>2</sub> batteries was investigated. The batteries were tested with a capacity limitation of 800 mAh g<sup>-1</sup> (on the basis of the total mass of ZCO/SWCNTs composite for ZCO-based electrodes or the mass of SWCNTs for control electrodes) at 0.1 mA cm<sup>-2</sup> to evaluate the cycle life of Li-O<sub>2</sub> batteries with and without ZCO catalyst (see Figure V- 355). The onset of ORR is reduced from ~4.3 V to ~3.4 V for the ZCO/SWNT composite electrode, which is a reduction of ~0.9 V. Even at the end of the charge process (800 mAh g<sup>-1</sup>), the ZCO/SWCNTs electrode still exhibits an overpotential of ~0.54 V below that of the SWCNT-alone electrode, thus demonstrating the efficient OER catalytic activity of ZCO in Li-O<sub>2</sub> batteries. At the same time, the ZCO/SWCNTs composite electrode retains almost the same discharge/charge voltage profiles for 50 cycles and leads to quite stable cycling performance at constant capacity of 800 mAh g<sup>-1</sup>-ZCO/SWCNT within the cutoff voltages. In contrast, the capacity of the SWCNT-alone electrode drops sharply after 25 cycles.

As shown in Figure V-354, among the cells with the air electrodes described above, the cell with the in situ grown ZCO/SWCNT composite exhibits the highest first discharge capacity (2750 mAh g<sup>-1</sup> based on the total weight of ZCO and SWCNTs in the air electrode, or 3667 mAh g<sup>-1</sup> based on the weight of SWCNTs). It also possesses more stable cycling capability and higher reversible capacity (~1500 mAh g<sup>-1</sup>-ZCO/SWCNTs at the tenth cycle). In contrast, the ex situ mixture of ZCO+SWCNT and SWCNT alone electrodes show fast capacity decay. More importantly, compared to the ex situ blended ZCO+SWCNTs mixture; the in situ

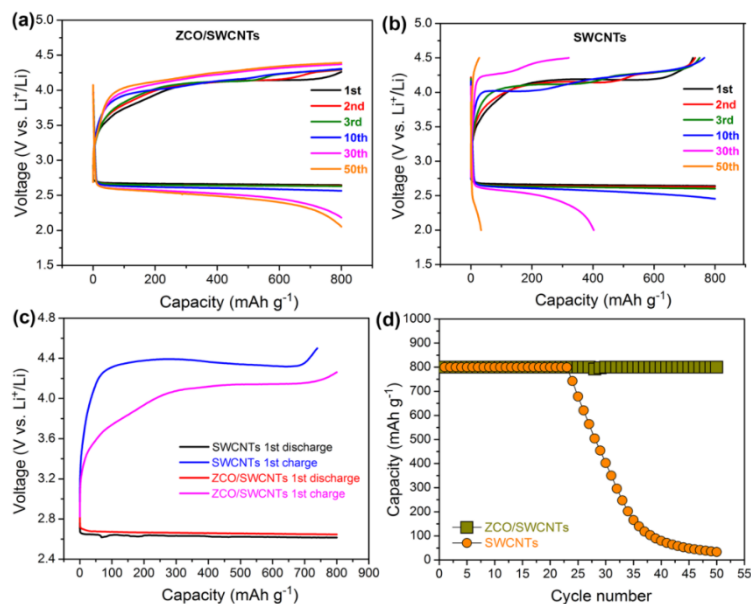


Figure V-355: Voltage profiles of selected cycles for ZCO/SWCNTs composite a) and sole SWCNTs b) electrodes at a current density of 0.1 mA cm<sup>-2</sup> under a capacity-limited cycling protocol with the controlled capacity of 800 mAh g<sup>-1</sup>. c) Comparison of the first discharge/charge curves for ZCO/SWCNTs composite and SWCNTs. d) The corresponding cycling performance of ZCO/SWCNTs composite and SWCNTs for 50 cycles.

remaining and a more extensive corrosion layer. These results reveal that ZCO/SWCNT composites catalyzed air electrodes can enhance the stability of Li-metal anodes, resulting in the improved Li-O<sub>2</sub> battery performance.

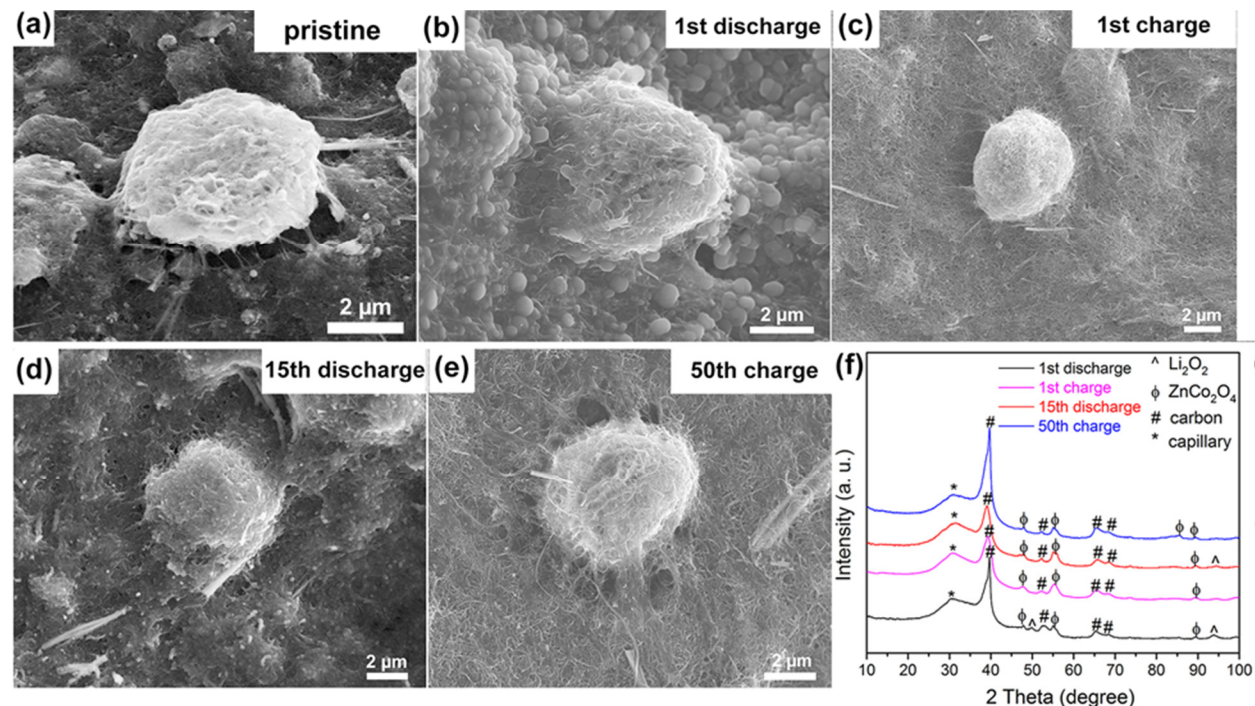


Figure V-356: SEM images of ZCO/SWCNT composite electrodes at different states: a) pristine, b) after the first discharge, c) after the first charge, d) after the 15<sup>th</sup> discharge, and e) after the 50<sup>th</sup> charge. f) The corresponding XRD patterns of these cycled ZCO/SWCNTs composite electrodes

The cycled air electrodes were analyzed by SEM, micro-XRD, and XPS to understand the enhanced cycling stability of the ZCO/SWCNT composite electrodes developed in this work. The surface morphology of ZCO/SWCNT composite electrodes after the 50<sup>th</sup> charge (Figure V-356e) is very close to that of the pristine electrode (Figure V-356a). The morphology and size of the ZCO microspheres remained very similar even after 50 cycles, confirming the excellent stability of ZCO catalyst during electrochemical reactions of oxygen reduction and evolution. The SEM images of cycled Li-metal anodes also showed that more retention of the compact Li metal layer and a thinner corrosion layer are observed for the Li-metal anodes from cycled coin cells with ZCO/SWCNT composite air electrodes, compared to the Li-metal anodes from the cells based on SWCNT alone, which has less compact Li metal

### Binder-Free Air Electrode Based on Metal Oxide Catalyzed Carbon Cloth

A binder-free air electrode based on metal oxide catalyst on carbon cloth (CC) was synthesized. The obtained binder-free catalytic air electrode was tested in Li-O<sub>2</sub> coin cells with 1-M LiTf-tetraglyme electrolyte

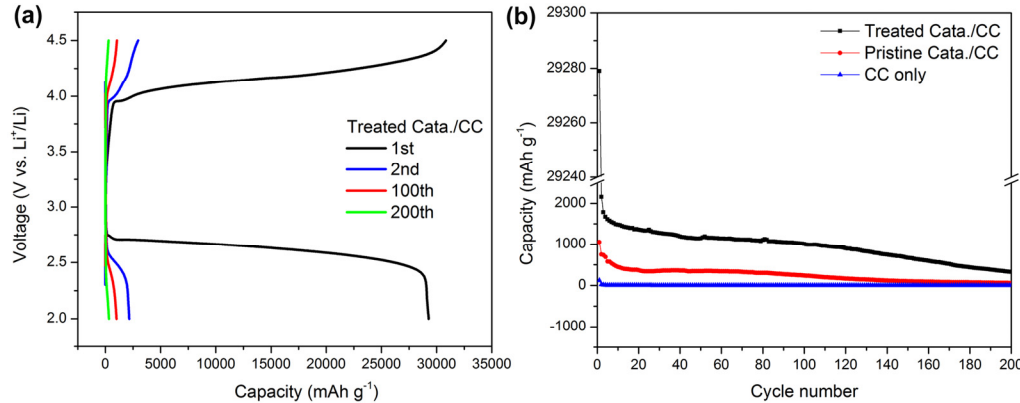


Figure V-357: (a) Voltage profiles of treated catalyst/carbon cloth air electrode in Li-O<sub>2</sub> coin cells at selected cycles. (b) Cycling stability of Li-O<sub>2</sub> coin cells with air electrodes of treated catalyst/CC, pristine catalyst/CC, and pure carbon cloth under full discharge/charge (2.0~4.5 V) cycling

using the full discharge/charge (2.0~4.5 V) protocol, and compared with the pristine catalyst/CC and pure CC air electrodes. The treated catalyst/CC electrode showed extremely high discharge and charge capacities at the first cycle (Figure V-357). Although the capacities at the second cycle were significantly lower, the treated catalyst/CC electrode still showed stable cycling at a capacity >1200 mAh g<sup>-1</sup> for 120 cycles and 1000 mAh g<sup>-1</sup> for 140 cycles. As a comparison, the pristine catalyst/CC electrode showed stable cycling at a capacity of ~300 mAh g<sup>-1</sup>, which is significantly lower than the treated catalyst/CC air electrode.

### Enhanced Cycling Stability of Rechargeable Li-O<sub>2</sub> Batteries Using High Concentration Electrolytes

We further investigated the effect of Li salt concentration on the cycling performance of rechargeable Li-O<sub>2</sub> batteries with CNT/PVDF air electrodes. The compound lithium bis(trifluoromethanesulfonyl)-imide (LiTFSI) in 1,2-dimethoxyethane (DME) with three salt concentrations (1 M, 2 M, and 3 M) were used. The cells were cycled at 0.1 mA cm<sup>-2</sup> under a capacity-limited (1000 mAh g<sup>-1</sup>) protocol. As shown in Figure V-358, the discharge capacity of the cells with 1-M and 2-M electrolytes can only maintain at 1000 mAh g<sup>-1</sup> for 2 and 8 cycles within the given voltage range (2 to 4.5 V), and finally decrease to below 100 mAh g<sup>-1</sup> after 19 and 29 cycles. In contrast, the Li-O<sub>2</sub> cells with 3-M electrolyte were able to maintain very stable discharge capacity at 1000 mAh g<sup>-1</sup> for 55 cycles. When the cells using electrolytes with different concentration were tested at a

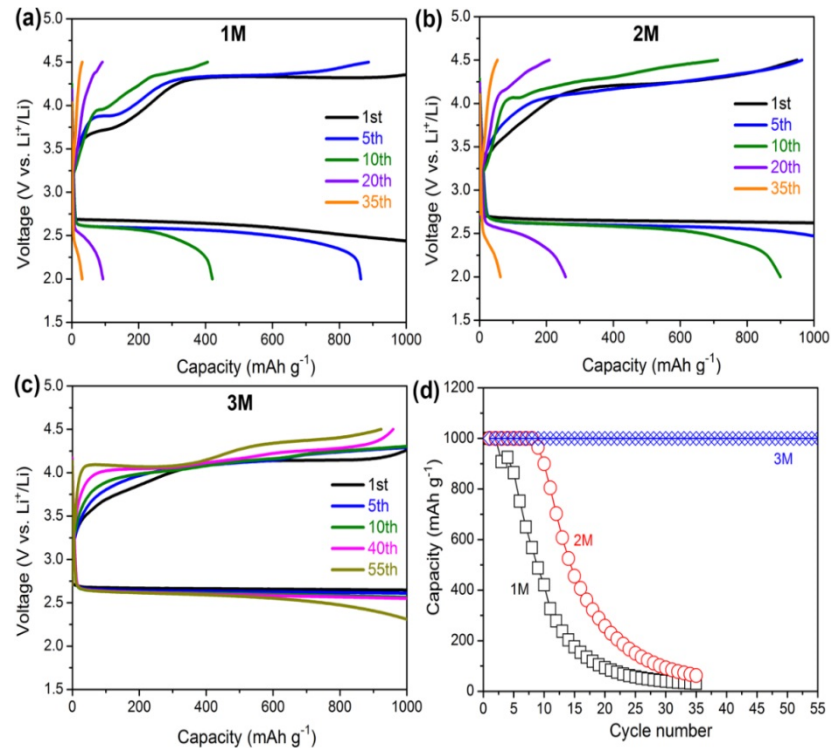


Figure V-358: Electrochemical performance of Li-O<sub>2</sub> cells using electrolyte with three salt concentrations cycled at a capacity (1000 mAh g<sup>-1</sup>) limited protocol between 2.0 and 4.5 V at 0.1 mA cm<sup>-2</sup>. Voltage profiles of the cells using LiTFSI-DME electrolytes with salt concentrations of 1 M a), 2 M b), and 3 M c). d) The cycling stability of these three cells

full discharge/charge protocol after stabilization (see Figure V- 359), the cells with all three electrolytes exhibited a similar first-cycle discharge capacity of  $\sim$ 1600 to 1840 mAh g $^{-1}$ , and also demonstrated similar sharp decreases in capacity over the first 10 cycles. The capacities at the tenth cycle are about 500, 700, and 800 mAh g $^{-1}$  for the cells with 1-M, 2-M and 3-M electrolytes, respectively. After that, the capacity of the cell with 1-M electrolyte continued to show a rapid capacity decrease over the next 10 cycles to less than 120 mAh g $^{-1}$ . As for the cells with the 2-M electrolyte, the capacity decreases slowly but monotonously from the 10<sup>th</sup> to the 40<sup>th</sup> cycle to about 250 mAh g $^{-1}$ . In contrast, the cells with the 3-M electrolyte exhibit a stable cycle behavior in the next 30 cycles and have a capacity retention at approximate 650 mAh g $^{-1}$  after 40 cycles. We demonstrated that the high salt concentration (i.e. 3-M) electrolyte enhances the cycling stability of Li-O<sub>2</sub> cells although they still exhibit fast capacity loss in the first 10 cycles. After 40 cycles, the resistance values of these Li-O<sub>2</sub> cells are in the order of 1 M > 2 M >> 3 M. The highly concentrated electrolyte (i.e., 3-M) leads to the lowest internal resistance in Li-O<sub>2</sub> cells after cycling, which is indicative of the fact that the high concentration electrolyte is much more stable during discharge/charge cycles.

As shown in Figure V- 360, the electrolytes with smaller salt concentrations (1 M and 2 M) led to a large amount of toroidal shaped nanostructured particles in the air electrode after 40 cycles, which are discharged products including Li<sub>2</sub>O<sub>2</sub> and LiOH, and exhibited more severe corrosion to the Li-metal anode and result in a thicker surface layer. In contrast, the 3-M concentrated electrolyte led to much cleaner surface and morphology of the air electrode ad showed good stability toward Li metal.

Density functional theory was adopted to calculate the molecular energies, the Mullikan charge of the pure DME and the Li $^{+}$ -(DME)<sub>n</sub> solvates, and the chemical reaction energies of DME solvent molecules or Li $^{+}$ -(DME)<sub>n</sub> solvates present in the LiTFSI-DME electrolytes with the superoxide radical anion O<sub>2</sub> $^{\cdot-}$ . The 3-M LiTFSI-DME electrolyte, which contains only 1-M Li $^{+}$ <sub>2</sub>-(DME)<sub>3</sub> solvate, shows significantly enhanced electrochemical oxidation stability at the air cathode. However, in the 1-M and 2-M LiTFSI-DME electrolytes, there exist 1-M Li $^{+}$ -(DME)<sub>2</sub> solvate and a large amount of pure DME. The DME molecule has the highest energy of the highest occupied molecular orbital energy, thus it has poor electrochemical oxidation stability.

Therefore, the Li-O<sub>2</sub> cells with the 1-M and 2-M electrolyte have poor cycling stability. Figure V- 361 shows the calculated Gibbs activation barriers for the reaction of O<sub>2</sub> $^{\cdot-}$  with the C-H bond scission from CH<sub>2</sub> groups in the DME, Li $^{+}$ -(DME)<sub>2</sub>, and Li $^{+}$ <sub>2</sub>-(DME)<sub>3</sub>, respectively. The Gibbs activation barrier increases from 152 kJ mol $^{-1}$  for pure DME without coordinating Li $^{+}$  to 184 kJ mol $^{-1}$  for Li $^{+}$ -(DME)<sub>2</sub> and 191 kJ mol $^{-1}$  for Li $^{+}$ <sub>2</sub>-(DME)<sub>3</sub>. The computational results indicate that the C-H bond scission of a DME molecule becomes more difficult when it coordinates with Li $^{+}$  ions, or the DME molecule is more stable under high Li $^{+}$  coordination conditions. Therefore, the highly concentrated LiTFSI-DME electrolytes in Li-O<sub>2</sub> systems can significantly mitigate electrolyte decomposition and stabilize with reduced oxygen intermediates, resulting in considerably enhanced cycling stability.

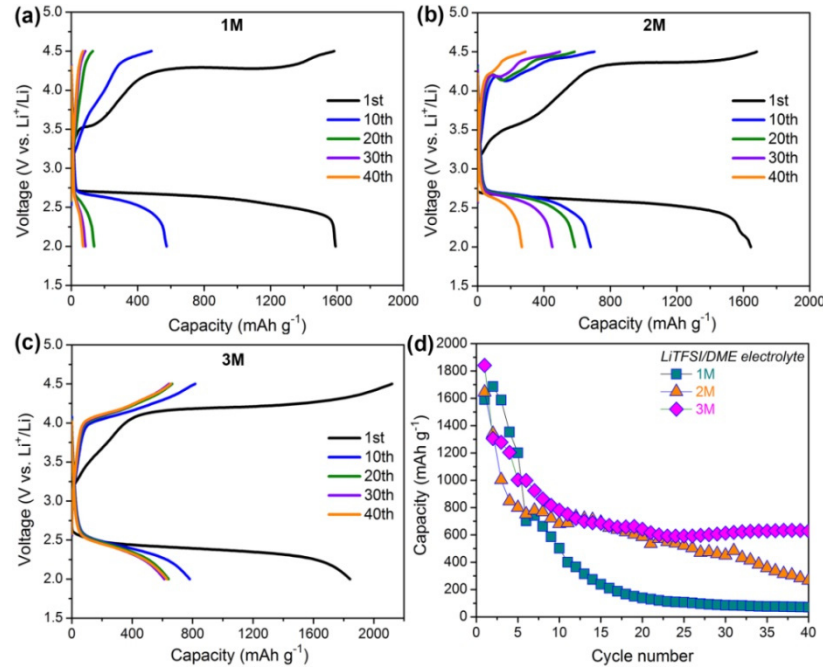
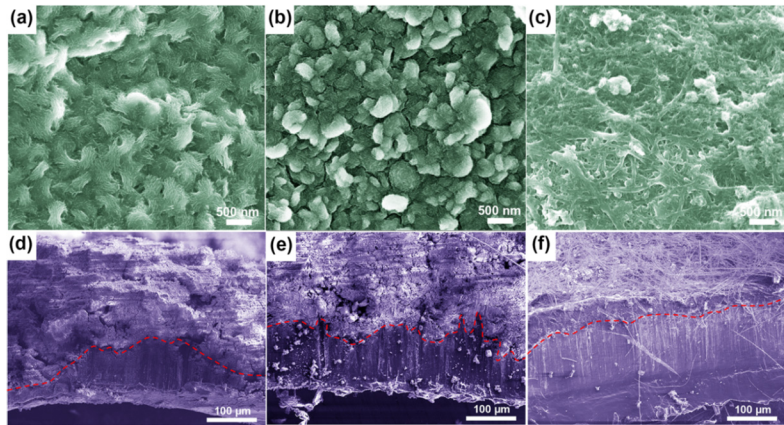


Figure V- 359: a-c) Voltage profiles of Li-O<sub>2</sub> coin-cells with the three concentration electrolytes cycled at a full discharge/charge protocol between 2.0 and 4.5 V at 0.1 mA cm $^{-2}$  for 40 cycles, and d) comparison of their corresponding cycling stability



**Figure V- 360:** SEM images of plan-view air-electrodes in the charged state (a-c) and cross-sectional Li metal anodes (d-f) after 40 discharge/charge cycles from LiTFSI-DME electrolytes of 1 M (a, d), 2 M (b, e), and 3 M (c, f). The fibers on the surface of the cycled Li metal anode in (f) are leftover glass fibers from the glass fiber paper used as separator in Li-O<sub>2</sub> cells

We also investigated the effects of concentrated LiTFSI-electrolytes with acetonitrile (AN) and dimethyl sulfoxide (DMSO) on the cycling performance of Li-O<sub>2</sub> batteries with CNT/PVDF/carbon paper air electrodes. We used three LiTFSI/solvent mole ratios of 1:4, 1:3, and 1:2 for each solvent-based electrolyte. The capacity limited test protocol (1000 mAh g<sup>-1</sup>) was used in this investigation. Unlike the concentrated LiTFSI-DME electrolytes tested above, three concentrated LiTFSI-AN electrolytes and the LiTFSI-2DMSO electrolyte cannot be cycled.

According to Bruce et al., the discharge in AN-electrolytes is surface chemistry due to the low donor number of AN, thus the air electrode surface is quickly passivated by the insulating Li<sub>2</sub>O<sub>2</sub> leads to a low discharge capacity. The LiTFSI-2DMSO probably has too low oxygen solubility and high viscosity so the discharge cannot be completed before the 1000 mAh g<sup>-1</sup> limit is reached. The electrolytes of LiTFSI-3DMSO and LiTFSI-4DMSO can be discharged and charged for 36 and 32 cycles, respectively (see Figure V- 362a, b), but the charging process is not reversible. When the two electrolytes were cycled at a lower capacity limitation (600 mAh g<sup>-1</sup>), their cycle lives could be extended to ~80 and 71 cycles, respectively (see Figure V- 362c, d). The limited cyclability in this electrolyte can be attributed to the instability of DMSO against reduced oxygen species and Li metal, and the low oxidation voltage of DMSO.

### Conclusions and Future Directions

We have developed a facile method for in situ synthesis and fabrication of ZCO/SWCNTs composites as air electrode materials with nanosheet-assembled ZCO microspheres and SWCNTs-supported ZCO ultrathin films as the effective bifunctional catalyst for ORR and OER in Li-O<sub>2</sub> batteries. The in situ grown ZCO/SWCNT composite electrodes exhibit largely improved discharge capacity, greatly reduced overvoltage (~0.9 V) in the onset of the oxygen evolution potential from the oxygen reduction potential, and enhanced cycling stability. The recently synthesized binder-free air electrode based on the metal-oxide catalyst on carbon cloth with certain special treatments can result in extremely high discharge and charge capacities at the first cycle and stable cycling at a capacity above 1200 mAh g<sup>-1</sup> for 120 cycles or 1000 mAh g<sup>-1</sup> for 140 cycles even under a full discharge/charge protocol. We also have demonstrated that the concentrated LiTFSI-DME electrolyte (3 M) leads to much less reaction-residual

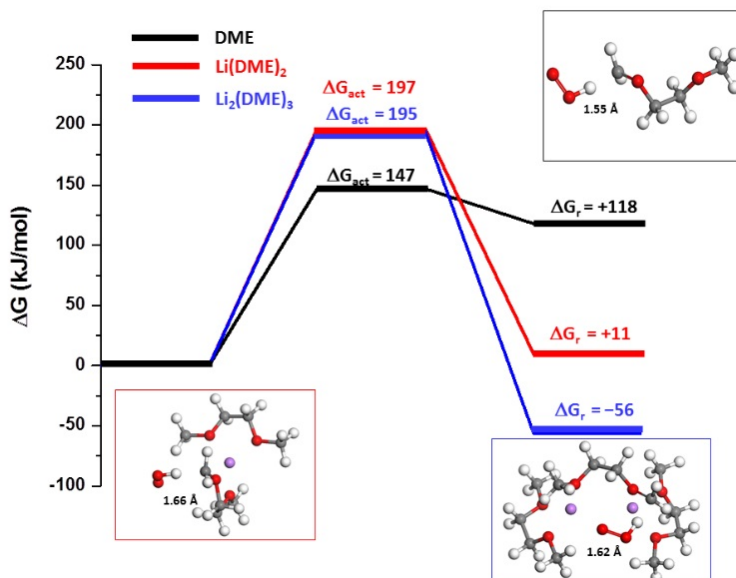


**Figure V- 361:** Computational simulations of the Gibbs activation barriers for the C-H bond scission from CH<sub>2</sub> groups a), and CH<sub>3</sub> groups b) in DME, Li<sup>+</sup>-(DME)<sub>2</sub>, and Li<sup>2+</sup>-(DME)<sub>3</sub> by the attack of O<sub>2</sub><sup>-</sup>

on the charged air electrode surface and much less corrosion to the Li-metal anode, leading to more stable cycling in Li-O<sub>2</sub> cells. The coordination with highly concentrated Li<sup>+</sup> ions strengthened the C-H bond on free DME molecules against the attack of reactive superoxide radical anion and significantly improved the stability of the electrolyte during Li-O<sub>2</sub> reactions. Similar results also observed when a concentrated LiTFSI-3DMSO electrolyte was tested. This work reveals deep insight into the fundamental mechanism of highly concentrated electrolytes enhancing the stability of air-cathodes and Li-metal anodes in rechargeable Li-O<sub>2</sub> batteries.

Future work will focus on investigating the mechanism of long-term cycling of the newly developed binder-free air electrode based on metal-oxide catalyst on carbon cloth with pre-treatments. Then, we will further improve the stability of the carbon air electrodes, searching for stable non-carbon air electrodes, and developing electrolytes that are stable against reactive reduced-oxygen species during ORR and OER.

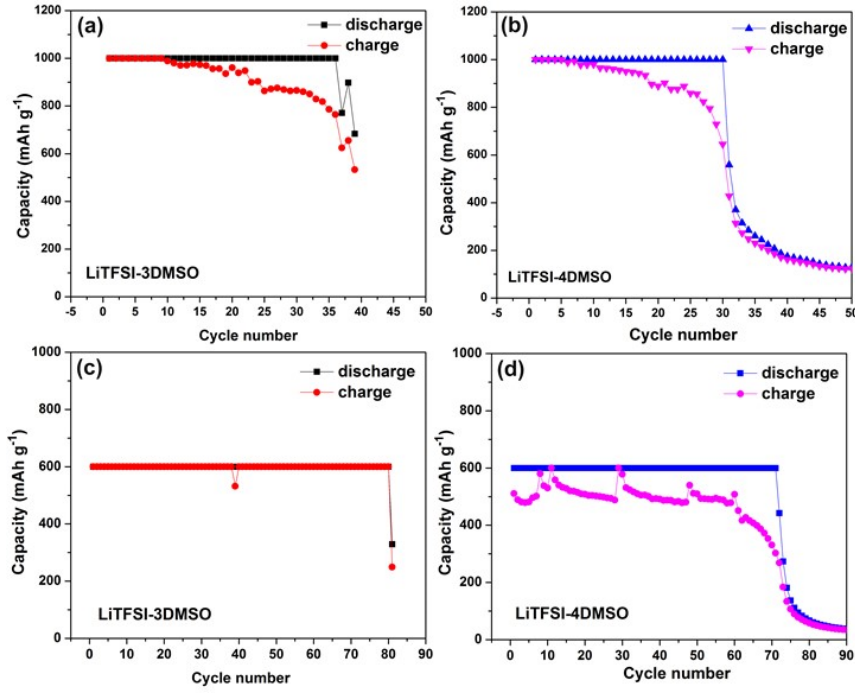


Figure V-362: Cycling stability of electrolytes, LiTFSI-3DMSO (a, c) and LiTFSI-4DMSO (b, d), in Li-O<sub>2</sub> coin cells at two different capacity limitations at 1000 mAh g<sup>-1</sup> (a, b) and 600 mAh g<sup>-1</sup> (c, d)

## FY 2015 Publications/Presentations

1. B. Liu, W. Xu, P. Yan, P. Bhattacharya, R. Cao, M. E. Bowden, M. H. Engelhard, C.-M. Wang, J.-G. Zhang, "In Situ Grown ZnCo<sub>2</sub>O<sub>4</sub> on Single Walled Carbon Nanotubes as Air Electrode Materials for Rechargeable Lithium-Oxygen Batteries", *ChemSusChem*, 2015, DOI: 10.1002/cssc.201500636.
2. B. Liu, W. Xu, P. Yan, X. Sun, M. E. Bowden, J. Read, J. Qian, D. Mei, C.-M. Wang, J.-G. Zhang, "Enhanced Cycling Stability of Rechargeable Li-O<sub>2</sub> Batteries Using High Concentration Electrolytes", accepted for publication by *Advanced Functional Materials*.
3. J.-G. Zhang, W. Xu, "Rechargeable Lithium-Air Batteries", Oral presentation at *2015 BMR Program Review Meeting*, LBNL, CA, January 21, 2015.
4. B. Liu, W. Xu, P. Yan, P. Bhattacharya, R. Cao, M. E. Bowden, M. H. Engelhard, C.-M. Wang, J.-G. Zhang, "ZnCo<sub>2</sub>O<sub>4</sub> Catalyzed Single Walled Carbon Nanotubes as Air Electrodes for Rechargeable Lithium-Oxygen Batteries", presented in *Beyond Lithium-Ion VIII*, Oak Ridge, TN, June 2-4, 2015.
5. J.-G. Zhang, W. Xu, J. Qian, R. Cao, B. Liu, Y. Zhang, L. Xiao, P. Bhattacharya, W. A. Henderson, M. H. Engelhard, E. Nasybulin, O. Borodin, J. Zheng, and F. Ding, "Electrolyte strategy for stabilizing lithium metal anodes in batteries", Poster presentation at *Pacific Northwest Energy Storage Symposium*, Seattle, WA, September 10-11, 2015; and at *EMSL Science Meeting on Energy Materials and Processes for Advanced Batteries and Catalysis*, Richland, WA, September 17, 2015.

## V.J.2 Efficient Rechargeable Li/O<sub>2</sub> Batteries Utilizing Stable Inorganic Molten Salt Electrolytes (Liox Power, Inc.)

### Objectives

- The objective of this project is to develop high specific energy, rechargeable Li/O<sub>2</sub> (Li/Air) batteries having lower overpotential and improved robustness under ambient air compared to current Li/O<sub>2</sub> batteries. The technical approach involves replacing traditional organic and aqueous electrolytes with a nonvolatile, inorganic molten salt comprising nitrate anions and operating the cell at elevated temperature (>80 °C). The research methodology includes powerful *in situ* spectroscopic techniques coupled to electrochemical measurements (e.g. electrochemical mass spectrometry) designed to provide quantitative information about the nature of chemical and electrochemical reactions occurring in the air electrode.

#### Project Details

**Christopher D. Johnson (NETL Program Manager)**  
DE-EE0006799 Recipient: Liox Power, Inc.

**Vincent Giordani (Liox Power, Inc. – PI)**  
129 N. Hill Avenue, Suite 107  
Pasadena, CA 91106  
Phone: 626-389-6311; Fax: 626-389-6302  
E-mail: [vincent@liox.com](mailto:vincent@liox.com)

Start Date: October 2014  
Projected End Date: October 2017

### Technical Barriers

Barriers addressed for Li/Air:

- Electrolyte stability.
- Fast electrode kinetics and high reversibility.
- Air tolerance.

### Technical Targets

The long term goal of this project is to develop Li/O<sub>2</sub> batteries comprising inorganic molten salt electrolytes and protected Li anodes which demonstrate high (>500 Wh/kg) specific energy and efficient cycleability in ambient air (>200 cycles at appreciable depth of discharge). By the end of the project it is anticipated that problems hindering the use of both the Li anode and air electrode will be overcome due to materials advances and strategies enabled within the intermediate (>80 °C) operating temperature range of the system under development.

### Accomplishments

- We demonstrated alkali metal eutectic compositions having eutectic points below 120 °C allowing cell operation to be reduced from 150 to 120 °C.
- We have measured ionic conductivity and lithium cation transference number in eutectic compositions.
- We have implemented an electrochemical cell setup to perform Rotating Disk Electrode studies in molten nitrate electrolytes at elevated temperatures. We measured diffusion coefficients and solubilities of lithium salts such as Li<sub>2</sub>O, Li<sub>2</sub>O<sub>2</sub>, LiOH and Li<sub>2</sub>CO<sub>3</sub> in LiNO<sub>3</sub>-KNO<sub>3</sub> melt. We demonstrated enhanced solubilities of Li<sub>2</sub>O<sub>2</sub> - the discharge product of Li/O<sub>2</sub> batteries - compared to room temperature non-aqueous electrolytes.
- We synthesized boron-doped carbon nanotubes with various doping amounts, in replacement of typical carbon black such as Super P carbon, for the O<sub>2</sub> cathode.
- We quantified e<sup>-</sup>/O<sub>2</sub> molar ratios and OER/ORR ratios for baseline Super P carbon O<sub>2</sub> electrodes, demonstrating a 2 e<sup>-</sup>/O<sub>2</sub> for both discharge and charge cell reactions. We demonstrated extremely low overpotentials for the O<sub>2</sub> electrode at reasonable current densities (up to 0.5 mA/cm<sup>2</sup> or 150 mA/g<sub>carbon</sub>).

- We demonstrated using electrochemical mass spectrometry that O<sub>2</sub> is the main gas being evolved during cell charge without CO<sub>2</sub> evolution, which is always detected in room temperature non-aqueous cells.
- We demonstrated that LiOH and Li<sub>2</sub>CO<sub>3</sub>, possible ORR side products, can be bulk oxidized in molten nitrate eutectics near equilibrium potentials.
- We have shown a new morphology of lithium peroxide, and begun to develop a mechanism for why it forms. In addition, we have explored the effect of various cell parameters such as discharge rate on the morphology of the resulting lithium peroxide.
- We demonstrated the instability of amorphous carbon black such as Super P carbon in presence of ORR products, responsible for limited cycle life (30-40 cycles at ~50% DOD). We proposed a mechanism for coulombic inefficiency and cell death.

## Introduction

The rechargeable lithium-oxygen battery has attracted attention due to its large theoretical energy density compared to modern lithium-ion batteries. This large energy density is attributed to the reaction of lithium with molecular oxygen to form lithium peroxide, which grows on the surface of the cathode. While this is a promising chemistry, there are many practical challenges that remain to be solved, such as the decomposition of organic electrolyte in the presence of superoxide anions and large overpotentials on charge. We propose a system which inherently avoids many of the issues associated with organic electrolyte decomposition, while also forming lithium peroxide with a unique morphology. By using a LiNO<sub>3</sub>/KNO<sub>3</sub> eutectic molten salt in place of a conventional solvent/salt electrolyte, solvent decomposition is obviated. In addition, the elevated temperature of the molten salt as well as the large concentration of lithium ions encourage faster diffusion and kinetics.

## Approach

**Innovative Approach:** Replace volatile, unstable and air-intolerant organic electrolytes common to prior research with inert molten nitrate electrolytes and operate cell above liquidus temperature (> 80 °C). Improve reversibility and rate capability since discharge products (Li<sub>2</sub>O<sub>2</sub>, Li<sub>2</sub>O, LiOH and Li<sub>2</sub>CO<sub>3</sub>) are stable and sparingly soluble in molten nitrate electrolytes. Combine quantitative gas analysis (pressure monitoring, mass spectrometry) with precise coulometry, as well as in situ spectroscopic techniques such as Raman to analyze air electrode processes.

## Results

We have achieved the following progress:

### Low voltage hysteresis compared to conventional room temperature organic electrolyte Li/O<sub>2</sub> cells

We have investigated the electrochemistry of O<sub>2</sub> at 150 °C in LiNO<sub>3</sub>-KNO<sub>3</sub> molten salt electrolyte (Cyclic Voltammetry, see Figure V- 363). We compared the results to a conventional room-temperature organic electrolyte, namely lithium perchlorate in DMSO. Both cells used the same Super P carbon electrode material (5% PTFE binder) with comparable carbon loading (~5 mg/cm<sup>2</sup>). The results clearly demonstrate the superior behavior of the molten salt electrolyte cell.

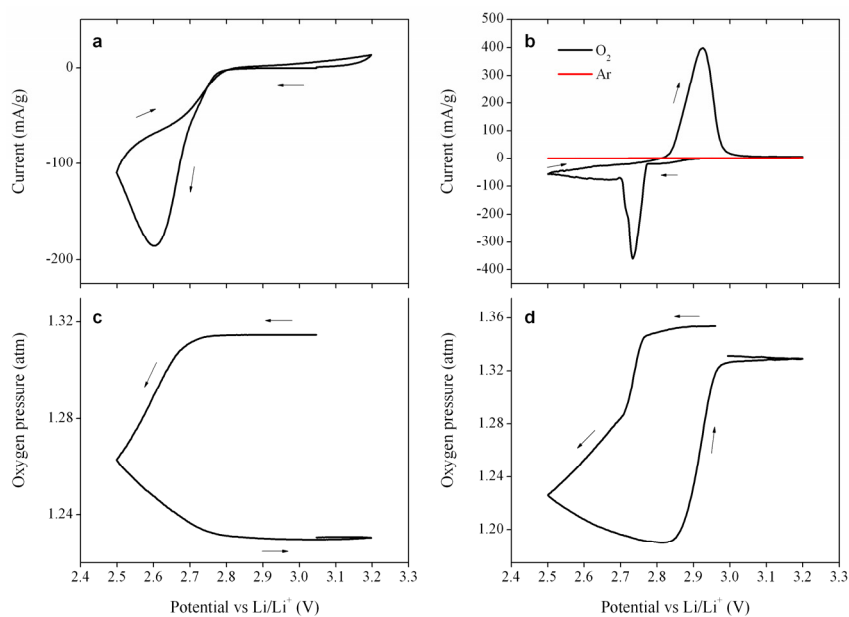


**Figure V- 363:** Cyclic voltammetry study of O<sub>2</sub> reduction in a Li/O<sub>2</sub> cell electrolyte: a,c) 0.1 M LiClO<sub>4</sub>-DMSO at 30 °C and b,d) LiNO<sub>3</sub>-KNO<sub>3</sub> eutectic at 150 °C. Working electrode: Super P porous carbon ( $A=0.785\text{ cm}^2$ ), carbon loading  $\sim 5\text{ mg/cm}^2$ . Counter and reference electrodes: Li metal. Scan rate: 0.05 mV/s. Voltage window: 2.5–3.2 V vs Li/Li<sup>+</sup>. Current density expressed in mA per g of carbon

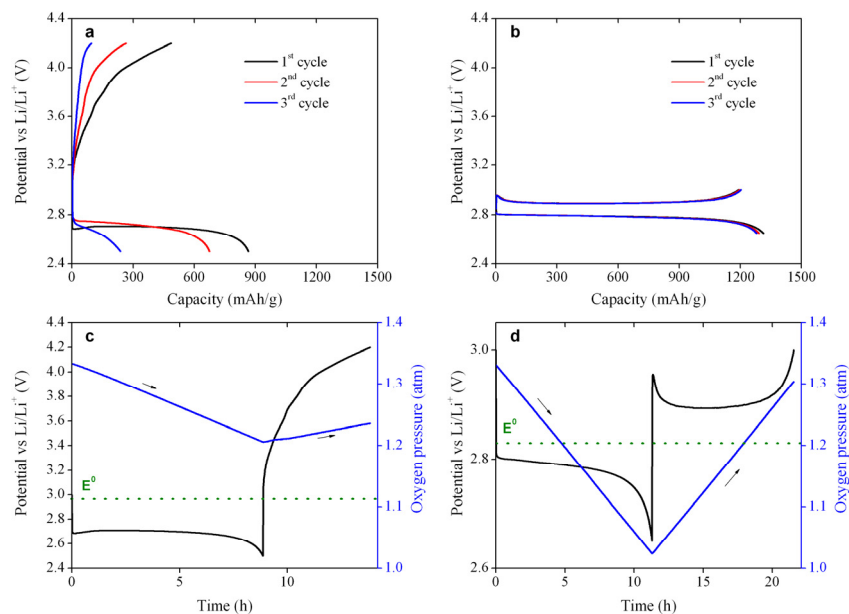


**Figure V- 364:** Li/O<sub>2</sub> cell voltage and pressure profiles measured in a,c) 0.1 M LiClO<sub>4</sub>-DMSO at 30 °C between 2.5 and 4.2 V and b,d) LiNO<sub>3</sub>-KNO<sub>3</sub>-CsNO<sub>3</sub> molten salt electrolyte at 120 °C between 2.65 and 3 V. Positive electrode: Super P Carbon:PTFE 95:5 wt.%, current: 0.32 mA/cm<sup>2</sup> (~80 mA/g carbon). Electrolyte loading: ~ 150 μL. Carbon loading: ~4 mg/cm<sup>2</sup>. Pressure profiles depicted in c and d) are for the first cycle of the cell. Cell capacity expressed in mAh per g of carbon

demonstrate high reversibility with low voltage polarization, good capacity retention and minimized oxygen pressure loss (pressure slopes during discharge and charge half-cycle perfectly overlap), suggesting high chemical stability of the molten nitrate electrolyte in a Li/O<sub>2</sub> cell.

While the reduction of O<sub>2</sub> in the organic electrolyte is highly irreversible (no oxidation peak during the anodic scan and no pressure variation, Figure V- 363 a and c), we observed a reversible behavior at 150 °C in the molten nitrate electrolyte (Figure V- 363 b and d), with both oxidation peak and pressure increase during the anodic scan consistent with oxidation of Li<sub>2</sub>O<sub>2</sub> back to lithium ions and oxygen gas.

This is further confirmed by galvanostatic cycling data shown in Figure V- 364. Displayed are the first 3 cycles recorded at 0.32 mA/cm<sup>2</sup> (~80 mA/g carbon) both for the organic electrolyte at 30 °C (Figure V- 364a) and for the LiNO<sub>3</sub>-KNO<sub>2</sub>-CsNO<sub>3</sub> molten salt electrolyte at 120 °C (Figure V- 364 b). Figure V- 364 c and d show the O<sub>2</sub> pressure variation during the 1<sup>st</sup> cycle as we discharge/charge the cell. Large polarization during charge, poor discharge capacity retention and irreversible oxygen pressure loss are typical features commonly observed with the organic electrolyte Li/O<sub>2</sub> cell. This is due to the fact that organic electrolytes react with ORR products during cycling and rapidly decompose. Here we

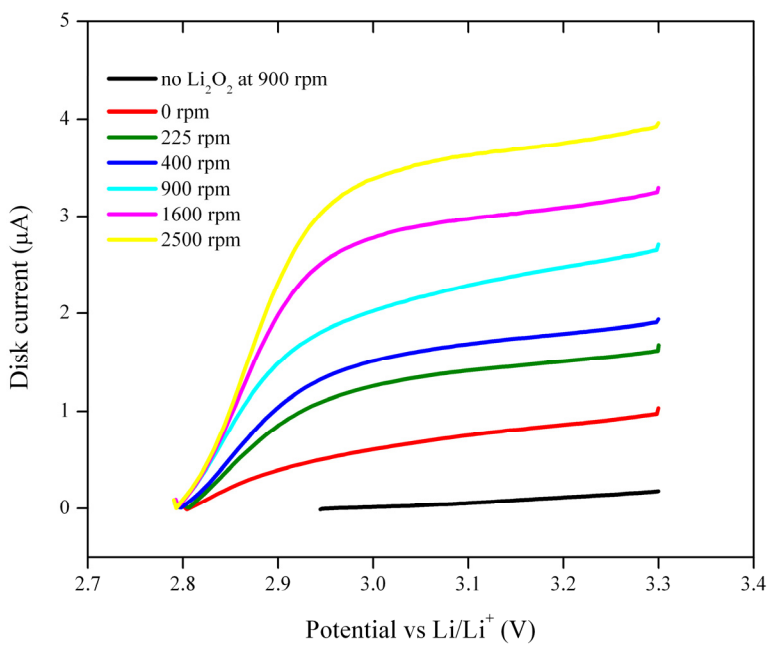


**Figure V- 365:** Linear sweep voltammograms recorded at a Pt RDE ( $A = 0.196 \text{ cm}^2$ ) from a  $\text{LiNO}_3\text{-KNO}_3$  molten salt electrolyte containing  $\text{Li}_2\text{O}_2$ .  $v = 1 \text{ mV/s}$ , from OCV to 3.3 V vs  $\text{Li}/\text{Li}^+$ .  $T = 150^\circ \text{C}$ . Counter electrode: Pt wire, reference electrode: Li metal rod

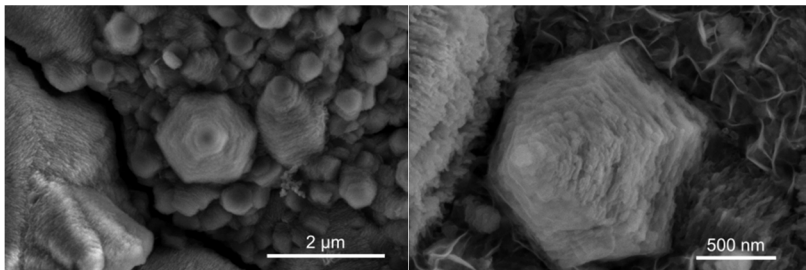


**Figure V- 366:** SEM images of a discharge  $\text{O}_2$  electrode in  $\text{LiNO}_3\text{-KNO}_3$  electrolyte at  $150^\circ \text{C}$ . Cell was discharged to 2.5 V cutoff at  $80 \text{ mA/g}_{\text{carbon}}$

Further evidence for enhanced solubility of the discharge products was obtained by scanning electron microscopy and morphological study of the discharge products in the  $\text{O}_2$  electrode (Figure V- 366). Typically, large particles ranging from 500 nm to several microns were observed at the carbon surface. Of note, a new morphology of  $\text{Li}_2\text{O}_2$  was observed empirically for the first time which consists of stacks of hexagonal layers. Intriguingly, this conforms to theoretical predictions of the equilibrium Wulff construction of  $\text{Li}_2\text{O}_2$  as a hexagonal prism. We conjecture that a solution-mediated precipitation of lithium peroxide is responsible for the growth of such large crystals.

#### Discharge product characterization and in situ gas analysis during charge half-cycle

Figure V- 367(a) shows in situ gas analysis performed during a  $\text{Li}/\text{O}_2$  battery charge half cycle in  $\text{LiNO}_3\text{-KNO}_3$  electrolyte at  $150^\circ \text{C}$ . The cell is first discharged under  $\text{O}_2$  to roughly 30% depth of discharge ( $\sim 400 \text{ mAh/g}$ ). Then, during OCV between discharge and charge, the valve connecting the battery to the mass spectrometer is opened and gases are allowed to flow from the cell head-space directly into the mass spectrometer. In other words the charge cycle is carried out under “vacuum conditions” which would not be possible with common organic electrolytes due to solvent volatility. As the electrode begins to recharge, oxygen signal (blue curve) increases and remains steady throughout the entire charge. Other gases such as carbon dioxide (red curve) and nitric oxide (brown curve) remain at background levels.

#### Determine $\text{Li}_2\text{O}_2$ solubility in the molten nitrate electrolyte

Lithium peroxide solubility in molten nitrates was investigated by rotating disk electrode (RDE) measurements (Figure V- 365). Typically a PTFE-based electrochemical cell containing  $\sim 40 \text{ mL}$  of molten salt was used inside an Ar-filled glovebox. The working electrode consisted of a Pt RDE, the counter electrode a Pt wire and the reference electrode a Li metal rod. Once reproducible cyclic voltammograms were obtained in the 2.8-3.3 V range, lithium peroxide powder was added to the molten salt electrolyte, and using the RDE tip, the solution was vigorously stirred for several minutes until saturation was reached. Linear sweep voltammograms were performed at 1 mV/s, varying the electrode rotation rate from 100 to 2500 rpm. Levich/Cottrell analysis was used to determine bulk concentration of  $\text{Li}_2\text{O}_2$  in the molten nitrate electrolyte. A concentration of  $5.2 \times 10^{-4} \text{ mol/L}$  was found which is one order of magnitude greater than values calculated in organic solvents such as DMSO or DMF at  $30^\circ \text{C}$  (in the  $10^{-5} \text{ mol/L}$  range).

XRD patterns of the carbon electrode before discharge, following a ~1200 mAh/g discharge under O<sub>2</sub> to 2.6 V cathodic cutoff, and after a completed cycle (electrode fully recharged to 3 V) are depicted in Figure V-367(b). It clearly demonstrates that crystalline Li<sub>2</sub>O<sub>2</sub> forms on the carbon surface during discharge and can subsequently be oxidized upon cell charge. Furthermore, XRD also reveals the presence of Li<sub>2</sub>CO<sub>3</sub> alongside lithium peroxide, confirming sustained reaction between carbon and the oxygen reduction products.

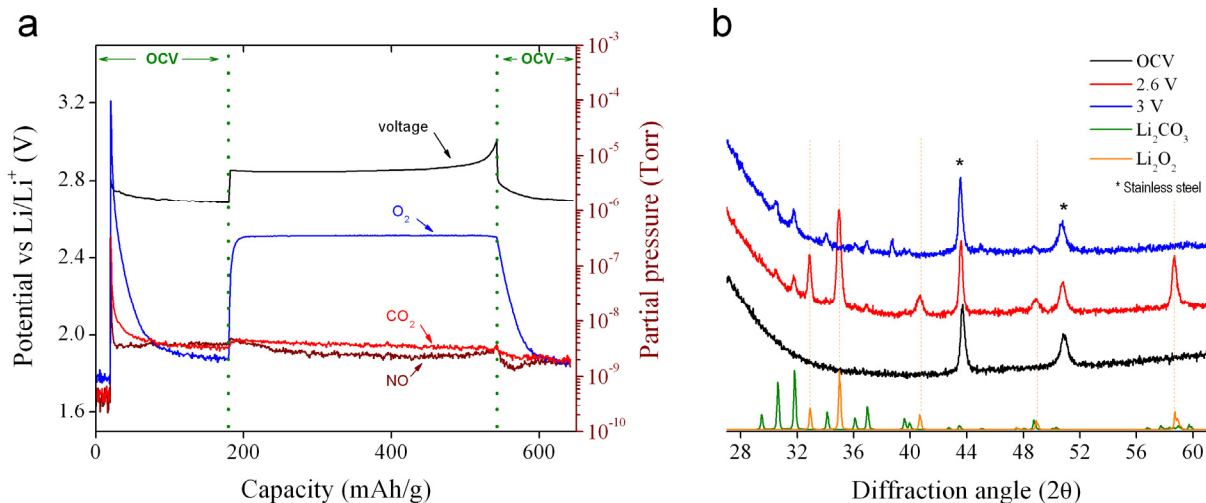


Figure V-367: a) Li/O<sub>2</sub> cell charging profile with in situ gas analysis. Cell employed a LiNO<sub>3</sub>-KNO<sub>3</sub> molten salt electrolyte, a Super P Carbon:PTFE cathode, and was charged at 150 °C, 80 mA/g<sub>carbon</sub> to a 3 V cutoff. Capacity expressed in mAh per g of carbon. b) First cycle XRD patterns of a Super P Carbon cathode discharged/charged in a molten nitrate Li/O<sub>2</sub> cell between 2.6 and 3 V, respectively

### Understand the origin of cell failure

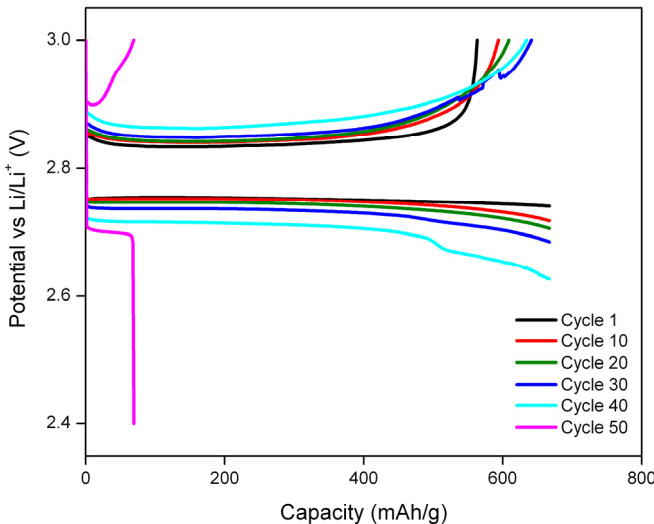
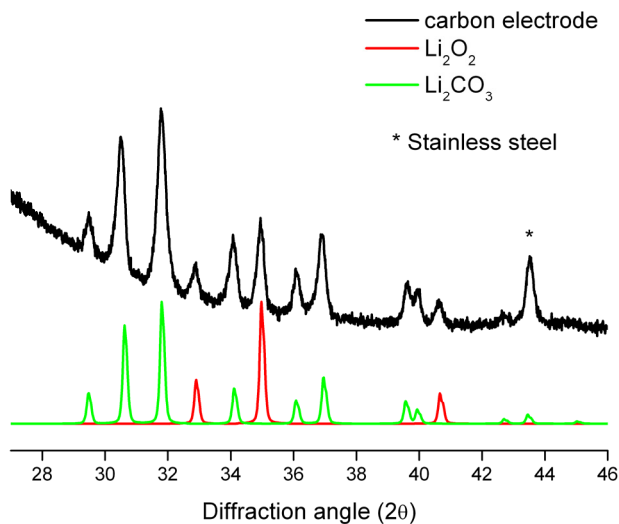


Figure V-368: Li/O<sub>2</sub> cell voltage profile. LiNO<sub>3</sub>-KNO<sub>3</sub> electrolyte. T= 150°C

after a full cycle, XRD analysis revealed the presence of lithium peroxide at the carbon surface, alongside lithium carbonate (Figure V-369). We believe that electrically disconnected lithium peroxide accumulates away from the electrode during cycling while lithium carbonate passivates carbon and is responsible for the continuous increase in cell polarization with cycle number. To further support this argument, we performed SEM analysis of our cycled carbon cathode. Large clusters of lithium peroxide (>10 microns in size) were observed on residual separator glass microfibers leftover on the carbon side. This is consistent with uncontrolled reprecipitation of dissolved lithium peroxide during battery cycling. Furthermore large crystals of lithium carbonate could be seen all across the carbon surface (Figure V-370).

Electrode passivation by Li<sub>2</sub>CO<sub>3</sub>, often reported as “carbon corrosion”, is a known phenomenon. As cycle number increases, the overall energy efficiency of the battery decreases, consistent with the growth in electrode impedance (Figure V-368). The cell was galvanostatically cycled in LiNO<sub>3</sub>-KNO<sub>3</sub> eutectic at 150 °C at 0.5 mA (0.64 mA/cm<sup>2</sup> or ~165 mA/g of carbon) with limited depth of discharge (2 mAh discharge, ~45% DOD). The cell was stopped after 50 cycles (~340 hours of cycling) when the discharge capacity had significantly dropped and the cathode was analyzed by XRD and SEM.

Despite ending the cycling at 3 V



**Figure V- 369:** XRD analysis of the carbon electrode following 50 cycles (cell death). XRD pattern references for  $\text{Li}_2\text{O}_2$  and  $\text{Li}_2\text{CO}_3$

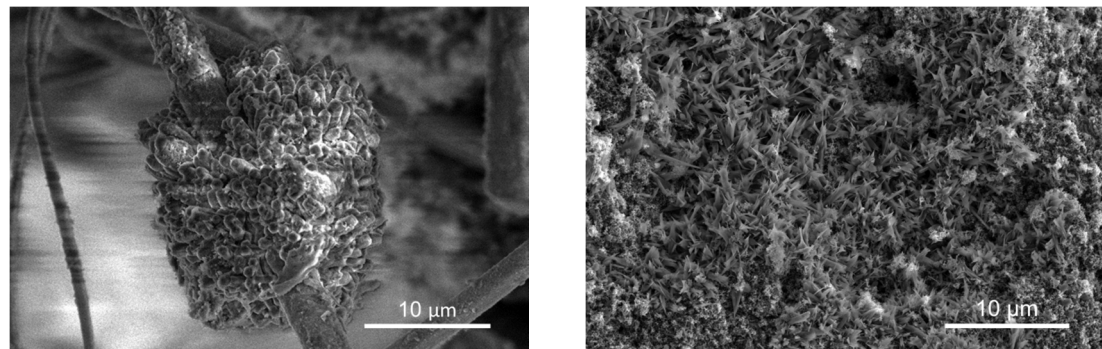


**Figure V- 370:** SEM images of the carbon electrode following 50 cycles. Top image:  $\text{Li}_2\text{O}_2$  particles precipitated onto separator glass fiber. Right image:  $\text{Li}_2\text{CO}_3$  particles covering carbon surface

### Conclusions and Future Directions

Project technical approach enables significant improvements in overpotential and stability in  $\text{Li}/\text{O}_2$  cells and may lessen certain system-level constraints. Future, near-term technical objectives include:

- Identify non-carbonaceous air electrode materials,
- Manage  $\text{Li}_2\text{O}_2$  dissolution and precipitation.

High performance  $\text{Li}/\text{O}_2$  cell chemistry depends on the stability of the anode/electrolyte and cathode/electrolyte interfaces. Of critical importance is 1) the design of protective layers (ceramic or polymer) to separate the lithium anode from the molten salt electrolyte and the cathode, and 2) the design of cathode materials that will provide high stability towards ORR products. Solubility of  $\text{Li}_2\text{O}_2$  allows growth of large particles and clusters via a solution phase mechanism which enables high areal capacity and low overpotential, but creates challenges in achieving high coulombic efficiency. We need to control  $\text{Li}_2\text{O}_2$  morphology and growth within cathode compartment in order to improve coulombic efficiency. Low  $\text{O}_2$  solubility is a challenge for achieving high rate capability (need to identify catalytic materials facilitating chemical absorption of  $\text{O}_2$  in melt). Long-term stability of cell components (current collector, ceramic  $\text{Li}^+$  conducting membrane, cell housing) with molten nitrates must be determined.

**FY 2015 Publications/Presentations**

**Patents**

1. PCT Application No. WO2014153551 “Alkali Metal/Oxygen Batteries Employing Molten Nitrate Electrolytes”.
2. PCT Application No. WO2015021451 “Rechargeable Batteries Employing Catalyzed Molten Nitrate Positive Electrodes”.

**Presentations**

1. Oral Presentation by Dan Addison at *Lithium Battery Power* conference in Washington, D.C. (November 2014).
2. Poster Presentation by Dylan Tozier at The Nanomaterials for Applications in Energy Technology Gordon Research Conference in Ventura, CA (February 2015).
3. Oral Presentation by Vincent Giordani at *Materials Research Society* conference in San Francisco, CA (April 2015).
4. Oral Presentation by Dan Addison at *Next Generation Batteries 2015* conference in San Diego, CA (April 2015).
5. Oral Presentation by Dylan Tozier at *228<sup>th</sup> ECS Meeting* in Phoenix, AZ (October 2015).

## V.J.3. Li-Air Batteries (ANL)

### Objectives

- Develop stable electrolytes and new cathode architectures in lithium air batteries to lower the charge overpotential, improve the cell efficiency and cycle life.
- Understand the oxygen crossover effect at the anode on the electrochemical performance of Li-air battery.

### Technical Barriers

- **Unstable electrolytes:** electrolyte decomposition (in particular the ether-based electrolytes) in the presence of the reduced oxygen species, especially superoxide anion ( $O_2^-$ ).
- **Inefficient cathode structure and catalysis:** Commonly used carbons and cathode catalysts do not access the full capacity of the oxygen electrode and cause significant charge overpotentials. This lowers rates.
- **Lithium electrode poisoning** due to oxygen crossover and reaction with the electrolyte destroys the integrity and functioning of the cell. This lowers cycle life.

### Technical Targets

The goal of this project is to demonstrate that a practical Li-air battery is achievable. The targets are to achieve 300 cycles and an energy density of 600~700 Wh/kg. This will provide the necessary breakthroughs and a firm basis for follow-on optimization and incremental improvements.

### Accomplishments

- A combined experimental and theoretical study has provided new insight into how interfacial effects can stabilize lithium superoxide, which may play an important role in the charge and discharge chemistries of a Li-O<sub>2</sub> battery.
- We have investigated a number of metal nanoparticles as catalysts for Li-O<sub>2</sub> batteries. Pd nanoparticles on an alumina coated carbon surface were found to significantly reduce the charge overpotential and increase efficiency.
- Molybdenum carbide (MoC<sub>2</sub>) nanoparticles have been investigated as catalysts for Li-O<sub>2</sub> batteries and found to significantly reduce the charge overpotential and increase cycle life.

### Introduction

Lithium-air batteries can be considered the ‘holy grail’ of lithium batteries because they offer, in principle, at least ten times the energy density of conventional lithium-ion systems. The lithium-ion cell chemistry, the best to date, would provide a theoretical specific energy of ~900 Wh/kg if the calculation is based on the masses of the anode and cathode materials alone; in practice, 150-200 Wh/kg has been accomplished at the cell level. In contrast, a lithium-air cell, when discharged to Li<sub>2</sub>O<sub>2</sub> at an average 3.1 V would provide a theoretical specific energy of 3623 Wh/kg, or when discharged to Li<sub>2</sub>O at the same voltage, 5204 Wh/kg. Note that gasoline (octane) offers a theoretical energy of ~13,000 Wh/kg if the mass of the injected oxygen is not considered in

### Project Details

Tien Duong (Program Manager)

Subcontractor: ANL

Khalil Amine & Jun Lu

Chemical Sciences and Engineering Division

Argonne National Laboratory

9700 S. Cass Avenue, Building 205

Argonne, IL 60439-4837

Phone: 630-252-3838; Fax: 630-972-4440

E-mail: [amine@anl.gov](mailto:amine@anl.gov); and [junlu@anl.gov](mailto:junlu@anl.gov)

Larry Curtiss

Material Science Division

Argonne National Laboratory

9700 S. Cass Avenue, Building 200

Argonne, IL 60439-4837

Phone: 630-252-7380

E-mail: [curtiss@anl.gov](mailto:curtiss@anl.gov)

Start Date: October 2014

Projected End Date: September 2018

the calculation because it is supplied externally and combusted within, and exhausted from, the engine. By the same token, a lithium-air cell would offer a specific energy of ~11,000 Wh/kg if the ‘free’ oxygen supplied during discharge and released during charge is ignored in the calculation.

While the inherent energy potential of lithium metal approaches that of gasoline, today’s battery manufacturers have not yet been able to unlock this potential. While today’s lithium-ion batteries may provide acceptable power for hybrid electric vehicles (HEVs) and all-electric vehicles (EVs), they do not provide sufficient energy for an acceptable driving distance. This range limitation and the absence of a battery charging infrastructure have limited public interest in electric vehicles. A breakthrough in Li-air battery technology would significantly increase the possibility of extending the electric range of these vehicles with the added advantages of reducing battery cost and weight.

This promising Li-air battery technology is still in its infancy and, no doubt, will require significant research efforts in a variety of fields to unlock its full potential. The successful implementation of non-aqueous Li-air cells has been hampered because of severe materials problems that have limited electrochemical performance: (1) the non-aqueous electrolytes are unstable at high potentials and are easily oxidized by the oxygen released during charge, thereby seriously limiting cycle life; (2) during discharge, the solid and insoluble  $\text{Li}_2\text{O}_2$  and/or  $\text{Li}_2\text{O}$  products are deposited on the surface or within the pores of the carbon cathode, thereby clogging the pores and restricting oxygen flow; (3) poisoning of the lithium electrode due to oxygen crossover destroys the integrity and functioning of the cell; and (4) commonly used cathode catalysts, such as  $\text{MnO}_2$  or Mn metal, do not access the full capacity of the oxygen electrode or enable sufficiently high rates.

The team led by Dr. Khalil Amine at Argonne National Laboratory (ANL) is working on problems that limit the electrochemical performance of the Li-air battery, including the stability of the organic electrolyte, cathode catalysts and structures, and stability of the lithium anode under oxygen-crossover conditions. This effort will lead to the development of a reversible lithium air battery that provides 10 times the energy density of the state-of-the-art lithium ion battery for powering electric vehicles. The technology, if successful, can also benefit many military applications that require very high energy density such as satellite, military vehicles for silent watch and operation.

### **Approach**

Issues that limit the performance of the Li-air battery include (1) electrolytes decomposition; (2) inefficient cathode materials; and (3) lithium electrode corrosion. During the previous year (FY13) we made significant progress in finding cathode materials that can reduce the charge overpotential that was leading to the larger inefficiencies in the performance of the  $\text{Li}-\text{O}_2$  battery. Although the lower charge potential reduces sources of electrolyte instability, the cycle life remained poor. The possible reasons for this include other sources of electrolyte instabilities and cathode degradation leading to increased charge potentials with cycling.

This project addresses the cycle life problem of Li-air batteries through investigation of (a) the discharge formation mechanism and relationship to electrolytes, (b) investigation of the morphology and composition of the discharge product, and (c) investigation of electrolyte decomposition mechanisms. This understanding is being used to (a) develop new electrolytes that will be more stable than ethers towards oxygen reduction species in the electrolyte, (b) new carbon based cathodes that will promote formation of discharge morphologies such as those involving superoxides to prevent degradation of the cathode materials with cycling, and (c) investigation of techniques to protect the lithium anode.

The experimental designs to create advanced electrolytes, carbons, catalysts, cathodes, and anodes will be guided by theory and modeling. The experimental results will be thoroughly analyzed with very sophisticated analytical techniques and used to fine-tune the computational studies. Fundamental understanding of the underlying principles will be provided to greatly facilitate the next steps in the development cycle.

### **Results**

We have achieved the following progress:

#### **Suppression of lithium superoxide disproportionation in $\text{Li}-\text{O}_2$ batteries.**

The suppression of lithium superoxide disproportionation has been investigated in a  $\text{Li}-\text{O}_2$  battery based on an activated carbon cathode, a lithium anode, and an electrolyte composed of tetraglyme and lithium triflate. The

results indicate that interfacial effects can suppress disproportionation of a LiO<sub>2</sub> component in the discharge product.

High intensity XRD and TEM measurements were first used to show that there is a LiO<sub>2</sub> component along with Li<sub>2</sub>O<sub>2</sub> in the discharge product. The stability of the discharge product was then probed by investigating the dependence of the charge potential and Raman intensity of the superoxide peak with time. The results indicate that the LiO<sub>2</sub> component can be stable for possibly up to days when an electrolyte is left on the surface of the discharged cathode. Density functional calculations reveal that the disproportionation process will be slower at an electrolyte/LiO<sub>2</sub> interface compared to a vacuum/LiO<sub>2</sub> interface. The combined experimental and theoretical results provide new insight into how interfacial effects can stabilize LiO<sub>2</sub> and suggest that these interfacial effects may play an important role in the charge and discharge chemistries of a Li-O<sub>2</sub> battery.

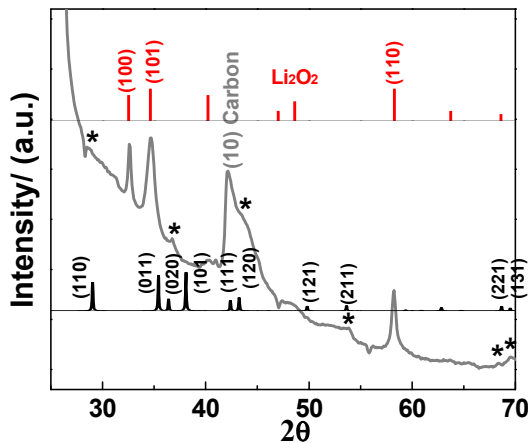


Figure V- 371: XRD pattern of the discharged AC cathode for 1000 mAh/g. The red histogram corresponds to the standard Li<sub>2</sub>O<sub>2</sub> patterns. The LiO<sub>2</sub> pattern (black histogram) is from the structure calculated from density functional theory

The stability of the discharge product from this activated carbon based Li-O<sub>2</sub> cell was further investigated by varying the interface conditions of the discharge product and characterizing the subsequent effect on the disproportionation process with time. Six different ageing conditions were investigated. The Raman spectra for these six different cases are shown in Figure V- 372. The electrolyte is kept in the cell (except for #5) for the noted period of time after which it is dried with dimethyl carbonate (see supplemental information). The Raman spectra from these six different discharged cathodes all have a peak at ~1123 cm<sup>-1</sup> (denoted as S1) associated with the presence of a LiO<sub>2</sub> species in the toroids. Another peak at ~1505 cm<sup>-1</sup> (denoted as S2) in the Raman spectra is due to the coupled interface between the LiO<sub>2</sub> component and the carbon electrode surface and thus is another signature for the presence of LiO<sub>2</sub> component in the discharge product. For conditions #2-#4 the relative intensity of Raman peaks S1 and S2 for the discharge product are found to be similar to that of the Raman spectra taken of the discharge product with no aging (#1). This suggests that the LiO<sub>2</sub> component has not significantly

In this work, the discharged AC electrode was examined by high energy XRD, as shown in Figure V- 371. Three distinct peaks are identified as the (100), (101), and (110) peaks of LiO<sub>2</sub>. There are several weaker peaks marked with an asterisk "\*" that do not match with Li<sub>2</sub>O<sub>2</sub> or other possible products. Interestingly, these XRD peaks are consistent with the XRD pattern of a LiO<sub>2</sub> crystalline phase based on theoretical study. Based on these results, the XRD data suggests at least some of the discharge product is crystalline LiO<sub>2</sub>.

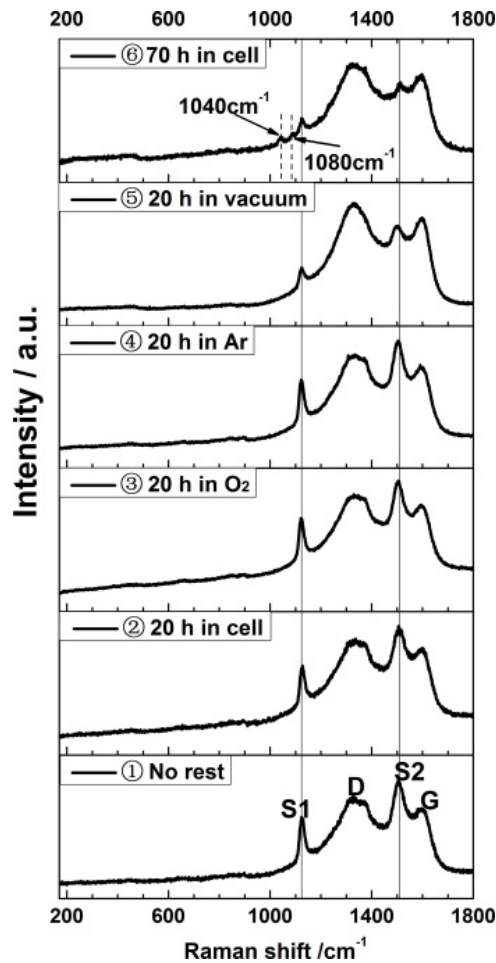


Figure V- 372: Raman spectra of the toroids on the surface of the discharged activated carbon cathode for the six different conditions noted in the figure. The values of the peaks (in cm<sup>-1</sup>) are: 1123 (S1), 1505 (S2), 1340 (D), 1600 (G)

disproportionated further under the cell/O<sub>2</sub>/Ar gas conditions for 20 hours. In contrast for the discharged AC cathodes kept in vacuum for 20 hours or in cell for 70 hours, the intensity of peaks S1 and S2 becomes weaker relative to the Raman spectra taken of the discharge product with no aging (#1). This again further confirms that some of the LiO<sub>2</sub> component disproportionates when exposed to vacuum for 20 hours or ages in the cell for 70 hours.

In order to gain insight into this new experimental evidence for stability of LiO<sub>2</sub>, we investigated the effect of the presence of an electrolyte on the stability of an LiO<sub>2</sub> surface covered using Density Functional Theory (DFT) calculations. An amorphous LiO<sub>2</sub> slab is found to be quite stable with the outermost surface-bounded superoxide groups not coming off as oxygens. In contrast to a bare amorphous LiO<sub>2</sub> surface exposed to vacuum, the under-coordinated superoxide species are stabilized through interaction with the solvent and LiCF<sub>3</sub>SO<sub>3</sub> molecules in the density functional calculations.

Thus, the experimental results are explained by DFT calculations that find the disproportionation process to be slower at an electrolyte/LiO<sub>2</sub> interface compared to a vacuum/LiO<sub>2</sub> interface. The combined experimental and theoretical results provide new insight into how interfacial effects can stabilize LiO<sub>2</sub>, which may play an important role in the charge and discharge chemistries of a Li-O<sub>2</sub> battery.

### Metal nanoparticles as effective electrochemical catalysts for Li-O<sub>2</sub> batteries

We have investigated a number of metal nanoparticles as catalysts for Li-O<sub>2</sub> batteries to find one that can reduce the charge overpotential and increase efficiency. Pd nanoparticles were found to be especially effective at this. In this work uniformly dispersed Pd nanoparticles on ZnO-passivated porous carbon were synthesized via an atomic layer deposition (ALD) technique. They were tested as a cathode material in a rechargeable Li-O<sub>2</sub> battery. They showed a highly active catalytic effect toward the electrochemical reactions—in particular, the oxygen evolution reaction as shown in Figure V- 373.

Transmission electron microscopy (TEM) showed discrete crystalline nanoparticles decorating the surface of the ZnO-passivated porous carbon support in which the size could be controlled in the range of 3–6 nm, depending on the number of Pd ALD cycles performed. X-ray absorption spectroscopy (XAS) at the Pd K edge revealed that the carbon-supported Pd existed in a mixed phase of metallic palladium and palladium oxide. The ZnO-passivated layer effectively blocks the defect sites on the carbon surface, minimizing the electrolyte decomposition. Our results suggest that ALD is a promising technique for tailoring the surface composition and structure of nanoporous supports for Li-O<sub>2</sub> batteries to achieve low charge overpotentials.

### Metal carbide nanoparticles as effective electrochemical catalysts for Li-O<sub>2</sub> batteries

Molybdenum carbide (MoC<sub>2</sub>) nanoparticles have been investigated as catalysts for Li-O<sub>2</sub> batteries to find one that can reduce the charge overpotential and increase efficiency. In this work done in collaboration with Y.-K. Sun of Hanyang University, Korea, a nanostructured cathode based on Mo<sub>2</sub>C nanoparticles dispersed on carbon nanotubes, dramatically increases the electrical efficiency up to 88% with a cycle life of more than 100 cycles compared to just the carbon nanotubes. The Mo<sub>2</sub>C nanoparticle catalysts contribute to the formation of a well-dispersed lithium peroxide nanolayers (Li<sub>2</sub>O<sub>2</sub>) on the Mo<sub>2</sub>C/carbon nanotubes with large contact area during oxygen reduction reaction (ORR). This Li<sub>2</sub>O<sub>2</sub> structure can be decomposed at low potential upon oxygen evolution reaction (OER) by avoiding the energy loss associated with the decomposition of the typical Li<sub>2</sub>O<sub>2</sub> discharge products.

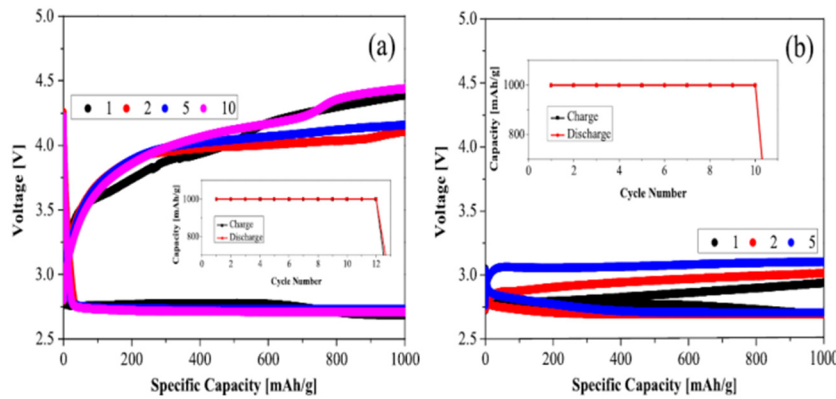


**Figure V- 373:** Voltage profiles showin the how the Pd nanoparticle based cathode material dramatically reduces the charge overpotential in a Li-O<sub>2</sub> battery. (a) Porous carbon only, (b) porous carbon with Al<sub>2</sub>O<sub>3</sub> coating and Pd nanoparticles

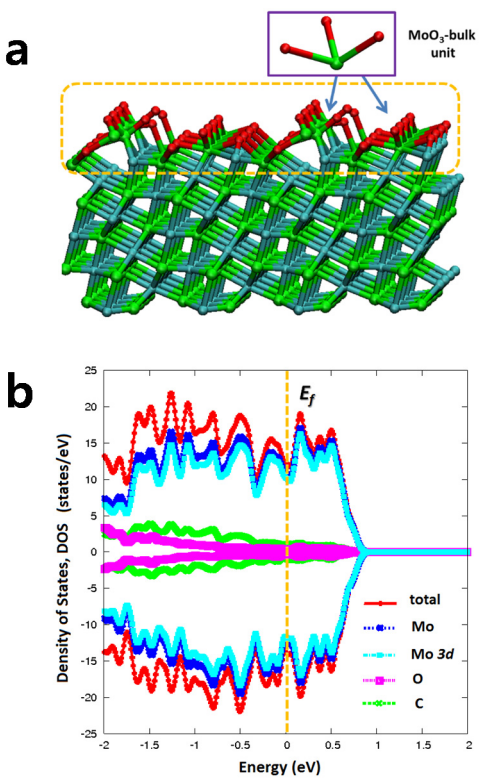


**Figure V- 374:** a) The oxidized  $\text{Mo}_2\text{C}$  (101)-Mo surface with a  $\text{MoO}_3$ -like portion (the highlighted region shows a  $\text{MoO}_3$ -bulk unit-like configuration in the inset) on top surface layer after the adsorbed  $\text{O}_2$  molecules dissociate. b) The electronic density of states (e-DOS) around the Fermi-level ( $E_f$ )

- We have investigated a number of metal nanoparticles as catalysts for  $\text{Li-O}_2$  batteries. Pd nanoparticles on an alumina coated carbon surface were found to significantly reduce the charge overpotential and increase efficiency.
- Molybdenum carbide ( $\text{MoC}_2$ ) nanoparticles have been investigated as catalysts for  $\text{Li-O}_2$  batteries and found to significantly reduce the charge overpotential and increase cycle life.

Future research will focus on an integrated effort using these results on the mechanism of lithium oxygen formation and electrolytes for increasing the cycle life and energy density of the  $\text{Li-O}_2$  battery.

#### FY 2015 Publications/Presentations

1. Jun Ming, Won-Jin Kwak, Jin-Bum Park, Chang-Dae Shin, Jun Lu, Larry Curtiss, Khalil Amine, and Yang-Kook Sun, "Physical pulverization strategy to prepare highly active composite of CoOx and crushed graphite for lithium-oxygen battery", *ChemPhysChem*, **15**, 2070-2076, 2014. (Invited Article)
2. "Understanding and mitigating some of the key factors that limit non-aqueous lithium-air battery performance," J. Lu, K. C. Lau, Y.-K. Sun, L. A. Curtiss and K. Amine, *Journal of the Electrochemical Society*, **162**, A1-A8 (2015).
3. Study on the Catalytic Activity of Noble Metal Nanoparticles on Reduced Graphene Oxide for Oxygen Evolution Reactions in Lithium–Air Batteries, Y. S. Jeong, J.-B. Park, H.-G. Jung, J. Kim, X. Luo, J. Lu, L. Curtiss, K. Amine, Y.-K. Sun, B. Scrosati, and Y. J. Lee, *Nanoletters*, **15**, 4261–4268 (2015) 10.1021/nl504425h
4. Theoretical Exploration of Various Lithium Peroxide Crystal Structures in a Li-Air Battery, K. C. Lau, D. Qiu, X. Luo, J. Greeley, L. A. Curtiss, J. Lu, and K. Amine, *Energies*, 529-548 (2015). doi:10.3390/en8010529

Density functional calculations indicate that layered crystalline  $\text{MoO}_3$  bulk is insulating (band gap  $\sim 2$  eV), whereas the noncrystalline amorphous phase of  $\text{MoO}_3$  bulk is metallic shown in Figure V- 374. Thus, we suspect that the formation of metallic noncrystalline  $\text{MoO}_3$ -like layers on the  $\text{Mo}_2\text{C}$  nanoparticles along with the carbon nanotubes are responsible for the low charge overpotentials and the high cyclability found in the  $\text{Li-O}_2$  cell ls based on these new materials.

Although no electrolyte and electrode can be 100% stable yet, we expect that this effective composite cathode can be a good reference to help improve the electrical efficiency and cyclability in the  $\text{Li-O}_2$  battery system.

#### Conclusions and Future Directions

In this project, an integrated experimental and theoretical approach was used to address the technical barriers for non-aqueous  $\text{Li}$ -air battery. This project addresses the cycle life and energy density of  $\text{Li}$ -air batteries through investigation of (a) the discharge formation mechanism and relationship to electrolytes, (b) investigation of the morphology and composition of the discharge product, and (c) investigation of electrolyte decomposition mechanisms.

Accomplishments during the past year include:

- A combined experimental and theoretical study has provided new insight into how interfacial effects can stabilize lithium superoxide, which may play an important role in the charge and discharge chemistries of a  $\text{Li-O}_2$  battery.

5. “A Mo<sub>2</sub>C/Carbon Nanotube Composite Cathode for Lithium–Oxygen Batteries with High Energy Efficiency and Long Cycle Life,” W.-J. Kwak, K. C. Lau, C.-D. Shin, K. Amine, L. A. Curtiss, and Y.-K. Sun, *ACS Nano*, **9**, 4129–4137 (2015), 10.1021/acsnano.5b00267
6. Interfacial Effects on Lithium Superoxide Disproportionation in Li-O<sub>2</sub> Batteries, D. Zhai, K. C. Lau, H.-H. Wang, J. Wen, D. J. Miller, J. Lu, F. Kang, B. Li, W. Yang, J. Gao, E. Indacochea, L. A. Curtiss, and K. Amine *Nano Lett.*, **15** (2), 1041–1046 (2015).
7. Implications of the Unpaired Spins in Li–O<sub>2</sub> Battery Chemistry and Electrochemistry: A Minireview, K. C. Lau, J. Lu, X. Luo, L. A. Curtiss, K. Amine, *ChemPlusChem*, *ChemPlusChem* **80** (2), 336-343 (2014)
8. Pd nanoparticles on ZnO-passivated porous carbon by atomic layer deposition: an effective electrochemical catalyst for Li-O<sub>2</sub> batteries, X. Luo, M. Piernavieja-Hermida, J. Lu, T. Wu, J. Wen, Y. Ren, D. Miller, Z. Zak Fang, Y. Lei and K. Amine, *Nanotechnology* **26**, 164003 (2015)

#### Invited Talks

1. “Stability of Lithium Superoxide and Its Role in Charge and Discharge Chemistries in Lithium–Oxygen Batteries,” L. A. Curtiss, Spring ACS National Meeting, Denver, CO March 22-26, 2015.
2. “New insights into the role of lithium superoxide in lithium-oxygen batteries Beyond Lithium Ion,” L. A. Curtiss, VII Meeting, Oak Ridge National Laboratory, June 2-4, 2015.
3. “Catalytic Reactivity of Supported Subnanometer Clusters: A Computational Perspective,” L. A. Curtiss, International Conference on Chemical Bonding, Kauai, Hawaii, July 2-6, 2015.
4. “Lithium-oxygen batteries: computational studies of growth and nucleation mechanisms and effect on cell performance,” L. A. Curtiss, Fall ACS National Meeting, Boston, MA August 15-20, 2015.

# V.J.4 Overcome the Obstacles for the Rechargeable Li-air Batteries (BNL/UWM)

## Objectives

- We propose to investigate the root causes of the major obstacles of the air cathode in the Li-air batteries, which impede the realization of high energy, high power, and long cycle life Li-air batteries. The research is to focus on the investigation of catalytic disproportionation of superoxide ions by borane compounds; the impact of carbon structure and designation of a Li-air flow cell.

## Technical Barriers

- The poor cycle life of Li air batteries.
- The poor rate capability of Li-air batteries
- A feasible engineering design of a Li-air batteries.
- The lack of High efficient O<sub>2</sub> reduction catalyst.

## Technical Targets

- Compete investigation of carbon catalytic activity for O<sub>2</sub> reduction.
- Determine the rate constant for the borane catalyzed superoxide disproportionation.
- Synthesize borane catalysts with various structures.
- Design and test a Li-air flow cell.

## Accomplishments

- We found that strong Lewis acid such as Tris(pentafluorophenyl)borane can catalyse a rapid superoxide (O<sub>2</sub><sup>-</sup>) disproportionation. The reaction is faster than the reaction between superoxide and solvents. The reaction rate constants were determined.
- The solvation number of Li ion with commonly used non-aqueous electrolytes were determined as well as the relative strength of the solvents for the solvation of Li ion. The impact of the solvated Li cation on the O<sub>2</sub> redox reaction was determined.
- The kinetics for the redox couple O<sub>2</sub>/O<sub>2</sub><sup>-</sup> are very fast, therefore no catalyst seems necessary to assist the charge transfer process. Apparently, the main source of the overpotential for the O<sub>2</sub> reduction reaction is from mass diffusion. However, Li<sub>2</sub>O<sub>2</sub> becomes soluble in non-aqueous electrolytes in the presence of the tetraethylammonium tetrafluoroborate additive. The soluble B-O<sub>2</sub><sup>2-</sup> ions can be oxidized electro-catalytically.
- Based on the fundamental studies, a Li-air flow cell was designed and tested.

## Introduction

A Li-air system promises extraordinary theoretical energy density. Like many battery systems, this impressive capacity is accompanied with a trade-off in complexity. In the case of rechargeable Li-air batteries, besides the metallic Li anode, such complexities result from the redox reaction of oxygen in non-aqueous electrolytes. For example, the superoxide (O<sub>2</sub><sup>-</sup>) ions formed as a product of O<sub>2</sub> reduction in non-aqueous electrolytes can react with the carbonate solvents typically used in Li-ion batteries, e.g. propylene carbonate (PC) and ethylene carbonate (EC). In order to unlock the potential of Li-air redox chemistry, it is crucial to overcome those

## Project Details

### Tien Duong (Program Manager)

Subcontractor: BNL

### Deyang Qu (University of Wisconsin Milwaukee)

College of Engineering

3200 N Cramer Street

Milwaukee, WI 43211

Phone: 414-229-3716; Fax: 414-229-6958

E-mail: [gud@uwm.edu](mailto:gud@uwm.edu)

### Xiao-Qing Yang (Brookhaven National Laboratory)

Chemistry Department

Building 555, Brookhaven National Laboratory

Upton, NY 11973

Phone: 631-344-3663; Fax: 631-344-5815

E-mail: [xyang@bnl.gov](mailto:xyang@bnl.gov)

obstacles e.g. to prevent chemical reactions between  $O_2^-$  and the solvents, pre-mature passivation of the gas diffusion electrode caused by  $Li_2O_2$  precipitation.

### Approach

The research was based on the fundamental understanding of the mechanism of the  $O_2$  redox reaction. Through the comprehensive knowledge gained in the research, the obstacles of Li-air cathode were tackled. Innovative approaches to overcome the barriers were suggested and tested.

### Results

#### 1. Determination of the reaction rate constants and reaction orders for the catalytic disproportionation of superoxide ions and its reaction with PC.

Superoxide reacts with carbonate solvents in Li-air batteries. Tris(pentafluorophenyl)borane is found to catalyze a more rapid superoxide ( $O_2^-$ ) disproportionation reaction than the reaction between superoxide and propylene carbonate (PC). (See Figure V- 375.) With this catalysis, the negative impact of the reaction between the electrolyte and  $O_2^-$  produced by the  $O_2$  reduction can be minimized. A simple kinetic study using ESR spectroscopy was reported to determine reaction orders and rate constants for the reaction between PC and superoxide, and the disproportionation of superoxide catalyzed by Tris(pentafluorophenyl)borane and Li ions (see Table V- 13). The reactions are found to be first order and the rate constants are 0.033 s<sup>-1</sup>M<sup>-1</sup>, 0.020 s<sup>-1</sup>M<sup>-1</sup> and 0.67 s<sup>-1</sup>M<sup>-1</sup> for reactions with PC, Li ion and Tris(pentafluorophenyl)borane, respectively.

**Table V- 13: Reaction rate constants (Initial concentration for  $O_2^-$  - 0.01 M)**

	Concentration (M)	STD	R	$k'$ (s <sup>-1</sup> )	$k$ (s <sup>-1</sup> M <sup>-1</sup> )
PC	0.08	$6.87 \times 10^{-5}$	0.998	0.003	0.037
Li-ion	0.2	$3.78 \times 10^{-4}$	0.960	0.004	0.02
TPFPB	0.009	$1.59 \times 10^{-4}$	0.997	0.006	0.67

Lewis acids were found to catalyze the disproportionation of  $O_2^-$  ions in aprotic solution. The catalytic effect is related to the strength of the Lewis acidity, which is evident that strong Lewis acid TPFPB catalyse much faster disproportionation reaction than weak one like Li ion. Strong Lewis acids like tris(pentafluorophenyl)borane can also catalyse the disproportionation of  $O_2^-$  much faster than it can react with a carbonate solvent like PC. Therefore, the negative impacts of the chemical interaction between  $O_2^-$  and carbonate solvents can be minimized in Li-air batteries.

#### 2. The impact of solvation of $Li^+$ Cation on the $O_2$ redox reactions

The solvation of  $Li^+$  with eleven non-aqueous solvents commonly used as the electrolytes for Li batteries were studied.

The solvation preferences of different solvents were compared by means of electrospray mass spectrometry and collision-induced dissociation. The relative strength of the solvent for the solvation of  $Li^+$  was determined. The Lewis acidity of the solvated  $Li^+$  cations was determined by the preferential solvation of the solvent in the solvation shell. The kinetics of the catalytic disproportionation of the  $O_2^-$  depends on the relative Lewis acidity of the solvated  $Li^+$  ion. The impact of the solvated  $Li^+$  cation on the  $O_2$  redox reaction was also investigated. (See Table V- 14 and Figure V- 376.)

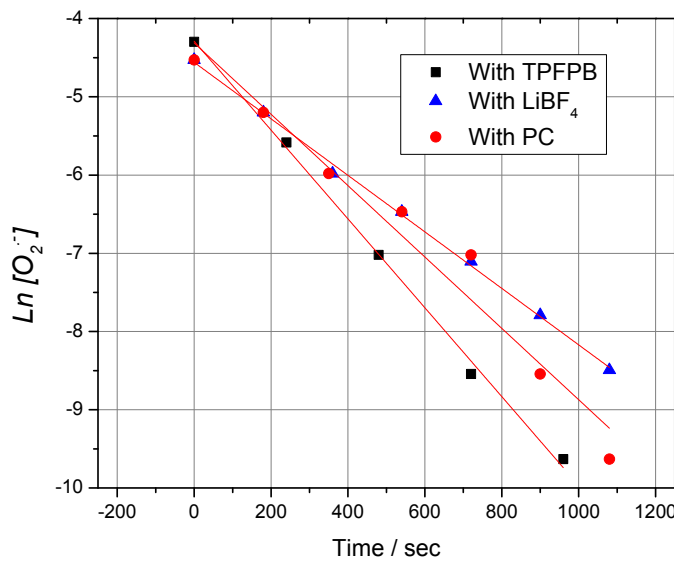


**Figure V- 375: The change of the natural logarithm of  $O_2^-$  concentration with time**

**Table V- 14: Relative molar ratio of different solvents in the Li<sup>+</sup> solvation adducts obtained from ESI-MS spectra of 5mM LiBF<sub>4</sub> DMSO and other solvents (1:1) mixture. The voltages of Cone and Extractor are 20 and 0V for ESI-MS**

Solvent X=	Mol% of solvent X in Li <sup>+</sup> solvation shell	Solvent Y=	Mol% of solvent Y in Li <sup>+</sup> solvation shell
DMSO	98.2	Py	1.8
DMSO	97.1	ACN	2.9
DMSO	69.9	DME	30.1
DMSO	43.1	DEDME	56.9
DMSO	98.6	EC	1.4
DMSO	91.8	PC	8.2
DMSO	99.4	DMC	0.6
DMSO	98.6	DEC	1.4
DMSO	69.2	DMF	30.8
DMSO	97.7	GBL	2.3
DMSO	48.9	DMSO <sup>d6</sup>	51.1

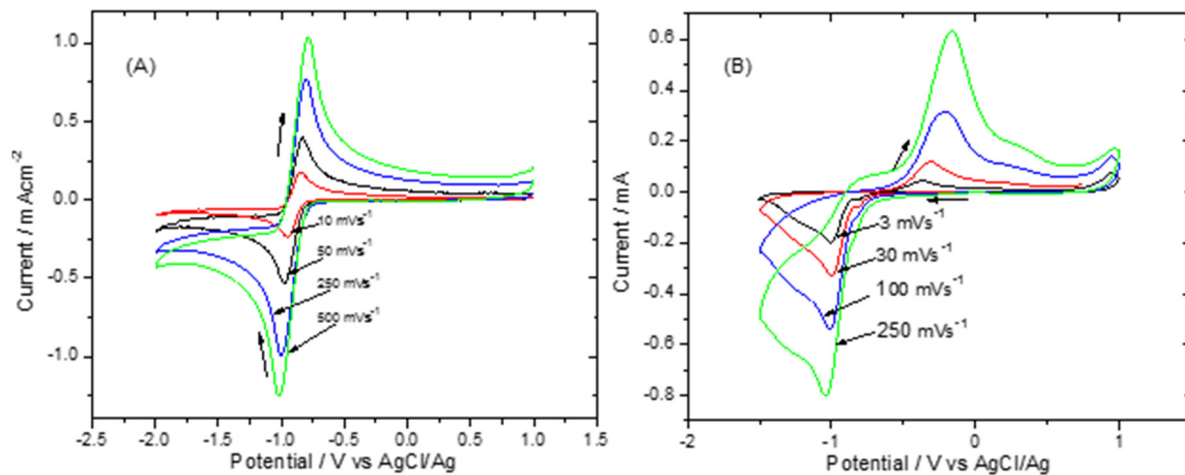


**Figure V- 376: Cyclic voltammograms at various scan rates in 1 M TEABF<sub>4</sub> DMSO electrolyte (A) and 1 M LiBF<sub>4</sub> DMSO electrolyte (B) saturated with O<sub>2</sub> on a glassy carbon-disc electrode**

The local structure of solvation around a Li<sup>+</sup> cation in a mixed solvent electrolyte plays important roles in the properties of an electrolyte (e.g. the conductivity and viscosity of the electrolyte). Using ESI-MS and CID, we indeed observed the selective solvation of a Li<sup>+</sup> cation (Table V- 14). Such selective solvation was proven to be related to the relative strength of the interaction between the solvent and Li<sup>+</sup>. The electrochemical behaviors of a Li-air battery are dramatically affected by the kind of solvent used in the electrolytes which was attributed, at least partially, to the manner in which Li<sup>+</sup> cations were solvated. The solvent effects on the O<sub>2</sub> redox reaction were attributed to the alteration of the acidity of the solvated Li<sup>+</sup> cation. The superoxide (O<sub>2</sub><sup>-</sup>), which is the product of O<sub>2</sub> reduction, is a Lewis base and can be catalytically disproportioned by a Lewis acid. The inclination is that the Lewis acidity of a solvated Li<sup>+</sup> ion decreases if solvated with a solvent that strongly interacts with it. Figure V- 376 A and B show the cyclic voltammetry profiles at various scan rates for a glassy carbon electrode in the O<sub>2</sub> saturated DMSO solution containing 1M tetraethyl ammonium tetrafluoroborate (TEABF<sub>4</sub>) and 1M LiBF<sub>4</sub>, respectively.

### 3. Electrocatalytic O<sub>2</sub> redox reaction

Oxygen reduction and oxygen evolution reactions were studied on graphite electrodes with different crystal orientations. The kinetics for the redox couple O<sub>2</sub>/O<sub>2</sub><sup>-</sup> are very fast, therefore no catalyst seems necessary to assist the charge transfer process. Apparently, the main source of the overpotential for the O<sub>2</sub> reduction reaction is from mass diffusion. Li<sub>2</sub>O<sub>2</sub> becomes soluble in non-aqueous electrolytes in the presence of the tetraethylammonium tetrafluoroborate additive. The soluble B-O<sub>2</sub><sup>2-</sup> ions can be oxidized electro-catalytically. The edge orientation of graphite demonstrates superior catalytic activity for the oxidation over basal orientation. The findings reveal an opportunity for recharging Li-air batteries efficiently and a new strategy of developing the catalyst for oxygen evolution reaction.

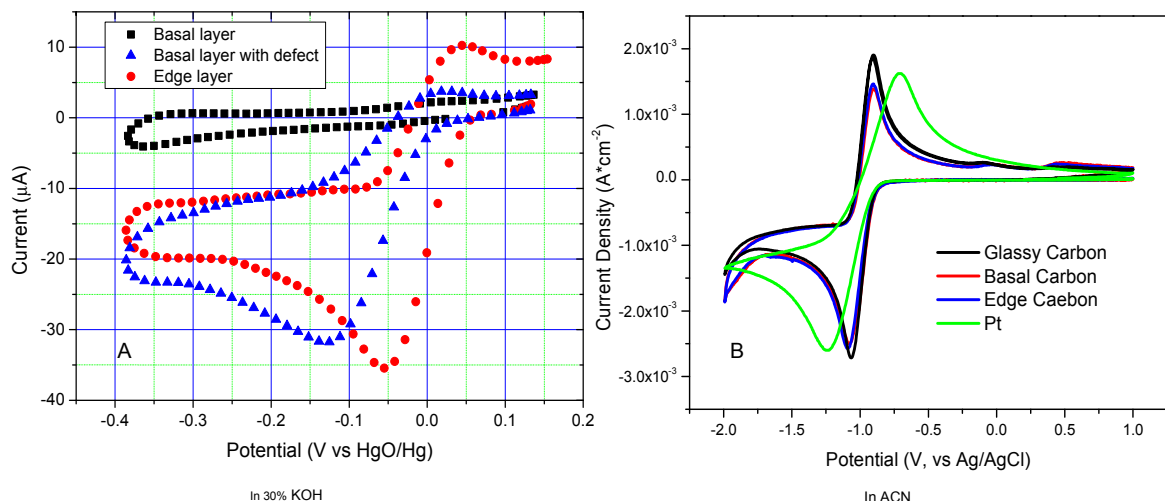


Figure V- 377: Cyclic voltammetry for the O<sub>2</sub> redox reaction on the surface of pyrolytic graphite (PG) edge layer, PG basal layer and glassy carbon in 30% KOH aqueous electrolyte (A) 0.1 M TEABF<sub>4</sub> acetonitrile electrolyte (B) saturated with O<sub>2</sub>

Unlike in aqueous electrolyte, no difference can be observed for the electrocatalytic activity for the ORR on the various carbon surfaces in acetonitrile based electrolyte. One can easily observe the differences between the cyclic voltammetry for the ORR in alkaline electrolyte (Figure V- 377A) and that in non-aqueous electrolyte (Figure V- 377B). Besides the clear difference in the electrocatalytic activity on various carbon orientations, the O<sub>2</sub> redox reaction was very irreversible in the alkaline electrolyte, but very reversible in acetonitrile-based electrolyte. Hence, the activation energy or the over-potential for the ORR and OER in acetonitrile would be considerably lower. Since a catalyst increases the rate of a reaction by reducing the activation energy, with an already low activation energy, the catalyst would have minimal impact on the kinetics of the O<sub>2</sub> redox reaction in acetonitrile. In addition, the possible absorption of organic molecules on the graphite electrodes could also level the electrochemical catalytic capability or even poison a catalyst as shown in Figure V- 378, Pt metal demonstrates less catalytic activity.

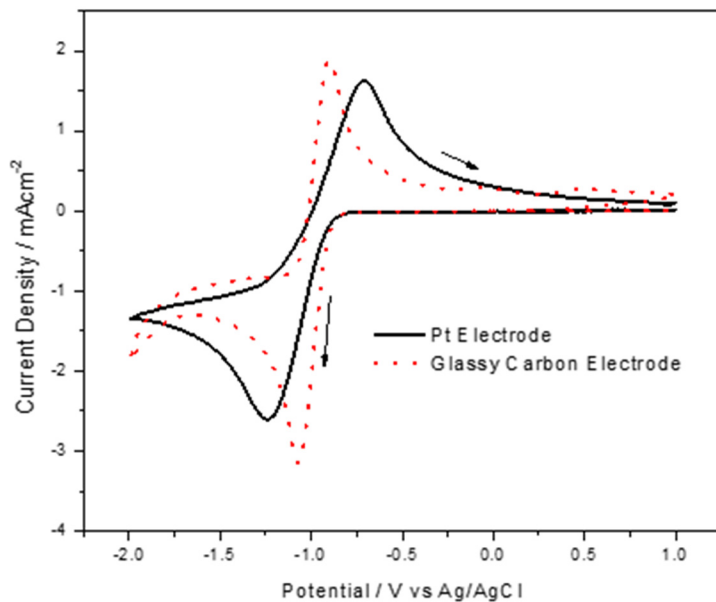


Figure V- 378: Comparison of cyclic voltammetry of O<sub>2</sub> redox reaction on glass carbon and Pt electrodes in 0.1 M TEABF<sub>4</sub> acetonitrile electrolyte saturated with O<sub>2</sub>. The scan rate is 50mv/s

reaction of O<sub>2</sub>/O<sub>2</sub><sup>•</sup> is very rapid. The overpotential for the ORR on a Li-air cathode is limited by mass diffusion. A highly active catalyst, such as Pt, could catalyze other side reactions and poison the surface of electrode, which could have a negative impact on the kinetics of the redox reaction. Li<sub>2</sub>O<sub>2</sub> can become soluble in a non-aqueous electrolyte if a strong Lewis acid additive is added such as TPFPB, which results in the formation of a stable Lewis acid-O<sub>2</sub><sup>2-</sup> complex ion (for example, B-O<sub>2</sub><sup>2-</sup>). The boron-superoxide complex can be electrocatalytically oxidized. The edge orientation of graphite demonstrated higher catalytic activity to the oxidation of B-O<sub>2</sub><sup>2-</sup> than to that of the basal orientation. These findings reveal a new opportunity to develop highly effective catalysts for the charge process for Li-air batteries.

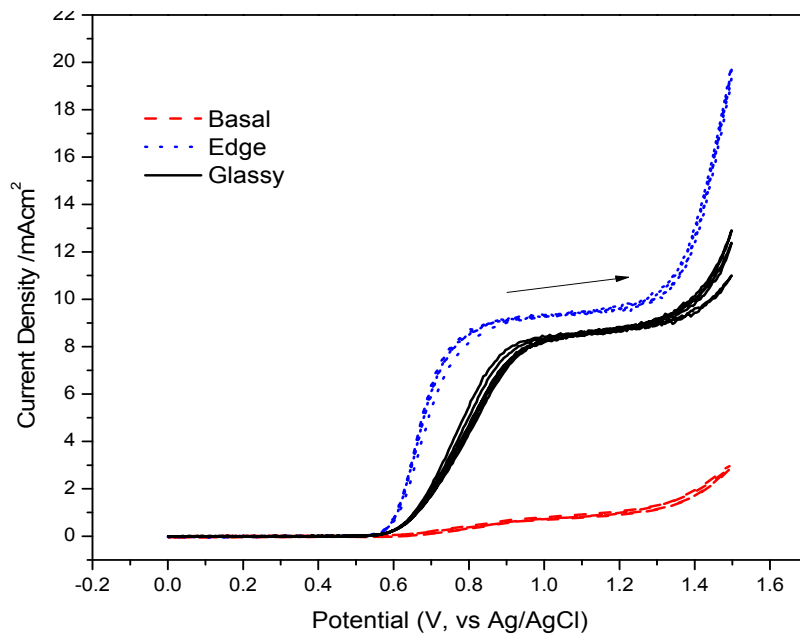


Figure V- 379: Comparison of linear voltammetry of the oxidation of soluble B-O<sub>2</sub><sup>2-</sup> in 0.1M LiClO<sub>4</sub> acetonitrile electrolyte containing 20mM TPFPB and saturated with Li<sub>2</sub>O<sub>2</sub>. The experiments were done on rotating disk electrode. Rotating rate is 800 rpm, scan rate is 50mv/s

We reported in the FY2013 and 2014 annual reports that Li<sub>2</sub>O<sub>2</sub> can become dissolved by forming B-O<sub>2</sub><sup>2-</sup> in Tris(pentafluorophenyl)borane (TPFPB). Figure V- 379 shows the significant difference between the oxidation reaction of the B-O<sub>2</sub><sup>2-</sup> anion on the basal and edge orientations of graphite. The oxidation of B-O<sub>2</sub><sup>2-</sup> was inhibited on the basal orientation, while the electrocatalytic activity was found to be the highest on the edge orientation. Besides the lack of unsatisfied valences on the basal orientation to provide active sites for the adsorption of the reactant, it was believed that the different electrocatalytic properties of edge and basal orientations were also due to the fact that the applied potential falls across the space charge region of the basal orientation.

In summary, the kinetics of the redox Li-air cathode is limited by mass diffusion. A highly active catalyst, such as Pt, could catalyze other side reactions and poison the surface of electrode, which could have a negative impact on the kinetics of the redox reaction. Li<sub>2</sub>O<sub>2</sub> can become soluble in a non-aqueous electrolyte if a strong Lewis acid additive is added such as TPFPB, which results in the formation of a stable Lewis acid-O<sub>2</sub><sup>2-</sup> complex ion (for example, B-O<sub>2</sub><sup>2-</sup>). The boron-superoxide complex can be electrocatalytically oxidized. The edge orientation of graphite demonstrated higher catalytic activity to the oxidation of B-O<sub>2</sub><sup>2-</sup> than to that of the basal orientation. These findings reveal a new opportunity to develop highly effective catalysts for the charge process for Li-air batteries.

#### 4 Design a Li-air flow cell.

A lab flow cell was made and the preliminary tests of cycling was done. The results are shown in Figure V- 380. Clearly, the capacity of the cell without the strong Lewis acid additive decreased very rapidly while the efficiency was low; both the capacity and efficiency improved significantly when the additive was added. We believe the strong Lewis acid additive, on one hand, accelerate the superoxide disproportion rate which minimized its chemical interaction with the electrolyte; one the other hand, make the Li<sub>2</sub>O<sub>2</sub> more soluble which delayed the cathode passivation due to solid precipitation.

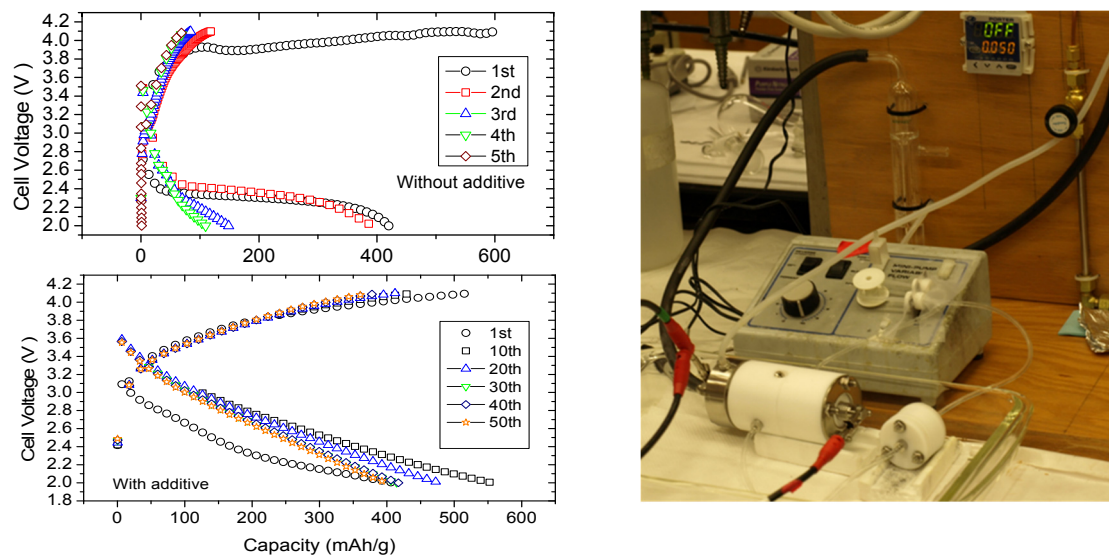


**Figure V-380: First 50 cycles for a Li-air flow cell with and without B additive**

#### FY 2015 Publications/Presentations

1. Q. Wang, D. Zheng, M.E. McKinnon, X.Q. Yang, D.Y. Qu, "Kinetic Investigation of Catalytic Disproportionation of Superoxide Ions in the Non-aqueous Electrolyte used in Li-Air Batteries", *J. Power Sources* 274(2015)1005-1008.
2. Dong Zheng, Xuran Zhang, Deyu Qu, Xiao-Qing Yang, Hung-Sui Lee, D.Y. Qu, Investigation of the Electrocatalytic Oxygen Reduction and Evolution Reactions in Lithium-Oxygen Batteries, *J. Power Sources*, 288(2015)9-12
3. Dong Zheng, Xiaoqing Yang, D. Qu, Preferential Solvation of Lithium Cations and the Impacts on the Oxygen Reduction in Li-Air Batteries, *ACS Appl. Mater. & Interface ACS Appl. Mater. & Interface* 7(2015)19923-19929.

# V.K Sodium-Ion Batteries

## V.K.1 Exploratory Studies of Novel Sodium-Ion Battery Systems (BNL)

### Objectives

- To determine the contributions of electrode materials changes, interfacial phenomena, and electrolyte decomposition to the cell capacity and power decline for Na-ion batteries.
- To develop and apply synchrotron based *in situ* X-ray techniques such as x-ray diffraction (XRD) and x-ray absorption spectroscopy (XAS) to study materials in an environment that is close to the real operating conditions for na-ion cells.
- To develop new diagnostic tools for Na-ion battery studies.

### Technical Barriers

- Na-ion batteries with long calendar and cycle life
- Na-ion batteries with superior abuse tolerance
- To reduce the production cost of a PHEV batteries

### Technical Targets

- Complete the particle size effects on kinetic properties of  $\text{Li}_4\text{Ti}_5\text{O}_{12}$  as anode materials for Na-ion batteries using synchrotron based *in situ* x-ray diffraction.
- Complete the *in situ* x-ray diffraction studies of sodium iron ferrocyanide (Prussian Blue Analogous) as cathode materials for Na-ion batteries during charge-discharge cycling.
- Complete the *in situ* x-ray absorption near edge structure (XANES) studies of sodium iron ferrocyanide (Prussian Blue Analogous) at Fe k-edge as cathode materials for Na-ion batteries during charge-discharge cycling.
- Complete the *in situ* extended x-ray absorption fine structure (EXAFS) studies of sodium iron ferrocyanide (Prussian Blue Analogous) at Fe k-edge as cathode materials for Na-ion batteries during charge-discharge cycling.

### Accomplishments

- Through collaboration with Prof. Yongsheng Hu at Institute of Physics, Chinese Academy of Sciences, the the structural changes in a new cathode materials  $\text{Na}_{0.44}[\text{Mn}_{0.44}\text{Ti}_{0.56}]\text{O}_2$  during Na insertion and extraction were studied using *in situ* XRD experiment. The results show continuous peak shift during Na insertion/extraction but no new phase formation upon Na insertion/extraction into/from  $\text{Na}_{0.44}[\text{Mn}_{0.44}\text{Ti}_{0.56}]\text{O}_2$  in a wide Na content rangewas observed. Although a significant amount of  $\text{Mn}^{3+}$  was reserved in  $\text{Na}_{0.44}[\text{Mn}_{0.44}\text{Ti}_{0.56}]\text{O}_2$  structure for the entire range of electrochemical cycles, the main crystal structure was maintained during the entire charge/discharge process without any obvious structure transformation. This is further supported by *ex situ* STEM results. The results of this study were published on Nature communications
- Through collaboration with Prof. Yuguo Guo at Institute of chemistry, Chinese Academy of Sciences, Structure evolution of sodium iron ferrocyanide (Prussian Blue Analogous) as cathode materials for

### Project Details

#### Xiao-Qing Yang

Chemistry Department  
Building 555, Brookhaven National Laboratory  
Upton, NY 11973  
Phone: 631-344-3663; Fax: 631-344-5815  
E-mail: [xyang@bnl.gov](mailto:xyang@bnl.gov)

#### Xiqian Yu

Chemistry Department  
Building 555, Brookhaven National Laboratory  
Upton, NY 11973  
Phone: 631-344-4142; Fax: 631-344-5815  
E-mail: [xyu@bnl.gov](mailto:xyu@bnl.gov)

Start Date: October 2014

Projected End Date: September 2015

Na-ion batteries has been studied using *ex situ* X-ray absorption near edge spectroscopy (XANES) and Extended X-ray absorption fine structure spectroscopy (EXAFS) at different charge or discharge states at the Fe k-edge. The energy of the absorption maximum (7,131 eV) for the fully charged electrode (4.4 V) is similar to that of the  $K_3Fe(CN)_6$ , which confirms that most of Fe in the charged states are in the  $Fe^{3+}$  state. The results of this study was published on Nano Research.

## Introduction

Recently, due to the abundant sodium resources and their potentially low cost in raw materials, research and development of room-temperature sodium (Na)-ion batteries have attracted extensive interest for application in large-scale stationary energy storage and smart grid. Unlike what might be assumed that sodium insertion and extraction is similar as lithium, recent detailed structural studies on  $Na_xCoO_2$ ,  $Na_xVO_2$  and Sb show that sodium storage mechanisms in most cathode/anode materials could be quite complicated and significantly different from the corresponding lithium compounds. Unfortunately, for many electrode materials used in Na-ion batteries, the sodium storage mechanisms and the relationship between the structural changes and their electrochemical performance are far from well understood. Therefore, completely structural or physical characterization of the materials is quite necessary and the development of new and facile *in situ* techniques, especially dedicated to sodium storage system, will be very desirable. In collaboration with Prof. Yongsheng Hu at Institute of Physics, Chinese Academy of Sciences, BNL has completed the structural studies of  $Li_4Ti_5O_{12}$  during chemically sodium insertion using synchrotron based *in situ* X-ray diffraction (XRD). The structural evolution of another new cathode materials  $Na_{0.44}[Mn_{0.44}Ti_{0.56}]O_2$  during charge-discharge cycling was also studied using *in situ* X-ray diffraction (XRD) and x-ray absorption (XAS) techniques. Through collaboration with Prof. Yuguo Guo at Institute of chemistry, Chinese Academy of Sciences, Structure evolution of sodium iron ferrocyanide (Prussian Blue Analogous) as cathode materials for Na-ion batteries has been studied using *ex situ* X-ray absorption spectroscopy (XAS) at different charge or discharge states at the Fe k-edge.

## Approach

1. Synchrotron based X-ray diffraction (XRD), X-ray absorption spectroscopy (XAS), to elucidate and differentiate the contribution from each component and element to the capacity and structural changes of various cathode and anode materials for Na-ion batteries
2. Extended collaboration with other US and international academic institutions.

## Results

We have achieved the following progress:

### **Study the particle size effects on kinetic properties of $Li_4Ti_5O_{12}$ as anode materials for Na-ion batteries**

The structural revolution of  $Li_4Ti_5O_{12}$  during chemically sodium insertion was studied using synchrotron based *in situ* X-ray diffraction (XRD). The sodium insertion behavior into  $Li_4Ti_5O_{12}$  is strongly size dependent. A solid solution reaction behavior in a wide range has been revealed during sodium insertion into the nano-sized  $Li_4Ti_5O_{12}$  ( $\sim 44$  nm), which is quite different from the well-known two-phase reaction of  $Li_4Ti_5O_{12}/Li_7Ti_5O_{12}$  system during lithium insertion, and also has not been fully addressed in the literature so far.

Figure V- 381(a), (b) and (c) show the SEM images and the crystallite size distribution of nano-size ( $r=44$  nm,  $r=120$ nm) and sub micro-size ( $r=440$  nm)  $Li_4Ti_5O_{12}$ . Figure V- 381 (d) shows the *in situ* XRD patterns collected during chemical sodiation of the nano-size 44nm (top), 120nm (middle) and sub micro-size (bottom)  $Li_4Ti_5O_{12}$ , the sodium insertion caused phase transition behavior is strongly related to the particle size of the material. Fully sodium insertion can be finished within 2 hours for 44nm nano-sized  $Li_4Ti_5O_{12}$ , while for the sub micro- sized  $Li_4Ti_5O_{12}$ , no new phase can be observed within the initial 8 hours during chemical sodiation. Figure V- 381 (e) shows the enlarged view of the (111) reflections for the pristine  $Li_4Ti_5O_{12}$  with different particle sizes. Figure V- 381 (f) shows XRD patterns of the sub micro-sized  $Li_4Ti_5O_{12}$  collected after chemical sodiation of 20 h, 40 h and 80 h respectively, new  $Na_6LiTi_5O_{12}$  phase emerged after long time reaction. Full sodiation was obtained in 2h and 24h respectively for 44nm and 120nm  $Li_4Ti_5O_{12}$ . Figure V- 381 (g) shows the charge-discharge curve (1st: dash line and 30th: solid line) of Na insertion and extraction into  $Li_4Ti_5O_{12}$  (0.1C, 0.5 V-3 V).

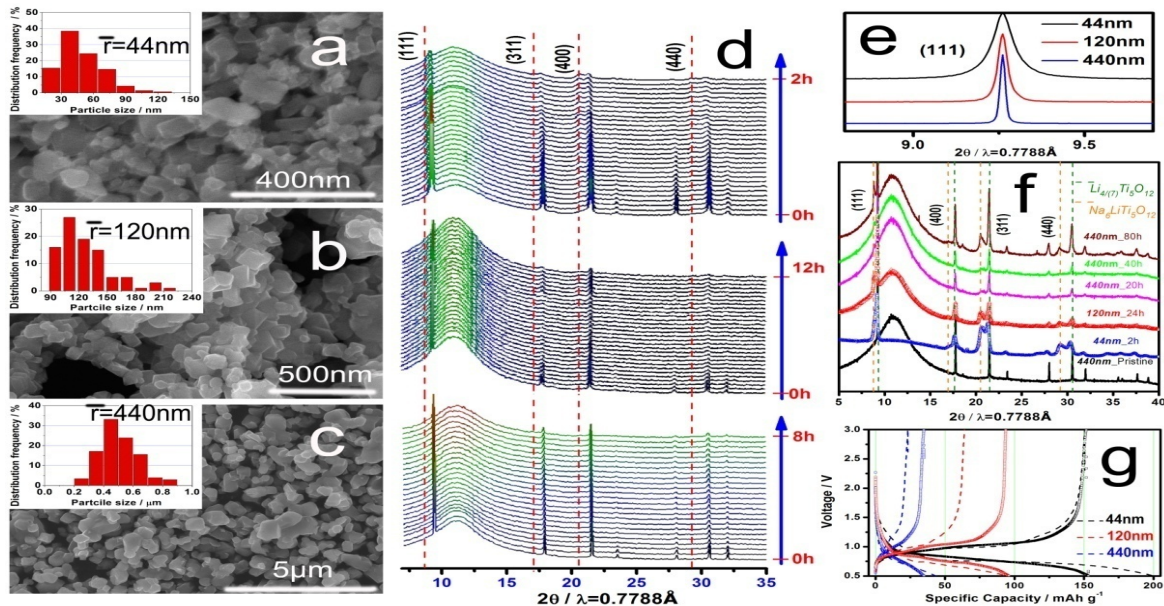


Figure V- 381: (a), (b) and (c) The SEM images and the crystallite size distribution of nano-size ( $r=44$  nm,  $r=120$ nm) and sub micro-size ( $r=440$  nm)  $\text{Li}_4\text{Ti}_5\text{O}_{12}$ ; (d) *in situ* XRD patterns collected during chemical sodiation of the nano-size 44nm (top), 120nm (middle) and sub micro-size (bottom)  $\text{Li}_4\text{Ti}_5\text{O}_{12}$ , the sodium insertion caused phase transition behavior is strongly related to the particle size of the material (e) Enlarge view of the (111) reflections for the pristine  $\text{Li}_4\text{Ti}_5\text{O}_{12}$ ; (f) XRD patterns of the sub micro-sized  $\text{Li}_4\text{Ti}_5\text{O}_{12}$  collected after chemical sodiation of 20 h, 40 h and 80 h respectively, new  $\text{Na}_6\text{LiTi}_5\text{O}_{12}$  phase emerged after long time reaction; Sodiation completed in 2h and 24h respectively for 44nm and 120nm  $\text{Li}_4\text{Ti}_5\text{O}_{12}$ ; (g) The charge-discharge curve (1st: dash line and 30th: solid line) of Na storage into  $\text{Li}_4\text{Ti}_5\text{O}_{12}$  (0.1C, 0.5 V-3 V)

### Structure evolution of sodium iron ferrocyanide (Prussian Blue Analogous) cathode materials for Na-ion batteries

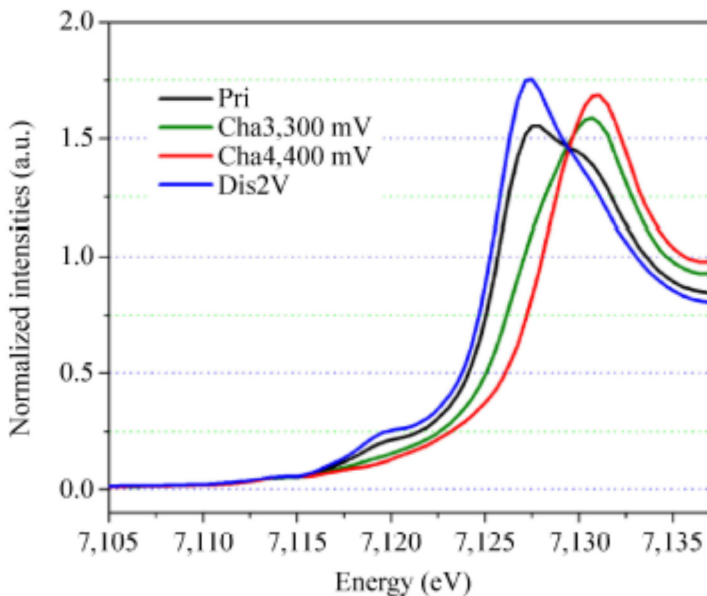
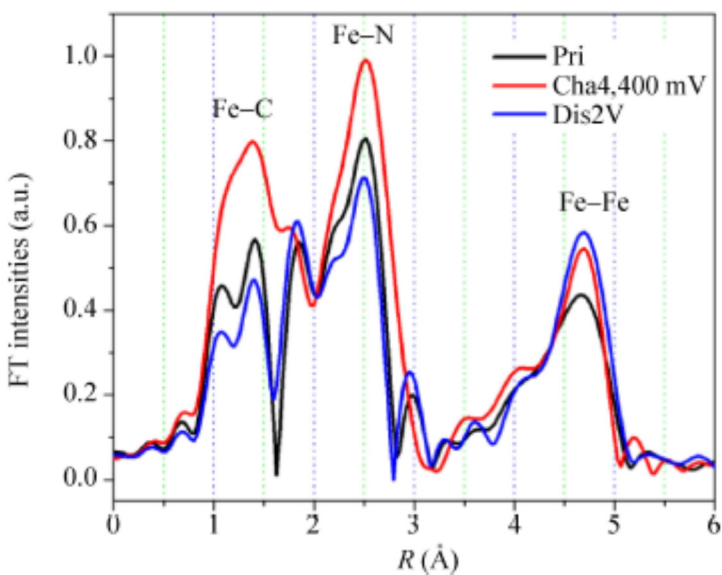


Figure V- 382: Ex situ Fe K-edge XANES spectra of the  $\text{NaFe}(1.63)$  electrode collected at different charge and discharge states

absorption ramp (at about 7,118–7,120 eV) which can be assigned to a shakedown process involving the 1s to 4p transition followed by ligand-to-metal charge transfer (LMCT).

Structure evolution of sodium iron ferrocyanide (Prussian Blue Analogous) as cathode materials for Na-ion batteries has been studied using *ex situ* X-ray absorption near edge spectroscopy (XANES) at different charge or discharge states at the Fe k-edge. More fundamental information about the electronic structure of Fe was revealed by XAS. XANES measurements at the Fe K-edge were performed to quantitatively determine the average valence state of Fe in the charged/discharged  $\text{NaFe}(1.63)$  electrodes and their spectra are shown in Figure V- 382. All the XANES features are similar to those of PBAs reported in the literature. The spectra for the pristine and discharged (2.0 V) materials display a small hump in the beginning of the



**Figure V- 383:** *Ex situ* Fourier transformed magnitude of Fe K-edge EXAFS spectra of the NaFe(1.63) electrode collected at different charge and discharge states

(7,131 eV) for the fully charged electrode (4.4 V) is similar to that of the  $K_3Fe(CN)_6$ , which confirms that most of Fe in the charged states are in the  $Fe^{3+}$  state.

Structure evolution of sodium iron ferrocyanide (Prussian Blue Analogous) as cathode materials for Na-ion batteries has been studied using *ex situ* Extended X-ray absorption fine structure spectroscopy (EXAFS) at different charge or discharge states at the Fe k-edge. Fourier transformed magnitudes of the Fe K-edge EXAFS spectra of the pristine, fully charged and discharged samples are shown in Figure V- 383. Three dominant peaks are observed in all the spectra; the peaks at 1.5, 2.5, and 4.4–4.8 Å can be ascribed to the Fe–C, Fe–N, and Fe–Fe shells, respectively. The significant splitting of the Fe–C and Fe–N peaks for the pristine and discharged samples reveals an irregular or distorted iron octahedral environment due to lower symmetry of the rhombohedral structure which agrees well with XRD results. The intensities of these peaks increased for the fully sodium-extracted sample (4.4 V), which agrees well with the XRD observation of the phase transformation from rhombohedral to a higher symmetry cubic phase upon  $Na^+$  extraction. An obvious change of the peak attributed to the Fe–Na shell (3.0 Å) can also be observed for the pristine and fully discharged electrodes in which sufficient  $Na^+$  ions occupy the interstitial sites in the lattice.

#### Structural evolutions of Ti substituted tunnel-type $Na_{0.44}MnO_2$ oxide as negative electrode for aqueous sodium-ion batteries

To further understand the structural changes in  $Na_{0.44}[Mn_{0.44}Ti_{0.56}]O_2$  during Na insertion and extraction, *in situ* XRD experiment was performed and the results are presented in Figure V- 384. Most of the XRD reflections (e.g. (040), (130), (140)) reveal continuous peak shift during Na insertion/extraction. There is no evident appearance of a new phase upon Na insertion/extraction into/from  $Na_{0.44}[Mn_{0.44}Ti_{0.56}]O_2$  in a wide Na content range. Although a significant amount of  $Mn^{3+}$  was reserved in  $Na_{0.44}[Mn_{0.44}Ti_{0.56}]O_2$  structure for the entire range of electrochemical cycles, the main crystal structure was maintained during the entire charge/discharge process without any obvious structure transformation. This is further supported by *ex situ* STEM results. Interestingly, visible biphasic region can be observed at the end of the discharge process, which is probably due to the smaller unit cell volume of  $Na_{0.44}[Mn_{0.44}Ti_{0.56}]O_2$  compared to  $Na_{0.66}[Mn_{0.44}Ti_{0.56}]O_2$ , and the slow kinetics of the phase transition. All of the XRD patterns recorded during the *in situ* investigations have been refined. From the evolution of the lattice parameters, Vegard's law is verified in general within the regions separated by the dash line as marked in Figure V- 384b. Two-phase transition range, if exist, may only occur in narrow regions across the dash line. These observations are in good agreement with the charge-discharge profile. Overall, it is most likely that the phase transition may proceed through several solid solution

Appearance of this peak suggests the strong covalent bonding nature of Fe ions with CN ligands. The strong main absorption peaks at around 7,127 eV for  $Na^+$  inserted (i.e., discharged) samples and around 7,132 eV for  $Na^+$  extracted (i.e., charged) samples are ascribed to the purely dipole-allowed 1s to 4p transition. The pre-edge features seen in most transition metal oxides due to dipole forbidden 1s to 3d transition are less discernible in our samples due to either the weak signal/noise ratio and/or overlapping with the LMCT features. The XANES for the Fe K-edge after Na extraction (i.e. 3.3 and 4.4 V states) showed a clear edge shift to higher energy indicating an increased average valence state of Fe. The energy of the absorption maximum

reactions during Na insertion/extraction into/from  $\text{Na}_{0.44}[\text{Mn}_{0.44}\text{Ti}_{0.56}]O_2$ , different from the significant consecutive two-phase reaction behavior observed in  $\text{Na}_{0.44}\text{MnO}_2$

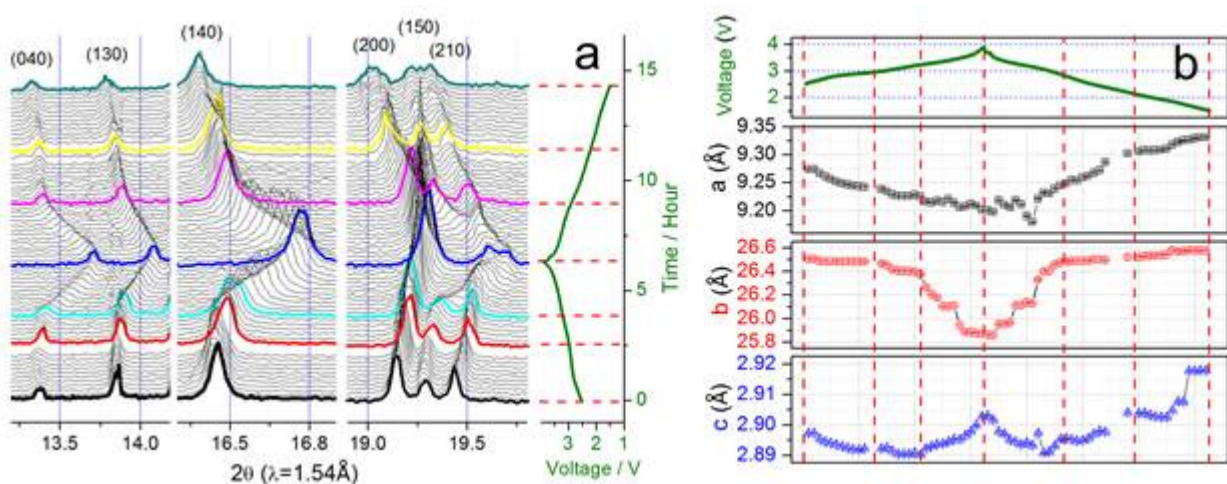


Figure V- 384: Structure evolution upon Na extraction/insertion. (a) In situ XRD patterns collected during the first discharge/charge of the  $\text{Na}/\text{Na}_{0.44}[\text{Mn}_{0.44}\text{Ti}_{0.56}]O_2$  cell under a current rate of C/10 at a voltage range between 1.5 and 3.9 V. For easy comparison with results in the literature, the  $2\theta$  angle has been converted to values corresponding to the more common laboratory Cu Ka radiation ( $\lambda = 1.54 \text{ \AA}$ ). (b) Evolution of the Lattice parameters during charge/discharge process

*In situ* Mn K-edge XAS spectra were collected to examine the variations of the oxidation states during cycling. The corresponding X-ray absorption near edge spectroscopy (XANES) results are shown in a. An entire edge shift of the XANES spectra can be observed during the charge and discharge process, which represents a redox reaction of Mn ions for the entire electrochemical cycle. To semi-quantitatively determine the oxidation states of Mn, the evolution of the edge energy of the XANES spectra was plotted in Figure V- 385b along with  $\text{Mn}_2\text{O}_3$  ( $\text{Mn}^{3+}$ ) for reference. The average oxidation state of Mn, changes from around +3 in the pristine material towards a higher value (< +4) during charge process. During discharge, Mn ions are continuously reduced, and the average oxidation state of Mn is lower than +3 at the fully discharged state. The *ex situ* Mn XANES results further confirm the charge compensation mechanism of Mn. Due to the strong absorption from other components of the *in situ* cell and the lower k-edge energy nature of Ti, it is difficult to perform *in situ* Ti K-edge XAS experiment. Therefore, *ex situ* Ti K-edge XANES spectra were collected at selected charge and discharge states as shown in Figure V- 385c. All spectra remain at the same edge position as the reference material  $\text{Li}_4\text{Ti}_5\text{O}_{12}$ , indicating Ti ions remain at  $\text{Ti}^{4+}$  during the entire charge/discharge process. The charge compensations can be concluded to be solely taken place on Mn ions. In addition, since it is generally accepted that the square pyramidal Mn(5) site will remains at  $\text{Mn}^{3+}$  state during Na insertion/extraction<sup>35</sup>, portion of the Mn ions on other sites should be reduced to  $\text{Mn}^{2+}$  to match the observed discharge capacity in  $\text{Na}_{0.44}[\text{Mn}_{0.44}\text{Ti}_{0.56}]O_2$ . This is different from the observation in  $\text{Na}_{0.44}\text{MnO}_2$ , where  $\text{Mn}^{3+}/\text{Mn}^{4+}$  redox reaction on Mn(2) and Mn(3) sites can compensate the charge during entire Na extraction/insertion process. The site preference of the  $\text{Mn}^{2+}$  in the discharged  $\text{Na}_{0.44}[\text{Mn}_{0.44}\text{Ti}_{0.56}]O_2$  will be further interpreted by DFT calculation in the following discussion.

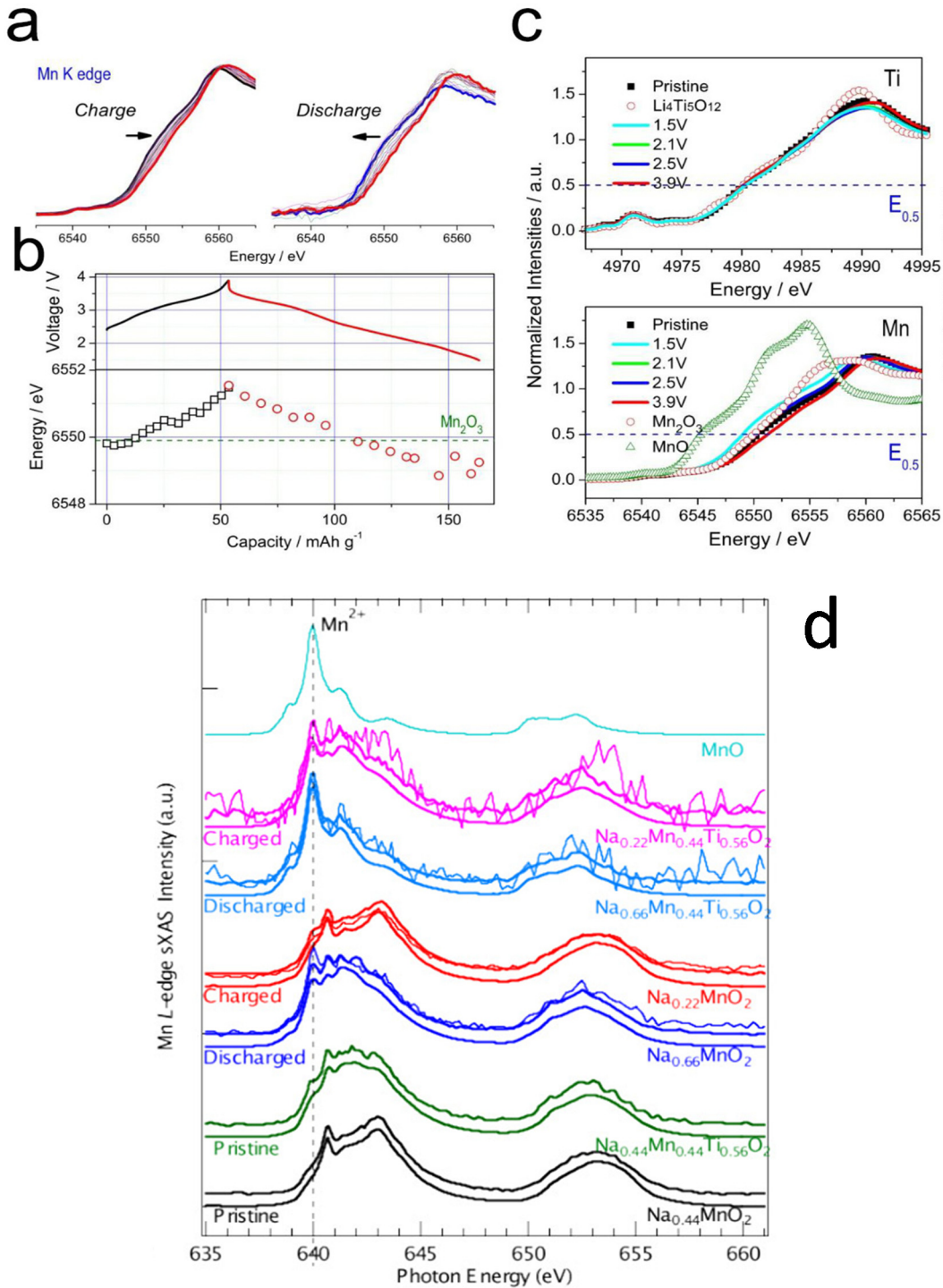


Figure V-385: Charge transfer mechanism upon Na extraction/insertion in  $\text{Na}_{0.44}[\text{Mn}_{0.44}\text{Ti}_{0.56}]_{\text{O}_2}$ . (a) In situ XANES spectra at Mn K-edge collected during initial charge and discharge at a current rate of C/8 between 1.5 and 3.9 V voltage range (Data are obtained in two different in situ cells for charge and discharge process separately); (b) Variation of Mn K-edge position during initial charge and discharge; (c) Ti and Mn K-edge XANES spectra ex situ collected at different charge/discharge states. Spectra of reference materials were represented for comparison. (d) Mn L-edge sXAS spectra collected on  $\text{Nax}[\text{Mn}_{0.44}\text{Ti}_{0.56}]_{\text{O}_2}$  samples in comparison with that of  $\text{NaxMnO}_2$  ( $x = 0.22, 0.44$  and  $0.66$ ). The spectra of chemically prepared samples are shown in thick solid lines, while those of electrochemically prepared ones are in thin dot lines. The calculated spectra (thick dash lines) using the linear combination of the  $\text{Mn}^{2+}$ ,  $\text{Mn}^{3+}$  and  $\text{Mn}^{4+}$  reference spectra agree well with experiments

Soft X-ray absorption spectroscopy (sXAS) enables us to study the evolution of the manganese oxidation states on the electrode surface with the higher energy resolution. Mn *L*-edge sXAS offers a direct probe of the Mn 3d electrons through dipole-allowed 2p-to-3d transition. Comparing with the hard X-ray spectroscopy, sXAS is more surface sensitive with the probing depth around several nanometers if the total electron yield is measured. Figure V- 385d shows Mn *L*-edge sXAS spectra collected on pristine Na<sub>0.44</sub>MnO<sub>2</sub> and Na<sub>0.44</sub>[Mn<sub>0.44</sub>Ti<sub>0.56</sub>]O<sub>2</sub> powder samples, as well as on both chemically- and electrochemically-prepared Na<sub>x</sub>MnO<sub>2</sub> and Na<sub>x</sub>[Mn<sub>0.44</sub>Ti<sub>0.56</sub>]O<sub>2</sub> powder and electrode samples with nominally x = 0.22 and 0.66. The spectra consist of well-separated absorption features in two regions, *L*<sub>2</sub> (638–646eV) and *L*<sub>3</sub> (649–656eV), resulting from the 2p core-hole spin-orbital splitting. In general, manganese compounds with the manganese ions of the same oxidation state in the octahedral crystal field display similar Mn *L*-edge sXAS spectra in spite of their different compositions and crystal structures. While for these with different manganese oxidation states, dramatically different absorption features are observed and the overall absorption intensity shifts to higher photon energy along with the increased manganese oxidation states. This enables us to quantitatively analyze the evolution of the manganese oxidation states in complex battery material.

#### FY 2015 Publications

1. Kai He, Huolin L. Xin, Kejie Zhao, Xiqian Yu, Dennis Nordlund, Tsu-Chien Weng, Jing Li, Yi Jiang, Christopher, A. Cadigan, Ryan M. Richards, Marca Doeff, Xiao-Qing Yang, Eric A. Stach, Ju Li, Feng Lin, and Dong Su, “Transitions from Near-Surface to Interior Redox upon Lithiation in Conversion Electrode Materials”, *Nano Lett.*, 2015, 15 (2), pp 1437–1444, DOI: 10.1021/nl5049884, Publication Date (Web): January 29, 2015.
2. Yong-Ning Zhou, Mahsa Sina, Nathalie Pereira, Xiqian Yu, Glenn G. Amatucci, Xiao-Qing Yang, Frederic Cosandey, and Kyung-Wan Nam, “FeO0.7F1.3/C nanocomposite as a high capacity cathode material for sodium-ion batteries”, *Advanced Functional Materials*, Volume 25, Issue 5, pages 696–703, February 4, 2015, DOI: 10.1002/adfm.201403241
3. J. Song, L. Wang, Y. Lu, J. Liu, B. Guo, P. Xiao, J.-J. Lee, X.-Q. Yang, G. Henkelman, J. B. Goodenough, "Removal of interstitial H<sub>2</sub>O in hexacyanometallates for a superior cathode of a sodium-ion battery", *J. Am. Chem. Soc.* (2015), 137, 2658, DOI: 10.1021/ja512383b, Publication Date (Web): February 13, 2015.
4. Ji-Li Yue, Yong-Ning Zhou, Si-Qi Shi, Zulipiya Shadike, Xuan-Qi Huang, Jun Luo, Zhen-Zhong Yang, Hong Li, Lin Gu, Xiao-Qing Yang, Zheng-Wen Fu, “Discrete Li-occupation versus pseudo-continuous Na-occupation and their relationship with structural change behaviors in Fe<sub>2</sub>(MoO<sub>4</sub>)<sub>3</sub>”, *Scientific Reports* 5, Article number: 8810 doi:10.1038/srep08810, Published 06 March 2015.
5. H. Li, X. Yu, Y. Bai, F. Wu, C. Wu, L. Liu, X.-Q. Yang, "Effects of Mg doping on the remarkably enhanced electrochemical performance of Na<sub>3</sub>V<sub>2</sub>(PO<sub>4</sub>)<sub>3</sub> cathode materials for sodium ion batteries", *J. Mater. Chem. A.* (March 2015), 3, 9578.
6. Y. Wang, J. Liu, B. Lee, R. Qiao, Z. Yang, S. Xu, X. Yu, L. Gu, Y.-S. Hu, W. Yang, K. Kang, H. Li, X.-Q. Yang, L. Chen, X. Huang, "Ti-substituted tunnel-type Na<sub>0.44</sub>MnO<sub>2</sub> oxide as a negative electrode for aqueous sodium-ion batteries", *Nature Communications*. (March 2015), 6, 6401. .

#### FY 2015 Presentations

1. Seongmin Bak, Yongning Zou, Enyuan Hu, Xiqian Yu, Kyung-Wan Nam, and Xiao-Qing Yang, “Synchrotron-Based X-Ray Characterization on the Thermal Decomposition Mechanism of Charged Cathode Materials for Na-Ion Batteries”, presented at the 2015 MRS Spring Meeting, April 6-10, 2015 San Francisco, USA.

## Appendix A: List of Contributors

Contributor	APR FY2015 Section(s)
Abouimrane, Ali (ANL)	IV.D.1
Abraham, Daniel P. (ANL)	IV.B.1, IV.B.2, IV.C.1, IV.C.2, IV.C.3, IV.E.2
Achary, D. Krishnan (University of Pittsburgh)	V.I.1
Adam, Tornheim (ANL)	IV.C.1, IV.C.2, IV.C.3
Ahmad, Iftikhar (Lambda Technologies)	IV.F.2
Ahmed, Shabbir (ANL)	III.A.1
Alamgir, Mohamed (LG Chem Power)	II.A.2, II.A.7
Albano, Fabio (XALT Energy)	II.B.1
Allcorn, Eric (SNL)	IV.B.3
Allu, S. (ORNL)	III.C.3, III.C.5
Alsup, Charles (NETL)	V.D.2
Amine, Khalil (ANL)	IV.D.1, V.I.3, V.J.3.
Andrew, Michael G. (JCI)	II.C.1
Arnold, John (Miltec UV)	II.C.2, IV.F.3
Arsenault, Renata (USABC)	II.A.5, II.C.1
Aude, Hubaud (ANL)	IV.C.1, IV.C.2, IV.C.3
Bae, Chulheung (USABC)	II.A.2
Baker, Dominick N. (ANL)	IV.B.1
Balasubramanian, Mahalingam (ANL)	IV.C.1, IV.C.2, IV.C.3
Balbuena, Perla B. (Texas A&M U.)	V.G.4, V.I.7
Balsara, Nitash (LBNL)	V.I.2
Ban, Chunmei (NREL)	IV.C.1, IV.C.2, IV.C.3, V.C.3
Bareño, Javier (ANL)	IV.B.4, IV.C.1, IV.C.2, IV.C.3
Basco, John (ANL)	III.B.1
Battaglia, Vince (LBNL)	V.B.1, V.B.5
Billings, J. (ORNL)	III.C.3
Bloom, Ira (ANL)	III.B.1, III.B.3, IV.B.3, IV.B.4, IV.C.1, IV.C.2, IV.C.3
Brodie, Bradley (DENSO International)	II.B.5
Burrell, Anthony (ANL)	IV.C.1, IV.C.2, IV.C.3, IV.E.1
Busbee, John (Xerion)	II.A.5
Cabana, Jordi (UIC)	IV.E.1

<b>Contributor</b>	<b>APR FY2015 Section(s)</b>
Carlson, Steven A. (Optodot)	II.C.4
Ceder, Gerbrand (MIT)	V.G.3
Chen, Guoying (LBNL)	V.F.1
Chen, Zonghai (ANL)	IV.D.1, V.I.3
Chiang, Yet-Ming (MIT)	V.B.3
Christophersen, Jon P. (INL)	III.B.2
Croy, Jason R. (ANL)	IV.C.1, IV.C.2, IV.C.3, IV.E.1, V.D.10, V.D.5, V.F.8
Cui, Yangie (ANL)	IV.D.1
Cui, Yi (Stanford U.)	V.C.2, V.H.5, V.I.6
Cunningham, Brian (DOE)	II.D, III
Curtiss, Larry (ANL)	V.J.3
Daniel, Claus (ORNL)	IV.C.1, IV.C.2, IV.C.3, IV.E.4
Datta, Moni (University of Pittsburgh)	V.I.1
Dees, Dennis W. (ANL)	III.A.1, IV.B.1, IV.B.2, IV.C.1, IV.C.2, IV.C.3
Deppe, Jack (Deppe Consulting)	All
Dietz-Rago, Nancy (ANL)	IV.B.4
Doeff, Marca (LBNL)	V.D.8
Dogan, Fulya (ANL)	IV.C.1, IV.C.2, IV.C.3
Dudney, Nancy (ORNL)	V.H.1, V.H.3
Dufek, Eric J. (INL)	III.B.2, III.B.3
Dunn, Jennifer (ANL)	III.A.2
Duong, Tien (DOE)	V
Dzwiniel, Trevor (ANL)	IV.E.2
Elwasif, W. (ORNL)	III.C.3
Faguy, Peter (DOE)	IV
Fenton, Kyle R. (SNL)	IV.B.3
Feridun, Ozgenur K. (ANL)	IV.E.1
Gaines, Linda (ANL)	III.A.2
Gallagher, Kevin G. (ANL)	III.A.1, IV.B.1, IV.B.2, IV.C.1, IV.C.2, IV.C.3
Gan, Hong (BNL)	V.I.4
Geller, Tony (SNL)	III.C.5
George, Steven M. (UC Boulder)	IV.B.3, V.C.3
Gilbert, James A. (ANL)	IV.B.1, IV.C.1, IV.C.2, IV.C.3

<b>Contributor</b>	<b>APR FY2015 Section(s)</b>
Giordani, Vincent (Liox Power)	V.J.2
Goodenough, John B. (UTA)	V.D.9
Grey, Clare (U. Cambridge)	V.F.4
Ha, Seonbaek (IIT)	IV.B.2
Hakim, Iddir (ANL)	IV.C.1, IV.C.2, IV.C.3
Halalay, Ion (General Motors)	IV.E.2
Han, Taeyoung (General Motors)	III.C.2
Hendershot, Ron (Daikin America)	V.H.7
Herbert, Erik (Michigan Tech U.)	V.H.1
Howell, David (DOE)	All
Ingram, Brian (ANL)	IV.C.1, IV.C.2, IV.C.3
Ishwait, Manar (ANL)	IV.B.2, IV.C.1, IV.C.2, IV.C.3
Jacobs, Alex (Sila Nano)	IV.F.6
Jansen, Andrew N. (ANL)	IV.B.1, IV.B.2, IV.B.3, IV.C.1, IV.C.2, IV.C.3, IV.E.1, IV.E.2
Johnson, Christopher (ANL)	IV.B.2, IV.C.1, IV.C.2, IV.C.3
Johnson, Christopher (NETL)	II.B.1, II.B.4, IV.D.5, IV.D.6, V.H.2, V.H.4, V.H.7, V.J.2
Jorgensen, Scott (USABC)	II.A.6, II.A.7
Kaczmarek, Susan (Energetics)	All
Kalnaus, S. (ORNL)	III.C.3
Kee, R. (Colorado School of Mines)	III.C.5
Kelly, Kenneth (NREL)	III.A.3
Kepler, Keith (Farasis Energy)	IV.D.3
Kercher, Andrew (ORNL)	V.D.7
Keyser, Matthew (NREL)	III.B.4
Kiggans, Jim (ORNL)	V.D.7
Kim, Gi-Heon (NREL)	III.C.1, III.C.2, III.C.7
Kim, Jeffrey (Maxwell)	II.A.6
Klett, Matilda (ANL)	IV.B.1
Kostecki, Robert (LBNL)	V.F.2
Krumdick, Gregory (ANL)	IV.B.3, IV.C.1, IV.C.2, IV.C.3, IV.E.1, IV.E.2
Kumar, BJ (Energetics)	All
Kumta, Prashant (University of Pittsburgh)	V.C.1, V.I.1
Lamb, Joshua (SNL)	III.B.3

<b>Contributor</b>	<b>APR FY2015 Section(s)</b>
Lee Walker (ANL)	III.B.1
Lee, Sehee (UC Boulder)	V.C.3
Li, Jianlin (ORNL)	IV.B.1, IV.C.1, IV.C.2, IV.C.3, IV.E.4
Liao, Chen (ANL)	IV.C.1, IV.C.2, IV.C.3
Liu, Gao (BNL)	IV.D.1, IV.E.2, V.B.4
Liu, Jun (PNNL)	V.C.1, V.I.5
Long, Brandon (BASF)	IV.E.1
Looney, J. Patrick (BNL)	V.D.4
Lopatin, Sergey (Applied Materials)	II.C.3
Lopez, Herman (Envia Systems)	II.A.1
Lu, Jun (ANL)	IV.D.1, V.J.3
Lu, Wenquan (ANL)	IV.B.1, IV.B.2, IV.C.1, IV.C.2, IV.C.3
Maiti, Spandan (University of Pittsburgh)	V.I.1
Manivannan, A. (NETL)	V.I.1
Manthiram, Arumugam (UTA)	V.D.6
Maroni, Victor (ANL)	IV.B.2
Martin, Jerry (Boulderionics)	IV.E.2
Masias, Al (USABC)	II.A.3
Mazzeo, Brian (BYU)	V.G.6
McCaskey, A. (ORNL)	III.C.3
Meng, Ying Shirley (UCSD)	V.F.5
Michelbacher, Christopher J. (INL)	III.B.2
Miller, Dean (ANL)	IV.E.1
Mixer, Bruce (NETL)	II.B.5, IV.D.3, IV.D.4, IV.F.2, IV.F.4, IV.F.5, V.H.8
Moffat, Harry (SNL)	III.C.5
Mohanty, Debasish (ORNL)	IV.C.1, IV.C.2, IV.C.3, IV.E.4
Mukherjee, Partha P. (Texas A&M U.)	V.I.7
Mullin, Scott (Seeo)	II.A.4
Murphy, Michael, (ANL)	IV.C.1, IV.C.2, IV.C.3
Nagasubramanian, Ganesan (SNL)	IV.B.3
Nanda, Jagjit (ORNL)	IV.C.1, IV.C.2, IV.C.3, V.D.1
Nelson, Paul A. (ANL)	III.A.1
O'Connor, Ian (Saft America)	II.A.8

<b>Contributor</b>	<b>APR FY2015 Section(s)</b>
O'Hanlon, Daniel (ANL)	IV.C.1, IV.C.2, IV.C.3
Orendorff, Christopher J. (SNL)	III.B.3, IV.B.3, IV.E.2
Ozge, Feridun (ANL)	IV.C.1, IV.C.2, IV.C.3
Pannala, S. (ORNL)	III.C.3
Paul, James C. (Ricardo)	III.A.3
Peebles, Cameron (ANL)	IV.C.1, IV.C.2, IV.C.3
Persson, Kristin (LBNL)	V.G.2
Pesaran, Ahmad (NREL)	III.B.3, III.C.2, III.C.4
Pol, Vilas (Purdue U.)	V.I.7
Polzin, Bryant J. (ANL)	IV.B.1, IV.B.2, IV.C.1, IV.C.2, IV.C.3, IV.E.1, IV.E.2
Powell, Bob (General Motors)	IV.E.2
Prendergast, David (LBNL)	V.I.2
Prezas, Panos (ANL)	III.B.1
Privette, Rob (XG Sciences)	IV.B.3
Pupek, Krzysztof (ANL)	IV.E.2
Qi, Yue (Michigan State U.)	V.G.5
Qu, Deyang (U. of Wisconsin, Milwaukee)	V.J.4
Rempel, Jane (TIAX LLC)	IV.D.6
Ren, Yang (ANL)	V.I.3
Risco, Andrew (Boulderionics)	IV.E.2
Robertson, David (ANL)	III.B.1
Ross, Philip (LBNL)	V.F.6
Roumi, Farshid (Parthian Energy)	IV.F.5
Sahore, Ritu (ANL)	IV.C.1, IV.C.2, IV.C.3
Sakamoto, Jeff (U. of Michigan)	V.H.1, V.H.2
Santhanagopalan, Shriram (NREL)	III.C.8
Sazhin, Sergiy V. (INL)	III.B.2
Seminario, Jorge M. (Texas A&M U.)	V.G.4
Shaffer, Christian (EC Power)	III.C.6
Shin, Youngho (ANL)	IV.C.1, IV.C.2, IV.C.3, IV.E.1
Shirk, Matthew G. (INL)	III.B.2
Simunovic, S. (ORNL)	III.C.3
Singh, Jagat Deep (3M)	II.B.3, IV.D.2

<b>Contributor</b>	<b>APR FY2015 Section(s)</b>
Somorjai, Gabor A. (UC Berkeley)	V.F.6
Sprague, Michael A. (NREL)	III.C.8
Srinivasan, Venkat (LBNL)	V.G.1
Steele, Leigh Anna M. (SNL)	III.B.3
Stefan, Ionel (Amprius)	II.A.3, IV.F.4
Strand, Dee (Wildcat Discovery)	V.H.8
Su, Xin (ANL)	IV.B.2
Sun, Chengjun (ANL)	V.I.3
Sun, Xiao-Guang (ORNL)	IV.E.2
Sunstrom, Joe (Daikin America)	V.H.7
Tabacchi, John (NETL)	II.B.2, II.B.3, II.C.2, II.C.3, II.C.4, II.C.5, IV.D.2, IV.F.3, V.I.1, V.I.2
Takeuchi, Esther (SBU)	V.I.4
Tan, Taison (24M)	IV.F.1
Tataria, Harshad (USABC)	II.A.4, II.A.8
Tenant, Robert C. (NREL)	IV.B.1, IV.C.1, IV.C.2, IV.C.3, IV.E.5
Thackeray, Michael (ANL)	IV.E.1, V.D.10, V.D.5, V.F.8
Tomsia, Antoni P. (LBNL)	V.B.3
Trask, Stephen E. (ANL)	IV.B.1, IV.B.2, IV.C.1, IV.C.2, IV.C.3, IV.E.1
Turner, John A. (ORNL)	III.C.3
Vadivel, Nicole (ANL)	IV.C.1, IV.C.2, IV.C.3
Vaughey, John (ANL)	IV.C.1, IV.C.2, IV.C.3
Velikokhatnyi, Oleg (University of Pittsburgh)	V.I.1
Venkatachalam, Subramanian (Envia Systems)	IV.D.4
Voelker, Gary (Miltec UV)	II.C.2, IV.F.3
Wachsman, Eric (U. of Maryland)	V.H.4
Walker, Lee K. (INL)	III.B.2
Wang, Chong-Min (PNNL)	V.F.7
Wang, Chunsheng (U. of Maryland)	V.I.3
Wang, Donghai (PSU)	II.B.4, IV.D.5
Wang, Feng (BNL)	V.D.4
Waterhouse, Robert (AMTEK)	II.A.9
Wheeler, Dean (BYU)	V.G.6
Whittingham, Stanley (Binghamton U.)	V.D.2

<b>Contributor</b>	<b>APR FY2015 Section(s)</b>
Wixom, Mike (Navitas)	II.C.5
Wood III, David L. (ORNL)	IV.B.1, IV.C.1, IV.C.2, IV.C.3, IV.E.3, IV.E.4
Wood, Weston (AMTEK)	II.A.9
Wu, Huiming (ANL)	IV.D.1.
Wu, Qingliu (ANL)	IV.B.1, IV.B.2
Xiao, Jie (PNNL)	V.D.3, V.I.5
Xiao, Xingcheng (GM)	V.G.5
Xin, Su (ANL)	IV.C.1, IV.C.2, IV.C.3
Xu, Wu (PNNL)	V.H.6, V.J.1
Yang, Xiao-Qing (BNL)	IV.D.1., V.F.3, V.J.4, V.K.1
Yu, Xiqian (BNL)	V.F.3, V.K.1
Zaghib, Karim (HydroQuebec, IREQ)	V.B.2
Zhang, Chao (NREL)	III.C.8
Zhang, Ji-Guang (PNNL)	V.C.1, V.D.3, V.H.6, V.J.1
Zhang, Zhengcheng (ANL)	IV.C.1, IV.C.2, IV.C.3, IV.E.2, V.E.1
Zheng, Jim (Florida State U.)	V.C.1
Zhu, Yimin (OneD Material)	II.B.2

## Appendix B: List of Acronyms

Acronym	Explanation
3M	Minnesota Mining and Manufacturing Company
AABC	Advanced Automotive Batteries Conference
AAO	Anodic aluminum oxide
AB	Acetylene black
ABA	Anion Binding Agent
ABDT	ANSYS Battery Design Tool
ABMR	Advanced Battery Materials Research
ABR/ABRT	Applied Battery Research for Transportation
AC	Alternating Current
ACN	Acetonitrile
ACS	American Chemical Society
ADF	Annular dark-field (imaging)
ADFSTEM	Annular dark-field (imaging in) scanning transmission electron microscope
ADP	Advanced drying process
AER	All electric range
AEY	Auger electron yield
AFM	Atomic force microscopy
AIMD	Ab initio molecular dynamics
ALD	Atomic layer deposition
ALS	Advanced Light Source
AMR	Annual Merit Review
ANL	Argonne National Laboratory
ANOVA	Analysis of variance
AOP	(VTO) Annual operating plan
AP-ALD	Atmospheric pressure atomic layer deposition
AP-CVD	Atmospheric pressure chemical vapor deposition
APS	Advanced Photon Source
ARC	Accelerated rate calorimetry
ARL	Army Research Laboratory
ARPA-E	Advanced Research Projects Agency - Energy
ARRA	American Recovery & Reinvestment Act

Acronym	Explanation
ASAP	As Soon As Publishable
ASI	Area-specific impedance
ASR	Area specific resistance
ATR-FTIR	Attenuated total reflection-Fourier transform infrared spectroscopy
AVS	American Vacuum Society
BATT	Batteries for Advanced Transportation Technologies
BD	Bulk-doped
BDS	Battery Design Studio
BERC	Berkeley Energy and Resources Collaborative
BES	Basic Energy Sciences (DOE Office)
BET	Brunauer, Emmett, and Teller (surface area analysis)
BEV	Battery electric vehicle
BLAST	Battery Lifetime Analysis Simulation Tool
BLE	Battery Life Estimator
BMF	Battery manufacturing facility
BMR	(Advanced) Battery Materials Research (Program)
BMS	Battery management system
BNL	Brookhaven National Laboratory
BOL	Beginning of life
BOM	Battery ownership model
BTC	Battery Technology Center
BV	Butler-Volmer (expression)
BYU	Brigham Young university
CAD	Computer-aided Design
CAE	Computer-aided engineering
CAEBAT	Computer-aided engineering of batteries
CAFE	Corporate Average Fuel Economy (Standards)
CAMP	Cell analysis, modeling, and prototyping (facility)
CATARC	China Automotive Technology and Research Center
CB	Carbon black
CBD	Carbon binder domain
CC	Constant-concentration
CCD	Charge-coupled device

<b>Acronym</b>	<b>Explanation</b>
CD	Charge depleting
CDM	Cell domain model
CE	Coulombic efficiency
CEC	California Energy Commission
CEF	Cathode Energy Factor
CEI	Cathode electrolyte interfaces
CERC	Clean Energy Research Center
CFM	Complex framework materials
CFT	Characterization, Fabrication, and Testing (facility)
CG	Concentration gradient
CID	Collision-induced dissociation
CMC	Carboxymethyl cellulose
CNT	Carbon nano-tubes
COP	Coefficient of performance
COSY	Correlation spectroscopy
COTS	Commercial-Off-The-Shelf
CPE	Constant phase element
CPI	Compact Power Inc.
CPU	Central Processing Unit
CRADA	Cooperative Research and Development Agreement
CS	Charge-sustaining
CSE	Cumulative strain energy
CSM	Contract Security Management (Team)
CSTR	Continuous stirred tank reactor
CSWG	Crash Safety Work Group
CT	(X-ray) Computed tomography
CV	Cyclic voltammetry
CVD	Chemical vapor deposition
CY	Calendar year
DC	Direct current
DCR	Direct current resistance
DDPM	Discrete diffusion particle model
DEC	Diethyl carbonate

Acronym	Explanation
DFT	Density function theory
DI	Deionized (water)
DLP	Double layer pouch (cells)
DLS	Dynamic light scattering
DMC	Dimethyl carbonate
DME	Dimethyl ether
DMF	Dimethylformamide
DMSO	Dimethylsulfoxide
DOD	Depth-of-discharge
DOE	Department of Energy
DOL	Dioxolane
DOPA	3,4-Dihydroxyphenyl-L-alanine
DOS	Density of states
DOSY	Diffusion-ordered spectroscopy
DOT/NHTSA	Department of Transportation/National Highway Traffic Safety Administration
DP	Dry process
DPA	Destructive physical analysis
DPGDME	Dipropylene glycol dimethyl ether
DPP	Dynamic particle-packing (model)
DSC	Differential scanning calorimetry
DST	Dynamic stress test
EADL	Electrochemical Analysis and Diagnostic Laboratory (ANL)
EC	Ethylene carbonate
ECM	Equivalent Circuit Model
ECP	EC Power
ECS	Electrochemical Society
ECT	Electrochemical thermal (model)
ED	Electrode domain
EDAX	Energy dispersive X-ray analysis
EDC	Ethylene dicarbonate
EDL	Electrolyte deposition layer
EDM	Electrode-domain model
EDOT	Ethylenedioxathiophene

<b>Acronym</b>	<b>Explanation</b>
EDS	Energy dispersive spectroscopy
EDV	Electric Drive Vehicle
EDX	Energy-dispersive x-ray (spectroscopy)
EELS	Electron energy loss spectroscopy
EERE	Energy Efficiency and Renewable Energy (DOE Office)
EIS	Electrochemical Impedance Spectroscopy
EM	Electro-magnetic
EMC	Electron Microscopy Center
EMSL	Environmental Molecular Sciences Laboratory
EOL	End of life
EP	Engineered pore (anode)
EPA	Environmental Protection agency
EPR	Electron paramagnetic resonance
EREV	Extended range electric vehicle
ESI-MS	Electrospray ionization mass spectrometry
ESR	Electron spin resonance
ETS	Error-corrected Time-domain Series (solution)
EUCAR	European Council for Automotive Research and Development
EV	Electric vehicle
EVI	Electric Vehicle Initiative
EXAFS	Extended X-ray absorption fine structure
FC	Fast-charge
FCE	First cycle efficiency
FCG	Full concentration gradient
FCTO	Fuel Cell Technologies Office (at DOE)
FEC	Fluoro ethylene carbonate
FFT	Fast Fourier Transforms
FIB	Focused Ion Beam
FIR	First cycle irreversible loss
FMR	Focused Melt Resistance (welding)
FMVSS	Federal Motor Vehicle Safety Standards
FOA	Federal Opportunity Anouncement
FP	First principles

Acronym	Explanation
FT	Fourier Transform
FTIR	Fourier Transform InfraRed spectroscopy
FY	Fiscal year
GC	Gas chromatography
GC-MS	Gas chromatography - mass spectroscopy
GHG	Green house gases
GITT	Galvanostatic intermittent titration technique
GM	General Motors
GO	Graphene oxide
GPC	Growth rate per rotation cycle
GPE	Gel polymer electrolyte
GREET	Greenhouse gases, Regulated Emissions, and Energy use in Transportation (model)
GSC	Glass-state conversion
GUI	Graphic user interface
HAADF	High Angle Annular Dark Field
HCA	High capacity anode
HCC	High capacity cathode
HCMRTM	High capacity manganese rich cathode materials
HD	High dielectric
HE	High energy
HEHV	High energy high voltage
HEMR	High-energy mechanochemical reduction
HEV	Hybrid electric vehicle
HF	Hydrofluoric acid
HFET	Highway Fuel Economy Test
HOMO	Highest occupied molecular orbital
HP	High power
HPC	High performance computing
HPPC	Hybrid pulse power characterization
HQ	Hydro-Québec
HR-TEM	High resolution transmission electron microscopy
HSE	Heyd-Scuseria-Ernzerhof (exchange-correlation functional)

<b>Acronym</b>	<b>Explanation</b>
HV	High voltage
IA	(IEA) Implementing Agreement
IA-HEV	Implementing Agreement - hybrid electric vehicles
IAPG	Interagency Advanced Power Group
IBA	International Battery Materials Association
IC	Ion chromatography
ICE	Internal combustion engine
ICL	Irreversible capacity loss
ICP	Inductively coupled plasma
ICV	Internal combustion engine vehicle
ID	Intensity of the carbon D-band
IEA	International Energy Agency
IEA-HEV	International Energy agency - hybrid electric vehicle
IEA-HEV-IA	International energy Agency - Hybrid Electric Vehicles - Implementing Agreement
IEC	International Electrotechnical Commission
INL	Idaho National Laboratory
IP	Intellectual property
IR	Infra-red
ISC	Internal short circuit
JCESR	Joint center for energy storage research
JCI	Johnson Controls, Incorporated
JPL	Jet Propulsion Laboratory
KMC	Kinetic Monte Carlo (algorithm)
LATP	Lithium aluminum titanium phosphate
LBNL	Lawrence Berkeley National Laboratory
LCA	Life cycle analysis
LCO	Lithium cobalt oxide
LCV	Lower cutoff voltage
LEESS	Lower-energy energy storage systems
LFMO	$\text{Li}_2\text{Fe Mn}_3\text{O}_8$
LFP	Li iron phosphate
LIB	Lithium-ion battery

Acronym	Explanation
LIBS	Laser induced breakdown spectroscopy
LIC	Lithium-ion conducting
LL	Layered-layered
LLNL	Lawrence Livermore National Laboratory
LLR	Low lithium-rich (cathode)
LLS	Layered-layered spinel
LLTO	(Li,La)TiO <sub>3</sub>
LLZ	Li <sub>7</sub> La <sub>3</sub> Zr <sub>2</sub> O <sub>12</sub>
LLZO	Lithium lanthanum zirconate
LMCT	Ligand-to-metal charge transfer
LMNO	Lithium manganese nickel oxide
LMO	Lithium manganese oxide
LMR	Lithium Manganese-rich (layered cathode material)
LNMO	LiNi <sub>0.5</sub> Mn <sub>0.5</sub> O <sub>2</sub>
LPCVD	Low pressure chemical vapor deposition
LPV	Linear Parameter Variable
LS	Low spin
LT	Low temperature
LTI	Linear Time Invariant
LTO	Lithium titanate, Li <sub>4</sub> Ti <sub>5</sub> O <sub>12</sub>
LUMO	Lowest unoccupied molecular orbital
LVOPF	Li(Na) <sub>1+x</sub> VOPO <sub>4</sub> F <sub>x</sub>
LVP	Li <sub>3</sub> V <sub>2</sub> (PO <sub>4</sub> ) <sub>3</sub>
MAA	Methacrylate-co-methacrylic acid
MAS	Magic angle spinning
MBP	Midland Battery Park
MCMB	Mesocarbon micro beads
MD	Molecular dynamics
MERF	Materials Engineering Research Facility
MF2	Metal binary fluoride
MFCA	Multifunctional cathode additive
MIT	Massachusetts Institute of Technology
MLD	Molecular layer deposition

<b>Acronym</b>	<b>Explanation</b>
MP	Methyl propionate
MRS	Materials Research Society
MS	Mass spectroscopy
MSMD	Multi-scale, multi-domain
MSRL	Environmental Molecular Sciences Research Laboratory
MSU	Michigan State University
MW-ST	Microwave-assisted solvothermal
MYPP	Multi-year program plan
NASA	National Aeronautics and Space Administration
NASA-JPL	NASA Jet Propulsion Laboratory
NCA	$\text{LiNi}_{0.8}\text{Co}_{0.15}\text{Al}_{0.05}\text{O}_2$
NCEM	National Center for Electron Microscopy
NCM	$\text{Li}_{1+w}[\text{Ni}_x\text{Co}_y\text{Mn}_z]_{1-w}\text{O}_2$
NDE	Non-destructive evaluation
NEI	Natural Energy Institute (Hawaii)
NERSC	National Energy Research scientific Computing Center
NETL	National Energy Technology Laboratory
NHTSA	National Highway Transportation Safety Administration
NLDFT	Non-local density functional theory
NMC	$\text{LiNi}_{1/3}\text{Co}_{1/3}\text{Mn}_{1/3}\text{O}_2$
NMCT	Ti-substituted NMC
NMP	N-methylpyrrolidone
NMR	Nuclear magnetic resonance
NRE	Non-recurring engineering (cost)
NREL	National Renewable Energy Laboratory
NSLS	National Synchrotron Light Source
NTG	Newman-Tiedemann-Gu (electrochemistry model)
NUANCE	Northwestern University Atomic and Nanoscale Experimental Center
OAS	Open architecture software
OCP	Open-circuit potential
OCV	Open circuit voltage
OEM	Original equipment manufacturer
OER	Oxygen evolution reaction

Acronym	Explanation
OMC	Ordered microporous carbon
ORNL	Oak Ridge National Laboratory
ORR	Oxygen reduction reaction
PAA	Polyacrylic acid
PAN	Polyacrylonitrile
PBE	Perdew Burke Ernzerhof (correlation)
PC	Propylene carbonate
PCA	Principal component analysis
PCB	Printed circuit board
PCET	Proton coupled electron transfer
PCM	Polarized continuum model
PDCA	Plan-Do-Check-Act (cycle)
PDF	Pair density function
PDM	particle-domain model
PE	Polyethylene
PEDOT	Poly(3,4-ethylenedioxythiophene)
PEFM	Poly(2,7-9,9-dioctylfluorene-co-2,7-9,9-(di(oxy-2,5,8-trioxadecane)) fluorine-co-2,7-fluorenone-co-2,5-1-methylbenzoic ester)
PEN	Polyethylene naphthalate
PEO	Polyethyleneoxide
PET	Polyethylene Terephthalate
PETT	Pentaerythritol tetrakis (3-mercaptopropionate)
PEV	Plug-in electric vehicle
PEY	Partial electron yield
PFG	Pulse field gradient
PFM	Poly(9,9-dioctylfluorene-co-fluorenone-co-methylbenzoic ester)
PFPE	Perfluoropolyether
PG	Pyrolytic graphite
PHEV	Plug-in hybrid electric vehicle
PHEV10	PHEV with 10-mile range
PHEV40	PHEV with 40-mile range
PI	Principal Investigator
PM	Project manager

<b>Acronym</b>	<b>Explanation</b>
PMMA	Poly(methyl methacrylate)
PNNL	Pacific Northwest National Laboratory
POC	Proof of concept
POD	Proper Orthogonal Decomposition
POP	Porous organic polymer
PP	Polypropylene
PPS	Polyphenylene sulfide
PS	Polystyrene
PSA	Particle size analysis
PSD	Pore size distribution
PSU	Pennsylvania State University
PTC	Positive temperature coefficient (device)
PTF	Post Test Facility
PTFE	Poly(tetrafluoroethylene) (cathode)
PVD	Physical vapor deposition
PVDF	Poly(vinylidenefluoride)
PVP	Polyvinylpyrrolidone
QA	Quality assurance
QC	Quality control
R&D	Research and Development
R2R	Roll-to-roll
RAL	Rutherford Appleton Laboratory
RC	Resistance-Capacitor (circuit)
RDE	Rotating disk electrode
RE	Reference electrode
RF	Radio frequency
RFP	Request for proposals
RFPI	Request for proposal information
RH	Relative humidity
RIHP	Rapid induction hot pressing
RMS	Root mean square
ROE	Return on Equity
ROM	Reduced Order Modeling

Acronym	Explanation
RPM	Revolutions per minute
RPT	Reference performance test
RS	Representative sandwich (model)
RT	Room temperature
SAE	Society of Automotive Engineers
SAED	Selected area electrode diffraction
SBIR	Small Business Innovation Research
SBIR/STTR	Small Business Innovation Research/Small Business Technology Transfer
SBR	Styrene-butadiene rubber (binder)
SDS	Safety data sheet
SEI	Solid electrolyte interphase
SEM	Scanning electron microscopy
SEM-EDS	Scanning electron microscopy/Energy Dispersive X-ray spectroscopy
SEO	Poly(styrene)-b-poly(ethylene oxide)
SFG	Sum Frequency Generation
SIC	Single ion conductor
SIMS	Secondary ion mass spectrometry
SLAC	Stanford acceleration laboratory
SLMP	Stabilized lithium metal powder
SLP	Single layer pouch (cells )
SMTC	Single-Module Thermal Chamber
SNL	Sandia National Laboratories
SNS	Spallation Neutron Source
SOA	State of the art
SOC	State of charge
SOFC	Solid oxide fuel cell
SP	Super-P (carbon)
SPPC	Single Potential-Pair Continuum
SRL	Surface reconstruction layer
SS	Solid-state
SSE	Solid-state electrolyte
SSRL	Stanford Synchrotron Radiation Lightsource
STDEV	Standard deviation

<b>Acronym</b>	<b>Explanation</b>
STEM	Scanning transmission electron microscopy
STEM/EELS	Scanning transmission electron microscopy/electron energy loss spectroscopy
STF	Standard test fixture
STTR	Small Business Technology Transfer Program
SVM	State Variable Model
SWCNT	Single-walled carbon nanotube
TAC	Technical Advisory Committee
TACLE	Tailored Aqueous Colloids for Lithium-Ion Electrodes
TALE	Total arbitrary Lagrangian Eulerian (capability)
TAMU	Texas A&M University
TCO	Total cost of ownership (model)
TD	Transverse direction
TEG	Tetraethylene glycol
TEGDME	Tetraethyleneglycoldimethyl
TEM	Transmission electron microscopy
TEP	Trisethyl phosphite
TEY	Total electron yield
TFSI	Bis(trifluoromethanesulfonyl)imide
TGA	Thermal gravimetric analysis
THF	Tetrahydrofuran
TM	Transition metal
TMA	Tri-methyl aluminum
TOF-SIMS	Time-of-flight – secondary ion mass spectroscopy
TPFPB	Tris(pentafluorophenyl) borane
TR-XRD	Time-resolved X-ray diffraction
TTFP	Tris(2,2,2,-trifluoroethyl)phosphite
TVR	Taylor Vortex Reactor
TXM	Transmission X-ray Microscopy
TXM-XANES	Transmission X-ray microscopy with X-ray near edge absorption spectroscopy
UC	University of California
UCAP	Ultracapacitor
UCB	University of California, Berkeley
UCSD	University of California, San Diego

Acronym	Explanation
UCV	Upper cut-off voltage
UDDS	Urban Dynamometer Driving Schedule
UDF	User defined function
UHMWPE	Ultra High Molecular Weight Polyethylene
UK	United Kingdom
USA	United States of America
USABC	United States Advanced Battery Consortium
USCAR	United States Council for Automotive Research
USDRIVE	Driving Research and Innovation for Vehicle efficiency and Energy sustainability
USPTO	United States Patents and Trademarks Office
UTA	University of Texas, Austin
UV	Ultraviolet
VASP	Vienna Ab-initio Simulation Package
VC	Vinylene carbonate
VF	Voltage fade
VFM	Variable frequency microwave
VGCF	Vapor grown carbon fiber
VIBE	Virtual Integrated Battery Environment
VOC	Volatile organic compound
VT, VTO	Vehicle Technologies Office
WP	Wet process
XAFS	X-ray absorption fine structure
XANES	X-ray absorption near edge structure
XAS	X-ray absorption spectroscopy
XEDS	X-ray energy dispersive spectroscopy
XML	eXtensible Markup Language
XPS	X-ray photoelectron spectroscopy
XR	X-ray reflectivity
XRD	X-ray diffraction
ZCO	ZnCo <sub>2</sub> O <sub>4</sub>

## **Disclaimer**

This report was prepared as an account of work sponsored by an agency of the United States government. Neither the United States government nor any agency thereof, nor any of their employees, makes any warranty, express or implied, or assumes any legal liability or responsibility for the accuracy, completeness, or usefulness of any information, apparatus, product, or process disclosed or represents that its use would not infringe privately owned rights. Reference herein to any specific commercial product, process, or service by trade name, trademark, manufacturer, or otherwise does not necessarily constitute or imply its endorsement, recommendation, or favoring by the United States government or any agency thereof. The views and opinions of authors expressed herein do not necessarily state or reflect those of the United States government or any agency thereof.



Energy Effi  
le Energy

*Cover: Battery multiscale multidomain modeling framework (Courtesy: NREL)*

For more information, visit: [vehicles.energy.gov](http://vehicles.energy.gov)

DOE/EE-1317 • April 2016